LLE 2008 Annual Report

UR
LLE

October 2007 – September 2008

Cover Photos

Top left: The off-axis parabola (OAP) optic is being moved into position in the OMEGA Target Bay. The optic was installed for joint OMEGA and OMEGA EP shots.

Middle Left: High school student Rachel Kurchin (The Harley School) examines a spherical target inside a glass hohlraum. Rachel was one of 15 students participating in the 2008 Summer High School Research Program. She is also one of two students from LLE's summer program selected as a semifinalist in the Intel Science Talent Search.

Middle center: The lower housing of a neutron time-of-flight (nTOF) detector shown shortly after being machined at LLE. The completed nTOF will be used to obtain ion temperatures from integrated fast-ignition experiments on OMEGA. It will also be used as an nTOF detector prototype for downscattered-neutron measurements on the NIF.

Bottom left: The OMEGA EP Laser System was completed on time and within budget and initial experiments were started in the fourth quarter of FY08.

Top right: On 16 May 2008, Dr. Robert McCrory, Vice Provost, Director, and CEO of the Laboratory for Laser Energetics (LLE), along with special guests, which included University of Rochester President Joel Seligman and University Provost Ralph Kuncl, U.S. Senator Charles Schumer, U.S. Congressman Thomas Reynolds, and Undersecretary for Nuclear Security for the U.S. Department of Energy Thomas D'Agostino, dedicated the new OMEGA EP laser at the Robert L. Sproull Center for Ultra High Intensity Laser Research at the Laboratory for Laser Energetics. Senator Charles Schumer is shown giving the keynote address at the dedication ceremony.

Middle right: NIF PAM arrived at LLE for integration into the OMEGA EP Laser System. It was installed in the OMEGA EP Sources Bay and will be used for beam-smoothing studies.

Bottom right: An image of one of the first short-pulse target shots on OMEGA EP.

LLE 2008 Annual Report

**UR
LLE**

October 2007 – September 2008

Inertial Fusion Program and
National Laser Users' Facility Program

Contents

Executive Summary

The fiscal year ending September 2008 (FY2008) concluded the first year of the third five-year renewal of Cooperative Agreement DE-FC52-08NA28302 with the U.S. Department of Energy (DOE). This annual report summarizes progress in inertial fusion research at the Laboratory for Laser Energetics (LLE) during the past fiscal year. It also reports on LLE's progress on laser, optical materials, and advanced technology development; the completion of the OMEGA EP High-Energy, Petawatt-Class Laser System on time and on budget; operation of OMEGA for the National Laser Users' Facility (NLUF) and other external users; and programs focusing on the education of high school, undergraduate, and graduate students during the year.

Progress in Inertial Confinement Fusion (ICF) Research

The research program at the University of Rochester's Laboratory for Laser Energetics (LLE) focuses on inertial confinement fusion (ICF) research supporting the goal of achieving ignition on the National Ignition Facility (NIF). This program includes the full use of the OMEGA EP Laser System. Within the National Ignition Campaign (NIC), LLE is the lead laboratory for the validation of the performance of cryogenic target implosions, essential to all forms of ICF ignition. LLE has taken responsibility for a number of critical elements within the Integrated Experimental Teams (IET's) supporting the demonstration of indirect-drive ignition on the NIF and is the lead laboratory for the validation of the polar-drive approach to ignition on the NIF. LLE is also developing, testing, and building a number of diagnostics to be deployed on the NIF for the NIC.

During this past year, progress in the inertial fusion research program was made in three principal areas: NIC experiments; development of diagnostics for experiments on OMEGA, OMEGA EP, and the National Ignition Facility (NIF); and theoretical analysis and design efforts aimed at improving direct-drive-ignition capsule designs and advanced ignition concepts such as fast ignition and shock ignition.

1. National Ignition Campaign Experiments

In FY08, LLE, in collaboration with the Plasma Science Fusion Center–MIT, RSI Corporation, Naval Research Laboratory (NRL), and the Nuclear Research Center Negev, continued investigations of ignition-scaled cryogenic capsule implosions. Successful ignition target designs depend on two important issues: the ability to maintain the fuel adiabat at a low level and the control of nonuniformity growth during the implosion. A series of experiments were carried out on OMEGA (p. 16) to study the physics of low-adiabat, high-compression cryogenic capsule assembly. High-areal-density (with $\rho R > 0.2$ g/cm^2) cryogenic-fuel assembly is reported on OMEGA designs where the shock timing was optimized using the nonlocal treatment of the heat conduction and the suprathermal electron preheat by the two-plasmon-decay instability was mitigated.

The current status and future development of LLE's work on layering cryogenic D$_2$ and DT targets are presented in a report on p. 57. This essential effort achieved the milestone of routinely providing cryogenic DT capsules that meet the 1.0-μm (rms) OMEGA ice-surface-quality specification. The best D$_2$ layers achieved so far (rms roughness of 1.1 μm) are approaching the quality achieved in DT targets. Efforts to improve the consistency of this process are reported along with investigations that support the National Ignition Campaign's study of issues relevant to ignition-scale indirect-drive and direct-drive cryogenic targets.

The results of a collaborative project (including LLE, LLNL, and the University of California, Davis) on suprathermal electron production in gas-filled hohlraums are reported beginning on p. 139. Two bursts of high-energy electrons are observed when such hohlraums are driven with 13.5 kJ of 351-nm light on OMEGA. The two-plasmon-decay (TPD) instability in the exploding laser-entrance-hole (LEH) window appears to produce up to 20 J of hot electrons with $T_{hot} \sim 75$ keV at very early times and a very sharp laser-intensity threshold at $\sim 0.5 \times 10^{15}$ W/cm^2. The second pulse, produced by stimulated

Raman scattering (SRS) during the main laser drive, has more energy (~200 J) but significantly lower $T_{hot} \sim 20$ keV. This was the first such observation of the TPD instability in a hohlraum-configuration target.

Studies of energy transfer from high-intensity laser pulses into solid-density targets address basic issues in laser–plasma interactions, including electron acceleration, ion acceleration, and secondary radiation generation. In this volume (p. 1) we report on target experiments using LLE's Multi-Terawatt (MTW) Laser Facility to study isochoric heating of solid-density targets by fast electrons produced from intense, short-pulse laser irradiation. Electron refluxing occurs due to the target-sheath field effects and contains most of the fast electrons within the target volume. This process can efficiently heat the solid-density plasma through collisions. X-ray spectroscopic measurements of the absolute K_α photon yields and variations of the K_α/K_β emission ratio both indicate that laser energy couples to fast electrons with a conversion efficiency of ~20%. Bulk electron temperatures of at least 200 eV are inferred for the smallest-mass targets.

A collaborative team including LLE, Plasma Science and Fusion Center–MIT, LLNL, RAL, and GA reports on a comprehensive program underway at LLE to explore the physics of fast ignition (p. 120). The OMEGA EP Laser Facility, completed in April 2008, is located adjacent to the 60-beam, 30-kJ OMEGA Laser Facility and consists of four beamlines with a NIF-like architecture. Two of the beamlines can operate as high-energy petawatt (HEPW) lasers, with up to 2.6 kJ each with 10-ps pulse duration. These beams can be either injected into the OMEGA EP target chamber or combined collinearly into the existing OMEGA target chamber for integrated fast-ignitor experiments. Fuel-assembly experiments on OMEGA have achieved high fuel areal densities, and the effects of a cone on the fuel assembly are being studied. Experiments on short-pulse laser systems in collaboration with other institutions are being pursued to investigate the conversion efficiency from laser energy to fast electrons. A coherent transition radiation diagnostic is being developed to study the transport of the electrons in high-density material. Integrated experiments with room-temperature targets were performed in 2008 on OMEGA. Simulations of these integrated experiments show significant heating of up to 1 keV due to the hot electrons from the short-pulse laser.

Measurements of time-resolved absorption in cryogenic and room-temperature, direct-drive implosions on OMEGA are reported on p. 36. Time-dependent and time-integrated absorp-

tion fractions are inferred from scattered-light measurements that agree reasonably well with hydrodynamic simulations that include nonlocal electron-heat transport. Discrepancies in the time-resolved scattered-light spectra between simulations and experiments remain for complex laser pulse shapes, indicating beam-to-beam energy transfer and commensurate coupling losses. Time-resolved scattered-light spectra near $\omega/2$ and $3\omega/2$, as well as time-resolved hard x-ray measurements, indicate the presence of a strongly driven TPD instability at high intensities that may influence the observed laser light absorption. Experiments indicate that energetic electron production due to the TPD instability can be mitigated with high-Z-doped plastic shells.

A collaborative team comprised of scientists from LLE, LLNL, Plasma Science and Fusion Center–MIT, and Nuclear Research Center Negev presents initial results from experiments on the shock-ignition inertial confinement fusion concept (p. 25). Shock ignition is a two-step inertial confinement fusion concept where a strong shock wave is launched at the end of the laser pulse to ignite the compressed core of a low-velocity implosion. Initial shock-ignition technique experiments used 40-μm-thick, 0.9-mm-diam, warm surrogate plastic shells filled with deuterium gas. These experiments showed a significant improvement in the performance of low-adiabat, low-velocity implosions compared to conventional "hot-spot" implosions. High areal densities with average values exceeding ~0.2 g/cm^2 and peak areal densities above 0.3 g/cm^2 were measured, in good agreement with one-dimensional hydrodynamic simulation predictions. Shock-ignition-technique implosions with cryogenic deuterium and deuterium–tritium ice shells also produced areal densities close to the 1-D prediction and achieved up to 12% of the predicted 1-D fusion yield.

A physical understanding of heating generated by shock waves, radiation, and energetic electrons is required to effectively control the pressure in the main fuel layer of direct-drive capsules. On p. 185, we report on studies of shock-wave–heated and compressed planar targets using time-resolved Al $1s$–$2p$ absorption spectroscopy as a diagnostic. Significant discrepancies between the measured and predicted shock-wave heating were observed at late times in the drive, which can be explained by reduced radiative heating due to lateral heat flow in the coronal plasma.

We report on the effectiveness of a laser shinethrough barrier for direct illumination of a spherical target in direct-drive inertial confinement fusion experiments (p. 144). In the earliest stages of irradiation, before the plasma forms a critical-

density surface, laser light can penetrate into the target. This "shinethrough" light can be sufficiently intense to undergo filamentation and to damage the inside of the target, thereby seeding hydrodynamic instabilities. Laser shinethough can be blocked by a thin coating of opaque material such as aluminum (Al). For cryogenic direct-drive targets, the shinethrough barrier material must also be compatible with cryogenic target fabrication procedures, which rules out Al layers since they would interfere with the permeation filling and optical characterization of cryogenic targets. Silicon (Si) has been found to be a promising candidate for a direct-drive cryogenic target shinethrough barrier material. Several cryogenic targets have been coated with Si, successfully permeation filled with either D_2 or DT, and subsequently layered and optically characterized. Various thicknesses of Si coatings have been applied to planar targets and tested under relevant irradiation conditions. Experiments have shown that 200 μm of Si is sufficient to protect targets from laser shinethrough.

2. Target Diagnostics for OMEGA, OMEGA EP,
    and the NIF

In collaboration with LLNL and SNL, LLE achieved an important diagnostic milestone in FY08 by validating a technique to measure multi-shock timing on the NIF. Shock timing is performed with optical diagnostics (VISAR and ASBO) using the experimental configuration illustrated in Fig. 1. For this measurement, the target is placed at the end of a cone inserted inside a NIF-scale hohlraum that reaches radiation temperatures of ~165 eV. The capsule and cone are filled with liquid deuterium, and an external window enables the optical diagnostics to view the internal surface of the capsule along the axis of the cone. This measurement was highlighted in

E16369JR
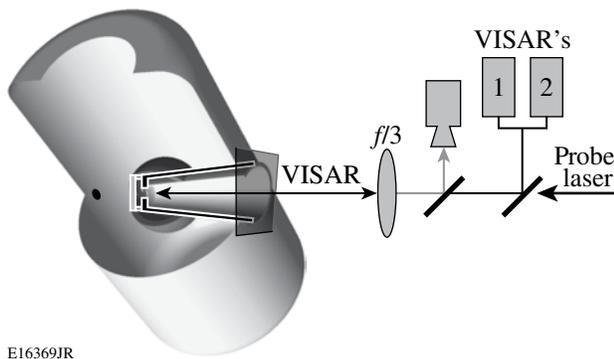
Figure 1
Schematic of experimental configuration for multi-shock timing experiments on hohlraum-driven cryogenic D_2 targets.

an invited paper delivered at the 50th Annual Meeting of the American Physical Society Division of Plasma Physics in November 2008.

A collaborative effort by the Plasma Science and Fusion Center–MIT and LLE on monoenergetic proton radiography of field and density distributions in inertial confinement fusion implosions is reported on p. 47. This unique imaging technique reveals field structures through deflection of proton trajectories, and areal densities are quantified through energy lost by protons while traversing the plasma. Two distinctly different types of electromagnetic-field configurations are observed during implosions, and the capsule size and areal-density temporal evolution are measured. The first field structure consists of many radial filaments with complex striations and bifurcations that permeate the entire field of view with 60-T magnetic field magnitudes, while another coherent, centrally directed electric field of the order of 10^9 V/m is seen near the capsule surface. Although the mechanisms for generating these fields are not yet fully understood, their effect on implosion dynamics is expected to be consequential.

In related work, a collaborative team including the Plasma Science and Fusion Center–MIT, LLE, Nuclear Research Center Negev, LLNL, and General Atomics reports on time-gated, monoenergetic proton radiography that provides unique measurements of implosion dynamics of spherical targets in direct-drive inertial confinement fusion (ICF) (p. 81). Radiographs obtained at different implosion times, from acceleration through coasting and deceleration to final stagnation, display a comprehensive picture of a spherical ICF implosion. Critical information inferred from such images characterizes the spatial structure and temporal evolution of self-generated fields and plasma areal density.

Scientists from LLE and the University of Rochester's Institute of Optics report on the design of a high-resolution optical transition radiation diagnostic for fast-electron-transport studies on the MTW Laser Facility (p. 9). Coherent transition radiation is generated as relativistic electrons, generated in high-intensity laser–plasma interactions, exit the target's rear surface and move into vacuum. High-resolution images of the rear-surface optical emission from high-intensity ($I \sim 10^{19}$ W/cm^2) laser-illuminated metal foils have been recorded using a transition radiation diagnostic (TRD). The detector is a scientific-grade charge-coupled-device (CCD) camera that operates with a signal-to-noise ratio of 10^3 and a dynamic range of 10^4. The TRD has demonstrated a spatial resolution of 1.4 nm over a 1-mm field of view, limited only by the CCD pixel size.

3. Theoretical Analysis and Design

A systematic investigation of the effect of low-ℓ-mode perturbations on neutron-yield degradation of direct-drive, low-adiabat ($\alpha \sim 2$ to 3) cryogenic D_2 implosions is reported (p. 172). This study uses 2-D *DRACO* simulations to show that for thin-shell targets (~5 μm), the yield degradation can be explained by the combined perturbations for the target offset, the low-ℓ-mode ice roughness, and the low-ℓ-mode laser illumination nonuniformities. For similar pulse shapes, thick-shell targets generally do not perform as well as thinner-shell targets. This indicates that high-ℓ-mode perturbations such as laser imprinting may play a role in further reducing neutron yields in thick-shell targets.

We report (p. 204) on theoretical work to develop an accurate representation of measurable Lawson criterion for inertial fusion with DT fuel. This ignition condition is found using an analytical dynamic model of ignition, and it is confirmed by the results of one-dimensional simulations of marginally ignited direct-drive targets (gain ~ 1). A simple fit of the ignition condition can be written as $\left\langle T_i^{\text{no }\alpha} \right\rangle_n^{2.6} \times \left\langle \rho R_{\text{tot}} \right\rangle_n > 50 \text{ keV}^{2.6} \times \text{g} / \text{cm}^2$. This ignition condition is given in terms of only two measurable parameters of the fuel: (1) the burn-averaged total areal density $\left\langle \rho R_{\text{tot}} \right\rangle_n$ and (2) the neutron-averaged hot-spot ion temperature $\left\langle T_i^{\text{no }\alpha} \right\rangle_n$ without accounting for the α-particle deposition.

The creation of relativistic, hot electron–positron plasma in the laboratory is an ambitious experimental challenge that has yet to be realized. Electron–positron pair plasmas are theoretically interesting because of the mass symmetry between plasma components. Electron–positron plasmas are important in astrophysical settings, and there have been proposals to use electron–positron plasmas as energy sources for space propulsion. We report on theoretical calculations (p. 161) of the expected electron–positron pair production that may be attained on future experiments on OMEGA EP. It is shown that a yield of ~5×10^{11} pairs may be possible on OMEGA EP provided that the hot-electron temperature is consistent with the ponderomotive scaling.

Lasers, Optical Materials, and Advanced Technology

An improved laser speckle smoothing scheme is reported (p. 73) that augments the current NIF 1-D SSD system by using multiple-FM modulators (MultiFM 1-D SSD). With a judicious choice of modulator frequencies, MultiFM 1-D SSD smoothes resonances that are produced at the higher spatial frequencies and can attain similar or even faster smoothing rates compared to the baseline NIF 2-D SSD system. *DRACO* simulations have shown that MultiFM 1-D SSD beam smoothing is sufficient

for the direct-drive-ignition targets and pulse shapes analyzed thus far and may even make it possible to reduce the bandwidth enough to eliminate the need for dual-crystal frequency conversion on the NIF.

A single-shot cross-correlator based on a pulse replicator that produces a discrete sequence of sampling pulses that are nonlinearly mixed with the pulse under test is discussed (p. 86). The combination of a high reflector and partial reflector replicates an optical pulse by multiple internal reflections and generates a sequence of spatially displaced and temporally delayed sampling pulses. This principle is used in a cross-correlator characterizing optical pulses at 1053 nm, where a dynamic range higher than 60 dB is obtained over a temporal range larger than 200 ps. The dynamic range can be extended with standard optical-density filters and the temporal range extended with larger optics.

A novel focal-spot diagnostic developed for OMEGA EP will be used to characterize on-shot focal spots to support high-quality laser–matter interaction experiments (p. 94). The complex fields in the region of the high-energy focus are calculated using high-resolution measurements of the main beam wavefront using the focal-spot diagnostic (FSD) located on the short-pulse diagnostic package and a careful calibration of the transfer wavefront between the FSD instrument and target chamber center. The concept of this calibration procedure is experimentally verified in the Multi-Terawatt (MTW) Laser System, which serves as a development platform for OMEGA EP. A technique based on phase retrieval is employed for the transfer-wavefront calibration since the OMEGA EP infrastructure cannot be replicated in the MTW laser; however, this approach also shows promise as an alternative method for OMEGA EP.

A systematic study has been conducted to improve the laser-damage resistance of multilayer high-reflector coatings for use at 351 nm on the OMEGA EP Laser System (p. 103). A series of hafnium-dioxide monolayer films deposited by electron-beam evaporation with varying deposition rates and oxygen backfill pressures were studied using transmission electron microscopy (TEM), x-ray diffraction (XRD), and refractive-index modeling. These coatings exhibit microstructural changes for sufficiently slow deposition rates and high oxygen backfill pressures, resulting in an absence of crystalline inclusions and a lower refractive index. This process was used to fabricate reduced-electric-field–type multilayer, high-reflector coatings that achieved laser-damage thresholds as high as 16.6 J/cm^2, which represents exceptional improvement over previous dam-

age thresholds measured at this wavelength of the order of 3 to 5 J/cm^2.

Two large-aperture (1.5-m) tiled-grating compressors—each consisting of four sets of tiled-grating assemblies—have been built and successfully implemented on the OMEGA EP laser (p. 113). The techniques used for tiling individual tiled-grating assemblies and for optimizing the overall performance of a tiled-grating compressor are described. Both compressors achieved subpicosecond-pulse duration without tiling-induced temporal degradation. A ray-tracing model predicted that the static wavefront of the grating tiles dominate focal-spot degradations when submicroradian tiling accuracy is achieved. The tiled-grating compressors delivered a tighter focal spot compared to sub-aperture grating compressors with single central tiles.

An on-shot focal-spot diagnostic is presented for characterizing high-energy, petawatt-class laser systems (p. 130). Accurate measurements at full energy are demonstrated using high-resolution wavefront sensing in combination with techniques to calibrate on-shot measurements with low-energy sample beams. Results are shown for full-energy activation shots on OMEGA EP.

The suppression and elimination of self-pulsing in a watt-level, dual-clad, ytterbium-doped fiber laser are reported (p. 150). Self-pulsations are caused by the dynamic interaction between the photon population and the population inversion. The addition of a long section of passive fiber in the laser cavity makes the gain recovery faster than the self-pulsation dynamics, allowing only stable continuous-wave lasing. This scheme provides a simple and practical method for eliminating self-pulsations in fiber lasers at all pumping levels.

A collaborative team from LLE and the Kavli Institute of Nanoscience, Delft University of Technology reports on a new readout scheme for NbN superconducting single-photon detectors (SSPD's), using a low-noise, cryogenic high-electron mobility transistor and a high-load resistor directly integrated with the detector to achieve amplitude resolution of dark and photon counts (p. 153). This scheme makes it possible to study the physical origin of dark counts in SSPD's and may enable both photon-number-resolving and energy-resolving capabilities of the standard, meander-type SSPD.

Superconductivity is still regarded as a very promising technology to be applied to high-performance electronics (e.g., Josephson junction digital circuits, ultrasensitive

magnetometers) and optoelectronics (e.g., broadband x-ray to visible-light photoconductors, optical single-photon and photon-counting detectors). A comprehensive study of the time-resolved dynamics of Cooper pairs and quasiparticles in Hg-based superconductors begins on p. 219.

OMEGA Extended Performance (OMEGA EP)
The OMEGA EP project was completed in April 2008—on time and on budget. The formal Critical Decision 4 (CD-4) milestone was approved by the NNSA Acquisition Executive on 6 May 2008. OMEGA EP accomplished all project completion criteria, demonstrating short- and long-pulse capability. In total there were over 3000 test shots on OMEGA EP during the period from August 2006 to 30 April 2008. Highlights of the activation and CD-4 demonstration shots included Beams 1 and 2 being successfully operated to the OMEGA EP and OMEGA target chambers. Beam 1 achieved 600 J of infrared (IR) short-pulse energy (400 J required) at <100-ps duration, and Beam 2 achieved 424 J of IR short-pulse energy (400 J required) at ~10 ps. All four beams were operated at >1-kJ ultraviolet (UV) in long-pulse operational mode. During the week of 31 March 2008, the OMEGA EP laser fired 22 shots into the OMEGA target chamber. A CD-4 Project Completion review was conducted on-site by NNSA on 23–24 April to validate project completion. The system performance requirements were met with two minor exceptions (described below) and the facility transitioned to operations in May 2008.

The project completion criteria were established in a formal Project Completion and Certification Plan. Project completion was based on compliance with all sections of this plan. All appropriate project documentation was made available for review by NNSA to verify that applicable requirements of DOE Order 413.3A *Program and Project Management for the Acquisition of Capital Assets* for project completion and start of operations had been satisfied. The top-level system technical and functional performance requirements for the project were specified at the start of the project. The performance characteristics for each beamline were divided between the short- and long-pulse beam characteristics. These criteria were as follows:

Short-pulse beams
Beamlines 1 and 2 activated for high-intensity experiments with a joint OMEGA target shot to include the following conditions:

- Beamline 1 having a pulse width of ≤100 ps, Beamline 2 a pulse width of ≤10 ps

- Beamline 2 timed with respect to Beamline 1 to the desired delay with an uncertainty of less than 10-ps rms

- OMEGA EP beams timed to the OMEGA beams to the desired delay with an uncertainty of less than 20-ps rms

- Each beam having an on-target energy of ≥400 J

- Focal-spot conditions where >80% of the on-target energy will be within a 40-μm-diam spot

- Irradiation of a backlighter foil in OMEGA using Beamline 1 or 2 to include the criteria above and repeated within 2 h

Long-pulse beams

All four beamlines activated for the single-sided irradiation of a foil target in the auxiliary target chamber to include the following conditions:

- Pulse durations between 1 to 10 ns for each beam, configurable

- On-target total energy ≥1000 J per beam at 351 nm, at 2 ns or longer

- All four beamlines co-timed to less than 40-ps rms

- Focal-spot conditions where >95% of the UV energy is contained in a 1-mm-diam spot

These system performance criteria were deemed to have been met with two exceptions, neither of which precluded OMEGA EP from satisfying the primary functional requirements defined in the Statement of Mission Need. The first exception was that the OMEGA EP short-pulse suite of diagnostics includes a new and novel method for measuring the focal-spot size on target. This instrument, the Focal-Spot Diagnostic, acquired high-quality data on its initial use. The focal-spot size during the CD-4 shot campaign to OMEGA was measured on one beam to be 30- to 35-μm radius (radius that contains 80% of the energy, R_{80}), whereas the requirement is $R_{80} < 20$ μm. The other short-pulse beam focal spot was not measured. Subsequent to project completion the focal spots of both beams were improved and are, as of the end of FY08, very near the R_{80} requirement. The second exception was that Beamlines 1 and 2 were not shot on target in long-pulse mode due to the unavailability of UV focus lenses. The beamlines were, however, shot at >1000-J-equivalent on-target energy

with the beam terminated at the UV diagnostics. The UV focus lenses were awaiting conditioning, initiation, and mitigation (CIM) at LLNL to achieve high UV laser damage fluence. In order not to impact the National Ignition Facility schedule, a programmatic decision was made to wait until LLNL could reasonably process the optics and deliver them to LLE.

National Laser Users' Facility (NLUF) and External Users' Programs

During FY08, a governance plan was implemented to formalize the scheduling of the OMEGA Laser Facility as an NNSA User Facility. Under this plan, OMEGA shots are allocated by campaign. The majority of the FY08 target shots were allocated to the National Ignition Campaign (NIC), and integrated experimental teams from LLNL, LANL, SNL, and LLE conducted a variety of NIC-related experiments primarily at the OMEGA facility. Shots were also allocated in FY08 to the high-energy-density (HED) physics programs from LLNL and LANL.

Under the governance plan 25% of the facility shots are allocated to Basic Science experiments. Roughly half of these are dedicated to University Basic Science under the National Laser Users' Facility Program and the remaining shots are allotted to Laboratory Basic Science, comprising peer-reviewed basic science experiments conducted by the national laboratories and LLE/FSC.

In total, nearly 49% of the OMEGA shots in FY08 were dedicated to external users including the NLUF programs, LLNL, LANL, SNL, CEA (France), and AWE (UK, Atomic Weapons Establishment).

1. NLUF Experiments

In FY08, the Department of Energy (DOE) issued a solicitation for NLUF grants for the period of FY09–FY10. A total of 13 proposals were submitted to DOE for the NLUF FY09–FY10 program. An independent DOE Technical Evaluation Panel reviewed the proposals and recommended that 11 of the proposals receive DOE funding and shot time on OMEGA in FY09–FY10. Table I lists the successful proposals.

Fiscal year 2008 was the second year of a two-year period of performance for the NLUF projects approved for FY07–FY08 funding and OMEGA shots. A total of 125 shots were conducted for six NLUF projects. The progress of some this work is detailed beginning on p. 228 in the following reports:

- *Experimental Astrophysics on the OMEGA Laser*
  (R. P. Drake, University of Michigan)

- *Laboratory Experiments on Supersonic Astrophysical Flows Interacting with Clumpy Environments*
  (P. Hartigan, Rice University)

- *Multiview Tomographic Study of OMEGA Direct-Drive-Implosion Experiments*
  (R. Mancini, University of Nevada, Reno)

- *Monoenergetic Proton Radiography of ICF Implosions*
  (R. D. Petrasso and C. K. Li, Massachusetts Institute of Technology)

- *X-Ray Thompson-Scattering Spectra in Shock-Compressed Beryllium*
  (R. Falcone and H. J. Lee, University of California at Berkeley)

2. FY08 LLNL OMEGA Experimental Programs

In FY08, Lawrence Livermore National Laboratory (LLNL) led 238 target shots on the OMEGA Laser System. Approximately half of these experiments were dedicated to the National Ignition Campaign (NIC); the other half were dedicated to supporting the high-energy-density stewardship experiments (HEDSE's).

Objectives of the LLNL-led NIC campaigns on OMEGA included the following:

- *Laser–plasma interaction studies of physical conditions relevant for the National Ignition Facility (NIF) ignition targets*

- *Studies of the x-ray flux originating from the laser entrance hole (LEH) window of a hohlraum, which might impact the performance of a fusion capsule*

- *Characterization of the properties of warm dense matter—specifically radiatively heated Be*

Table I: Approved NLUF proposals for FY09–FY10.

Principal Investigator	Institution	Project Title
Farhat Beg	University of California, San Diego	Systematic Study of Fast Electron Transport and Magnetic Collimation in Hot Plasmas
Paul Drake	University of Michigan	Experimental Astrophysics on the OMEGA Laser
Roger Falcone	University of California, Berkeley	Detailed *In-Situ* Diagnostics of Multiple Shocks
Uri Feldman	ARTEP, Inc.	EP-Generated X-Ray Source for High-Resolution 100–200 keV Point Projection Radiography
Yogendra Gupta	Washington State University	Ramp Compression Experiments for Measuring Structural Phase Transformation Kinetics on OMEGA
Patrick Hartigan	Rice University	Dynamics of Shock Waves in Clumpy Media
Raymond Jeanloz	University of California, Berkeley	Recreating Planetary Core Conditions on OMEGA, Techniques to Produce Dense States of Matter
Karl Krushelnick	University of Michigan	Intense Laser Interactions with Low Density Plasmas Using OMEGA EP
Roberto Mancini	University of Nevada, Reno	Three-Dimensional Studies of Low-Adiabat Direct-Drive Implosions at OMEGA
Mark Meyers	University of California, San Diego	Response of BCC Metals to Ultrahigh Strain Rate Compression
Richard Petrasso	Massachusetts Institute of Technology	Monoenergetic Proton and Alpha Radiography of Laser-Plasma-Generated Fields and ICF Implosions

- *Studies of the physical properties of capsules based on Cu-doped Be, high-density carbon, and conventional plastics, including new high-resolution shock-velocimetry measurements*

- *Determining ablator performance during the implosion of NIC-candidate ablators*

- *Experiments to study the physical properties (thermal conductivity) of shocked fusion fuels*

- *High-resolution measurements of velocity nonuniformities created by microscopic perturbations in NIF ablator materials*

- *Demonstration of $T_r = 100$-eV foot-symmetry tuning using a re-emission sphere*

- *Demonstration of $T_r = 100$-eV foot-symmetry tuning using a backlit thin-shell capsule*

- *Quantification of x-ray foot preheat caused by laser–window interaction*

  The LLNL HEDSE campaigns included the following:

- *Quasi-isentropic [isentropic compression experiment (ICE)] drive used to study material properties such as strength, equation of state, phase, and phase-transition kinetics under high pressure*

- *Development of long-duration, point-apertured, point-projection x-ray backlighters*

- *Development of an experimental platform to study non-local thermodynamic equilibrium (NLTE) physics using direct-drive implosions*

- *Opacity studies of high-temperature plasmas under LTE conditions*

- *Development of multikilovolt x-ray sources using underdense NLTE plasmas for x-ray source applications*

- *Studies of improved hohlraum heating efficiency using cylindrical hohlraums with foam walls*

- *Laser-driven dynamic-hohlraum (LDDH)-implosion experiments*

- *High-speed hydrodynamic jets for code validation*

3. FY08 LANL OMEGA Experimental Programs

Los Alamos National Laboratory (LANL) successfully fielded a range of experiments on the OMEGA laser during FY08 studying the physics relevant to inertial confinement fusion (ICF) and high-energy-density laboratory plasma (HEDLP) in support of the national program. LANL conducted a total of 85 target shots on OMEGA. Collaborations with LLNL, LLE, MIT, and AWE remain an important component of LANL's program on OMEGA.

As reported beginning on p. 248, the LANL-led campaign included the following experiments:

- *AGEX-EOS experiments aimed at exploring radiative preheating in Richtmyer–Meshkov (RM) mix of large-Atwood-number interfaces*

- *"DT ratio–^{3}He" experiment to investigate the effect of helium on yield and reaction history of DT implosions*

- *The "Hi-Z" experiment to study the effects of instability growth and the resulting mix*

- *NIF Platform #5—aimed at developing x-ray diagnostic techniques to measure temperature in future NIF radiation transport experiments*

- *The "symergy" experiment to test the concept of using thin shells to quantify asymmetry during the foot of an NIF ignition drive pulse*

4. FY08 CEA OMEGA Experimental Programs

During FY08, CEA scientists led 39 target shots on OMEGA—four more than the nominal allocation. Reports on the experiments begin on p. 253 and include the following:

- *Development and testing of data acquisition systems that can operate under harsh radiation environments*

- *Exploration of monocrystaline diamond CVD detectors for time-resolved neutron measurements*

- *Development of neutron imaging on OMEGA*

5. FY08 AWE OMEGA Experimental Programs

AWE scientists conducted 32 OMEGA target shots in FY08—two more than the nominal allocation. The experiments focused on studies of radiation transport and hohlraum symmetry.

FY08 Laser Facility Report

The OMEGA facility conducted 1169 target shots on OMEGA and 85 target shots on OMEGA EP for a variety of users in FY08 (see Table II). The OMEGA Availability and Experimental Effectiveness averages for the year were 91.3% and 96.1%, respectively. Highlights of the year included the following:

- *Pulse-shaping capability was enhanced to include double and triple picket pulses for cryogenic experiments on OMEGA.*

- *The picket-generation hardware has been upgraded to allow for the creation of independent timing/amplitude control of the pickets.*

- *A new harmonic energy detector (HED) system was designed and implemented to replace the legacy system on OMEGA.*

- *The Fiducial Laser System was upgraded to solid-state, diode-pumped regenerative amplifier technology.*

- *All rod amplifier power conditioning unit control systems were upgraded with improved trigger boards.*

- *A new Target Viewing System (TVS) was installed on the OMEGA target chamber. The new system features real-time image processing, up to a 50-mm field of view, up to 2000-frames/s data collection, cryogenic target imaging improvements, remote focus capability, and target detection improvements.*

- *New environmental controls were added to the Pulse-Generation Room (PGR).*

- *The OMEGA EP Laser Facility completed the integration to target of two short-pulse beamlines and two long-pulse UV beamlines.*

- *Two additional ten-inch manipulators (TIM's) were commissioned for the OMEGA EP chamber, bringing the total to three.*

- *A suite of new target diagnostics were qualified for OMEGA EP.*

- *A NIF preamplifier module (PAM) was installed in the OMEGA EP Laser Sources Bay.*

Education at LLE

As the only major university participant in the National ICF Program, education continues to be an important mission for the Laboratory. A report on this year's Summer High School Research Program is described in detail on p. 224. Fourteen students participated in this year's program. The William D. Ryan Inspirational Teacher Award was presented to Ms. Jane M. Bowdler, an Advanced Placement (AP) calculus and pre-calculus teacher at Brockport High School.

Table II: The OMEGA target shot summary for FY08.

Laboratory	Planned Number of Target Shots	Actual Number of Target Shots	IDI NIC	DDI NIC	Total NIC	Non NIC
LLE	607	600	145	409	554	46
LLNL	221	237	117	0	117	120
NLUF	114	125	0	0	0	125
LANL	85	85	22	0	22	63
LBS	50	51	0	0	0	51
CEA	35	39	0	0	0	39
AWE	30	32	0	0	0	32
Total	1142	1169	284	409	693	476

Graduate students are using the OMEGA laser for fusion research and other facilities for HED research and technology development. They are making significant contributions to LLE's research activities. Twenty-five faculty from five departments collaborate with LLE's scientists and engineers. Presently, 87 graduate students are involved in research projects at LLE, and LLE directly sponsors 39 students pursuing Ph.D. degrees via the NNSA-supported Frank Horton Fellowship Program in Laser Energetics. Their research includes theoretical and experimental plasma physics, high-energy-density physics, x-ray and atomic physics, nuclear fusion, ultrafast optoelectronics, high-power-laser development and applications, nonlinear optics, optical materials and optical fabrications technology, and target fabrication.

Approximately 66 undergraduate students participated in work or research projects at LLE this past year. Student projects include operational maintenance of the OMEGA Laser System; work in laser development, materials, and optical-thin-film– coating laboratories; and programming, image processing, and diagnostic development. This is a unique opportunity for students, many of whom will go on to pursue a higher degree in the area in which they gained experience at the Laboratory.

In addition, LLE directly funds research programs within the Plasma Science and Fusion Center–MIT, the State University of New York (SUNY) at Geneseo, the University of Nevada, Reno, and the University of Wisconsin. These programs involve a total of approximately 16 graduate students, 27 undergraduate students, and 7 faculty members.

Robert L. McCrory
Director, Laboratory for Laser Energetics
Vice Provost, University of Rochester

High-Intensity Laser–Plasma Interactions in the Refluxing Limit

Introduction

Studies of energy transfer from high-intensity laser pulses into solid-density targets address basic issues in laser–plasma interactions, including electron acceleration, ion acceleration, and secondary radiation generation.[1–5] At laser irradiances $I\lambda^2 > 10^{18}$ (W/cm^2)μm^2, where I is the laser intensity and λ is the laser wavelength, electrons are accelerated to relativistic energies and can be used to create unique states of matter. These studies are motivated by a variety of applications in high-energy-density science,[6] including bright backlighter source development[7] and advanced inertial confinement fusion schemes such as fast ignition.[8,9]

Many uncertainties exist in the transport and energy deposition of laser-generated high-current electron beams in dense plasmas. Their propagation is strongly affected by self-generated electromagnetic fields and the ability of the plasma to draw a return current.[10–17] Simple, well-characterized target geometries can identify the dominant laser–plasma and energy-deposition phenomena and can be used for detailed code benchmarking. Of particular interest are methods for isochorically heating solid-density targets to hundreds of eV and many keV using fast electrons[18–24] to infer laser–plasma coupling and heating as a function of laser intensity, wavelength, pulse duration, and preplasma scale length.[25–33]

The fast electrons generated during high-intensity laser–plasma interactions with solid targets of just tens or hundreds of microns in extent and less than a few microns in thickness rapidly create a solid-density, high-energy-density plasma.[25,26] The electrons typically have energies of up to a few MeV and ranges of many hundreds of microns—far greater than the target thickness. The Debye sheath fields that rapidly form at the target surfaces constrain the majority of fast electrons to multiple transits through the target. This process is known as refluxing[3,34,35] and is a particularly efficient mechanism for transferring fast-electron energy into thermal-plasma energy prior to any significant hydrodynamic disassembly.[27–29]

Refluxing in small-mass targets provides a simple geometry for testing laser coupling, fast-electron generation, and plasma-heating models. For example, K-shell spectroscopy using buried fluors, a widely used technique for diagnosing fast-electron transport in massive solid targets,[18,21–23,33,36–38] is not necessary here. The target is so small that by choosing an appropriate mid-Z material (to simplify the ion de-excitation cascades and reabsorption of fluorescent x rays[21,37,39]), the target is the fluor. This is a unique property of the refluxing limit and provides insightful simplifications to the modeling of fast-electron stopping and secondary radiation generation and transport.[28]

Theobald et al.[27] have shown that the energy in K_α emission, per joule of laser energy, from a small-mass target is insensitive to the fast-electron spectrum and laser intensity in the relativistic regime. Myatt et al.[28] have published modeling of these experiments, taking into account the effect of spatial and temporal gradients, target expansion and heating, and fast-electron refluxing on the absolute and relative emission of K_α and K_β fluorescent lines. This is used to infer the laser-to-electron energy-conversion efficiency $\eta_{L\to e}$, accounting for classical fast-electron stopping and relativistic K-shell ionization cross sections.[40]

This article describes experiments that demonstrate the effect of bulk heating on L $\longrightarrow$ K and M $\longrightarrow$ K electron transitions in small-mass copper targets. It has previously been demonstrated using high-resolution K_α spectroscopy that high bulk-electron temperatures can be achieved (hundreds of eV) in a refluxing geometry.[25,26] In our experiment, variations in the K_β/K_α ratio as a function of target volume diagnose the bulk-electron temperature during the rapid isochoric heating phase. This allows the laser-to-electron energy-conversion efficiency $\eta_{L\to e}$ to be inferred by comparing experimental K_β/K_α measurements to numerical target-heating calculations, in addition to inferring the conversion efficiency from the absolute K_α yield.

This is a robust technique for inferring the deposited fraction of laser energy into the target bulk by fast electrons, which is required to create the experimentally observed K-photon yields. In the cold material limit, a laser-to-electron energy-conversion efficiency of $\eta_{L \to e} = (20\pm10)\%$ has been inferred. Laser pulses of 5 J and 1 ps at intensities of $I > 10^{19}$ W/cm^2 are shown to heat smaller-volume targets, culminating in $20 \times 20 \times 2$-μm^3 copper targets reaching the highest bulk-electron temperatures of $T_e > 200$ eV. An average laser-to-electron energy-conversion efficiency of around 20% has been inferred over a wide range of target volumes, in good agreement with cold K$_\alpha$ measurements.

The following sections (1) describe the experimental setup; (2) compare K$_\alpha$-emission measurements to a model of K$_\alpha$ production from small-mass targets; (3) compare bulk-heating measurements with numerical target-heating calculations; and (4) provide a discussion and summary.

Experimental Setup

The experiments were performed using the Multi-Terawatt (MTW) Laser System at the Laboratory for Laser Energetics. MTW is a hybrid laser system, which operates in the conventional chirped-pulse–amplification (CPA) mode and combines optical parametric amplification (OPA) with Nd-doped laser-glass amplification.[41] The measured contrast ratio after the OPCPA stage is around 10^8 during the 100-ps period prior to the main laser pulse. Maximum output energies >10 J in a transform-limited subpicosecond pulse duration provide peak powers of the order of 10 TW. The energy in the laser pulse, the pulse duration, and the spatial distribution of the laser beam on the compressor output are monitored on a shot-to-shot basis. Typical short-term stability over a period of a few days is 3% rms in energy and 10% rms in the pulse duration.

For the experiments described here, the laser delivered 1- to 5-J, 1-ps pulses and was focused at normal incidence onto planar-foil targets using an $f/2$ off-axis parabola. The focal-spot full width at half maximum was between 4 to 6 μm and provided a peak intensity of up to 2×10^{19} W/cm^2. The targets were copper foils that ranged in cross-sectional area and thickness between $20 \times 20 \times 2$ μm^3 and $500 \times 500 \times 50$ μm^3. Two types of target mounts were used, depending on the target size: 1- to 2-μm-diam spider-silk threads and 17-μm-diam silicon carbide stalks.

Measurements of the time-integrated copper K$_\alpha$ (8.05-keV) and copper K$_\beta$ (8.91-keV) emission were performed using a spectrometer based on an x-ray charge-coupled-device (CCD) camera operating in the single-photon–counting mode.[42] The spectrometer was located 23° to the target front-surface normal and incorporated extensive lead shielding and collimation tubes to optimize the signal to noise and minimize the detection of hard x-ray photons. It is assumed that K photons are emitted uniformly over 4π steradians and only weakly attenuated by the target plasma itself, prior to reaching the spectrometer. Copper filters of 75- to 150-μm thickness attenuated the K-shell emission, allowing K$_\alpha$ and K$_\beta$ photons to be transmitted just below the K edge of the filter. The final K-shell spectrum is calculated taking into account the solid angle sampled by the detector, the x-ray CCD quantum efficiency, and the filter transmission.

Measurements of the K$_\alpha$ Yield

High-intensity laser pulses interact with solid-density targets in a short-density-scale-length preplasma. The collisionless absorption of laser energy into relativistic electrons occurs up to the relativistic critical-density surface through $\mathbf{v} \times \mathbf{B}$ acceleration, resonance absorption, vacuum heating, and parametric instabilities.[24,43–45] Electron transport and heating away from the focal spot require that the fast-electron current be opposed by an inductively or electrostatically generated electric field that draws a return current from the thermal background. At the target boundaries, escaping fast electrons rapidly form a Debye sheath that, for sufficiently small targets, provides a potential that prevents a significant fraction of fast electrons from escaping. A MeV electron, for example, which has a range of around 1 mm and a characteristic slowing-down time of approximately 1 ps at solid density, will make multiple transits across a micron-scale-thickness, solid-density plasma before stopping. The high-energy electrons essentially provide their own return current. This reduces the enhanced stopping due to resistive electric fields associated with cold return currents that are found in more-massive targets.[46,47] In this case, resistive inhibition is not important because the characteristic electron range in the resistive electric fields is greater than the foil thickness. A resistive electric field $E_{res} \approx 2 \times 10^5$ kV/cm, which is representative of interaction conditions for copper at a few hundred eV, would stop a 1-MeV electron in 50 μm, assuming a minimum conductivity $\sigma = 1 \times 10^6$ $(\Omega m)^{-1}$ (Ref. 28). This resistive range is greater than the target thickness, allowing the electrons to contribute to the return current over time scales greater than their characteristic target transit time.

K$_\alpha$ emission has been used in many experiments to diagnose fast-electron-energy spectra and electron angular distributions during high-intensity laser–plasma interactions.[18,21,22,33,37] K-photon emission is generated during inelastic collisions

between fast electrons (with energies exceeding the K-shell binding energy) and electrons in the K shell. The fast-electron–induced K-shell vacancy is short lived ($<10^{-12}$ s) and decays through radiative and nonradiative de-excitation. The most important processes for mid-Z elements such as copper is the competition between Auger decay and K-shell fluorescence, which is quantified by the K-shell fluorescence probability.[48] K_α and K_β emission is thus generated during L $\longrightarrow$ K and M $\longrightarrow$ K electronic transitions.

The copper K-shell spectrum was investigated as a function of laser intensity using $500 \times 500 \times 20$-μm^3 copper targets to access the cold-material limit by using relatively large-mass targets, while keeping them thin enough to maintain the Debye sheath fields that cause refluxing and minimize opacity effects. Figure 113.1 shows a series of K_α emission measurements (normalized to the laser energy) using 1-ps-duration laser pulses over an intensity range of 5×10^{16} W/cm^2 $< I < 5 \times 10^{20}$ W/cm^2. The intensity on target is varied by changing the laser-spot size and laser energy. Data from the MTW laser (solid circles) are shown and compared to previously published data from the Vulcan PW laser (open circles).[27,28,49]
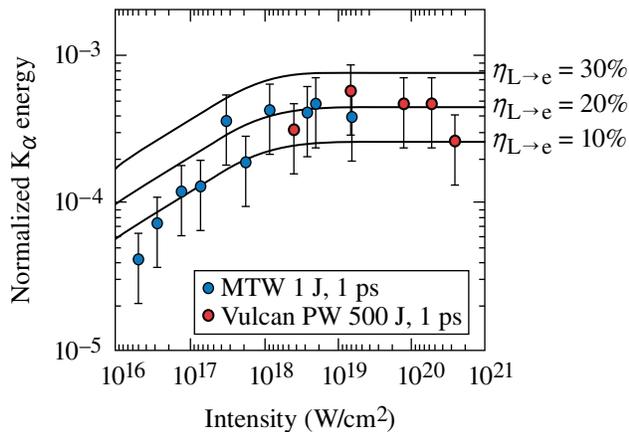
Figure 113.1
K_α energy (normalized to the laser energy) as a function of laser intensity. Data are shown for $500 \times 500 \times 20$-μm^3 copper targets from the MTW laser (solid circles) and the Vulcan PW laser (open circles).[27,28] Predictions from the K_α-production model are shown (solid lines) for laser-to-electron energy-conversion efficiencies $\eta_{L \to e} = 10\%$, 20%, and 30%.

The experimental data in Fig. 113.1 are compared to a model of K_α production (solid black lines) as described in Ref. 27. The model accounts for collisional fast-electron energy transfer only and makes no inference to the spatial homogeneity of the energy deposition, but simply allows the fast electrons to slow down. An exponential fast-electron-energy spectrum is

specified using a scaling relationship between the fast-electron temperature T_e and the laser intensity I. The ponderomotive scaling $T_e [\text{MeV}] = 0.511 \left[\left(1 + I_{18} \lambda_{\mu m}^2 / 1.37 \right)^{1/2} - 1 \right]$ is used for $I > 10^{18}$ W/cm^2 (Ref. 24), where I_{18} is the laser intensity in units of 10^{18} W/cm^2 and $\lambda_{\mu m}$ is the laser wavelength in microns. Such a scaling has been shown to become increasingly less accurate at lower laser intensities and is replaced by $T_e [\text{MeV}] = 0.05 \, I_{18}^{1/3}$, for interactions $I < 10^{18}$ W/cm^2. This phenomenological scaling is extrapolated from existing experimental measurements that are summarized in the review by Gibbon *et al.*[10]

The K_α-production model accounts for two distinct properties afforded by the refluxing process. The fast electrons are allowed to lose all of their energy inside the target, independent of their range, described using the classical slowing-down approximation. Energy is transferred to atomic electrons with high efficiency ($>90\%$),[28] and K-shell vacancies are created during each transit of the target by electrons with energy above the copper K-shell binding energy. This is accounted for in the K-shell ionization cross section, which is modified for relativistic effects.[39,40] There is also a correction for reabsorption of the emitted photons. The K_α transmission of a 20-μm-thick foil, for example, is 70%, which assumes a uniform fast-electron density and an attenuation length of $L = 25 \, \mu m$.

The fraction of incident laser energy deposited by fast electrons in the target, which generates the observed K-photon emission, is, to a good approximation, the laser-to-electron energy-conversion efficiency $\eta_{L \to e}$, with ion acceleration effects representing a small energy correction. For laser parameters consistent with the experiments reported here, the measured conversion efficiencies of laser energy into ion acceleration (including protons from surface contamination) are in the range of 0.1% to 2% (Refs. 34, 50–52). The experimentally inferred laser-to-electron energy-conversion efficiency therefore represents, to within experimental error, a minimum of the absolute $\eta_{L \to e}$ value.

The refluxing model predicts the K_α yield as a function of laser intensity for various laser-to-electron energy-conversion efficiencies $\eta_{L \to e}$. Figure 113.1 demonstrates good agreement between the energy emitted by K_α photons (normalized to the laser energy) and the K_α-production model. A conversion efficiency of laser energy into fast electrons $\eta_{L \to e} = (20 \pm 10)\%$ is inferred for $I > 10^{18}$ W/cm^2. If refluxing were not considered, K-photon production would fall dramatically for $I > 10^{18}$ W/cm^2 because there is insufficient time or material in a single pass of the plasma to support appreciable fast-electron-

energy loss or significant K-shell vacancy creation with an increasing electron range.

The data show that K_α conversion efficiency is a weakly increasing function of laser intensity above $I = 10^{18}$ W/cm^2. This is also a feature of the model, caused by the interplay between the energy dependence of the K-shell ionization cross section and the insensitivity of the K_α generation mechanism to the fast-electron temperature and energy spectrum in the refluxing regime. The effect is demonstrated in both data sets using both 1-J and 500-J laser pulses with comparable 1-ps pulse durations. For $I < 10^{18}$ W/cm^2, the fast-electron temperature T_e reduces and the K_α signal is predicted to decrease with laser intensity. This is a result of the particular energy dependence of the fast-electron range and the K-shell ionization cross section. This has been confirmed experimentally by defocusing the MTW laser and entering the nonrelativistic regime.

Influence of Target Heating on K-Shell Line Emission

The bulk-electron temperature that an initially cold target reaches during refluxing is governed by the target mass and the energy content of the laser-accelerated electrons. Numerical target-heating calculations[28] predict that volumetric heating to $T_e > 100$ eV in small-mass ($<300 \times 300 \times 20$-$\mu$m^3) copper targets is sufficient to collisionally ionize and partially deplete the M shell. Filling of the K-shell vacancy from the M shell will be suppressed and provides diagnostic access to the bulk-plasma environment through variations of the K_β/K_α ratio from that expected in the cold-material limit, as shown in Fig. 113.2. This

effect can be used to provide a self-consistency check on the total fast-electron-energy content.

The variation of K_β/K_α as a function of local bulk-electron temperature is shown in Fig. 113.3, based on the calculation reported in Ref. 28, which takes into account the LTE ion population, using the code *PrismSPECT*.[53] Here, K_β/K_α is normalized to the expected cold-material value $K_\beta/K_\alpha = 0.14$. A dramatic reduction in K_β/K_α is demonstrated for bulk-electron temperatures of up to 400 eV, beyond which there are negligible numbers of ions with populated M shells and no K_β emission is possible.

E16147JRC
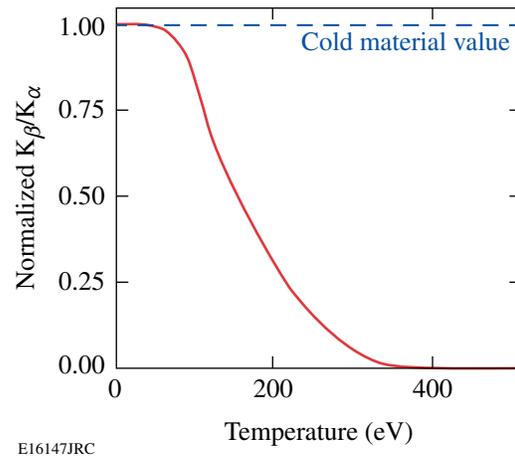
Figure 113.3
K_β/K_α ratio variation with bulk-electron temperature (normalized to the cold-material value).

E16143JRC
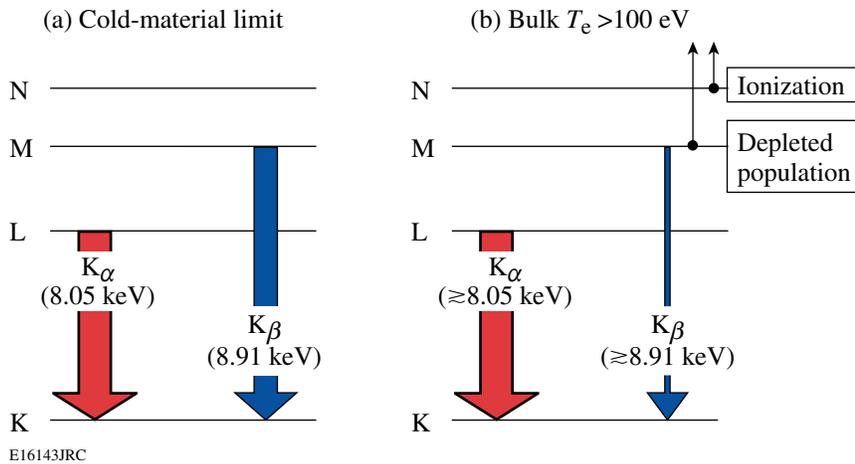
Figure 113.2
Copper-energy levels showing L $\longrightarrow$ K and M $\longrightarrow$ K electronic transitions that produce K_α and K_β radiative emission. Two examples are given: (a) a solid-density plasma in the cold-material limit (constant K_β/K_α) and (b) a solid-density plasma with bulk $T_e > 100$ eV (suppressed K_β/K_α). The number of emitted photons during L $\longrightarrow$ K and M $\longrightarrow$ K transitions is represented schematically by the relative arrow widths.

Figure 113.4 shows that the influence of bulk heating on K-shell emission predicted by the estimate in Fig. 113.3 is indeed observed experimentally. Examples of copper K-shell spectra are shown for (a) $500 \times 500 \times 50$-μm^3 and (b) $20 \times 20 \times 3$-μm^3 copper targets. The spectra were measured from interactions with 5-J, 1-ps laser pulses at an intensity of $I = 2 \times 10^{19}$ W/cm^2. The K$_\alpha$ and K$_\beta$ peaks are fit to Gaussian line shapes with a FWHM of 220 eV. M-shell depletion in the $20 \times 20 \times 3$-μm^3 target has significantly reduced the K$_\beta$ emission in comparison to that measured from the $500 \times 500 \times 50$-μm^3 target.
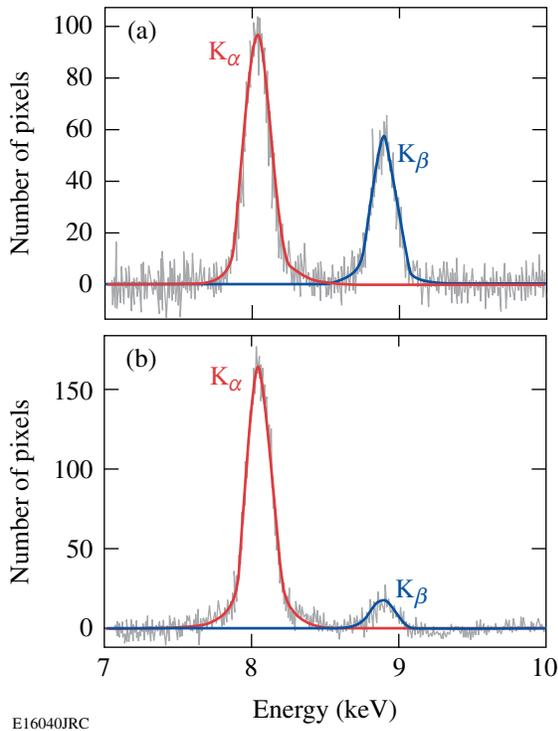

Figure 113.4
Example spectra for (a) $500 \times 500 \times 50$-μm^3 and (b) $20 \times 20 \times 3$-μm^3 copper targets and 5-J, 1-ps laser pulses at intensities $I = 2 \times 10^{19}$ W/cm^2. The K$_\alpha$ and K$_\beta$ peaks are shown.

The copper K-shell spectrum was measured as a function of target volume for a 1-ps pulse duration and constant laser intensity of $I = 2 \times 10^{19}$ W/cm^2. This shows the variation of K$_\beta$/K$_\alpha$ with increasing energy density, achieved by depositing a similar amount of fast-electron energy within decreasing target plasma volumes. Figure 113.5 shows variations in the energy emitted by K$_\alpha$ and K$_\beta$ photons (normalized to the laser energy) for target volumes of 5×10^{-6} mm$^3 < V < 1 \times 10^{-1}$ mm^3. Three distinct regions are highlighted. In region 1 ($V > 10^{-3}$ mm^3) the ratio of energy emitted in K$_\alpha$ and K$_\beta$ is constant, consistent with the cold-material value. In region 2 (5×10^{-6} mm$^3 < V < 1 \times$

10^{-3} mm^3) the energy emitted in K$_\alpha$ remains approximately constant but K$_\beta$ emission is increasingly suppressed for decreasing plasma volumes. This is consistent with M-shell depletion due to collisional ionization from the thermal background plasma. Any shifts in the K$_\beta$ emission as M-shell electrons are being removed, however, are not resolved by our spectrometer. At sufficiently high-energy densities, achieved in region 3 ($V < 5 \times 10^{-6}$ mm^3), the energy in both K$_\alpha$ and K$_\beta$ emission is dramatically suppressed. It is possible that for these very small targets, expansion during the period of active K-shell emission might impact the K$_\alpha$ and K$_\beta$ yields. In all cases, a hot plasma corona of less than solid density is always present but will contribute negligibly to the total K$_\alpha$ and K$_\beta$ signal because the emission is naturally weighted toward higher densities. Nonetheless, the total mass of the solid part is, in all cases, considerably larger than in the preplasma/corona during the time of K-shell emission. Figure 113.5 shows the insensitivity of K$_\alpha$ yield to target mass for volumes ranging between 5×10^{-6} to 1×10^{-3} mm^3, suggesting that a significant fraction of the target remains at solid density. Over the same range, however, K$_\beta$/K$_\alpha$ drops by almost an order of magnitude.
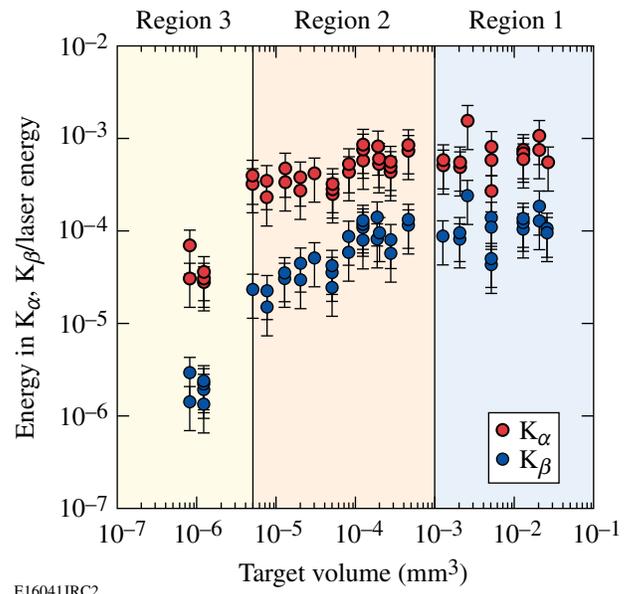
Figure 113.5
Energy in K$_\alpha$ and K$_\beta$ (normalized to the laser energy) as a function of target volume. Three distinct regions of behavior (1, 2, and 3) in the K-photon emission are identified for increasing energy densities (see text for details).

Figure 113.6 shows the experimentally measured variation in K$_\beta$/K$_\alpha$ (left axis; taken from the data presented in Fig. 113.5) as a function of target volume. The error associated with each K$_\beta$/K$_\alpha$ value is given by the standard deviation from a number
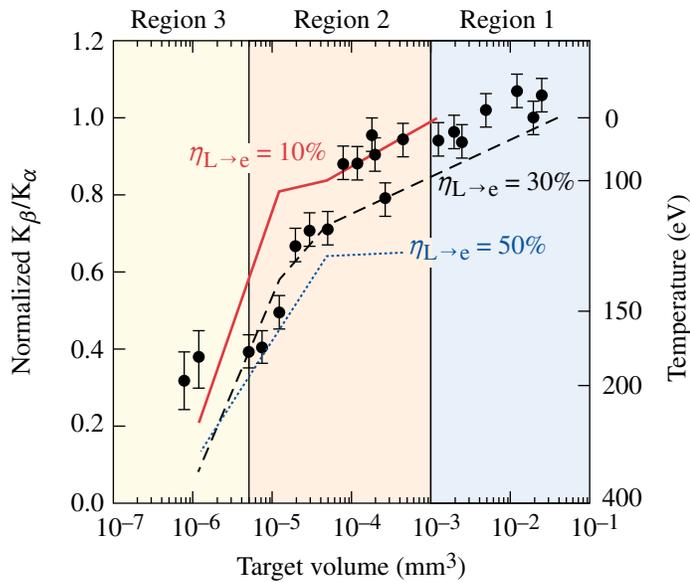
Figure 113.6

K_β/K_α (normalized to the cold-material value—left axis) and bulk-electron temperature (right axis) as a function of target volume. Calculated K_β/K_α [assuming laser-to-electron energy-conversion efficiencies $\eta_{L\rightarrow e}$ = 10% (solid line), 30% (dashed line), and 50% (dotted line)] as a function of target volume.

of shots at a given target volume. The right axis shows the corresponding bulk-electron temperatures using the model shown in Fig. 113.3. A 3.5× reduction in K_β/K_α for target volumes $V = 10^{-6}$ mm^3 below the cold-material value is consistent with a bulk-electron temperature $T_e \approx 200$ eV. The drop in K_α yield in region 3 may indicate temperatures even greater than 200 eV, causing L-shell depletion through collisional ionization.

A thorough analysis of K_β/K_α variations requires numerical calculations to take into account the spatial and temporal variations in the fast-electron distribution and the target heating. This is achieved by combining ion-population distribution calculations from the collisional-radiative code *PrismSPECT*[53] with 3-D numerical target-heating calculations[28] using the implicit-hybrid PIC code *LSP*.[54] The fast-electron source is defined in *LSP* by promoting electrons from the cold bulk-electron population at a rate consistent with a constant fraction ($\eta_{L\rightarrow e}$) of the laser power. The use of a collisional-radiative code to calculate the ion-population distribution is justified because a copper plasma at a few hundred eV and $n_e = 10^{23}$ cm^{-3} reaches a steady state in around 1 ps and the charge-state dynamics in the plasma is governed by the thermal background, with little influence from the MeV-scale fast-electron component of the distribution function.

Results of this calculation are shown in Fig. 113.6. The calculated variation in K_β/K_α as a function of target volume is shown for $\eta_{L\rightarrow e}$ = 10% (solid line), 30% (dashed line), and 50% (dotted line). Good agreement is demonstrated between the experimental K_β/K_α measurements and numerical calculations for $\eta_{L\rightarrow e}$ =

(20±10)% in the cold-material limit (region 1), consistent with the previous section (p. 4) on K_α emission. This demonstrates that the dominant physical phenomena present in the refluxing limit have been reasonably accounted for in the cold K-photon production model. On average, the variation of K_β/K_α is broadly consistent with a mean laser-to-electron energy-conversion efficiency of around 20%, except for the very smallest mass targets. For target volumes $V < 2 \times 10^{-5}$ mm^3, the theoretical curves begin to converge, making data comparisons increasingly challenging within the experimental uncertainties. Nonetheless, the significant reduction of K_β/K_α in this region below the cold-material limit remains consistent with the smallest mass targets, reaching the highest bulk-electron temperatures.

Discussion and Summary

In summary, high-temperature, solid-density plasmas have been produced and characterized on the MTW Laser System and compared to previous measurements from the Vulcan PW laser. Experiments have shown that absolute K_α yields from copper-foil targets, which are not heated significantly by the refluxing process, are constant for laser–plasma interactions in the relativistic regime. The measured K_α yields are compared to a K_α-production model, which shows good agreement, confirming the weak dependence of K_α generation on laser intensity, fast-electron temperature, and fast-electron range for $I > 10^{18}$ W/cm^2. Using this comparison, a laser-to-electron energy-conversion efficiency of $\eta_{L\rightarrow e} = (20\pm10)$% has been inferred in the cold-material limit. Variations in K_β/K_α over a range of target volumes (and energy density) for $T_e > 100$ eV have been measured. Experiments show numerical target-heating calcula-

E16434JRC2

tions are in good agreement with experimental observations over a wide range of target volumes that are broadly consistent with laser-to-electron energy-conversion efficiencies inferred from the simple K_α-production model.

The exploitation of refluxing in small-mass targets offers exciting potential. It provides a readily achievable method for the creation of extremely high-energy-density plasmas using the next generation of multikilojoule-class, high-intensity laser facilities, such as OMEGA EP.[55] These studies will provide new insights into electron generation, transport, and radiative emission of plasmas at unprecedented energy densities and under conditions relevant to fast ignition. On the basis of these experiments, the combined use of absolute K_α yields and K_β/K_α variations with increasing bulk-electron temperatures presents a method for determining the fast-electron-energy content. This implies that for picosecond-pulse-duration interactions in the relativistic regime, the laser energy is more important than the laser intensity for maximizing the fast-electron-energy content. This has far-reaching ramifications for the creation of high-energy-density plasmas using fast-electron–induced isochoric heating. Future experiments on OMEGA EP, for example, will use small-mass targets to access unprecedented energy densities using fast-electron–driven isochoric heating. Variations in the laser intensity and pulse duration up to the multikilojoule, 10-ps regime will make possible the formation of high-temperature, solid-density plasma in the 1- to 10-keV range.

ACKNOWLEDGMENT

REFERENCES

1. F. N. Beg *et al.*, Phys. Plasmas **4**, 447 (1997).

2. E. L. Clark *et al.*, Phys. Rev. Lett. **85**, 1654 (2000).

3. S. P. Hatchett, C. G. Brown, T. E. Cowan, E. A. Henry, J. S. Johnson, M. H. Key, J. A. Koch, A. B. Langdon, B. F. Lasinski, R. W. Lee, A. J. MacKinnon, D. M. Pennington, M. D. Perry, T. W. Phillips, M. Roth, T. C. Sangster, M. S. Singh, R. A. Snavely, M. A. Stoyer, S. C. Wilks, and K. Yasuike, Phys. Plasmas **7**, 2076 (2000).

4. R. D. Edwards *et al.*, Appl. Phys. Lett. **80**, 2129 (2002).

5. M. H. Key, M. D. Cable, T. E. Cowan, K. G. Estabrook, B. A. Hammel, S. P. Hatchett, E. A. Henry, D. E. Hinkel, J. D. Kilkenny, J. A. Koch, W. L. Kruer, A. B. Langdon, B. F. Lasinski, R. W. Lee, B. J. MacGowan, A. MacKinnon, J. D. Moody, M. J. Moran, A. A. Offenberger, D. M. Pennington, M. D. Perry, T. J. Phillips, T. C. Sangster, M. S. Singh, M. A. Stoyer, M. Tabak, G. L. Tietbohl, M. Tsukamoto, K. Wharton, and S. C. Wilks, Phys. Plasmas **5**, 1966 (1998).

6. B. A. Remington *et al.*, Science **284**, 1488 (1999).

7. H.-S. Park, D. M. Chambers, H.-K. Chung, R. J. Clarke, R. Eagleton, E. Giraldez, T. Goldsack, R. Heathcote, N. Izumi, M. H. Key, J. A. King, J. A. Koch, O. L. Landen, A. Nikroo, P. K. Patel, D. F. Price, B. A. Remington, H. F. Robey, R. A. Snavely, D. A. Steinman, R. B. Stephens, C. Stoeckl, M. Storm, M. Tabak, W. Theobald, R. P. J. Town, J. E. Wickersham, and B. B. Zhang, Phys. Plasmas **13**, 056309 (2006).

8. M. Tabak *et al.*, Phys. Plasmas **1**, 1626 (1994).

9. M. H. Key, Phys. Plasmas **14**, 055502 (2007).

10. P. Gibbon and E. Förster, Plasma Phys. Control. Fusion **38**, 769 (1996).

11. M. Tatarakis *et al.*, Phys. Rev. Lett. **81**, 999 (1998).

12. M. Borghesi *et al.*, Phys. Rev. Lett. **83**, 4309 (1999).

13. L. Gremillet *et al.*, Phys. Rev. Lett. **83**, 5015 (1999).

14. J. A. Koch *et al.*, Phys. Rev. E **65**, 016410 (2001).

15. Y. T. Li *et al.*, Phys. Rev. E **64**, 046407 (2001).

16. R. J. Kingham and A. R. Bell, Phys. Rev. Lett. **88**, 045004 (2002).

17. J. R. Davies *et al.*, Phys. Rev. E **56**, 7193 (1997).

18. J. D. Hares *et al.*, Phys. Rev. Lett. **42**, 1216 (1979).

19. S. J. Gitomer *et al.*, Phys. Fluids **29**, 2679 (1986).

20. B. Luther-Davies, A. Perry, and K. A. Nugent, Phys. Rev. A **35**, 4306 (1987).

21. H. Chen, B. Soom, B. Yaakobi, S. Uchida, and D. D. Meyerhofer, Phys. Rev. Lett. **70**, 3431 (1993).

22. K. B. Wharton *et al.*, Phys. Rev. Lett. **81**, 822 (1998).

23. K. Yasuike *et al.*, Rev. Sci. Instrum. **72**, 1236 (2001).

24. S. C. Wilks *et al.*, Phys. Rev. Lett. **69**, 1383 (1992).

25. G. Gregori *et al.*, Contrib. Plasma Phys. **45**, 284 (2005).

26. S. N. Chen *et al.*, Phys. Plasmas **14**, 102701 (2007).

27. W. Theobald, K. Akli, R. Clarke, J. Delettrez, R. R. Freeman, S. Glenzer, J. Green, G. Gregori, R. Heathcote, N. Izumi, J. A. King, J. A. Koch, J. Kuba, K. Lancaster, A. J. MacKinnon, M. Key, C. Mileham, J. Myatt, D. Neely, P. A. Norreys, H.-S. Park, J. Pasley, P. Patel, S. P. Regan, H. Sawada, R. Shepherd, R. Snavely, R. B. Stephens, C. Stoeckl, M. Storm, B. Zhang, and T. C. Sangster, Phys. Plasmas **13**, 043102 (2006).

28. J. Myatt, W. Theobald, J. A. Delettrez, C. Stoeckl, M. Storm, T. C. Sangster, A. V. Maximov, and R. W. Short, Phys. Plasmas **14**, 056301 (2007).

29. P. M. Nilson, W. Theobald, J. Myatt, C. Stoeckl, C. Mileham, I. A. Begishev, J. Brown, J. D. Zuegel, R. Betti, D. D. Meyerhofer, and T. C. Sangster, "Laser-to-Electron Energy Conversion Efficiency and Bulk Heating of Solid-Density Matter During High-Intensity Laser-Plasma Interactions in the Refluxing Limit," submitted to Physical Review Letters.

30. K. Eidmann *et al.*, J. Quant. Spectrosc. Radiat. Transf. **81**, 133 (2003).

31. A. Saemann *et al.*, Phys. Rev. Lett. **82**, 4843 (1999).

32. Z. Jiang *et al.*, Phys. Plasmas **2**, 1702 (1995).

33. A. Rousse *et al.*, Phys. Rev. E **50**, 2200 (1994).

34. A. J. Mackinnion, Phys. Rev. Lett. **88**, 215006 (2002).

35. R. A. Snavely, M. H. Key, S. P. Hatchett, T. E. Cowan, M. Roth, T. W. Phillips, M. A. Stoyer, E. A. Henry, T. C. Sangster, M. S. Singh, S. C. Wilks, A. MacKinnon, A. Offenberger, D. M. Pennington, K. Yasuike, A. B. Langdon, B. F. Lasinski, J. Johnson, M. D. Perry, and E. M. Campbell, Phys. Rev. Lett. **85**, 2945 (2000).

36. R. Kodama *et al.*, Phys. Plasmas **8**, 2268 (2001).

37. D. C. Eder *et al.*, Appl. Phys. B **70**, 211 (2000).

38. R. Kodama *et al.*, Nature **412**, 798 (2001).

39. M. Green and V. E. Cosslett, J. Phys. D **1**, 425 (1968).

40. H. Kolbenstvedt, J. Appl. Phys. **38**, 4785 (1967).

41. V. Bagnoud, I. A. Begishev, M. J. Guardalben, J. Puth, and J. D. Zuegel, Opt. Lett. **30**, 1843 (2005).

42. C. Stoeckl, W. Theobald, T. C. Sangster, M. H. Key, P. Patel, B. B. Zhang, R. Clarke, S. Karsch, and P. Norreys, Rev. Sci. Instrum. **75**, 3705 (2004).

43. F. Brunel, Phys. Rev. Lett. **59**, 52 (1987).

44. N. A. Ebrahim *et al.*, Phys. Rev. Lett. **45**, 1179 (1980).

45. K. Estabrook and W. L. Kruer, Phys. Fluids **26**, 1888 (1983).

46. A. R. Bell *et al.*, Plasma Phys. Control. Fusion **39**, 653 (1997).

47. F. Pisani *et al.*, Phys. Rev. E **62**, R5927 (2000).

48. W. Bambynek *et al.*, Rev. Mod. Phys. **44**, 716 (1972).

49. Previously published data[27] incorrectly accounted for photon attenuation by the target. The diagnostic observation angle with respect to the target normal was incorrectly stated as 16°; in fact it was 60° and the present data set takes the correct angle into account.

50. L. Robson *et al.*, Nat. Phys. **3**, 58 (2007).

51. J. Fuchs *et al.*, Nat. Phys. **2**, 48 (2006).

52. P. K. Patel *et al.*, Phys. Rev. Lett. **91**, 125004 (2003).

53. Prism Computational Sciences, Inc., Madison, WI 53711.

54. D. R. Welch *et al.*, Phys. Plasmas **13**, 063105 (2006).

55. C. Stoeckl, J. A. Delettrez, J. H. Kelly, T. J. Kessler, B. E. Kruschwitz, S. J. Loucks, R. L. McCrory, D. D. Meyerhofer, D. N. Maywar, S. F. B. Morse, J. Myatt, A. L. Rigatti, L. J. Waxer, J. D. Zuegel, and R. B. Stephens, Fusion Sci. Technol. **49**, 367 (2006).

A High-Resolution Optical Transition Radiation Diagnostic for Fast-Electron Transport Studies

Introduction

High-current relativistic electron beams are generated by high-intensity laser interactions with solids.[1] These electron beams may have applications in compact, tabletop-based, high-brightness laser–plasma particle accelerators,[2] narrowband x-ray sources for medical applications,[3] x-ray sources for high-density inertial fusion energy (IFE) target backlighter radiography,[4] and collimated electron beams required for the fast-ignition approach to IFE.[5] The MeV fast electrons are generated in high-intensity laser–matter interactions, and their subsequent motion must be understood if their potential applications are to be fully realized. A promising technique that provides information about the fast-electron energy and divergence, as well as spatial and temporal distribution inside the target, is spatially resolving the spectrum of transition radiation (TR).[6] TR is emitted when a charged particle passes through a refractive index interface,[7] as in the case of fast electrons exiting a metal foil into vacuum. The emitted electromagnetic energy is undetectably small for a single electron; however, laser–solid interactions typically produce a large number of fast electrons whose individual contributions sum to provide a measurable signal. If the fast-electron beam possesses a strongly correlated longitudinal electron-density structure, the electromagnetic emission can undergo a considerable coherent enhancement, producing coherent transition radiation (CTR).[8] This enhancement is restricted to a narrow spectral band determined by the details of the longitudinal fast-electron density profile. Electrons accelerated by laser–matter interactions have the required longitudinal density profile to generate the CTR.[9] The exact form of this profile depends on the nature of the dominant acceleration mechanism. For example, the resonance absorption process[10] accelerates electrons into the target once per optical cycle, whereas the $\vec{v} \times \vec{B}$ component of the Lorentz force[11] accelerates electrons twice every optical cycle. These electrons then travel through the target as a train of microbunches separated in time by an optical period or half an optical period, generating a CTR signal at the fundamental or second harmonic of the laser frequency, respectively. The spatial-intensity distribution and spectrum of the CTR emission provide information about the electron-transport physics in solid density.[12]

Experimental Setup

A transition radiation diagnostic (TRD) has been designed to acquire high-resolution images of rear-side optical emission at the second harmonic ($\lambda \sim 527$ nm) of the laser frequency from laser-illuminated planar targets. In the optical design shown in Fig. 113.7, a 20× infinity corrected objective,[13] with a 20-mm working distance, a numerical aperture of 0.42, a 1.2-mm field of view, a 1.6-μm depth of focus, and a 0.7-μm resolving power, collects the optical emission from the target's rear surface. A 150-μm-thick sacrificial glass microscope cover slip, acting as a debris shield, is placed on the target side of the objective. The objective is mounted on a motorized 1-D linear actuator[14] with a 10-mm full range of motion and a 20-nm step size. The objective has an exit pupil diameter of 8.4 mm. A 4-mm-thick Schott KG5 glass filter with $\sim 10^{-10}$ transmission at $\lambda = 1053$ nm and $\sim 70\%$ transmission from $\lambda = 400$ to 600 nm prevents laser light from propagating through the system.[15] A 200-mm-focal-length achromatic lens focuses the light through a pinhole that blocks stray light. A narrowband 50/50 beam splitter steers the signal beam through 90°, and a unit magnification optical arrangement relays the light to the detector. A 24-nm bandpass filter centered on $\lambda = 529$ nm is placed in the collimated region of this path.[16] Optical-quality, neutral-density (ND) filters can be placed here to control the level of the signal without significantly compromising the spatial resolution. The overall transmission of the TRD at $\lambda = 527$ nm is $\sim 20\%$. The detector is a Spectral Instruments (SI) 800-series charge-coupled-device (CCD) camera with a dynamic range of 10^4 (Ref. 17). The 14-mm × 14-mm front-illuminated chip is composed of 1024 × 1024, 13.5-μm × 13.5-μm pixels with a full-well capacity of 10^5 electrons. At $\lambda = 527$ nm the CCD quantum efficiency is 20%. The CCD chip is cooled to –40°C to minimize dark current (<0.1 e$^-$/pixel/s). The readout rate for the 16-bit analog-to-digital converter can be varied from 100 to 800 kHz, with a read noise of <5 electrons at the slowest speed.

To obtain high-resolution images of the target's rear-surface emission, the microscope objective must be positioned 20 mm away from the rear surface with $\sim$1-μm precision. This is accomplished by using the second arm of the optical system
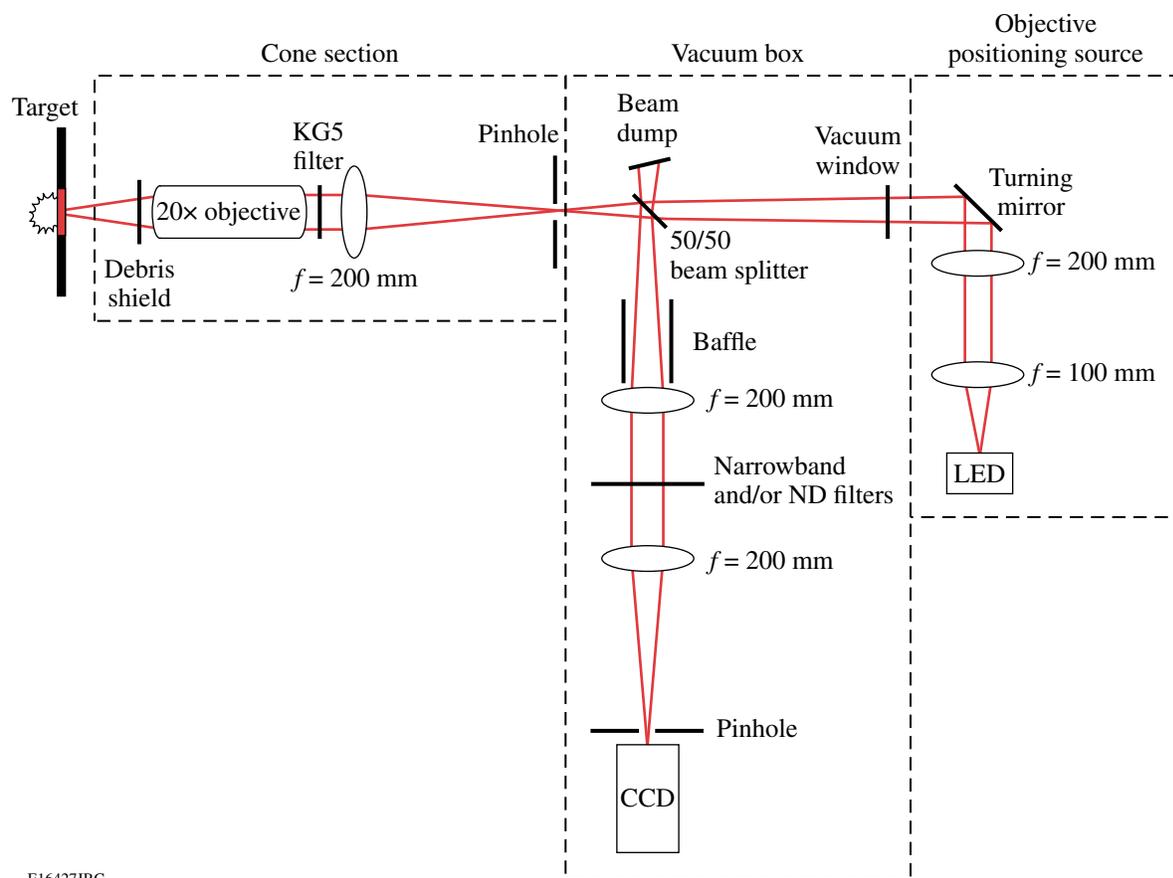
Figure 113.7

A schematic layout of the TRD optical system. Light emitted from the rear side of the target is magnified and relayed to a CCD camera. Filters and pinholes minimize background contributions. The right arm of the system is used only for pre-shot focusing on the rear surface.

(Fig. 113.7). Light from an ultrabright green LED[18] is transmitted through the collection optics and reflected off the target's rear side. Small-scale surface features present on the rear surface of the target act as focusing fiducials and are imaged onto the CCD camera. The camera's external shutter control channel is used to synchronize the LED illumination with the CCD chip exposure period. The CCD exposure time and readout speed are selected to accommodate the ND filter strength for the duration of this procedure. They are returned to standard values of 1 s and 400 kHz, respectively, for the experiment. The baffle and beam dump shown in Fig. 113.7 minimize the propagation of stray LED light through the system during positioning.

The TRD shown in Fig. 113.8 is comprised of two sections: The cone section resides inside the target chamber and is mounted on a target chamber port flange. The rear section, the TRD vacuum box, is attached to the outside face of the cone section. The rear panel of the vacuum box can be removed (as
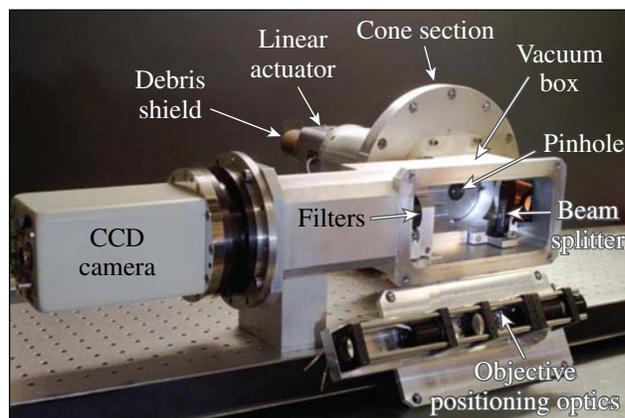

Figure 113.8

A photograph of the TRD with the rear-side access panel removed and laid along side. A detailed discussion of the device is found in the text.

shown in Fig. 113.8) for easy access to the filtering optics and pinhole between shots. Vent holes in the KG5 filter mount link the TRD vacuum box volume to that of the target chamber, allowing the TRD to be pumped. This allows the CCD camera to be operated in vacuum without an independent vacuum system. Operating pressure is reached within 12 min. The TRD vacuum box can be isolated from the main volume of the target chamber by replacing the KG5 filter mount and allowing the KG5 filter to act as a vacuum window. A computer-controlled linear actuator provides high-precision positioning of the microscope objective (see Fig. 113.9). The objective is mounted to the carriage and driven by a pico-motor with a 20-nm step size over a 10-mm range. An encoder using a holographically ruled grating[19] provides closed-loop control of the objective position with ~0.5-μm precision. The system is enclosed in an aluminum casing. To mitigate the risks posed to the actuator circuitry by electromagnetic pulses, it is disconnected during the shot. The actuator maintains its position when powered down.
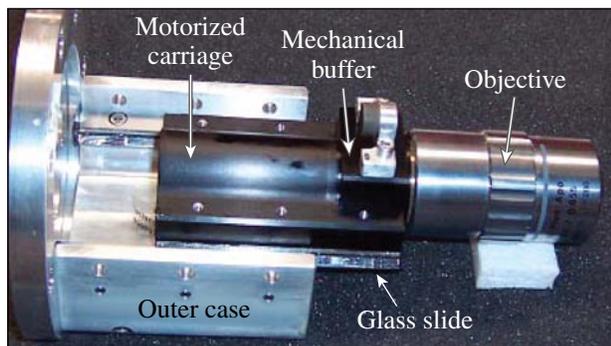
E16429JRC

Figure 113.9

The microscope objective is firmly held by the carriage, which glides in and out smoothly on rails attached to the inside of the outer case. The New Focus pico motor (not shown) is housed in the upper outer case and attached to the carriage via the mechanical buffer. It moves the objective in 20-nm steps over a range of 10 mm. Attached to the under side of the carriage is a glass slide encoded with a holographic ruler with 1-μm graduations. The hologram is read out from below by a reader embedded in the lower outer case to provide closed-loop positioning control.

The TRD was deployed on experiments conducted on LLE's Multi-Terawatt (MTW) Laser Facility.[20] This system is a front-end prototype for OMEGA EP.[21] The TRD is mounted on the MTW target chamber (shown in Fig. 113.10), where it occupies the port directly facing the off-axis parabolic focusing mirror. This assignment drove many components of the mechanical design. Significant amounts of γ radiation are produced in the forward direction during a high-intensity laser-target shot.[22] To prevent this radiation from contaminating the CTR signal, the system is folded through 90° so that the detector can be
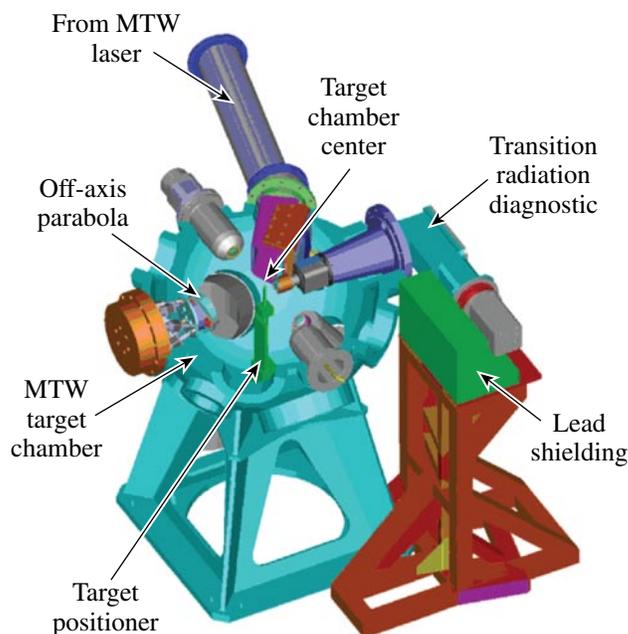
E16430JRC

Figure 113.10

A 3-D model of the MTW target chamber. An off-axis parabola (OAP) steers the MTW laser beam to focus at target chamber center (TCC). The TRD is housed in the port directly opposite the OAP. It images the rear-side optical emission from a normally illuminated target placed at TCC. The TRD optical system is folded through 90° so that the CCD camera lies in the γ-ray shadow of the TRD lead shielding.

shielded behind a 10-cm-thick lead brick wall. An additional 2-mm lead shield (not shown in Fig. 113.10) is placed around the CCD camera to minimize single hits by scattered γ rays arriving from the rear and top sides. Figure 113.11 illustrates the effect of the lead shielding in suppressing the number of γ-ray single hits. The images were taken under nearly identical experimental conditions. The solid-curve histogram was taken with no lead shielding in place. Individual γ rays are seen to produce pixel values of up to ~4000 analog-to-digital units. A reduction in the number of single hits by more than an order of magnitude was observed on the subsequent shot with the lead shielding in place (dashed-curve histogram).

System Performance

The calculated optical transmission curve for the TRD is shown in Fig. 113.12. The transmission of individual optical components was obtained either from the corresponding data sheet or by direct measurement using a spectrophotometer.[23] The curve shows that the transmission varies by 15 orders of magnitude between λ = 1053 nm and λ = 527 nm, so the laser light makes no contribution to an image obtained using the TRD. This was verified with 3-J laser shots taken on 20-μm-

thick, 500-μm-sq iron foils with the 24-nm bandpass filter replaced by an RG1000 filter glass.[15] This material efficiently transmits at the laser frequency while strongly attenuating its second harmonic. The results indicate that no light at the laser frequency enters the optical system.

The optical resolution of the TRD was determined by measuring the modulation transfer function (MTF).[24] The MTF of an imaging system is a measure of the image contrast at the object spatial frequencies; it describes with what efficiency
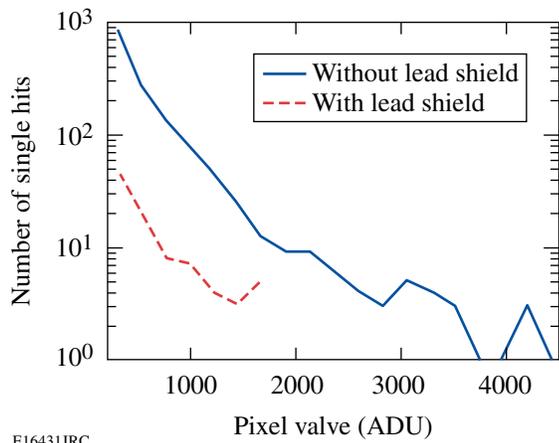
Figure 113.11
Histogram of the number of γ-ray single hits from two shots conducted under almost identical conditions. The pixel values are shown in analog-to-digital units (ADU's). The solid curve corresponds to a shot taken without lead shielding; the dashed curve corresponds to a shot with the lead shielding in place, demonstrating the efficiency of TRD shielding in suppressing the number of γ-ray photons incident on the CCD.
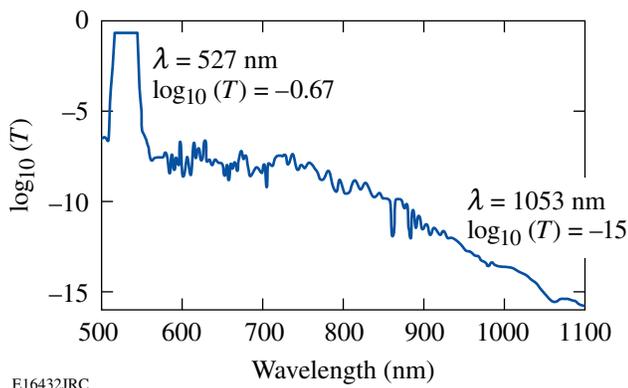
Figure 113.12
The optical transmission curve for the TRD. The transmission efficiency at the laser second harmonic, $\lambda = 527$ nm, is ~20%. The transmission efficiency at the laser wavelength, $\lambda = 1053$ nm, is ~15 orders of magnitude lower.

the system can pass each spatial frequency in the object plane. The optical resolution can be defined as the reciprocal of the highest frequency passed at which the contrast is maintained above a specified value. Tatian[25] has shown that the MTF can be obtained directly by analyzing equally spaced samples of the image edge function, which is the image space conjugate of a back-illuminated half plane as described below.

The experimental half plane was provided by an edge in a scanning electron microscope (SEM) 400-resolution grid [see Fig. 113.13(b)]. The grid was placed in the focal plane of the 20$\times$ objective, and an ultrabright LED illuminated the grid from its front side. The illumination was evenly distributed over the object plane to ensure good contrast in the object. The amount of stray light entering the optical system was minimized by mounting the SEM grid in a pinhole and constructing a set
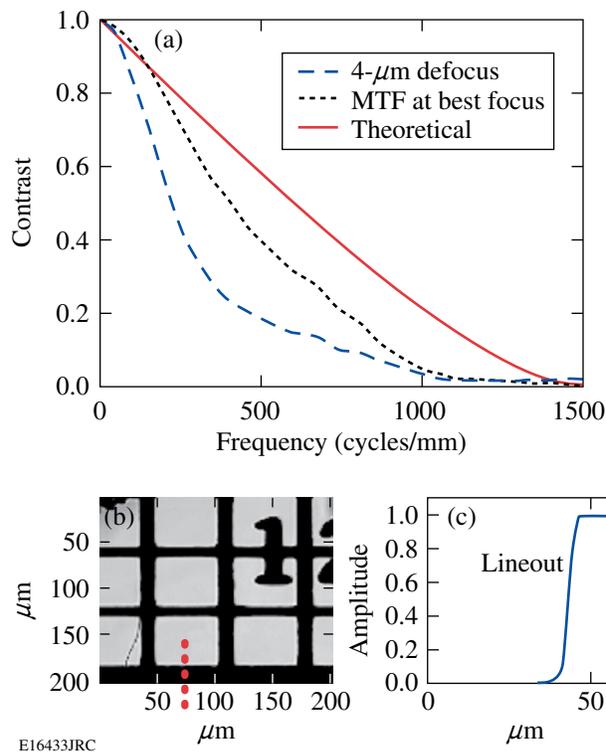
Figure 113.13
(a) The modulation transfer function (MTF) of the TRD. The curves are produced by analyzing images obtained using the TRD fitted with a 20$\times$ microscope objective. The solid line shows the theoretical MTF. The measured MTF at best focus is indicated by the dotted line; the contrast falls to ~1/10 at around 900 cycles/mm corresponding to a spatial resolution of ~1.1 μm. The dashed-line MTF expresses the effect of defocusing the collection optics. A 4-μm defocus reduces the optical performance of the system. (b) A section of an SEM 400-resolution grid. The dotted line indicates the position from which the lineout shown in (c) was taken. The lineout is normalized and used to calculate the MTF.

of opaque screens around the objective. The objective was positioned so that the grid was slightly defocused before being scanned through best focus. An image of the SEM grid was obtained every 500 nm, after which the images were post-processed to obtain the MTF. Figure 113.13(c) shows a normalized lineout, at best focus, taken through the image edge function. The CCD camera cannot sufficiently sample the image edge function with a 20× magnification, so it was necessary to linearly interpolate the data to effectively double the sampling rate to avoid aliasing in the MTF. Figure 113.13(a) shows the MTF for the case where a debris shield was placed in front of the objective. The solid line is the theoretical MTF; the dotted line shows the measured MTF at best focus. The limit of the spatial resolution is defined here to be the point at which the contrast ratio is ~10%. At best focus this corresponds to a spatial frequency of approximately 900 cycles/mm or 1.1 μm. Since it was necessary to linearly interpolate the image edge function, the value of 1.1 μm corresponds to the MTF of the optical part of the system. The CCD camera limits the optical resolution of the full system to ~1.4 μm, the size of a CCD pixel over the full field of view. This pixel-size–imposed limit could be reduced by increasing the system's magnification. The effect of defocus is illustrated in Fig. 113.13(a) by the dashed line MTF. A 4-μm defocus of the TRD collection optics reduces the MTF-limited resolution

to about 1.5 μm at 10% contrast with the contrast falling about twice as fast as in the best-focus case.

The TRD has been fielded on experiments conducted to diagnose electron transport in a variety of solid materials of varying thickness under differing laser conditions. Figure 113.14 shows three characteristic images of the rear-side emission in both a linear (top) and a logarithmic (bottom) scale. From left to right the targets are 20-μm-thick aluminum, 30-μm-thick aluminum and 50-μm-thick copper; all are 500 μm in the transverse directions. These images are produced by light emitted at the target's rear surface in a narrow spectral window around $\lambda = 527$ nm, the laser second harmonic. The emission can be explained as CTR caused by a density-modulated relativistic electron beam generated by the $\vec{v} \times \vec{B}$ component of the Lorentz force. The upper-frame images clearly indicate the presence of small-scale structures, ~≥2 μm in the emission region, which is indicative of electron-beam filamentation.[26] The lower-frame images show that the filamentary structures are superimposed onto a ring-like structure. The annular pattern is almost always observed and suggests that only the electrons accelerated along the beam envelope possess the required density modulation to be observed with the CTR technique. Our calculations suggest that these electrons make up only a small fraction, <5%, of the total fast-electron population.
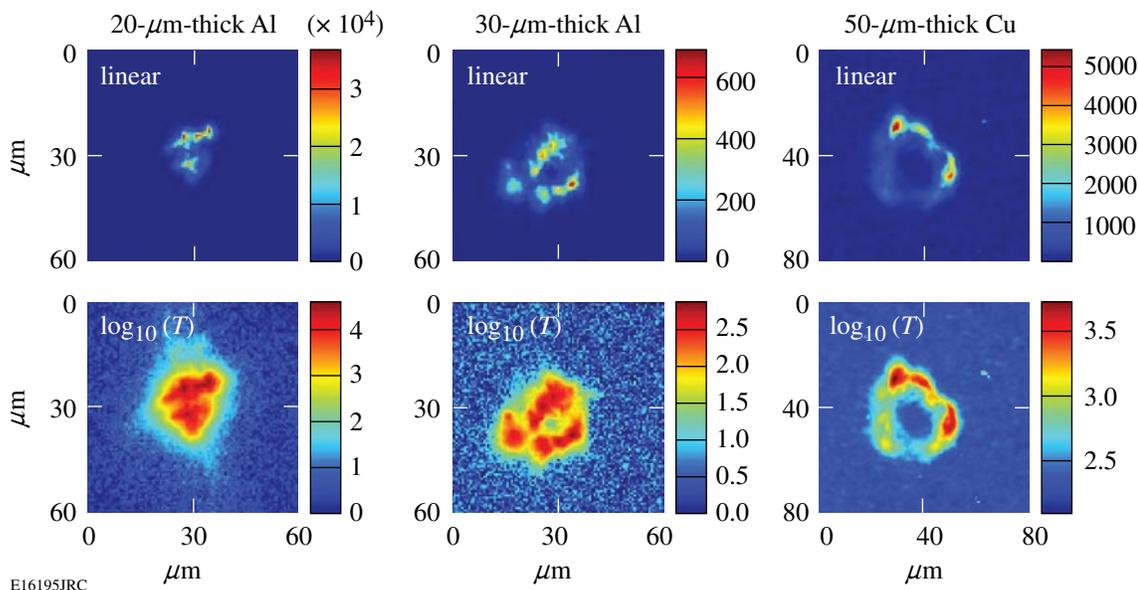
Figure 113.14
Images of the rear-side optical emission from thin foil targets normally illuminated with a laser intensity of 10^{19} W/cm^2. The upper row shows the images plotted on a linear scale, while the lower row shows the corresponding log-scale representation. From left to right the images are from 20-μm-thick aluminum, 30-μm-thick aluminum, and 50-μm-thick copper. The upper-frame images indicate the presence of filamentary structures in the emission pattern. The lower images are demonstrating that the background emission pattern possesses an annular property.

Figure 113.14 further indicates that the spatial size of the emission region increases with target thickness. This is presented explicitly in Fig. 113.15, where the radius of the observed emission pattern is plotted against the target thickness. A least squares fit to the data shows that the beam diverges inside the target with a half angle of ~16°. The corresponding intercept with the radius axis indicates that the beam emerges from a source of radius ~4 μm, consistent with the spatial size of the focused MTW laser beam.

E16198JRC
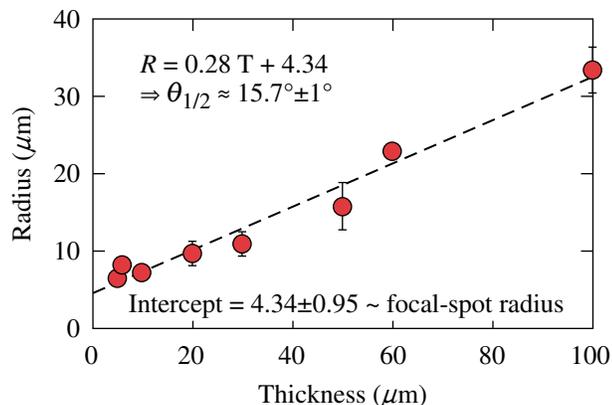
Figure 113.15
The size of the rear-surface emission region grows with target thickness. The growth is consistent with a fast-electron divergence angle of 16°. The data has been fitted using a least squares routine. The intercept of the least squares fit with the radius axis, representing the size of the electron source, is ~4.5 μm and consistent with the size of the laser focus.

Summary

A coherent transition radiation diagnostic has been developed to image the rear-side emission from high-intensity-laser–irradiated foil targets. The device has been optimized to measure radiation in a 24-nm bandwidth around $\lambda = 529$ nm with a dynamic range of 10^4. The transmission at $\lambda = 527$ nm is 15 orders of magnitude higher than the transmission at the laser frequency, and no laser light has been detected in the system during experiments. We have demonstrated, by measuring the modulation transfer function, that the CCD pixel size limits spatial resolution to 1.4 μm. The diagnostic is being used to infer information about the transport of high-current relativistic electron beams through solid targets. Small-scale structures, ~2 μm in size, have been observed in the rear-surface emission of metal foils irradiated with laser intensities of ~10^{19} W/cm^2. These are indicative of electron-beam filamentation.

REFERENCES

1. M. H. Key, M. D. Cable, T. E. Cowan, K. G. Estabrook, B. A. Hammel, S. P. Hatchett, E. A. Henry, D. E. Hinkel, J. D. Kilkenny, J. A. Koch, W. L. Kruer, A. B. Langdon, B. F. Lasinski, R. W. Lee, B. J. MacGowan, A. MacKinnon, J. D. Moody, M. J. Moran, A. A. Offenberger, D. M. Pennington, M. D. Perry, T. J. Phillips, T. C. Sangster, M. S. Singh, M. A. Stoyer, M. Tabak, G. L. Tietbohl, M. Tsukamoto, K. Wharton, and S. C. Wilks, Phys. Plasmas **5**, 1966 (1998).

2. T. Katsouleas, Nature **444**, 688 (2006).

3. K. K. Kainz *et al.*, Med. Phys. **31**, 2053 (2004).

4. H.-S. Park, D. M. Chambers, H.-K. Chung, R. J. Clarke, R. Eagleton, E. Giraldez, T. Goldsack, R. Heathcote, N. Izumi, M. H. Key, J. A. King, J. A. Koch, O. L. Landen, A. Nikroo, P. K. Patel, D. F. Price, B. A. Remington, H. F. Robey, R. A. Snavely, D. A. Steinman, R. B. Stephens, C. Stoeckl, M. Storm, M. Tabak, W. Theobald, R. P. J. Town, J. E. Wickersham, and B. B. Zhang, Phys. Plasmas **13**, 056309 (2006).

5. M. Tabak *et al.*, Phys. Plasmas **1**, 1626 (1994).

6. S. D. Baton *et al.*, Phys. Rev. Lett. **91**, 105001 (2003).

7. V. L. Ginzburg, Phys.-Usp. **39**, 973 (1996).

8. J. Zheng *et al.*, Phys. Plasmas **10**, 2994 (2003).

9. J. C. Adam, A. Héron, and G. Laval, Phys. Rev. Lett. **97**, 205006 (2006).

10. W. L. Kruer, *The Physics of Laser Plasma Interactions*, Frontiers in Physics (Westview Press, Boulder, CO, 2003), pp. 39–43.

11. S. C. Wilks *et al.*, Phys. Rev. Lett. **69**, 1383 (1992).

12. H. Popescu *et al.*, Phys. Plasmas **12**, 063106 (2005).

13. M-plan Apo 20×, Mitutoyo, Japan.

14. New Focus, Inc., a division of Brookham, San Jose, CA, 2004, http://www.newfocus.com (14 December 2004).

15. Schott North America, Inc., Elmsford, NY 10523.

16. Semrock, Rochester, NY 14624.

17. Spectral Instruments, Tucson, AZ 85745 (http://www.specinst.com/files/datasheets/4204-.pdf).

18. Luxeon III Star, Philips Lumileds Lighting Company, San Jose, CA 95131.

19. LIP 481R, Heidenhain, 83301 Traunreut, Germany.

20. V. Bagnoud, in *Frontiers in Optics 2004* (Optical Society of America, Rochester, NY, 2004), Paper FMM2.

21. J. H. Kelly, L. J. Waxer, V. Bagnoud, I. A. Begishev, J. Bromage, B. E. Kruschwitz, T. J. Kessler, S. J. Loucks, D. N. Maywar, R. L. McCrory, D. D. Meyerhofer, S. F. B. Morse, J. B. Oliver, A. L. Rigatti, A. W. Schmid, C. Stoeckl, S. Dalton, L. Folnsbee, M. J. Guardalben, R. Jungquist, J. Puth, M. J. Shoup III, D. Weiner, and J. D. Zuegel, J. Phys. IV France **133**, 75 (2006).

22. S. P. Hatchett, C. G. Brown, T. E. Cowan, E. A. Henry, J. S. Johnson, M. H. Key, J. A. Koch, A. B. Langdon, B. F. Lasinski, R. W. Lee, A. J. MacKinnon, D. M. Pennington, M. D. Perry, T. W. Phillips, M. Roth, T. C. Sangster, M. S. Singh, R. A. Snavely, M. A. Stoyer, S. C. Wilks, and K. Yasuike, Phys. Plasmas **7**, 2076 (2000).

23. Lambda900 Spectrophotometer, PerkinElmer, Waltham, MA 02451.

24. J. W. Goodman, *Introduction to Fourier Optics*, 3rd ed. (Roberts and Company Publishers, Englewood, CO, 2005), Chap. 6, p. 127.

25. B. Tatian, J. Opt. Soc. Am. **55**, 1014 (1965).

26. L. Gremillet, G. Bonnaud, and F. Amiranoff, Phys. Plasmas **9**, 941 (2002).

Performance of Direct-Drive Cryogenic Targets on OMEGA

Introduction

In the inertial confinement fusion (ICF) approach to fusion, a spherical shell filled with a deuterium–tritium (DT) mixture is compressed to reach a temperature of 10 to 12 keV in the lower-density central core region (hot spot) to initiate a burn wave through the higher-density colder main fuel surrounding the core.[1–3] The main fuel areal density (ρR) at that time must be large enough to burn a significant fraction of the fuel.[1,2] The peak areal density depends mainly on the fuel adiabat (defined as a ratio of the shell pressure to the Fermi-degenerate pressure at the shell density) and laser energy:[4]

$$(\rho R)_{\max} = \frac{2.6}{\alpha^{0.54}} E_{MJ}^{1/3}. \qquad (1)$$

To study the physics of low-adiabat, high-compression fuel assembly, a series of experiments with cryogenic D_2 and DT fuel was designed and performed on OMEGA.[5] Figure 113.16


TC8038JRC
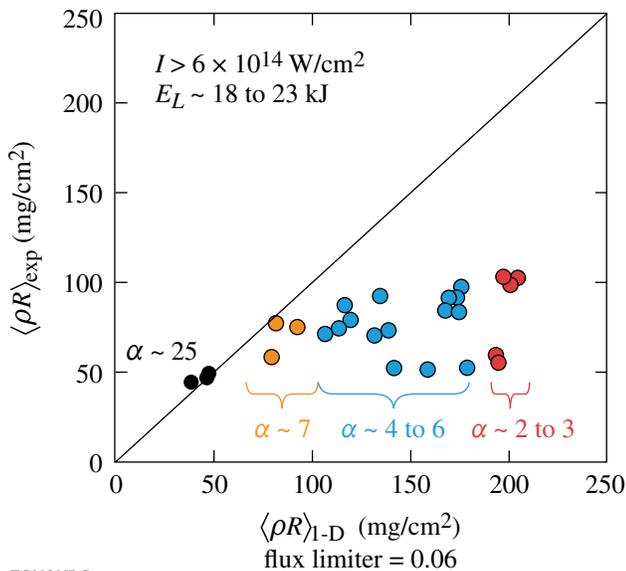
Figure 113.16
Measured neutron-averaged areal density $\langle \rho R \rangle$ as a function of the simulated value using the hydrocode *LILAC*, which uses a thermal conduction model with a constant flux limiter. The drive intensities were above 6×10^{14} W/cm^2 and the laser energy varied from 18 to 23 kJ.

summarizes the experimental results reported earlier.[6,7] The targets used in these experiments were D_2-filled CD shells with an outer diameter of ~860 μm, a shell thickness of 3 to 5 μm, and a cryogenic layer thickness between 92 and 98 μm. The targets were driven with shaped laser pulses at peak intensities of 6 to 10×10^{14} W/cm^2 to set the fuel adiabat at $\alpha = 2$ to 25. Figure 113.16 compares the experimental areal density $\langle \rho R \rangle_{\exp}$ inferred from the energy loss of the secondary protons[8] while they propagate through the compressed fuel and the simulated areal density $\langle \rho R \rangle_{1-D}$ averaged over the 1-D neutron-production history calculated using the hydrocode *LILAC*.[9] The constant flux-limiter thermal conduction model[10] with $f = 0.06$ was used in such simulations. As seen in the figure, the experimental data significantly deviate from simulation results for the implosions with a mid-to-low designed adiabat when the predicted $\langle \rho R \rangle_{1-D} > 100$ mg/cm^2. The goal of the current study presented here is to identify the main sources of the measured $\langle \rho R \rangle$ deviation from the theoretical predictions. Equation (1) is used for guidance in this study. According to this equation, the observed degradation in the areal density comes from the underestimation of the predicted adiabat.

In this article we consider several sources for the adiabat degradation during the implosion, including the shock heating and the preheat due to the suprathermal electrons. Based on the result of this study, target designs were optimized using the improved nonlocal thermal-conduction model implemented in the 1-D hydrodynamic code *LILAC*. High-areal-density[11] cryogenic fuel assembly with $\langle \rho R \rangle > 200$ mg/cm^2 has been achieved on OMEGA in designs where the shock timing was optimized and the suprathermal-electron preheat generated by the two-plasmon-decay instability was mitigated. The following sections (1) describe the modeling of the shock heating; (2) consider both the preheat effects due to the suprathermal electrons and the reduction in the measured areal density due to the burn truncation before the peak shell ρR is reached; and (3) present conclusions.

Modeling of Shock Heating

A typical laser pulse for a low-adiabat, direct-drive design consists of a lower-intensity foot (or, as shown in Fig. 113.17,

a picket used in adiabat-shaping designs[12,13] to mitigate the Rayleigh–Taylor instability growth[14]), a transition region, and the higher-intensity main pulse. At the beginning of the pulse, a shock wave (SW) is launched into the shell. Its strength determines the shell adiabat α. The compression wave (CW), initiated as the intensity rises during the transition region, must be properly timed to avoid an excessive adiabat increase at the inner part of the shell. Indeed, if the CW catches the SW too early in the shell, the SW strength increases, raising the adiabat. Delaying the CW, on the other hand, steepens up its front and turns into a shock as the CW travels along the density gradient produced by a rarefaction wave (RW) that is formed after the SW breaks out at the inner surface of the cryogenic layer. To prevent an excessive reduction in the fuel areal density, the coalescence of the RW with the CW must occur within the last 10% of the main fuel mass, as observed in calculations. This condition limits allowable mistiming of the shock breakout to $\Delta t_s / t_s \le 5\%$ and constrains the modeling accuracy in the absorbed laser energy E_s during the shock propagation. For a constant-intensity foot pulse, the shock-propagation time is $t_s = \Delta_0 / U_s$, where $U_s \sim \sqrt{P_a}$ is the shock speed and Δ_0 is the initial shell thickness. The ablation pressure scales as[1] $p_a \sim P^{2/3}$, where P is the laser power, and writing $E_s \sim P t_s$ gives $t_s \sim \Delta_0^{3/2} E_s^{-1/2}$. The same scaling can be obtained when the shock is launched by a narrow picket. The shock-breakout time in this case[12] is $t_s \sim \left(E_p^{-1/3} \Delta_0 \right)^{\beta}$, where $\beta = \left[1 - \sqrt{2\gamma(\gamma-2)} \big/ 2(2\gamma-1) \right]^{-1}$, γ is the ratio of specific heats, and t_p and E_p are the picket duration and energy, respectively. For $\gamma > 1.2$, the exponent is $\beta \simeq 3/2$ with less than 10% error, leading to $t_s \sim E_p^{-1/2}$, similar to the case of a constant-intensity pulse. Using $\Delta t_s / t_s < 5\%$, the requirement for the modeling accuracy in the absorbed picket energy becomes $\Delta E_p / E_p < 10\%$.


TC7809JRC
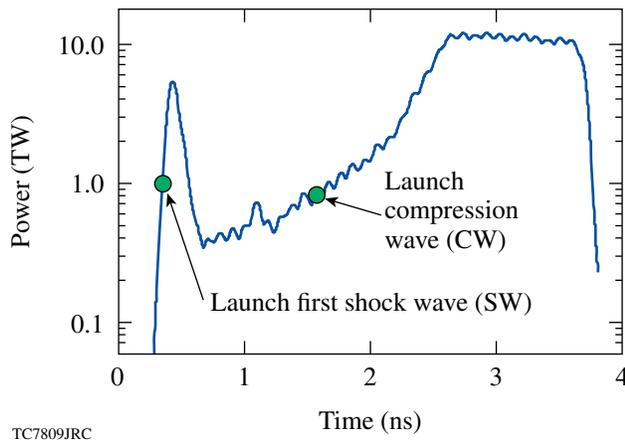
Figure 113.17
A typical pulse shape for the OMEGA direct-drive, low-adiabat design.

Inverse bremsstrahlung is the main absorption mechanism for the $\lambda = 0.351$-μm-wavelength laser irradiation. The absorption fraction depends on the electron-temperature and electron-density profiles.[15] These profiles, in turn, are determined by the thermal conduction near the location of the peak in the laser-energy deposition. Thermal-conduction modeling is crucial, therefore, when calculating the laser-energy deposition. In addition to inverse bremsstrahlung, resonance absorption[15] can be important at early times when the electron density at the critical surface is steep enough for the electric field to tunnel from the laser turning point to the critical density and excite plasma waves. The next two subsections study the contribution of resonance absorption and the effects of nonlocal electron transport to the laser absorption in ICF plasmas.

1. Resonance Absorption Modeling

The effect of resonance absorption was studied for direct-drive–relevant conditions using a numerical solution of the wave equations in planar geometry. The results of these calculations[16] were used to develop a simplified analytical model that can be implemented into hydrodynamic codes to model spherical implosions. The model is based on the approach described in Ref. 15. We consider a p-polarized electromagnetic wave with incident angle θ between the direction of propagation and the density gradient, which points along the z direction. The z component of the electric field E_z tunnels through from the laser turning point to the critical density, depositing a fraction f_A of the incident laser energy into the plasma waves (resonance absorption[15]). Propagating down the density gradient, the energy of these waves is damped into the electrons. Calculations show[16] that the average temperature of the resonance electrons for $\lambda_L = 0.351$-μm-wavelength laser irradiation does not exceed $\sim$5 keV. Resonance absorption, therefore, enhances the local absorption due to the inverse bremsstrahlung. Resonance absorption is calculated by evaluating the energy flux[15] $I_{abs} = \int_0^{\infty} \nu E_z^2 \big/ 8\pi \, dz$, where ν is the damping rate of the plasma waves. The main contribution to this integral comes near the resonance point, in the vicinity of the critical density, resulting in

$$I_{abs} = \frac{\omega L_n}{8} \left(\sin\theta B_{cr} \right)^2, \tag{2}$$

where B_{cr} and L_n are the magnetic field and the density scale length at the critical density, respectively. The resonance field is calculated by multiplying the field amplitude at the turning point, $B_t = 0.9 \, E_0 \left(c / \omega L_n \right)^{1/6}$, by a tunneling factor.[15] Here, E_0 is the laser field in free space. In deriving B_t the laser-energy absorption in the region below critical density was neglected, leading to an overestimate in the resonance field. Corrected

for this absorption and adding the intensity of the incoming and outgoing waves, $f_t E_0^2$ and $(f_t - f_A)E_0^2$, respectively, the magnetic field becomes $0.9\sqrt{2f_t - f_A}\, E_0 (c/\omega L)^{1/6}/2$, where f_t is the fraction of the laser energy that reaches the turning point. Multiplying B_t by the tunneling factor $\exp\left(-\omega/c \int_{z_t}^{z_c} \sqrt{-\epsilon}\, dz\right)$, we obtain $f_A = \phi^2 (2f_t - f_A)/8$ and

$$f_A = \frac{2f_t}{8/\phi^2 + 1}, \tag{3}$$

where $\phi = 2.3\tau \exp\left(-2\tau^3/3\right)$, $\tau = \left(3\omega/2c \int_{z_t}^{z_c} \sqrt{-\epsilon}\, dz\right)^{1/3}$, $\epsilon = 1 - n/n_{cr}$ is the dielectric function, n and n_{cr} are the electron and critical densities, respectively, and z_t and z_c are the position of the turning point and critical density, respectively. Since the incident laser light in ICF experiments consists of a mixture of s and p polarizations, the resonance absorption fraction in a hydrocode simulation is taken as a half value predicted by Eq. (3). Simulations show that Eq. (3) agrees very well with the results of more rigorous calculations.[16]

The tunneling factor depends on the density scale length at the critical surface. Thus, an accurate calculation of both the inverse bremsstrahlung and resonance absorption relies on thermal transport modeling, which affects hydrodynamic profiles in the energy-deposition region. The next subsection discusses electron thermal transport in laser-produced plasmas.

2. Heat-Transport Modeling

Because of the steep temperature and density profiles where the laser deposition is at maximum, the validity of Spitzer thermal conduction[17] breaks down (the mean free path of the heat-carrying electrons is comparable to or larger than the temperature scale length). In a model using flux limitation,[10] the thermal flux is calculated as a fraction f of the free-stream flux $q_{fs} = nTv_T$, when the Spitzer heat flux $q_{sp} > f q_{fs}$. Here, $v_T = \sqrt{T/m}$ is the electron thermal velocity and m, T, and n are the electron mass, temperature, and free electron density, respectively. Since the flux-limiter value f cannot be determined directly from the physical principles, its value, usually taken to be a constant in time, is obtained by comparing the simulation results with experimental observables. Remarkably, such a simple model is able to successfully explain a large number of experiments with simple pulse shapes. However, for the shaped, low-adiabat pulses, the flux limiter, as first shown in the Fokker–Planck simulations,[18] must be time dependent. The time dependence is especially important in simulating the adiabat-shaping designs,[12,13] where a narrow picket is introduced at the beginning of the laser pulse to tailor the shell adiabat and mitigate the

Rayleigh–Taylor instability growth.[14] Accurate accounting for the absorbed picket energy as well as for the laser coupling during the transition region (see Fig. 113.17) is crucial for the shock-timing calculation. Since it is highly impractical to obtain the temporal shape of the flux limiter based only on the experimental data, a thermal-transport model must be developed for self-consistent flux calculations. Such a model was proposed in Ref. 19, where the simplified Boltzmann equation was solved using the Krook approximation.[20] The main disadvantage of such a model is the lack of particle and energy conservation because of the energy-dependent collisional frequency. Calculations show that, for the conditions relevant to ICF experiments, the error in calculating the local electron density and energy using the solution of the model described in Ref. 19 does not exceed 5%. Despite the fact that the error is small, the model used in the present calculations is modified to recover the conservation properties. This is accomplished by renormalizing the local density and temperature used in evaluating the symmetric part of the electron-distribution function. Similar modifications appear in the classical limit when the ratio of the electron mean-free path λ_{ei} to the temperature scale length L_T is small.[21] The second-order deviations from the Maxwellian f_M, $f_{sym} = f_M + f_n + v^2 f_T$, where $f_{n,T} \sim O\left[(\lambda_{ei}/L_T)^2\right]$, are due in such a limit to the contribution from the electron–electron collisions.[21] These corrections are equivalent to the renormalization in the electron density and temperature used in the local Maxwellian distribution, $f_{sym} = f_M(n', T')$. Next, we describe the renormalization procedure used in the present nonlocal model.

The Boltzmann equation with the Krook collisional operator[20] $v_x \partial_x f + (eE_x/m) \partial_v f = -\nu_{ei}(v)(f - f_0)$ can be solved analytically by substituting f_0 into the second term of the left-hand side:[19]

$$f = f_0 - \int^x G(x', v) e^{\xi/y} d\xi,$$
$$G = \lambda_{ei}(x')\left(\frac{\partial f_0}{\partial x} + \frac{eE_x}{T}\frac{\partial f_0}{\partial \epsilon}\right), \tag{4}$$

where

$$\xi(x') = \int_x^{x'} dx'' / \lambda_{ei}(x''),$$

$\epsilon = mv^2/2T$, $y = \cos\theta$, $\lambda_{ei} = v/\nu_{ei}$, $\nu_{ei} \sim v^{-3}$ is the electron–ion collisional frequency, and E_x is the slowly varying electric field. Assuming that f_0 is a function of the renormalized density n' and temperature T', the relations between (n', T') and (n,T) are found by integrating Eq. (4), multiplied by 1 and $mv^2/2$, yielding $n = n' - R_1$ and $3nT/2 = 3n'T'/2 - R_2$, respectively, where

$$R_1 = 2\pi \int_0^\infty dv v^2 \int_0^1 dy (H_L - H_R),$$

$$R_2 = \pi m \int_0^\infty dv v^4 \int_0^1 dy (H_L - H_R),$$

$$H_L = \int_{x_L}^x G e^{\xi/y} d\xi,$$

and

$$H_R = \int_x^{x_R} G e^{-\xi/y} d\xi.$$

The integration limits are defined as

$$\int_x^{\{x_R, x_L\}} dx'' / \lambda_{ei} = \{+, -\} \infty.$$

The electric current and the heat flux are calculated using the standard definitions $j_x = e\int d^3 v v_x f$ and $q_x = m\int d^3 v v^2 v_x f/2$. The electric field E_x is defined by the zero-current condition $j_x = 0$. This condition yields an integral equation for E_x, which is solved by the iteration method.[19] For the distribution function f_0, we use the Maxwellian function with the corrections due to the laser field[22] $f_0 = f_M \exp(-0.07 \alpha_L \epsilon^{5/2})$, where $\alpha_L = Z v_e^2 / v_T^2$, Z is the average ion charge, and v_e and $v_T = \sqrt{T/m}$ are the electron quiver and thermal velocities, respectively.

Two main effects are introduced by the nonlocal treatment of the thermal transport: First, the flux is reduced from the Spitzer value in the regions with steep temperature gradients; second, the main fuel is heated by the long-range electrons from the hotter plasma corona. The heat flux calculated using the distribution function in Eq. (4) does not correctly reproduce the nonlocal heating because the integrand in Eq. (4) does not go to zero at $\int_{x'}^x dx'' / \lambda_E = 1$, where λ_E is the electron-deposition range. Since the calculations must accurately account for every preheat source, it is essential to include a deposition cutoff. In the previous version of the nonlocal model,[19] this was accomplished by replacing the exponential kernel $e^{\xi/y}$ in Eq. (4) with $\sqrt{1 - \xi/y}$. Such a substitution, however, does not properly recover the Spitzer limit. In the current version of the model, a test-particle approximation is used in evaluating λ_{ei} to produce the deposition cutoff. This approach gives Spitzer conductivity when $\lambda_{ei}/L_T \ll 1$. In the test-particle approximation, λ_{ei} is calculated along the particle trajectory using the energy-loss equation $dK/ds = -K/2 \lambda_E$. Since $\lambda_E \sim K^2$, we obtain

$$K = K_0 \sqrt{1 - \int_{x'}^x dx'' / y \lambda_E},$$

where $ds = dx/y$ is a path element. Then, the deposition cutoff is introduced in Eq. (4) by replacing $\lambda_{ei}(x')$ with

$$\lambda_{ei}(x', x) = \lambda_{ei}(x')\left(1 - \int_{x'}^x dx'/y\lambda_E\right).$$

Next, we compare the results obtained using the described nonlocal model with simulations based on the flux-limited Spitzer conduction. Figure 113.18 shows the effective flux limiter (defined as a maximum ratio of the nonlocal heat flux to the free-stream flux q_{fs} in the vicinity of maximum q_{sp} in the plasma corona) as a function of time for an $\alpha = 2$ cryogenic implosion. The higher value of the flux limiter during the picket indicates a larger predicted laser absorption and a stronger SW, relative to calculations based on the constant flux-limiter model. Then, as the laser intensity relaxes after the picket, the effective flux limiter takes on a reduced value, leading to a weaker CW. If these effects are not properly modeled in a simulation, they lead to a significant shock mistiming and areal-density reduction.
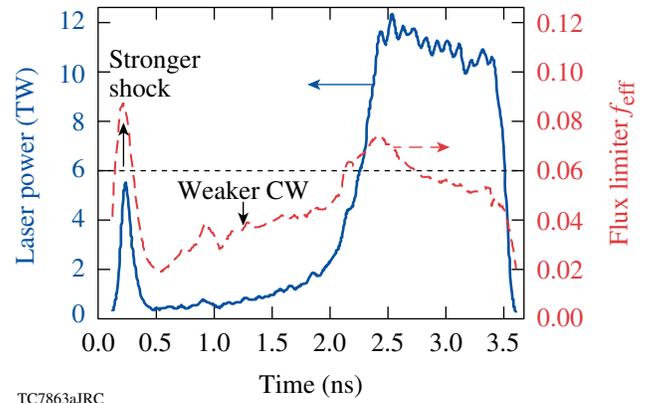

Figure 113.18
Laser pulse (solid line, left axis) and the effective flux limiter f_{eff} (dashed line, right axis) obtained using the nonlocal model for an $\alpha = 2$ cryogenic OMEGA design with a 95-μm-thick D_2 layer and a 10-μm-thick CD overcoat. The thin dashed line shows standard values of the flux limiter used in the hydrocode *LILAC*.

To test the accuracy of the absorption calculations with the nonlocal transport model, the simulation results were compared with experimental absorption data[23] for implosions of 20-μm-thick plastic shells driven with a 200-ps Gaussian pulse at peak intensities varied from 5×10^{13} to 1.5×10^{15} W/cm^2. Figure 113.19 shows the laser absorption fraction calculated using the flux-limited transport model with $f = 0.06$ and no resonance absorption (open squares), the flux-limited model with resonance absorption (solid squares), and the nonlocal model with resonance absorption (triangles). The resonance absorption
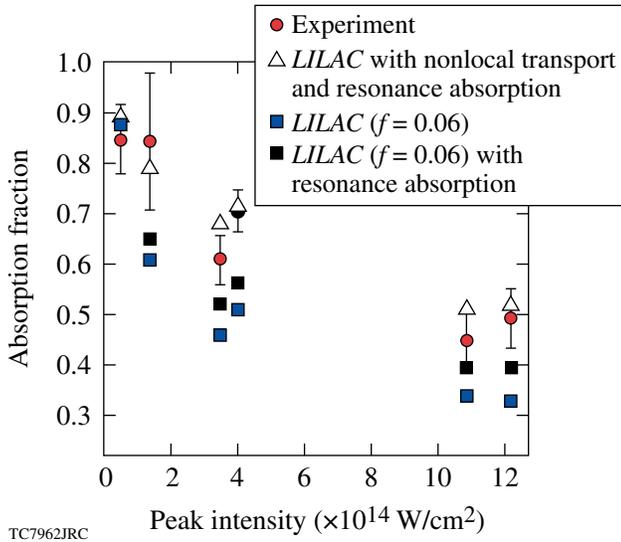
Figure 113.19
Absorption fraction of the incident laser energy for a 20-μm-thick CH shell driven by a 200-ps Gaussian pulse at different peak intensities.

Figure 113.20
Measured $\langle \rho R \rangle$ in a thin CD cryogenic shell as a function of the simulated value using the hydrocode *LILAC* with a constant flux limiter $f = 0.06$ (diamonds) and the nonlocal (squares) thermal conduction models. Arrows indicate reduction in calculated $\langle \rho R \rangle$ when the nonlocal model is used.

effects are small when the nonlocal thermal-transport model is used. These results, therefore, are not shown in Fig. 113.19. The flux-limited transport model produces much steeper electron-density profiles near the laser turning point, resulting in larger resonance absorption in comparison with the nonlocal model calculations. However, even with resonance absorption taken into account, the flux-limited model underestimates the laser absorption fraction for most of the cases shown in Fig. 113.19. The nonlocal model, on the other hand, reproduces the experimental results very well. The non-monotonic behavior of the absorption fraction with peak intensity is due to shot-to-shot variations in the picket width and the rate of intensity rise.

Next, the areal densities for the cryogenic implosions shown in Fig. 113.16 were recalculated using the nonlocal thermal-transport model. The data are plotted in Fig. 113.20. The improved agreement with the experimental data is due to a reduction in the calculated areal density, resulting from significant shock mistiming predicted by the nonlocal model (see arrows in Fig. 113.20 showing this reduction for individual shots). Even though the calculations with the nonlocal model are in better agreement with the experimental data, some discrepancy still remains. In the next section we examine possible sources for the remaining discrepancy, starting with suprathermal-electron preheat.

Suprathermal-Electron Preheat and ρR Sampling

Several laser–plasma interaction processes are capable of generating suprathermal electrons in the plasma corona. As dis-

cussed in the **Introduction** (p. 16), the degradation in ρR is significant if the adiabat at the inner part of the shell is increased. The electron preheat is important, therefore, if the electron-deposition ranges exceed the thickness of the cold part of the shell during the implosion. Thus, for the OMEGA designs, only electrons with energy in excess of 50 keV can reduce the peak shell compression. To estimate the amount of the energy deposited in the shell required to degrade the fuel areal density, we use the pressure–density relation[1] $p \sim \alpha \rho^{5/3}$ and assume the ideal gas equation of state. This gives $\alpha \sim T^{5/3} / p^{2/3}$. The shell pressure is proportional to the ablation pressure p_a, which is determined by the laser intensity. Therefore, for a given drive intensity, according to Eq. (1), $\rho R = (\rho R)_0 / (T/T_0)^{0.09}$, where $(\rho R)_0$ and T_0 are the areal density and electron temperature without the effects of preheat. The shell temperature during the acceleration phase in a typical low-adiabat design is ~20 eV. A 20% reduction in the areal density corresponds to a 6-eV increase in the shell temperature. For an OMEGA target, this leads to ~10 J of preheat energy deposited into the unablated part of the shell. The lowest-threshold mechanism capable of producing energetic electrons with $T_{\text{hot}} > 50$ keV is the two-plasmon-decay instability.[15] The threshold parameter η for this instability[24] is

$$\eta = \frac{I_{14} L_n (\mu\text{m})}{230 \, T_{\text{keV}}} \frac{\lambda_L}{0.351 \, \mu\text{m}}, \quad (5)$$

where I_{14} is the laser intensity in units of 10^{14} W/cm^2, L_n is the density scale length, and λ_L is the laser wavelength. The instability develops when $\eta > 1$. For a typical OMEGA implosion, $L_n \sim$

150 μm and $T_{keV} \sim 1$ at $I_{14} \sim 1$. Thus, the instability is expected to develop when the drive intensity exceeds a few 10^{14} W/cm^2.

The experimental signature of the suprathermal-electron preheat is the measured hard x-ray[25] signal. This correlates with the $3/2\omega$ signal,[23] indicating that the two-plasmon-decay instability is the main mechanism producing the energetic electrons. The hard x-ray signal measured in cryogenic implosions, shown in Fig. 113.21, increases with the laser intensity.[26] Taking this result into account, the peak drive intensity was reduced to below 3×10^{14} W/cm^2 to minimize the suprathermal-electron-preheat effect on the target performance.[26] The measured and predicted areal densities, together with the data for $I > 5 \times 10^{14}$ W/cm^2, are plotted on Fig. 113.22. The improved agreement observed for the lower-intensity shots suggests that suprathermal-electron preheat contributes to a modest degradation in ρR at higher drive intensities.

As the next step, the peak drive intensity was raised to 5×10^{14} and the CD overcoat thickness was increased from 5 to 10 μm. The thicker plastic shell was used to prevent the laser from burning through the plastic to the deuterium during the target implosion and thus mitigate the suprathermal-electron preheat at higher intensity. If the higher-Z plastic burns through during the pulse, as in the case of a 5-μm-thick shell, lower-Z D$_2$ penetrates into the subcritical-density region, reducing the laser absorption. This in turn leads to a drop in the coronal temperature and an increase in the laser intensity at the quarter-critical surface. All of these factors raise the value of η, exciting the two-plasmon-decay instability at the time when
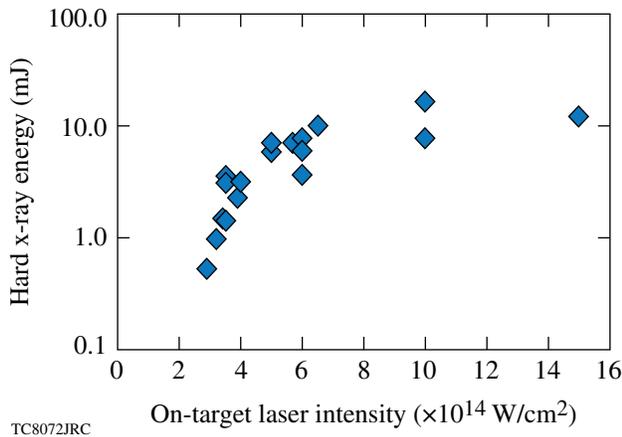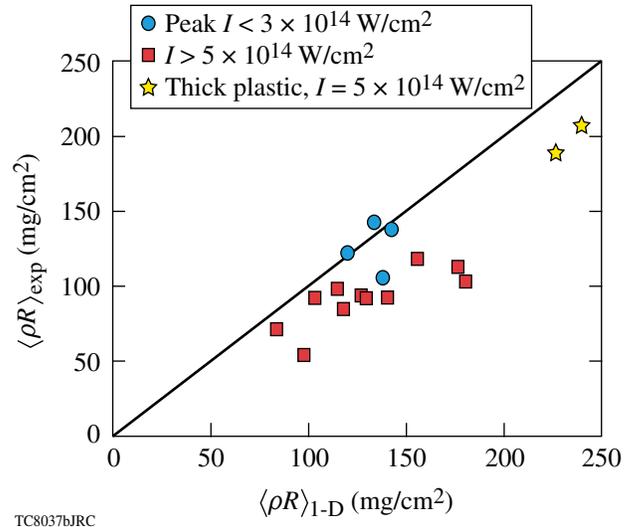
Figure 113.22
Measured $\langle \rho R \rangle$ as a function of the simulated value using the hydrocode *LILAC* with the nonlocal transport model for cryogenic implosions at peak intensities $I > 5 \times 10^{14}$ W/cm^2 (squares) and $I < 3 \times 10^{14}$ W/cm^2 (circles), and for a 10-μm-thick CD shell at $I = 5 \times 10^{14}$ W/cm^2 (stars).

the CD layer burns through. Increasing the CD overcoat thickness to 10 μm allowed the drive intensity to be raised to 5×10^{14} W/cm^2. This produced a significantly less amount of the hard x-ray signal compared to the thinner plastic shell, indicating lower suprathermal preheat. The stars in Fig. 113.22 show the high areal densities (up to 202±7 mg/cm^2) measured in the implosions, which are described in greater detail in Ref. 11. Despite the small hard x-ray signal, the measured areal densities were ~18% lower than the 1-D prediction, indicating that additional mechanisms could be responsible for the measured ρR deviation from the predicted value.

The areal density in the experiment is inferred from the energy downshift in the secondary protons created in the D^{3}He reaction.[8] The experimentally inferred $\langle \rho R \rangle$, therefore, is affected by the timing of the production of these protons with respect to the ρR temporal evolution. Shown in Fig. 113.23(a) are the experimental and predicted neutron-production histories for a cryogenic implosion with a 10-μm-thick CD overcoat that yielded the highest $\langle \rho R \rangle_{exp}$. The predicted areal-density history is plotted on the same figure. The figure shows that the experimental burn rate is significantly reduced (presumably by the perturbation growth during the shell deceleration) at the time when the shell ρR reaches its peak value.[27] This could explain the lower measured areal density with respect to the results of 1-D calculations [compare solid (measurement) and dotted (calculation) curves in Fig. 113.23(a)]. To address the


Figure 113.21
Measured bremsstrahlung radiation above 40 keV for the thin-CD-shell cryogenic implosions. The inferred hard x-ray temperature in these implosions is above 50 keV.

sampling issue, Fig. 113.23(b) plots the predicted D^3He proton spectrum averaged over the experimental burn history (dashed curve), showing good agreement with the measured spectrum (solid curve) averaged over five individual measurements at different views of the implosion.

The suprathermal-electron–generation efficiency for the NIF-scaled targets, not fully understood at present time, is currently under investigation. Preliminary experiments have been carried out to study the preheat mitigation by doping the outer layer of the ablator with high-Z elements. In these experiments, warm plastic shells filled with 15 atm of D_2 gas were imploded using two pulse shapes to set the shell adiabat to $\alpha = 2$ and 3, respectively. The outer 3 μm to 10 μm of the shell were doped with 6%/atom of Si or 2% to 2.6%/atom of Ge. The total shell thickness was 27 μm. The increased laser absorption caused by the higher averaged ion charge in the plasma corona is predicted to raise the threshold for the two-plasmon-decay instability [see Eq. (5)], reducing the suprathermal-electron preheat. Figure 113.24 shows the hard x-ray signal measured
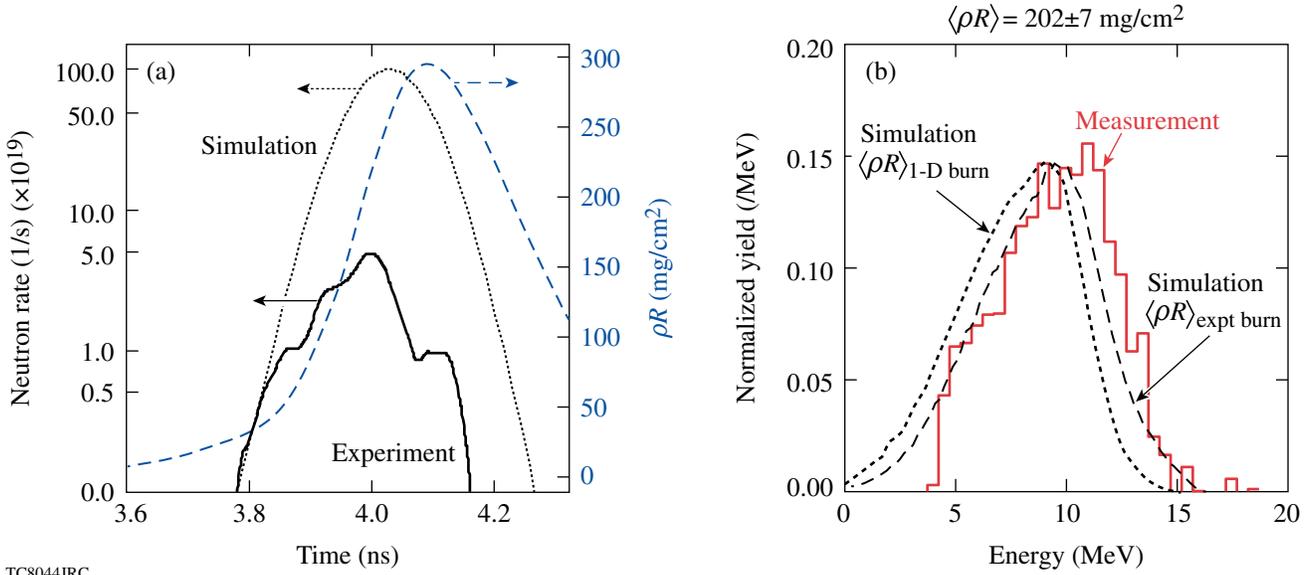
Figure 113.23

(a) The burn history measured (solid line) and predicted (dotted line). Also shown is the ρR evolution calculated with the 1-D code *LILAC* (dashed line, right axis). (b) Measured secondary-proton spectrum (solid line) for a 10-μm-thick CD shell with a 95-μm-thick D_2 cryogenic layer driven on an $\alpha = 2$ adiabat at $I = 5 \times 10^{14}$ W/cm^2. The dotted line shows the calculated spectrum averaged over the predicted 1-D burn, and the dashed line represents the calculated spectrum averaged over the experimental burn history.
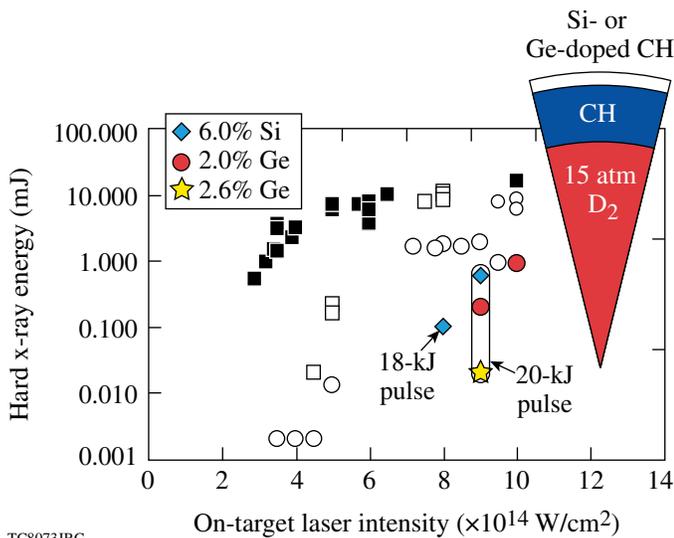
Figure 113.24

Measured bremsstrahlung radiation above 40 keV for the implosions with warm plastic (open circles), doped plastic (diamond, solid circle, and star), cryogenic 5-μm-thick CD (solid squares), and cryogenic 10-μm-thick CD (open squares) shells.

in pure-CH and CH shells doped with Si or Ge. The observed significant reduction in the signal level confirms the lower preheat level in the doped ablators. For comparison, Fig. 113.24 also shows the signal for cryogenic targets with 5- and 10-μm-thick CD shells.

In addition to the reduction in the hard x-ray signal, the shells with Si-doped layers show improved hydrodynamic stability. The radiation from the higher-Z dopant preheats the shell, reducing both the initial imprint levels[28,29] and the Rayleigh–Taylor instability growth. The improved stability of Si-doped shells with respect to the pure-CH shells results in an increase in both the experimental yields and the ratio of the experimental to the predicted yield. The latter is shown in Fig. 113.25. The increased yield is especially pronounced in the most-unstable, $\alpha = 2$ implosions when the thickness of the doped layer is 3 μm or greater. The stabilizing property of the high-Z dopants will be used in the future OMEGA cryogenic designs. Calculations show that the radiation from the dopant preferably preheats the higher-opacity CD layer without significantly heating the lower-opacity main fuel. This enhances cryogenic shell stability without compromising the fuel adiabat.


TC7964JRC
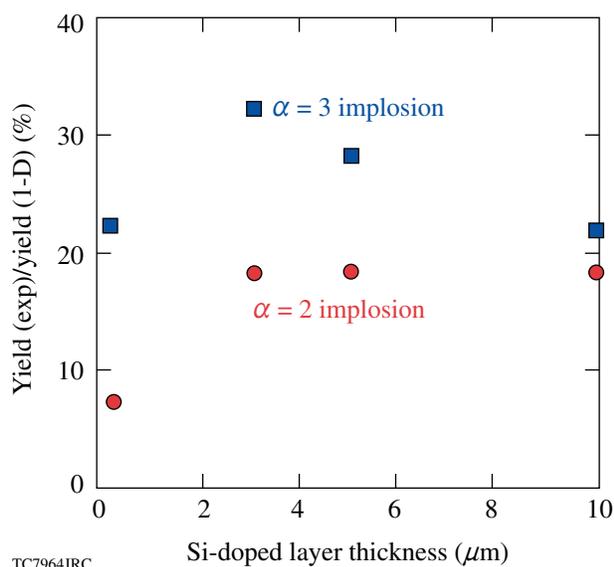
Figure 113.25
Ratio of the experimental yield and the predicted yield for warm-plastic-shell implosions with different Si-doped layer thicknesses.

Conclusions

Ignition target designs rely on low-adiabat, high-areal-density fuel compression. A series of implosions with 92- to 95-μm-thick cryogenic D_2 layers were performed on OMEGA to study the physics of ignition-relevant, low-adiabat fuel

assembly using the direct-drive configuration. The main sources of the adiabat degradation, observed in earlier experiments,[6,7] were attributed to (1) the shock mistiming resulting from inaccuracies in the laser-absorption modeling, (2) suprathermal-electron preheat generated by the two-plasmon-decay instability, and (3) under-sampling of higher ρR in the shell due to burn truncation. To increase the calculation accuracy, the nonlocal transport model was implemented in the 1-D hydrocode *LILAC*. High cryogenic areal density with $\langle \rho R \rangle > 200$ mg/cm^2 was measured in the experiments[11] when the shock timing was optimized using the nonlocal treatment of the heat transport and the suprathermal-electron-preheat source was mitigated.

REFERENCES

1. S. Atzeni and J. Meyer-ter-Vehn, *The Physics of Inertial Fusion: Beam Plasma Interaction, Hydrodynamics, Hot Dense Matter*, International Series of Monographs on Physics (Clarendon Press, Oxford, 2004).

2. J. D. Lindl, *Inertial Confinement Fusion: The Quest for Ignition and Energy Gain Using Indirect Drive* (Springer-Verlag, New York, 1998).

3. S. E. Bodner, D. G. Colombant, J. H. Gardner, R. H. Lehmberg, S. P. Obenschain, L. Phillips, A. J. Schmitt, J. D. Sethian, R. L. McCrory, W. Seka, C. P. Verdon, J. P. Knauer, B. B. Afeyan, and H. T. Powell, Phys. Plasmas **5**, 1901 (1998).

4. R. Betti and C. Zhou, Phys. Plasmas **12**, 110702 (2005).

5. T. R. Boehly, D. L. Brown, R. S. Craxton, R. L. Keck, J. P. Knauer, J. H. Kelly, T. J. Kessler, S. A. Kumpan, S. J. Loucks, S. A. Letzring, F. J. Marshall, R. L. McCrory, S. F. B. Morse, W. Seka, J. M. Soures, and C. P. Verdon, Opt. Commun. **133**, 495 (1997).

6. F. J. Marshall, R. S. Craxton, J. A. Delettrez, D. H. Edgell, L. M. Elasky, R. Epstein, V. Yu. Glebov, V. N. Goncharov, D. R. Harding, R. Janezic, R. L. Keck, J. D. Kilkenny, J. P. Knauer, S. J. Loucks, L. D. Lund, R. L. McCrory, P. W. McKenty, D. D. Meyerhofer, P. B. Radha, S. P. Regan, T. C. Sangster, W. Seka, V. A. Smalyuk, J. M. Soures, C. Stoeckl, S. Skupsky, J. A. Frenje, C. K. Li, R. D. Petrasso, and F. H. Séguin, Phys. Plasmas **12**, 056302 (2005).

7. T. C. Sangster, R. Betti, R. S. Craxton, J. A. Delettrez, D. H. Edgell, L. M. Elasky, V. Yu. Glebov, V. N. Goncharov, D. R. Harding, D. Jacobs-Perkins, R. Janezic, R. L. Keck, J. P. Knauer, S. J. Loucks, L. D. Lund, F. J. Marshall, R. L. McCrory, P. W. McKenty, D. D. Meyerhofer, P. B. Radha, S. P. Regan, W. Seka, W. T. Shmayda, S. Skupsky, V. A. Smalyuk, J. M. Soures, C. Stoeckl, B. Yaakobi, J. A. Frenje, C. K. Li, R. D. Petrasso, F. H. Séguin, J. D. Moody, J. A. Atherton, B. D. MacGowan, J. D. Kilkenny, T. P. Bernat, and D. S. Montgomery, Phys. Plasmas **14**, 058101 (2007).

8. F. H. Séguin, C. K. Li, J. A. Frenje, D. G. Hicks, K. M. Green, S. Kurebayashi, R. D. Petrasso, J. M. Soures, D. D. Meyerhofer, V. Yu. Glebov, P. B. Radha, C. Stoeckl, S. Roberts, C. Sorce, T. C. Sangster, M. D. Cable, K. Fletcher, and S. Padalino, Phys. Plasmas **9**, 2725 (2002).

9. J. Delettrez, R. Epstein, M. C. Richardson, P. A. Jaanimagi, and B. L. Henke, Phys. Rev. A **36**, 3926 (1987).

10. R. C. Malone, R. L. McCrory, and R. L. Morse, Phys. Rev. Lett. **34**, 721 (1975).

11. T. C. Sangster, V. N. Goncharov, P. B. Radha, V. A. Smalyuk, R. Betti, R. S. Craxton, J. A. Delettrez, D. H. Edgell, V. Yu. Glebov, D. R. Harding, D. Jacobs-Perkins, J. P. Knauer, F. J. Marshall, R. L. McCrory, P. W. McKenty, D. D. Meyerhofer, S. P. Regan, W. Seka, R. W. Short, S. Skupsky, J. M. Soures, C. Stoeckl, B. Yaakobi, D. Shvarts, J. A. Frenje, C. K. Li, R. D. Petrasso, and F. H. Séguin, "High-Areal-Density Fuel Assembly in Direct-Drive Cryogenic Implosions," submitted to Physical Review Letters.

12. V. N. Goncharov, J. P. Knauer, P. W. McKenty, P. B. Radha, T. C. Sangster, S. Skupsky, R. Betti, R. L. McCrory, and D. D. Meyerhofer, Phys. Plasmas **10**, 1906 (2003).

13. K. Anderson and R. Betti, Phys. Plasmas **11**, 5 (2004).

14. S. Chandrasekhar, in *Hydrodynamic and Hydromagnetic Stability*, International Series of Monographs on Physics (Clarendon Press, Oxford, 1961), p. 428.

15. W. L. Kruer, *The Physics of Laser–Plasma Interactions*, Frontiers in Physics, Vol. 73, edited by D. Pines (Addison-Wesley, Redwood City, CA, 1988), Chap. 4, p. 39.

16. I. V. Igumenshchev, V. N. Goncharov, W. Seka, D. Edgell, and T. R. Boehly, Phys. Plasmas **14**, 092701 (2007).

17. L. Spitzer, Jr. and R. Härm, Phys. Rev. **89**, 977 (1953).

18. A. Sunahara, J. A. Delettrez, C. Stoeckl, R. W. Short, and S. Skupsky, Phys. Rev. Lett. **91**, 095003 (2003).

19. V. N. Goncharov, O. V. Gotchev, E. Vianello, T. R. Boehly, J. P. Knauer, P. W. McKenty, P. B. Radha, S. P. Regan, T. C. Sangster, S. Skupsky, V. A. Smalyuk, R. Betti, R. L. McCrory, D. D. Meyerhofer, and C. Cherfils-Clérouin, Phys. Plasmas **13**, 012702 (2006).

20. N. A. Krall and A. W. Trivelpiece, *Principles of Plasma Physics* (San Francisco Press, Inc., San Francisco, 1986), p. 316.

21. A. V. Maksimov, V. P. Silin, and M. V. Chegotov, Sov. J. Plasma Phys. **16**, 331 (1990).

22. V. N. Goncharov and G. Li, Phys. Plasmas **11**, 5680 (2004).

23. W. Seka, D. H. Edgell, J. P. Knauer, J. F. Myatt, A. V. Maximov, R. W. Short, T. C. Sangster, R. E. Bahr, R. S. Craxton, J. A. Delettrez, V. N. Goncharov, I. V. Igumenshchev, and D. Shvarts, "Time-Resolved Absorption in Cryogenic and Room-Temperature, Direct-Drive Implosions," submitted to Phys. Plasmas (invited).

24. A. Simon, R. W. Short, E. A. Williams, and T. Dewandre, Phys. Fluids **26**, 3107 (1983).

25. C. Stoeckl, V. Yu. Glebov, D. D. Meyerhofer, W. Seka, B. Yaakobi, R. P. J. Town, and J. D. Zuegel, Rev. Sci. Instrum. **72**, 1197 (2001).

26. V. A. Smalyuk, D. Shvarts, R. Betti, J. A. Delettrez, D. H. Edgell, V. Yu. Glebov, V. N. Goncharov, R. L. McCrory, D. D. Meyerhofer, P. B. Radha, S. P. Regan, T. C. Sangster, W. Seka, S. Skupsky, C. Stoeckl, B. Yaakobi, J. A. Frenje, C. K. Li, R. D. Petrasso, and F. H. Séguin, "The Role of Hot-Electron Preheat in the Compression of Direct-Drive Imploding Targets with Cryogenic D_2 Ablators," submitted to Physical Review Letters.

27. P. B. Radha, V. N. Goncharov, T. J. B. Collins, J. A. Delettrez, Y. Elbaz, V. Yu. Glebov, R. L. Keck, D. E. Keller, J. P. Knauer, J. A. Marozas, F. J. Marshall, P. W. McKenty, D. D. Meyerhofer, S. P. Regan, T. C. Sangster, D. Shvarts, S. Skupsky, Y. Srebro, R. P. J. Town, and C. Stoeckl, Phys. Plasmas **12**, 032702 (2005).

28. M. Karasik *et al.*, Bull. Am. Phys. Soc. **49**, 276 (2004).

29. A. N. Mostovych, D. G. Colombant, M. Karasik, J. P. Knauer, A. J. Schmitt, and J. L. Weaver, "Enhanced Direct-Drive Implosion with Thin High-*Z* Ablation Layers," to be published in Physical Review Letters.

Initial Experiments on the Shock-Ignition Inertial Confinement Fusion Concept

Introduction

Shock ignition is a concept for direct-drive laser inertial confinement fusion (ICF)[1–3] that was recently proposed by Betti *et al.*[4,5] It promises to achieve ignition with ~3×-lower driver energy than the conventional isobaric hot-spot ignition concept.[6] The fuel is assembled to a high areal density (ρR) on a low adiabat (α) with a sub-ignition implosion velocity using shaped nanosecond laser pulses. The adiabat[3] is defined as the ratio of the plasma pressure to the Fermi pressure of a degenerate electron gas and is typically $\alpha \sim 1$ to 2. Because of the low implosion velocity, the temperature of the central hot spot is too low for conventional ignition to occur. A strong shock wave launched at the end of the laser pulse with an intensity spike hits the compressed core, further compresses the hot spot, and triggers ignition. The resulting burn wave ignites the entire dense core, producing high yields due to the large areal densities. Similar to fast ignition[7] and impact ignition,[8] the fuel assembly and ignition are separated and the energy gain (G) scales as $G \sim \theta / v_i^{1.25}$ (Ref. 9), where θ is the burnup fraction that increases with ρR (Ref. 2) and v_i denotes the implosion velocity. A low implosion velocity and high ρR are advantageous to producing the highest ICF gains.[4] The peak areal density is approximately independent of the shell's implosion velocity and depends on the in-flight adiabat according to $(\rho R)_{\text{max}} \sim \alpha^{-0.6}$ (Ref. 4), favoring as low an adiabat as achievable. Low-velocity, high-ρR, $\alpha \approx 1.5$ implosions have recently demonstrated experimentally a neutron-averaged areal density of 0.13 g/cm^2 and peak ρR of ~0.24 g/cm^2 (Ref. 10). In fast ignition, the implosion laser facility must be combined with a high-intensity, short-pulse, multipetawatt-ignitor laser facility delivering a particle beam for ignition. Shock ignition makes use of the pulse-shaping capabilities of the implosion laser facility, significantly relaxing the technical constraints on the concept.

The strong shock wave that triggers ignition is achieved by adding a sharp intensity spike at the end of the main drive pulse.[4] The laser power must rise to several hundred terawatts in a few hundred picoseconds to drive the ignitor shock. The spike pulse is timed so that the shock wave meets with the return shock driven by the rising hot-spot pressure during the deceleration phase in the shell close to the cold fuel/hot spot interface. The colliding shocks generate two new shock waves with one propagating inward, leading to further compression of the hot spot and a peaked pressure profile with its maximum in the center. The resulting fuel assembly is nonisobaric with a hot-spot pressure greater than the surrounding dense fuel pressure[4] and, to achieve ignition, requires a lower energy than the conventional isobaric hot-spot ignition.[4,5] The required driver energy is lowered roughly by the factor $\left(p_{\text{hs}} / p_{\text{iso}}\right)^{2.5}$ (Ref. 5), where p_{hs} is the nonisobaric hot-spot pressure and p_{iso} is the isobaric pressure. A pressure ratio of ~1.6 results in a 3×-lower ignition energy. This mechanism is very effective in thick-shell implosions, where the ignitor shock wave significantly increases its strength as it propagates through the converging shell. Massive shell implosions have good hydrodynamic-stability properties during the acceleration phase because of low acceleration and small in-flight aspect ratio (IFAR). The number of e foldings of Rayleigh–Taylor (RT) instability growth for the most-dangerous modes with wave numbers about equal to the inverse in-flight target thickness is roughly proportional to the square root of IFAR.[3] Low IFAR implosions are not significantly affected by RT instability.

This article describes initial implosion experiments of the shock-ignition concept that were performed on the OMEGA Laser System[11] using warm plastic surrogate shells and cryogenic shell targets. The power of the OMEGA laser is limited to about 20 TW, thus preventing the investigation of the shock-ignition scheme in ignition-relevant regimes (requiring more than 300 TW). Nevertheless, by lowering the power during the assembly pulse to about 7 TW, a late shock can be launched by a fast rise to about 18 TW. Such OMEGA experiments are used to study important features of the shock-ignition scheme such as hydrodynamic stability, shell compression, and hot-spot compression induced by the late shock. One of the most important aspects to be investigated is the uniformity of the shock-induced hot-spot compression. Since the ignitor shock is launched late in the pulse, its uniformity might be compromised by the large amplitude modulations of the ablation front.

The ignitor shock could transfer such perturbations from the ablation front to the hot spot, thus reducing the uniformity of the compression and possibly quenching the thermonuclear burn. By comparing the implosion performance with and without a shock, we infer the relative effectiveness of the shock compression and hot-spot heating. The low-mode uniformity of the compression is assessed by measuring the modulation in the areal density and by the magnitude of the neutron yield with respect to the calculated 1-D yield. Varying the timing of the peaks in the laser pulse shape optimizes the timing of the shock waves and the implosion performance. Plastic-shell implosions study how fuel–shell mixing affects the yield performance for shock-ignition pulse shapes, compared to standard low-adiabat picket-pulse capsule implosions.[10] Significantly improved performance using shock-ignition–type pulse shapes has been observed, leading to peak ρR exceeding ~0.3 g/cm^2. The following sections present the target types, the laser pulse shapes, and diagnostics; fusion-reaction yield measurements in plastic-shell implosions; areal-density analysis of plastic-shell implosions; and initial spike pulse cryogenic-shell implosions. A summary and conclusions are also presented.

Targets, Laser Pulse Shapes, and Diagnostics

Figure 113.26 shows the targets that were used in the experiments: (a) 40-μm-thick, 430-μm-outer-radius, plastic (CH) shells coated outside with a 0.1-μm layer of aluminum and filled with D$_2$ gas with pressures ranging from 4 to 45 atm and (b) cryogenic targets comprising a 10-μm-thick, strong deuterated plastic shell and frozen layers of 95-μm-deuterium (D$_2$) and 78-μm-deuterium–tritium (DT) ice, respectively. Details of the direct-drive cryogenic-target program can be found in Refs. 12–14.

The capsules were imploded by relaxation adiabat pulse shapes[9] for ~16- to 20-kJ UV laser pulses. The 351-nm-wavelength laser light was smoothed with polarization smoothing[15] and distributed phase plates,[16] and in some shots the laser beam was smoothed with 1-THz-bandwidth, 2-D smoothing by spectral dispersion (SSD).[17] Typical experimental pulse shapes with and without spike for warm plastic targets and $\alpha \sim 1.5$ are compared in Fig. 113.27. The shaped pulses comprise an 80-ps full width at half maximum (FWHM) Gaussian prepulse ("picket pulse") and a subsequent shaped main-drive portion consisting of an ~1-TW foot power and a moderate ~6- to 8-TW plateau; the solid curve comprises a high-intensity spike portion ("spike pulse") with a peak power of about ~17 TW. The corresponding nominal laser intensity in the spike portion exceeds 7×10^{14} W/cm^2. The nominal laser intensity refers to the initial target size, while the actual intensity at the critical-
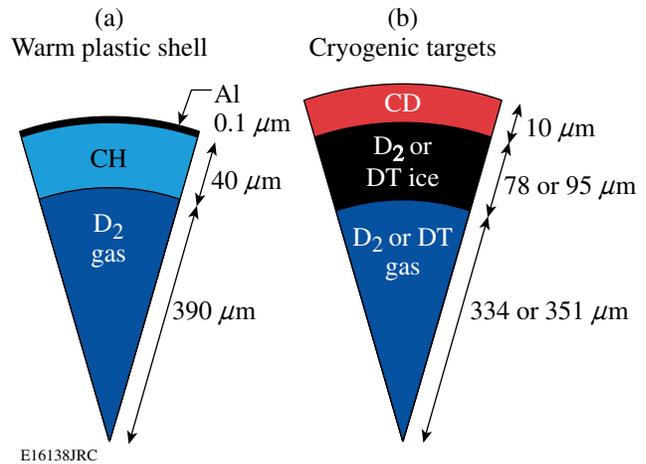
Figure 113.26
Targets that were used to test shock-ignition pulse-shape implosions on the OMEGA Laser Facility.
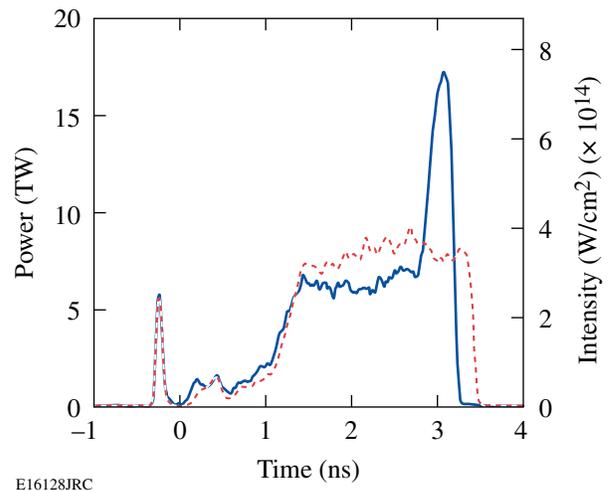
Figure 113.27
Pulse shapes with (solid curve, 46078) and without (dashed, 46073) spike, no SSD. The laser energies were 18.6 kJ (46078) and 19.4 kJ (46073), respectively. The onset of the spike pulse was at 2.8 ns.

density surface at the pulse end is a factor of ~2 higher due to compression. A similar pulse shape without spike but the same laser energy is shown by the dashed curve. The pulse shapes are very similar in the first nanosecond, including the picket intensity, the picket timing, and the foot of the main drive pulse. The no-spike shape reaches a slightly higher power in the plateau. The energy difference in the plateau is transferred to form the spike (solid curve). Zero time marks the onset of the foot of the main drive laser pulse. The picket pulse in front of the foot of the main pulse launches a shock wave that sets the

adiabat of the implosion and generates a shaped-adiabat profile within the shell that is monotonically decreasing from the outer (ablation) surface toward the inner shell surface (see Fig. 2 in Ref. 10). The use of adiabat-shaping pulses in the context of fast-ignition implosions was suggested in Ref. 9. The relaxation technique[18,19] for adiabat shaping simplifies the laser pulse by lowering the contrast ratio between the peak laser power and the power in the foot of the main pulse. It also improves the hydrodynamic stability of the implosion by decreasing the in-flight aspect ratio and increasing the ablation velocity.

Figure 113.28 shows a schematic of the timing of the various shock waves in a warm surrogate shock-ignition implosion. The picket pulse that is optimally timed with respect to the main drive pulse launches a shock wave (SW) and sets the adiabat of the implosion. The slowly rising part of the main drive launches a compression wave (CW) steepening up while propagating through the shell and then overtakes the SW just before shock breakout at the inner interface. A sharp rise in intensity at the end (spike pulse) generates a "spike shock wave" (SSW) that must be properly timed to meet the return shock in the inner region of the cold shell material. The colliding shocks then generate the shock wave that travels back to the capsule center. In the experiments, the implosion was optimized by measuring the fuel assembly performance as a function of the timing of the picket and spike pulses. The picket pulse was timed by a variable delay line, and the spike pulse timing was varied by using different pulse shapes that were designed so that the low-intensity foot drive was kept the same but had a different temporal onset of the spike portion, which was varied in 100-ps time increments. The trailing edge of the main drive pulse was designed to keep the total laser energy constant.

The diagnostics that were used to measure the implosion performance include proton wedged range filters (WRF's),[20] a nuclear temporal diagnostic (NTD),[21,22] and neutron time-of-flight diagnostics comprising scintillator counters coupled to fast photomultipliers for primary and secondary neutron yield measurements.[23] The kinetic energy downshift of protons generated by the D^{3}He fusion reactions, which is a secondary-proton production reaction in D$_2$ fuel, was used to infer areal density[24,25]

$$D + D \longrightarrow {}^3\text{He} + n, \qquad (1)$$

followed by

$$ {}^3\text{He} + D \longrightarrow p(12.6 - 17.5\,\text{MeV}) + {}^4\text{He}. \qquad (2)$$

The secondary protons have a considerable energy spread due to the kinetic-energy spread of ^{3}He produced in the primary reaction. The protons produced in the central hot-spot region pass through the dense, cold shell where their kinetic energy suffers a considerable downshift. Therefore the measurement of the downshifted kinetic-energy spectrum provides information about the shell areal density. By using wedges with an appropriate range of thicknesses and a CR-39 plastic detector, it is possible to make an accurate reconstruction of the proton spectrum by applying the technique discussed by Séguin et al. in Ref. 20. The lower detection limit given by the thinnest
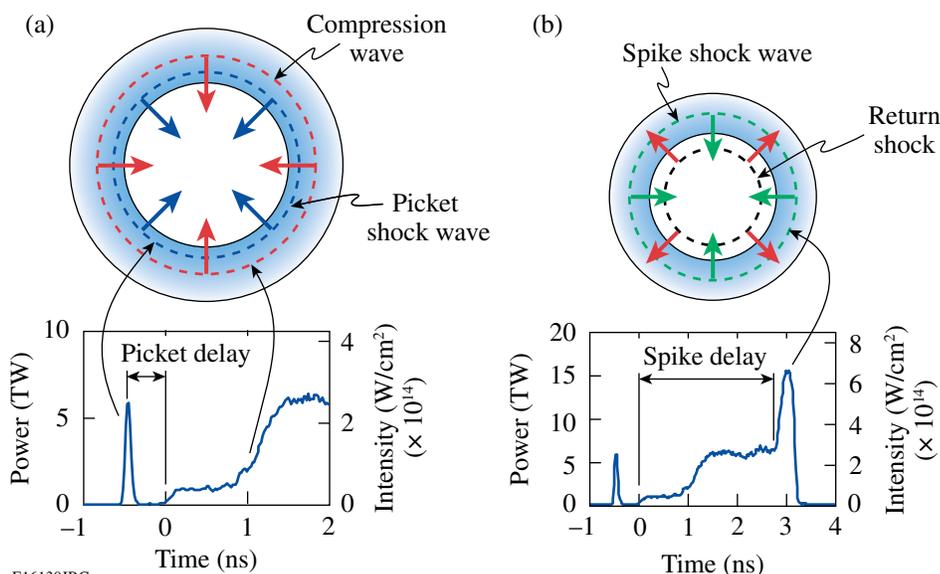
Figure 113.28
Schematic of the timing of the various shock waves generated by the picket pulse, the drive pulse, and the high-intensity spike pulse.

E16130JRC

wedge section is ~4 MeV. The proton spectra were measured at four locations around the target. Areal-density measurements based on the fusion proton-spectrum downshift are routinely used at LLE.[25,26]

Measurements of Fusion-Reaction Yield
in Plastic-Shell Implosions

A series of plastic-shell implosions with D_2-fill pressures in the range of 9 to 45 atm were performed with and without SSD using a low-adiabat pulse shape without a spike portion [Fig. 113.29(a)]. The pulse shapes were similar to that shown in Fig. 113.27 (dashed curve) but with a higher main-drive power of ~11 to 13 TW. The ratio of the measured primary neutron yield to that predicted by 1-D simulations using the hydrodynamic code *LILAC*,[27] or neutron yield-over-clean (YOC), is shown in Fig. 113.29(b) for these implosions as a function
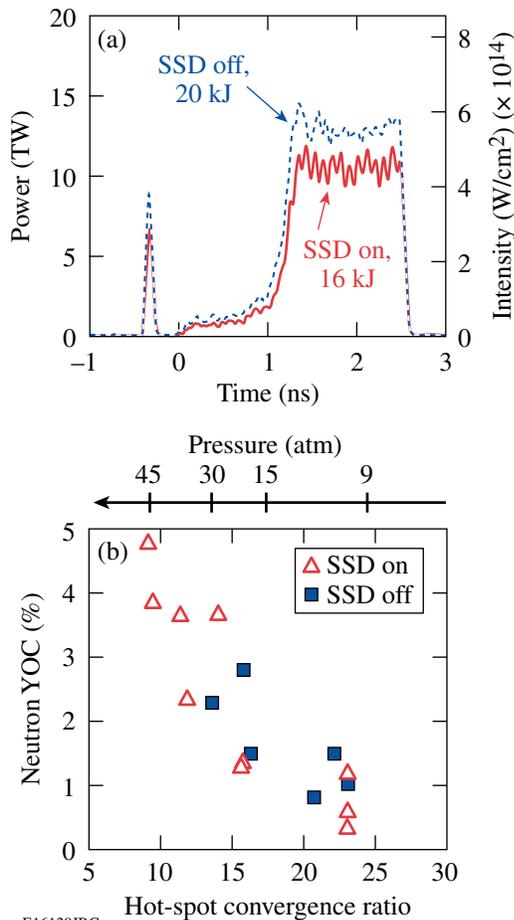

Figure 113.29

(a) Low-adiabat relaxation laser pulse shapes without a spike pulse. (b) Measured neutron yield over clean versus hot-spot convergence ratio (bottom) and D_2-fill pressure (top) of plastic-shell implosions. The open triangles depict measurement with SSD; the solid squares depict measurement without SSD.

of the calculated hot-spot convergence ratio (bottom) and fill pressure (top). The calculated hot-spot convergence ratio (CR) is defined as the initial inner target-shell radius divided by the minimum radius of the gas–shell interface at peak compression. The YOC is ~4% at 45 atm and decreases with lower pressure and higher CR to ~1%. SSD has no significant effect on the yield performance, indicating that thermal conductivity in the plasma formed by the picket pulse effectively smoothes short-wavelength structures in the laser beams (imprinting). A YOC decrease by a factor of ~4 when CR increases from ~9 to ~23 indicates an increased small length mixing for smaller hot-spot radii. Large convergence ratios of the fuel and the slow assembly make plastic shells inherently RT instable during the deceleration phase, giving rise to a substantial shell–fuel mixing[28] that quenches fusion reactions and typically results in YOC of a few percent.[10] Mixing is enhanced in these low-velocity implosions because the hot spot is small relative to the target size.[29] In comparison, shock-ignition–type pulse shapes considerably improve the performance (see Fig. 113.32 on p. 30).

A systematic study of low-adiabat ($\alpha \approx 1.5$) plastic-shell implosions with a short picket and a high-intensity spike was performed at a constant pressure of 25 atm, a fixed laser energy of 17 kJ, and a fixed spike-pulse timing of 2.8 ns as a function of picket timing (see Fig. 113.30). The measured neutron (open circles) and proton (solid squares) numbers are shown in Fig. 113.30(a) as a function of the picket-pulse delay. Zero determines the onset of the foot of the main drive, and an increased delay shifts the picket earlier in time away from the foot. The neutron and proton yields increase by a factor of ~2 from $3.5\pm0.4 \times 10^9$ to $8.0\pm0.8 \times 10^9$ and $2.6\pm0.5 \times 10^6$ to $6.2\pm1.2 \times 10^6$, respectively, when shifting from –550 ps to zero, which is the optimum picket timing. Calculated neutron and proton yields using the 1-D hydrocode *LILAC*[27] and a constant flux limiter of 0.06 show a similar trend, but the predicted yield variation is not as pronounced as in the measurement. Figure 113.30(b) shows that the picket timing also affects the measured average areal density ($\langle\rho R\rangle$). An ~100-ps mistiming lowers the yield by ~25%, which is significant compared to the neutron-yield measurement uncertainty of ~10%, and a delay by up to approximately –550 ps degrades the yield by a factor of ~2 and $\langle\rho R\rangle$ by ~20%. The measurement shows how shock-wave timing of SW and CW affects the implosion performance of these surrogate targets (see Fig. 113.28). If the CW is too late, the first shock enters the fuel, prematurely compressing and heating it, while if the CW is too early, the inner target portion is placed on too high an adiabat, reducing its compressibility. For direct-drive, hot-spot ignition target designs, the CW must overtake the first shock within ±150 ps of the design
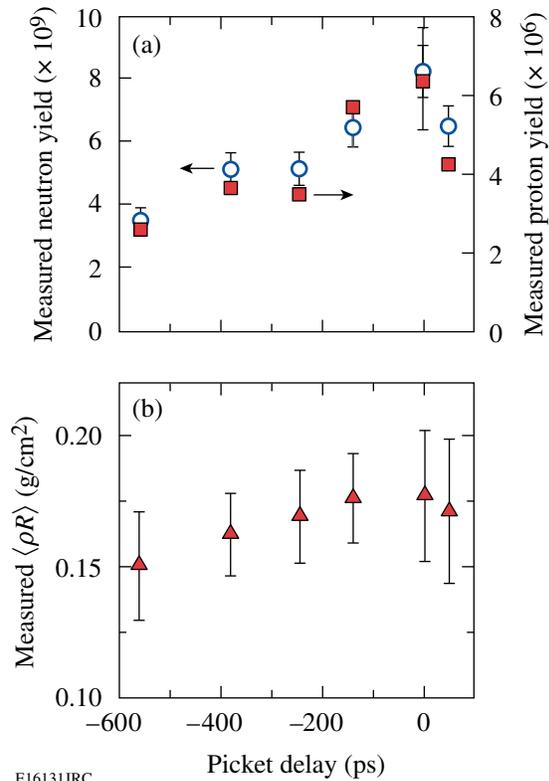
Figure 113.30

(a) Measured neutron (open circles) and proton (solid squares) yields as functions of the picket-pulse timing. Zero determines the onset of the foot of the main drive and an increased delay shifts the picket earlier in time away from the foot. (b) Corresponding measured average areal density. The relative $\langle \rho R \rangle$ error bars are shown.

specification.[30] For the surrogate CH experiments, the best results were obtained for time-zero for both the yield and $\langle \rho R \rangle$ with $\langle \rho R \rangle = 0.18 \pm 0.02$ g/cm^2 under the experimental conditions of Fig. 113.30. This shows that the correct timing of SW and CW has been obtained. More details on the areal-density measurements are discussed in **Areal-Density Analysis of Plastic-Shell Implosions** (p. 30).

The implosion was further optimized by studying how the timing of the SSW affects the implosion performance. This was done with different pulse shapes that were designed to have the same low-intensity foot and plateau, but a different spike-pulse timing. Figure 113.31(a) shows an overview of the neutron-yield measurements. The solid circle data point represents a measurement for a pulse shape without a high-intensity spike, yielding $1.8 \pm 0.2 \times 10^9$ neutrons with 19.4-kJ laser energy. In comparison, a spike pulse with a 2.8-ns delay and slightly less laser energy (18.6 kJ) results in 4$\times$ more neutrons (8.0$\pm$0.8 $\times$ 10^9, upper triangle). The proton yield increases by a factor of

~5 from $1.3 \pm 0.3 \times 10^6$ to $6.2 \pm 1.2 \times 10^6$. All other data points were measured with ~17-kJ laser energy, which explains why the second triangle at 2.8 ns is lower. The triangles represent the measurement for a picket delay of –300 ps, and the squares are a series with –100-ps picket delay. Figure 113.30(a) shows that a shorter picket delay results in an improved yield, which is consistent with the fact that the square data points in Fig. 113.31(a) are slightly higher than the triangles. The measurement in Fig. 113.31(a) demonstrates an optimum timing of the spike-pulse delay at 2.8 ns. A mistiming by 100 ps significantly affects the yield. One-dimensional hydrodynamic simulations using the code *LILAC* do not predict a maximum in neutron yield at 2.8 ns and show very little sensitivity of the fusion-product yield on SSW timing [see Fig. 113.31(b)]. The calculated 1-D yield for the SSW implosion with 18.6 kJ (upper triangle at 2.8 ns) is only slightly higher than a comparable implosion without SSW and 19.4 kJ of laser energy. Calculations for exactly the same laser energy predict ~30%
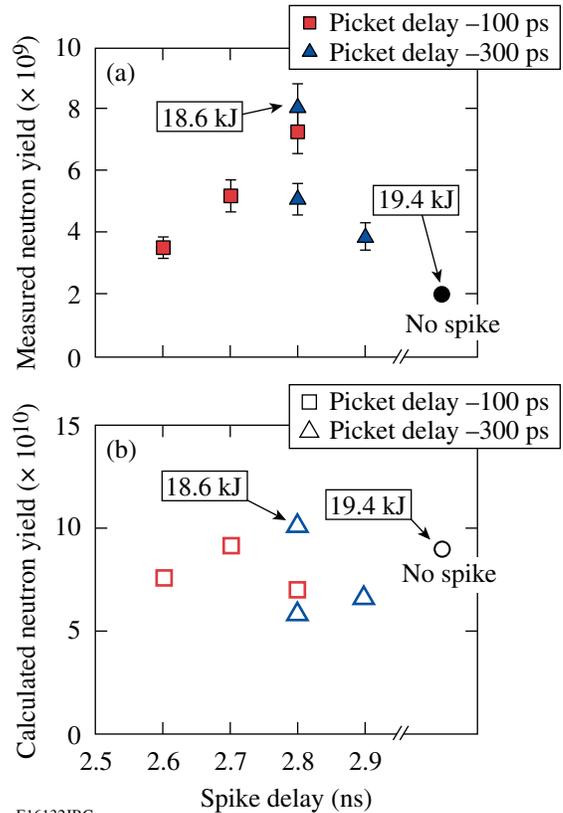
Figure 113.31

(a) Measured neutron yield as a function of the onset of the spike pulse, for two different picket-pulse delays. The targets were filled with 25 atm of D$_2$. The pulse without spike (solid circle) used a –300-ps picket delay. (b) Calculated neutron yield versus spike-pulse delay.

yield enhancement by the SSW, which is much lower than measured. As mentioned before, the SSW energy coupling into the hot spot is optimal for thick-shell targets because the ignitor shock strength increases significantly when traveling through the converging shell. Compared to an ignition design with a target shell thickness of ~350 μm (Ref. 5), the present targets (40 μm CH, ~100 μm cryo) are thin-shell targets, which explains why the simulated enhancement is only marginal. It is not yet clear why the targets perform much better than predicted, but there are several possible explanations. Plastic shells with low-pressure fills are inherently RT instable during the deceleration phase, giving rise to substantial shell–fuel mixing that quenches fusion reactions, which is believed to be the main cause for the YOC's in the percent range. The experiments presented here suggest that for optimal SSW timing, the mixing processes are mitigated, which might be caused by the impulse acceleration by the SSW that shortens the time period for the instability growth or by a steepening of the density profile at the inner shell surface. Another possibility, which is not very likely, would be that the hot-spot heat-transport losses are not modeled correctly and that the temperature increase produced by the SSW is larger than predicted, leading to the higher yield. Multidimensional hydrodynamic simulations have been started to study this effect in more detail.

The implosion performance was studied with the optimized spike-pulse shape for various shell-fill pressures between 4 and 25 atm. Figure 113.32 compares the YOC versus CR for implosions with an optimized spike-pulse shape (circles) and various pulse forms without a spike pulse (diamonds), including the data from Fig. 113.29(b). The implosions without a spike pulse were not optimized with respect to shock-wave timing. The experiments demonstrate that YOC close to 10% has been obtained for plastic-shell, $\alpha = 1.5$ to 1.9, low-adiabat implosions and CR of up to 30, indicating an improved stability with shock-ignition–type pulse shapes.

Areal-Density Analysis of Plastic-Shell Implosions

Figure 113.33 shows the measured proton spectrum, which is the average of four individual proton spectra taken from different lines of sight, for an 8.3-atm, D_2-fill implosion with a laser energy of 18 kJ without SSD. All of the measurements described in this section were performed without SSD. A mean downshift of 6.38±0.13 MeV was measured where the error represents the standard deviation over the four measurements. Following Refs. 20 and 24, an areal density averaged over the proton spectral distribution of $\langle \rho R \rangle = 0.204 \pm 0.003$ g/cm^2 is inferred where the uncertainty represents the standard deviation of $\langle \rho R \rangle$ from the four measurements. SSD smoothing was

E16133JRC
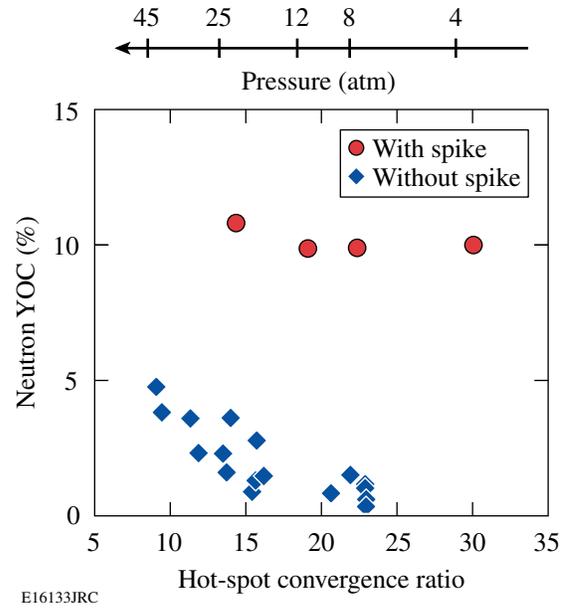
Figure 113.32
The neutron YOC versus 1-D calculated hot-spot convergence ratio. The YOC is close to 10% for a hot-spot convergence of up to 30.

E16134JRC
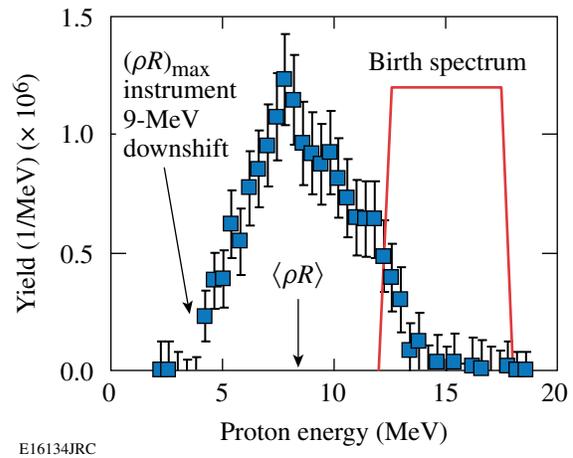
Figure 113.33
Measured proton spectra for shot 48674, which is the average of four spectra taken from different directions. The 8.3-atm, D_2-filled CH shell was imploded with 18.0 kJ without SSD. The average areal density was measured with $\langle \rho R \rangle = 0.204 \pm 0.014$ g/cm^2, and the measured maximum areal density of 0.3 g/cm^2 is restricted by the detection limit of the instrument.

found to have no significant effect on ρR for relaxation-type low-adiabat implosions,[10] and the small standard deviation of the ρR measurement indicates high shell stability. Notice that the lower limit of the detector given by the thickness of the Al wedges[20] is at a proton energy of 4 MeV, which appears as a cutoff in the measured spectrum. The protons need to be

downshifted by ~9 MeV to reach the cutoff that corresponds to a ρR value of ~0.3 g/cm^2. Therefore, the proton spectrum indicates that areal densities even higher than 0.3 g/cm^2 were experimentally realized. Calculations with the 1-D code *LILAC*[27] using a constant flux limiter of 0.06 predict, for shot 48674, $(\rho R)_{max} = 0.345$ g/cm^2 and with a time-dependent flux limiter (Refs. 31 and 32) $(\rho R)_{max} = 0.331$ g/cm^2. The time-dependent flux-limiter calculations model the nonlocal heat transport by introducing an effective temporal varying flux limiter.[32] For the ρR inference a fusion-reaction-rate–averaged density of 110 g/cm^3 and a temperature of 0.1 keV were taken from simulations. The inferred ρR value depends slightly on the density. A density variation of ± 50 g/cm^3 changes the areal density by ~± 0.01 g/cm^2. The temperature dependence is negligible. The absolute calibration uncertainty of the WRF is ± 0.4 MeV for the mean value of the proton spectral distribution corresponding to ± 0.01 g/cm^2. Taking the statistical fluctuation, the density variation, and the calibration uncertainty into account, an absolute measurement error of ~± 0.014 g/cm^2 is estimated, leading to $\langle \rho R \rangle = 0.204 \pm 0.014$ g/cm^2.

Areal-density measurements were performed for various fill pressures corresponding to various hot-spot convergence ratios. Figure 113.34 shows that implosions with optimized spike pulse shapes (open triangles) achieve the highest $\langle \rho R \rangle$ values that have a tendency to increase with CR from ~15 to ~25. The data point at CR ~ 30 falls below the scaling, indicating that for


E16136JRC
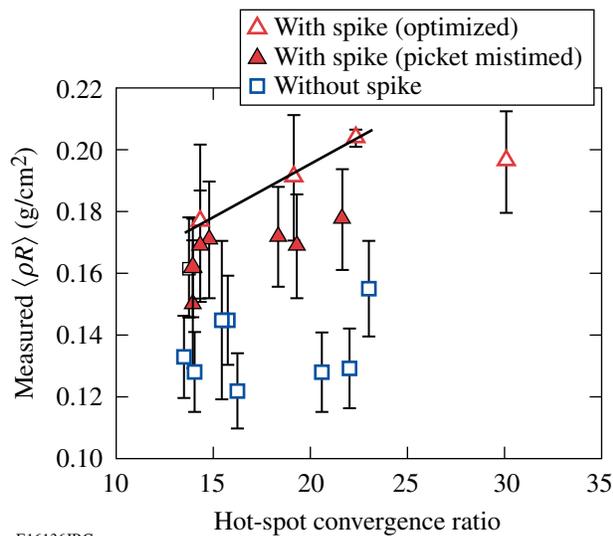
Figure 113.34
$\langle \rho R \rangle$ versus CR for 2.8-ns spike-delay pulse implosions (optimized pulse shape—open triangles; picket mistimed—solid triangles) and no-spike pulse-shape implosions (open squares). The relative $\langle \rho R \rangle$ error bars are shown.

large CR the $\langle \rho R \rangle$ measurement is affected by the instrumental cutoff and by the sampling over the $\langle \rho R \rangle$ time evolution (see Fig. 113.35). The solid line is a linear fit through the first three open triangle data points. In contrast, lower $\langle \rho R \rangle$ values are measured for a mistimed picket (solid triangles) and the lowest $\langle \rho R \rangle$ values are observed without SSW (squares), showing also a larger data scattering. Figures 113.32 and 113.34 reveal that optimum timed shock-ignition pulse-shape implosions show an improved performance with higher $\langle \rho R \rangle$ and suggest less instability growth.

Figure 113.35(a) shows all of the measured SSW implosion $\langle \rho R \rangle$ data versus the 1-D prediction with a time-dependent flux limiter. To relate the measured $\langle \rho R \rangle$ obtained from the mean of the proton spectrum to the 1-D calculation, the predicted ρR evolution is averaged over a time window in which the fusion products are generated and weighted according to the production rate.[33] The simulations in Fig. 113.35(b) show that the ρR (thick solid curve) increases during neutron production and that the fusion reactions are quenched near the time of a peak areal density of 0.33 g/cm^2. The measured neutron rate (thin solid curve) is lower and truncated compared to the 1-D simulated fusion rate (dashed), probably caused by shell–fuel mixing. Mixing is a time-dependent process that is small in the initial phase of ρR buildup and then grows during the deceleration, leaving a clean hot-spot radius equal to the so-called free-fall line.[34] The corresponding time-integrated proton spectrum is shown in Fig. 113.33; each point of the spectrum corresponds to a different downshift and, therefore, to a different ρR. The energy downshift of the low-energy tail of the spectrum represents a measure of the peak ρR during the neutron production, which was limited by the instrument indicating peak ρR exceeding 0.3 g/cm^2, in agreement with the simulations. The temporal shape of the neutron-production rate is close to the secondary-proton–production rate[26] and is used to calculate the neutron-rate–averaged $\langle \rho R \rangle_n$ [Fig. 113.35(a)]. The experimental error of the absolute timing of NTD[22] is ~50 ps and, considering that the neutron-production duration is typically less than 300 ps, the calculated $\langle \rho R \rangle_n$ values are very sensitive to the timing of the measured neutron rate. The timing error of the measured rate was taken into account for these calculations, leading to the uncertainties in the calculated $\langle \rho R \rangle_n$ shown as x-error bars in Fig. 113.35(a). Figure 113.35 shows that the fuel assembly is close to the burn-weighted 1-D predictions of the code *LILAC* with measured ρR values achieving larger than 90% of the 1-D prediction. The slight deviation at high compression is partially due to the instrumental cutoff resulting in a slightly lower $\langle \rho R \rangle$ reading.
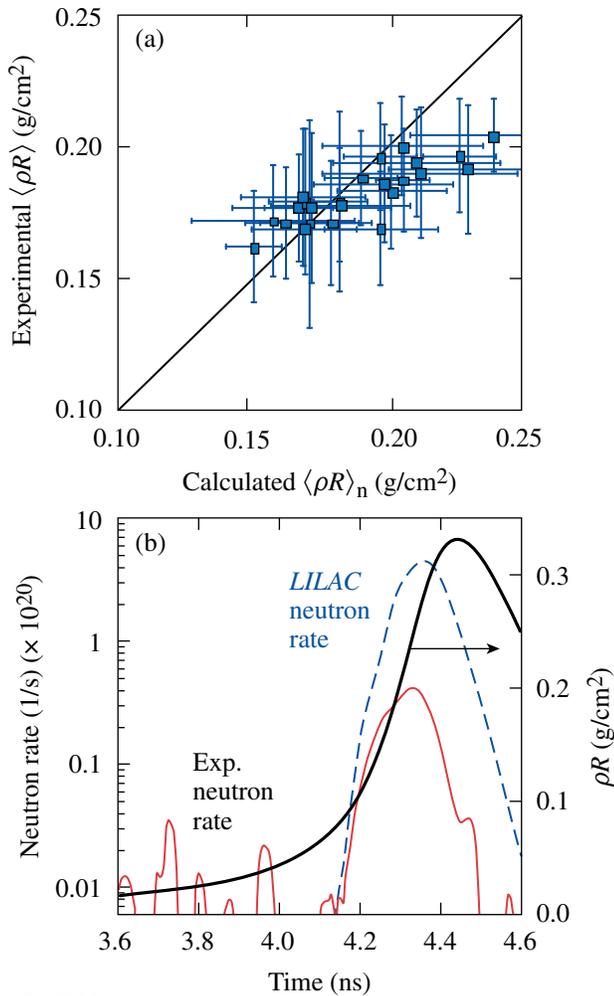
Figure 113.35
(a) Measured spike-pulse implosion $\langle\rho R\rangle$ versus *LILAC*-calculated neutron-rate–averaged $\langle\rho R\rangle_n$ and (b) comparison of measured neutron rate (thin solid curve), 1-D predicted neutron rate (dashed curve), and predicted ρR evolution (thick solid curve) for shot 48674 (proton spectrum in Fig. 113.33). The absolute measurement $\langle\rho R\rangle$ uncertainties are shown in (a).

Initial Spike-Pulse Cryogenic-Shell Implosions

Initial shock-spike implosions with cryogenic D_2 and DT targets [Fig. 113.26(b)] were performed using spike-pulse shapes similar to that shown in Fig. 113.27 with a total laser energy of 16.0 kJ for the D_2 target and 17.9 kJ for the DT target. In both cases SSD was used. High-quality targets with ice-layer nonuniformities of $\sigma_{rms} = 1.5~\mu$m (D_2) and $0.9~\mu$m (DT) were imploded. The D_2 target implosion suffered from a large 49 ± 3-μm offset of the capsule center from target chamber center, which caused a significant drive asymmetry. A low-mode ρR modulation was measured with the higher areal density toward the higher-intensity drive

side. By averaging the four lines of sight, an areal density of $\langle\rho R\rangle = 0.18\pm0.05$ g/cm^2 was measured, which is compared to a calculated value of 0.20 g/cm^2 (time-dependent flux limiter)[32] taking the measured fusion-reaction history into account. Therefore, the assembled fuel reaches ~90% of the 1-D prediction. The neutron yield is ~5% of the 1-D prediction. A similar D_2 cryogenic-target implosion using a similar waveform but without a spike pulse and with a better target offset of $19\pm3~\mu$m yielded a slightly higher YOC of ~7% and $\langle\rho R\rangle = 0.20\pm0.02$ g/cm^2 (Ref. 35). Table 113.I compares the implosion performance of cryogenic targets using low-adiabat picket-pulse shapes with and without a high-intensity spike at the end of the drive pulse. No measured ρR data are available for the DT implosions because the WRF diagnostic is compromised by the large neutron influx. DT target shot 48734 (with a late spike pulse) had very good ice-layer quality and small target offset resulting in YOC of ~12%, while a comparable shot without a spike pulse (48304) gave a YOC of ~10%. Due to a diagnostic error, no target-offset data are available for shot 48304. The first few shock-ignition cryo implosions on OMEGA were among the best performing (in terms of yield and ρR) but did not yet exceed the performance of standard pulse shapes. This is likely due to a non-optimal pulse shape when SSD was employed. The SSD bandwidth broadened the spike pulse sufficiently so that *LILAC* simulations do not show a SSW. The spike-pulse rise time without SSD in the plastic-shell implosions is about twice as fast and generates a significant SSW. Further experimental studies will assess the implosion performance of cryogenic targets without SSD, working toward an improved pulse shape with SSD, which will then allow a strong enough shock with the late spike pulse to be generated.

Parametric plasma instabilities are of concern in an ignition target design[5] with spike-pulse intensities in the range of 10^{15} to 10^{16} W/cm^2 and an ~150-ps FWHM pulse. The instabilities increase the back-reflection of laser light from the target and therefore lower the coupling efficiency into the capsule, while an increased fraction of the coupled energy will be transferred into suprathermal electrons, which are a potential source of preheat. No measurable amount of stimulated Raman and Brillouin backscatter is detected in the above-discussed cryogenic implosions having nominal laser peak intensities of ~8×10^{14} W/cm^2. The actual intensity at the critical-density surface is a factor of ~2 higher when the target compression is taken into account. There is a measurable amount of hard x-ray yield above ~50 keV due to fast electrons produced by the two-plasmon–decay (TPD) instability. Since $\langle\rho R\rangle$ reaches ~90% of the 1-D prediction, there is no significant degradation of the implosion due to preheat. There are no parametric-

E16137JRC

Table 113.I: A comparison of the implosion performance of cryogenic targets using low-adiabat picket-pulse shapes with and without a high-intensity spike at the end of the drive pulse.

Shot #	47206	48386	48304	48734
Target	D_2	D_2	DT	DT
Ice layer σ (μm)	2.4	1.5	0.7	0.9
Target offset (μm)	19±3	49±3	No data	10±5
Spike pulse	No	Yes	No	Yes
E_{laser} (kJ)	16.5	16.0	19.3	17.9
Adiabat	1.8	2.0	2.0	2.0
$\langle \rho R \rangle_{exp}$ (g/cm^2)	0.201±0.021	0.182±0.046	No data	No data
$\langle \rho R \rangle_{LILAC}$ (g/cm^2)	0.216	0.204	0.186	0.194
T_{ion} (keV) (exp)	2.1±0.5	1.8±0.5	2.5±0.5	1.9±0.5
T_{ion} (keV) (LILAC)	2.0	1.9	2.3	2.3
Y_n	7.70×10^9	3.40×10^9	1.60×10^{12}	1.43×10^{12}
(YOC)	7.3%	5.3%	9.8%	12.3%

instability measurements for shock-ignition-target–relevant conditions available (spherical cryogenic target, long density scale length, and intensities above 2×10^{15} W/cm^2). However, measurements of parametric instabilities for indirect-drive–relevant ignition-plasma conditions with millimeter-density scale length and 15% critical-density targets report a backscatter of the order of a few percent to 10% at 5×10^{15} W/cm^2 (Ref. 36). The density scale lengths in shock-ignition targets are shorter, and for similar laser intensities the backscatter is expected to be of the order of ~10% or less. Parametric instability and fast-electron–generation scaling measurements at direct-drive-ignition–relevant intensities and long density scale lengths in warm surrogate targets show that the TPD-generated preheat starts to saturate at intensities above ~1×10^{15} W/cm^2 (Ref. 37). Moderate-energy fast electrons (~100 keV) generated by the late high-intensity spike might even be beneficial for the shock-ignition concept. The effect of preheating was studied in marginal-igniting, 350-μm-thick massive shells with the 1-D *LILAC* code using a multigroup diffusion model for the fast-electron transport and a Maxwellian hot-electron-energy distribution of 150-keV characteristic energy.[5] There is considerable compression at the time when the fast electrons are generated with $\langle \rho R \rangle \approx 70$ mg/cm^2, compared to a 17-mg/cm^2 stopping range of a 100-keV electron in the cryogenic DT shell. The majority of the fast electrons are stopped in the outer layers of the shell and pose no threat of the implosion performance being compromised by preheat. Moderate-energy fast electrons actually increase the strength of the SSW, therefore widening the shock-launching ignition window.[5]

Summary and Conclusions

Fuel assembly that is relevant for the shock-ignition ICF concept has been experimentally studied for the first time. The experiments were performed on the OMEGA laser using shock-ignition laser pulse shapes and warm plastic surrogate and cryogenic targets. Systematic studies of low-adiabat ($\alpha \approx 1.5$) implosions with a short picket and a high-intensity spike were performed. It was demonstrated that the fuel assembly with warm plastic targets is close to 1-D simulation predictions with neutron-rate–averaged areal densities exceeding ~0.2 g/cm^2 and maximum ρR above ~0.3 g/cm^2, which are significantly higher than without the spike pulse. Implosions of D_2-filled, 40-μm-thick plastic shells were optimized by measuring the performance as a function of the timing of the picket and spike pulses. The spike-shock–generated implosion produces a factor of ~4–enhanced neutron yield compared to a laser pulse shape without intensity spike for 25-atm fill pressure and the same laser energy. For an optimized spike-pulse shape with respect to shock-wave timing, the measured neutron yields are ~10% of the yields calculated by 1-D simulations (YOC) for fill pressures down to 4 atm, while the YOC without a spike pulse (not optimized) is less than 1% for pressures below 9 atm. These are the highest YOC's reported so far for $\alpha \approx 1.5$ implosions of warm plastic shells and a hot-spot convergence ratio of ~30. Plastic shells with low fill pressures are inherently RT unstable during the deceleration phase, giving rise to a substantial shell–fuel mixing that quenches fusion reactions, which is not described by 1-D simulations. The measurements have shown that the shock-ignition concept is very promising by achieving higher

compression and better stability than comparable low-adiabat, relaxation-picket plastic-shell implosions without a spike pulse. Initial experiments with cryogenic D_2 and DT targets and $\alpha = 2$, spike and no-spike pulse shapes were performed, showing close to 1-D performance and a neutron YOC of ~12%.

ACKNOWLEDGMENT

REFERENCES

1. J. Nuckolls *et al.*, Nature **239**, 139 (1972).

2. J. D. Lindl, *Inertial Confinement Fusion: The Quest for Ignition and Energy Gain Using Indirect Drive* (Springer-Verlag, New York, 1998), p. 4.

3. S. Atzeni and J. Meyer-ter-Vehn, *The Physics of Inertial Fusion: Beam Plasma Interaction, Hydrodynamics, Hot Dense Matter*, International Series of Monographs on Physics (Clarendon Press, Oxford, 2004), p. 52.

4. R. Betti, C. D. Zhou, K. S. Anderson, L. J. Perkins, W. Theobald, and A. A. Solodov, Phys. Rev. Lett. **98**, 155001 (2007).

5. R. Betti, W. Theobald, C. D. Zhou, K. S. Anderson, P. W. McKenty, D. Shvarts, and C. Stoeckl, "Shock Ignition of Thermonuclear Fuel with High Areal Density," to be published in the Journal of Physics: Conference Series (Institute of Physics).

6. M. C. Herrmann, M. Tabak, and J. D. Lindl, Phys. Plasmas **8**, 2296 (2001).

7. M. Tabak *et al.*, Phys. Plasmas **1**, 1626 (1994).

8. M. Murakami and H. Nagatomo, Nucl. Instrum. Methods Phys. Res. A **544**, 67 (2005).

9. R. Betti and C. Zhou, Phys. Plasmas **12**, 110702 (2005); R. Betti, K. Anderson, T. R. Boehly, T. J. B. Collins, R. S. Craxton, J. A. Delettrez, D. H. Edgell, R. Epstein, V. Yu. Glebov, V. N. Goncharov, D. R. Harding, R. L. Keck, J. H. Kelly, J. P. Knauer, S. J. Loucks, J. A. Marozas, F. J. Marshall, A. V. Maximov, D. N. Maywar, R. L. McCrory, P. W. McKenty, D. D. Meyerhofer, J. Myatt, P. B. Radha, S. P. Regan, C. Ren, T. C. Sangster, W. Seka, S. Skupsky, A. A. Solodov, V. A. Smalyuk, J. M. Soures, C. Stoeckl, W. Theobald, B. Yaakobi, C. Zhou, J. D. Zuegel, J. A. Frenje, C. K. Li, R. D. Petrasso, and F. H. Séguin, Plasma Phys. Control. Fusion **48**, B153 (2006).

10. C. D. Zhou, W. Theobald, R. Betti, P. B. Radha, V. A. Smalyuk, D. Shvarts, V. Yu. Glebov, C. Stoeckl, K. S. Anderson, D. D. Meyerhofer, T. C. Sangster, C. K. Li, R. D. Petrasso, J. A. Frenje, and F. H. Séguin, Phys. Rev. Lett. **98**, 025004 (2007).

11. T. R. Boehly, D. L. Brown, R. S. Craxton, R. L. Keck, J. P. Knauer, J. H. Kelly, T. J. Kessler, S. A. Kumpan, S. J. Loucks, S. A. Letzring, F. J. Marshall, R. L. McCrory, S. F. B. Morse, W. Seka, J. M. Soures, and C. P. Verdon, Opt. Commun. **133**, 495 (1997).

12. C. Stoeckl, C. Chiritescu, J. A. Delettrez, R. Epstein, V. Yu. Glebov, D. R. Harding, R. L. Keck, S. J. Loucks, L. D. Lund, R. L. McCrory, P. W. McKenty, F. J. Marshall, D. D. Meyerhofer, S. F. B. Morse, S. P. Regan, P. B. Radha, S. Roberts, T. C. Sangster, W. Seka, S. Skupsky, V. A. Smalyuk, C. Sorce, J. M. Soures, R. P. J. Town, J. A. Frenje, C. K. Li, R. D. Petrasso, F. H. Séguin, K. Fletcher, S. Padalino, C. Freeman, N. Izumi, R. Lerche, and T. W. Phillips, Phys. Plasmas **9**, 2195 (2002).

13. T. C. Sangster, J. A. Delettrez, R. Epstein, V. Yu. Glebov, V. N. Goncharov, D. R. Harding, J. P. Knauer, R. L. Keck, J. D. Kilkenny, S. J. Loucks, L. D. Lund, R. L. McCrory, P. W. McKenty, F. J. Marshall, D. D. Meyerhofer, S. F. B. Morse, S. P. Regan, P. B. Radha, S. Roberts, W. Seka, S. Skupsky, V. A. Smalyuk, C. Sorce, J. M. Soures, C. Stoeckl, K. Thorp, J. A. Frenje, C. K. Li, R. D. Petrasso, F. H. Séguin, K. A. Fletcher, S. Padalino, C. Freeman, N. Izumi, J. A. Koch, R. A. Lerche, M. J. Moran, T. W. Phillips, and G. J. Schmid, Phys. Plasmas **10**, 1937 (2003).

14. T. C. Sangster, R. Betti, R. S. Craxton, J. A. Delettrez, D. H. Edgell, L. M. Elasky, V. Yu. Glebov, V. N. Goncharov, D. R. Harding, D. Jacobs-Perkins, R. Janezic, R. L. Keck, J. P. Knauer, S. J. Loucks, L. D. Lund, F. J. Marshall, R. L. McCrory, P. W. McKenty, D. D. Meyerhofer, P. B. Radha, S. P. Regan, W. Seka, W. T. Shmayda, S. Skupsky, V. A. Smalyuk, J. M. Soures, C. Stoeckl, B. Yaakobi, J. A. Frenje, C. K. Li, R. D. Petrasso, F. H. Séguin, J. D. Moody, J. A. Atherton, B. D. MacGowan, J. D. Kilkenny, T. P. Bernat, and D. S. Montgomery, Phys. Plasmas **14**, 058101 (2007).

15. T. R. Boehly, V. A. Smalyuk, D. D. Meyerhofer, J. P. Knauer, D. K. Bradley, R. S. Craxton, M. J. Guardalben, S. Skupsky, and T. J. Kessler, J. Appl. Phys. **85**, 3444 (1999).

16. Y. Lin, T. J. Kessler, and G. N. Lawrence, Opt. Lett. **21**, 1703 (1996).

17. S. Skupsky, R. W. Short, T. Kessler, R. S. Craxton, S. Letzring, and J. M. Soures, J. Appl. Phys. **66**, 3456 (1989).

18. K. Anderson and R. Betti, Phys. Plasmas **11**, 5 (2004).

19. J. P. Knauer, K. Anderson, R. Betti, T. J. B. Collins, V. N. Goncharov, P. W. McKenty, D. D. Meyerhofer, P. B. Radha, S. P. Regan, T. C. Sangster, V. A. Smalyuk, J. A. Frenje, C. K. Li, R. D. Petrasso, and F. H. Séguin, Phys. Plasmas **12**, 056306 (2005).

20. F. H. Séguin, J. A. Frenje, C. K. Li, D. G. Hicks, S. Kurebayashi, J. R. Rygg, B.-E. Schwartz, R. D. Petrasso, S. Roberts, J. M. Soures, D. D. Meyerhofer, T. C. Sangster, J. P. Knauer, C. Sorce, V. Yu. Glebov, C. Stoeckl, T. W. Phillips, R. J. Leeper, K. Fletcher, and S. Padalino, Rev. Sci. Instrum. **74**, 975 (2003).

21. R. A. Lerche, D. W. Phillion, and G. L. Tietbohl, Rev. Sci. Instrum. **66**, 933 (1995).

22. C. Stoeckl, V. Yu. Glebov, S. Roberts, T. C. Sangster, R. A. Lerche, R. L. Griffith, and C. Sorce, Rev. Sci. Instrum. **74**, 1713 (2003).

23. V. Yu. Glebov, D. D. Meyerhofer, C. Stoeckl, and J. D. Zuegel, Rev. Sci. Instrum. **72**, 824 (2001).

24. C. K. Li, D. G. Hicks, F. H. Séguin, J. A. Frenje, R. D. Petrasso, J. M. Soures, P. B. Radha, V. Yu. Glebov, C. Stoeckl, D. R. Harding, J. P. Knauer, R. L. Kremens, F. J. Marshall, D. D. Meyerhofer, S. Skupsky, S. Roberts, C. Sorce, T. C. Sangster, T. W. Phillips, M. D. Cable, and R. J. Leeper, Phys. Plasmas **7**, 2578 (2000).

25. R. D. Petrasso, J. A. Frenje, C. K. Li, F. H. Séguin, J. R. Rygg, B. E. Schwartz, S. Kurebayashi, P. B. Radha, C. Stoeckl, J. M. Soures, J. Delettrez, V. Yu. Glebov, D. D. Meyerhofer, and T. C. Sangster, Phys. Rev. Lett. **90**, 095002 (2003).

26. V. A. Smalyuk, P. B. Radha, J. A. Delettrez, V. Yu. Glebov, V. N. Goncharov, D. D. Meyerhofer, S. P. Regan, S. Roberts, T. C. Sangster, J. M. Soures, C. Stoeckl, J. A. Frenje, C. K. Li, R. D. Petrasso, and F. H. Séguin, Phys. Rev. Lett. **90**, 135002 (2003).

27. J. Delettrez, R. Epstein, M. C. Richardson, P. A. Jaanimagi, and B. L. Henke, Phys. Rev. A **36**, 3926 (1987); M. C. Richardson, P. W. McKenty, F. J. Marshall, C. P. Verdon, J. M. Soures, R. L. McCrory, O. Barnouin, R. S. Craxton, J. Delettrez, R. L. Hutchison, P. A. Jaanimagi, R. Keck, T. Kessler, H. Kim, S. A. Letzring, D. M. Roback, W. Seka, S. Skupsky, B. Yaakobi, S. M. Lane, and S. Prussin, in *Laser Interaction and Related Plasma Phenomena*, edited by H. Hora and G. H. Miley (Plenum Publishing, New York, 1986), Vol. 7, pp. 421–448.

28. P. B. Radha, T. J. B. Collins, J. A. Delettrez, Y. Elbaz, R. Epstein, V. Yu. Glebov, V. N. Goncharov, R. L. Keck, J. P. Knauer, J. A. Marozas, F. J. Marshall, R. L. McCrory, P. W. McKenty, D. D. Meyerhofer, S. P. Regan, T. C. Sangster, W. Seka, D. Shvarts, S. Skupsky, Y. Srebro, and C. Stoeckl, Phys. Plasmas **12**, 056307 (2005).

29. C. D. Zhou and R. Betti, Phys. Plasmas **14**, 072703 (2007).

30. T. R. Boehly, E. Vianello, J. E. Miller, R. S. Craxton, T. J. B. Collins, V. N. Goncharov, I. V. Igumenshchev, D. D. Meyerhofer, D. G. Hicks, P. M. Celliers, and G. W. Collins, Phys. Plasmas **13**, 056303 (2006).

31. A. Sunahara, J. A. Delettrez, C. Stoeckl, R. W. Short, and S. Skupsky, Phys. Rev. Lett. **91**, 095003 (2003).

32. V. N. Goncharov, O. V. Gotchev, E. Vianello, T. R. Boehly, J. P. Knauer, P. W. McKenty, P. B. Radha, S. P. Regan, T. C. Sangster, S. Skupsky, V. A. Smalyuk, R. Betti, R. L. McCrory, D. D. Meyerhofer, and C. Cherfils-Clérouin, Phys. Plasmas **13**, 012702 (2006).

33. P. B. Radha, V. Yu. Glebov, V. N. Goncharov, D. D. Meyerhofer, T. C. Sangster, S. Skupsky, J. A. Frenje, and R. D. Petrasso, Bull. Am. Phys. Soc. **51**, 106 (2006).

34. P. D. Roberts *et al.*, J. Phys. D **13**, 1957 (1980).

35. T. C. Sangster, V. N. Goncharov, P. B. Radha, V. A. Smalyuk, R. Betti, R. S. Craxton, J. A. Delettrez, D. H. Edgell, V. Yu. Glebov, D. R. Harding, D. Jacobs-Perkins, J. P. Knauer, F. J. Marshall, R. L. McCrory, P. W. McKenty, D. D. Meyerhofer, S. P. Regan, W. Seka, R. W. Short, S. Skupsky, J. M. Soures, C. Stoeckl, B. Yaakobi, D. Shvarts, J. A. Frenje, C. K. Li, R. D. Petrasso, and F. H. Séguin, "High-Areal-Density Fuel Assembly in Direct-Drive Cryogenic Implosions," submitted to Physical Review Letters.

36. J. D. Moody *et al.*, Phys. Rev. Lett. **86**, 2810 (2001).

37. C. Stoeckl, R. E. Bahr, B. Yaakobi, W. Seka, S. P. Regan, R. S. Craxton, J. A. Delettrez, R. W. Short, J. Myatt, A. V. Maximov, and H. Baldis, Phys. Rev. Lett. **90**, 235002 (2003).

Time-Resolved Absorption in Cryogenic and Room-Temperature, Direct-Drive Implosions

Introduction

Absorption of laser light in laser inertial confinement fusion (ICF) implosion experiments[1–4] is of pre-eminent importance since it provides the energy input. Current ICF implosions are scaled from future ignition experiments with thermonuclear gain and typically require laser pulses of complex temporal shape. These pulse shapes are chosen—among other considerations—to minimize the growth of hydrodynamic instabilities in the acceleration phase of the implosion.[5,6] They drive an optimized series of shock and compression waves that coalesce in the fuel and lead to hot-spot ignition, provided the fuel has been kept at a low adiabat α (α = minimum fuel pressure over Fermi-degenerate pressure).

An accurate understanding of the coupling of laser light to the target is essential for the success of implosion experiments. The laser light can be refracted, scattered, and absorbed. Hydrodynamic simulations are used to optimize the pulse shapes for specific target designs.[7–11] These simulations indicate that the scattered-light distribution in 60-beam implosion experiments is isotropic to within 1% or 2%. Experimental measurements of the laser light scattered into 4π strad are used to infer the absorption for comparison with hydrodynamic simulations.

Current implosion experiments on OMEGA are designed to study various parameters including the hydrodynamic stability of the implosion. The absorption of laser light crucially influences the hydrodynamics. All phases of laser absorption, refraction, and scattering in current experiments will be encountered in the early phases of future ignition experiments. Some potential problems of future ignition experiments cannot be fully investigated at present. The longer scale lengths that will be encountered in the future may favor nonlinear interaction processes beyond those in current implosion experiments[12] or dedicated long-scale-length planar interaction experiments.[13–16]

Time-integrated absorption measurements have been previously reported for direct-drive spherical target experiments.[2,4,17–21] Time-integrated measurements can mask dif-ferences in the time evolution of the absorption that can lead to significant hydrodynamic consequences, such as shock mistiming and an increased adiabat of the inner shell surface of the imploding target. This article describes the experimental conditions, followed by examples of time-resolved scattered-light measurements in implosion experiments and a discussion of the underlying absorption processes. Conclusions are also presented.

Experimental Conditions

The OMEGA Laser System[22] operating with 60 UV beams (λ_L = 351 nm) irradiates cryogenic and room-temperature targets of ~860-μm diameter. Total laser energies are ≤24 kJ in laser pulses of ≤4 ns with shapes with or without 100-ps pickets ahead of the main pulse. The maximum overlapped irradiation intensity is 1.5×10^{15} W/cm^2. All beams are equipped with distributed phase plates (DPP's),[23–25] polarization smoothing (PS),[26] and smoothing by spectral dispersion (SSD)[27] in most experiments. The energy irradiation nonuniformity on target is <3% rms with each of the 60 beams slightly overfilling the target with ~5% energy spillover around the cold target. The intensity nonuniformity on target during the slowly varying parts of the pulse shape ranges between 3% and 7% when averaged over 200 to 300 ps. In the rapidly varying parts of the pulse shape the intensity nonuniformity is more difficult to quantify since it depends on pulse-shape irregularities, timing jitter among beams, and the precision and accuracy of the pulse-shape measurements for each beam. The intensity nonuniformity during the rapidly varying parts of the pulse shapes is estimated to be ≤15% rms.

The cryogenic targets[28] are plastic (CD) shells of ~860-μm diameter and 3- to 10-μm wall thickness filled with ~1000 atm of DT or D$_2$ and cooled and frozen into uniform,[29,30] ~100-μm solid DT or D$_2$ "ice" layers at ~18 K. The room-temperature targets are either CH or CD shells with walls of 10 to 40 μm filled with D$_2$ or DT gas (3 to 40 atm). The room-temperature targets are coated with ~100 nm of Al for gas retention. Gas diffusion at cryogenic temperatures is negligible and no Al coating is applied.

The principal diagnostic for determining laser absorption in these implosion experiments is provided by two full-aperture backscattering stations (FABS) located in beams 25 and 30.[4,18,31] Time-resolved scattered-light spectroscopy and time-integrated calorimetry in these stations are used to infer the absorption of light by the target. The absolutely calibrated FABS calorimeters provide cross-calibration for all time-resolved scattered-light spectra. A schematic of the diagnostic arrangement is shown in Fig. 113.36(a) along with typical time-resolved scattered-light spectra for a narrowband (no SSD bandwidth), 1-ns, room-temperature implosion.

There are four spectrally and time-resolved scattered-light–measurement channels[31] (one channel in each FABS and two channels located between focusing lenses). Two typical time-resolved scattered-light spectra are shown in Figs. 113.36(b) and 113.36(c) with no SSD bandwidth applied. The temporal resolution is ~80 ps and the spectral resolution is ~0.08 nm.

The calorimeters are calibrated using shots through the target chamber without a target, yielding absolute errors on the energy measurements of 1% to 3% at ~10 J into the focusing lenses of beam 25 or 30. The detection threshold for these calorimeters is ~0.04 J. For a typical 20-kJ implosion with ~50%

absorption, this results in a calorimetry precision of ~1.5%. In the implosion experiments, the calorimeter measurements vary by 4% to 6%, leading to typical errors on the absorption of ~2% to 3%. These errors are about twice as large as expected but the source of these errors is not well understood at present. In addition to the FABS calorimeters, there are up to 17 scattered-light calorimeters located inside and outside of the target chamber. These calorimeters are cross-calibrated to the FABS calorimeters since absolute calibration of these calorimeters has proven to be very difficult to ascertain and maintain.

Near isotropy of the scattered light is predicted by hydro-dynamic simulations. The schematic ray trace in Fig. 113.36(a) shows a variety of scattered ray paths that contribute to the FABS calorimeter and streak camera channels. This figure is greatly simplified as each point on each lens receives rays from many different directions and each FABS sees contributions from all 60 beams. The fractional contributions from each beam vary with time and beam. Since the FABS stations are in the line of sight of opposing beams, some light passes around the targets at early times [unshifted signal in Fig. 113.36(b)] and contributes to the FABS energy measurements. This "blow-by" is not isotropic and must be subtracted from the scattered-light measurements before the isotropically scattered-light energy
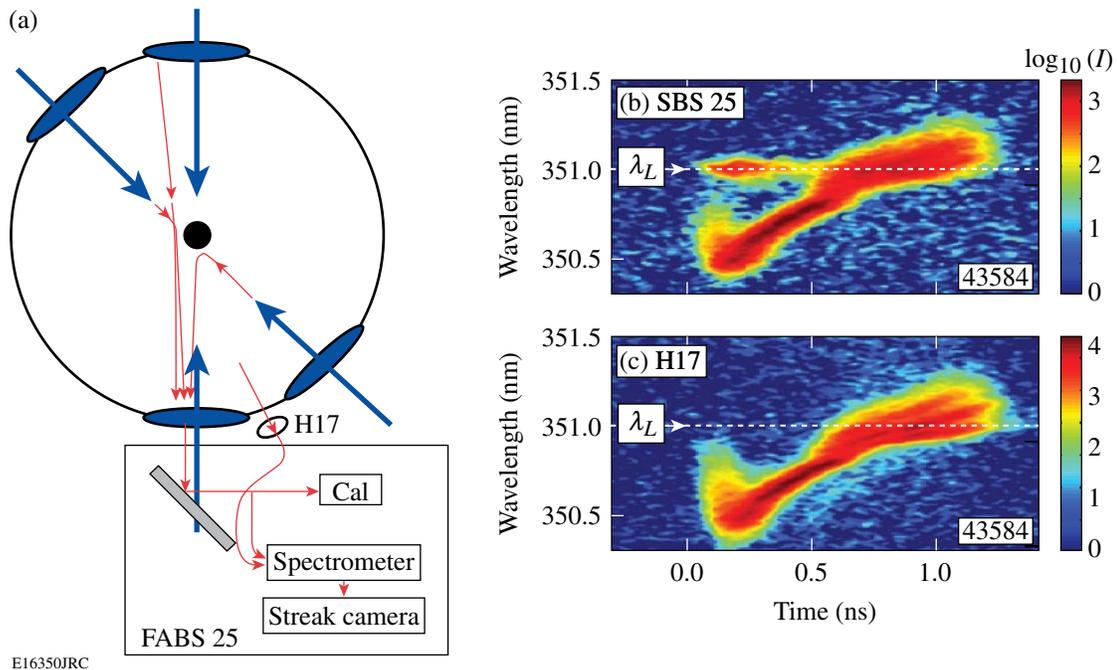

Figure 113.36

(a) Schematic of scattered-light diagnostics inside the OMEGA target chamber. The full-aperture backscatter station (FABS) is shown for beam 25 with its calorimeter and temporally and spectrally resolved backscatter channel. An additional channel for light scattered in between the focusing lenses is also shown (H17). Typical time-resolved backscatter spectra are shown in (b) for the FABS channel and (c) for the channel in between the focusing lenses for an imploding 20-μm-thick CH shell with DPP's and PS but no SSD bandwidth.

can be determined. This is done using target shots with only the beams opposing the two FABS stations. Since plasma formation on the limb of the target is minimal in this case, this measurement provides an upper limit of the blow-by. For consistency the two beams opposing the FABS can be turned off, which only minimally affects the FABS energy measurements for 58-beam shots but totally eliminates the need for blow-by corrections.

The two spectra shown in Fig. 113.36 clearly distinguish light that misses the target (blow-by) as it remains unshifted in wavelength [Fig. 113.36(b)]. For shots without beams opposing the FABS stations, the two spectra are practically indistinguishable. The time-resolved spectrum [Fig. 113.36(b)] allows for quantitative estimates of the blow-by, supporting the calorimetric estimates discussed above. The blow-by fraction depends on the pulse shape, pulse duration, and target and cannot be reasonably determined for all conditions. An estimated blow-by fraction of ~1.6% of the opposing beam energy is subtracted from the FABS calorimeter measurement to determine the diffusely scattered-light energy.

Results

Time-resolved scattered-light spectra are shown in Fig. 113.36 for a 1-ns square pulse implosion experiment and in Fig. 113.37(a) for an implosion using a complex pulse shape with 1-THz SSD bandwidth. The scattered-light power, obtained by integrating the spectra over the wavelength, is compared to predictions from hydrodynamic ($LILAC$[32]) simulations in Fig. 113.37(b). (Experimental time-resolved absorption fractions are not compared directly with simulations since the laser pulse shape and scattered-light spectra are recorded with different streak cameras and slight inaccuracies can lead to large errors upon division of one by the other.) To avoid the need for detailed blow-by corrections, the spectra taken in between the focusing lenses (e.g., H17) are used for most of the quantitative analyses. Two $LILAC$ predictions for the scattered-light power are shown in Fig. 113.37(b), one for standard flux-limited electron-heat transport with $f = 0.06$ (Ref. 33) and the second using a nonlocal heat-transport model developed at LLE.[34,35] The differences between the experimental observations and the $LILAC$ predictions apparent in Fig. 113.37(b) are typical for these experiments but the details differ depending on target and irradiation parameters.

The scattered-light spectra in Figs. 113.36 and 113.37 exhibit a similar rapid blue shift followed by a slow return to the initial laser wavelength and beyond. The spectra are modeled using ray-trace simulations based on density, velocity, and tempera-

ture profiles obtained from hydrodynamic ($LILAC$) simulations. Figure 113.38 shows schematically how all 60 beams of OMEGA contribute to the scattered light collected at any location. The contributions from each beam vary in time. The spectral shifts observed in Figs. 113.36 and 113.37 are due to the plasma evolution,[36] i.e., the temporally changing optical path length in the plasma traversed by any ray.
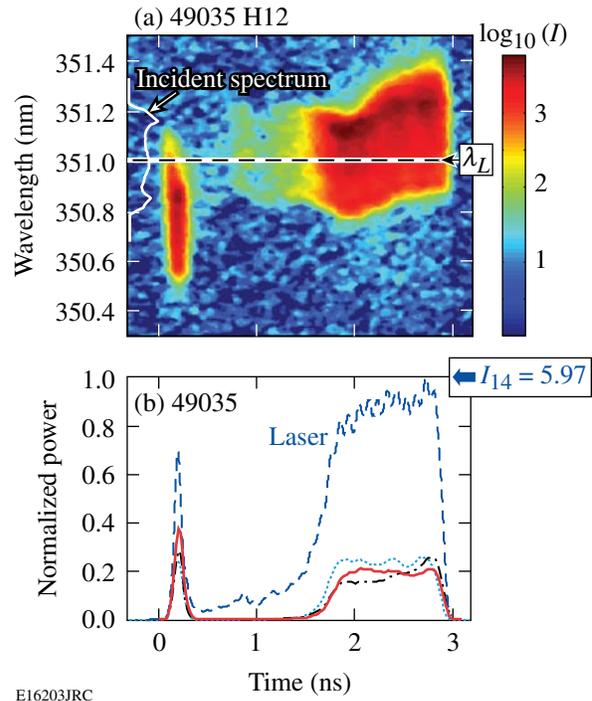

Figure 113.37
(a) Scattered-light spectrum and (b) incident and scattered-light powers for a cryogenic target (10-μm CH wall, 77-μm DT-ice layer, 858-μm diam) imploded with 17.7 kJ of fully smoothed laser energy (DPP's, PS, and 1-THz SSD bandwidth). The experimental scattered power is shown by the dotted line, the incident power by dashed lines, and $LILAC$ predictions with nonlocal and flux-limited transport by solid and dashed–dotted lines, respectively.
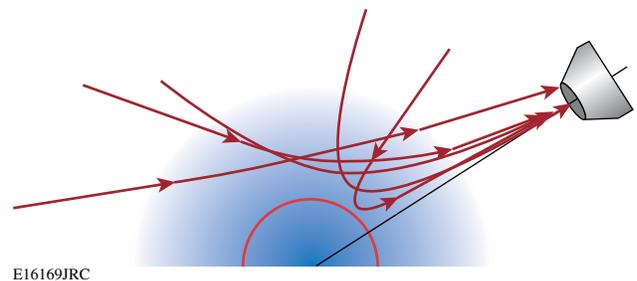

Figure 113.38
Illustration of scattered-light contributions from any of OMEGA's 60 beams to the light collected by a lens at the target chamber wall. The contributions from any one beam depend on both time and the position of the beam relative to the collector.

The experimental and simulated spectra are compared in Fig. 113.39 for a target irradiated with a 200-ps laser pulse without SSD corresponding to the picket shown in Fig. 113.37. For this narrowband experiment the anisotropic blow-by contribution to the scattered light observed in FABS25 is easily distinguished from the light that is isotropically scattered by the plasma. Simulations with the nonlocal electron-heat transport and the standard flux-limited transport are shown in Figs.113.39(b) and 113.39(c) with Fig.113.39(b) matching the experimental data better. The simulations include the blow-by around the target. The corresponding incident and scattered-light powers are shown in Fig. 113.40, where the blow-by has been removed from the spectrum. Excellent agreement between

simulations using nonlocal transport and experimental data is apparent in this figure. The time-integrated absorption fraction for a number of 200-ps irradiation experiments is shown in Fig. 113.41. The agreement between the *LILAC* predictions using nonlocal transport is apparent from these figures, whereas the standard flux-limited transport significantly underestimates the absorption.

E16206JRC
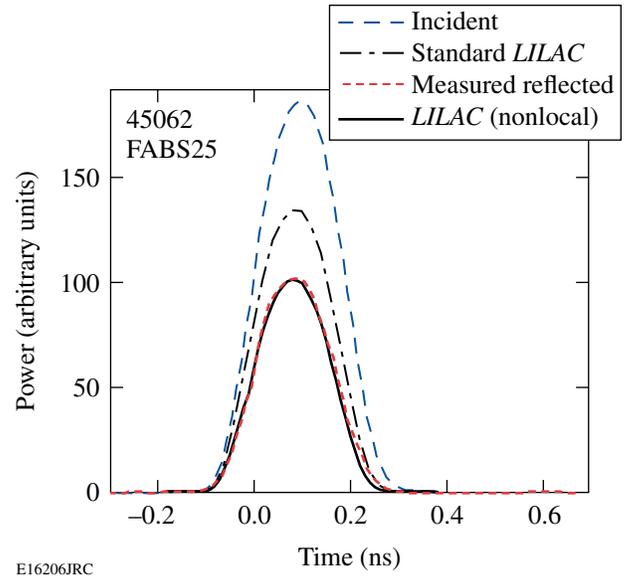
Figure 113.40
Power histories of the incident and scattered light for the spectra shown in Fig. 113.39: the measured scattered-light power (short-dashed line), the incident power (long-dashed line), the predictions based on nonlocal transport (solid line), and standard *LILAC* predictions using flux-limited heat transport with $f = 0.06$ (dashed–dotted line).

E16311JRC

Figure 113.39
Time-resolved scattered-light spectra for a 200-ps spherical irradiation experiment of a warm 20-μm CH shell with DPP's and PS but no SSD bandwidth. The experimental spectrum is shown in (a) and two simulated spectra are shown in (b) and (c). Nonlocal electron-heat transport was used for the plasma parameters in (b) and standard flux-limited ($f = 0.06$) heat transport was used in (c). The white circles are added for easier comparison of the simulated spectra with the experimental spectrum.

E16351JRC

Figure 113.41
The time-integrated absorption fractions for 200-ps irradiation experiments of CH targets (20-μm shells or solid spheres) with DPP's and PS. Most shots were without SSD bandwidth while two shots had 1-THz SSD bandwidth.

As shown in Fig. 113.37, hydrodynamic simulations using either flux-limited or nonlocal transport cannot accurately predict the scattered-light power at later times during the main part of the compression pulse ($t > 1.5$ ns in Fig. 113.37). A particularly striking example is shown in Fig. 113.42 where a warm plastic shell (20-μm CH wall, 873-μm diam) was imploded with a 1-ns square pulse, full beam smoothing, and 15.3-kJ laser energy. Instantaneously, the scattered-light spectra differ significantly from the incident spectrum as is evident from the lineouts in Fig. 113.42(a). The scattered-light power predicted by *LILAC* using constant flux-limited thermal transport significantly over-predicts the scattered power during the

first half of the pulse and then under-predicts it during the latter half. Simulations using nonlocal transport correctly estimate the scattered power during the first 150 ps but are consistently too low beyond that. The differences between the incident and scattered-light spectra [see lineouts in Fig. 113.42(a)] are indicative of a nonlinear interaction process as will be discussed on p. 43.

Another example of the measured and simulated scattered-light spectrum is shown in Fig. 113.43 for a cryogenic target implosion with a complex laser pulse designed to drive the target on a low fuel adiabat ($\alpha = 2$). Hydrodynamic simulations
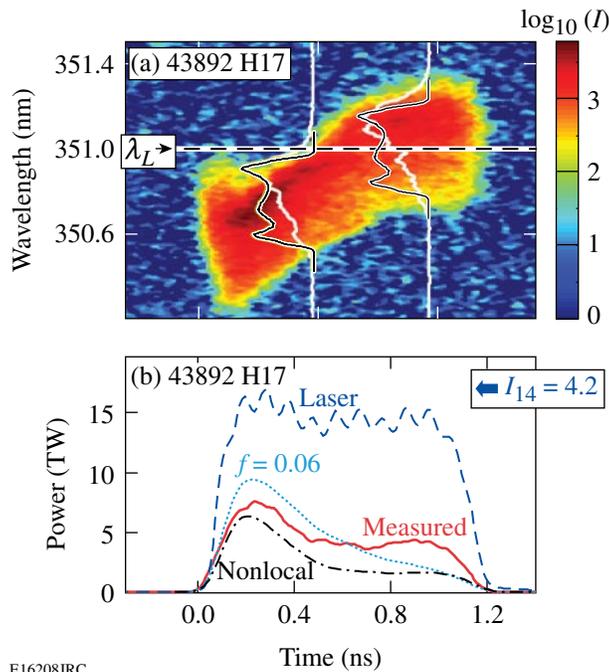

Figure 113.42
(a) Scattered-light spectrum and (b) incident, measured, and predicted scattered-light powers for a room-temperature target (20-μm CH wall, 873-μm diam, 15 atm of D_2) imploded with a 1-ns laser pulse of 15.3-kJ energy with full beam smoothing (DPP's and PS, 1-THz SSD bandwidth). Lineouts of the spectrum shown in (a) are in white with the incident spectrum superposed in black-on-white. In (b) the measured scattered-light power is shown as a solid line, *LILAC* predictions using standard flux-limited electron transport with $f = 0.06$ are shown as a dotted line, and those with nonlocal transport are shown as a dashed–dotted line.
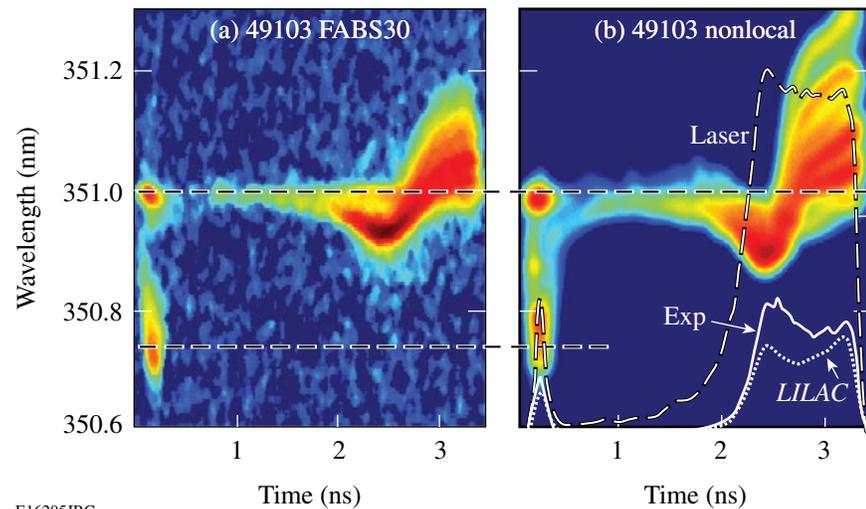
Figure 113.43
(a) Measured and (b) simulated time-resolved scattered-light spectra for an imploding cryogenic target (10-μm CD wall, 95-μm D_2-ice layer, 855-μm diam) with 16 kJ of laser energy smoothed with DPP's and PS but no SSD bandwidth. The laser pulse shape is shown as white dashes in (b) along with the measured (solid white) and simulated (dotted white) scattered-light powers. The hydrodynamic simulations used nonlocal electron transport. (For details of comparison see the **Discussion** section, p. 43.)

with nonlocal transport were used to calculate the simulated spectrum [Fig. 113.43(b)]. The general shape of the simulated spectrum is close to that measured. The incident laser power is shown in Fig. 113.43(b) along with the measured and predicted scattered laser power.

In addition to light scattered near the incident laser wavelength, laser light is scattered into half-harmonics ($\omega/2$ and $3\omega/2$) due to the two-plasmon-decay (TPD) instability. Stimulated Raman scattering (SRS)[37] has never been observed on OMEGA direct-drive-implosion experiments while half-harmonic spectra are regularly observed on OMEGA. The plasma waves produced by the TPD instability can generate energetic electrons leading to emission of hard x rays beyond 50 keV. Various scattered-light spectra and powers observed during a typical room-temperature implosion experiment are shown in Fig. 113.44. The wavelength scales of the half-harmonic spectra are chosen to have equal frequency (energy) scales for convenient comparison of the spectral features that are indicative of the TPD instability.

The half-harmonic and hard x-ray emission are superposed in Fig. 113.44(d). The power histories (two half-harmonics and hard x rays) are strikingly similar, suggesting their common TPD origin. Under well-controlled irradiation conditions (similar targets, same pulse shapes, but different intensities) the half-harmonic and hard x-ray signals exhibit an essentially identical exponential scaling with intensity (Fig. 113.45). An x-ray threshold around 4 to 5×10^{14} W/cm^2 is observed in Fig. 113.45. The half-harmonic emission has a threshold that is around 2×10^{14} W/cm^2, comparable to the theoretical threshold[38] as calculated for the average intensity in an equivalent linear density gradient for plane waves at normal incidence.

The intricate dependence of the TPD threshold to the density-gradient scale length (L_n), electron temperature (T_e), and intensity is seen in Fig. 113.46. A rough estimate for the TPD threshold is provided by the plane wave, linear-gradient-threshold parameter[38] $\alpha_{th} = I_{14}L_{n,\mu m}/230\,T_{e,keV} > 1$, where I_{14} is the average intensity on target in units of 10^{14} W/cm^2. The laser burns through the plastic shell of this cryogenic target around the dip of the α_{th}-curve in Fig. 113.46(b). It should also be noted that the instantaneous peak intensities on target are typically 5× larger than the average intensities.

Discussion

While time-integrated absorption measurements have been previously reported to be in good agreement with simulations,[4,21,39] the data presented here show the value of
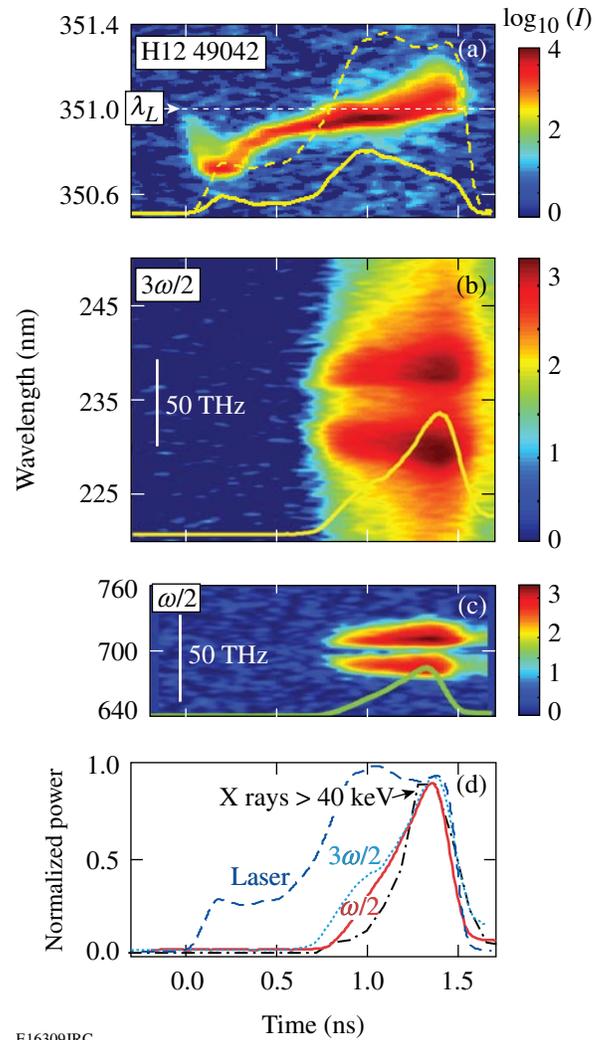
Figure 113.44
Time-resolved scattered-light spectra for a room-temperature implosion using 25 kJ of laser energy with DPP and PS smoothing but no SSD bandwidth. [Target: plastic shell, 24-μm wall, outer 10 μm are doped with 6% (atomic) Si, filled with 15 atm of D$_2$.] The spectrum of the scattered light around the laser frequency and the incident and scattered power are shown in (a). In (b) and (c) the $3\omega/2$ and $\omega/2$ spectra and powers are shown on a common frequency (energy) scale. The normalized incident laser, odd-integer half-harmonic powers, and the time-resolved x-ray emission for $h\nu_x > 40$ keV are shown in (d).

time-resolved data since compensating differences between experimental data and predictions can lead to erroneous interpretations. Time-resolved spectral measurements show a high sensitivity to the actual drive intensity on target. Time-resolved spectral measurements are particularly important for determining the hydrodynamic wave timing in the ignition-scaled experiments with complex pulse shapes presently carried out on OMEGA.
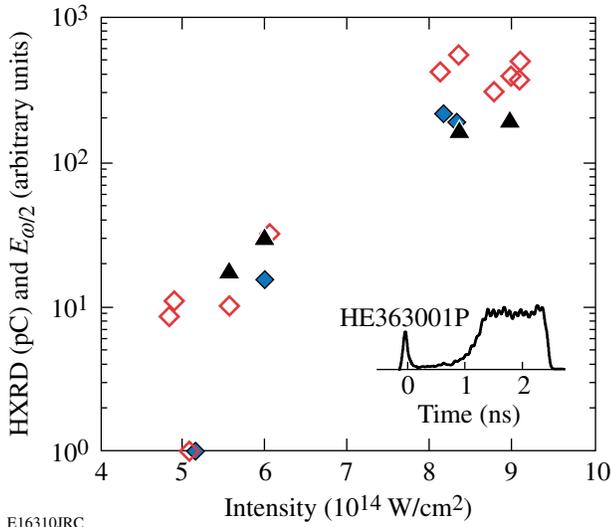
Figure 113.45

Intensity scaling of hard x rays (open and solid diamonds, $h\nu_x > 40$ keV) and the half-harmonic emission (solid triangles) for cryogenic shots with pulse shapes as shown in the insert. The targets were 10-μm CH or CD shells with a 95-μm D_2- or DT-ice layer. Shots with pure CD or CH shells are shown as open diamonds; those with Si-doped outer layers (5 μm) are shown as solid diamonds.
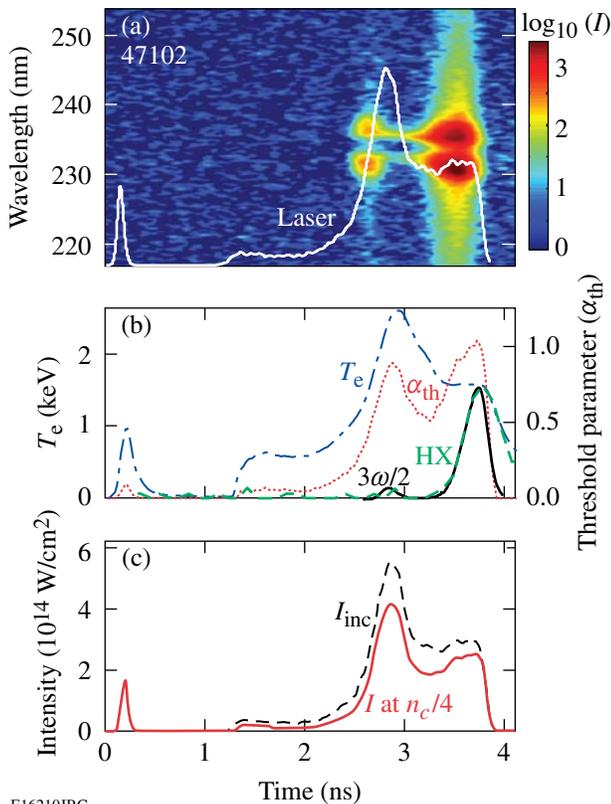
Discrepancies between the hydrodynamic predictions and experimental scattered-light data as shown in Fig. 113.37(b) are common. The initial spike of the incident laser pulse is typically more strongly absorbed than predicted by simulations using standard flux-limited electron-heat transport [dashed–dotted line in Fig. 113.37(b)]. In contrast, the *LILAC* prediction using nonlinear electron-heat transport is in excellent agreement for the scattered light of the initial spike. At later times (between 2 and 3 ns in Fig. 113.37) the experimental data tend to be predicted better using flux-limited electron transport. Both transport models consistently predict less scattered light than is observed.

The scattered-light spectra (Figs. 113.36, 113.37, 113.39, 113.42, and 113.43) contain a wealth of information about the plasma evolution and the laser–plasma interaction processes. Refraction in the plasma deflects part of all 60 beams of OMEGA into the collection optics as shown schematically in Fig. 113.38. The exact contribution of any beam varies in time and with the position of the beam relative to the collection optics. This is simulated numerically with a ray-trace code using the time-varying plasma profiles obtained from one-dimensional *LILAC* simulations.[40] These simulations show that the rapid blue shift during the initial irradiation of the target is due to the buildup of plasma[36] that occurs when the optical path length traversed by the scattered light decreases rapidly with time, since the index of refraction in the plasma is $\mu = \left(1 - n_e/n_c\right)^{1/2} < 1$, where n_e and n_c are the electron density and critical electron density. These ray-trace simulations show that the scattered light shifts to the blue whenever the mass ablation rate increases.

The remarkable sensitivity of the scattered-light spectra on the electron-heat-transport model used in the hydrodynamic simulations is shown in Fig. 113.39. For this narrowband shot (no SSD bandwidth) we note that the simulations reproduce both the refracted spectrum and the "blow-by" spectrum (the

Figure 113.46

Spectrum of the 3/2-harmonic emission (a) from a cryogenic target (4.5-μm CH shell and 95-μm D_2 ice layer) imploded with 11.7 kJ of laser energy and full beam smoothing (DPP, PS, and 1-THz SSD bandwidth). *LILAC* predictions for T_e and α_{th} are shown in (b). Also, shown in (b) are the normalized 3/2-harmonic and hard x-ray powers. (The extended hard x-ray emission is an artifact of the cryogenic target implosion and does not relate to extended fast electron production.) In (c) the incident intensity and the intensity at $n_c/4$ are shown. The thin CH shell burns through at ~3.2 ns.

small part of the laser beam opposing the FABS that misses the target entirely and is seen only when viewing the target through one of the focusing lenses). The experimental spectrum [Fig. 113.39(a)] is better (though not perfectly) matched by the simulations using nonlocal electron-heat transport [Fig. 113.39(b)] than by the standard flux-limited heat transport with $f = 0.06$ [Fig. 113.39(c)]. Figure 113.40 also shows much better agreement between observed and simulated scattered-light power with the nonlocal heat-transport model. The improved predictability of the hydrodynamic simulations for picket pulses is evident in the time-integrated absorption fractions for the 200-ps experiments shown in Fig. 113.41.

Obtaining accurate hydrodynamic simulations of these short-pulse experiments is crucial since the initial spikes in these ignition-relevant pulse shapes (Figs. 113.37, 113.42, 113.45, and 113.46) are intended to shape the adiabat of the implosion.[10]

The scattered laser power is generally underpredicted by *LILAC* during the main part of the laser pulse (see Figs. 113.37, 113.42, and 113.43). The scattered-light spectrum in Fig. 113.42 (20-μm CH shell, 1-ns square pulse, 1-THz SSD) shows a change from the symmetrical, incident SSD spectrum to one that is red peaked (see lineouts in Fig. 113.42). This change is evidence for nonlinear scattering in the plasma corona such as stimulated Brillouin scattering (SBS) with a strong electromagnetic (EM) seed.[15] Intrabeam forward SBS, where scattering of the blue spectrum seeds SBS in the red of the same beam, would be expected to give rise to a red-peaked spectrum with negligible net energy loss. In contrast, cross-beam energy transfer has been shown in planar geometry to be very effective[15,41] and can lead to significant loss of drive energy. The effects seen in spherical geometry are difficult to reproduce in planar geometry with its restricted number of beam angles. The multitude of contributing beams and varying beam paths render it difficult to numerically model these effects in spherical geometry. The enhanced scattering at later times tends to be less detrimental to a low-adiabat implosion than the increased absorption during the early phase of plasma formation that is better modeled using the nonlocal model.

The potential significance of the cross-beam energy transfer is seen in Fig. 113.43 for an implosion experiment without SSD bandwidth. The scattered light during the picket is well reproduced in spectrum and power by the simulations using nonlocal transport. In contrast, significant differences are observed between the experimental and simulated spectra and powers starting with the intensity rise to the main pulse. The simulated spectrum predicts a larger blue shift than is observed.

As mentioned previously, ray-trace simulations indicate that an increasing mass ablation rate leads to an increasing blue shift. The observed time-resolved spectrum in Fig. 113.43 indicates that there is less drive pressure at the onset of the main pulse than predicted, consistent with the observed increased scattered-light power at that time. The simulated spectrum in Fig. 113.43 between 2 and 3.3 ns shows two strongly red-shifted components not seen in the experimental data. These components are due to light rays with the closest approach to the critical surface; they also are the most intense rays in each beam and provide the most efficient drive. It is plausible that their absence indicates a loss due to cross-beam energy transfer. (Increased absorption for these rays could explain the absence of these red components but would be inconsistent with the reduced drive deduced from the reduced blue shift of the spectrum and the observed increased scattered-light power.) It should be noted that these detailed features of the spectra are only visible without SSD bandwidth as a 1-THz SSD bandwidth completely washes out these details.

The scattered-light spectra at various wavelengths are shown in Fig. 113.44 for a room-temperature, low-adiabat ($\alpha = 3$), narrowband (no SSD bandwidth) implosion. The outer 5 μm of this target are doped with 6% atomic Si in an effort to reduce hard x-ray production. Figures 113.44(a)–113.44(c) show the spectra and powers of the scattered light near the incident laser wavelength and the odd-integer half-harmonics. The wavelength scales of the $\omega/2$ and $3\omega/2$ spectra are chosen to have equal frequency scales. The existence of these odd-integer half-harmonic spectra is compelling evidence for the TPD instability,[2,13] while the separation of the two peaks reflects the different secondary scattering processes involved.[42]

The half-harmonic spectrum in Fig. 113.44(c) is consistent with plasmon-to-photon mode conversion[42] analogous to the conversion process underlying resonance absorption.[43] The red component of this spectrum is stronger since the lower-frequency TPD plasmon can convert near the point of its creation while the higher-frequency (blue) plasmon has to propagate to its turning point before conversion. The spectral splitting is consistent with linear TPD theory.[38]

The 3/2-harmonic emission [Fig. 113.44(b)] is due to Thomson scattering of incident photons off TPD plasmons. In spherical geometry, the relevant phase-matching conditions are easily satisfied due to the large number of available probe rays for Thomson scattering. This explains why the blue peak of the 3/2-harmonic spectrum tends to be more intense than the red peak since the phase-matching conditions

can be satisfied for the blue plasmon at its point of creation. For the red 3/2-harmonic component, the phase-matching conditions require that the red plasmon propagate down the density gradient and acquire the requisite k-vector length for Thomson scattering.[42]

Given these differences in the generation processes for the odd-integer half-harmonic emissions, it is surprising that their power histories are nearly identical, as seen in Fig. 113.44(d). It is equally surprising that the temporal hard x-ray emission follows the half-harmonic emission as shown in Fig. 113.44(d). This is probably a consequence of the extremely rapid growth of the TPD instability, which is followed by saturation.

The exponential scaling of the hard x-ray and half-harmonic emission with laser intensity is shown in Fig. 113.45. This kind of scaling is observed only if the target and pulse shapes are kept constant while the intensity alone is varied. Changing either the pulse shape or the target causes the simple scaling to break down. In particular, doping the outer layers of the target with high-Z elements (Si or Ge) reduces the hard x-ray emission while affecting the half-harmonics to a lesser extent.[44] The underlying cause for these changes can be partly attributed to changes in density scale length, electron temperature, and absorption of the incident light on the way to $n_c/4$. However, a Z-dependence in the saturation mechanisms for the TPD instability cannot be ruled out.

The TPD threshold (and presumably also its saturation) dependence on density scale length, electron temperature, and intensity is illustrated in Fig. 113.46. The 3/2-harmonic emission has an initial, weak burst at 2.8 ns before the peak of the laser pulse. Its main emission occurs at the end of the laser pulse when the laser intensity is only half of its peak value but the threshold parameter α_{th} is highest due to the reduced temperature. The fast-electron production also peaks at that time as indicated in Fig. 113.46(b). [The extended hard x-ray signal observed in Fig. 113.46(b) is consistently observed in cryogenic shots and is tentatively attributed to energetic electrons striking surfaces in the vicinity of the target that are present only during cryogenic shots.] As in room-temperature targets, the strong half-integer harmonic emission generally correlates well with the hard x-ray emission temporally. Weaker precursor half-integer harmonic emission is typically not reflected in the hard x-ray signals.

The threshold parameter α_{th} represents a simplified view of the actual experimental conditions, yet it appears to give useful insight into the threshold behavior (and possibly also its saturation behavior) of this instability. This instability is as ubiquitous for direct-drive laser-fusion experiments as it is intractable theoretically, particularly with regard to its ramifications of fast-electron generation and fast-electron preheat.

Conclusions

The spectra and powers of the scattered laser light during direct-drive ICF implosion experiments on OMEGA have been shown to be powerful tools for fine-tuning hydrodynamic code simulations and identifying laser–plasma interaction processes. Short pulses frequently precede the main laser pulse for adiabat shaping of the implosion. These pulses have been shown experimentally to have higher absorption than predicted by hydrodynamic code simulations using flux-limited diffusion. Comparisons of *LILAC* simulations with these experimental data have led to an improved nonlocal electron-transport model.

Later during target irradiation the scattered-light spectra and powers indicate the presence of enhanced scattering that reduces the laser drive of the target. The scattered-light spectra point to a nonlinear interaction process that is tentatively identified as EM-seeded SBS. The EM seed here is provided by the scattered light of any of the 60 beams of OMEGA and the required SBS gain is small. The spectra indicate that the increase in mass ablation during the rise of the main pulse is not as large as predicted by hydrodynamic simulations, supporting the reduced laser–plasma coupling observed in the power measurements.

The presence of the TPD instability is clearly seen in these direct-drive-implosion experiments through the emission of $\omega/2$ and $3\omega/2$ light as well as hard x rays above 50 keV. The sensitivity of the TPD instability to laser intensity, density-gradient scale lengths, and electron temperature has been identified using complex pulse shapes. Although there is no easily applicable theory for interpreting the details of the observation, the data obtained so far permit tailoring implosion experiments to minimize the detrimental effects of the energetic electron production associated with the TPD. In particular, doping of the outer plastic layers of the target with high-Z elements appears to mitigate hard x-ray production although the detailed mechanism is not well understood at present.

ACKNOWLEDGMENT

REFERENCES

1. R. S. Craxton and R. L. McCrory, Laboratory for Laser Energetics, University of Rochester, Rochester, NY, LLE Report No. 108 (1980).

2. M. C. Richardson, R. S. Craxton, J. Delettrez, R. L. Keck, R. L. McCrory, W. Seka, and J. M. Soures, Phys. Rev. Lett. **54**, 1656 (1985).

3. R. Cauble and W. Rozmus, Phys. Fluids **28**, 3387 (1985).

4. W. Seka, C. Stoeckl, V. N. Goncharov, R. E. Bahr, T. C. Sangster, R. S. Craxton, J. A. Delettrez, A. V. Maximov, J. Myatt, A. Simon, and R. W. Short, Bull. Am. Phys. Soc. **49**, 179 (2004).

5. P. W. McKenty, J. A. Marozas, V. N. Goncharov, K. S. Anderson, R. Betti, D. D. Meyerhofer, P. B. Radha, T. C. Sangster, S. Skupsky, and R. L. McCrory, Bull. Am. Phys. Soc. **51**, 295 (2006).

6. P. W. McKenty, T. C. Sangster, M. Alexander, R. Betti, R. S. Craxton, J. A. Delettrez, L. Elasky, R. Epstein, A. Frank, V. Yu. Glebov, V. N. Goncharov, D. R. Harding, S. Jin, J. P. Knauer, R. L. Keck, S. J. Loucks, L. D. Lund, R. L. McCrory, F. J. Marshall, D. D. Meyerhofer, S. P. Regan, P. B. Radha, S. Roberts, W. Seka, S. Skupsky, V. A. Smalyuk, J. M. Soures, K. A. Thorp, M. Wozniak, J. A. Frenje, C. K. Li, R. D. Petrasso, F. H. Séguin, K. A. Fletcher, S. Padalino, C. Freeman, N. Izumi, J. A. Koch, R. A. Lerche, M. J. Moran, T. W. Phillips, G. J. Schmid, and C. Sorce, Phys. Plasmas **11**, 2790 (2004).

7. V. N. Goncharov, P. McKenty, S. Skupsky, R. Betti, R. L. McCrory, and C. Cherfils-Clérouin, Phys. Plasmas **7**, 5118 (2000).

8. R. L. McCrory, R. E. Bahr, T. R. Boehly, T. J. B. Collins, R. S. Craxton, J. A. Delettrez, W. R. Donaldson, R. Epstein, V. N. Goncharov, R. Q. Gram, D. R. Harding, P. A. Jaanimagi, R. L. Keck, J. P. Knauer, S. J. Loucks, F. J. Marshall, P. W. McKenty, D. D. Meyerhofer, S. F. B. Morse, O. V. Gotchev, P. B. Radha, S. P. Regan, W. Seka, S. Skupsky, V. A. Smalyuk, J. M. Soures, C. Stoeckl, R. P. J. Town, M. D. Wittman, B. Yaakobi, J. D. Zuegel, R. D. Petrasso, D. G. Hicks, and C. K. Li, in *Inertial Fusion Sciences and Applications 99*, edited by C. Labaune, W. J. Hogan, and K. A. Tanaka (Elsevier, Paris, 2000), pp. 43–53.

9. S. Skupsky, R. Betti, T. J. B. Collins, V. N. Goncharov, D. R. Harding, R. L. McCrory, P. W. McKenty, D. D. Meyerhofer, and R. P. J. Town, in *Inertial Fusion Sciences and Applications 2001*, edited by K. Tanaka, D. D. Meyerhofer, and J. Meyer-ter-Vehn (Elsevier, Paris, 2002), pp. 240–245.

10. V. N. Goncharov, J. P. Knauer, P. W. McKenty, P. B. Radha, T. C. Sangster, S. Skupsky, R. Betti, R. L. McCrory, and D. D. Meyerhofer, Phys. Plasmas **10**, 1906 (2003).

11. R. Betti, K. Anderson, T. R. Boehly, T. J. B. Collins, R. S. Craxton, J. A. Delettrez, D. H. Edgell, R. Epstein, V. Yu. Glebov, V. N. Goncharov, D. R. Harding, R. L. Keck, J. H. Kelly, J. P. Knauer, S. J. Loucks, J. A. Marozas, F. J. Marshall, A. V. Maximov, D. N. Maywar, R. L. McCrory,

P. W. McKenty, D. D. Meyerhofer, J. Myatt, P. B. Radha, S. P. Regan, C. Ren, T. C. Sangster, W. Seka, S. Skupsky, A. A. Solodov, V. A. Smalyuk, J. M. Soures, C. Stoeckl, W. Theobald, B. Yaakobi, C. Zhou, J. D. Zuegel, J. A. Frenje, C. K. Li, R. D. Petrasso, and F. H. Séguin, Plasma Phys. Control. Fusion **48**, B153 (2006).

12. S. E. Bodner, D. G. Colombant, J. H. Gardner, R. H. Lehmberg, S. P. Obenschain, L. Phillips, A. J. Schmitt, J. D. Sethian, R. L. McCrory, W. Seka, C. P. Verdon, J. P. Knauer, B. B. Afeyan, and H. T. Powell, Phys. Plasmas **5**, 1901 (1998); J. Myatt, A. V. Maximov, W. Seka, R. S. Craxton, and R. W. Short, Phys. Plasmas **11**, 3394 (2004).

13. W. Seka, R. S. Craxton, R. E. Bahr, D. L. Brown, D. K. Bradley, P. A. Jaanimagi, B. Yaakobi, and R. Epstein, Phys. Fluids B **4**, 432 (1992).

14. W. Seka, R. S. Craxton, R. Bahr, D. Bradley, P. Jaanimagi, J. Knauer, S. Letzring, D. Meyerhofer, R. L. Short, A. Simon, and J. M. Soures, Bull. Am. Phys. Soc. **35**, 1944 (1990).

15. W. Seka, H. A. Baldis, J. Fuchs, S. P. Regan, D. D. Meyerhofer, C. Stoeckl, B. Yaakobi, R. S. Craxton, and R. W. Short, Phys. Rev. Lett. **89**, 175002 (2002).

16. W. Seka, R. E. Bahr, R. W. Short, A. Simon, R. S. Craxton, D. S. Montgomery, and A. E. Rubenchik, Phys. Fluids B **4**, 2232 (1992).

17. J. M. Soures, T. C. Bristow, H. Deckman, J. Delettrez, A. Entenberg, W. Friedman, J. Forsyth, Y. Gazit, G. Halpern, F. Kalk, S. Letzring, R. McCrory, D. Peiffer, J. Rizzo, W. Seka, S. Skupsky, E. Thorsos, B. Yaakobi, and T. Yamanaka, in *Laser Interaction and Related Plasma Phenomena*, edited by H. J. Schwarz, H. Hora, M. J. Lubin, and B. Yaakobi (Plenum Press, New York, 1981), Vol. 5, pp. 463–481.

18. W. Seka, R. S. Craxton, J. Delettrez, L. Goldman, R. Keck, R. L. McCrory, D. Shvarts, J. M. Soures, and R. Boni, Opt. Commun. **40**, 437 (1982).

19. W. Seka, L. M. Goldman, M. C. Richardson, J. M. Soures, K. Tanaka, B. Yaakobi, R. S. Craxton, R. L. McCrory, R. Short, E. A. Williams, T. Boehly, R. Keck, and R. Boni, in *Plasma Physics and Controlled Nuclear Fusion Research 1982* (IAEA, Vienna, 1983), Vol. I, pp. 131–137.

20. C. Garban-Labaune *et al.*, Phys. Fluids **28**, 2580 (1985).

21. S. P. Regan, H. Sawada, D. Li, V. N. Goncharov, R. Epstein, J. A. Delettrez, J. P. Knauer, J. A. Marozas, F. J. Marshall, R. L. McCrory, P. W. McKenty, D. D. Meyerhofer, P. B. Radha, W. Seka, T. C. Sangster, S. Skupsky, V. A. Smalyuk, R. Mancini, S. H. Glenzer, O. Landen, and G. Gregori, Bull. Am. Phys. Soc. **51**, 254 (2006).

22. T. R. Boehly, R. S. Craxton, T. H. Hinterman, P. A. Jaanimagi, R. L. Keck, J. H. Kelly, T. J. Kessler, R. L. Kremens, S. A. Kumpan, S. A. Letzring, R. L. McCrory, S. F. B. Morse, W. Seka, S. Skupsky, J. M. Soures, and C. P. Verdon, in *Proceedings of the IAEA Technical Committee Meeting on Drivers for Inertial Confinement Fusion*, edited by J. Coutant (IAEA, Vienna, 1995), pp. 79–86.

23. Kato *et al.*, Phys. Rev. Lett. **53**, 1057 (1984).

24. T. J. Kessler, Y. Lin, J. J. Armstrong, and B. Velazquez, in *Laser Coherence Control: Technology and Applications*, edited by H. T. Powell and T. J. Kessler (SPIE, Bellingham, WA, 1993), Vol. 1870, pp. 95–104.

25. T. J. Kessler, Y. Lin, L. S. Iwan, W. P. Castle, C. Kellogg, J. Barone, E. Kowaluk, A. W. Schmid, K. L. Marshall, D. J. Smith, A. L. Rigatti, J. Warner, and A. R. Staley, in *Second Annual International Conference Solid State Lasers for Application to Inertial Confinement Fusion*, edited by M. L. André (SPIE, Bellingham, WA, 1997), Vol. 3047, pp. 272–281.

26. J. E. Rothenberg, J. Appl. Phys. **87**, 3654 (2000).

27. S. Skupsky, R. W. Short, T. Kessler, R. S. Craxton, S. Letzring, and J. M. Soures, J. Appl. Phys. **66**, 3456 (1989).

28. D. R. Harding, D. D. Meyerhofer, S. J. Loucks, L. D. Lund, R. Janezic, L. M. Elasky, T. H. Hinterman, D. H. Edgell, W. Seka, M. D. Wittman, R. Q. Gram, D. Jacobs-Perkins, R. Early, T. Duffy, and M. J. Bonino, Phys. Plasmas **13**, 056316 (2006).

29. D. H. Edgell, W. Seka, R. S. Craxton, L. M. Elasky, D. R. Harding, R. L. Keck, and M. D. Wittman, Fusion Sci. Technol. **49**, 616 (2006).

30. D. H. Edgell, W. Seka, R. S. Craxton, L. M. Elasky, D. R. Harding, R. L. Keck, L. D. Lund, and M. D. Wittman, J. Phys. IV France **133**, 903 (2006).

31. W. Seka, V. N. Goncharov, J. A. Delettrez, D. H. Edgell, I. V. Igumenshchev, R. W. Short, A. V. Maximov, J. Myatt, and R. S. Craxton, Bull. Am. Phys. Soc. **51**, 340 (2006).

32. J. Delettrez, R. Epstein, M. C. Richardson, P. A. Jaanimagi, and B. L. Henke, Phys. Rev. A **36**, 3926 (1987).

33. R. C. Malone, R. L. McCrory, and R. L. Morse, Phys. Rev. Lett. **34**, 721 (1975).

34. V. N. Goncharov, T. C. Sangster, P. B. Radha, T. R. Boehly, T. J. B. Collins, R. S. Craxton, J. A. Delettrez, R. Epstein, V. Yu. Glebov, S. X. Hu, I. V. Igumenshchev, R. Janezic, S. J. Loucks, J. R. Marciante, J. A. Marozas, F. J. Marshall, D. N. Maywar, J. P. Knauer, P. W. McKenty, S. P. Regan, R. G. Roides, W. Seka, S. Skupsky, V. A. Smalyuk, J. M. Soures, C. Stoeckl, R. Betti, R. L. McCrory, D. D. Meyerhofer, D. Shvarts, J. A. Frenje, R. D. Petrasso, and C. K. Li, "Performance of Direct-Drive Cryogenic Targets on OMEGA," to be published Physics of Plasmas (invited).

35. V. N. Goncharov, O. V. Gotchev, E. Vianello, T. R. Boehly, J. P. Knauer, P. W. McKenty, P. B. Radha, S. P. Regan, T. C. Sangster, S. Skupsky, V. A. Smalyuk, R. Betti, R. L. McCrory, D. D. Meyerhofer, and C. Cherfils-Clérouin, Phys. Plasmas **13**, 012702 (2006).

36. T. Dewandre, J. R. Albritton, and E. A. Williams, Phys. Fluids **24**, 528 (1981).

37. W. L. Kruer, *The Physics of Laser–Plasma Interactions*, Frontiers in Physics, Vol. 73, edited by D. Pines (Addison-Wesley, Redwood City, CA, 1988), Chap. 4, pp. 37–43.

38. A. Simon, R. W. Short, E. A. Williams, and T. Dewandre, Phys. Fluids **26**, 3107 (1983).

39. A. L. Richard, J. P. Jadaud, N. Dague, M. C. Monteil, R. E. Turner, D. Bradley, R. J. Wallace, O. L. Landen, J. M. Soures, S. Morse, and G. Pien, in *ECLIM 2000: 26th European Conference on Laser Interaction with Matter*, edited by M. Kálal, K. Rohlena, and M. Šinor (SPIE, Bellingham, WA, 2001), Vol. 4424, pp. 23–26.

40. D. Edgell, W. Seka, J. A. Delettrez, R. S. Craxton, V. N. Goncharov, I. V. Igumenshchev, J. Myatt, A. V. Maximov, R. W. Short, T. C. Sangster, and R. E. Bahr, Bull. Am. Phys. Soc. **52**, 195 (2007).

41. R. K. Kirkwood, J. D. Moody, A. B. Langdon, B. I. Cohen, E. A. Williams, M. R. Dorr, J. A. Hittinger, R. Berger, P. E. Young, L. J. Suter, L. Divol, S. H. Glenzer, O. L. Landen, and W. Seka, Phys. Rev. Lett. **89**, 215003 (2002).

42. R. L. Berger and L. V. Powers, Phys. Fluids **28**, 2895 (1985).

43. W. L. Kruer, in *Laser Plasma Interactions*, edited by R. A. Cairns and J. J. Sanderson (Scottish Universites Summer School in Physics, Edinburgh, Scotland, 1980), pp. 387–432.

44. P. B. Radha, J. P. Knauer, T. C. Sangster, V. N. Goncharov, I. V. Igumenshchev, R. Betti, R. Epstein, D. D. Meyerhofer, and S. Skupsky, Bull. Am. Phys. Soc. **52**, 143 (2007); J. P. Knauer, P. B. Radha, V. N. Goncharov, I. V. Igumenshchev, R. Betti, R. Epstein, F. J. Marshall, S. P. Regan, V. A. Smalyuk, D. D. Meyerhofer, and S. Skupsky, Bull. Am. Phys. Soc. **52**, 233 (2007).

Monoenergetic Proton Radiography of Inertial Fusion Implosions

Identification and characterization of the physical phenomena associated with dynamic, extreme states of matter, such as those of high-energy-density physics[1,2] found in inertial fusion,[3,4] laboratory astrophysics,[2,5] and laser–plasma interaction physics,[6] are of fundamental scientific importance. A unique method of diagnosing inertial fusion implosions has resulted in the characterization of two distinct electromagnetic field configurations that have potentially consequential effects on implosion dynamics. This method also makes possible the quantitative study of the temporal evolution of capsule size and areal density.

The method involves radiography using a pulsed (0.1 ns), monoenergetic (15.0 MeV), quasi-isotropic proton source.[7] Fields are revealed in radiographs through deflection of proton trajectories, and areal densities are quantified through the energy lost by protons while traversing the plasma. The imaged samples are inertial confinement fusion (ICF) capsules of the fast-ignition (FI) variety,[8,9] initially 430 μm in radius, imploded by 36 laser beams that deposit 14 kJ of energy in a 1-ns pulse (see the appendix, p. 51).

For electricity generation[3,4] and for studies of high-energy-density physics in the laboratory,[1,2] ICF seeks to release copious energy by igniting a compressed pellet of fusion fuel. Fuel compression to densities of 300 g/cm^3 or higher will be achieved by energy deposition onto the surface of a fuel capsule over nanosecond time scales, either by laser light (direct drive) or by x rays generated in a cavity by laser light (indirect drive). Ignition and energy gain will occur in a central hot spot or, in the FI scheme, by the extremely rapid (~picoseconds) deposition of additional energy, either directly onto the compressed pellet,[8] or along the axis of a cone that keeps the path clear of plasma ablated from the pellet surface.[9]

The 15-MeV, monoenergetic proton radiography applied herein was recently used by Li *et al.* in a different context to investigate fields generated by laser–foil interactions.[10,11] MacKinnon *et al.*[12] used a broadband, non-isotropic proton source to study six-beam implosions, although they did not observe either striated or coherent field structures. In addition,

earlier workers, using optical techniques largely sensitive to density perturbations, observed very fine-scale radial filaments and jets[13,14] in targets driven by one to four laser beams. However, the character of these structures is qualitatively different in several ways from the striations described in this article (see the appendix, p. 51).

In the experiments reported here (Fig. 113.47), cone-in-shell FI targets were radiographed before and during implosion, 1.56 ns after the start of the laser drive (Fig. 113.48), shortly after the end of the acceleration phase.[4] The radiographs were taken perpendicular to the Au cone axis. Figure 113.49 shows the experimental results (which are also characteristic of many implosions without cones). Because the detector records proton fluence and energy, Fig. 113.49 shows images that illustrate the spatial distributions of both proton fluence and mean proton energy.

Five important features are apparent in these images: First, the character of the isotropic and monoenergetic proton source
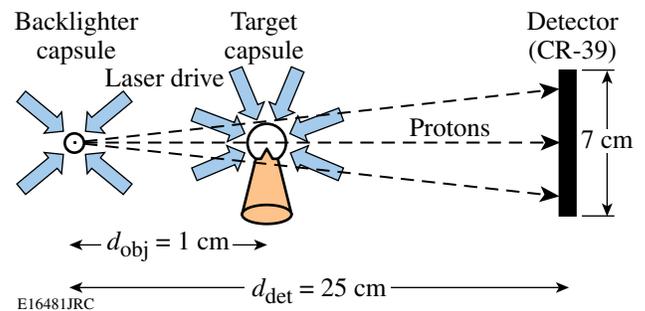

Figure 113.47
Schematic of experimental setup. A short (130 ps), monoenergetic (ΔE/E < 3%), quasi-isotropic pulse of 15.0-MeV D^{3}He fusion protons is generated by laser implosion of a backlighter capsule filled with D$_2$ and ^{3}He gas. The ~3 × 10^8 protons emitted from the 45-μm FWHM source region interact with matter and electromagnetic fields in a cone-in-shell capsule implosion. The position and energy of every proton reaching the detector are individually recorded on CR-39, encoding the details of the matter and field distributions surrounding the target capsule.

E16482JRC
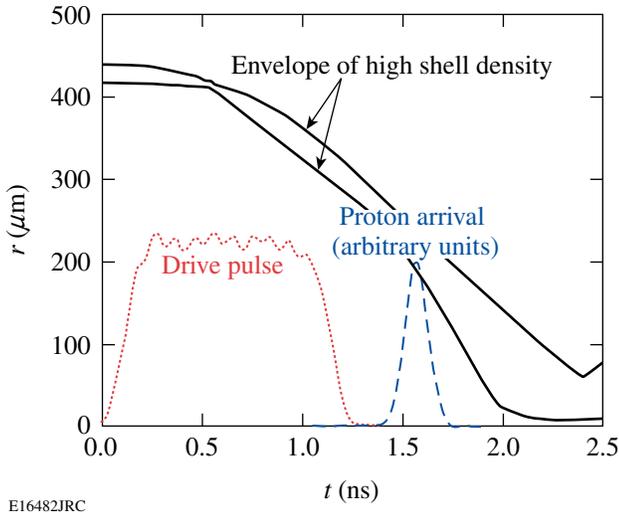
Figure 113.48
Cone-in-shell capsule drive pulse (dotted), simulated[16] shell trajectory (solid), and experimental backlighter proton arrival time (dashed). Simulations predict that the shell has compressed from its original radius by about a factor of 2, and the ρR has doubled to 5 mg/cm^2 when the backlighter protons arrive at 1.56 ns (OMEGA shot 46529).


E16483JRC
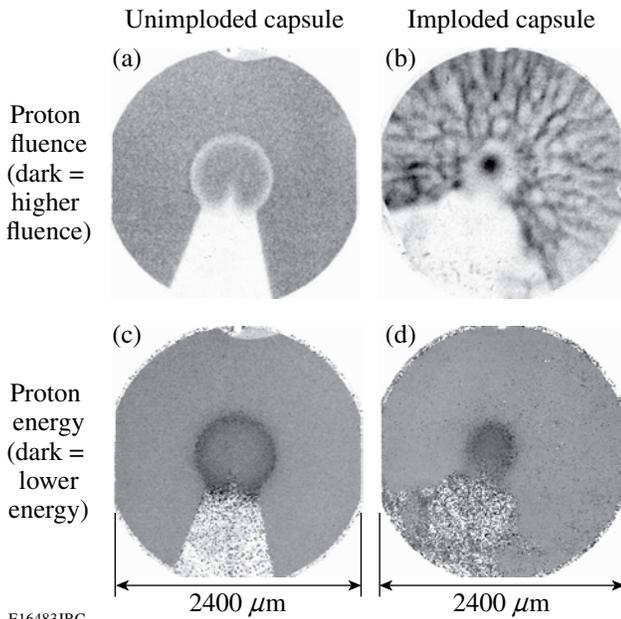
Figure 113.49
Images of a 430-μm-radius spherical CH capsule with attached gold cone, before and during implosion. Images (a) and (c) show the unimploded capsule used in OMEGA shot 46531. Images (b) and (d) show a capsule at 1.56 ns after the onset of the laser drive (shot 46529). In (a) and (b) dark areas correspond to regions of higher proton fluence, and in (c) and (d) dark areas correspond to regions of lower proton energy. The energy image values in the region shadowed by the cone are mostly noise since very few protons were detected in that region. See lineouts in Figs. 113.50 and 113.52 for image values.

is reflected in the uniform background of Figs. 113.49(a) and 113.49(c). Second, a complex filamentary structure is seen in the fluence image of Fig. 113.49(b). The uniform energy seen outside the capsule in Fig. 113.49(d) demonstrates that the fluence striations are caused by electromagnetic deflection rather than scattering through plasma density filaments. Third, substantial plasma blowoff from the cone casts a much wider shadow as the capsule is imploded. Fourth, a significant enhancement of the proton fluence at the center of the imploded target [Fig. 113.49(b)] suggests the presence of a radially directed, focusing electric field. Finally, radial compression of the capsule by a factor of 2 is seen in Fig. 113.49(d). The basic repeatability of the field structure and capsule compression was demonstrated using radiographs taken at the same relative time, but on different implosions.

In the images, field structure is studied by means of the spatial distribution of proton fluence. The proton-path–integrated electric (E) or magnetic (B) field can be estimated from the angular deflection θ of protons of energy E_p passing through the field region:

$$\int E_\perp d\ell = 2(E_p/e)\tan\theta, \tag{1}$$

$$\int B \times d\ell = (m_p v_p/e)\sin\theta, \tag{2}$$

$$\tan\theta = M\xi/(d_{\text{det}} - d_{\text{obj}}), \tag{3}$$

where m_p is the proton mass, v_p is the proton speed, e is the fundamental unit charge, the magnification $M = 25$, and d_{det} and d_{obj} are defined in Fig. 113.47. The deflection angle is determined by measuring the apparent displacement ξ of protons in the target plane using Eq. (3).

Areal density at different positions in the target capsule is studied through the downshift in proton energy relative to the incident energy of 15.0 MeV. It is proportional to the amount of matter traversed between the source and detector,[15] quantified by $\rho L (= \int \rho d\ell)$.

Radial lineouts of the images in Fig. 113.49 are shown in Fig. 113.50. In the fluence lineout [Fig. 113.50(b)] for the imploded target, the value near $r = 0$ μm is strikingly enhanced relative to the values at large radii (by a factor of 3) and at $r = 200$ μm (by a factor of 6). To explain this, a radial electric field of about 1.5×10^9 V/m is necessary to "focus" 15.0-MeV protons passing near $r = 200$ μm toward the center to the extent observed. Scattering is insufficient to explain this result (see Fig. 113.51).
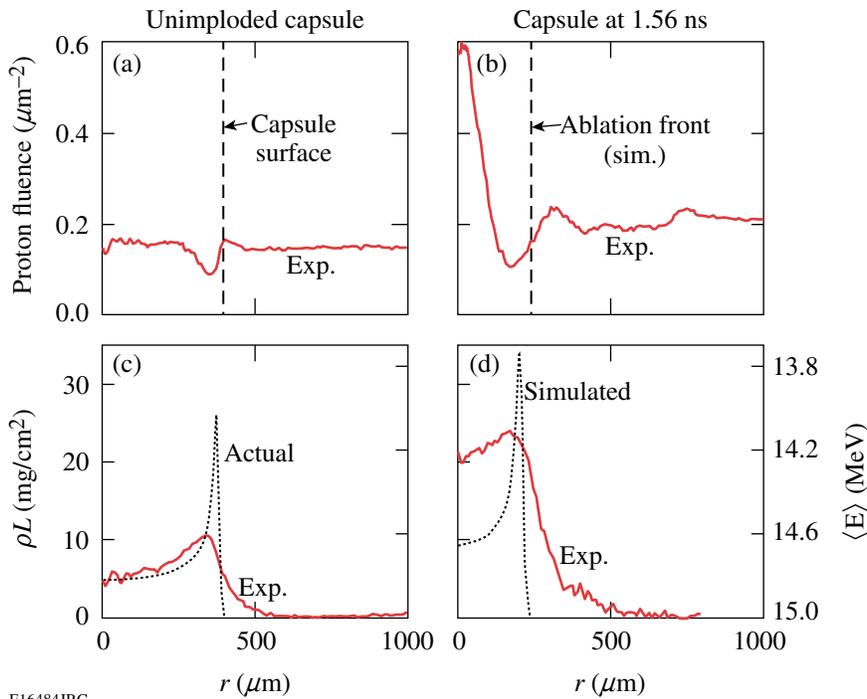
Figure 113.50
Radial lineouts of proton fluence and mean-path areal density (ρL) from Fig. 113.49. All lineouts are averaged over the azimuth, excluding the region of the cone shadow. (a) and (c): Unimploded capsule of shot 46531; (b) and (d): capsule of shot 46529, 1.56 ns after start of laser drive. The fluence lineout (a) shows the effects of angular scattering through the limb of the capsule shell. In (b), angular scattering effects alone are insufficient to explain the peak at $r = 0$. A radial electric field of $\sim 10^9$ V/m is necessary to "focus" the protons to the extent observed. In (c) and (d) radial lineouts of the mean energy images in Fig. 113.49 were converted to ρL. Also displayed are the (c) actual and (d) simulated ρL, assuming no angular scattering (dotted), where $\rho L/2 = \rho R$ at $r = 0$.
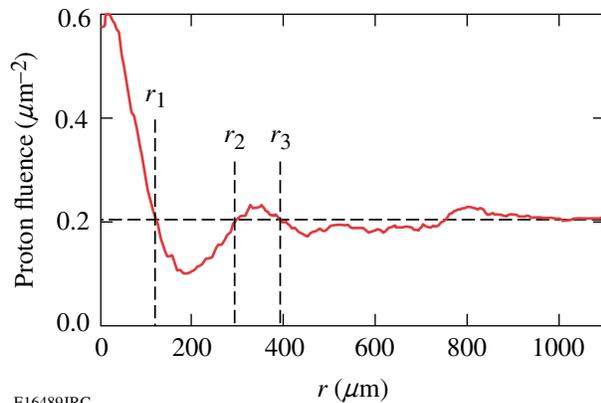
Figure 113.51
Reproduction of Fig. 113.50(b), marking the boundaries of the proton fluence enhancement at the center ($r < r_1$), the fluence depression through the capsule limb and E-field region ($r_1 < r < r_2$), and a secondary fluence enhancement outside the shell ($r_2 < r < r_3$). Fluence peaks and troughs in the far-field region ($r > 430$ μm = initial capsule radius) are the result of filamentary structures. Also marked is the proton fluence of 0.20 protons/μm^2, equal to the far-field average fluence. In the absence of a focusing electric field, one would expect that scattering of protons through the capsule limb should deflect an approximately equal number of protons inward as outward. The number of protons deflected out of the trough region $r_1 < r < r_2$ is about 12,300, calculated as the difference in the number of protons over an azimuthal integral in that region compared to the expected number based on the far-field fluence and the area of the region. The number of protons deflected into the inner and outer proton fluence peaks are 8200 and 4100, respectively. Therefore, angular scattering through the limb plasma can account for only about half of the protons in the central peak; we invoke the presence of a focusing E field to explain the remainder of the fluence enhancement at the center.

We conjecture that this coherent field is a consequence of a large, outward-directed electron pressure gradient that exists in the vicinity of the fuel–shell interface. Such a field might be expected to occur during, and shortly after, the acceleration phase of the implosion in which substantial shell mass is rapidly assembled and compressed. Such an electric field, given by $-\nabla P_e / e n_e$, has been observed in the context of other recent laser–plasma experiments.[10] In this case, future measurements of the evolution of this coherent E field might effectively map capsule pressure dynamics throughout the implosion. Such information would be invaluable in assessing implosion performance.

Lineouts of the mean energy images of Figs. 113.49(c) and 113.49(d) can be used to infer the mean-path areal density ρL, shown in Figs. 113.50(c) and 113.50(d). The ρL lineout [Fig. 113.50(c)] of the unimploded target gives an initial radial areal density (ρR) of 2.5 mg/cm^2, which is very close to the actual initial ρR of 2.4 mg/cm^2. Scattering of protons smears out measured ρL values near the limb of the shell at $r = 410$ μm. Both measurement and simulation[16] indicate a factor-of-2 reduction in capsule radius at 1.56 ns. However, the ρL lineout [Fig. 113.50(d)] of the imploded capsule at 1.56 ns implies that the capsule ρR has increased to 10 mg/cm^2, which is twice the 5 mg/cm^2 predicted by numerical simulation. This high apparent experimental ρR is due in part to scattering and in part to E-field focusing of the lower-energy protons passing through the limb of the capsule shell.

Returning to the filamentary fields, we note how the outer edge of the coherent field merges, at a boundary just outside the imploding capsule, into the striated fields. As illustrated in Fig. 113.52(c) and in Fig. 113.55 of the appendix, the striated fields originate inside the critical surface, which is extremely close to the capsule surface. Azimuthal lineouts of the proton fluence image of Fig. 113.49(b) at radii 430 μm and 860 μm show the amplitude and scale of proton fluence variations (Fig. 113.52) due to striations. Peak-to-valley fluence modulations of a factor of 4 are seen at both radii. The typical angular oscillation period is 20° and 10° for the inner and outer radii, respectively, corresponding to the same 150-μm spatial distance between striations. This distance implies a deflection angle of 0.45°, which gives a path-integrated magnetic field $\int B \times d\ell$ of 4000 T μm. Assuming an integration path length equal to the typical width of striations (75 μm) results in a magnetic field strength of $\sim$60 T. If the fluence variations are instead due to E fields, the field strength required is $\sim$3 × 10^9 V/m, although quasi-neutrality of the coronal plasma with no laser energy source makes this interpretation unlikely.

The occurrence of such strong inhomogeneities inside the critical surface $\sim$0.5 ns after the laser drive ends suggests that substantially larger fields are likely present just before laser shutoff.[17,18] This situation would be reflected in a Hall parameter ($\omega\tau$) of the order of 1 or larger, the inverse square of which reduces the classical electron heat transport.[17,18] This situation would result in the inhomogeneous inhibition of thermal transport over the capsule surface, altering even the zeroth-order hydrodynamics.[18,19] Whether the source of these inhomogeneities is Rayleigh–Taylor (RT),[20] electrothermal,[19] collisional Weibel,[13,17] or another instability, they will provide seeds for RT growth that, if too substantial, could degrade capsule compression and quench ignition during the final stagnation phase.[4,17,18] These issues are being actively investigated.

It seems plausible that either the electrothermal or RT instability could be the relevant source. Ongoing planar experiments, in which RT was purposely seeded, measured B fields of the order of 100 T using the method described here (see the appendix, p. 51). Furthermore, estimates (based on Ref. 18) of the RT-generated B field under similar conditions give fields of the same magnitude (see the appendix, p. 51). Radiography of driven solid-CH balls, which undergo no acceleration to drive RT growth, could be used to determine if RT is a contributing mechanism.

Finally, the vast spatial extent of these striated fields likely reflects their outward convection resulting from the plasma flow because the fields are tied to the out-flowing plasma due to high plasma electrical conductivity. We conjecture that these radiographic images thus provide snapshots of structures originally produced inside the critical surface at various times during the implosion.
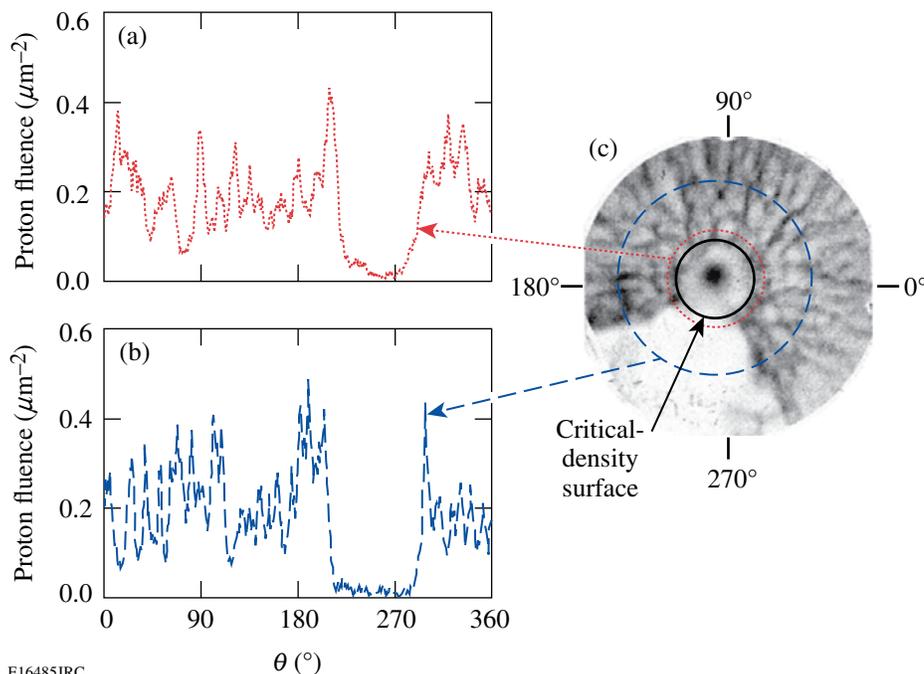

Figure 113.52
Circular lineouts of proton fluence obtained from shot 46529 at radii of (a) 430 μm and (b) 860 μm. The filamentary structures represent a 2-D projection of a 3-D field structure that originates inside the critical density surface (c).

E16485JRC

In summary, two distinctly different, simultaneously occurring electromagnetic field structures, with important implications for implosion dynamics, have been characterized in imploding ICF capsules. First, a complex filamentary field topology permeates the entire 2400-μm field of view with striations corresponding to 60-T magnetic fields. This field, through the inhomogeneous inhibition of heat flux in the vicinity of the ablation surface, could generate seeds for RT growth, thereby affecting the overall implosion dynamics.[4,6,18,19] Second, a coherent, radial electric field of magnitude 10^9 V/m exists in the immediate vicinity of the capsule, dramatically focusing protons toward the center.[21] This hitherto unobserved field is conjectured to originate from the gradient of electron pressure. If verified, a window for analyzing the evolution of the internal pressure dynamics is opened; this would be of immense value for critically assessing the entire implosion process.

Appendix: Monoenergetic Proton Radiography of Inertial Fusion Implosions

1. Materials and Methods

All experiments were performed at the OMEGA Laser Facility,[22] which delivers up to 30 kJ in 60 beams at a wavelength of 351 nm. Full beam smoothing[23] was used on each beam to reduce high-mode nonuniformities caused by laser speckle.

A schematic illustration of the proton radiography setup is shown in Fig. 113.47. The source of monoenergetic protons is a 220-μm-radius, 2.2-μm-thick spherical glass (SiO_2) shell filled with deuterium (D_2) and helium-3 (^{3}He) gas.[7] This backlighter capsule is illuminated by 17 laser beams, delivering 6.9 kJ of energy in a 1-ns pulse, which compresses and heats the gas such that the D-^{3}He fusion reaction, $D + {}^3He \longrightarrow {}^4He + p$, proceeds. The protons are quasi-isotropically emitted in a 130-ps pulse[24] at an energy of 15.0 MeV[25] with a spectral width[26] $\Delta E/E < 3\%$ and from a region 45 μm across[7] (see Fig. 113.53). Typical proton yields are 1 to 4×10^8, and the yields for the OMEGA shots shown in the manuscript were 2.9×10^8 (shot 46531) and 3.7×10^8 (shot 46529). The backlighter implosion has not yet been fully optimized for proton yield, pulse duration, or source size.

The target imaged is a 430-μm-radius, 23-μm-thick spherical plastic (CH) shell with an embedded gold (Au) cone of 5-mm height, 30-μm thickness, and an opening angle of 35°. The cone ends in a shelf (see Fig. 113.54) where the cone intersects the shell, and a smaller cone tip reaches inward to a distance of 40 μm from the capsule center. Forty beams in a spherically symmetric configuration are pointed at the spherical shell; the shell is then directly driven with 14.1 kJ using 36 of those beams (the four beams aimed nearest the cone axis remain off to avoid the laser hitting the inside of the cone), for an on-target illumination intensity of 6.7×10^{14} W/cm^2. Because the OMEGA system is optimized for a 60-beam spherical drive, the illumination uniformity is degraded in this configuration from <2% to ~7% rms.


E16486JRC
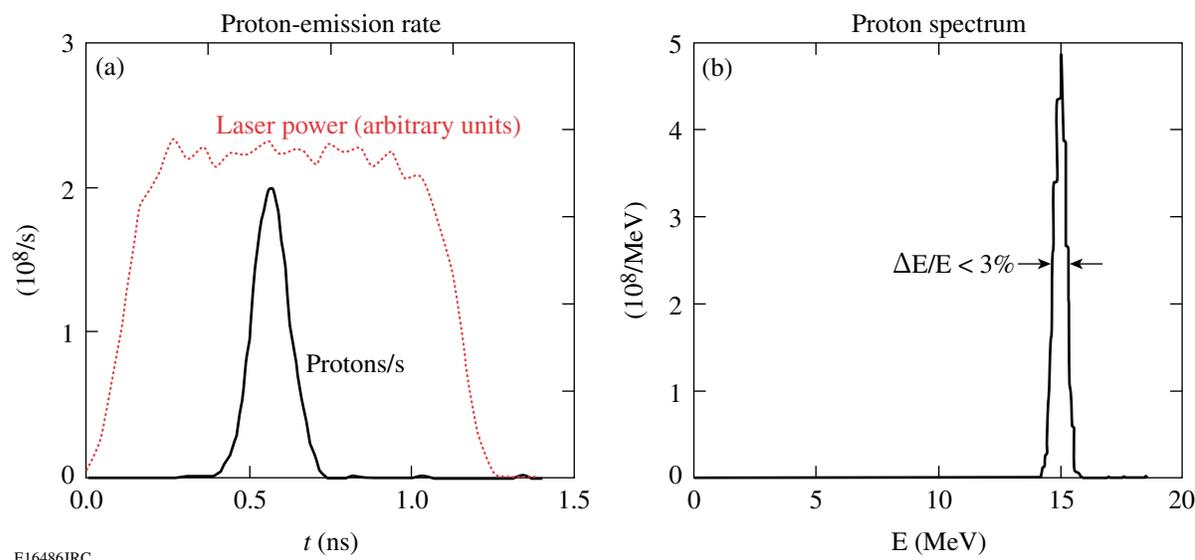
Figure 113.53
Measured characteristics of proton emission from the source implosion. (a) Emission history and (b) spectrum of emitted D^{3}He protons from the backlighter capsule on OMEGA shot 46531. The total D^{3}He proton yield was 2.9×10^8.
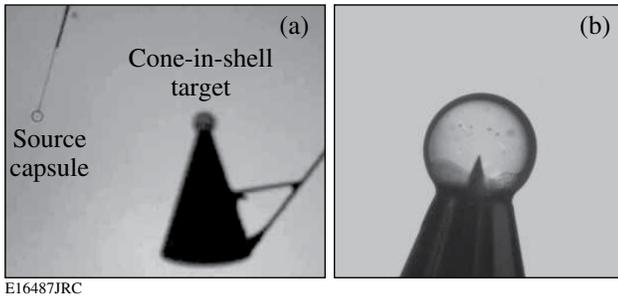
Figure 113.54
(a) Pre-implosion snapshot of source and target capsules. (b) A close-up photograph of the cone-in-shell target sphere. (See also Fig. 113.47.)

The imaging detector is CR-39, a plastic nuclear track detector with submicron spatial resolution, low sensitivity to electromagnetic and x-ray noise sources, and energy-resolving characteristics.[26] The position and energy of every incident proton are recorded. The center of the sphere in the subject target is placed 1.0 cm from the center of the backlighter capsule, and the detector is located 25 cm from the source, so structure in the subject is magnified by a factor $M = 25$ at the detector. The relative timing of the backlighter and subject-capsule laser drive beams is adjusted so the backlighter protons arrive at the subject capsule at a desired time interval following the onset of target-capsule drive (Fig. 113.54).

The spatial resolution of the system, neglecting scattering in the target, is limited primarily by the finite source size and results in convolution of structure in the target plane by a Gaussian of about 43-μm FWHM. Smaller structures cannot be observed in the capsule corona without further optimization of the backlighter source.

The energy resolution of the system is about 0.05 MeV, corresponding to an areal-density resolution of about 1.5 mg/cm^2. A more thorough analysis of the absolute accuracy of proton energy measurements on the radiographic CR-39, as well as an assessment of the effects of angular scattering of protons through plasma in the target plane, is currently in progress.

2. Other Relevant Work

Of direct relevance to this article, and in support of the presence of the observed field structures, Shiraga *et al.*[27] and Séguin *et al.*[28] inferred the presence of residual electromagnetic fields outside imploded capsules (exploding pushers and ablatively driven implosions similar to those studied here, respectively) on the basis of fluence variations in self-emitted, charged fusion products. Furthermore, character-

ization of capsule assembly and symmetry in ICF-relevant implosions has included extensive use of self-emitted fusion protons,[26,29] including those from implosions of fast-ignition (FI) targets.[30] Recently, Li *et al.*[7] suggested that a complementary way to study implosions and, in particular, the spatial structure of fields and areal density, is through monoenergetic proton radiography.

Filamentary and jet-like structures were previously observed near the critical surface using shadowgraphic, interferometric, and Faraday rotation techniques by several groups during laser illumination of both planar[31,32] and spherical targets.[13,14] As mentioned in the main text, there are substantial differences between the filamentary structures observed by these groups and those reported in this article: (1) The lateral spatial wavelength of structures was 10 μm, and examination of their data shows no evidence of the ~150-μm spatial scale that we see. (2) The radial extent of the earlier structures is much smaller and confined, whereas the structures reported here fill the entire field of view. (3) Fine structures originate well into the underdense plasma, while the structures here originate inside the critical surface, even approaching the ablation surface (see Fig. 113.55). (4) For uniformly illuminated implosions, fields greater than 10 T were not detected.[33] In addition, it is useful to point out that one of the unique advantages of the particle probe that we have used is that it is not "cut off" by critical-density plasma effects as is the case for optical probes.
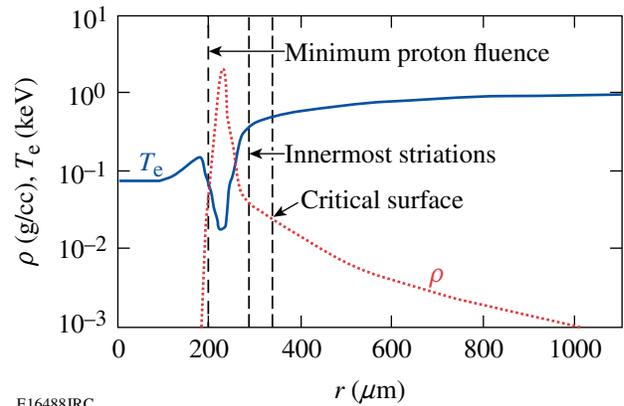

Figure 113.55
LILAC[36] simulation of the mass density and electron temperature profiles of the imploding capsule at 1.56 ns, ~0.3 ns after the laser has turned off. At this time, the capsule shell (the region of highest density near 230 μm) is imploding inward at approximately constant speed. The radius corresponding to the observed minimum proton fluence (Fig. 113.51) occurs at the inner shell surface in the simulation. The innermost striations are observed at about 300 μm [Fig. 113.49(b)], well inside the critical-density surface (for $\lambda = 0.351$ μm).

Previous studies of laser–capsule interactions using broad-band proton radiography[34] include Borghesi *et al.*[35] and MacKinnon *et al.*[12] Borghesi illuminated a sphere from one side using a short (1 ps), intense pulse and observed filamentary structures similar to those described in the previous paragraph. MacKinnon, however, saw no filamentary or focusing fields surrounding a capsule driven with six 1-ns laser beams. The fact that MacKinnon did not see these structures is not presently understood. There are, however, substantial differences in the implosion conditions compared to the current work. For example, MacKinnon used six beams at 1-μm wavelength and 1.5×10^{13}-W/cm^2 intensity; herein we used 36 beams at 1/3 μm and 6.7×10^{14} W/cm^2. In addition, MacKinnon's radiographic images were obtained substantially after (~1.5 ns) the end of the driving laser pulse, whereas in the current work, radiographs were obtained shortly after (~0.3 ns) the end of the pulse. If the observed field structures are produced and sustained by the laser (see Possible Mechanisms below), the structures may no longer be detectable 1 ns after their generating source has turned off.

The monoenergetic D^{3}He fusion proton emission from backlighter capsules has, for the purposes of these experiments, distinct advantages over broadband, non-isotropic proton emissions associated with intense-laser-beam experiments.[34] A single energy provides unambiguous quantitative relationships between proton energy loss through the target and areal density and also between proton trajectory bending and field strengths at the target. Quasi-isotropy allows for imaging of large objects, or even simultaneous imaging of multiple objects in totally different directions (as has been done in other contexts[11]).

3. Possible Mechanisms

Numerous instabilities that generate magnetic fields in laser–plasma experiments have been identified or proposed,[17] and take place over a wide range of plasma conditions. Instabilities generated outside the critical surface are the collisionless Weibel, thermomagnetic, and filamentation instabilities. Just inside the critical surface, the collisional Weibel, $\nabla T \times \nabla n$, and thermomagnetic instabilities will grow. Nernst convection can carry B fields generated by these instabilities inward.[17] The electrothermal instability occurs when the mean free path is shorter than the electron skin depth.[19] The Rayleigh–Taylor (RT) instability generates B fields at the ablation front.[18,20]

Monoenergetic proton radiography of planar foils seeded with RT ripples is currently in progress to investigate the generation and growth of fields by RT processes. Preliminary results have observed ~100-T-magnitude magnetic field struc-

tures, which are absent when the rippled RT seed is absent from the foil.

An estimate of the RT-induced B-field magnitude can be obtained using the work of Nishiguchi.[18] The capsule shell's acceleration g can be approximated from the experimental observations as the distance the shell has traveled over one half the square of the time it took to get there, $g = 2 \times (430\text{–}215\ \mu\text{m})/(1.5\ \text{ns})^2 \approx 200\ \mu\text{m/ns}^2$. The observed transverse spacing between filaments near the capsule surface is typically 150 μm. From *LILAC* simulations,[36] $L = 10\ \mu$m is typical of the plasma density scale length. From these values, $kL = 0.42$. Consulting Fig. 1 of Nishiguchi, this gives a peak B-field magnitude of about 300 T at the end of the linear phase of RT growth—only 5× the observed B-field magnitude "averaged" over the width of a filament.

Although RT processes could plausibly generate the observed B fields, other mechanisms cannot yet be ruled out. New experiments using monoenergetic proton radiography will be performed to investigate which instability mechanism(s) is (are) at work. A time sequence of radiographs would enable observation of the onset, growth, and decay of such filamentary structures. Variation of the intensity and other laser conditions could be used to elucidate the origin and any thresholds. Comparison of these radiography results with those from driven solid-CH balls, which undergo no acceleration to drive RT growth, would determine if RT is a dominant mechanism.

Whatever the mechanism, magnetic fields generated close to the ablation front would get "frozen in" to the ablating material and would follow the plasma flow off the capsule surface. Therefore, structures at the edge of the field of view were actually generated some several hundred picoseconds earlier, making it possible to record a history of the filamentary structure in a single radiographic snapshot.

In regard to the coherent focusing field, this article has emphasized the possible and likely connection between the central coherent electric field and the pressure gradient at the fuel–shell interface. Yet, another intriguing consequence is that this field could also opportunely reflect hot electrons that otherwise might preheat the fuel. To make such an assessment quantitative would require that we have information about both the evolution of this coherent field and how it is affected by the laser pulse shape and the capsule itself. (Because of shot limitations, for example, we have so far investigated only the coherent field for the 1-ns square pulse shape, as depicted in Fig. 113.48.) We would also need rather detailed information

about the bath of hot electrons, how it is generated, how it depends on pulse shape and the capsule, and, in general, how the hot-electron distribution evolves. In the course of exploring the full consequences of the central coherent field, we will investigate this preheat amelioration possibility.

ACKNOWLEDGMENT

REFERENCES

1. National Research Council (U.S.) Committee on High Energy Density Plasma Physics, *Frontiers in High Energy Density Physics: The X-Games of Contemporary Science* (National Academies Press, Washington, DC, 2003).

2. R. P. Drake, *High-Energy-Density Physics: Fundamentals, Inertial Fusion, and Experimental Astrophysics, Shock Wave and High Pressure Phenomena* (Springer, Berlin, 2006).

3. J. Nuckolls *et al.*, Nature **239**, 139 (1972).

4. S. Atzeni and J. Meyer-ter-Vehn, *The Physics of Inertial Fusion: Beam Plasma Interaction, Hydrodynamics, Hot Dense Matter*, International Series of Monographs on Physics (Clarendon Press, Oxford, 2004).

5. B. A. Remington, R. P. Drake, and D. D. Ryutov, Rev. Mod. Phys. **78**, 755 (2006).

6. W. L. Kruer, *The Physics of Laser Plasma Interactions, Frontiers in Physics* (Westview Press, Boulder, CO, 2003), pp. 39–43.

7. C. K. Li, F. H. Séguin, J. A. Frenje, J. R. Rygg, R. D. Petrasso, R. P. J. Town, P. A. Amendt, S. P. Hatchett, O. L. Landen, A. J. Mackinnon, P. K. Patel, V. Smalyuk, J. P. Knauer, T. C. Sangster, and C. Stoeckl, Rev. Sci. Instrum. **77**, 10E725 (2006).

8. M. Tabak *et al.*, Phys. Plasmas **1**, 1626 (1994).

9. R. Kodama *et al.*, Nature **418**, 933 (2002).

10. C. K. Li, F. H. Séguin, J. A. Frenje, J. R. Rygg, R. D. Petrasso, R. P. J. Town, P. A. Amendt, S. P. Hatchett, O. L. Landen, A. J. Mackinnon, P. K. Patel, V. A. Smalyuk, T. C. Sangster, and J. P. Knauer, Phys. Rev. Lett. **97**, 135003 (2006).

11. C. K. Li, F. H. Séguin, J. A. Frenje, J. R. Rygg, R. D. Petrasso, R. P. J. Town, O. L. Landen, J. P. Knauer, and V. A. Smalyuk, Phys. Rev. Lett. **99**, 055001 (2007).

12. A. J. Mackinnon *et al.*, Phys. Rev. Lett. **97**, 045001 (2006).

13. T. Mochizuki *et al.*, Jpn. J. Appl. Phys. **19**, L645 (1980).

14. O. Willi and P. T. Rumsby, Opt. Commun. **37**, 45 (1981).

15. C. K. Li and R. D. Petrasso, Phys. Rev. Lett. **70**, 3059 (1993).

16. Numerical simulations of full-sphere capsules, equivalent to the target capsule with no cone, were performed with the 1-D hydrodynamic code *LILAC*.[36] The use of 1-D spherical geometry to simulate the areal density of cone-in-shell capsules was previously used and found reasonable.[30]

17. M. G. Haines, Can. J. Phys. **64**, 912 (1986).

18. A. Nishiguchi, Jpn. J. Appl. Phys. **41**, 326 (2002).

19. M. G. Haines, Phys. Rev. Lett. **47**, 917 (1981).

20. K. Mima, T. Tajima, and J. N. Leboeuf, Phys. Rev. Lett. **41**, 1715 (1978).

21. The filamentary and focusing fields are present irrespective of whether the capsule is of the hot-spot or fast-ignition variety.

22. T. R. Boehly, D. L. Brown, R. S. Craxton, R. L. Keck, J. P. Knauer, J. H. Kelly, T. J. Kessler, S. A. Kumpan, S. J. Loucks, S. A. Letzring, F. J. Marshall, R. L. McCrory, S. F. B. Morse, W. Seka, J. M. Soures, and C. P. Verdon, Opt. Commun. **133**, 495 (1997).

23. S. Skupsky and R. S. Craxton, Phys. Plasmas **6**, 2157 (1999).

24. J. A. Frenje, C. K. Li, F. H. Séguin, J. Deciantis, S. Kurebayashi, J. R. Rygg, R. D. Petrasso, J. Delettrez, V. Yu. Glebov, C. Stoeckl, F. J. Marshall, D. D. Meyerhofer, T. C. Sangster, V. A. Smalyuk, and J. M. Soures, Phys. Plasmas **11**, 2798 (2003).

25. Hot electrons escaping from the backlighter capsule during laser irradiation results in a capsule charge of several hundred kV, which accelerates the escaping D^3He protons above their 14.7-MeV birth energy. This shift is measured to 0.1-MeV accuracy by the proton spectrometers.[26]

26. F. H. Séguin, J. A. Frenje, C. K. Li, D. G. Hicks, S. Kurebayashi, J. R. Rygg, B.-E. Schwartz, R. D. Petrasso, S. Roberts, J. M. Soures, D. D. Meyerhofer, T. C. Sangster, J. P. Knauer, C. Sorce, V. Yu. Glebov, C. Stoeckl, T. W. Phillips, R. J. Leeper, K. Fletcher, and S. Padalino, Rev. Sci. Instrum. **74**, 975 (2003).

27. H. Shiraga, T. Mochizuki, and C. Yamanaka, Appl. Phys. Lett. **37**, 602 (1980).

28. F. H. Séguin, C. K. Li, J. A. Frenje, S. Kurebayashi, R. D. Petrasso, F. J. Marshall, D. D. Meyerhofer, J. M. Soures, T. C. Sangster, C. Stoeckl, J. A. Delettrez, P. B. Radha, V. A. Smalyuk, and S. Roberts, Phys. Plasmas **9**, 3558 (2002).

29. H. Azechi *et al.*, Laser Part. Beams **9**, 193 (1991).

30. C. Stoeckl, T. R. Boehly, J. A. Delettrez, S. P. Hatchett, J. A. Frenje, V. Yu. Glebov, C. K. Li, J. E. Miller, R. D. Petrasso, F. H. Séguin, V. A. Smalyuk, R. B. Stephens, W. Theobald, B. Yaakobi, and T. C. Sangster, Plasma Phys. Control. Fusion **47**, B856 (2005).

31. B. Grek *et al.*, Phys. Rev. Lett. **41**, 1811 (1978).

32. G. Thiell and B. Meyer, Laser Part. Beams **3**, 51 (1985).

33. O. Willi, P. T. Rumsby, and C. Duncan, Opt. Commun. **37**, 40 (1981).

34. A. J. Mackinnon, P. K. Patel, R. P. Town, M. J. Edwards, T. Phillips, S. C. Lerner, D. W. Price, D. Hicks, M. H. Key, S. Hatchett, S. C. Wilks, M. Borghesi, L. Romagnani, S. Kar, T. Toncian, G. Pretzler, O. Willi, M. Koenig, E. Martinolli, S. Lepape, A. Benuzzi-Mounaix, P. Audebert, J. C. Gauthier, J. King, R. Snavely, R. R. Freeman, and T. Boehly, Rev. Sci. Instrum. **75**, 3531 (2004).

35. M. Borghesi *et al.*, Phys. Plasmas **9**, 2214 (2002).

36. J. Delettrez, R. Epstein, M. C. Richardson, P. A. Jaanimagi, and B. L. Henke, Phys. Rev. A **36**, 3926 (1987).

Cryogenic Targets: Current Status and Future Development

Introduction

Twenty years ago the beta-layering mechanism was proposed for achieving a uniformly thick deuterium–tritium (DT)-ice layer in an inertial confinement fusion (ICF) capsule.[1] Experiments with DT-filled capsules confirmed the feasibility of that mechanism,[2] but only now have DT cryogenic targets been demonstrated to be reliably produced with the inner surface of the DT layer possessing the quality required for achieving ignition: a roughness better than 1.0-μm root mean square (rms). Importantly, these results were accomplished in equipment that interfaces with the OMEGA laser, which enables the targets to be imploded in ignition-relevant experiments. Achieving the ice-quality milestone demonstrated the feasibility and adequacy of the beta-layering method, but repeatedly achieving high-quality ice layers is equally important since it allows ICF implosion experiments to be performed where other critical parameters can be varied.[3] This article discusses the process and presents the important issues that affect the quality of the ice layer.

While targets with DT-ice layers are required to achieve ignition, targets with pure-deuterium (D_2)-ice layers make it possible to (1) diagnose the areal density[3] and (2) increase the throughput of cryogenic targets for experiments that could otherwise be achieved with DT because of the radiological complications with handling tritium. In the absence of heating from the decay of tritium, an alternative volumetric heating technique in D_2 is based on the absorption of IR radiation.[4] However, achieving uniform illumination of the capsule while minimizing the effect of energy absorbed in the support structure of the target made it substantially more difficult to achieve the 1.0-μm-rms specification for D_2 than for DT. Nevertheless, as our understanding of the ice layer's sensitivity to the thermal environment has improved, so has our ability to better control the D_2-ice quality; currently we are very close to the ice-quality requirement. The issues and complexities associated with layering D_2 are discussed here.

As our ability to reliably provide high-quality cryogenic targets for implosion experiments has progressed to a produc-

tion process, new technical challenges for producing cryogenic targets have presented themselves. The greatest challenge is to provide new types of targets for use on the National Ignition Facility: plastic shells that incorporate a foam ablator, targets that are filled through a fill tube rather than by permeation, and targets that are sub-cooled below the liquid–solid transition (19.7 K). These new research opportunities and issues associated with them are presented in this article.

Cryogenic Target Production and Characterization

The design philosophy, equipment, capabilities, and operations used to produce cryogenic targets have been reviewed extensively.[5] In summary, 0.9-mm plastic shells (2- to 10-μm wall) are mounted on very thin (1-μm-diam) spider silks and filled with D_2, or DT, via permeation at 300 K, to a pressure of 1000 atm. The targets are subsequently cooled to 20 K, where the gas pressure is <1 atm, and transferred individually at cryogenic temperatures to portable equipment that contains the functionality to form the ice layer (60 to 100 μm thick) shown schematically in Fig. 114.1. Those aspects of the process
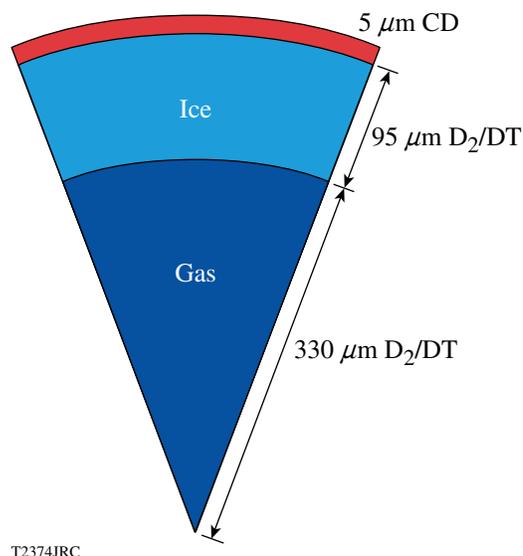

Figure 114.1
Schematic of an OMEGA-scale cryogenic target.

that relate directly to the quality of the ice layer are expounded upon in more detail in the following sections.

The method used to image and quantify the smoothness of the ice layer has also been reported previously,[6] but the salient points are summarized because they are relevant to this discussion. The cryogenic target is rotated around its north–south axis and is viewed by two cameras elevated 12° and 26° above the equator and displaced 100° azimuthally. These viewing angles are defined by the pre-existing viewing angles for the OMEGA target chamber. Typically an image of the target is acquired for each 15° rotational increment, as shown in Fig. 114.2(a). Two concentric circles are evident—the outer circle is the limb of the plastic capsule and the inner circle corresponds to the interface between the ice layer and the inner gas void. From these images the radial position of the ice and plastic surfaces is measured to better than 1-μm precision. By combining all the images, the center of the sphere can be calculated, and the rms deviation of the measured position of the ice-layer position from the averaged sphere radius is the first estimate of the ice roughness [see Fig. 114.2(b)]. A more precise analysis involves fitting the data to spherical-harmonic coefficients to determine the power in the low ℓ modes ($\ell < 12$) [see Fig. 114.1(c)]. This analysis is inappropriate for quantifying higher-mode roughness because the surface is not uniformly sampled, and the northern and southern poles of the surface (<6% by area) are not sampled at all. Both conditions are a consequence of the inclined viewing angles of the camera and the rotational axis of the target. These higher modes are determined by averaging the Fourier modes obtained from the individual images. Together, a representative power spectrum is determined for the whole surface.

Cryogenic DT Targets

The ice-roughness specification for a NIF cryogenic target is shown in Fig. 114.2(b). This value along with the associated power spectrum presumes that the outer-surface ice layer is substantially smoother than the inner surface, so the roughness value is effectively a measure of the uniformity of the ice wall thickness.

Achieving the roughness specification requires forming a high-quality ice crystal to (1) minimize light scattered within the crystal that degrades the sharpness and continuity of the bright band and affects the accuracy of the shadowgraphic analysis and (2) achieve a constant thermal conductivity throughout the shell. A high-quality crystal is one without any features in the shadowgram image that are either crystallographic dislocations (facets, grain boundaries) within the ice or cracks at the inner surface of the ice, both of which can develop during the crystal growth phase.

1. Seed Crystal and Ice-Layer Formation

Crystal formation involves initially freezing the liquid and then allowing 1 h for the beta-layering process to establish an ice layer, which invariably has a polycrystalline structure. That layer is melted (temperature raised in 0.050-K increments at 1-h intervals) until only a small ice crystal (<200-μm diam) remains at the north pole, as shown in Fig. 114.3. The temperature ramp is rapidly reversed (lowered 0.08 K in one step) and then lowered 0.02 K at the rate of 0.001 K every ~20 min. The time lapse between the decrements is a qualitative judgment that is based on the rate the crystal grows. When the layering process appears to have stalled, the temperature is lowered
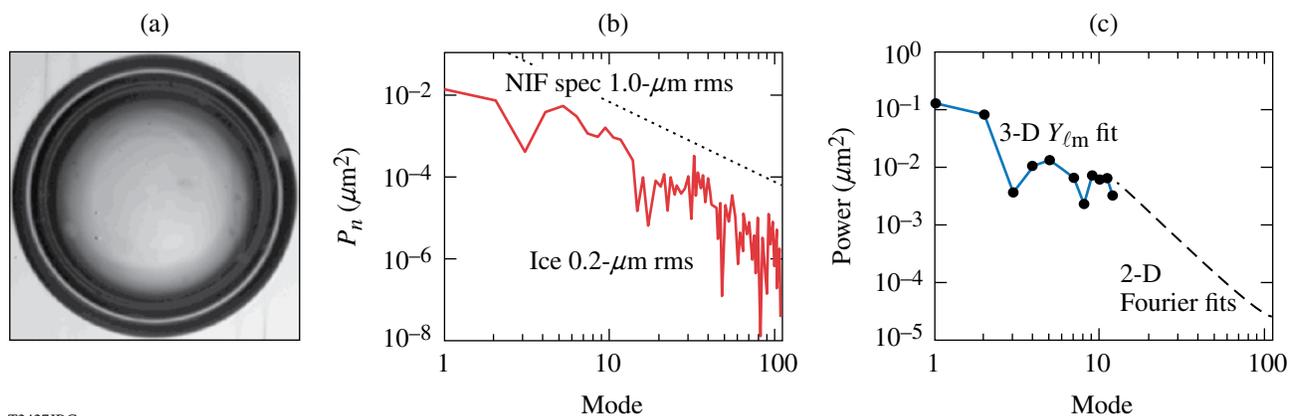
T2427JRC

Figure 114.2
(a) A shadowgraph image of a cryogenic target and (b) the Fourier power spectrum of the ice layer (the dotted line is the specification and the solid line the best recorded result of a single view of the target). (c) The spectral analysis of the 3-D surface is shown using a spherical-harmonic fit for the lower modes and an average of the 2-D Fourier fits for the higher modes.

another 0.02 K at the same rate. Once a contiguous ice layer exists, the temperature is decreased another 0.05 K at a constant rate (1 mK every 30 min), leaving an ice layer that is a single crystal, as shown in Fig. 114.4. Once all the liquid has solidified, the target is cooled another 0.1 K to complete the formation of a uniformly thick ice layer. The timing of the reversal of the temperature ramp is critical: if the seed crystal expands too rapidly, multiple dislocations and grain boundaries will develop

within the ice; alternatively, reversing the temperature ramp too late will melt the seed crystal because there is a thermal lag between the target and the layering sphere, which is the temperature-controlled surface.

While the protocol described above has been demonstrated to produce a desirable crystal structure, the dynamics of the crystal-growth phase is dependent on the environment around the target, the dimensions of the target and the layering sphere, and the amount of DT inside the capsule. A different protocol will be needed for forming ice layers in NIF-scale targets, especially when using the cryogenic equipment envisioned for the NIF, which requires that targets be filled through fill tubes. In the future, a NIF-scale target will be permeation filled with DT to determine whether the geometry and isothermal characteristics of the present layering sphere are sufficient for achieving the ice-roughness specification for the larger target. Separately, a newly constructed cryogenic system will be used to determine how to process targets possessing a fill tube (see **Future Development**, p. 69). Together, these data will guide the design of the front end of the NIF's Target Insertion Cryostat to field direct-drive targets.
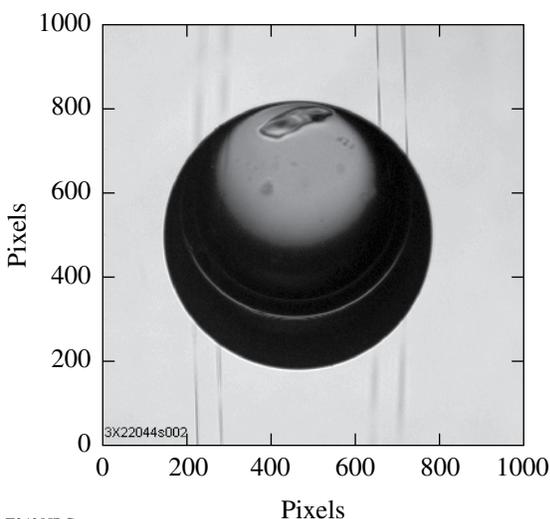

Figure 114.3
A cryogenic target containing liquid DT is shown at the beginning of the crystal formation phase. The small crystal at the top of the target seeds the ice layer.

2. DT-Ice-Layer Quality

Since DT cryogenic operations began in 2006, 21 target-filling operations have been undertaken and 39 targets have been produced for implosions and to study the layering process. The average ice roughness of 31 targets studied (without foam ablators) is 1.0 μm (rms) with a range from 0.6 μm to
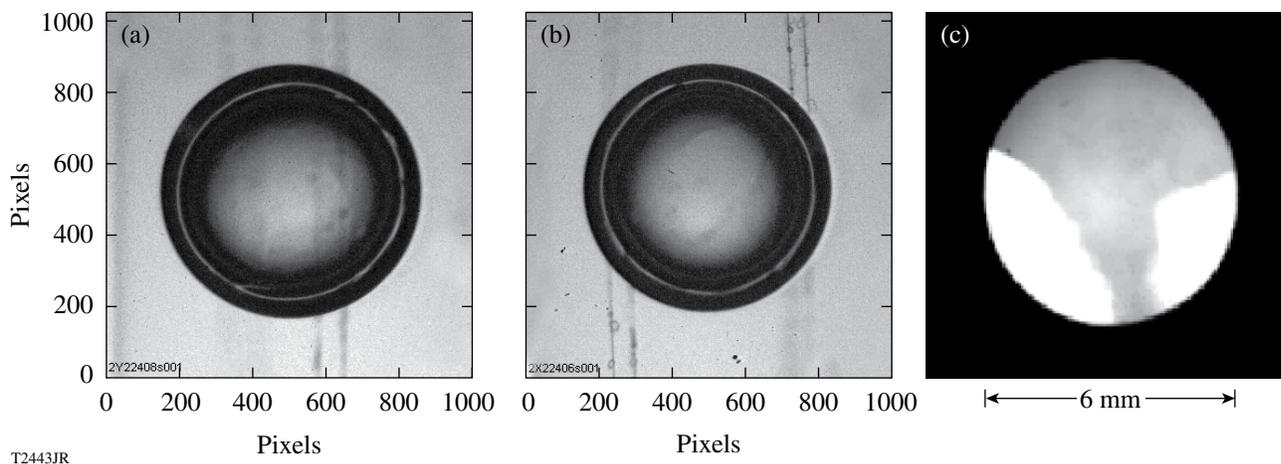

Figure 114.4
Images of the target shown in Fig. 114.3 after layering were acquired using polarized light. The absence of any contrast suggests that the ice layer is composed of a single crystal. Images (a) and (b) are from separate cameras looking at the same target. Image (c) is an ice crystal grown in a cylindrical cell viewed through polarizing optics and showing three separate grains.

2.0 μm. The protocol for forming and then characterizing the ice requires approximately 12 h to complete, and there is a 60% probability that the ice-roughness specification can be achieved within 24 h of receiving the target.

Good repeatability of the layering process was demonstrated by repeatedly melting and re-layering the ice in the same capsule using the same protocol, as shown in Fig. 114.5,

First ice layer

0.69-μm rms

Second ice layer

0.65-μm rms

Third ice layer

1.00-μm rms

−2   −1   0   1   2

Thickness variation (μm)
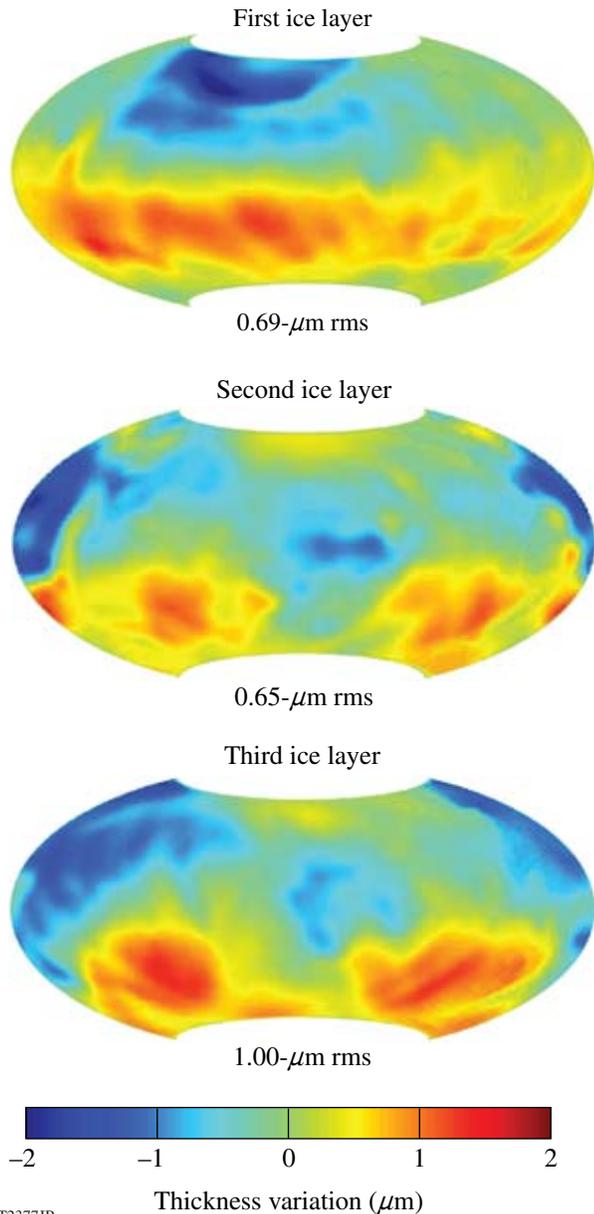
T2377JR

Figure 114.5
The variation in the thickness of three separate ice layers (shown in an Aitoff projection) formed in the same cryogenic target shows the repeatability of the process.

and then repeating this with different capsules. The variation in the ice roughness when the layer was melted and reformed was very small (<0.4 μm), and the location of the thicker and thinner regions of the ice in each layer was different after the melt–relayer cycle. The residual roughness present in all of the targets studied showed that there was no statistical correlation between the ice roughness and the plastic capsule or the thermal environment surrounding the target.

3. Fractionation

A consideration when using DT is the possibility that the deuterium and tritium fractions in the fuel will solidify at different temperatures because the heavier isotopes freeze at a slightly higher temperature (pure T_2 at 20.62 K and DT at 19.79 K). We may expect tritium (T_2 and DT) to freeze disproportionately early on during the cooling ramp, leaving excess tritium at the top of the target and closer to the plastic. This effect would be observed as a repeatable thickness variation in the ice (regions with excess tritium would be thinner due to heat generation from the tritium decay). The lack of any pattern in the ice-thickness distribution suggests that any fractionation that may occur is very small or that subsequent solid diffusion may minimize early-time fractionation.

4. Effect of Tritium Decay to ^{3}He

The decay of tritium to form ^{3}He can affect both the ice-layer quality and implosion performance. If helium entrapped within the ice has sufficient mobility to agglomerate into bubbles larger than 0.5 μm, the resulting perturbation will seed instabilities during the implosion.[7] These larger-sized bubbles may also buckle the ice, adding to the intrinsic roughness. Alternatively, helium that diffuses through the ice into the central void will increase the gas density, and the additional work required to compress the gas during implosions can have a marginal effect on the performance of ignition experiments. While either possibility has an adverse effect, the time scale over which these events occur is important and the data presented here are an attempt to better understand what happens to the ^{3}He produced.

A cryogenic-DT-ice layer was aged for 19 days at a temperature close (within 0.2 K) to the triple-point temperature (19.79 K). Figures 114.6(a) and 114.6(b) show the ice-layer distribution before and after the aging, respectively. No bubbles or voids were observed. Another set of experiments were performed by lowering the temperature to induce grain boundaries, dislocations, and fractures into an ice layer. Inducing disturbances in the ice is expected to enhance ^{3}He diffusion and provide voids where the gas could accumulate.

(a) Initial quality, 1.0-μm rms   (b) 19 days later, 2.0-μm rms

Thickness variation (out of 95 μm)

Initial   19 days at 19.5 K

T2379aJRC
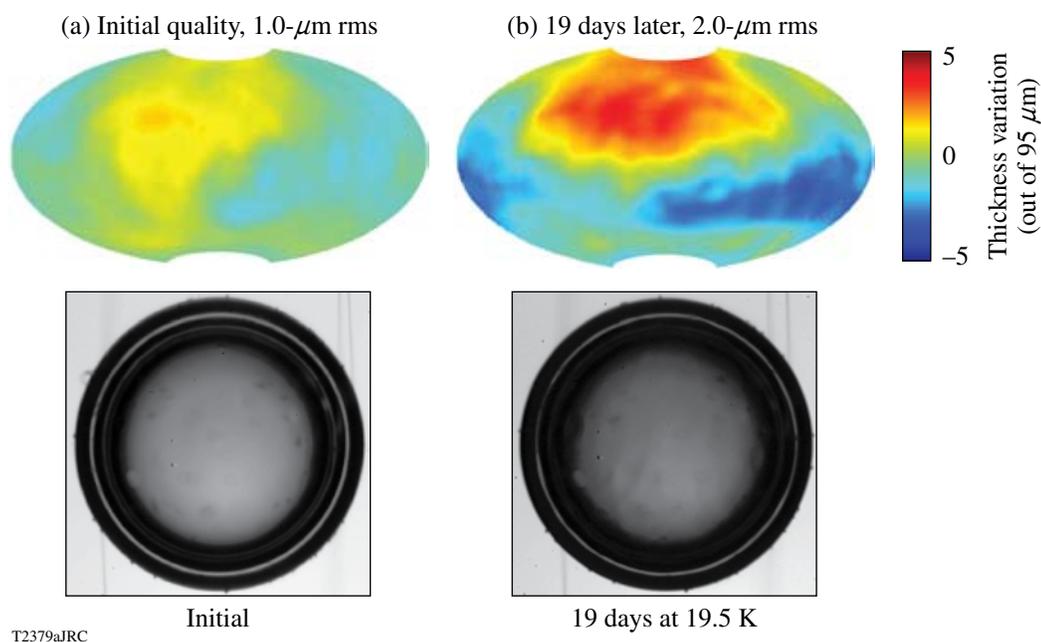
Figure 114.6
Images of a cryogenic DT target and the associated ice-thickness distribution (a) initially and (b) after 19 days.

Moreover, lowering the temperature increases the strain in the ice-crystal structure, which enhances the diffusivity of helium within the crystal.[8] A cryogenic-DT layer aged for two days at 2 K below the triple point [Fig. 114.7(a)] showed no evidence of bubble formation, but small clusters of voids attributed to ^{3}He were observed in another cryogenic-DT-ice layer [shown in Figs. 114.7(b) and 114.7 (c)], aged for seven days under the same conditions.

The appearance of bubbles many days after the ice layer was formed, and only when the ice was strained and fractured, suggests that the helium has limited mobility within a DT-ice crystal. The other possibility is that helium is highly mobile within the ice and diffuses rapidly to the center void; that eventuality would require helium atoms to be more mobile in defect-free, unstrained ice, which is counter to the observations and the general understanding of how gases diffuse through crystalline structures.[8]

Helium has very low solubility in hydrogen ice,[9] and the size of the helium atom (0.3 Å) relative to the open structure of the DT-ice crystal (hexagonally close-packed structure with a 2.2-Å interstitial radius) is expected to allow rapid diffusion. However, there are data that may support the notion that helium is effectively trapped in the ice, which would be very desirable since the unavoidable decay of tritium may not have the deleterious effect on the ICF implosion described at the beginning of the

(a)

40 h at 17.7 K—no bubbles

(b)   (c)

x-axis camera   y-axis camera

T2429JR
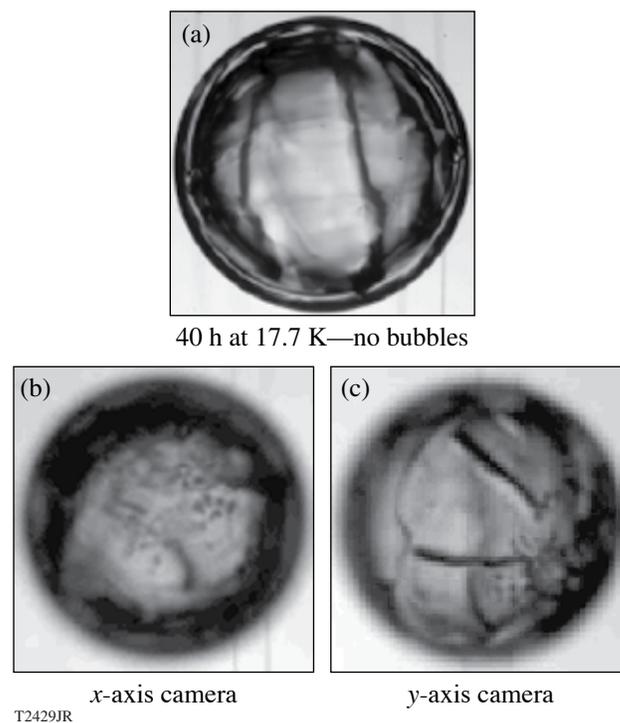
Figure 114.7
(a) A fresh DT-ice layer was cooled 2 K below the formation temperature and aged for two days. (b) and (c) When aged for seven days, 2 K below the formation temperature, black spots presumed to be ^{3}He bubbles were observed.

section. The decay product of tritium is a $(^3\text{HeD})^+$ or $(^3\text{HeT})^+$ ion (Ref. 10) that initially remains bonded to neighboring DT, D_2, or T_2 molecules in the lattice. A fraction of these ions will be neutralized by the electrons produced by the decay of nearby tritium atoms (which have a range of $\sim 0.6\ \mu$m in the ice), and then dissociate into ^3He and T or D atoms. The latter two atoms rapidly recombine and are re-adsorbed into the lattice. The remainder of the $^3\text{HeT}^+$ (and $^3\text{HeD}^+$) ions may become incorporated into the lattice at interstitial octahedral sites and unable to migrate.[10] Experimental evidence for this eventuality is from muon-catalyzed fusion studies[11] that measure the time-dependent change of the fusion–neutron disappearance rate in ice and liquid-DT mixtures. The disparity in the neutron disappearance rate between the liquid (where there was no change) and ice (where the change increased with time) was attributed to the accumulation of ^3He within the ice lattice.[11]

To provide a scale to the helium production rate, approximately 10^{10} ^3He atoms are produced per second in the 0.18-mm^3 ice volume of an OMEGA-scale target; that equates to $\sim 5 \times 10^4$ He atom/s in every 10-μm^3 voxel, which collectively would form a 0.1-μm-diam bubble every second. The 10-μm scale length was chosen to reflect the limited diffusion path of helium atoms and is based on the range of β electrons in the ice to neutralize ionic species into more-mobile neutral atoms. After 19 days, 1.6×10^{16} helium atoms would have been produced and bubbles that are clearly visible would be expected. (The size of the bubble depends on the Laplace pressure and permeability of the ice.) As observed, there were fewer than 10^3 bubbles (with a less than 10-μm-diam size) after the ice was aged for seven days, and then only when the ice was faceted and strained. The most likely inference from all the data is that He has limited mobility. Because this inference has far-reaching implications for the acceptable "shelf-life" of a DT-ice layer, this interpretation needs to be supported with direct measurements of the diffusivity of the ^3He by-product of tritium decay through hydrogenic ice.

What was noticeable in the DT target that had been allowed to age [see Fig. 114.7] was the progressive deterioration in the quality of the ice layer. Interestingly, the power in the added roughness was in the lower Legendre modes ($\ell < 10$). This phenomenon is attributed to the constant rearrangement of the DT structure caused by the high-energy β-decay electrons breaking and reforming the crystal bonding structure. Approximately 10^{10} tritium atoms disintegrate every second in an OMEGA-scale DT target, produces high-energy electrons (up to 18 keV) with each electron capable of rupturing up to 10^5 molecular bonds that hold the lattice together. Clearly these

bonds reform rapidly, as the lattice remains intact, but this constant realignment of the crystal will allow for sizeable diffusivity of deuterium and tritium through the lattice and, with time, a possible re-ordering, or fractionation, of the isotopes. If, due to gravity, the heavier tritium atoms diffuse away from the north pole, the resulting lower volumetric heating there would make the ice thicker—which is what was observed. Not only would this increase the rms roughness of the ice but it would also create a variable areal density around the target that would affect the dynamics of the implosion.

5. DT-Ice Layers in Foam Ablator Targets

Efforts to characterize ice layers formed in foam targets using the same protocol that worked for standard plastic ablators were unsuccessful because the resulting ice/foam layer was opaque and the ice/gas interface could not be imaged. Although the foam alone was transparent (it possesses a small pore size, $<0.2\ \mu$m) and remained transparent when filled with liquid, the target became opaque once the ice layer formed. The transparency was improved by minimizing the number of freeze/melt cycles and not cooling the target below 18 K. This minimized mechanical damage to the foam structure (maintained the pores sizes) from the shear forces that develop due to the different densities of the ice and liquid phases.[12]

It remains critically important to form the ice layer slowly in order to preserve the single-crystal structure of the ice. The presence of the foam does not appear to change how the layer grows provided that the process proceeds in a sufficiently controlled manner with a stable and gradual temperature ramp. This greater sensitivity to the cooling rate compared to non-foam targets is presumed to be due to the viscous drag that the foam has on the movement of the liquid. If the target is cooled too rapidly, the liquid does not have enough time to move to the ice/liquid interface (the void that can develop there is caused by the density mismatch), and the liquid can nucleate a crystal at a foam filament rather than attaching to the existing crystal, which results in a higher void content and greater opacity. At the extreme—flash freezing the target—there is a 13% decrease in the molar volume of DT due to the phase change and the ice turns instantly opaque. The transparency improves marginally as the layering mechanism functions to redistribute and densify the ice, but the resulting small-grain polycrystalline structure cannot be annealed into a single crystal and the inner ice surface cannot be imaged using shadowgraphy. Figure 114.8 shows a series of images of a DT-filled foam target containing initially (a) liquid and then an ice layer formed slowly (b) or rapidly (c). The quality of the ice layer when properly formed is approaching what is achievable in non-foam DT targets: 0.9- to

2.6-μm rms. Current development is directed at understanding how imperfections and variability in the foam structure affect the quality of the ice layer and the ability to characterize it.
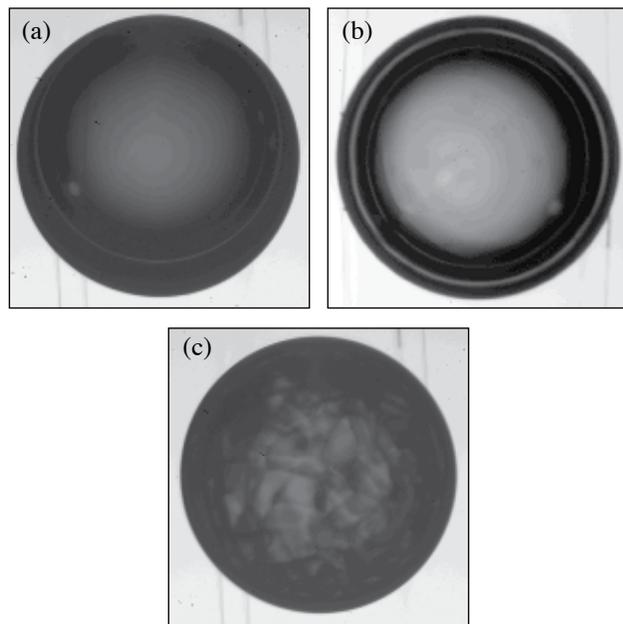
T2430JR

Figure 114.8
DT in a foam target (840-μm diameter; 0.5-μm-rms outer surface roughness; 0.73-μm-rms inner foam layer roughness; 47-μm-rms inner foam layer thickness): (a) liquid DT, (b) single-crystal ice layer, 54 μm thick, 1.2-μm rms, (c) rapidly cooled polycrystalline ice layer.

6. DT-Gas Density at Implosion

A special challenge with DT targets is to preserve the ice layer when the shrouds are retracted to shoot the target. A complication arises because the helium gas that surrounds the target to remove the heat from the target must be removed prior to the shrouds retracting, and its elimination results in the target warming. While the shroud retraction process can be extremely rapid[5] (<1 s total with the target exposed to ambient radiation for <60 ms), slower shroud retraction rates are used to allow more time for the mechanical impulses from the retraction process to attenuate in order to minimize target vibration. Currently there is a 6-s time lapse between the helium gas being exhausted and the target being imploded. During this time the temperature of the ice rises from 19.4 K to 19.7 K (the triple-point temperature). If the target is not initially sufficiently cold, the ice will begin to melt.

Cryogenic D$_2$ Targets

Despite the success in providing DT cryogenic targets that meet ice-roughness specifications, D$_2$ targets are still required for implosion experiments to measure the areal density generated

in the implosion[3] and to support additional cryogenic implosion experiments as the radiological issues associated with handling tritium complicates and slows the production of DT cryogenic targets. The best D$_2$-ice layers produced so far are approaching the quality typically achieved in DT targets, but the process is subject to more variability. Improving D$_2$ target layering has been a high priority and is described in this section.

Recent experiments with D$_2$ cryogenic targets and the experience with DT targets, which provides a benchmark for comparison, strongly suggest that ice-roughness variation in D$_2$ targets is caused by (1) nonuniform volumetric heating of the target and (2) the target-support structure distorting the spherical isotherms around the target. A surprising sensitivity of the ice roughness to even small thermal perturbations around the target has been observed. The sources of these perturbations must be identified and eliminated to reliably produce high-quality D$_2$ targets.

Lacking the intrinsic beta-decay heating method of tritium, volumetric heating of deuterium targets is achieved by irradiating the target with mid-infrared (mid-IR) light at the wavelength of a strong D$_2$ absorption resonance (3.16 μm) (Ref. 13). Uniform illumination is essential to achieve uniform volumetric heating required for high-quality ice layers, so the D$_2$ targets are located at the center of an integrating sphere that also sets the spherical isotherms.

Figure 114.9 shows a schematic of the "layering sphere." Mid-IR light is introduced by an optical fiber so that it does
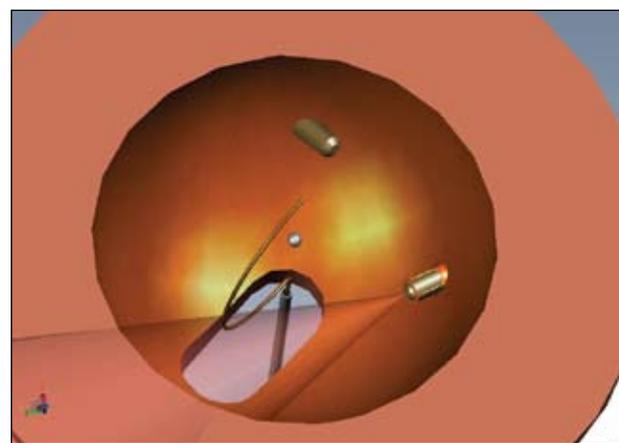
T2431JRC

Figure 114.9
A schematic of the lower hemisphere of the layering sphere showing the target mounted on the beryllium "C" support and two IR fibers projecting into the sphere. The cone of light from one of the fibers is projected and shown to intersect the beryllium support.

not directly illuminate the target. The inner surface of the layering sphere is deliberately roughened and coated with gold to provide a highly reflective scattering surface. Ideally, this scattering would be isotropic and would uniformly illuminate the target after a few bounces. Subsequent experiments showed that the surface forward scatters the light with a $\cos^9\theta$ angular distribution.[14]

Another limitation to forming high-quality D_2-ice layers is the nonuniform thermal environment surrounding the target. Mid-IR light absorbed by the target support, the plastic ablator, and the glue used to hold the target perturbs the spherical isotherms sufficiently to exceed the 1-μm-rms-roughness specification. Efforts to mitigate these effects have improved the ice-layer quality and are presented here.

The result of these efforts produced a D_2-ice layer with an rms roughness of 1.1 μm. This best D_2-ice layer, shown in Fig. 114.10, was achieved in a layering sphere that had received all the upgrades described in subsequent sections. Importantly, this good quality was not an isolated event; similar targets that were layered using the same protocol achieved ice layers that ranged from 1.5- to 2.5-μm rms roughness, considerably better than the historical 3- to 5-μm rms roughness. A necessary requirement for improved ice smoothness is the plastic capsule itself, specifically, the thinness of the walls (2.0 μm—the thinnest requested) and the composition of the plastic (low oxygen content) because this reduces the sensitivity of the target to nonuniform illumination.

1. Effect of IR Heating on Ice-Layer Quality

The strongest absorption bands in D_2 correspond to the $Q_1(1)+S_0(0)$ and $Q_1(0)+S_0(0)$ transitions that overlap at 3.16 μm and have a combined 10-nm bandwidth.[13] The $Q_1(1)$ and $Q_1(0)$ components of the absorption band are due to vibration-only transitions in ortho- and para-deuterium, respectively, while the $S_0(0)$ component is a rotation-only transition. Absorption is due to a dipole moment induced by motion in two neighboring D_2 molecules, where one molecule rotates (change in the rotational quantum number, $\Delta J = 2$) and the other vibrates (change in the vibrational quantum, $\Delta v = 1$). The absorption band possesses fine structure that varies according to the ratio of ortho- and para-deuterium (deuterium is 67% ortho and 33% para). The absorption coefficient is 4 cm^{-1}, corresponding to ~7% of the incident IR power being absorbed by the ice in a standard OMEGA-scale cryogenic target.

The current IR layering source is a tunable optical parametric oscillator (OPO)[15] with a bandwidth (0.03 to 0.3 nm) that is narrow compared to the D_2 absorption band.[13] The wavelength of the OPO can be adjusted in 10-nm steps that are comparable to the bandwidth of the strongest D_2 absorption band at 3.16 μm. This combination of narrow OPO bandwidth and coarse tuning can result in the output wavelength being offset
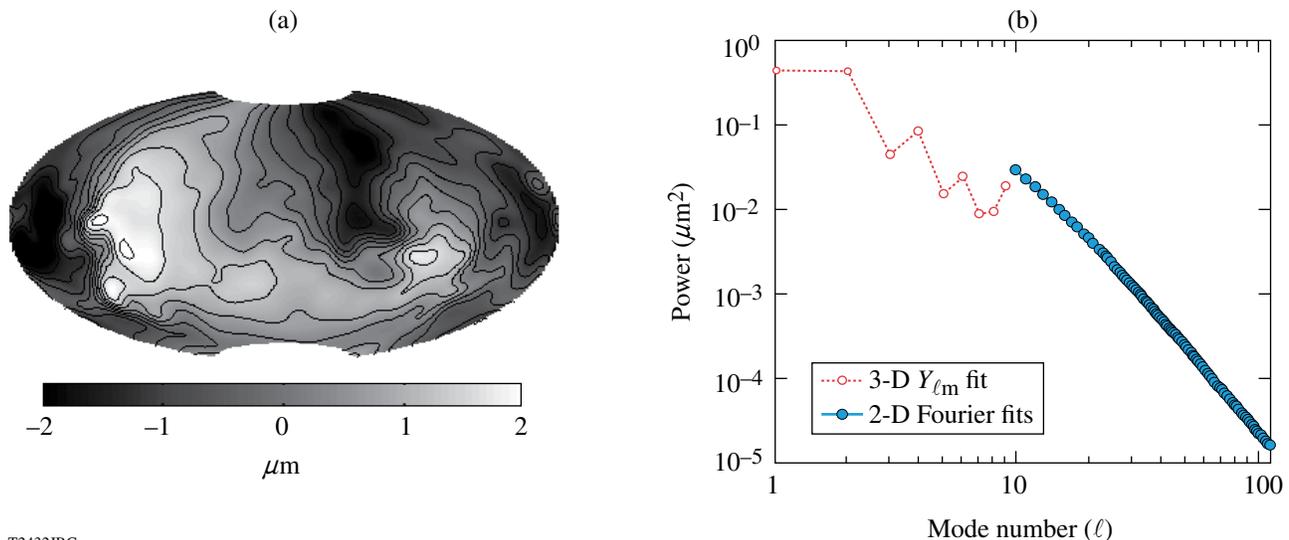
T2432JRC

Figure 114.10
(a) The variation in the thickness of a 99-μm deuterium ice layer (860-μm-diam, 2.0-μm wall capsule) is shown (b) with the associated power spectrum for the entire surface. The rms roughness value for all modes is 1.1 μm.

from the deuterium absorption peak, which would reduce the heat deposited in the ice and make the volumetric heating very dependent on the spectral stability of the OPO. The stability of the wavelength depends on the temperature stability of the lithium niobate crystal in the OPO, where a 5°C change corresponds to a 1-nm change in wavelength. The wavelength is not locked to a specific value; instead, the temperature of the crystal is closed-loop controlled using a chromel–alumel thermocouple. Consequently the spectral output depends on how well the crystal is thermally connected to the temperature sensor, the standard error limits of the sensor (2.2°C), the bandwidth on the temperature control circuit logic (2°C), and the sensitivity of the temperature measurement (a millivolt thermocouple signal) to external noise.

OPO output power and wavelength must both be stable since both affect the volumetric heat load during the initial crystal growth phase (15-min duration), and the rate of growth of the crystal determines whether single, or multiple, crystals form, and the presence of facets and low-angle grain boundaries in an ice layer with multiple crystals increases the ice roughness.

Once the layer is formed and the target is transported to the OMEGA target chamber, small drifts in wavelength and power may result in the ice layer melting (a 1% change in OPO power will slump the ice layer in 30 min).

The effect of OPO wavelength on ice-layer quality was determined by forming a layer at one wavelength and at maximum OPO output power and then changing the wavelength. The data are shown in Figs. 114.11 and 114.12. Operating the OPO wavelength closer to the peak of the D_2 absorption band produces targets with lower roughness. At wavelengths where D_2 does not absorb (3.15 and 3.21 μm), there is sufficient heat absorbed in the plastic to form a thermal gradient sufficient to give a rudimentary ice layer. These layers possess a dominant vertical P_1 mode that is symptomatic of insufficient heat being coupled into the ice. Separate experiments in which the power of the OPO was deliberately varied show that a minimum of 3 μW must be absorbed in the ice to form a uniformly thick ice layer. Higher heat loads in the target increase the speed at which a layer forms but only marginally improves the ice roughness. It has been impossible to explore the benefit of high
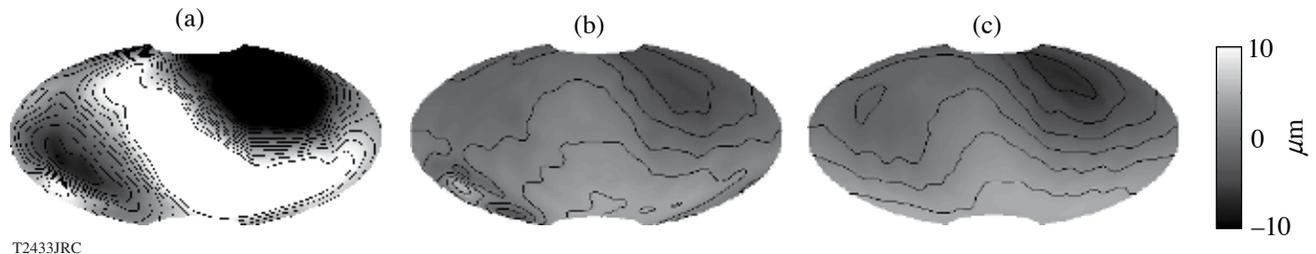

T2433JRC

Figure 114.11
Variation in the thickness of the ice layer when just the wavelength of the optical parametric oscillators (OPO's) is varied: (a) $\lambda = 3.21$ μm, roughness is 10.5-μm rms; (b) $\lambda = 3.17$ μm, roughness is 2.4-μm rms; (c) $\lambda = 3.16$ μm, roughness is 3.0-μm rms,
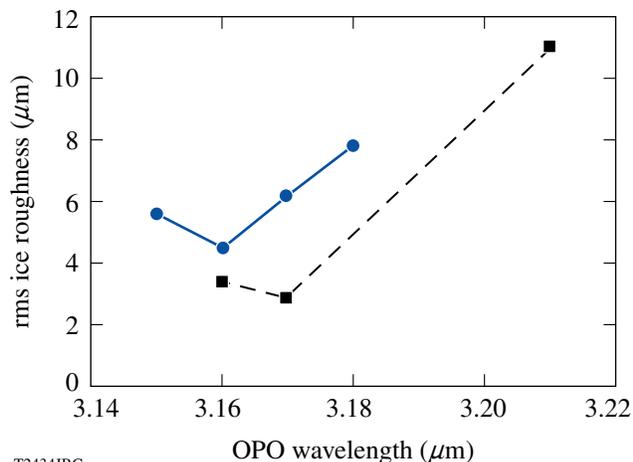

T2434JRC

Figure 114.12
The dependency of ice roughness on the wavelength of the IR source is shown for two OPO's. The variability in roughness depends on whether sufficient heat is coupled into the ice layer to complete the layering process. The output power of the OPO's was constant.

IR power because the maximum power that can be achieved in the ice is ~20 μW, which is twice the heat from beta decay in a comparably sized DT target.

2. IR Illumination Uniformity

From the beginning the importance of uniform IR illumination throughout the layering sphere was recognized, so the surface of the layering sphere was treated to provide Lambertian reflectance.[16] The observed behavior of the D_2 (and not DT) ice layers questioned that assumption of Lambertian reflectance, and tests of the layering sphere showed that the surface has a preferred forward scattering angle. Subsequent ray-trace modeling[17] showed large regions of the layering sphere volume where the IR intensity is substantially greater than elsewhere (see Fig. 114.13). A portion of these regions overlap the beryllium support, which is 22 mm long with a 7-mm radius of curvature and intersects a large portion of the cross-sectional area of the void in the layering sphere. The heat deposited in the beryllium structure perturbs the spherical isothermal structure around the target and, depending on how hot the beryllium becomes, determines how it will affect the ice (see **Effect of the Target Support on the Ice-Layer Quality**, p. 68).

IR uniformity was improved by adding a diffusive reflecting surface in front of the injection fiber to scatter the incident beam (5 to 20 mW) over a larger fraction of the layering-sphere surface and reduce the intensity of each subsequent reflection. This successfully eliminated the thermal influence of the beryllium support on the ice layer, but the new IR illumination pattern introduced a different and smaller perturbation to the ice layer that suggests that the target is no longer being uniformly illuminated—it appears that one of the multiple initial reflections of the beams is striking the target directly. This conclusion was reached by rotating the target and seeing the same ice-distribution pattern in the ice layer relative to the surface of the layering sphere regardless of the rotational position of the capsule. A similar ice distribution pattern is observed, at different magnitudes, in all the moving cryostats that were retrofitted with this modification to the IR injection fiber.

To estimate the ice layer's sensitivity to nonuniform illumination a finite-volume thermal calculation (*FLUENT*[18]) applied a 20%-larger volumetric heating load over two opposing sides of the target that total 14% of the target's volume. That nonuniformity redistributed the ice and the resulting roughness was 17-μm rms. The pattern of roughness and distribution of power in the low Fourier modes was similar to experimentally observed ice layers (see Fig. 114.14), which shows that the ice layer is very sensitive to illumination uniformity.

3. Effect of the Plastic Ablator's Composition on the Ice Layer

The effect of nonuniform IR illumination on the ice roughness is compounded if appreciable light is absorbed by the ablator. If the heat absorbed in the plastic is uniform, the main effect is to increase the temperature difference between the layering sphere and the target; however, as the ratio of heat in the plastic relative to the heat required to form an ice layer


T2435JRC
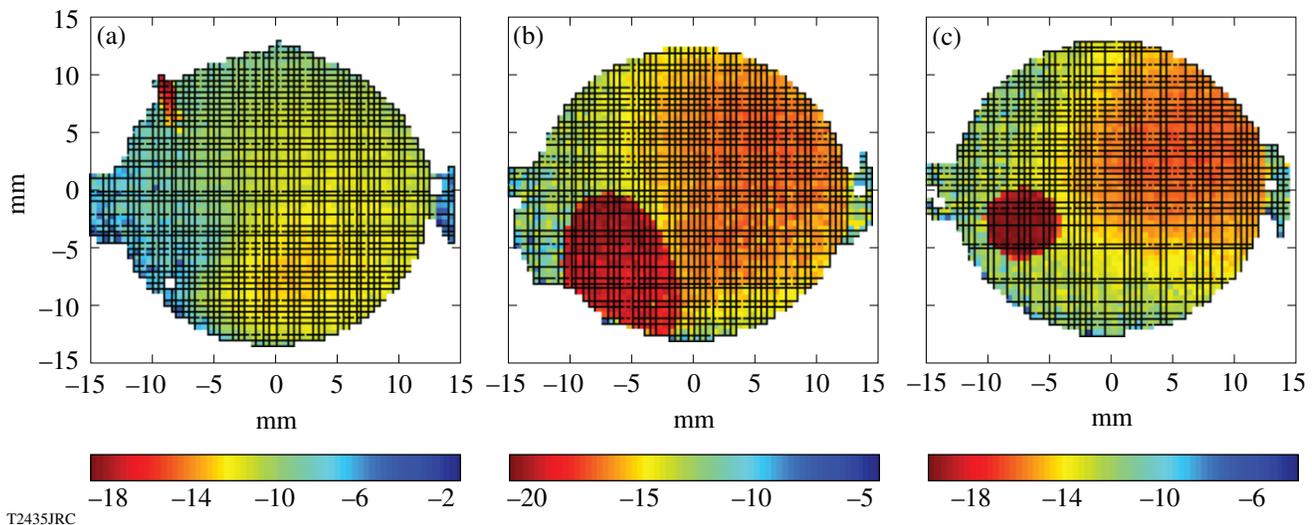
Figure 114.13
Calculated IR intensity distribution patterns shown in a logarithmic plot for discrete vertical planes through the layering sphere (a) 0°, (b) 60°, and (c) 120° (angles refer to OMEGA coordinates).

(~3 μW, or 1/3 Q_{DT}) increases and is not uniform throughout the plastic, the distortion to the spherical uniformity of the isotherms around the target increases.

The plastic ablator strongly absorbs IR light over the wavelength range of 2.85 to 3.4 μm, which includes the deuterium absorption band at 3.16 μm. This absorption increases with time, as shown in Fig. 114.15(a), due to the uptake of ambient moisture and oxygen that become chemically bonded in the plastic as a hydroxyl molecule.[19] The absorption coefficient increases markedly when a silicon dopant is added to the ablator, as shown in Fig. 114.15(b) (Ref. 20).


(a)

(b)

T2436JRC
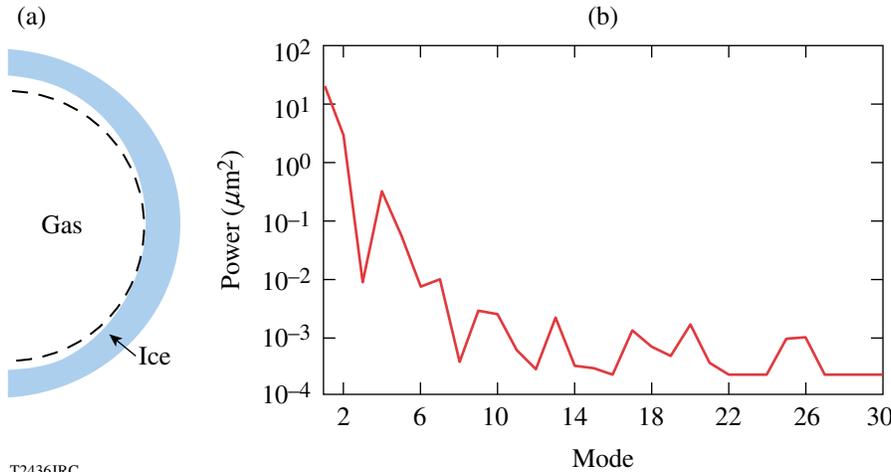
Figure 114.14
The calculated effect of 20% illumination nonuniformity on the ice-thickness distribution for a large volumetric heat load over a 14% volume at the north and south poles. (a) The ice is thinner at the poles (dashed line is a surface of constant radius for reference). (b) The Fourier power spectrum shows that the low-mode roughness (P1 through P4) is the greatest. The shape of the PSD is comparable to measured ice layers but the magnitude is ~50% larger.

T2437JRC
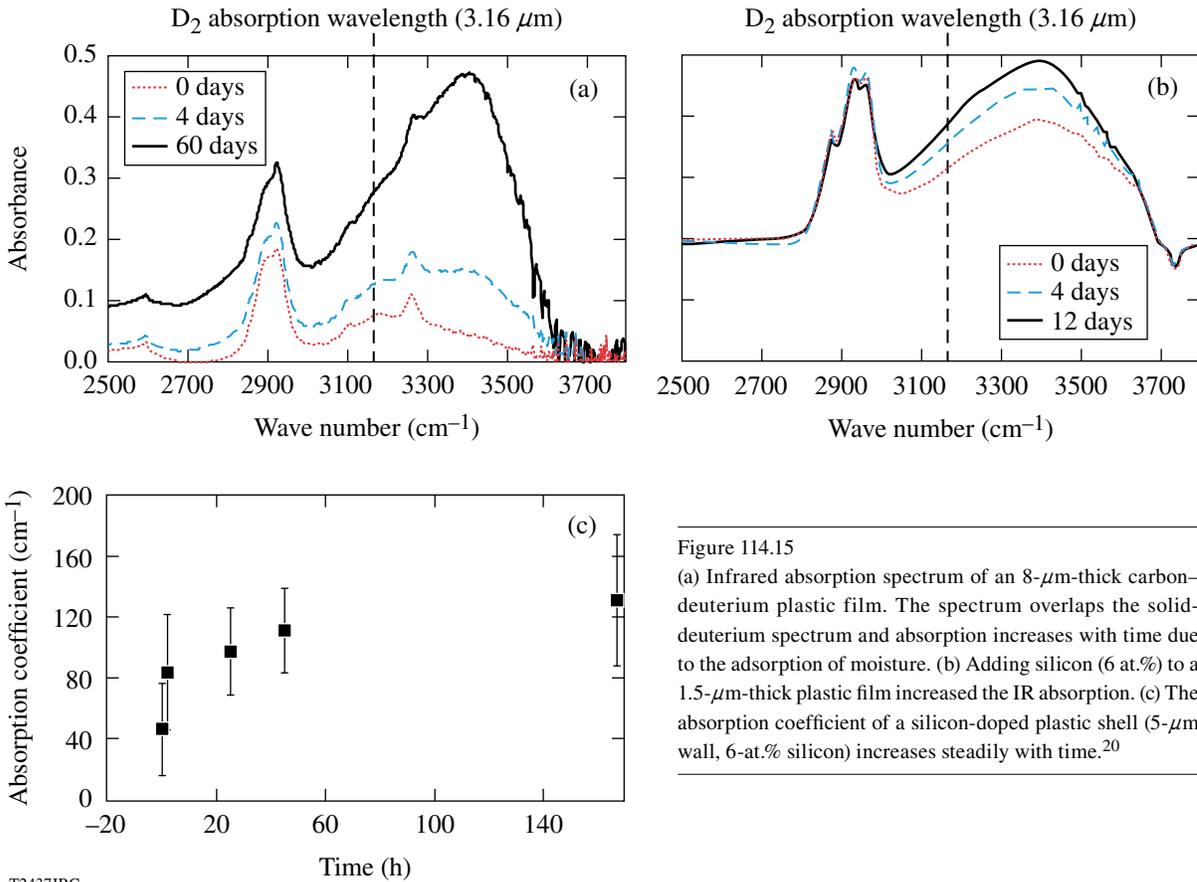
Figure 114.15
(a) Infrared absorption spectrum of an 8-μm-thick carbon–deuterium plastic film. The spectrum overlaps the solid-deuterium spectrum and absorption increases with time due to the adsorption of moisture. (b) Adding silicon (6 at.%) to a 1.5-μm-thick plastic film increased the IR absorption. (c) The absorption coefficient of a silicon-doped plastic shell (5-μm wall, 6-at.% silicon) increases steadily with time.[20]

The absorption coefficient of a standard plastic capsule is 5 to 26 cm^{-1} (one to six times that for D$_2$) as fabricated and increases to 16 cm^{-1} and 35 cm^{-1} after 4 and 60 days, respectively.[19,20] Absorption is due to the presence of the hydroxyl (–OH) species that possess a strong dipole moment that allows them to effectively absorb radiation. These species derive from the adsorption of moisture, or in the case of silicon-doped plastic, from the reaction of silicon free radicals present in the polymer with atmospheric oxygen. Free radicals within the plastic result from the plasma polymerization process. The presence of silicon in the CH ablator increases the absorption coefficient by a variable amount, depending on the fabrication conditions, up to a maximum measured value of ~6000 cm^{-1}, where 95% of the IR light is absorbed by the plastic ablator, effectively shielding the ice from the IR source. The problem with the presence of high-reactive silicon atoms was mitigated by heating the plastic to 300°C immediately following fabrication. Heat treatment reduces the number of reactive sites in the plastic, and the measured absorption coefficients were reduced to ~40 to 140 cm^{-1}, depending on how long the capsules are exposed to the atmosphere [Fig. 114.15(c)]. Currently there remains a sizeable variability in the magnitude of the absorption coefficient of the plastic.

The effect of the enhanced IR absorption in the plastic ablator on the ice-layer roughness is two-fold: (1) If the ablator absorbs the light so effectively that too little heat is absorbed in the ice, then insufficient heat density is available to drive the layering process, resulting in a roughness of ~10-μm rms, as seen in Fig.114.16(a). This behavior was also observed in deuterium–tritium targets with a low (0.1 and 1 at.%) tritium content where the heat from tritium decay was insufficient to form a symmetrical ice layer, as well as when the OPO wavelength was detuned from the D$_2$ absorption maximum. Heat treating significantly improved the silicon-doped target (2.5-μm rms) ice roughness [Figure 114.16(b)]. (2) If the ablator is not uniformly thick, or the IR illumination is not uniform over the surface of the target, the variable volumetric heating load will be accentuated by a high absorption in the plastic and will degrade the uniformity of the ice layer. Since the thickness of the plastic wall is measured interferometrically to vary less than 0.2 μm, illumination uniformity is the greatest concern. Figure 114.16(c) shows a silicon-doped target with two opposing regions of thinner ice that is presumed to be caused by a higher IR flux illuminating the target along this direction.

4. Effect of the Target Support on Ice-Layer Quality

The target is attached to four spider silks (<1-μm diam) on a beryllium wire (250-μm diam) that is bent into a semicircle (7-mm radius). The beryllium wire was shown in earlier experiments[21] to affect the ice layer: the thinnest region of the ice faced the beryllium support and this correlation was maintained when the target was rotated in the layering sphere, and when different targets were used. The cause was the beryllium support absorbing IR light, as shown in Fig. 114.9, and heat from the hot wire imprinting into the ice. Conclusive proof of the IR-induced heating effect of the beryllium is the absence of any similar imprint in DT-ice layers for targets that use the same support structure.

Glue is used to attach the capsule to the spider silk. Manipulating extremely small quantities of glue is difficult as surface tension rapidly wicks the glue from the dispenser to the surface. The glue strongly absorbs IR light and becomes a localized heat source on the capsule. To test the effect, a capsule was mounted in silk and four glue spots of different sizes were
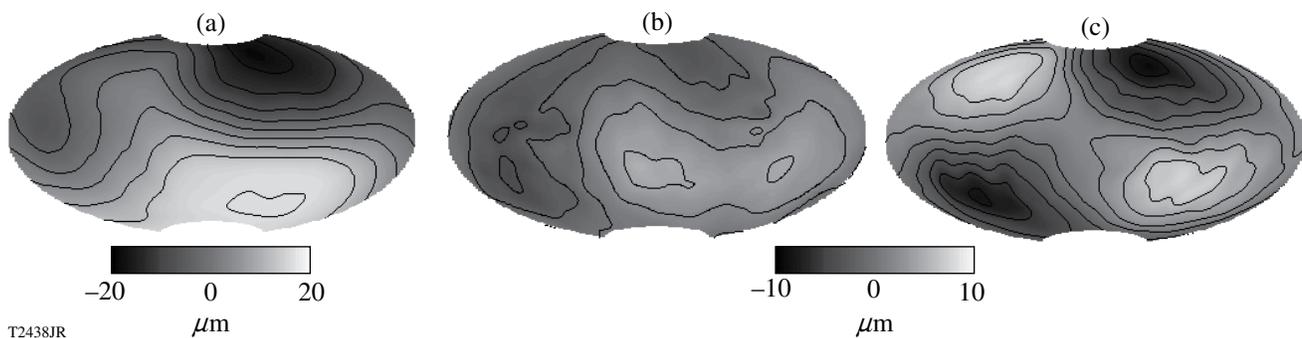
Figure 114.16
D$_2$-ice thickness distribution in a silicon-doped plastic capsule. A large P1 vertical mode is present when (a) the capsule is not heat treated to minimize adsorption of water (10-μm rms) and is reduced when (b) the capsule is heat treated (2.5-μm rms). (c) A third target shows two opposing thin regions of ice that lie on an inclined axis (30° from north and 50° azimuthally, in OMEGA coordinates), which suggests that the target is more strongly illuminated along this axis.

applied, as shown in Fig. 114.17. Glue spots smaller than 30-μm diam and 3 μm high (<1 ng) did not affect the ice, whereas a glue spot ~100-μm diam and 7 μm high (47 ng) generated a 20-μm-deep hole in the ice and a 26-ng glue spot generated a 10-μm-deep crater. The two smallest glue spots had no observable effect on the ice layer. An alternative to using glue is to overcoat the target and silks with a thin film of parylene less than 1 μm thick. The capsule is held without glue between four silks during the vapor-deposition process. Experience shows that this satisfactorily supports the capsule and eliminates the need for glue.


T2439JR
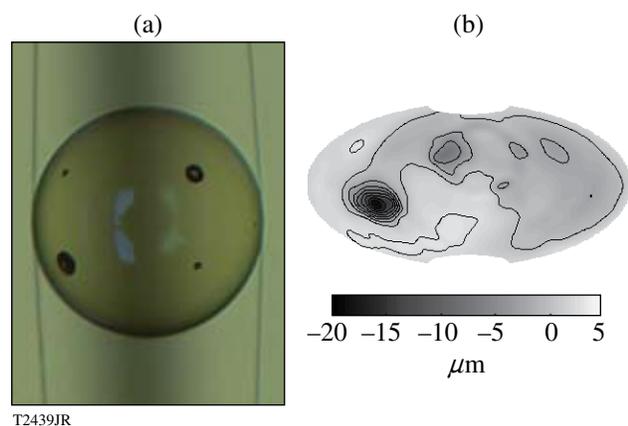
Figure 114.17
(a) A target is shown mounted on silk with four glue spots of varying size. Starting in the top left-hand corner and proceeding clockwise, they have masses of <1, 26, 1, and 47 ng. (b) The variation in the thickness of a 95-μm ice layer is shown as an Aitoff projection. The 47-ng glue mass (height of the glue is 7 μm) causes a 20-μm crater. Diagonally opposite this feature is a 10-μm crater caused by the 26-ng glue spot. The smaller glue masses had no effect.

5. Current Status
Smooth D$_2$-ice layers are feasible when sufficient heat is deposited in the ice, minimal heat is deposited in the plastic ablator, and the target is uniformly illuminated. We have no diagnostic to evaluate these phenomena that is more sensitive to these effects than the target itself. So only by accumulating statistics of the ice layer for different targets and layering-sphere environments is it possible to evaluate and improve the performance of cryogenic equipment for producing high-quality ice layers. Anytime one of the critical components is changed, the performance of the equipment can change, and it requires over a month to reestablish the performance of the system. These critical components are the IR injection fiber, the layering sphere, and the target type (wall thickness, ablator composition). Currently there is one moving cryostat that produces good-quality ice layers and two cryostats that produce moderate-quality layers. A concerted effort is underway to improve the design of a reflective optic for the injection fiber to improve the uniformity of IR illumination. Such a device should improve the repeatability of the layer quality in all the moving cryostats used for implosion experiments.

Future Development
1. Achieving 0.3-mg/cc Gas Density in a Cryogenic Target
Experience shows that the ice-roughness specification can be achieved only by forming the ice layer at the triple point (0.5 mg/cc at 19.7 K for DT). Implosions performed using a low-adiabat ($\alpha < 2$) laser pulse shape would benefit by lowering the gas density to 0.3 mg/cc, which corresponds to a temperature of 18 K for DT.[22] The consequence of cooling the target by the required 1.7 K raises the density of the ice by 0.8%, which induces a strain of 0.1% along the a axis and 0.2% along the c axis of the hexagonally closed packed crystal. This strain exceeds the yield stress[12] and plastically deforms the ice.

Experiments reported that this behavior can be minimized by rapidly cooling the ice layer, thereby creating a brief "time window" where the gas has the desired density (0.3 mg) and the ice-layer smoothness is preserved.[23] Repeating those experiments here with the OMEGA Cryogenic System suggests that the solution is not so straightforward. Rapidly cooling a target with a thick ablator wall (10 μm) and a 95-μm D$_2$-ice layer showed that a 10-s period existed during which the ice layer retained its roughness and the temperature was 1.7 K below the triple-point temperature, as seen in Fig. 114.18(a). The temperature of the target is calculated from the measured temperature of the layering sphere and the thermal diffusivity of helium. The heat capacity and heats of fusion and sublimation of the D$_2$ ice were included in the analysis.

Repeating this experiment with targets with thinner plastic ablators (2 to 5 μm) produced contradictory data. Features and roughness were observed in the ice once the temperature had dropped 1 K, as shown in Fig. 114.18(b). Sometimes the increased roughness was observed along only one viewing axis; other times the outer plastic surface roughened while the ice layer retained its smoothness. This observation confirms that the stresses induced when the ice contracts are substantial, as witnessed by the plastic and/or ice buckling. This raises the question of why targets with thicker plastic ablators did not show as rapid a degradation of ice quality as the targets with thinner ablators since the stresses should be similar. One possible explanation is that the ice layer may detach from the thicker plastic walls because the plastic is less likely to buckle to relieve the stress; the resulting higher thermal resistance

between the wall and ice layer may cause the actual temperature of the ice and gas to be higher than calculated.
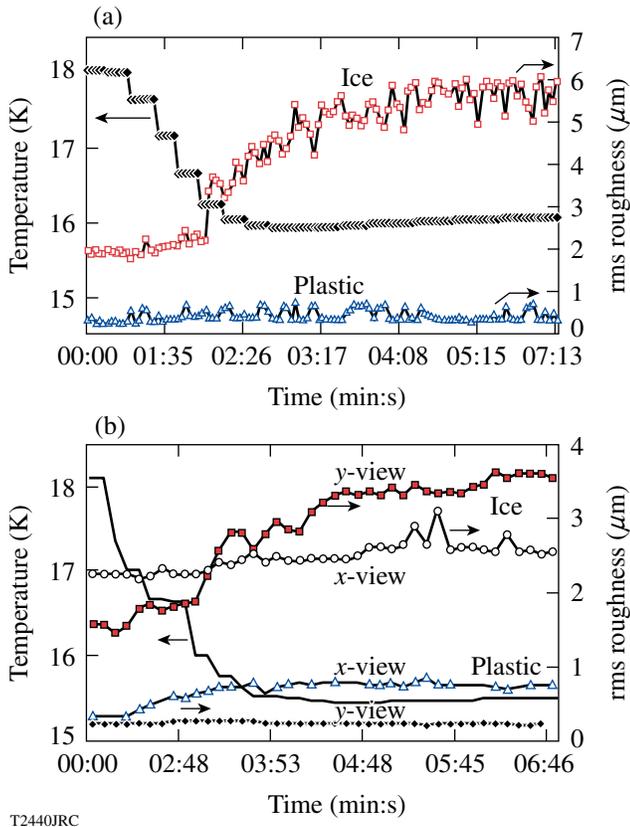
Figure 114.18

(a) Rapidly cooling a target with a 10-μm plastic wall shows that there is little change in the ice roughness until the temperature is 1.7 K below the triple point. Simultaneously there is no change in the roughness of the plastic ablator. In contrast, (b) rapidly cooling a thinner-wall (5 μm) capsule shows the ice roughness increased in one camera view and not the other. Concomitantly, the roughness of the plastic ablator increased in the camera view where the ice did not roughen and visa versa.

Current experience requires that we assume that dislocations and grain boundaries will develop in the ice as it cools and before it is imploded. What needs to be resolved is whether these features are crystallographic fractures within the ice or cracks at the inner ice surface. If they are the former, they would have nanometer scale lengths and would not be expected to affect the implosion; if they are the latter, they could affect the implosion if the total void volume due to the cracks were large. The current NIF specification for indirect-drive targets is that the void-volume in the cracks be less than 0.2% of the total ice volume. The features that form when the target is rapidly cooled appear circumferentially around portions of the target in discrete regions, as shown in Fig. 114.19, that appear to be correlated to a crystalline axis. Should there be a strong correlation between the

position and direction of these features and the crystallographic axis, then it is reasonable to assume that the features are a benign facet or low-angle grain boundary rather than a larger-scale crack at the inner ice surface. Current emphasis is to acquire those statistics to see if there is a correlation between the orientation of the growth crystal as determined from the solidification process and the fracture features observed during cooling.
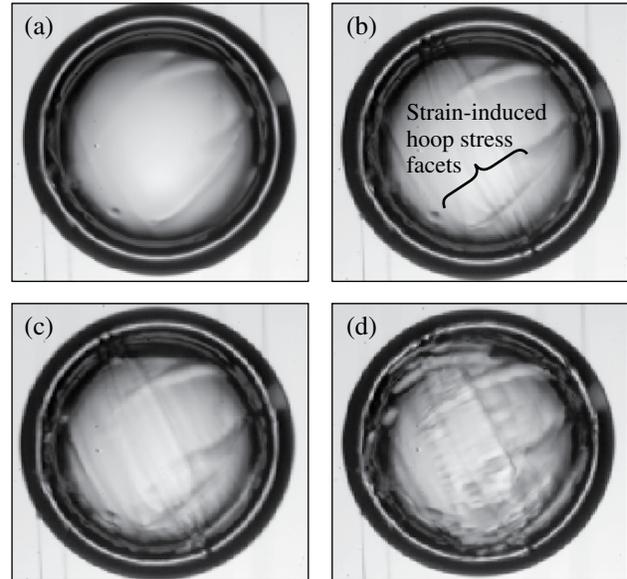
Figure 114.19
Images of the ice layer when it is rapidly cooled showing preferred orientation of cracks: (a) initial rms roughness is 2.2 μm; (b) +145 s and –1.4 K, 2.2 μm; (c) +180 s and –2 K, 2.3 μm; (d) +300 s and –2.6 K, 2.6 μm.

2. Cryogenic Fill-Tube Test Facility

Two new cryogenic systems designed specifically to study targets that are filled via a tube are now operational. This capability is needed to study cryogenic-target science issues that cannot be addressed with the existing OMEGA Cryogenic Target Handling System (CTHS). Two goals for the system will be (1) to prototype the environs surrounding a NIF-scale target and demonstrate that the design of the layering sphere is suitable for producing NIF-scale targets that meet the ice-thickness and ice-roughness specifications, and (2) to support specific studies of cryogenic targets that cannot be performed using the OMEGA CTHS.

The new equipment has capabilities and features not available on the CTHS, including (1) the ability to characterize a D_2-ice layer using both x-ray phase contrast (see Fig. 114.20) and shadowgraphy to cross-calibrate these techniques; (2) a cryogenic rotation stage small enough to be included in the NIF CTHS to preserve the ability to rotate a target through the

field of view of the diagnostics to compile a 3-D analysis of the entire surface of the target; and (3) a layering sphere environment that incorporates the target support structure and fill-tube accessories that will be used to field cryogenic targets on the National Ignition Facility (Fig. 114.21) (Ref. 24).

Targets to be tested in this equipment include fast-ignition, cone-in-shell OMEGA-scale targets; indirect-drive NIF-scale targets mounted in a transparent hohlraum; and foam NIF-scale targets in standard support structures and "Saturn-ring" support structures.[24]
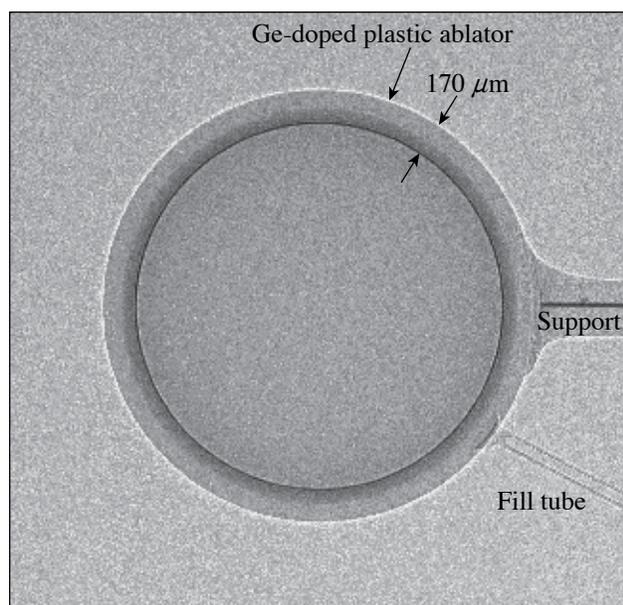
T2442JR

Figure 114.20
X-ray phase-contrast image of a 2.2-mm-diam NIF indirect-drive-scale capsule with a germanium-doped plastic ablator. The support for the target is horizontal and below it is the tube for filling the target.
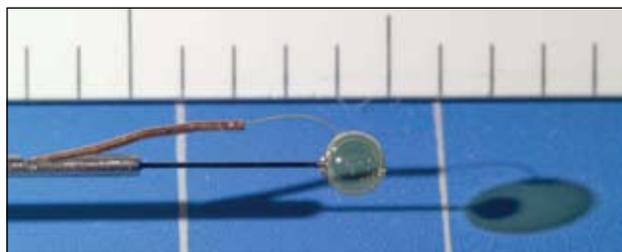
T2444JRC

Figure 114.21
NIF-scale, 3.0-mm-diam direct-drive target showing the horizontal support and fill tube.

The planned experiments include qualifying a thermal environment and protocol for forming targets that meet NIF specification, evaluating the dynamics of the targets' support to ensure accurate pointing and target stability, and optimizing the trade-off between these competing requirements.

Conclusion
The ability to form cryogenic targets with radioactive DT ice that meet the exacting specifications, and to deliver those targets for implosion experiments, demonstrates a substantial advancement in the capabilities of the OMEGA system. Current emphasis is on supplying these targets for experiments and on improving the operation, while simultaneously improving the consistency of D_2 cryogenic target quality.

Beyond the scope of supporting ongoing experiments, we are supporting the National Ignition Campaign by studying issues relevant to indirect-drive cryogenic targets. We are also extending our capability to studying the requirements for making larger-sized targets intended to achieve ignition on the NIF using direct illumination.

REFERENCES

1. J. K. Hoffer and L. R. Foreman, Phys. Rev. Lett. **60**, 1310 (1988).

2. J. Sater *et al.*, Fusion Technol. **35**, 229 (1999); J. D. Sheliak and J. K. Hoffer, Fusion Technol. **35**, 234 (1999).

3. T. C. Sangster, J. A. Delettrez, R. Epstein, V. Yu. Glebov, V. N. Goncharov, D. R. Harding, J. P. Knauer, R. L. Keck, J. D. Kilkenny, S. J. Loucks, L. D. Lund, R. L. McCrory, P. W. McKenty, F. J. Marshall, D. D. Meyerhofer, S. F. B. Morse, S. P. Regan, P. B. Radha, S. Roberts, W. Seka, S. Skupsky, V. A. Smalyuk, C. Sorce, J. M. Soures, C. Stoeckl, K. Thorp, J. A. Frenje, C. K. Li, R. D. Petrasso, F. H. Séguin, K. A. Fletcher, S. Padalino, C. Freeman, N. Izumi, J. A. Koch, R. A. Lerche, M. J. Moran, T. W. Phillips, and G. J. Schmid, Phys. Plasmas **10**, 1937 (2003).

4. G. W. Collins *et al.*, J. Vac. Sci. Technol. A **14**, 2897 (1996).

5. D. R. Harding, T. C. Sangster, D. D. Meyerhofer, P. W. McKenty, L. D. Lund, L. Elasky, M. D. Wittman, W. Seka, S. J. Loucks, R. Janezic, T. H. Hinterman, D. H. Edgell, D. Jacobs-Perkins, and R. Q. Gram, Fusion Sci. Technol. **48**, 1299 (2005).

6. *LLE Review Quarterly Report* **109**, 46, Laboratory for Laser Energetics, University of Rochester, Rochester, NY, LLE Document No. DOE/SF/19460-739 (2006).

7. T. J. B. Collins, A. Poludnenko, A. Cunningham, and A. Frank, Phys. Plasmas **12**, 062705 (2005); *LLE Review Quarterly Report* **100**, 227, Laboratory for Laser Energetics, University of Rochester, Rochester, NY, LLE Document No. DOE/SF/19460-578, NTIS Order No. PB2006-106672 (2004). (Copies may be obtained from the National Technical Information Service, Springfield, VA 22161.)

8. S. H. Leiden and F. A. Nichols, J. Nucl. Mater. **38**, 309 (1971).

9. M. J. Hiza, Fluid Phase Equilib. **6**, 203 (1981).

10. S. Raynor and D. R. Herschbach, J. Phys. Chem. **87**, 289 (1983); R. H. Scheicher *et al.*, Bull. Am. Phys. Soc. **48**, 434 (2003), Paper H12.005.

11. N. Kawamura *et al.*, Phys. Lett. B **465**, 74 (1999).

12. P. C. Souers, *Hydrogen Properties for Fusion Energy* (University of California Press, Berkeley, 1986).

13. A. Crane and H. P. Gush, Can. J. Phys. **44**, 373 (1966).

14. M. Alexander, *2002 Summer Research Program for High School Juniors at the University of Rochester's Laboratory for Laser Energetics*, University of Rochester, Rochester, NY, LLE Report No. 329, LLE Document No. DOE/SF/19460-479 (2003).

15. Aculight Corporation, Bothell, WA 98021.

16. Labsphere, Inc., North Sutton, NH 03260.

17. *FRED*, Photon Engineering, LLC, Tucson, AZ 85711.

18. ANSYS, Inc., Lebanon, NH 03766.

19. R. C. Cook *et al.*, Fusion Sci. Technol. **45**, 148 (2004).

20. A. Nikroo, General Atomics, private communication (2008).

21. D. R. Harding, D. D. Meyerhofer, S. J. Loucks, L. D. Lund, R. Janezic, L. M. Elasky, T. H. Hinterman, D. H. Edgell, W. Seka, M. D. Wittman, R. Q. Gram, D. Jacobs-Perkins, R. Early, T. Duffy, and M. J. Bonino, Phys. Plasmas **13**, 056316 (2006).

22. E. Mapoles, Lawrence Livermore National Laboratory, private communication (2008).

23. M. Martin *et al.*, Fusion Sci. Technol. **49**, 600 (2006).

24. R. S. Craxton and D. W. Jacobs-Perkins, Phys. Rev. Lett. **94**, 095002 (2005).

Multiple-FM Smoothing by Spectral Dispersion—An Augmented Laser Speckle Smoothing Scheme

Introduction

Polar-drive (PD)[1–4] implosions on the National Ignition Facility (NIF) require smoothing of the laser-imposed nonuniformities. The spot shape on target is controlled by employing distributed phase plates (DPP's).[5,6] Smoothing by spectral dispersion (SSD)[7–9] smoothes the far-field speckle pattern in a time-integrated sense by continuously changing the near-field phase front of the laser beam. The current configuration of the NIF has SSD in only one dimension (i.e., 1-D SSD), which is insufficient for directly driven targets. A two-dimensional (2-D) SSD system with a 1-THz ultraviolet bandwidth and two color cycles proposed for the NIF provides the requisite smoothing but it is an expensive option that adds considerable complexity.[10] An idea originally suggested by Rothenberg[11] further improved beam smoothing of all spatial frequencies by augmenting the 2-D SSD system with multiple-FM modulators in both dimensions at the expense of both increased complexity and cost. An alternative laser speckle smoothing scheme proposed here employs multiple-FM modulators in a single dimension (MultiFM 1-D SSD) with minimal cost increase and added system complexity since the added modulation can be applied in the all-fiber-optic front-end system. In addition, this system concentrates beam-smoothing improvements on the lower end of the spatial frequencies that most limit direct-drive implosions with a low in-flight aspect ratio.

MultiFM 1-D SSD employs multiple color cycles to improve the smoothing of lower-spatial-frequency nonuniformities without producing resonances at higher spatial frequencies because multiple modulators interact and effectively average the resonant features with a judicious choice of modulator frequencies. MultiFM 1-D SSD attains similar or even faster smoothing rates compared to the full 2-D SSD system, albeit with shorter asymptotic times. Two-dimensional hydrodynamic simulations using *DRACO*[12] show that MultiFM 1-D SSD is sufficient for the targets and pulse shapes analyzed thus far, even for smaller overall bandwidth (in the 0.5-THz range), which means that a single frequency-conversion crystal system can be used for the NIF with significant cost and complexity savings.

MultiFM Coherence Time

When SSD is employed, smoothing for any spatial frequency can be characterized by an inverse coherence time (or smoothing rate) and an asymptotic nonuniformity. The rms average of the inverse coherence times over all spatial frequencies is equivalent to the effective bandwidth applied to the laser beam; however, this bandwidth is not uniformly distributed over the spatial frequencies imposed in the far-field plane, which range from zero to the highest spatial frequency determined by the diffraction limited spot. The SSD system does not continue to smooth forever but is limited to the characteristic asymptotic level that is determined by the angular divergence of the near field imposed by SSD. Both of these characteristics can be represented by a fitted functional form

$$\sigma^2(t,\ell) = \sigma_0^2(\ell)\frac{t_c(\ell)}{t + t_c(\ell)} + \sigma_{\text{asym}}^2(\ell), \tag{1}$$

where $\sigma_0^2(\ell) \equiv \sigma^2(0,\ell)$ is the initial value of the nonuniformity and $\sigma_{\text{asym}}^2(\ell) \equiv \sigma^2(\infty,\ell)$ is the asymptotic level of the nonuniformity for the spatial mode given by ℓ.

After a few coherence times and prior to reaching the asymptotic level, Eq. (1) can be approximated by

$$\sigma^2(t,\ell) \simeq \sigma_0^2(\ell)\frac{t_c(\ell)}{t}, \quad t_c < t < t_{\text{asym}}. \tag{2}$$

During this time, the coherence time proportionally affects the level of nonuniformity, whereas the "slope" is given by t^{-1}. If the coherence time can be decreased by modifying the SSD design, the nonuniformity for a given mode will decrease proportionally. The asymptotic nonuniformity level σ_{asym} is determined by the angular divergence of the SSD system because this determines the number of independent modes in the far field. Increasing the angular divergence reduces σ_{asym}.

The smoothing performance of any SSD system, including MultiFM, is accurately calculated using a specialized, time-dependent far-field simulation, like *Waasikwa'*.[13] Figure 114.22 shows the smoothing performance of the ℓ-mode range $30 < \ell < 60$ for the NIF 1-D SSD system with 10.8 Å of applied IR bandwidth yielding 878 GHz of ultraviolet bandwidth.[a] The figure also indicates the relative improvements that could be made for this ℓ-mode range by increasing the applied bandwidth $\Delta\lambda$ or the angular divergence $\Delta\theta_{SSD}$. For ℓ modes lower than the first local maximum in the distributed inverse coherence time (roughly $\ell < 100$ for systems in this article; see Fig. 114.25), the inverse coherence time is approximately given by $t_c^{-1} \propto \ell\Delta\lambda N_{cc}$, where N_{cc} is the effective number of color cycles. The angular divergence of one dimension is given approximately by $\Delta\theta_{SSD} \propto \Delta\lambda N_{cc}/\nu_m$, where ν_m is the modulator frequency.
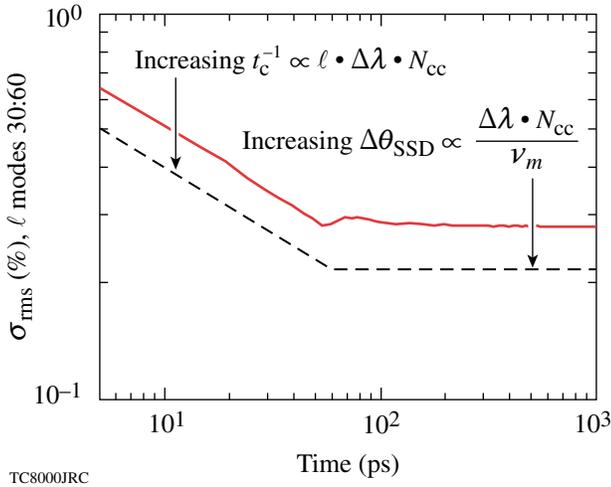

Figure 114.22
Time evolution of the nonuniformity summed over the ℓ-mode range $30 < \ell < 60$ for the NIF 1-D SSD system with 10.8 Å of applied bandwidth (878-GHz UV). The solid line represents the result of a *Waasikwa'* far-field simulation. The dashed line indicates the improvements possible by altering the coherence time and/or the angular divergence: (1) decreasing the coherence time of a mode proportionally decreases the level of nonuniformity during $t_c < t < t_{asym}$ and (2) increasing the angular divergence will decrease the asymptotic level σ_{asym}.

Figure 114.23 shows the smoothing effect on the lower ℓ modes by increasing the number of color cycles while holding the bandwidth and angular divergence constant. For early times in the laser pulse (not shown), the initial nonuniformity is the same $\left[\sigma^2(t,\ell) \rightarrow \sigma_0^2(\ell) \text{ as } t \rightarrow 0\right]$ for each case. However,

increasing the number of color cycles delivers asymptotic smoothing performance at earlier times. This illustrates that as the inverse coherence time is increased for this ℓ-mode range, the far field can be smoothed faster and the asymptotic level can be reached earlier.
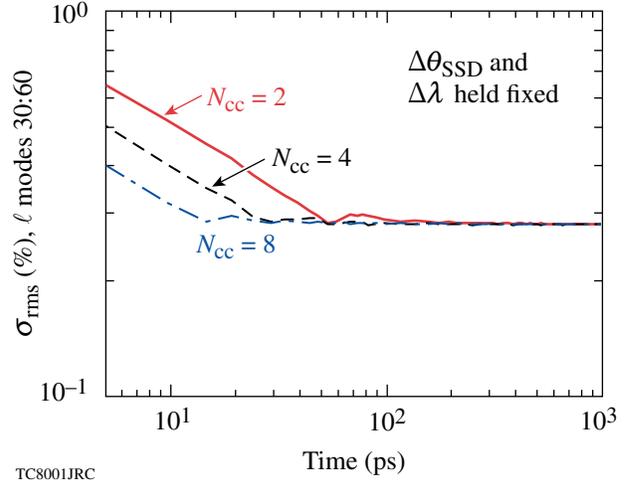

Figure 114.23
Time evolution of the nonuniformity rss-summed over the ℓ-mode range $30 < \ell < 60$ for three different realizations of a 1-D SSD system. The applied bandwidth and angular divergence are held fixed at 10.8 Å and 100 μrad, respectively, while the number of color cycles is varied as 2, 4, and 8, which correspond to modulator frequencies of 17.5, 35.5, and 70.5 GHz, respectively. All three traces represent full *Waasikwa'* far-field simulations. The effective bandwidth is 1.1 THz.

As previously noted, the inverse coherence time is not constant over the entire ℓ-mode range of the far-field intensity pattern. The inverse coherence time for each ℓ mode and the values of $\sigma_0^2(\ell)$ and $\sigma_{asym}^2(\ell)$ can be calculated by fitting Eq. (1) to time-dependent *Waasikwa'* far-field simulations, but this is a computationally intensive process. A simplified phenomenological formulation is desirable for evaluating or designing many SSD system variations. However, it is essential that the simple mathematical model given here is verified against a full far-field simulation prior to performing the even-lengthier hydrodynamic simulation. This is done by verifying a final MultiFM system design using the simple t_c^{-1} model against a time-dependent *Waasikwa'* simulation fitted to Eq. (1).

For a 1-D SSD system the inverse coherence time along a single spatial dimension[11] is given by

---

[a]Conventionally, the applied laser bandwidth is specified in two different units to distinguish to which end of the frequency-converted laser system the bandwidth refers. When the bandwidth is given in angstroms (Å), it refers to the bandwidth in the front-end IR system and when the bandwidth is specified in GHz or THz, it refers to the bandwidth following the frequency-conversion crystals in the UV range. An IR bandwidth of 12.3 Å corresponds to 1.0 THz in the UV.

$$t_c^{-1}{}_x(\ell_x) = 2\Delta\lambda \sin\left(\frac{1}{2}\ell_x \kappa N_{cc}{}_x\right) \tag{3}$$

along one of the two spatial-frequency directions, where $\ell_x \equiv k_{x_{ff}} r_{tar}$, $\kappa \equiv f_{NIF}\lambda_{UV}/(r_{tar}D_{NIF})$, and $k_{x_{ff}}$, f_{NIF}, λ_{UV}, r_{tar}, and D_{NIF} are the NIF spatial frequency, focal length, laser wavelength, target radius and near-field diameter, respectively. A similar functional form represents the second dimension for a 2-D SSD system; if no second dimension is included, then $t_c^{-1}{}_y = 0$. For a single-modulator 1-D SSD system, a 2-D plot of the inverse coherence time is shown in Fig. 114.24 for the two-color-cycle, 10.8 Å, 1-D SSD system described in Fig. 114.23. Note that in Fig. 114.24 the inverse coherence time periodically goes to zero for spatial frequencies where no beam smoothing is achieved. Equation (3) defines the inverse coherence time in only a single spatial-frequency dimension, but an azimuthal average is standard practice for comparing the effectiveness of different SSD systems (including MultiFM and 2-D SSD). The inverse coherence time for an effective ℓ mode in the 2-D plane is defined as

$$t_c^{-1}{}_{rss}(\ell) \equiv \sqrt{\left(t_c^{-1}{}_x\right)^2 + \left(t_c^{-1}{}_y\right)^2}, \tag{4}$$

where $\ell \equiv \ell(\theta) = \sqrt{\ell_x^2 + \ell_y^2}$ is the radial ℓ mode. In addition, it is necessary to account for the effect of the near-field beam envelope on the resultant inverse coherence time because the envelope affects the relevant weighting of the contribution of each spatial frequency in the 2-D spatial-frequency plane. The mathematical model of a 1-D or 2-D SSD system is then given by

$$t_c^{-1}(\ell) = \frac{\oint t_c^{-1}{}_{rss}(\ell)\,PSD_0(\ell)\,\ell\,d\theta}{\oint PSD_0(\ell)\,\ell\,d\theta}, \tag{5}$$

where $PSD_0(\ell)$ is the spatial-frequency power spectrum of the diffraction-limited spot or single speckle pattern.[16,17] Note that the $PSD_0(\ell)$ can be used to analyze the effect of partially filled near-field apertures.

Equation (5) is employed to calculate the inverse coherence time versus ℓ mode for the three realizations of the 1-D SSD system, as shown in Fig. 114.25. These curves illustrate distinct behavior for the large ℓ-mode and low ℓ-mode regions. The mean value of the inverse coherence time yields a measure of the effective bandwidth. For the 1-D SSD systems the


TC8074JRC

Figure 114.24
The inverse coherence time t_c^{-1} (in GHz) plotted in two dimensions as a function of the normalized-spatial-frequency, two-color-cycle system in Fig. 114.23 (1.1 THz, 100 μrad). Note that the number of zeros counted along the positive or negative axis for non-zero frequencies up to the effective round-aperture cut-off frequency yields the number of color cycles. In this case, there are two zeros along the positive or negative vertical axis. The axis has been normalized to a square NIF aperture and therefore is lengthened by $\sqrt{2}$ relative to a round aperture. A lineout in the SSD dispersion direction illustrates how the inverse coherence time periodically goes to zero. No beam smoothing is experienced at these spatial frequencies.

TC8002JRC

Figure 114.25
The inverse coherence time t_c^{-1} (in GHz) plotted as a function of the spatial ℓ-mode number for the three different 1-D SSD systems described in Fig. 114.23. The number of color cycles is varied as 2, 4, and 8. The divergences are fixed at 100 μrad. Note that the average inverse coherence time for the large ℓ modes is approximately 1.25× the applied bandwidth of 878 GHz and that the inverse coherence time for the lower ℓ modes ($\ell <$ first local maximum) is given by $t_c^{-1} \propto \ell\Delta\lambda N_{cc}$. The resultant effective bandwidth is 1.1 THz. The vertical dashed line indicates the approximate distinction between low ℓ and high ℓ modes.

effective bandwidth is 1.1 THz, which is roughly 1.25× the applied bandwidth for a single modulator system. In the large ℓ-mode range, the inverse coherence time is given roughly by the effective bandwidth. The peak of the first local maximum is $1.1\sqrt{2}$ of the applied bandwidth, as related to the maximum of Eq. (3) that is azimuthally averaged around the 2-D plane. In the ℓ-mode range lower than the first local maximum, the inverse coherence time is given by

$$t_c^{-1}(\ell) = \Delta\lambda\ell\kappa N_{cc}, \tag{6}$$

which can be understood by taking the small angle approximation to Eq. (3).

Another feature in Fig. 114.25 is the series of strong resonances in the large ℓ-mode range. This is due to the coherent effect of having multiple color cycles across the near-field plane. Each color cycle is a copy of its neighbors and does not lend to smoothing at the corresponding spatial frequency, which leads to the zeroes of Eq. (3). The zeroes of the resonant features are a 1-D effect, and their relative effect is lessened due to the azimuthal averaging of Eq. (5); however, the zeroes are still present in the 2-D plane and represent spatial frequencies that experience no smoothing and are a potential threat in an ICF implosion due to hydrodynamic instabilities. The only smoothing that these modes get is from multiple beam overlap on target.

The resonant features caused by multiple color cycles can be mitigated with MultiFM if the modulator frequencies are judiciously chosen. The effect of multiple overlaid patterns dramatically reduces the range of spatial frequencies that do not benefit from beam smoothing, as illustrated in Fig. 114.26. In the near field, the application of MultiFM in 1-D takes the form

$$E(x,y) = E_0(x,y) \prod_{n=1}^{N} e^{i3\delta_n \sin\left[\omega_n(t+\xi_x x)\right]}, \tag{7}$$

where $E_0(x,y)$ is the near-field beam envelope and δ_n, ω_n, and ξ_x are modulation depth, frequency, and grating dispersion for the nth modulators, respectively.

To calculate the inverse coherence time for the MultiFM case, Eq. (3) can be generalized by root-sum-square (rss) summing the values for each modulator. This approximation is valid when the modulation frequencies are incommensurate and the mixing of the modes in the far field temporally integrates to zero since terms like $\cos(\omega_m t) \cdot \cos(\omega_n t)$ average to zero
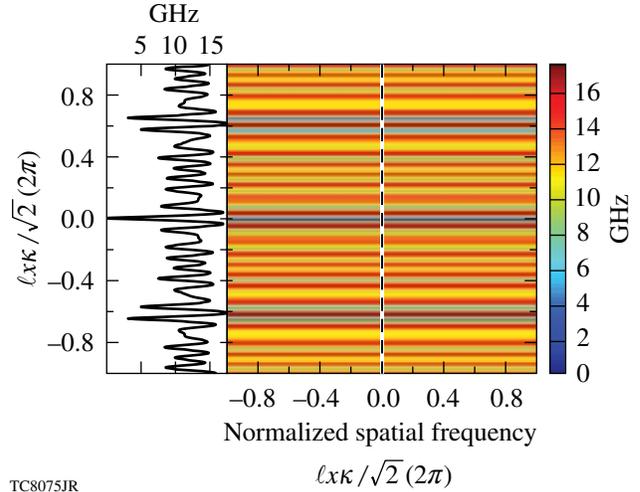

Figure 114.26
The inverse coherence time t_c^{-1} (in GHz) plotted in two dimensions as a function of normalized spatial frequency for a MultiFM 1-D SSD system employing three modulators at frequencies of 65, 75, and 95 GHz ($N_{cc} = 8$, 9, and 11, respectively) with a combined divergence of 175 μrad and effective ultraviolet bandwidth of 1.2 THz. A lineout in the 1-D SSD dispersion direction illustrates the significant improvement in beam smoothing compared to Fig. 114.24. Note that the inverse coherence time goes to zero for all modulators at the origin by definition.

when m is not equal to n. A three-modulator MultiFM case is compared in Fig. 114.27 to a single-modulator, eight-color-cycle case. Three modulators at frequencies of 65, 75, and 95 GHz ($N_{cc} = 8$, 9, and 11, respectively) produce a combined divergence of 175 μrad and effective ultraviolet bandwidth of 1.2 THz. Beam-smoothing rates are comparable for low ℓ modes, but the MultiFM configuration outperforms the single modulator for high ℓ modes due to the overlapped effect of multiple modulators, each with multiple color cycles. The effective color-cycle number is weighted by the bandwidth of each modulator,

$$N_{cc_{mFM}} \simeq \frac{\sqrt{\sum_{n=1}^{N}\left(N_{cc_n}\Delta\lambda_n\right)^2}}{\sqrt{\sum_{n=1}^{N}\Delta\lambda_n^2}}, \tag{8}$$

while the effective bandwidth and angular divergence can be estimated by rss-summing the contributions from each modulator. The total angular divergence, however, can have significant energy in the wings of the distribution as far out as the linear sum of the individual divergences.

An important observation is that improved lower ℓ-mode performance can also be achieved while decreasing the total
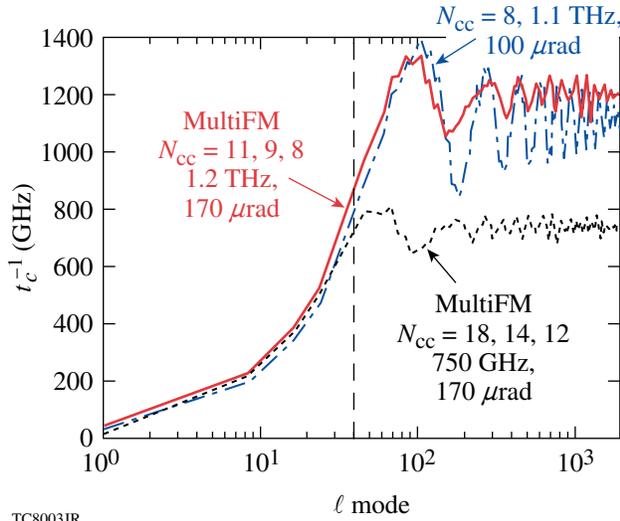
Figure 114.27

Azimuthally averaged inverse coherence time plotted as a function of spatial ℓ-mode number for an eight-color-cycle, 1-D SSD system (eight color cycles, 1.1 THz, 100 μrad) and MultiFM 1-D SSD system (8, 9, and 11 color cycles, 1.2 THz, 170 μrad). Another MultiFM 1-D SSD realization is also shown (12, 14, and 18 color cycles, 750 GHz, 170 μrad) using three modulators at 68, 77, and 94 GHz, respectively, but a smaller effective bandwidth of 750 GHz. The vertical dashed line indicates the approximate distinction between low ℓ and high ℓ modes.

Figure 114.28

The inverse coherence time plotted as a function of spatial ℓ mode number for a four-color-cycle, 1-D SSD system and a low ℓ-mode–matching MultiFM 1-D SSD system with two modulators and lower applied bandwidth. This realization of a MultiFM 1-D SSD system employs two modulators at frequencies of 55 and 60 GHz ($N_{cc} = 9$ and 10, respectively) and used a combined divergence of 110 μrad and only 600 GHz of effective UV bandwidth.

applied bandwidth, as long as the product $\Delta\lambda \cdot N_{cc}$ and the angular divergence $\Delta\theta$ are held constant. In general, high ℓ-mode nonuniformities decouple much sooner from directly driven targets with low in-flight aspect ratios than lower ℓ modes, which implies that the larger ℓ modes do not utilize all the potential smoothing of these modes. MultiFM 1-D SSD makes it possible to reduce the total bandwidth applied while maintaining the same performance of the lower ℓ modes. This phenomenon is depicted in the third plot (dashed) in Fig. 114.27, where a different set of modulation frequencies and color cycles achieves the same performance with a lower effective bandwidth of 750 GHz. Likewise, the two-modulator MultiFM 1-D SSD system shown in Fig. 114.28 matches the low ℓ-mode performance with only 600-GHz effective bandwidth and 110 μrad of divergence. Two-dimensional hydrodynamic *DRACO* simulations of NIF direct-drive targets with 1-μm (rms) inner ice roughness, 30-ps (rms) mistiming, 50-μm (rms) beam mispointing, and 8% (rms) energy imbalance for a 1.5-MJ CH-foam target in a symmetric-drive configuration show that this MultiFM system provides sufficient beam smoothing to achieve ignition. Further research is underway to determine if the bandwidth and the total energy delivered to target can be reduced, as well as to investigate MultiFM 1-D SSD for polar-drive implosions. Significant costs and complexity could be avoided on the NIF

if the applied bandwidth can be reduced to 0.5 THz, since only a single frequency-tripling crystal would be required.

MultiFM Divergence

The asymptotic level of nonuniformity, σ_{asym}, of the lower ℓ modes is governed by the angular divergence because more-independent speckle modes are created. The angular divergence is ultimately limited by the smallest pinhole in the laser system. The primary concern is pinhole closure during the main drive pulse. Currently, the angular divergence $\Delta\theta_{SSD}$ for the NIF is limited to 100 μrad (full angle), which is set by a minimum pinhole size of 300 μrad. Dynamic bandwidth reduction[14] should allow the angular divergence to be increased without the risk of pinhole closure since simulations indicate that strong beam smoothing is required only during the initial low-power portion of the laser pulse when significant laser imprinting occurs.[15] The angular divergence of SSD for a single modulator is given by

$$\Delta\theta_{SSD} \propto \frac{N_{cc}\Delta\lambda}{\nu_m}, \qquad (9)$$

where ν_m is the modulator frequency. The angular divergence can be increased by increasing the $N_{cc}\Delta\lambda$ product and/or decreasing the modulator frequency ν_m. Current investigations of MultiFM have limited divergence to a maximum full angle of 170 μrad, but increasing this limit could further improve

smoothing of these important modes. Detailed laser imprint experiments will be performed on OMEGA EP with a prototypical NIF beam-smoothing system to establish practical dynamic bandwidth reduction schemes. Additional experiments will also be performed to establish any lower limit of beam smoothing required late in the drive pulse to mitigate adverse laser–plasma interactions.

The asymptotic nonuniformity level and the time it takes to reach this level can be accurately calculated for a square pulse shape due to MultiFM 1-D SSD.[18] The nonuniformity as a function of time can also be calculated for arbitrary pulse shapes and 2-D SSD system configuration but is beyond the scope of this article and will be discussed in a forthcoming article. The asymptotic nonuniformity due to a MultiFM 1-D SSD system is given by

$$\sigma_{\mathrm{asym}}(\ell) = \frac{1}{2\pi} \oint \prod_{n=1}^{N} J_0\big[\zeta_n(\ell,\theta)\big]\mathrm{d}\theta, \qquad (10\mathrm{a})$$

where

$$\zeta_n(\ell,\theta) \equiv 6\xi_n \sin\left[\pi N_{\mathrm{cc}_n} \frac{\ell}{\ell_c} \cos(\theta)\right], \qquad (10\mathrm{b})$$

J_0 is a zeroth-order Bessel function of the first kind, and $\ell_c \equiv 2\pi r_{\mathrm{tar}} D_{\mathrm{NIF}}/(f_{\mathrm{NIF}}\lambda_{\mathrm{UV}})$ is the ℓ-mode cutoff. The angle θ is necessary because although the proposed MultiFM beam smoothing is applied only in a single direction, the spectrum is inherently 2-D and it facilitates the azimuthal average. The number of independent states is found by $N_{\mathrm{states}} = 1/\sigma_{\mathrm{asym}}^2(\ell)$. If the coherence time is known for the ℓ mode, then the asymptotic time is given by $t_{\mathrm{asym}} = t_c N_{\mathrm{states}}$. The formulation represented in Eqs. (10) is appropriate for all ℓ modes.

The statement that increasing the angular divergence, given by Eq. (9), decreases the σ_{asym}, given by Eqs. (10), can be understood by examining the arguments of the Bessel function. This applies only to the lower ℓ modes due to the sine function as an argument to the Bessel function and to the multi-color-cycle effects. As the argument of the Bessel function increases, the peak envelope of the Bessel function decreases. For ℓ modes lower than the peak of the first maximum of the sine function, the argument of the Bessel function increases when the product $\delta_m N_{\mathrm{cc}}$ increases. The product relates to the total angular divergence because $\delta_m N_{\mathrm{cc}} \propto \Delta\lambda N_{\mathrm{cc}}/(2\nu_m) \propto \Delta\theta$.

Beam-smoothing performance depends not only on the inverse coherence time and the total divergence but also on the shape of the spectral divergence. Some combinations of modulators yield excellent smoothing rates (inverse coherence time) for a given total divergence, but do not provide adequate beam smoothing due to the spectral distribution. The effectiveness of spectral modes is weighted by their amplitudes. The shape of the spectrum is found by taking the 2-D Fourier transform of the near-field beam with its associated SSD phase front applied but without a phase plate. In general, the shape of the far-field spectrum differs from the shape of the temporal frequency spectrum due to the near-field beam shape. Ideally, modes are evenly weighted for best smoothing performance, but edge-peaked spectra perform better than center-peaked spectra. An example is shown in Fig. 114.29, where the applied bandwidth and total divergences are identical for the two different MultiFM cases. The configuration with a more-uniform divergence but some edge peaking [Fig. 114.29(a)] gives better far-field simulation performance early in time than the strong, center-peaked divergence shown in Fig. 114.29(b), which is illustrated in Fig. 114.29(c).

Conclusion

Implementing MultiFM 1-D SSD beam smoothing on the NIF is a promising approach to meet the smoothing requirements for polar-drive implosions. It provides the flexibility to tailor the inverse coherence time spectrum to meet the target hydrodynamic-instability requirements while potentially reducing the overall bandwidth of the SSD system. Multiple color cycles are used to increase the performance of the lower ℓ modes and multiple modulators are used to reduce the resonant effects of multiple color cycles. Figure 114.30 shows how the MultiFM 1-D SSD system with 600-GHz effective bandwidth and 110 μrad of divergence described in Fig. 114.28 nearly attains the same target performance for a 1.5-MJ CH-foam target as the baseline 1-THz, 2-D SSD. Future work will extend these results to a 500-GHz MultiFM 1-D SSD system and a 1.0-MJ CH-foam target. It may require increasing the angular divergence and invoking dynamic bandwidth reduction.
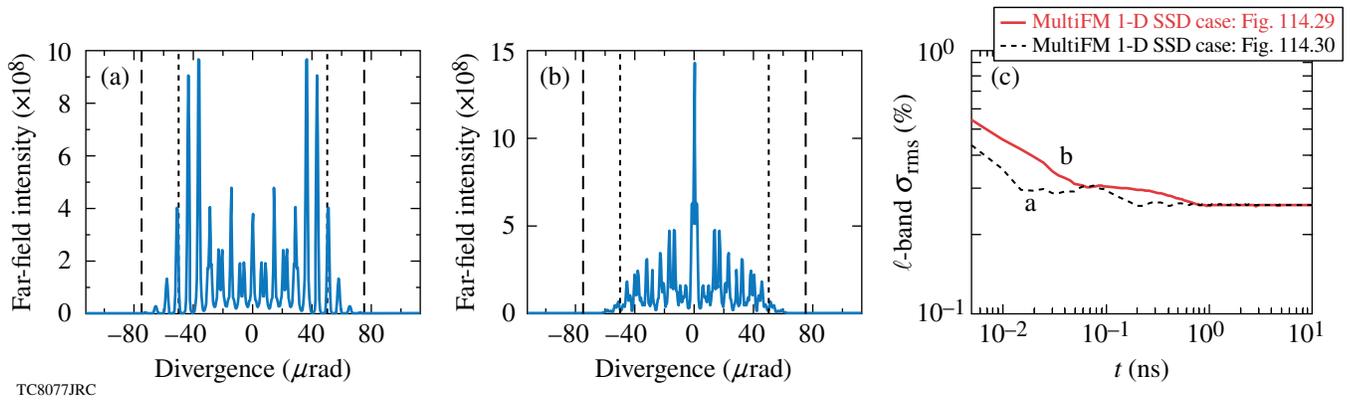
Figure 114.29

Angular divergence, plotted in the far field or pinhole plane, for two different MultiFM 1-D SSD systems with 820-GHz effective bandwidth and 110 μrad of divergence. The modulator frequencies were (a) 61 and 55 GHz with eight and seven color cycles, respectively, and (b) 61 and 45 GHz with eight and five color cycles, respectively. The thin dashed vertical line represents the 100-μrad specification and the thick dashed line represents the 150-μrad boundary. Note how the spectrum in (b) is more widely distributed and edge peaked relative to (a). (c) The nonuniformity calculated by *Waasikwa'* is rss-summed over ℓ modes 30 to 60 and is plotted as a function of time. Both systems have the same resulting asymptotic value but the system with the edge-peaked spectrum has improved performance early in time.
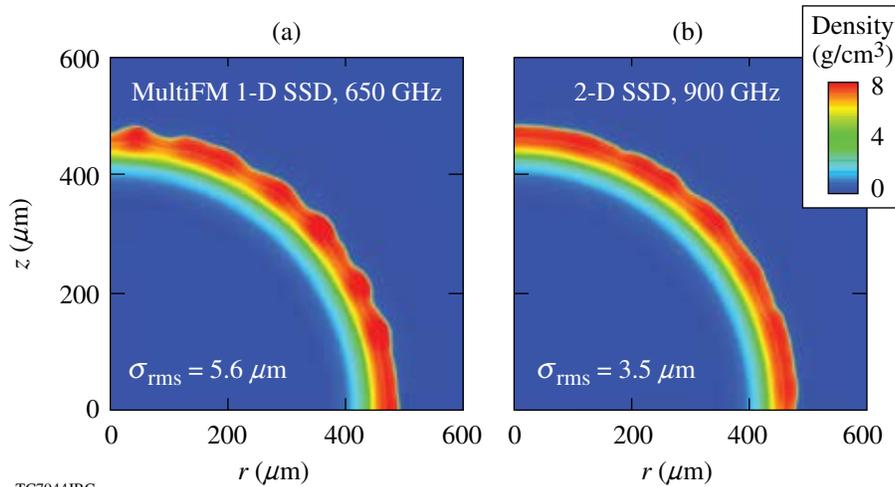
Figure 114.30

1.5-MJ CH-foam target at the end of the acceleration phase for three different SSD systems. (a) MultiFM 1-D SSD described in Fig. 114.28 and (b) 2-D SSD. Both the MultiFM 1-D SSD system and the 2-D SSD system attain nearly 1-D gain.

REFERENCES

1. S. Skupsky, J. A. Marozas, R. S. Craxton, R. Betti, T. J. B. Collins, J. A. Delettrez, V. N. Goncharov, P. W. McKenty, P. B. Radha, T. R. Boehly, J. P. Knauer, F. J. Marshall, D. R. Harding, J. D. Kilkenny, D. D. Meyerhofer, T. C. Sangster, and R. L. McCrory, Phys. Plasmas **11**, 2763 (2004).

2. J. A. Marozas, F. J. Marshall, R. S. Craxton, I. V. Igumenshchev, S. Skupsky, M. J. Bonino, T. J. B. Collins, R. Epstein, V. Yu. Glebov, D. Jacobs-Perkins, J. P. Knauer, R. L. McCrory, P. W. McKenty, D. D. Meyerhofer, S. G. Noyes, P. B. Radha, T. C. Sangster, W. Seka, and V. A. Smalyuk, Phys. Plasmas **13**, 056311 (2006).

3. R. S. Craxton and D. W. Jacobs-Perkins, Phys. Rev. Lett. **94**, 095002 (2005).

4. R. S. Craxton, F. J. Marshall, M. J. Bonino, R. Epstein, P. W. McKenty, S. Skupsky, J. A. Delettrez, I. V. Igumenshchev, D. W. Jacobs-Perkins, J. P. Knauer, J. A. Marozas, P. B. Radha, and W. Seka, Phys. Plasmas **12**, 056304 (2005).

5. J. A. Marozas, J. Opt. Soc. Am. A **24**, 74 (2007).

6. T. R. Boehly, D. L. Brown, R. S. Craxton, R. L. Keck, J. P. Knauer, J. H. Kelly, T. J. Kessler, S. A. Kumpan, S. J. Loucks, S. A. Letzring, F. J. Marshall, R. L. McCrory, S. F. B. Morse, W. Seka, J. M. Soures, and C. P. Verdon, Opt. Commun. **133**, 495 (1997).

7. S. Skupsky, R. W. Short, T. Kessler, R. S. Craxton, S. Letzring, and J. M. Soures, J. Appl. Phys. **66**, 3456 (1989).

8. *LLE Review Quarterly Report* **78**, 62, Laboratory for Laser Energetics, University of Rochester, Rochester, NY, LLE Document No. DOE/SF/19460-295 (1999).

9. S. P. Regan, J. A. Marozas, R. S. Craxton, J. H. Kelly, W. R. Donaldson, P. A. Jaanimagi, D. Jacobs-Perkins, R. L. Keck, T. J. Kessler, D. D. Meyerhofer, T. C. Sangster, W. Seka, V. A. Smalyuk, S. Skupsky, and J. D. Zuegel, J. Opt. Soc. Am. B **22**, 998 (2005); S. P. Regan, J. A. Marozas, J. H. Kelly, T. R. Boehly, W. R. Donaldson, P. A. Jaanimagi, R. L. Keck, T. J. Kessler, D. D. Meyerhofer, W. Seka, S. Skupsky, and V. A. Smalyuk, J. Opt. Soc. Am. B **17**, 1483 (2000).

10. S. Skupsky and R. S. Craxton, Phys. Plasmas **6**, 2157 (1999).

11. J. E. Rothenberg, J. Opt. Soc. Am. B **14**, 1664 (1997).

12. P. B. Radha, V. N. Goncharov, T. J. B. Collins, J. A. Delettrez, Y. Elbaz, V. Yu. Glebov, R. L. Keck, D. E. Keller, J. P. Knauer, J. A. Marozas, F. J. Marshall, P. W. McKenty, D. D. Meyerhofer, S. P. Regan, T. C. Sangster, D. Shvarts, S. Skupsky, Y. Srebro, R. P. J. Town, and C. Stoeckl, Phys. Plasmas **12**, 032702 (2005).

13. J. A. Marozas, S. P. Regan, J. H. Kelly, D. D. Meyerhofer, W. Seka, and S. Skupsky, J. Opt. Soc. Am. B **19**, 7 (2002).

14. *LLE Review Quarterly Report* **85**, 39, Laboratory for Laser Energetics, University of Rochester, Rochester, NY, LLE Document No. DOE/SF/19460-378, NTIS Order No. PB2006-106656 (2000).

15. P. W. McKenty, J. A. Marozas, V. N. Goncharov, K. S. Anderson, R. Betti, D. D. Meyerhofer, P. B. Radha, T. C. Sangster, S. Skupsky, and R. L. McCrory, Bull. Am. Phys. Soc. **51**, 295 (2006).

16. J. W. Goodman, *Introduction to Fourier Optics* (McGraw-Hill, New York, 1988).

17. J. W. Goodman, *Statistical Optics*, Wiley Series in Pure and Applied Optics (Wiley, New York, 1985).

18. J. A. Marozas and P. B. Radha, Bull. Am. Phys. Soc. **47**, 99 (2002).

Monoenergetic Proton Radiography Measurements of Implosion Dynamics in Direct-Drive Inertial Confinement Fusion

The goal of inertial confinement fusion (ICF) is ignition and high gain,[1–3] which require that a cryogenic deuterium–tritium (DT) spherical capsule be symmetrically imploded. This implosion results in a small mass of low-density, hot fuel at the center, surrounded by a larger mass of high-density, low-temperature fuel.[2,3] Shock coalescence ignites the hot spot, and a self-sustaining burn wave subsequently propagates into the main fuel region. In the direct-drive approach to ICF, such an implosion occurs in response to a large number of high-power individual laser beams illuminating the surface of a capsule. Understanding and controlling implosion dynamics are essential to ensure the success of the entire implosion process.[1–3]

Implosion dynamics have been studied experimentally with a number of diagnostics, including x-ray imaging,[2–5] fusion-product spectrometry,[6] and fusion-product imaging,[7,8] but none of these provide a complete picture of the time evolution of mass assembly and self-generated electric (E) and magnetic (B) fields.

This article presents new nuclear observations of implosion dynamics for direct-drive spherical capsules on the OMEGA Laser System,[9] using a novel method of monoenergetic proton radiography.[10,11] The combination of characteristics in our approach allows us to, first, probe distributions of self-generated E + B fields; second, determine ρR by measuring the energy loss of backlighting protons; and third, sample all the implosion phases from acceleration, through coasting and deceleration, to final stagnation, to provide a more-comprehensive picture of ICF

spherical implosions. The result is the first use of proton radiography to study ICF implosion dynamics. We note that earlier work by Mackinnon et al.[12] successfully demonstrated the feasibility of imaging implosions with protons (produced, in his case, by laser–plasma interactions), backlighting plastic (CH) capsules that were imploded by six 1-μm-wavelength laser beams.[13]

The experiment is illustrated schematically in Fig. 114.31. A CH capsule—the imaged subject—had an 860-μm initial diameter, a 20-μm-thick shell, and a 15-atm H_2 gas fill. It was imploded through direct drive with 40 beams of frequency-tripled (0.35 μm) UV laser light. The laser pulse was square, with a 1-ns duration and a total energy of ~16 kJ. The individual laser beams were smoothed using a single-color-cycle, 1-THz, two-dimensional (2-D) smoothing by spectral dispersion (SSD), and polarization smoothing (PS).[14,15] Implosions were backlit with monoenergetic protons (14.7 MeV) generated from D^3He-filled, exploding-pusher implosions driven by 19 OMEGA laser beams (details of this technology have been reported elsewhere[10,11]). The duration of the backlighting was ~130 ps, and the relative timing of backlighter and subject implosions was adjusted in each experiment so the proton radiograph would reflect the condition of the subject capsule at a desired time during its implosion. The effective FWHM of the backlighter was ≈40 μm (Ref. 10)—the primary limit on the intrinsic spatial resolution of the imaging system. In images of imploded capsules, spatial resolution was degraded somewhat by scattering of the imaging protons as they passed through the capsules.[16,17]
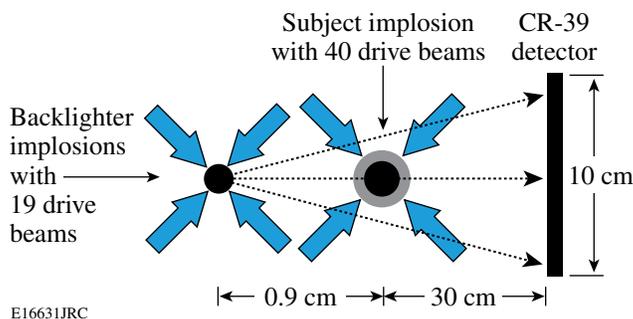

Figure 114.31
Experimental setup, with proton backlighter, subject implosion, CR-39 imaging detectors and laser beams. The field of view at the subject is ~3 mm.

E16631JRC

Figure 114.32 shows a series of proton radiographs that cover a complete ICF implosion process from beginning through peak compression. Each individual image contains both spatial and energy information because the CR-39 detector records the position and energy of every individual proton. Such images can therefore be displayed to show either proton fluence versus position [Fig. 114.32(a)] or proton mean energy versus position [Fig. 114.32(b)], providing important information about field distributions and capsule compression.

A striking feature of Fig. 114.32(a) is that a central peak occurs in the fluence images during the early stages of implosion ($t = 0.8$ to 1.4 ns), while a fluence dip occurs at the centers at later times ($t = 1.6$ to 2.1 ns).[19] This indicates that trajectories of imaging protons were deflected by radial E fields in the capsule. (Proton trajectories are also altered by scattering in the capsule shell, but this process cannot account for the observed fluence peaks and dips.[20]) At early times the field must have been centrally directed in order to focus the protons passing within the capsule shell toward the center of the imaging detector. To account for the rapid change from a central fluence peak to a central fluence dip at ~1.5 ns, the radial field must have either reversed direction or suddenly become at least three times larger at that time (as shown by Monte Carlo simulations), in which case all protons would strike the detector outside the shadow of the capsule.

An E-field source that is consistent with the data is the gradient of plasma electron pressure $\left(E \approx -\nabla p_e / en_e\right)$.[21,22] Other possible sources do not fit as naturally with the data.[23] The pressure gradient has the correct sign at early times, and it reverses direction at about the correct time. This is illustrated in the electron pressure and density profiles at 0.8 ns and 1.9 ns, calculated by the *LILAC* hydro simulation program[24] and shown in Fig. 114.33. Using calculated ∇p_e and n_e at different times, we estimate the resultant E-field magnitude in the range $\sim -10^9$ to $\sim 10^8$ V/m, as shown in Fig. 114.34. Figure 114.34 also shows experimental field values deduced from the data of Fig. 114.32(a).[25] The predictions match the data in three crucial ways: the field strength and sign before the reversal ($\sim -10^9$ V/m, directed inward), the time of the field reversal (~1.5 ns), and the field strength after the reversal ($\sim 10^8$ V/m directed outward). This match leads to a high level of confidence that ∇p_e is the source of the observed phenomena. Note that the detailed structures of the fluence images in Fig. 114.32(a) are also modified, in ways that do not affect our conclusions, by the in-flight movement of the shell ($V_{imp} \sim -2.5 \times 10^7$ cm/s), which is ~30 μm during the backlighter nuclear burn time (~130 ps).

Quantitative information about capsule sizes and ρR's at different times is extracted from the lineouts through the centers of each of the individual images in Fig. 114.32(b); the mean

(a) Proton fluence

|←1.1 mm→|

(b) Proton energy

0.0 ns　　0.8 ns　　1.2 ns　　1.4 ns　　1.6 ns　　1.9 ns　　2.1 ns

E16632JR
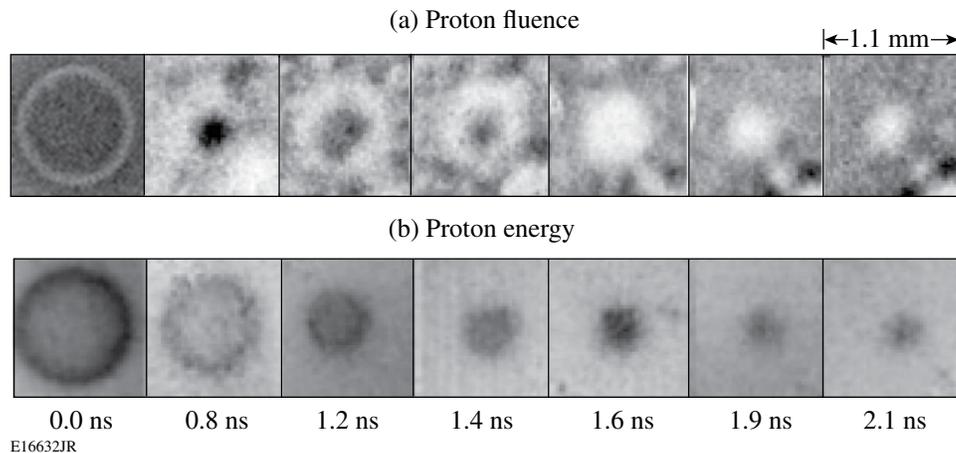
Figure 114.32
Proton radiographs of imploding capsules at different times. Images in (a) show proton fluence (within each image, darker means higher fluence), while images in (b) show proton energy (within each image, darker means more proton energy loss and more matter traversed). The gray-scale mapping for image display is different in each image. Note that the capsule-mounting stalk appears in the lower right corner of each fluence image. Note also that the field of view of these images is only part of the total indicated in Fig. 114.31; the area outside this region is the subject of another study of external fields.[18]
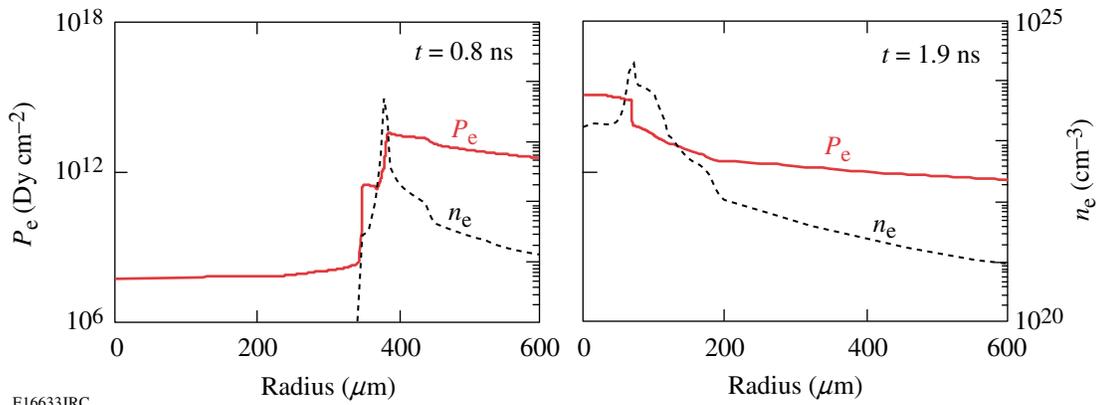
Figure 114.33
Profiles of electron pressure (solid lines) and density (dashed lines) at 0.8 ns and 1.9 ns, calculated by *LILAC*.
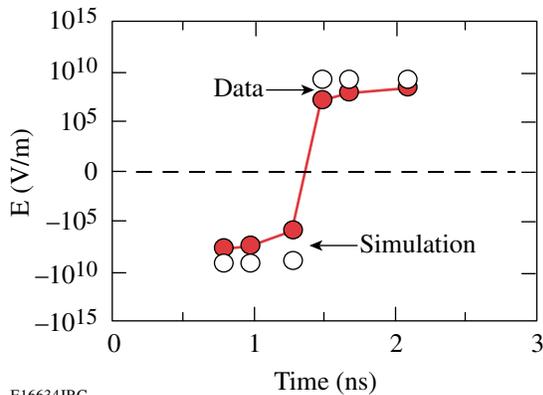
Figure 114.34
Radial E fields estimated from experimental measurements (open circles) and from *LILAC* simulations (solid circles) versus implosions times. The differences between simulation and data may result from effects of proton scattering.

width provides the averaged capsule size ($\approx 2R$), while the mean height indicates the total ρL ($\approx 2 \times \rho R$). The measurements are compared with *LILAC* simulations in Figs. 114.35(a) and 114.35(b), respectively. The simulations come reasonably close to matching the observed evolution of capsule convergence and ρR during the acceleration and coasting phases (~0 to 1.6 ns), but they predict somewhat smaller values of radius, and larger values of ρR, than measured at the times of nuclear burn (~1.9 ns) and peak compression (~2.1 ns). Overall, this indicates that the implosions had approximately 1-D performance, with little impact from hydrodynamic instabilities, before deceleration. It has been suggested that performance approaches 1-D because of full single-beam smoothing, which significantly improves the shell integrity during the acceleration phase, and because thickening of the shell during subsequent coasting further enhances shell integrity.[15] The apparent degradation of capsule performance at later times relative to the 1-D simulation could be largely a consequence of fuel–shell mixing and implosion asymmetry.[2,3]

It is worthwhile to compare these measured ρR values with a value obtained using a completely different method during an equivalent implosion. The open black data point in Fig. 114.35(b) was obtained by using proton spectrometry to determine the energy of self-emitted D^{3}He protons;[26] the downshift in the energy of these protons implies a ρR at bang time of ~25 mg/cm^2. This is slightly higher than the measurement made here but statistically consistent with it given the measurement uncertainties. On the other hand, the spectrometry-implied value is closer to the 1-D value, which raises the possibility that the radiography-implied value loses accuracy when the capsule becomes sufficiently compressed that images are seriously affected by proton scatter. This is currently being investigated, and we plan to develop a more accurate technique for deconvolving the effects of scatter in our analyses.

Finally, the residual mass during the implosion process can be estimated in terms of the measured R [Fig. 114.35(a)] and measured ρR [Fig. 114.35(b)]: $m/m_0 \approx C_r^{-2} \rho R(t)/\rho R(0)$,

where $C_r \equiv R(0)/R(t)$ is the target convergence ratio. This indicates that ~30%–40% of the shell has been ablated by bang time. Although the mass estimates have large uncertainties due to those associated with both R and ρR measurements, they are helpful for illustrating the dynamics of mass ablation during implosions.
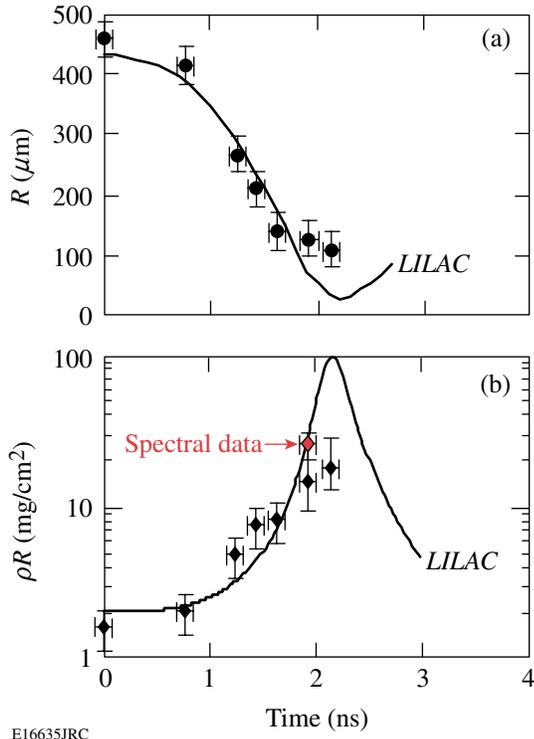

Figure 114.35
Measured capsule radii [(a) solid circles] and ρR [(b) solid diamonds] compared with *LILAC* 1-D simulations (solid lines). Horizontal error bars represent uncertainties in backlighter burn time. One data point [open diamond in (b)] represents the ρR of a comparable implosion of a D^3He-filled capsule at bang time, measured by several proton spectrometers in different directions; this completely different type of measurement is statistically consistent with the data derived here from radiography images.

In summary, new observations and measurements of direct-drive spherical implosions have been made with time-gated, monoenergetic proton radiography. Quantitative information inferred from proton images characterizes the spatial structure and temporal evolution of an imploding capsule, dynamically displaying a more-comprehensive picture of direct-drive ICF spherical implosions. The observations have also shown the first experimental evidence of radial E fields inside the imploding capsules, as well as their reversal in direction and their probable connection with plasma pressure gradients.

REFERENCES

1. J. Nuckolls *et al.*, Nature **239**, 139 (1972).

2. J. D. Lindl, *Inertial Confinement Fusion: The Quest for Ignition and Energy Gain Using Indirect Drive* (Springer-Verlag, New York, 1998).

3. S. Atzeni and J. Meyer-ter-Vehn, *The Physics of Inertial Fusion: Beam Plasma Interaction, Hydrodynamics, Hot Dense Matter*, International Series of Monographs on Physics (Clarendon Press, Oxford, 2004).

4. F. J. Marshall, J. A. Delettrez, R. Epstein, R. Forties, R. L. Keck, J. H. Kelly, P. W. McKenty, S. P. Regan, and L. J. Waxer, Phys. Plasmas **11**, 251 (2004).

5. R. S. Craxton, F. J. Marshall, M. J. Bonino, R. Epstein, P. W. McKenty, S. Skupsky, J. A. Delettrez, I. V. Igumenshchev, D. W. Jacobs-Perkins, J. P. Knauer, J. A. Marozas, P. B. Radha, and W. Seka, Phys. Plasmas **12**, 056304 (2005).

6. F. H. Séguin, J. A. Frenje, C. K. Li, D. G. Hicks, S. Kurebayashi, J. R. Rygg, B.-E. Schwartz, R. D. Petrasso, S. Roberts, J. M. Soures, D. D. Meyerhofer, T. C. Sangster, J. P. Knauer, C. Sorce, V. Yu. Glebov, C. Stoeckl, T. W. Phillips, R. J. Leeper, K. Fletcher, and S. Padalino, Rev. Sci. Instrum. **74**, 975 (2003).

7. L. Disdier, A. Rouyer, I. Lantuéjoul, O. Landoas, J. L. Bourgade, T. C. Sangster, V. Yu. Glebov, and R. A. Lerche, Phys. Plasmas **13**, 056317 (2006).

8. F. H. Séguin, J. L. DeCiantis, J. A. Frenje, S. Kurebayashi, C. K. Li, J. R. Rygg, C. Chen, V. Berube, B. E. Schwartz, R. D. Petrasso, V. A. Smalyuk, F. J. Marshall, J. P. Knauer, J. A. Delettrez, P. W. McKenty, D. D. Meyerhofer, S. Roberts, T. C. Sangster, K. Mikaelian, and H. S. Park, Rev. Sci. Instrum. **75**, 3520 (2004).

9. J. M. Soures, R. L. McCrory, C. P. Verdon, A. Babushkin, R. E. Bahr, T. R. Boehly, R. Boni, D. K. Bradley, D. L. Brown, R. S. Craxton, J. A. Delettrez, W. R. Donaldson, R. Epstein, P. A. Jaanimagi, S. D. Jacobs, K. Kearney, R. L. Keck, J. H. Kelly, T. J. Kessler, R. L. Kremens, J. P. Knauer, S. A. Kumpan, S. A. Letzring, D. J. Lonobile, S. J. Loucks, L. D. Lund, F. J. Marshall, P. W. McKenty, D. D. Meyerhofer, S. F. B. Morse, A. Okishev, S. Papernov, G. Pien, W. Seka, R. Short, M. J. Shoup III, M. Skeldon, S. Skupsky, A. W. Schmid, D. J. Smith, S. Swales, M. Wittman, and B. Yaakobi, Phys. Plasmas **3**, 2108 (1996).

10. C. K. Li, F. H. Séguin, J. A. Frenje, J. R. Rygg, R. D. Petrasso, R. P. J. Town, P. A. Amendt, S. P. Hatchett, O. L. Landen, A. J. Mackinnon, P. K. Patel, V. Smalyuk, J. P. Knauer, T. C. Sangster, and C. Stoeckl, Rev. Sci. Instrum. **77**, 10E725 (2006).

11. C. K. Li, F. H. Séguin, J. A. Frenje, J. R. Rygg, R. D. Petrasso, R. P. J. Town, P. A. Amendt, S. P. Hatchett, O. L. Landen, A. J. Mackinnon,

P. K. Patel, V. A. Smalyuk, T. C. Sangster, and J. P. Knauer, Phys. Rev. Lett. **97**, 135003 (2006).

12. A. J. Mackinnon *et al.*, Phys. Rev. Lett. **97**, 045001 (2006).

13. In Ref. 12, Mackinnon reported no fields surrounding the capsule, in contrast to the observations shown here, and this is not presently understood. There are, however, significant differences in the implosion conditions: for example, Mackinnon *et al.* used six beams at 1 μm to irradiate a 250-μm-radius capsule. Herein we used 36 beams at 1/3 μm to irradiate 430-μm-radius capsules. In addition, there are differences in their proton backlighter, such as the fact that the proton spectrum is broadband, a circumstance that will lead to some additional blurring and washout of field structures.

14. S. Skupsky and R. S. Craxton, Phys. Plasmas **6**, 2157 (1999).

15. D. D. Meyerhofer, J. A. Delettrez, R. Epstein, V. Yu. Glebov, V. N. Goncharov, R. L. Keck, R. L. McCrory, P. W. McKenty, F. J. Marshall, P. B. Radha, S. P. Regan, S. Roberts, W. Seka, S. Skupsky, V. A. Smalyuk, C. Sorce, C. Stoeckl, J. M. Soures, R. P. J. Town, B. Yaakobi, J. D. Zuegel, J. Frenje, C. K. Li, R. D. Petrasso, D. G. Hicks, F. H. Séguin, K. Fletcher, S. Padalino, C. Freeman, N. Izumi, R. Lerche, T. W. Phillips, and T. C. Sangster, Phys. Plasmas **8**, 2251 (2001).

16. V. L. Highland, Nucl. Instrum. Methods **129**, 497 (1975).

17. A simple analytic model[16] can be used to estimate the characteristic scattering angle in radians for protons passing through a plasma with areal density ρL. It is $\langle\theta_{sc}\rangle = z(15\,\mathrm{MeV}/p\beta c)(\rho L/\rho L_{rad})^{1/2}$, where $z = 1$ for protons, $p\beta c = 30$ MeV for 15-MeV protons, and $\rho L_{rad} = 4.34 \times 10^4$ mg/cm^2 for carbon. For example, if $\rho L \approx 20$ mg/cm^2, then $\langle\theta_{sc}\rangle \sim 0.6°$.

18. F. H. Séguin, C. K. Li, J. R. Rygg, J. A. Frenje, R. D. Petrasso, R. Betti, O. V. Gotchev, J. P. Knauer, F. J. Marshall, D. D. Meyerhofer, and V. A. Smalyuk, "Monoenergetic Proton Radiography Observations of E and B Field Evolution Outside Imploding, Direct-Drive ICF Capsules," in preparation.

19. It has been confirmed by Monte Carlo simulations of the imaging system that, for a given amount of deflection, the character of focusing or defocusing in the image is relatively insensitive to the specific distance of the detector position.

20. There are two reasons why scatter cannot account for the observed features: First, simulations show that the Coulomb scattering angles are not large enough to deflect protons to the image center at the earlier times. Second, scatter could not account for the level of fluence reduction seen in the center region at later implosion times. Monte Carlo simulations indicate that proton scattering at later times reduces the central proton fluence in radiographs by ~30% relative to values outside the capsule. The reductions in the actual images [Fig. 114.32(b)] are ~90%, indicating that scattering is not the dominant mechanism behind the observed central fluence deficit.

21. L. Spitzer, *Physics of Fully Ionized Gases*, 2nd rev. ed., Interscience Tracts on Physics and Astronomy (Interscience, New York, 1962).

22. S. I. Braginskii, in *Reviews of Plasma Physics*, edited by Acad. M. A. Leontovich (Consultants Bureau, New York, 1965).

23. For example, the charge separation around the convergent shock front due to the imbalance of ion mean free paths between the shocked and unshocked plasmas. This contribution can be ruled out as the dominant source because it will neither reverse direction nor suddenly increase as the data require. (We have ignored contributions from the outgoing shock front at later times due to its relatively weaker strength.)

24. J. Delettrez, R. Epstein, M. C. Richardson, P. A. Jaanimagi, and B. L. Henke, Phys. Rev. A **36**, 3926 (1987).

25. The electric field E was derived from the images by using E $\sim$ $2\zeta\varepsilon_p (A + a) (eAaL)^{-1}$, where $\varepsilon_p = 15$ MeV is the proton energy; e is electron charge; $a = 0.9$ cm and $A = 30.9$ cm are distances from backlighter to implosion and from backlighter to detector, respectively; $|\zeta| \sim (0.5-1) \times R$ is the apparent displacement of protons in the subject plane due to the effects of E on the proton trajectories; and $L \sim (0.5-2) \times R$ is the proton pathlength.

26. C. K. Li, D. G. Hicks, F. H. Séguin, J. A. Frenje, R. D. Petrasso, J. M. Soures, P. B. Radha, V. Yu. Glebov, C. Stoeckl, D. R. Harding, J. P. Knauer, R. L. Kremens, F. J. Marshall, D. D. Meyerhofer, S. Skupsky, S. Roberts, C. Sorce, T. C. Sangster, T. W. Phillips, M. D. Cable, and R. J. Leeper, Phys. Plasmas **7**, 2578 (2000).

High-Dynamic-Range, Single-Shot Cross-Correlator Based on an Optical Pulse Replicator

Introduction

New temporal diagnostics are constantly being developed to match the evolution of optical sources and their applications. Laser systems can now generate optical intensities as high as 10^{21} W/cm^2 (Ref. 1), and short-pulse laser systems delivering energies higher than 1 kJ are currently being developed.[2] The characterization of high-energy laser systems is challenging because their repetition rate is usually low. Incoherent processes such as laser and parametric fluorescence can induce significant variations of the intensity from shot to shot. Large shot-to-shot variations preclude the use of averaging and scanning diagnostics. The interaction regime of an optical pulse with a target is set by the peak intensity on target, but the prepulse intensity can significantly influence the interaction. The temporal intensity of the pulse must be known over an extended temporal range (for example, hundreds of picoseconds before the main pulse) with a high dynamic range (for example, eight orders of magnitude below the peak intensity of the pulse). These requirements are currently beyond the capabilities of single-shot optical pulse characterization techniques.[3–5]

Scanning nonlinear cross-correlators have been used for high-dynamic-range intensity measurements.[6,7] These diagnostics gate the pulse under test using an instantaneous nonlinear interaction with another optical pulse. The representation of the intensity of the pulse under test is obtained by scanning the delay between the interacting pulses. The scanning range can be very large since it is limited only by the ability to scan the relative delay between optical pulses. The dynamic range is set for each time slot by adjusting the signal level on the detector. For example, a combination of variable attenuation at the input of the diagnostic and variable gain at the detection stage may be used to adapt the signal level before detection. These diagnostics are fundamentally multi-shot devices.

Single-shot cross-correlators using time-to-space encoding have been demonstrated.[8,9] In these devices, nonlinear interaction in an appropriate arrangement maps the temporal intensity of the pulse under test onto a spatial-intensity distribution, which can be measured in a single shot. If the pulse-front tilt from a diffraction grating is used,[9] a large temporal coverage can be obtained. Since photodetectors and analog-to-digital converters are usually limited to a dynamic range of the order of 1000, the different temporal slices of the gated signal were selectively attenuated in Ref. 9 to make it possible to measure a 60-dB dynamic range using a low-dynamic-range detector. In practice, custom, continuous, spatially varying, neutral-density filters would be required to adjust the sensitivity of the device.

This article demonstrates a single-shot cross-correlator based on an optical pulse replicator. The replicator generates a discrete sequence of sampling pulses that are cross-correlated with the source under test in a nonlinear crystal. Advantages of this technique include (1) long temporal ranges, (2) sensitivity adjustments on the sampling pulses using standard neutral-density filters, and (3) constant temporal resolution over the full temporal range of the diagnostic. The remaining three sections describe the design of the cross-correlator, review various experimental results, and present conclusions.

Design of a Single-Shot, High-Dynamic-Range Cross-Correlator Based on a Pulse Replicator

1. General Principle

Following Fig. 114.36(a), the single-shot, high-dynamic-range cross-correlator correlates the pulse under test with a sequence of sampling pulses in a nonlinear crystal, and the spatial intensity of the resulting signal maps the temporal intensity of the input pulse. For the purpose of this explanation and demonstration, the following approximate optical frequencies apply: 1ω for the pulse under test, 2ω for the sequence of sampling pulses, and 3ω for the resulting nonlinear signal. The sampling pulses are temporally delayed and spatially displaced to ensure that the pulse under test is sampled at different times and the nonlinear signals corresponding to different times are spatially distinguishable. These pulses are generated by an optical pulse replicator (OPR) composed of a high reflector (HR) and a partial reflector (PR) appropriately aligned. This arrangement is an adjustable version of a Fabry–Perot etalon with an uncoated entrance window,[10] which has
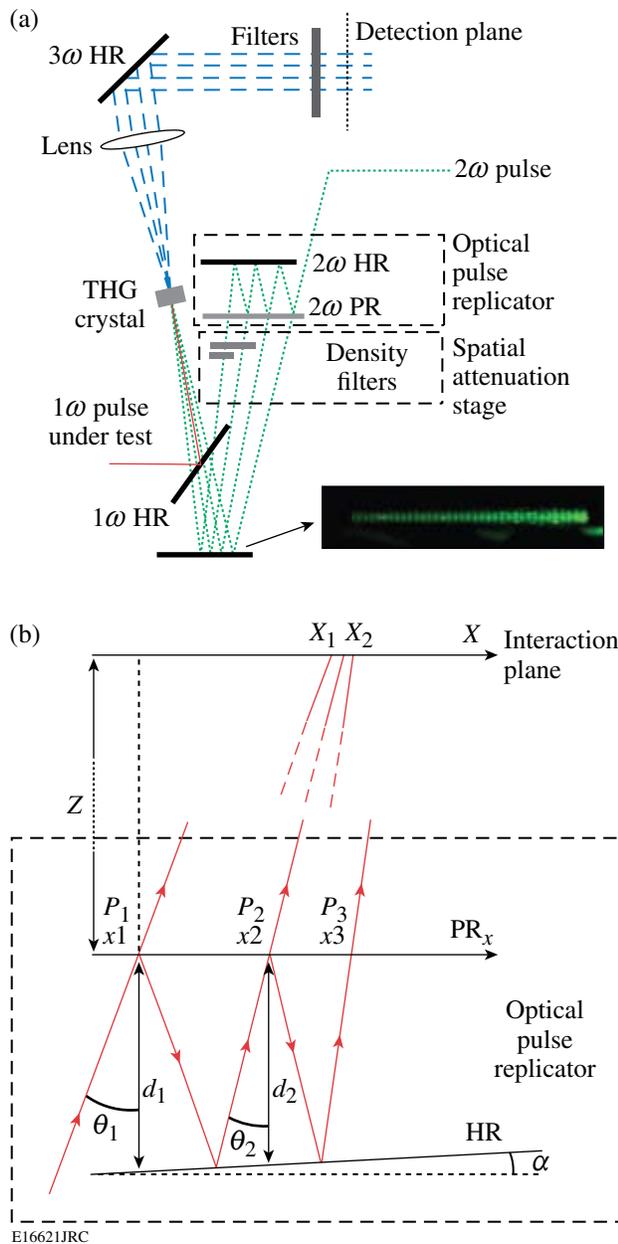
Figure 114.36

(a) Design of a single-shot cross-correlator based on the nonlinear interaction of the pulse under test with a sequence of sampling pulses from an optical pulse replicator. (b) Layout for the calculation of the spatial and temporal properties of the sequence of pulses from the optical pulse replicator. HR: high reflector; PR: partial reflector.

been used to generate discrete sequences of optical pulses.[11] In this demonstration, the pulse entering the OPR has an optical frequency of 2ω and has been obtained by doubling the input pulse under test. After the OPR, a set of neutral-density filters can selectively attenuate the sampling pulses corresponding

to high-intensity portions of the pulse under test. This allows one to balance the intensity of the nonlinear signals. The pulse under test and sampling sequence are combined in a quasi-collinear fashion and interact in a third-harmonic-generation (THG) crystal. The time-to-wave-vector encoding performed by the OPR at 2ω at the nonlinear crystal is converted into a time-to-space encoding of the 3ω signals with a lens of focal length f located a distance f away from the nonlinear crystal and the detection plane. This makes it possible to measure each individual signal corresponding to the nonlinear interaction of the pulse under test with each sampling pulse; i.e., the discrete temporal slices gated by the sequence of sampling pulses are located at discrete, spatially distinct locations of the detection plane.

2. Design and Characteristics of the Replicator

The pulse replicator is a combination of a high reflector (HR) and a partial reflector (PR) set to provide a sequence of sampling pulses after multiple reflections. Following Fig. 114.36(b), the input pulse is incident on the PR at point P_1, and part of the pulse is transmitted, generating the first sampling pulse. The remaining part of the pulse is reflected toward the HR and reflected back by the HR. The beam reflected by the HR is incident on the PR at point P_2. The pulse transmitted through the PR is the second sampling pulse, and the main part of the pulse is reflected again toward the HR to generate successive sampling pulses. For an energy E_0 at the input of the OPR, the energy of pulse n coming out of the OPR is $E_0 R^{n-1} T$, where R and T are, respectively, the intensity reflection and transmission coefficients of the partial reflector. Assuming $R = 99\%$ and a perfect high reflector, the energy of the first sampling pulse is 1% of the input pulse energy, while the energy of the 50th sampling pulse is 0.61%.

The replicator generates a sequence of sampling pulses that can be used either in the far field (i.e., the pulses are focused in the nonlinear crystal), or in a quasi near field (i.e., the pulses propagate in free space between the replicator and the nonlinear crystal). In the far-field implementation, the beams from the replicator are parallel in the near field and focused to a single point in the far field. This requires a good-quality lens with a large aperture (e.g., 2 in. for a 2-in. OPR). Care must also be taken to optimize the angular phase matching of focused beams. The overlap of multiple beams from the OPR with the pulse under test between beams might also be difficult to achieve. It was found that the sensitivity of the near-field implementation was satisfactory for the targeted application, so the near-field implementation described in the next paragraph was used.

A geometrical treatment of the near-field implementation is shown in Fig. 114.36(b). The two reflectors are set at an angle α. The existence of an optimal angle α for which all the beams from the replicator are in the same vicinity (with a tolerance associated to the beam size) at a given distance from the replicator must be proven. In practice, one of the reflectors can be set on a gimbal/kinematic mount. An interaction plane at a distance Z from the PR, where the nonlinear interaction will take place, is considered. The input beam is incident on the PR at an angle θ_1 in the point P_1 chosen as the spatial origin. The distance between the PR and the HR following a line perpendicular to the PR at point P_1 is d_1. Naming θ_n and d_n the corresponding quantities for point P_n, one can show that

$$\theta_n = \theta_{n-1} - 2\alpha \tag{1}$$

$$d_n = d_{n-1} \frac{1 - \tan(\alpha)\tan(\theta_{n-1} - 2\alpha)}{1 + \tan(\theta_{n-1})\tan(\alpha)} \tag{2}$$

$$x_n = x_{n-1} + d_{n-1} \frac{\tan(\theta_{n-1}) + \tan(\theta_{n-1} - 2\alpha)}{1 + \tan(\alpha)\tan(\theta_{n-1})}. \tag{3}$$

The sampling pulse coming out of the replicator at point P_n crosses the plane parallel to the PR at a distance Z at the coordinate $X_n = x_n + Z\tan(\theta_n)$. The corresponding optical path length L_n relative to point P_1 is the sum of the length accumulated in the replicator and the length between the PR and the interaction plane. One has the relation

$$L_n = L_{n-1} + \frac{d_{n-1}}{\left[1 + \tan(\alpha)\tan(\theta_{n-1})\right]}$$

$$\times \left[\frac{1}{\cos(\theta_{n-1})} + \frac{1}{\cos(\theta_{n-1} - 2\alpha)}\right] + \frac{Z}{\cos(\theta_n)} \tag{4}$$

with $L_1 = Z/\cos(\theta_1)$. Equations (1)–(4) allow one to calculate the position of the replicas at the interaction plane (i.e., the collection of X_n) and the delays between replicas (i.e., the delays calculated from the collection of L_n). The nonlinear crystal and the 1ω beam can be set to match the average value of the positions X_n of the sampling pulses, and the spatial performance of the OPR depends on the spreading of the X_n relative to their average value. The distance between the two reflectors sets the average delay between replicas (i.e., the sampling rate), and the temporal performance of the OPR depends on the nonuniformity of the sampling rate over the measured temporal range.

Figure 114.37 shows a simulation of the spatial characteristics of a pulse replicator with $\theta_1 = 20°$ and $Z = 1$ m. The results are plotted as a function of the sampling pulse number (between 1 and 50) and angle α. This corresponds to the situation where the distance Z is fixed in the diagnostic and the angle α is tuned. For the particular value $Z = 1$ m, the sampling pulses optimally overlap for $\alpha = 0.31$ mrad. Figure 114.37(b) displays the values of X_n for this value of α. The intersections of the sampling pulses with the reference plane are spread within 300 μm of the mean position. Such spreading will have minimal impact provided that it is small relative to the
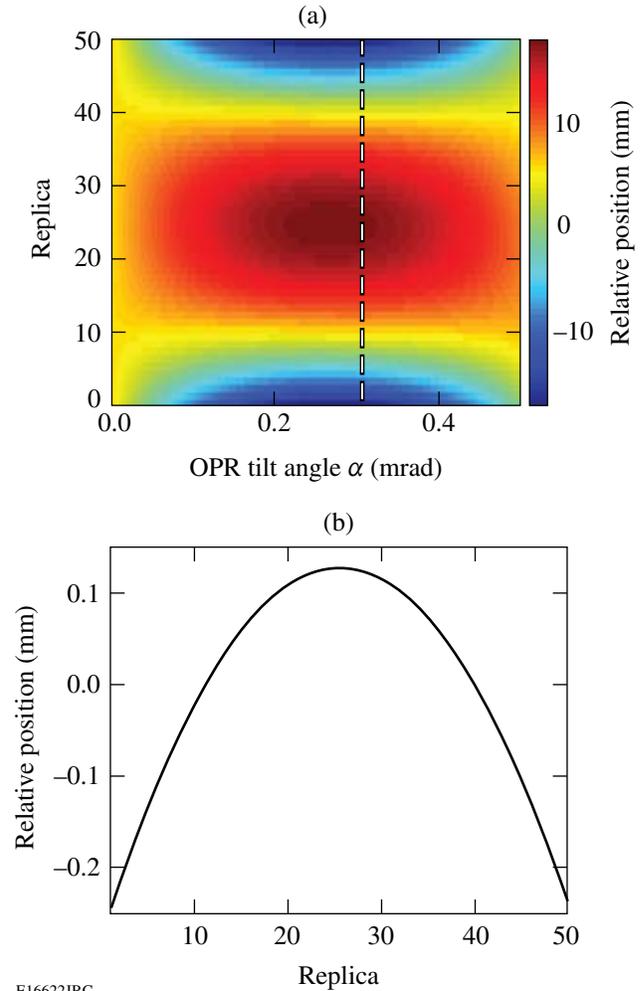
Figure 114.37
(a) Relative position (mm) of 50 replicas from the pulse replicator versus relative angle of the two reflectors of the OPR. The value of α minimizing the spread of the relative positions is indicated by a white dashed line. (b) Relative position of 50 replicas from the pulse replicator for the relative angle minimizing the standard deviation of the relative positions.

E16622JRC

size of the interacting beams. Figure 114.38(a) shows the non-uniformity of the sampling rate versus the sampling pulse number. Figure 114.38(b) displays the delay for the value of α leading to the optimal overlap plotted in Fig. 114.37(a). The average delay between replicas is 6.26 ps, and an insignificant change of the sampling rate of 0.3 ps over the 50 replicas is observed. Signal variation due to imperfect spatial overlap can be calibrated, as described in the following section, since it is a property of the diagnostic for a specific input beam size that does not depend on the temporal characteristics of the pulse.
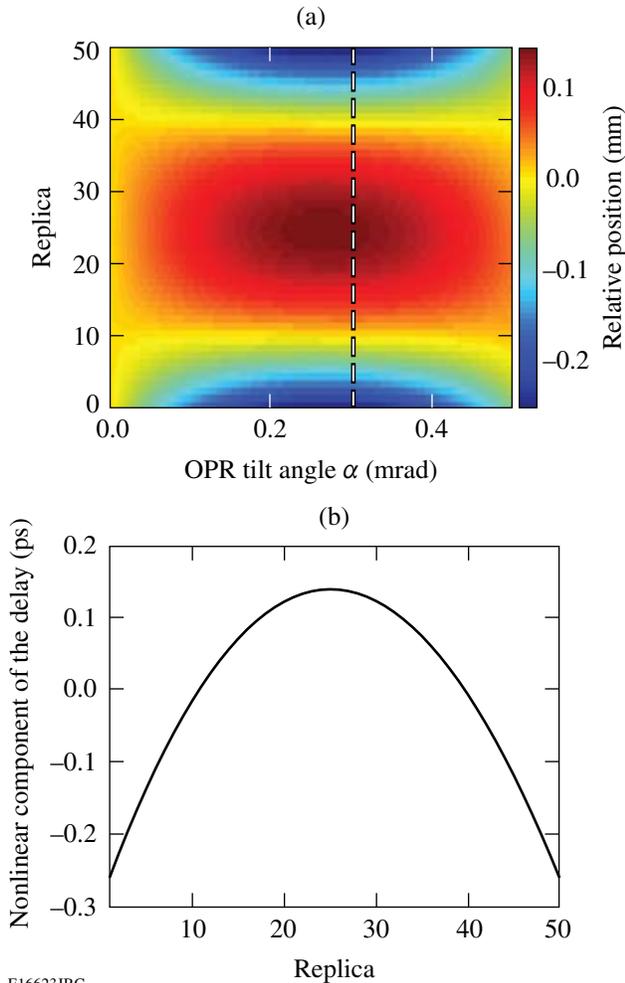
Figure 114.38

(a) Nonlinear component of the delay (ps) for 50 replicas from the pulse replicator versus the relative angle of the two reflectors of the OPR. The value of α minimizing the spread of the relative positions is indicated by a white dashed line. (b) Nonlinear component of the delay for 50 replicas from the pulse replicator for the relative angle minimizing the standard deviation of the relative positions.

Experimental Results

1. Experimental Setup

A prototype single-shot cross-correlator was built with 2-in. reflectors. The off-the-shelf commercial reflectors have a surface figure of $\lambda/10$ at 633 nm. The partial reflector has $R = 99\%$ at $0°$. The angle between the input beam and the reflectors is approximately $20°$. The layout is similar to that of Fig. 114.36(a), with a metal mirror between the beam combiner and the THG crystal folding the 1ω and 2ω beam paths to reduce the footprint of the device. The horizontal width of the 2ω beam before replication was reduced by using a telescope to increase the number of replicas produced by the replicator. The distance Z between the OPR and nonlinear crystal is 130 cm. The nonlinear crystal is a 5-mm, type-II DKDP cut for THG ($\theta \sim 59°$). The polarizations of the 1ω and 2ω beams are vertical and horizontal, respectively, and the crystal is oriented accordingly. The angular spread of the 2ω beams after the replicator is in the horizontal direction, which is aligned with the ordinary axis of the crystal to decrease the phase-matching angular variation. The 1ω and 2ω beams are multiplexed vertically with a small angle so that they overlap in the THG crystal.

Optical pulses from a diode-pumped regenerative amplifier (DPRA) operating at 1053 nm were used to demonstrate the single-shot, high-dynamic-range cross-correlator. The DPRA is seeded by a short optical pulse (sub-200 fs) from a mode-locked laser. After amplification and gain narrowing, the amplifier delivers an ~8-ps pulse at 5 Hz with an energy per pulse of approximately 250 μJ. Second-harmonic generation is performed in a 10-mm, type-I lithium triborate (LBO) crystal. The 2ω energy before the replicator is 60 μJ. With the 5-mm DKDP crystal, the noise-equivalent input 1ω energy of the contrast diagnostic is approximately 7 pJ. The sampling pulses need not be derived from the pulse under test, and a low-energy pulse under test could be characterized using sampling pulses generated by another source.

The THG signal is measured with a video camera connected to a frame grabber. The 1ω and 2ω sources are blocked before detection with colored filters. The dynamic range of the diagnostic using this eight-bit frame grabber was determined by measuring the signal corresponding to a single 3ω replica versus input 1ω energy. For a spatially extended 3ω beam, the dynamic range is higher than at each point in the beam because lower-intensity parts of the beam can linearly contribute to the signal even when other parts are saturated. A dynamic range of the order of 30 dB was obtained (Fig. 114.39). Additionally, the 3ω signal versus input 1ω energy was measured when a

E16623JRC
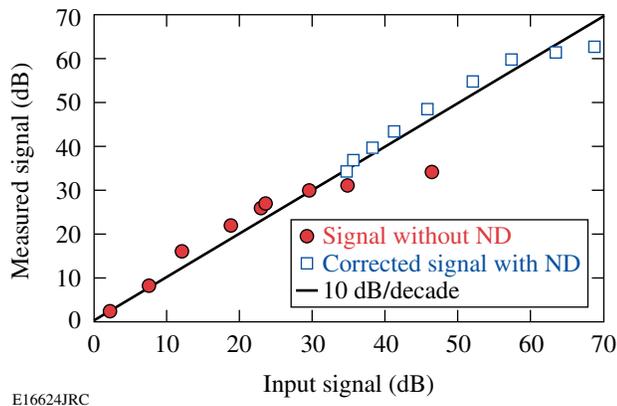
E16624JRC

Figure 114.39
Measured 3ω signal versus 1ω signal without neutral-density (ND) filters on the sampling pulse (circles) and with a 30-dB attenuation on the sampling pulse after signal correction (squares). The solid line corresponds to the expected linear relation between the input and output signals.

neutral-density filter with an optical density of 3 was set in front of the 2ω replicas used for up-conversion. As expected from the THG process, the THG signal decreases by three orders of magnitude for the same input 1ω energy, and a 30-dB decrease in the 2ω sampling energy is compensated by a 30-dB increase in 1ω energy. This demonstrates the potential enhancement of the dynamic range of the diagnostic using density filters on specific sampling pulses that are known to correspond to high-intensity portions of the pulse under test. Thanks to the discrete spatial-intensity distribution of the sampling pulses, attenuation can be performed with off-the-shelf density filters. Attenuation of the sampling source, as opposed to the attenuation of the signal after interaction,[9] was chosen to minimize scattering. Scattering of the sampling pulses at a non-detected wavelength before the nonlinear interaction is preferred over scattering of a high-intensity signal at the detected wavelength after the nonlinear interaction to preserve the high dynamic range of the diagnostic.

The sampling rate was calibrated by temporally scanning the 1ω pulse relative to the train of sampling pulses. The variations of the 3ω signal intensity in each time slot were calibrated using this scan to correct the measured signals. These variations potentially arise from the non-identical spatial overlap of the sampling pulses with the 1ω pulse in the crystal, from the 2ω energy-per-replica variation at the output of the OPR, and from the phase-matching variations in the tripling crystal among different 2ω pulses arriving at different angles.

2. Measurement of a Train of Pulses
   from a Fabry–Perot Etalon

The intensity and temporal calibration of the diagnostic were tested by inserting a Fabry–Perot etalon in the 1ω optical beam path. The etalon generates a sequence of optical pulses separated by the intracavity round-trip time, 40 ps in this case. Figure 114.40 shows the intensity histogram measured over 1000 shots, which is similar to the infinite-persistence mode of sampling oscilloscopes. Five pulses from the pulse train are well resolved by the diagnostic. As expected, the separation between pulses is approximately 40 ps, and their intensity decreases monotonically. Energy fluctuations from the DPRA can also be seen.
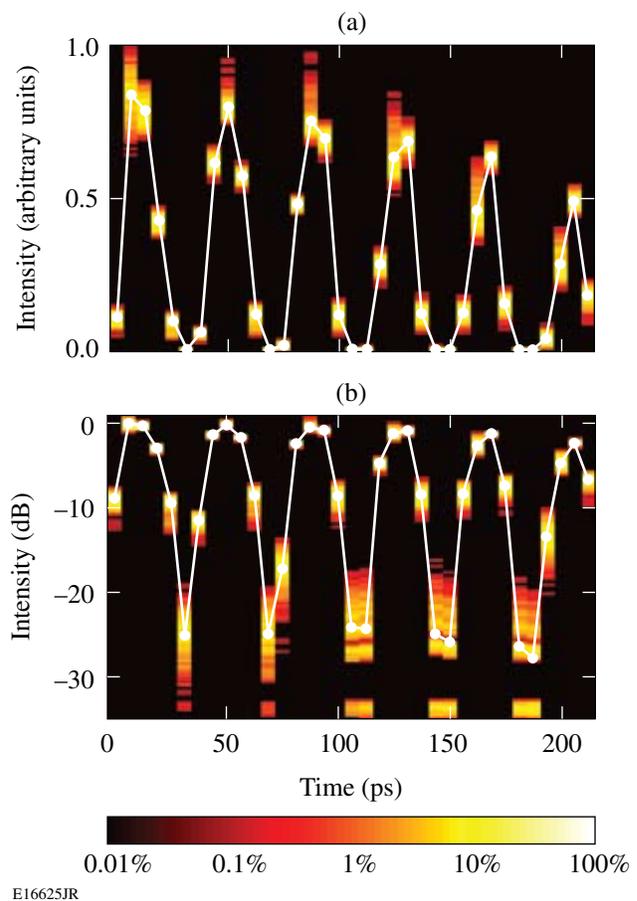

E16625JR

Figure 114.40
Intensity histogram of the output of a Fabry–Perot etalon on (a) a linear scale and (b) logarithmic scale. In each case, the average value of the intensity at each time slot is plotted with white circles.

3. High-Dynamic-Range Measurements

Figure 114.41 demonstrates the high dynamic range of the diagnostic. The sensitivity of the device was adapted to measure

the prepulse contrast. A neutral-density filter with an optical density of 3 at 2ω was set at the output of the pulse replicator to attenuate the seven last sampling pulses, which were timed to coincide with the main pulse from the DPRA. This effectively allows one to map the signal intensity over more than 60 dB onto the detector. The intensity histogram of 10,000 successive shots of the DPRA shows the presence of a prepulse approximately 100 ps before and 40 dB below the main pulse. Amplified spontaneous emission (ASE) has an average intensity approximately 45 dB below the peak intensity of the pulse, although there are large shot-to-shot intensity variations due to the incoherent nature of ASE. Figure 114.42(a) shows the intensity of one DPRA shot, while Fig. 114.42(b) shows the intensity averaged over 10,000 shots.
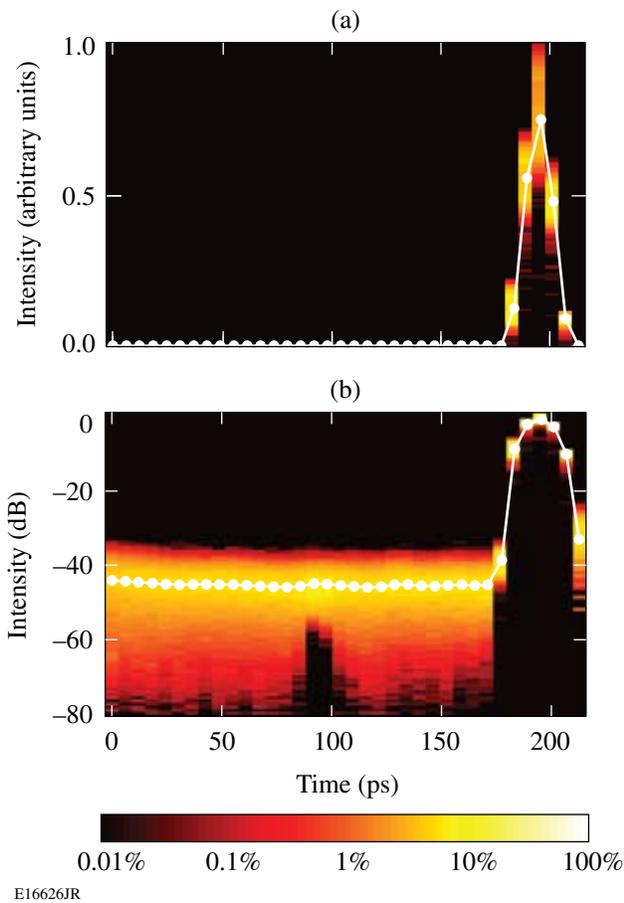

Figure 114.41
Intensity histogram of 10,000 successive shots of the DPRA on (a) linear and (b) logarithmic scales. In each time slot, brighter intensity corresponds to a larger proportion of samples in a given intensity bin. The average intensity is plotted with white circles. A prepulse can be observed approximately 100 ps before the main pulse.
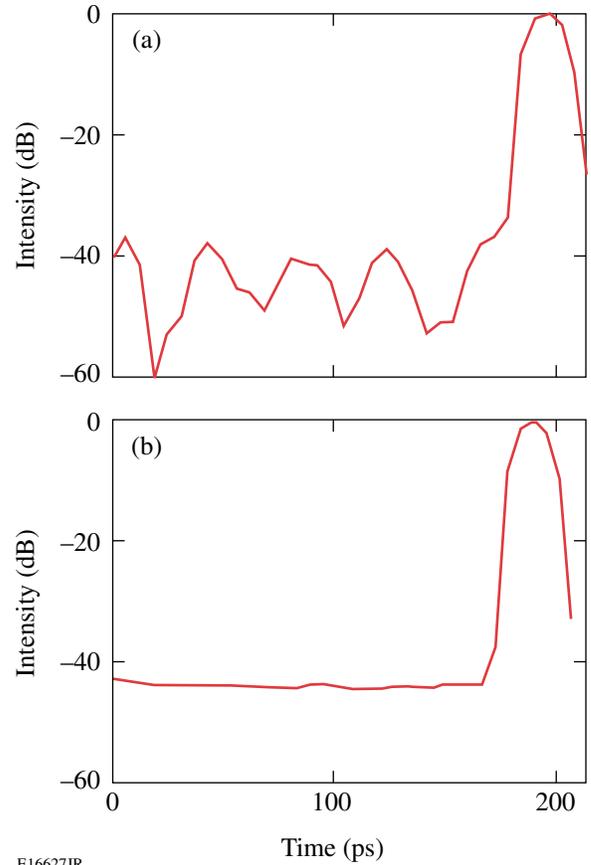

Figure 114.42
(a) Intensity of one DPRA shot and (b) intensity averaged over 10,000 shots.

4. Measurement of Amplified Spontaneous Emission

ASE is a time-stationary incoherent process, and one expects that its statistical temporal properties do not depend on time. The observation window of the cross-correlator was moved significantly in front of the pulse from the DPRA. Figure 114.43 shows the histogram of the measured intensity, with the average value plotted with white circles. Very uniform distribution of the intensity samples can be observed on the linear and logarithmic plots.

5. Statistical Analysis

Incoherent laser and parametric fluorescence are commonly present on high-energy laser pulses. The statistical properties of the intensity of ASE are well documented.[12] For ASE with a degree of polarization equal to 1 (i.e., linearly polarized ASE), the intensity probability density is

$$P(I) = \frac{1}{\langle I \rangle} \exp\left(-\frac{I}{\langle I \rangle}\right), \tag{5}$$

91
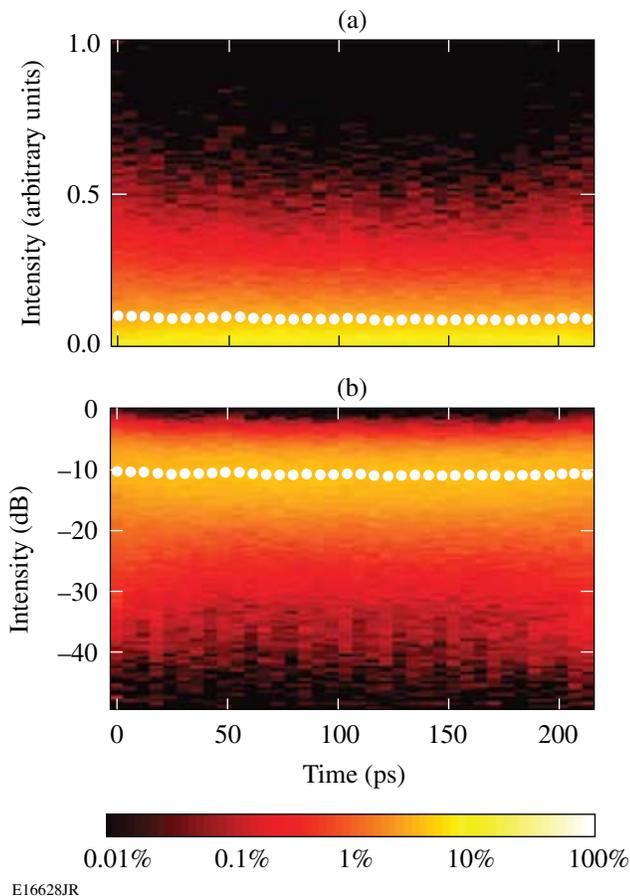
Figure 114.43
Intensity histogram of 10,000 realizations of ASE on (a) linear and (b) logarithmic scales. In each case, the average value of the intensity at each time slot is plotted with white circles.


Figure 114.44
Intensity probability density distribution for amplified spontaneous emission. Plots (a) and (c) correspond to an overlap of the distributions obtained at each of the 36 time slots characterized by the diagnostic on a linear and logarithmic scale, respectively. Plots (b) and (d) correspond to the distribution calculated with all the measured samples on a linear and logarithmic scale, respectively. Experimental distributions are plotted with thin solid lines, and the theoretical prediction of Eq. (5) is plotted with circles.

where $\langle I \rangle$ is the average value of the intensity. Equation (5) is remarkable since it does not rely on any free parameter. A collection of samples of the intensity of an incoherent process should match this distribution and confirm that the measured variations are indeed on the signal under test and are not due to the diagnostic. Figure 114.44(a) shows the measured intensity probability distributions at each of the 36 measured time slots (i.e., 36 different probability density distributions are calculated, each of them using the 10,000 intensity samples measured at a given time). An excellent overlap of the distributions and a good agreement with the expected distribution of Eq. (5) are obtained. Figure 114.44(b) corresponds to the measured intensity probability distribution when all the collected samples (i.e., 36,000 samples) are considered as a single set. An excellent agreement with the expected distribution is again obtained. Figures 114.44(c) and 114.44(d) are logarithmic representations of the data plotted in Figs. 114.44(a) and 114.44(b), respectively. They reinforce the property that accurate intensity measurements are performed over a 30-dB dynamic range.

Figure 114.45 displays the normalized quantity $\sigma_N(I) = \sigma(I)/\langle I \rangle$ for the data from Figs. 114.41 and 114.43. For the incoherent process described by Eq. (5), one expects $\sigma_N(I) = 1$. Values slightly higher than 1 are measured, with a slightly increased value at the edges of the measurement range [Fig. 114.45(a)]. Higher noise is attributed to photodetection noise. In these measurements, the signal corresponding to the outer replicas before intensity calibration is lower, and the relative detection noise would be higher. For a coherent process, it is expected that $\sigma_N(I) = 0$, while for a combination of a coherent and incoherent process, all values of $\sigma_N(I)$ between 0 and 1 are achievable. Figure 114.45(b) displays $\sigma_N(I)$ for the data in Fig. 114.41. This quantity is very close to 0 at times corresponding to the main pulse. It is essentially identical to its values in Fig. 114.45(a) at times corresponding to ASE only. The small prepulse approximately 100 ps before the main pulse corresponds to an observable decrease of $\sigma_N(I)$. While the noise at
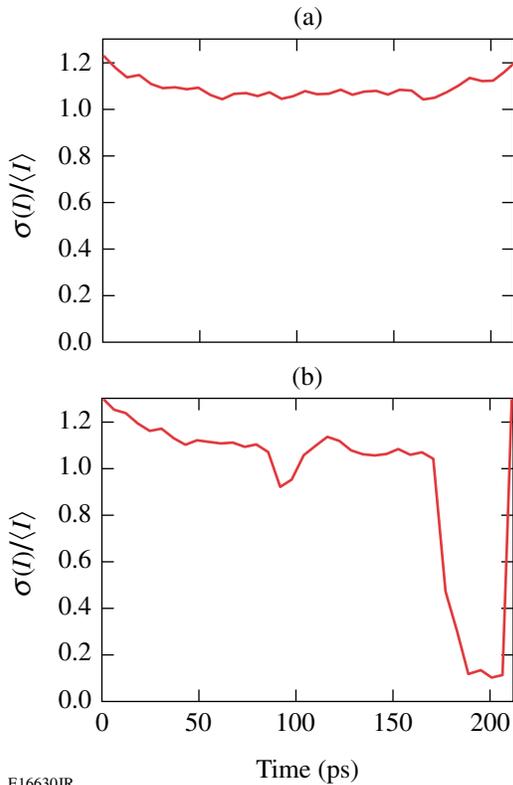
Figure 114.45

Normalized intensity standard deviation as a function of time for amplified spontaneous emission (in relation to Fig. 114.43) and for a 200-ps window including the main laser pulse (in relation to Fig. 114.41).

in various directions. The temporal range can be directly increased by using larger reflectors in the optical pulse replicator. The temporal dynamic range can be improved by increasing the dynamic range of the spatial-intensity measurement of the gated signal. For example, additional optical densities can be used after the pulse replicator to characterize optical sources with higher contrast requirements.

REFERENCES

1. S.-W. Bahk, P. Rousseau, T. A. Planchon, V. Chvykov, G. Kalintchenko, A. Maksimchuk, G. A. Mourou, and V. Yanovksy, Opt. Lett. **29**, 2837 (2004).

2. J. D. Zuegel, S. Borneis, C. Barty, B. LeGarrec, C. Danson, N. Miyanaga, P. K. Rambo, C. LeBlanc, T. J. Kessler, A. W. Schmid, L. J. Waxer, J. H. Kelly, B. Kruschwitz, R. Jungquist, E. Moses, J. Britten, I. Jovanovic, J. Dawson, and N. Blanchot, Fusion Sci. Technol. **49**, 453 (2006).

3. D. J. Kane and R. Trebino, Opt. Lett. **18**, 823 (1993).

4. C. Dorrer, B. de Beauvoir, C. Le Blanc, S. Ranc, J.-P. Rousseau, P. Rousseau, and J.-P. Chambaret, Opt. Lett. **24**, 1644 (1999).

5. J. Bromage, C. Dorrer, I. A. Begishev, N. G. Usechak, and J. D. Zuegel, Opt. Lett. **31**, 3523 (2006).

6. S. Luan *et al.*, Meas. Sci. Technol. **4**, 1426 (1993).

7. E. J. Divall and I. N. Ross, Opt. Lett. **29**, 2273 (2004).

8. J. Collier *et al.*, Laser Part. Beams **19**, 231 (2001).

9. I. Jovanovic *et al.*, presented at the CLEO/QELS Conference, Baltimore, MD, 6–11 May 2007 (Paper JThD137).

10. C. Dufour, Rev. Opt. **24**, 11 (1945).

11. S. Xiao, J. D. McKinney, and A. M. Weiner, IEEE Photonics Technol. Lett. **16**, 1936 (2004).

12. L. Mandel and E. Wolf, *Optical Coherence and Quantum Optics* (Cambridge University Press, Cambridge, England, 1995).

these times is small relative to the main pulse, it is significant relative to the intensity of the prepulse.

Conclusion

A single-shot cross-correlator based on a discrete sequence of sampling optical pulses has been demonstrated. Versatile operation has allowed the characterization of different optical sources. The demonstrated high dynamic range (60 dB) and large temporal coverage (200 ps) make this temporal diagnostic a valuable tool to measure the temporal contrast of optical pulses. The capabilities of this cross-correlator can be extended

Application of Phase Retrieval for Characterizing a High-Intensity Focused Laser Field

Introduction

Focal-spot diagnostics (FSD's) for a high-intensity laser is one of the basic diagnostic requirements for analyzing high-field laser–matter interaction experiments. Many different parameters of a focal spot might be of interest to an experimenter—encircled energy per a given radius, the peak power density of a focal spot, the evolution of local hot spots along the propagation direction, or a full two-dimensional complex-field distribution for a more-comprehensive laser–matter interaction study. The difficulties of implementing focal-spot diagnostics for high-power lasers lie mostly in the necessity of devising an indirect technique because no instrument can survive direct measurements. The indirect technique, therefore, needs thorough qualification regarding how closely it is capable of representing real focal spots.

One of the appealing approaches to FSD is to measure near-field amplitude and phase to predict the field at the focus. This approach can determine the full complex-field distribution at any plane near the focus using well-known diffraction theories. In addition, the on-shot focal spot can be calculated easily without interfering with target experiments. Since the focal-spot is more affected by wavefront error than by fluence error, it is important that the wavefront error be minimized in this approach. One source of wavefront error is the non-common-path aberrations (NCPA's)—the difference between the measured wavefront through the sample beam path and the on-shot wavefront. We designate this difference as "transfer wavefront." We also designate the aberrations belonging only to the diagnostic path as "intrinsic NCPA's" and the aberrations not captured by the diagnostic setup as "extrinsic NCPA's." The transfer wavefront is obtained by subtracting the intrinsic NCPA from the extrinsic NCPA.

Transfer wavefront is characterized by sending probe beams through the optical beam path under consideration. There are, in general, two approaches for characterizing transfer wavefront depending on the arrangement of probe sources and the number of wavefront-measurement locations. In the first approach a single probe source, or so-called reference beam, is sent out

to characterize both intrinsic and extrinsic NCPA's; but the wavefronts are measured at two different locations: at the end of the diagnostic beam path and after the final focusing optic in the experimental chamber. This approach was demonstrated in a 100-TW class laser.[1] In the second approach, two probe sources are used at each end of the diagnostic and on-shot path and the wavefront is measured at only a single location, which is at the end of the diagnostic beam path. These two approaches are conjugate to each other in concept. For convenience the first approach is called single-source FSD or FSD-1, and the second is called double-source FSD or FSD-2.

Schematics for both versions of FSD are shown in Fig. 114.46. The on-shot wavefront is measured by a wavefront sensor located at a diagnostic table. The intrinsic NCPA's (W_i) of the measured wavefront are the down-collimator aberrations and other aberrations in the optics located in the diagnostic table. The aberrations from the leaky mirror through the transport optics to the off-axis-paraboloidal (OAP) mirror are extrinsic NCPA's (W_e). In FSD-1, the calibration source as noted in Fig. 114.46(a) is a low-energy reference beam co-propagating with the main beam. The wavefront of this reference beam is measured at the diagnostic table and in the target chamber. The wavefront at location W_2 in the target chamber can be directly measured using a near-field imaging setup.[1] In our case, we chose to use a phase-retrieval method using multiple focal spots measured with a high-resolution focal-spot microscope (FSM) at different longitudinal locations.

Using a reference beam, at W_1,

$$W_{r1} = W_{\text{ref}} + W_i, \tag{1}$$

where W_{ref} is the aberrations in the reference beam itself before the leaky mirror and W_{r1} is the wavefront measured at the sensor location.

At W_2,

$$W_{r2} = T(W_{\text{ref}} + W_e) - W_t, \tag{2}$$
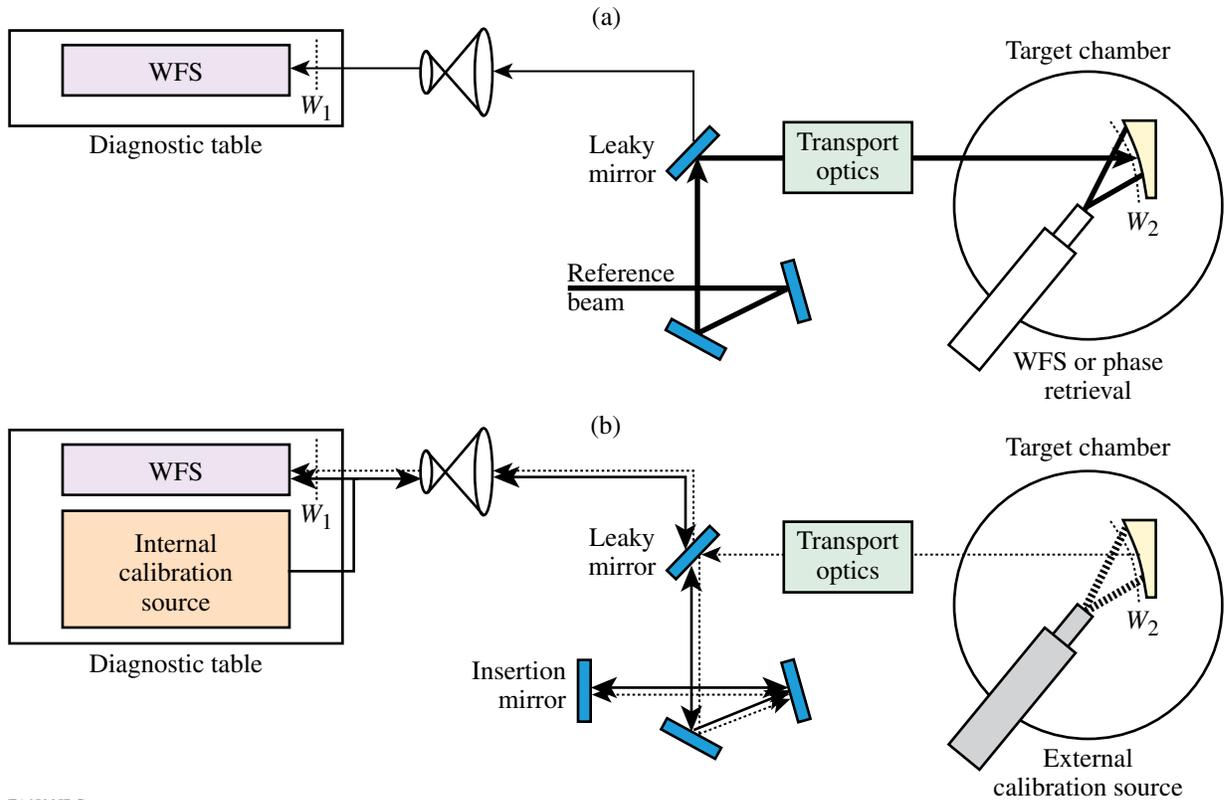
E16590JRC

Figure 114.46

(a) FSD-1 uses one calibration source, and wavefronts are measured at two locations to calculate the transfer wavefront. (b) FSD-2 uses two calibration sources, and the wavefront is measured at only one location. WFS: wavefront sensor

where W_{r2} is obtained by the phase-retrieval method or by direct measurement. W_t is an instrument error either in the wavefront-sensor imaging system or in the focal-spot microscope used in the phase retrieval. $T(\ )$ is a transformation function describing the spatial coordinate difference and the image distortion after the reflection off of the off-axis paraboloid.[2] For a large f-number focusing, T can be a simple linear transformation because the distortion is negligible.

The transfer wavefront is

$$W_{\text{transfer}} = W_e - W_i = T^{-1}(W_{r2} + W_t) - W_{r1}, \qquad (3)$$

and the on-shot wavefront in the target chamber is calculated as

$$W_{2,\,\text{on-shot}} = W_{1,\,\text{on-shot}} + W_{\text{transfer}}. \qquad (4)$$

The locations of W_1 and W_2 are shown in Fig. 114.46.

In the FSD-2 approach, the wavefront sensor located at the diagnostic table measures the intrinsic term, characterized by sending a source twice through the diagnostic path reflected by a temporary insertion mirror [Fig. 114.46(b)]. Let us refer to this quantity as W_s and the source as the "internal calibration source." If we send another source located at the center of the target chamber backward through the system, the extrinsic term as well as the intrinsic term will be detected at the sensor location. We denote this measured quantity as W_p and call the calibration source "external calibration source":

$$W_s = W_{i,0} + 2W_i, \qquad (5)$$

$$W_p = T^{-1}(W_{e,0}) + W_e + W_i, \qquad (6)$$

where $W_{i,0}$ and $W_{e,0}$ are the aberrations that are inherent to the intrinsic and extrinsic calibration sources, respectively. Each has to be measured separately. The inverse transformation is needed to remap the extrinsic source error in a planar space, whereas it is not necessary to apply the inverse transformation to $W_{i,0}$ because the internal calibration source is usually created by a simple on-axis beam collimator that does not distort the beam; it is easily measured by inserting an extra mirror close to the wavefront-sensor location.

The transfer wavefront is calculated as

$$W_{\text{transfer}} = W_e - W_i = \left(W_p - W_s\right) - \left[T^{-1}\left(W_{e,0}\right) - W_{i,0}\right]. \quad (7)$$

A concern with this calibration scheme is the necessity of using a high-power source during the measurement of W_s because of the energy loss associated with the double-pass transmission through the leaky mirror. The main signal might also suffer severe ghost reflections from other optics in the intermediate locations.

In either calibration procedure, the resulting transfer wavefront map should cover the on-shot main beam in the area for the calibration map to be meaningful. The advantage of FSD-2 is that beam registration is automatic and it is easy to subtract and add wavefronts from the internal or external source. However, in the presence of non-negligible aberrations in the external calibration source, the registration task becomes non-trivial and one might have to apply the distortion transformation. Also, the requirement that the two calibration beams should be co-propagating without a centering error poses some alignment challenges. FSD-1, however, has the advantage of being insensitive to the aberrations in the reference beam. It also allows a more direct adaptive-optic correction of the incoming beam as a whole due to the presence of a wavefront-sensing scheme after the final focusing optic.

OMEGA EP is a petawatt laser currently being built at LLE. The focal-spot diagnostics for OMEGA EP is based on the FSD-2 approach. Owing to the complexity of the system, there is always a risk that relying on only one approach might limit our capability to characterize the transfer wavefront under certain conditions. Along with the baseline OMEGA EP FSD development, we investigate the feasibility of implementing FSD-1, especially using a phase-retrieval method. In the **Phase-Retrieval Formalism** section that follows, the mathematical formalism of the phase-retrieval method will be discussed. In the **Off-line FSD Test-Bed Results** section (p. 97), the wavefronts at W_2 obtained by FSD-2 and by the phase-retrieval FSD will be compared and shown to agree well with each other, thus confirming the phase-retrieval method. In the **FSD Demonstration in the MTW Laser System** section (p. 99), phase-retrieval FSD will be applied to predict a focal spot in the Multi-Terawatt (MTW) Laser System, which is compared with the direct focal-spot measurements.

Throughout this article the criterion of FSD accuracy is measured in terms of R_{80} error. R_{80} is an encircle radius that captures 80% of the total energy at the focus. Although the true R_{80} value is not known, R_{80} from a direct focal-spot measure-ment is considered as the true R_{80} for the purpose of R_{80} error calculation. Currently OMEGA EP requires less than 10% error in R_{80} prediction.

Phase-Retrieval Formalism

Phase retrieval is a calculation technique that retrieves phase information from available intensity measurements that are connected by an integral or differential form of a propagation equation. A phase profile is sought that recreates all the measured intensity profiles under the propagation constraint. One can systematically find a solution using one of the search methods typically available from commercial optimization packages. In this section we describe a phase-retrieval method based on multiple near-focus measurements and one near-field fluence measurement. Increasing the number of measurement planes improves the accuracy of the result as well as the dynamic range of the retrieved phase.[3]

In Fig. 114.47, the measurement schemes and notations are described. A complex near field $g(x,y)$ is focused by a focusing optic with a focal length of F. The focused intensity profiles are measured at N locations defocused from the focus by Δz_k. The complex field at the kth plane (G_k) is calculated by the Fourier transform after multiplying $g(x,y)$ with a defocusing term; $g(x,y)$ is described by the measured near-field intensity $I_0(x,y)$ and an unknown phase, which is to be retrieved. The phase term can be expressed as a sum of basis functions (ξ_n) multiplied by modal coefficients a_n:

$$g(x,y) = \sqrt{I_0(x,y)} \exp\left[i\sum_n a_n \xi_n(x,y)\right]. \quad (8)$$

Here we chose to use modal expansion instead of a point-by-point phase representation. If the two-dimensional phase map is allowed to vary point by point, the retrieved phase is susceptible

$$G_k(x',y') = \text{FT}\left\{g(x,y)\exp\left[-i\frac{\pi\Delta z_k}{\lambda F^2}\left(x^2 + y^2\right)\right]\right\},$$
$$k = 1, \cdots, N$$
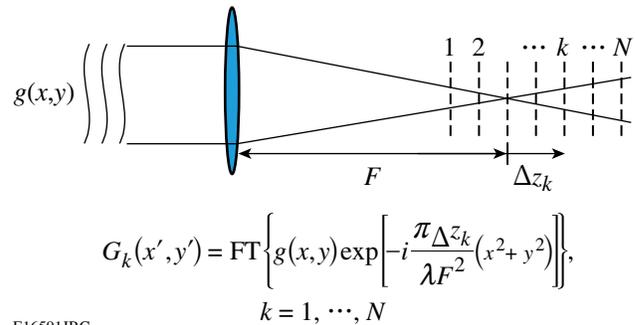
E16591JRC

Figure 114.47
Phase retrieval using a multiple-focal-plane intensity measurement.

to discontinuities due to noise in the focal-spot measurements. A modal approach allows one to obtain a smooth phase map but sacrifices resolution for high-spatial-frequency terms not captured by the employed modes. The basis functions commonly used are Zernike polynomials for a circular beam shape or Legendre polynomials for rectangular shapes. For the actual laser beam, which is neither a perfect circle nor a rectangle, one chooses a circle or a rectangle whose size is just large enough to include the whole laser beam. The inner product, however, is defined only within the laser-beam boundary. As long as the beam shape is close to the ideal geometrical figure, this quasi-modal expansion closely represents the original surface.

The error metric to be minimized is

$$\varepsilon(\{a_n\}) = \sum_{k=1}^{N} \lambda_k \iint \left[|G_k(x',y')| - \sqrt{I_k(x',y')} \right]^2 \mathrm{d}x'\mathrm{d}y', \quad (9)$$

where λ_k is a weighting factor for the measurement plane k. Using the expression of the far field for the kth plane (G_k), the error metric can be seen as a function of the modal coefficients a_n, where we search for a set of coefficients that minimize the magnitude of the error metric. Generally the searching process can be made more efficient when the gradients of the error metric with respect to each search variable are available as an analytic form.[4] In this case the gradient for the coefficient a_n is

$$\frac{\partial \varepsilon}{\partial a_n} = 2\,\mathrm{Imag}\left\{ \iint \mathrm{IFT}\left[\sum_{k=1}^{N} \lambda_k \left(G_k - \sqrt{I_k}\, e^{i\psi_k} \right) \right]^* \xi_n\, g\, \mathrm{d}x\mathrm{d}y \right\}, \quad (10)$$

where IFT is the inverse Fourier transform, ψ_k is the phase of the complex field G_k, and I_k is the measured intensity at the kth plane. The measured intensity usually contains noise that can be negative after background subtraction, so the negative values are set to zero. To measure focal spots, it is ideal to measure intensity by placing a CCD (charge-coupled device) camera directly at the focal planes; however, for low-f-number focusing, a microscope imaging system is needed to resolve a small focal spot. For such a case, the aberrations in the microscope system should be negligible. The modal coefficients for tip and tilt terms are allowed to vary independently for each plane because the mechanical translation is not typically linear. That is, if the number of coefficients to be retrieved is M, the actual number of coefficients that are optimized is $M + 2(N–1)$.

With the error metric and the gradients given, a MATLAB® optimization routine ("fminunc") is used to retrieve the modal coefficients. The routine uses a trust-region approach.[5] The typical number of iterations for successful retrieval is less than 20, using five measurement planes.

Off-line FSD Test-Bed Results

Before applying the phase-retrieval method in the MTW Laser System, it was first tested in an off-line FSD test bed where it is possible to compare a directly measured wavefront and a retrieved wavefront. The experimental setup is shown in Fig. 114.48. The setup is designed to mimic basic configurational features of OMEGA EP focal-spot diagnostics; it contains a wavefront sensor, a focal-spot microscope, transport optics, an OAP, down-collimation telescopes, a leaky mirror, and an insertion mirror as well as internal and external calibration sources [Fig. 114.46(b)]. The same wavefront sensor and focal-spot microscope were used in both the test-bed setup and the FSD demonstration in the MTW Laser System.

The wavefront sensor chosen for OMEGA EP is a Shack–Hartmann wavefront sensor—HASO—manufactured by Imagine Optic. It has a 128×128 lenslet array with a 14×14-mm^2 CCD sensor area. The focal length of each microlens is 6.3 mm, which can measure local slopes up to 15 mrad. The accuracy of the defocus term was measured to be better than 0.01 waves at 1.053 μm, and the relative error of astigmatism was found to be within 2%. Accuracy in higher-order aberrations was studied using custom-designed sinusoidal phase plates of one wave peak-to-valley. Wavefront measurements up to one quarter of the maximum spatial frequency were confirmed to be within less than 1% discrepancy with the interferometric measurements. Measurements at higher spatial frequency with the reference phase plates were limited by the maximum slope limit of the sensor.

The prototype FSM consists of a high-quality microscope objective (Mitutoyo, 10×, N.A. = 0.26, nominal focal length = 20 mm), a tube lens (nominal focal length = 200 mm), and a scientific-grade, 16-bit CCD camera (SI-800, Spectral Instruments). The microscope objective has a long working distance suitable for high-fluence measurements. The objective is infinity corrected, so a tube lens refocuses the image at the CCD. The actual dynamic range of the camera is reduced to 14 bits due to read noise. The camera was cooled at –35°C in all cases to minimize noise.

The thick black line in Fig. 114.48 represents the main beam line. W_s is measured by the external calibration source placed at the FSM image plane, and W_p is measured by the internal calibration source placed next to the wavefront sensor. W_2 is calculated according to Eq. (4). All the calibration beams and
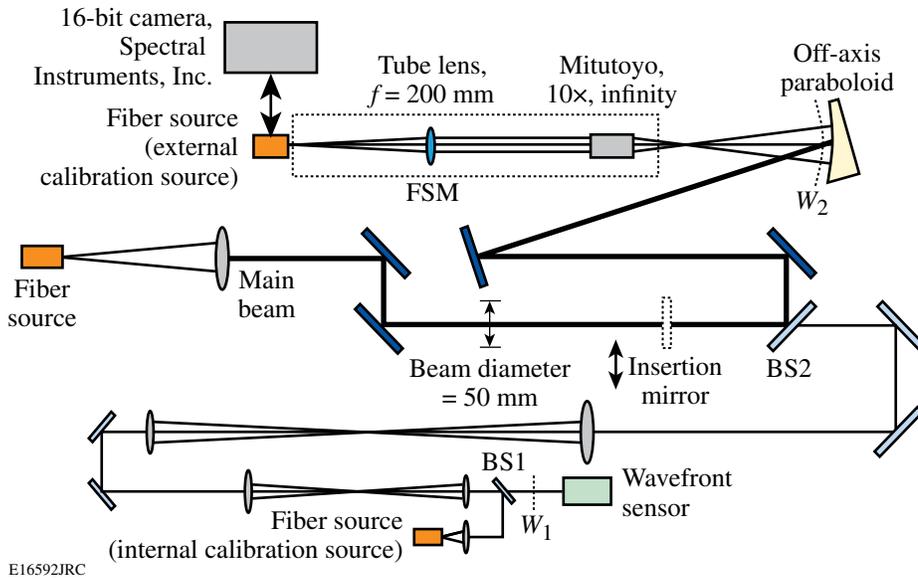
Figure 114.48
The test-bed setup with a geometry similar to the OMEGA EP FSD setup. BS: beam splitter; FSM: focal-spot microscope unit.

the main beam source are obtained from collimating the diverging beam from a single-mode fiber tip injected with a 1053-nm continuous-wave laser. The main beam is a 2-in.-diam round beam down-collimated at the sensor location by a factor of 5. The beam is attenuated before the fiber sources so there are no filter-induced aberrations in the setup. The whole setup was covered with acrylic glass to prevent measurement corruption from air turbulence. The lenses in the two down-collimators and the collimator lens for the main beam were intentionally tilted to introduce aberrations. The main beam is focused by a 200-mm effective-focal-length OAP mirror and the focus is imaged to the FSM.

Figure 114.49 summarizes the wavefronts measured by the FSD-2 procedure. The measured and the calculated focal spots are also shown in Fig. 114.50. The fine details of the calculated focal spot are in excellent agreement with those of the measurement, but the relative R_{80} discrepancy (12%) slightly exceeds the OMEGA EP accuracy requirement (10%) at the best-focus position [Fig. 114.50(d)]. R_{80} errors for five different focal spots measured at $\Delta z = -500, -250, 0, 250,$ and 500 μm are $-2.1, -5.4, -12, -6.2,$ and 2%, respectively. It appears that this discrepancy in R_{80}, which is more pronounced near the best-focus position, actually results from an incoherent background halo in the FSM measurements,[6] which spreads focused light away from the center of focus.

With the direct characterization of wavefront using the FSD-2, we can compare this with the retrieved wavefront from the multiple focal plane phase-retrieval method, which uses the aforementioned five focal-spot measurements. The best-fitting
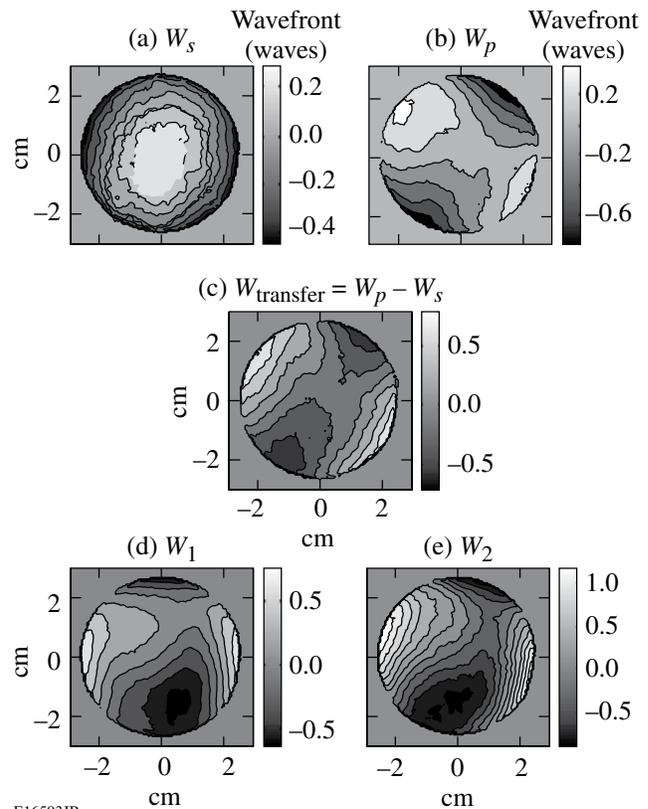
Figure 114.49
Summary of wavefront measurements in the test-bed setup. (a) W_s, (b) W_p, (c) $W_{transfer}$, and (d) a wavefront measured at the wavefront sensor location (W_1), and (e) a calculated wavefront after the paraboloidal mirror ($W_2 = W_1 + W_{transfer}$). The wavefront units are in waves.
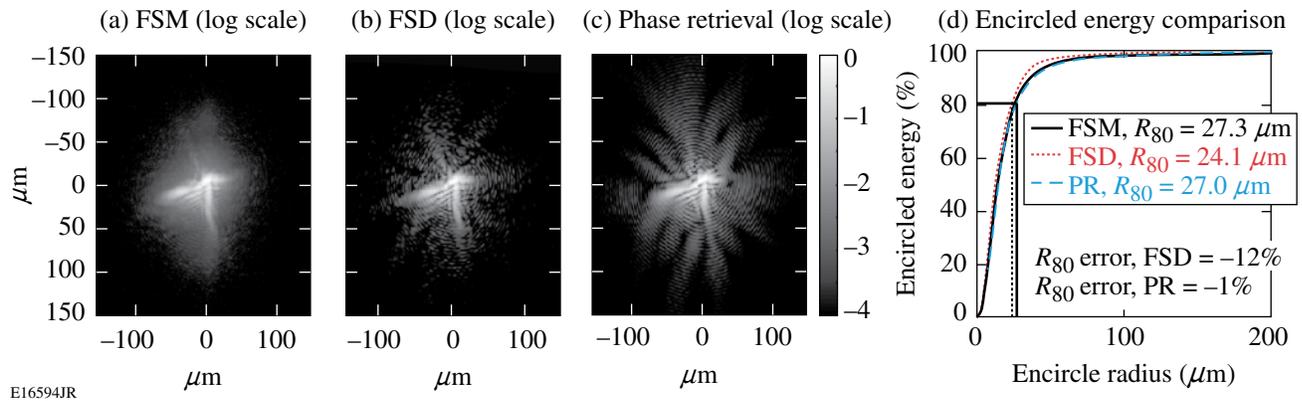
Figure 114.50
The calculated and measured focal spots for the test-bed experiment. (a) Directly measured focal spot by FSM, (b) calculated focal spot based on FSD cali-bration, (c) calculated focal spot from the retrieved Zernike coefficients, and (d) encircled energy comparisons and the relative R_{80} errors with respect to the R_{80} value of the directly measured focal spot.

Zernike coefficients that minimize the difference between the measured and the calculated focal spots are calculated by an optimization routine. The retrieved wavefront, corresponding to W_2, agrees well with the W_2 from the baseline FSD. Figure 114.51 compares Zernike coefficients and the wavefront difference. The rms (root-mean-square) difference between the two wavefronts is 0.074 waves. Although one might expect that the R_{80} prediction from the retrieved phase coefficients would have similar errors as in the FSD-2 approach, the R_{80} errors in the five different focal planes in the phase-retrieval case are actually all within 2%. Putting more weight on the direct measurements, it shows that it is possible for the phase-retrieval process to produce a wavefront map that fits all the focal-spot
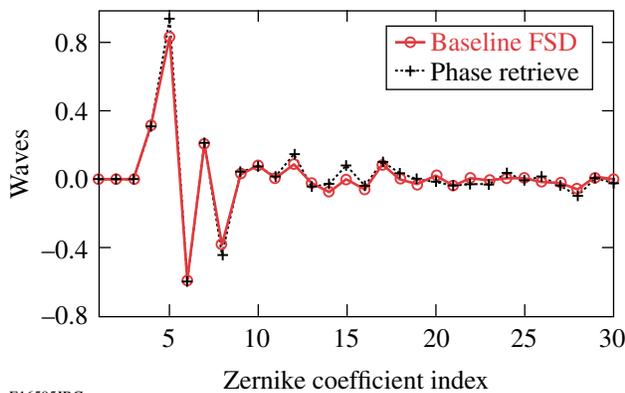

Figure 114.51
Zernike coefficients from the FSD calibrated wavefront and from phase retrieval from multi-focal-plane data agree well with each other. The rms wavefront difference is 0.074 waves.

data while still being slightly off from the true wavefront. Throughout this experiment the external and internal source errors were assumed negligible; also, the distortion mapping was not applied because the *f* number (~4) is relatively large.

FSD Demonstration in the MTW Laser System

The MTW FSD setup (Fig. 114.52) is based on phase-retrieval FSD (FSD-1) because an external calibration source is not available in the target chamber. In this case the pulse energetics is a practical concern. The attenuation was prepared in three steps; first through wave plates and a polarizer, second by Fresnel reflection off an uncoated wedge (M2), and finally by neutral-density filters inside the FSM. The main glass amplifier was not fired throughout the experiment.

Similar to the FSD test-bed case, the beam is focused by an *f*/4 off-axis paraboloidal mirror; we measured focal spots at five different planes near focus separated by 250 μm. The objective was mounted on a remotely controlled translation stage for operation under vacuum, and the position of the objective was optically monitored using a target-viewing system. We obtained a set of modal phase coefficients that minimize an error metric, which quantifies the difference between the measured data and the intensity computed from the phase estimate, by an optimization routine under the assumption that the field is monochromatic. The modal basis is represented by Legendre polynomials because the beam shape is close to square. Figure 114.53 shows lineout comparisons at each plane after completion of the algorithm. We note generally good agreement in every plane except at the focused plane (first row, third column); the blurring of the focal spot in the horizontal direction is due to angular dispersion caused by a
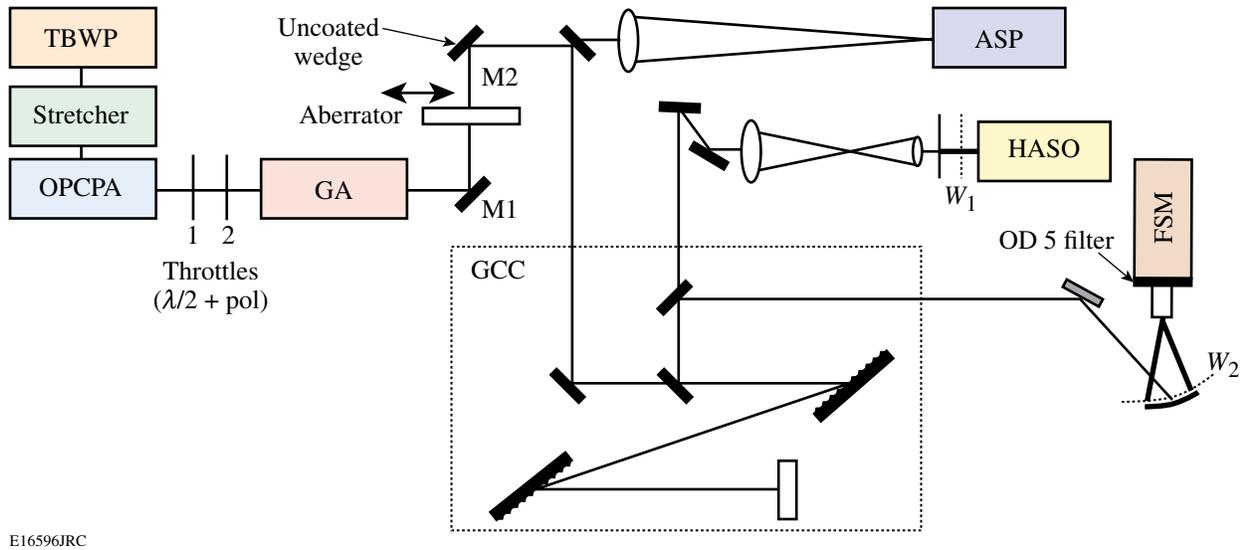
E16596JRC

Figure 114.52
Experimental setup for a phase-retrieval FSD demonstration in the MTW Laser System. TBWP: a mode-locked oscillator; OPCPA: parametric amplifier; GA: 15-cm-thick glass amplifier (inactive); HASO: wavefront sensor; ASP: pointing sensor; GCC: compressor chamber; FSM: focal-spot microscope.
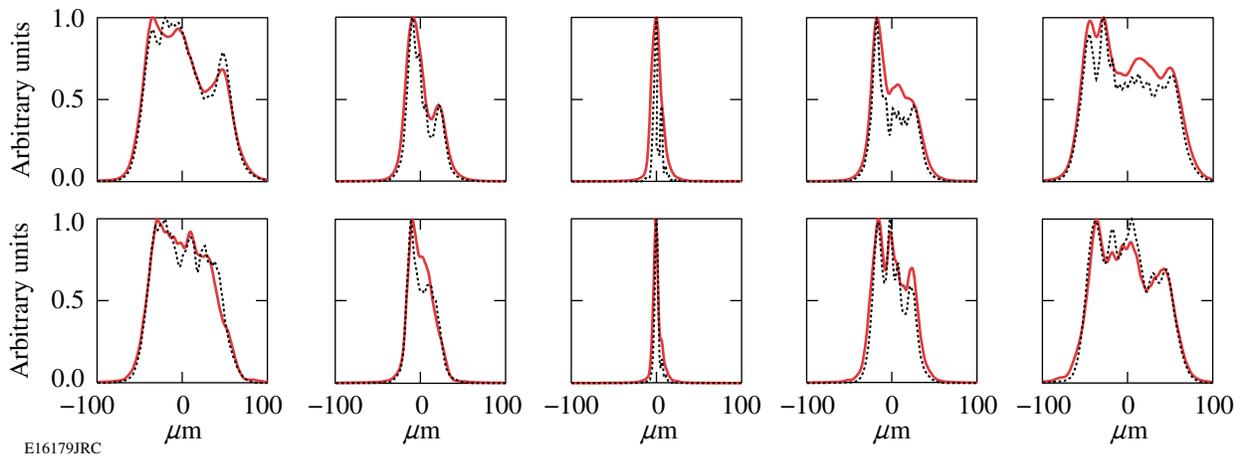
E16179JRC

Figure 114.53
Horizontal (first row) and vertical (second row) lineout comparisons at each plane. The solid lines are from measurements; the dashed lines are from the phase-retrieval calculations. Distances are 500, 250, 0, –250, and –500 μm from the left column to the right.

slight misalignment of the compressor gratings. The angular dispersion was independently measured to be 47 μrad over the 7-nm bandwidth by marking the bandpass-filtered focal-spot position change from 1050 nm to 1057 nm. Therefore we find it better to exclude the zero-defocus plane measurement in the search algorithm. On the other hand, the focus plane measurement can be used to estimate the amount of angular dispersion. The amount of angular dispersion estimated from phase-retrieval results is 50 μrad, which agrees with the independently measured value within 7% relative error.

Once the wavefront of the focusing beam is successfully characterized, this information can be used to characterize focal spots at higher energies by separately measuring the differential wavefront change. As shown in Fig. 114.54, the wavefront sensor on the diagnostic table measures sets of wavefronts belonging to the same beam used in the phase retrieval. The transfer wavefront is calculated according to Eq. (7) [Fig. 114.54(c)]. With the transfer wavefront quantified, the characterization of focal-spot distribution under a different circumstance should be possible by a single wavefront

measurement at the diagnostic table. To validate this idea, an aberrated, transmissive element was placed before the leaky mirror (Fig. 114.52). The directly measured focal spot [Fig. 114.55(a)] morphologically agrees well with the predicted focal spot using the wavefront of Fig. 114.54(e) as shown in Fig. 114.55(b), whereas the agreement is poor without using the transfer wavefront [Fig. 114.54(d) and Fig. 114.55(c)]. The calculated and directly measured focal spots are also compared in logarithmic scale in Figs. 114.56(a) and 114.56(b). The R_{80} error [Fig. 114.56(c)] is 13%, which falls slightly short of the OMEGA EP requirement. The encircled energy of the FSM focal spot shows that it has more energy scattering beyond R_{80} than FSD test-bed measurements; this may result from the extra use of filters in the FSM for attenuating the beam.
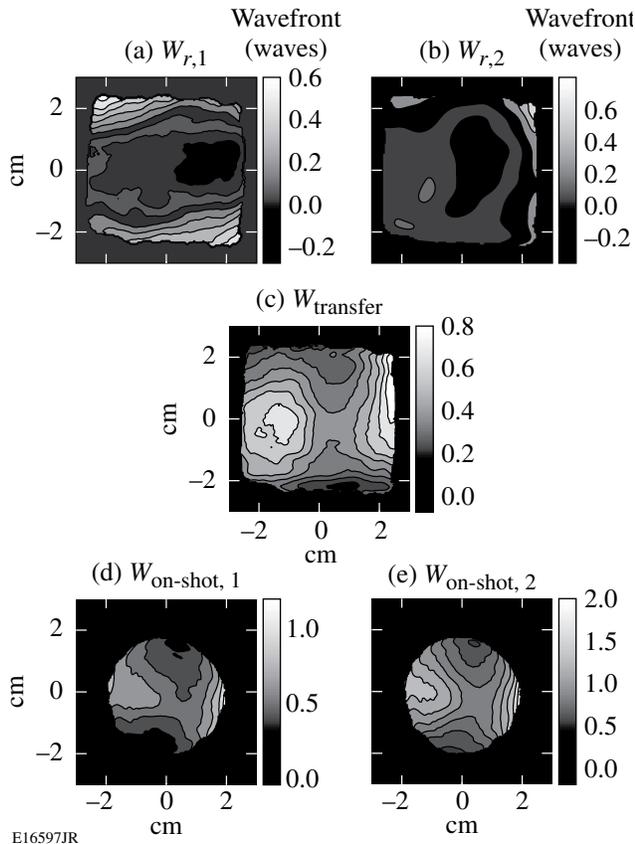

Figure 114.54

Wavefront summary of an OPCPA laser beam. (a) Wavefront measured at the wavefront sensor location, (b) wavefront after OAP reflection, from phase retrieval, (c) transfer wavefront [Eq. (3)], (d) wavefront measured at the wavefront sensor location after the insertion of an aberrator, and (e) calibrated wavefront for the W_2 plane using the transfer wavefront. Wavefront unit is in waves.
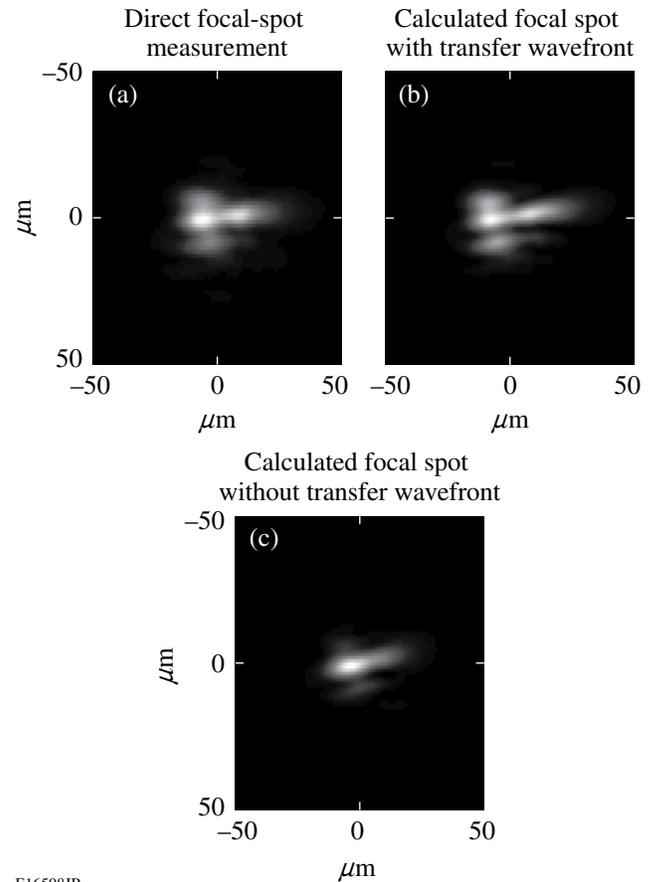
Figure 114.55

Linear scale comparison of the directly measured focal spot (a) in the presence of an aberrator with the calculated focal spot, (b) using the transfer wavefront obtained from phase retrieval, and (c) not using the transfer wavefront.

Conclusions

This work presented focal-spot diagnostic concepts for a high-power laser system, which is based on measuring a near-field complex field for predicting a far field. Since the wavefront at the target chamber is not directly measurable, we demonstrated two calibration procedures to characterize a "transfer wavefront" with which the measured wavefront at the diagnostic table can be easily converted to the actual wavefront at the target chamber location. One FSD approach (FSD-2) is based on direct wavefront measurements using multiple calibration sources, whereas the phase-retrieval FSD (FSD-1) is based on phase retrieval using multiple focal-plane measurements. The two calibration methods were successfully demonstrated in the FSD test-bed setup. The test-bed results show that phase retrieval agrees with the direct measurement within 0.07 waves rms. In the MTW system, the phase-retrieval FSD was applied to characterize the transfer wavefront and a focal
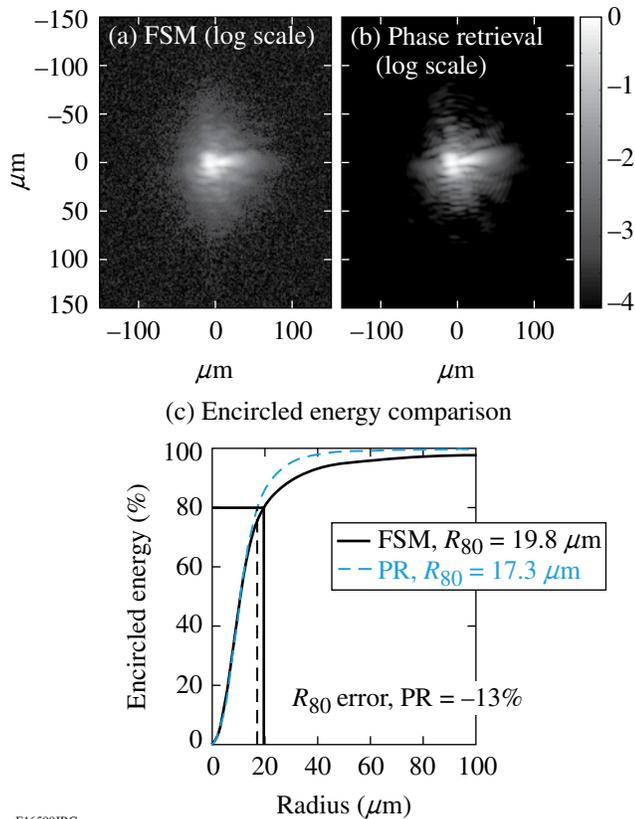
E16599JRC

Figure 114.56

Logarithm scale comparison of the directly measured focal spot (a) in the presence of an aberrator with the calculated focal spot and (b) using the transfer wavefront obtained from phase retrieval. Encircled energy comparisons (c) show 13% of relative R_{80} error.

spot. The disagreement in R_{80} seen in both the test-bed setup and the MTW system suggests that the FSM data may have been corrupted by an incoherent background halo. Currently the R_{80} error is not smaller than 10% from the experimental verification point of view. On the other hand, the availability of the phase-retrieval technique will complement the application of the baseline FSD in OMEGA EP, which might be impaired by system complexity.

REFERENCES

1. S.-W. Bahk, P. Rousseau, T. A. Planchon, V. Chvykov, G. Kalintchenko, A. Maksimchuk, G. A. Mourou, and V. Yanovksy, Opt. Lett. **29**, 2837 (2004).

2. S.-W. Bahk, P. Rousseau, T. A. Planchon, V. Chvykov, G. Kalintchenko, A. Maksimchuk, G. Mourou, and V. Yanovsky, Appl. Phys. B **80**, 823 (2005).

3. V. Yu. Ivanov, V. P. Sivokon, and M. A. Vorontsov, J. Opt. Soc. Am. A **9**, 1515 (1992).

4. J. R. Fienup, Appl. Opt. **32**, 1737 (1993).

5. T. F. Coleman and Y. Li, SIAM J. Optim. **6**, 418 (1996).

6. G. Kuwabara, J. Opt. Soc. Am. **43**, 53 (1953).

Optimization of Laser-Damage Resistance of Evaporated Hafnia Films at 351 nm

Introduction

Highly reflective coatings for laser applications in the ultraviolet region of the spectrum pose significant challenges since laser-damage thresholds decrease significantly as the absorption edge of the film materials is approached. Damage initiation at 351 nm for pulsed laser systems in the nanosecond-pulse regime tends to be dominated by the intrinsic absorption of the film materials, as well as defect density and the standing-wave electric-field distribution within the interference structure.[1–3] High reflectors in the near ultraviolet are typically constructed of oxides, utilizing silica as the low-index material and a refractory oxide as the high-index material. Material selection proceeds to fluorides as the wavelengths continue to become shorter and the absorption in the oxides becomes unacceptable. Silica, while somewhat challenging to evaporate, is a stable, low-absorption, high-laser-damage-threshold material that consistently outperforms the high-refractive-index component in multilayer reflectors.[1,4] The influence of the electric field distribution is quite well understood, leaving as the primary need improved high-index film materials that may be deposited with low defect density, low absorption, and high laser-damage resistance.[5,6]

Evaporated hafnia films are of particular interest for large-aperture laser applications due to the relatively high bandgap, ease of scale-up, ability to deposit uniform films, high degree of control throughout the deposition process, and relatively low intrinsic film stress.[7–10] Adjusting the deposition temperature and oxygen backfill pressure during reactive deposition may modify material parameters such as laser-damage resistance, complex refractive index, and film stress in hafnia/silica multilayers.[11–13] Furthermore, the use of hafnium metal as a source material provides a cleaner deposition than hafnium dioxide, with fewer ejected particulates, since hafnia undergoes a crystalline phase transition with a rapid change in volume while it is being heated.[14,15]

The microstructure of the deposited film is also of concern, for both mechanical and optical performance. A weak, loosely bound film structure may be environmentally and mechani-cally fragile, while potentially exhibiting increased tensile stress.[16–18] As roughness increases, optical scatter will also increase, reducing the efficiency of lasers incorporating such coatings.[19] In pursuing improved laser-damage resistance of the material, it is important to continue to evaluate the influence that process changes have on these other properties of the overall coating. The structure of an evaporated hafnia film tends to be quite porous, with relatively distinct zone-1 columnar growth.[20–22] This open microstructure is sensitive to the relative humidity of the use environment and is prone to tensile stress, potentially leading to cracking of the film structure. Ideally, the film microstructure could be deterministically controlled to reduce the environmental influence on film properties as well as achieve a neutral film stress in the final use environment, but there is minimal control over such properties for standard evaporated films. As porosity is increased in the film, there is a corresponding decrease in refractive index, requiring additional layers to achieve desired reflectivity specifications for reflective coatings.

A great deal of effort has been expended in determining the laser-damage mechanisms in hafnia films. The presence of "nanoclusters" of hafnium within the layers, which provide localized heating when irradiated by a laser, has been hypothesized.[23] These defects may be of the order of a few tens of atoms, leading to a reduction in laser-damage resistance as evidenced by localized initiation sites.[23] Modifications to the deposition process that avoid the formation of nanoclusters, or break existing clusters, are expected to lead to significant improvements in the laser-damage resistance of the deposited hafnia.

This effort is centered around the need to improve the laser-damage resistance of multilayer high-reflector coatings for use at a 351-nm wavelength at a 0.5-ns pulse duration. This requires the reduction, or ideally the avoidance, of nanoclusters or nano-absorbers in the growing hafnia layers. Monolayers of hafnia are deposited for characterization by pulsed-laser-damage testing, x-ray diffraction (XRD), transmission electron microscopy (TEM), and spectrophotometry. Ideally, x-ray diffraction will be

capable of resolving the presence of any significant crystalline inclusions within the hafnia films, providing the opportunity to characterize these inclusions for size and composition. The refractive index of the film will also be characterized, in an effort to understand the impact of any changes in deposition conditions with the overall density of the film structure. Finally, multilayer high-reflector coatings will be fabricated by utilizing the established deposition process to determine the influence of the process on the performance of finished mirrors for use in a 351-nm laser.

Experimental Procedure

Depositions of hafnia films were performed in a Vacuum Process Technology (VPT) 56-in., box-type evaporation system (see Fig. 114.57). The system is cryopumped to provide a clean base vacuum of less than 3×10^{-6} Torr. The chamber is equipped with a planetary rotation system and fixed-position uniformity masks to achieve a consistent film-thickness distribution within 1% peak-to-valley. The interior of the chamber is heated using a 12-kW array of quartz heater lamps. Two Ferrotec EV-M8 electron-beam guns are utilized as evaporation sources, one equipped with six 25-cc pockets and the other a 400-cc continuously rotating pan. Deposition control is performed with an Inficon IC5 deposition controller and an array of six quartz-crystal monitor (QCM) heads, with four of


G8212JRC

Figure 114.57
The 56-in. evaporation system used to prepare hafnia monolayers. The system uses quartz heater lamps and cryopumps and provides uniform evaporation from the electron-beam guns through the use of planetary rotation and fixed-position uniformity masks. Film-thickness control is achieved with multi-point quartz-crystal monitoring (QCM).

the six used in a weighted average to monitor the evaporant flux from each source. This provides improved noise reduction in the thickness measurement, while averaging measurements in different regions of the chamber to minimize the effects of shifts in the vapor plume.

A cleaved-float-glass sample and a polished fused-silica substrate were placed in substrate fixtures in the planetary rotation system. The cleaved-float-glass substrate provides a virgin glass surface for more accurate determination of the laser-damage threshold, with no contaminants from cleaning or polishing processes.[4] The polished fused-silica sample is suitable for spectral measurement, x-ray diffraction, or electron microscopy. A shutter system installed on the planet made it possible to load four such pairs of substrates into the system, while only one pair is exposed at any given time. As a result four different sets of deposition conditions can be tested for each pumping cycle of the chamber.

The six-pocket electron-beam gun was loaded with 99.9%-purity hafnium metal supplied by Aran Isles. A monolayer of hafnia, with a nominal layer thickness of 177 nm, was deposited on each pair of substrates. The deposition rate was varied for each value of the oxygen backfill pressure, as outlined in Table 114.I, while the substrate temperature was maintained at 200°C for all depositions.

Measurements of Deposited Layers

The performance of the hafnia film was evaluated relative to three primary concerns: spectral/photometric performance, film stress, and laser-damage resistance. Changes in material properties were evaluated based on differences in refractive index, porosity, and crystallinity, as well as imaging of the film structure. The presence of different material phases and inclusions is of particular interest since such differences may significantly impact the laser-damage resistance of the material. Further evaluation of the material properties of the coating, such as relative elemental content or bonding structure, may be pursued in future work but was not undertaken at this time. The influence on film stress will be studied in the future for deposition conditions that yield films with sufficiently high laser-damage resistance.

First, spectral measurements were performed on all fused-silica samples at approximately 40% relative humidity using a Perkin–Elmer Lambda 900 spectrophotometer operating in a normal-incidence transmittance configuration. The transmittance measurements for the coated samples are shown in Fig. 114.58.
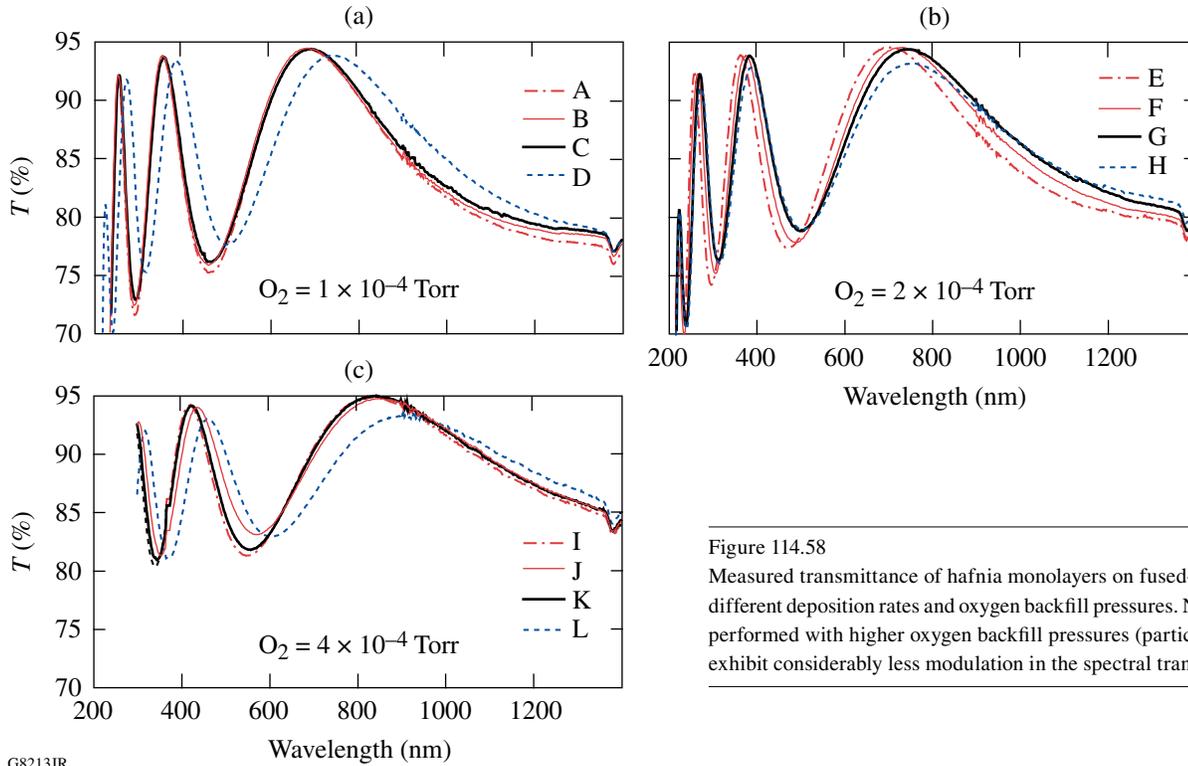
Figure 114.58
Measured transmittance of hafnia monolayers on fused-silica substrates for different deposition rates and oxygen backfill pressures. Note that depositions performed with higher oxygen backfill pressures (particularly samples I–L) exhibit considerably less modulation in the spectral transmission data.

Table 114.I: Sample identifiers A–N are assigned to substrates coated at one of six different deposition rates while using one of three oxygen backfill pressures.

Sample	O_2 Backfill Pressure (Torr)	Deposition Rate (Å/s)
A	1×10^{-4}	1.2
B	1×10^{-4}	0.9
C	1×10^{-4}	0.6
D	1×10^{-4}	0.3
E	2×10^{-4}	1.2
F	2×10^{-4}	0.9
G	2×10^{-4}	0.6
H	2×10^{-4}	0.3
I	4×10^{-4}	1.2
J	4×10^{-4}	0.9
K	4×10^{-4}	0.6
L	4×10^{-4}	0.3
M	2×10^{-4}	0.1
N	2×10^{-4}	0.2

All of the samples were characterized for their laser-damage resistance at 351 nm, using a 0.5-ns pulsed laser in a standard testing procedure.[23] Samples were tested in both 1:1 and N:1 configurations, with multiple threshold measurements used to establish a mean and standard deviation for each sample. Results are shown in Fig. 114.59.
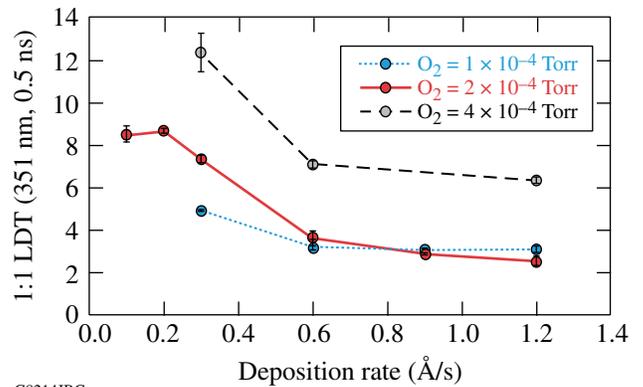
Figure 114.59
Measured laser-damage resistance of hafnia monolayers (as a function of deposition rate) at 351 nm and 0.5-ns pulse length, tested in 1:1 mode. Note the strong dependence on O_2 backfill at low deposition rates, with the slowest depositions and the greatest O_2 backfill leading to the highest laser-damage thresholds.

To better understand the material changes in the hafnia, samples were prepared for cross-section TEM, to provide high-resolution imaging of the film growth structure. Samples were prepared from multilayers consisting of hafnia layers deposited at 0.3 to 1.2 Å/s, alternated with identical silica layers, to determine the influence of changing process conditions within a single sample. Images of hafnia layers deposited at rates of 0.3 and 1.2 Å/s are shown in Fig. 114.60. Selected area electron diffraction and microdiffraction were used with a spot size of the order of 2 nm in an attempt to ascertain the presence of any crystalline nature to the hafnia material. Neither method was able to distinguish the presence of crystallites, although this may indicate that this method is not sufficiently sensitive on the thin TEM samples to properly evaluate crystalline content of these films.
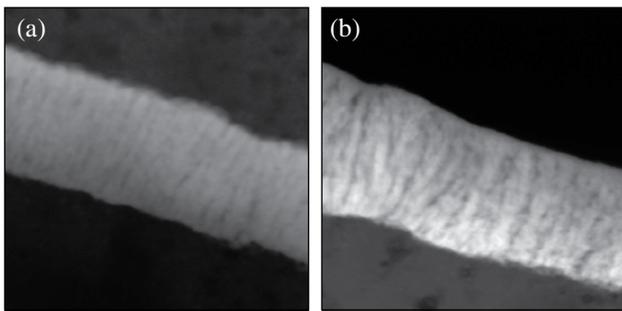
G8215JR

Figure 114.60
(a) TEM image of a layer of hafnia deposited at 1.2 Å/s in an O_2 backfill of 2.0×10^{-4} Torr. Columns are relatively distinct and perpendicular to the substrate surface. (b) TEM image of a layer consisting of hafnia deposited at 0.3 Å/s in an O_2 backfill of 4.0×10^{-4} Torr. Columns are not as distinct (more branching), and the film exhibits a greater porosity than that deposited at a higher rate. Image is in dark field, 126×126 nm.

Finally, XRD measurements of the hafnia films on samples "E" and "H" were collected using a Phillips MRD diffractometer with a Cu K_α source to evaluate the crystallinity of the hafnia structure. The coated sample was oriented in a near-grazing incidence configuration, with the incident angle $\theta = 2.2°$ and the diffracted angle 2θ incremented in steps of 0.02°, with a 13-s integration time at each position. The resulting scans are shown in Fig. 114.61.

Analysis of Hafnia Performance
The spectral transmission measurements of all of the samples in Fig. 114.58 were analyzed by fitting the measured data to a Sellmeier dispersion relationship, given by[24]

$$n^2(\lambda) = A_0 + \frac{A_1\lambda^2}{\lambda^2 - A_2},$$ (1)

where n is the wavelength-dependent real part of the index of refraction, λ is the wavelength, and A_i are the calculated constants allowing the experimental data to be fit. The refractive-index data and film thickness can be used to directly determine the theoretical transmittance of the coating by any of the standard film performance calculations or software.[24] The real part of the refractive indices determined for each of the samples is depicted in Fig. 114.62. Reducing the deposition rate decreases the real refractive index, while an increase in the oxygen backfill pressure further decreases the real refractive index. This decrease in refractive index indicates a change in the density of the film, which corresponds to an increase in film porosity. This may be experimentally observed by changes in the mechanical stability of the material and the influence of relative humidity on the film's optical thickness, which increases for highly porous films.

Results of the laser-damage testing indicate two primary features of interest. First, there is a distinct increase in the laser-damage threshold as the deposition rate is decreased. This was explored further for deposition rates below 0.3Å/s for a backfill of 2.0×10^{-4} Torr. Deposition rates of 0.2 and 0.1Å/s exhibited damage thresholds within the measurement
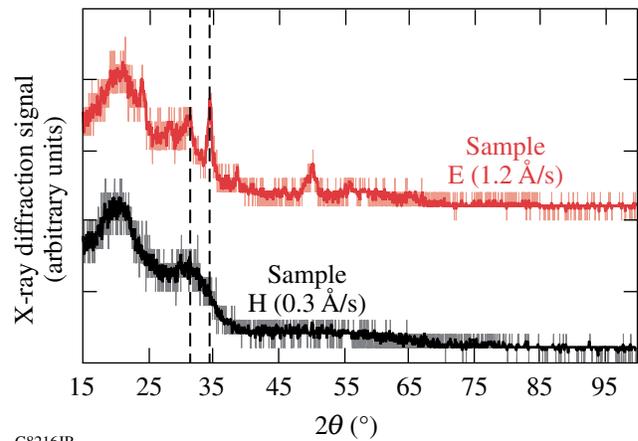
G8216JR

Figure 114.61
X-ray diffraction analysis of hafnia films deposited on silica substrates. Samples were measured in a grazing-incidence configuration, with $\theta_{incident} = 2.2°$ and 2θ incremented in steps of 0.02°, with a 13-s integration time at each position. The signal is background subtracted and smoothed with a boxcar average to clarify the diffraction peaks. As the deposition rate is increased, there is a clear increase in the crystalline signature for the film.
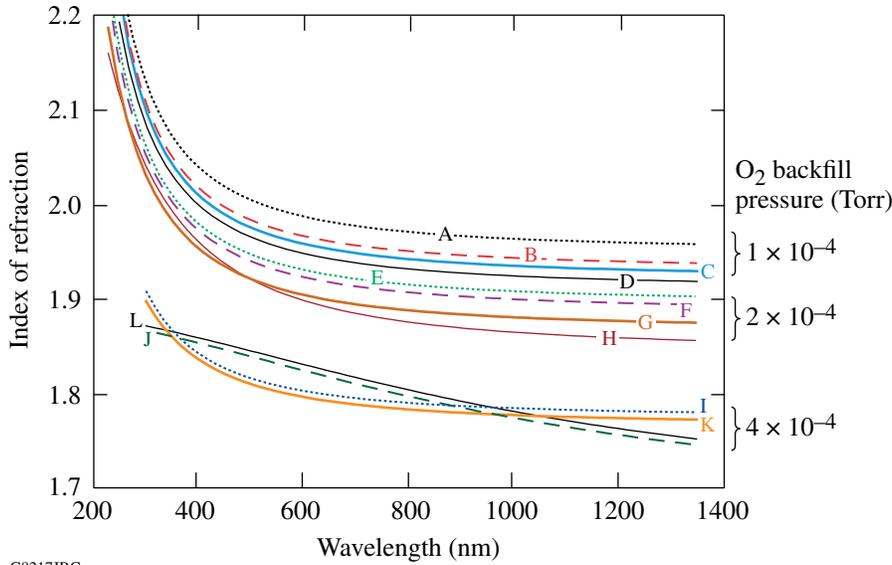
Figure 114.62
Modeled refractive indices for each of the hafnia-coated samples indicate a dependence on O_2 backfill and deposition rate. An increase in the O_2 backfill significantly reduces the hafnia refractive index, while a decrease in the deposition rate provides a lesser reduction in refractive index. Samples prepared with a backfill pressure of 4.0×10^{-4} Torr appear to have an abnormal dispersion curve, with a relatively poor fit to the Sellmeir function. This is likely due to the presence of scatter at shorter wavelengths, which also reduces transmittance.

uncertainty of each other, indicating that further decreasing the rate below 0.2 Å/s is not beneficial. Second, the laser-damage resistance at higher deposition rates is independent of the oxygen backfill pressure for the two "typical" backfill pressures (1×10^{-4} and 2×10^{-4} Torr), but a high oxygen backfill pressure of 4×10^{-4} Torr provides a substantial benefit. This likely indicates that the reduction in damage resistance at high deposition rates is not due to oxygen/hafnium adatom arrival ratios, and a resulting improvement in film stoichiometry, but some other effect of the relative deposition rates, such as film density. Hacker *et al.* argue that oxygen in excess of that needed for stoichiometric oxides benefits laser-damage resistance by increasing film porosity due to increased evaporant flux collisions with oxygen that may provide a mechanism for additional oxygen incorporation in the film.[3] This excess oxygen influences the behavior of absorptive regions in the film undergoing heating during laser interactions, as well as during recrystallization and oxidation/reduction reactions. It may saturate regions susceptible to damage, providing excess oxygen during melting and cooling, and significantly increasing the probability of formation and preservation of stoichiometric material.

Conversely, laser-damage resistance at very low deposition rates depends significantly on oxygen backfill pressure, denoting the absence of this other effect. It is suggested that this difference in laser-damage resistance is due to the presence, or lack thereof, of nanoclusters of hafnium metal (or oxide) deposited within the film. As the deposition rate is increased, the hafnium source must be heated more aggressively with a

higher electron-beam current. This added energy increases the probability of ejecting very small solid particulates from the source, creating defects that will limit the laser-damage resistance. The laser-damage threshold appears independent of oxygen backfill for rates in the 0.6 to 1.2 Å/s range, except for the highest backfill pressure of 4×10^{-4} Torr, where there is a dramatic improvement. The reason for this notable improvement is not known but may relate to the interaction of the nanocluster during formation or in the surrounding film structure with the available oxygen. Further investigation is necessary to better understand this phenomenon. As the deposition rate is decreased, and the presence of these nanocluster defects is reduced or eliminated, the absorption in the film becomes the limiting damage criterion and the presence of additional oxygen further improves the film stoichiometry.

XRD Analysis

To verify the potential presence of nanoclusters or other inclusions within the hafnia film, two of the monolayers were characterized using XRD. It was expected that the nanoclusters would exhibit the crystalline nature of the hafnium source material or would be oxidized like the hafnium dioxide film, so these signatures were sought in the diffraction patterns. The size of any crystallites present may be determined based on the peak broadening given by Scherrer's equation:[25]

$$t = \frac{0.9\lambda}{B \cos \theta_B}, \tag{2}$$

where t is the crystallite size, λ is the wavelength of the x-ray illumination, B is the width of the diffraction peak in radians,

and θ_B is one-half the diffracted angle ($2\theta_B$) of the x-ray radiation. The diffraction patterns of samples E and H are shown in Fig. 114.61.

The first goal in evaluating the films with XRD is to detect the presence of crystalline nanoclusters, but of equal importance is the identification of the phase of any film inclusions. The presence of a metal inclusion, versus an oxide inclusion, should significantly affect the absorption, thermal conductivity, and resulting influence on laser-damage resistance for the component. Samples E and H exhibit a clear difference in crystallinity, as illustrated in Fig. 114.61, although the overall magnitude of the diffraction peaks is quite low, as evidenced by the relative degree of noise surrounding the peaks. The diffraction peaks observed for sample E can be analyzed to determine the phase content in the crystalline inclusions using Philips X'Pert HighScore XRD software.[26] Peak locations clearly indicate that the crystalline phase present is hafnium dioxide, not hafnium metal.

The widths of the peaks in the scan of sample E were determined to calculate the size of the crystalline inclusions. The peak at 34.59° has a measured width of 0.47°, but this is actually a double peak as indicated in hafnia reference file 78-0049 of the ICDD database. The peak at 31.44° is a good single peak with a width of 0.96°. This leads to a calculated crystallite size of 9.7 nm, in good agreement with the maximum 10-nm inclusion size determined by thermal modeling of laser-damage morphology.[23]

Application to Mirror Fabrication

The ultimate goal of this effort is to produce a mirror with a greater ability to withstand high incident laser fluence at 351 nm. Such a mirror typically consists of alternating quarter-wave optical thicknesses of hafnia and silica, so that constructive interference will lead to greater than 99% reflectivity of the incident intensity. Previous tests of silica monolayers show that the laser-damage resistance is significantly higher than that of hafnia.[4] The highest laser-damage resistance for a hafnia monolayer in this study was achieved with the lowest deposition rate (0.3 Å/s) and high oxygen backfill pressure. In order to reduce scatter, the oxygen backfill pressure was limited to 2.0×10^{-4} Torr.

A 23-layer mirror design was established to achieve the desired reflectance at 351 nm at near-normal incidence. The spectral performance of the deposited mirror shown in Fig. 114.63 is shifted to a slightly shorter wavelength than the targeted 351-nm central wavelength.


G8218JRC
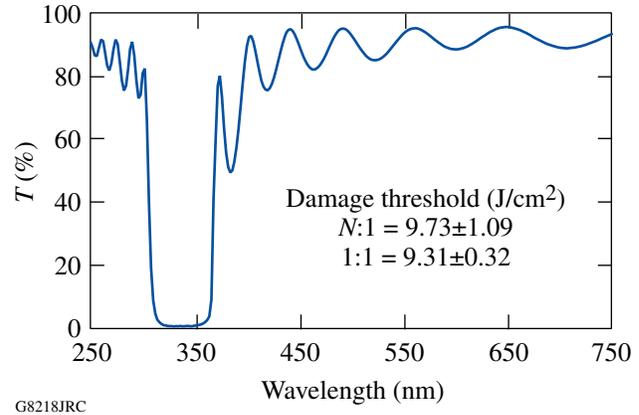
Figure 114.63
Spectral performance of a 23-layer mirror designed for near-normal incidence at 351 nm and produced by the deposition process used for sample H.

Laser-based reflectometry measurements at 351 nm indicate that the reflectivity of the mirror is 99.2% with approximately 0.5% loss due to scatter from the porous film structure. Laser-damage testing of this multilayer at 351 nm and 0.5-ns pulse length yields an N:1 threshold of 9.73 ± 1.09 J/cm^2, while the 1:1 procedure results in a threshold of 9.31 ± 0.32 J/cm^2. By comparison, hafnia/silica multilayers prepared with the standard process (hafnia deposition rate of 1.2 to 1.5 Å/s) in the past four years at LLE have yielded 1:1 damage thresholds of 1.16 to 5.64 J/cm^2, with an average threshold of 3.36 J/cm^2. Even when targeting defects in the improved mirror, the laser-damage resistance is substantially higher than that of any comparable mirror previously produced.

A 31-layer suppressed-electric-field design[5] was selected to further improve laser-damage resistance in the hafnia layers. The slow-rate deposition technique provides a great deal of flexibility in depositing the coating design since deposition rates and/or oxygen backfill pressures are readily varied for each layer deposited. More-rapid deposition may be utilized for layers interacting with lower-amplitude electric fields, providing not only faster processing, but also minimizing the number of necessary layers and decreasing the surface roughness and associated scatter. The electric-field profile of the outermost 14 layers of this design is illustrated in Fig. 114.64, indicating the deposition rates of any reduced-rate hafnia layers, all of which were deposited with an oxygen backfill pressure of 4×10^{-4} Torr. Laser-damage threshold of this coating undergoing N:1 testing reached 13.13 ± 1.15 J/cm^2, while the 1:1 procedure resulted in a threshold of 12.11 ± 0.51 J/cm^2.
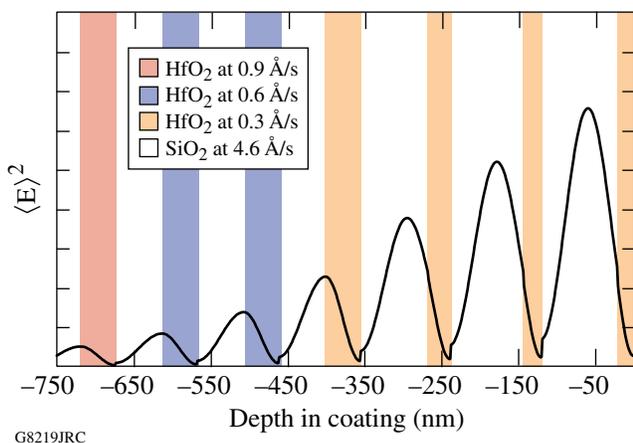
Figure 114.64

Time-averaged electric-field squared in the outer 14 layers of a hafnia/silica reflector designed for 28° incidence, p-polarization at 351 nm. The hafnia layer thicknesses are reduced from typical quarter-wave optical thicknesses in the outer layers to shift the peak electric fields into the more-damage-resistant silica layers. The deposition process is also adjusted to provide maximum laser-damage resistance in regions of the highest standing-wave electric-field intensity.

This testing led to the deposition of production UV transport mirrors (UVHR1 and UVHR2) for LLE's OMEGA EP Laser System. Coatings were produced on BK7 substrates with a measured N:1 laser-damage resistance at 351 nm and 0.5-ns pulse duration, ranging from 9 to 16.63 J/cm^2. Additionally, a strong dependence of laser-damage threshold with respect to relative humidity was noted. The measured laser-damage threshold of a single sample changed from 13.08 to 16.63 J/cm^2 as the relative humidity of the testing environment increased from 24% to 44%, respectively.

Results and Discussion

It is clear that the changes in deposition parameters of evaporated hafnia films significantly alter the refractive index, crystallinity, and laser-damage resistance. XRD makes it possible to quantitatively analyze the film structure, leading to the conclusion that higher deposition rates lead to crystalline inclusions of hafnium dioxide within the amorphous structure. The presence of smaller nanocluster inclusions of hafnium metal has been hypothesized based on laser-damage morphology, but the signature of such inclusions was not observed in the XRD measurements, nor was it apparent in the electron diffraction work. If these nanoclusters are the precursor of damage, then decreasing deposition rate must be reducing the absorption cross-section of the nanoclusters. It is likely that this results from a decrease in the mean size of the nanoclusters con-

tained within the film, or possibly the thermal coupling of the cluster to the surrounding hafnia matrix. A sufficiently gentle evaporation, with a source temperature held very close to the evaporation temperature of the material, provides insufficient energy for the ejection of nanoclusters and improves the overall laser-damage resistance of the material.

The presence of a high oxygen backfill pressure can be expected to scatter coating molecules during transport from the source to the substrate, since the purpose of the vacuum is to increase the mean free path of the coating molecules to avoid this effect. By increasing the oxygen pressure, a greater percentage of the coating will be scattered and the film will condense with less energy at the substrate surface.[17] This energy reduction leads to a more porous film, with reduced mechanical integrity, but, as shown, the laser-damage resistance is significantly improved.

The porosity and resulting influence on the optical properties of the film may explain the relationship between relative humidity and film performance, as past experience has shown a decrease of approximately 2.7% in optical thickness for films in nominal 40% relative humidity versus purged or vacuum environments with approximately 0% relative humidity. This would lead to changes in the standing-wave electric-field profile, altering intensities within the layers and the corresponding damage thresholds. However, it is also possible that the presence of additional moisture increases the available oxygen within the film, decreasing both the hafnium-to-oxygen ratio and the absorption.[3]

It is expected that chamber geometry and e-beam sweep pattern play a significant role in the rate dependence of hafnia deposition. If the nanocluster explanation is accurate, then chamber geometries that provide a greater deposited film rate for an equivalent source heating would lead to a shifting of the inflection point in the damage graph to higher deposition rates. If the absorption and subsequent damage are primarily due to film non-stoichiometry, then higher deposition rates due to changing geometry should lead to further reductions in laser-damage resistance as oxidation becomes more incomplete. Further investigation of the film structure due to the process modifications, as well as the fundamental cause of the change in laser-damage resistance, is necessary to better understand and utilize these results.

Future Work

Reducing the deposition rate for slow film growth substantially improves laser-damage performance at 351 nm.

Further work is needed to verify the change in the size of the crystalline inclusions, using cross-section and plan-view TEM imaging. Process modifications for e-beam evaporation will be extended to deposition rates below 0.3 Å and higher oxygen backfill pressures during reactive deposition to further improve laser-damage resistance. The influence of the changing film morphology—specifically reduced density leading to potentially higher scatter in the UV—will also be explored to determine the impact on optical and mechanical properties of multilayer coatings. Texture of the film crystallinity should be investigated with XRD to better separate nucleation and film structure from the crystalline signature of film inclusions.

Conclusions

Laser-damage testing of samples processed under different deposition conditions clearly suggests that multiple factors are influencing the damage resistance of the layers. It is hypothesized that, at higher deposition rates, nanoclusters of hafnium metal are ejected from the source and embedded within the growing film, reducing the laser-damage threshold of the material. These clusters are sufficiently small that oxidation is still complete, but the presence of the crystalline inclusion in the overall amorphous structure leads to a degradation of laser-damage resistance. By reducing deposition rates, the range of cluster sizes and the corresponding absorption cross-section is also reduced, enhancing laser-damage resistance. The manipulation of the film porosity and damage resistance through the use of deposition rate and oxygen backfill pressure provides the freedom to modify only those layers interacting with the highest-intensity electric fields, where laser damage is most likely to occur. The use of this process adjustment results in significantly higher laser-damage resistance for multilayer hafnia/silica mirrors at 351 nm.

REFERENCES

1. A. M. Piegari, M. R. Perrone, and M. L. Protopapa, in *Sixth Conference on Optics: 2000*, edited by V. I. Vlad (SPIE, Bellingham, WA, 2001), Vol. 4430, pp. 869–881.

2. M. Reichling, A. Bodemann, and N. Kaiser, Thin Solid Films **320**, 264 (1998).

3. E. J. Hacker, H. Lauth, and P. Weissbrodt, in *Laser-Induced Damage in Optical Materials*: 1995, edited by H. E. Bennett *et al.* (SPIE, Bellingham, WA, 1996), Vol. 2714, pp. 316–330.

4. S. Papernov, D. Zaksas, J. F. Anzellotti, D. J. Smith, A. W. Schmid, D. R. Collier, and F. A. Carbone, in *Laser-Induced Damage in Optical Materials: 1997*, edited by G. J. Exarhos *et al.* (SPIE, Bellingham, WA, 1998), Vol. 3244, pp. 434–445.

5. J. H. Apfel, Appl. Opt. **19**, 1880 (1977).

6. M. L. Protopapa *et al.*, J. Vac. Sci. Technol. A **20**, 643 (2002).

7. J. B. Oliver and D. Talbot, Appl. Opt. **45** 3097 (2006).

8. J. B. Oliver, J. Howe, A. Rigatti, D. J. Smith, and C. Stolz, in *Optical Interference Coatings*, OSA Technical Digest (Optical Society of America, Washington, DC, 2001), p. ThD2.

9. J. DiJon *et al.*, in *Laser-Induced Damage in Optical Materials: 1999*, edited by G. J. Exarhos *et al.* (SPIE, Bellingham, WA, 2000), Vol. 3902, pp. 158–168.

10. C. J. Stolz, C. L. Weinzapfel, A. L. Rigatti, J. B. Oliver, J. Taniguchi, R. P. Bevis, and J. S. Rajasansi, in A*dvances in Mirror Technology for X-Ray, EUV Lithography, Laser, and Other Applications*, edited by A. M. Khounsary, U. Dinger, and K. Ota (SPIE, Bellingham, WA, 2004), Vol. 5193, pp. 50–58.

11. R. Thielsch, A. Gatto, and N. Kaiser, Appl. Opt. **41**, 3211 (2002).

12. B. Andre, J. Dijon, and B. Rafin, U.S. Patent No. 7,037,595 (2 May 2006).

13. H. Leplan *et al.*, J. Appl. Phys. **78**, 962 (1995).

14. R. Chow *et al.*, Appl. Opt. **32**, 5567 (1993).

15. C. J. Stolz *et al.*, in *Advances in Optical Interference Coatings*, edited by C. Amra and H. A. Macleod (SPIE, Bellingham, WA, 1999), Vol. 3738, pp. 318–324.

16. L. B. Freund and S. Suresh, *Thin Film Materials: Stress, Defect Formation, and Surface Evolution* (Cambridge University Press, Cambridge, England, 2003).

17. M. Ohring, *Materials Science of Thin Films: Deposition and Structure*, 2nd ed. (Academic Press, San Diego, 2002), pp. 723–730.

18. J. A. Floro *et al.*, MRS Bull. **27**, 19 (2002).

19. A. V. Tikhonravov *et al.*, Appl. Opt. **42**, 5140 (2003).

20. B. A. Movchan and A. V. Demchishin, Fiz. Met. Metalloved **28**, 653 (1969).

21. J. V. Sanders, in *Chemisorption and Reactions on Metallic Films*, edited by J. R. Anderson, Physical Chemistry, A Series of Monographs (Academic Press, London, 1971), pp. 1–38.

22. J. A. Thorton, in *Modeling of Optical Thin Films*, edited by M. R. Jacobson (SPIE, Bellingham, WA, 1988), Vol. 821, pp. 95–103.

23. S. Papernov and A. W. Schmid, J. Appl. Phys. **82**, 5422 (1997).

24. A. V. Tikhonravov and M. K. Trubetskov, OptiLayer Thin Film Software, Optilayer Ltd., http://www.optilayer.com (9 June 2005).

25. B. D. Cullity, *Elements of X-Ray Diffraction*, 2nd ed. (Addison-Wesley, Reading, MA, 1978).

26. PANalytical, Inc., Westborough, MA 01581 (see http://www.panalytical.com).

Development and Demonstration of Large-Aperture Tiled-Grating Compressors for the OMEGA EP Petawatt-Class Laser System

Introduction

The OMEGA EP chirped-pulse–amplification system at LLE requires two 1.5-m large-aperture grating compressors to achieve high-energy petawatt capability.[1] The current state-of-the-art multilayer dielectric (MLD) diffraction gratings cannot meet this size requirement.[2] Several institutes have explored the possibility of tiling gratings.[3–6] Kessler and Cotel have demonstrated the coherent addition of small-scale gold gratings in a compressor using a far-field method.[5,6]

Due to the wavefront of large gratings and the general difficulty in achieving diffraction-limited, far-field performance with a 0.5-m-aperture beam, a far-field method alone cannot provide sufficient tiling accuracy for large-scale grating tiling. We have developed and automated an interferometric tiling method and, for the first time, demonstrated a 1.5-m tiled-grating assembly (TGA) composed of three full-size gratings (0.47 m × 0.43 m, 0.5 m in diagonal).[7] In this article, we report the first demonstration of two large-aperture tiled-grating compressors. The architecture and tiling performance of all eight TGA's developed for the two compressors of OMEGA EP are reported. The tiling technique and the method used for constructing a tiled-grating compressor are described. The full spatial and temporal performance of the tiled-grating compressors is reported.

The following sections (1) describe the pulse compression architecture of OMEGA EP and the development of the tiled-grating assemblies; (2) analyze tiling effect on focal-spot performance and the method for constructing a tiled-grating compressor; (3) present the near-field tiling technique in vacuum and the performance of each tiled TGA; and (4) report on tiling optimization and the characterization of the spatial and temporal performances.

OMEGA EP Pulse-Compression Architecture and Tiled-Grating-Assembly Development

OMEGA EP has two separate grating compressors that produce two short-pulse beams (1 ~ 100 ps). Figure 115.1(a) shows the pulse-compression scheme for OMEGA EP. Each compressor consists of four sets of TGA's, each having three 0.47-m × 0.43-m gratings. In total, eight TGA's and 24 grating tiles are required to construct the two compressors. The beam size of the OMEGA EP laser is 0.37 m × 0.37 m. The incident angle on TGA1 is 72.5°, which offers a large pulse-compression ratio and relaxes the damage-threshold requirements for the gratings. Figure 115.1(b) shows the rear view of one TGA, which holds three full-size OMEGA EP grating tiles. Each tile is mounted on a triangular support frame. All three tile support frames are mounted on a mechanical platform, with the center support frame fixed to the mechanical platform to provide structural stability. The mechanical platform is positioned on a rotary stage, which allows the entire TGA to rotate between
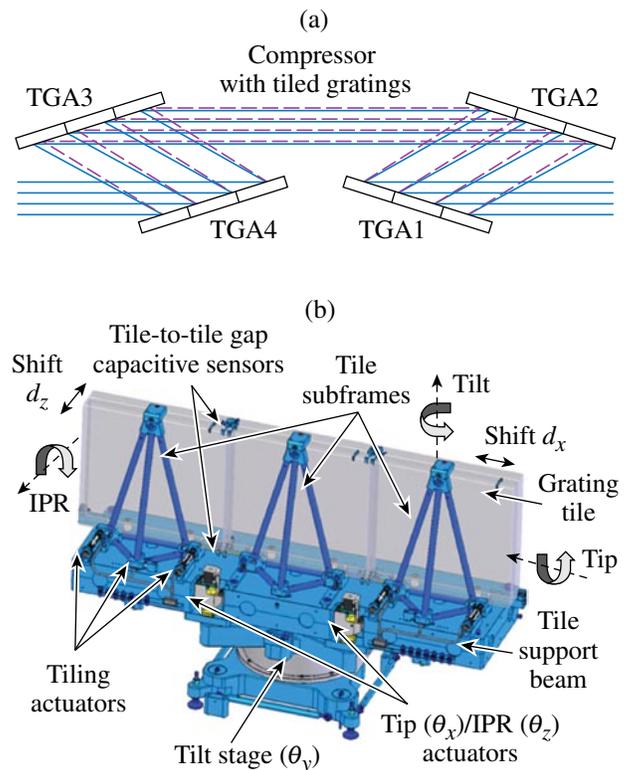
Figure 115.1

(a) OMEGA EP compressor consists of four tiled-grating assemblies (TGA's). The size of each TGA is 1.41 m × 0.43 m. (b) TGA assembly and tiling parameters.

–175° to +175° (θ_y rotation). Tip (θ_x) and in-plane rotation (IPR/ θ_z) movements are provided by two motorized linear actuators mounted on the back of the mechanical platform.

Tile-to-tile alignment is realized by maintaining the central tile static and by moving the two outboard tiles relative to the central tile. For each outboard tile, there are six degrees of freedom relative to the central tile: tilt θ_y, tip θ_x, IPR θ_z, lateral shift d_x, longitudinal shift (also referred to as piston d_z), and relative groove-spacing change Δ_d. The six parameters form three independent pairs: piston and lateral shift, tip and IPR, and tilt and groove spacing change. The two parameters within each pair compensate each other;[8] therefore, each of the outboard tile support frames incorporates only three electrostrictive actuators to provide tile-to-tile alignment by modifying tip, tilt, and piston. Each actuator is paired with a capacitive sensor to form a closed control loop to hold its position. The resolution for holding the position of an actuator is ±4 nm. For coarse alignment, the TGA is positioned at normal and Littrow angles iteratively to remove the tip and IPR of the central tile by adjusting the two linear actuators. The grating grooves of outboard tiles can be aligned to that of the central tile by manually adjusting the tip and IPR through three screws underneath the tile support beam. The initial aligned position is determined by interferometric analysis. The changes from the aligned positions in terms of piston and lateral shift, tip, and IPR are monitored by two pairs of capacitive sensors across the tile gap mounted on the top and bottom surfaces of the tile substrates. The aligned position is then maintained in real time by compensating the temporal drift of the lateral shift and the in-plane rotation with the piston and tip, respectively. Eight sets of TGA's have been built for the two compressors of OMEGA EP.

Modeling for Focal-Spot Analysis and Tiled-Compressor Construction

A ray-tracing model has been developed to perform tiling tolerance analysis for the full tiled-grating compressor system followed by an $f/2$ parabola for focusing (i.e., 12 gratings grouped in four TGA's). This model simulates the influence of misalignment on all four TGA's of a compressor taking into account the measured wavefronts of the grating tiles. The performance of a tiled-grating compressor is fundamentally determined by the initial tiling performance and the long-term stability of a TGA. The initial tiling is constrained by the interferometric measurement, which is subject to disturbance caused by turbulence and vibration; the long-term stability of a TGA is determined by environmental stability, such as temperature and vibration. Taking into account the sensitivity of the tiling interferometer and the mechanical and environmental stabil-

ity of a TGA, the best-achievable tiling accuracy for each tile of each TGA was determined to be approximately ±0.2 μrad, ±0.2 μrad, and ±0.13 μm for tilt plus groove spacing change, tip plus IPR, and piston plus lateral shift, respectively. For each OMEGA EP compressor, there are eight outboard tiles to be aligned to their corresponding central tiles. Since there are three independent tiling parameters for each tile, the total number of independent tiling parameters is 24. It is necessary to understand and predict the combined effect of the tiling errors described above on the focal spot of the tiled-grating compressor. For each outboard tile of a TGA of the compressor, the tilt, tip, and piston were chosen as the independent tiling parameters to perform a Monte Carlo tolerance analysis, i.e., each outboard tile's position in terms of tilt, tip, and piston was randomly perturbed within the tiling accuracy. This simulation was done in the case of a flat grating-tile wavefront and a measured non-flat grating-tile wavefront. For both cases, the input beam of the compressor was flat. The mean and standard deviation values of the radius of 80% encircled energy, R_{80}, and Strehl ratio were calculated for 500 runs. Figure 115.2 shows the histograms of the far-field performance of 500 randomly realized tiled-grating compressors with a tiling accuracy tilt/ tip = ±0.2 μrad and piston = 0.13 μm for the grating tiles with a flat wavefront. The mean and standard deviation of R_{80} are 4.2 μm and 0.66 μm, respectively.

The size of each of the 12 holographically recorded MLD diffraction-grating tiles is 0.47 m × 0.43 m. The state-of-the-art wavefront quality for this size of grating tile is approximately 0.25 λ (peak-to-valley), λ (wavelength) = 1053 nm. Grating wavefront error consists of a substrate mirror term due to coat-
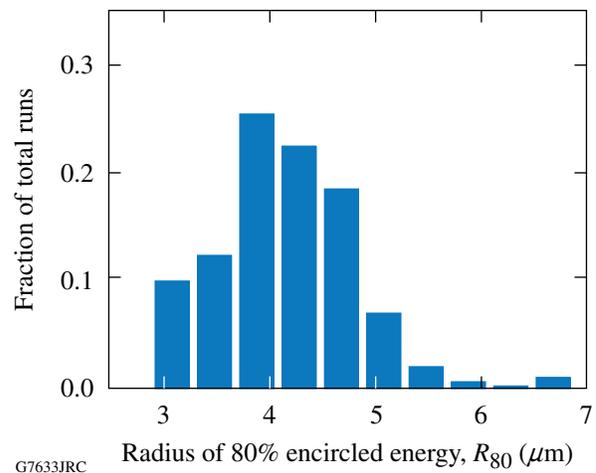

Figure 115.2
The histograms of R_{80} for 500 simulations considering the experimental tiling error and flat grating-tile wavefront.

ing and a holographic term, which could add or cancel each other, depending on the orientation of the grating relative to the beam. The final wavefront of the compressor varies with the choice, order, and orientation of each of its 12 gratings. These properties were optimized to minimize the overall wavefront of the compressor using a matrix-based procedure that considers the measured wavefront of each individual grating tile at both orientations. We have modeled the focal-spot degradation caused by the static wavefront of all grating tiles for various compressor configurations. In these simulations, the three glass substrates of each TGA are perfectly aligned, i.e., there is no tiling error. The compressor configurations producing the minimum total wavefront error were selected for actual construction. Figure 115.3(a) shows the minimized wavefront map of one realization. The peak-to-valley and rms wavefront are 0.73 λ and 0.07 λ, respectively. The corresponding R_{80} is 7.3 μm. The design baseline corresponding to a flat wavefront is 2.6 μm. A Monte Carlo tiling-tolerance analysis predicted the focal-spot degradation under imperfect tiling conditions by using the measured wavefront of the tiles and the experimental tiling accuracy of tilt/tip ± 0.2 μrad and piston ± 0.13 μm. Figure 115.3(b) shows the histogram of R_{80} for 500 simulations. The mean and standard deviation of R_{80} are 7.7 μm and 0.8 μm, respectively. Considering the focal-spot size without tiling error (R_{80} = 7.3 μm) and the design baseline (R_{80} = 2.6 μm), we conclude that the focal-spot degradation is dominated by the static grating wavefront when submicroradian tiling accuracy can be achieved. We can also conclude that, given the same tiling accuracy, the focal-spot degradation caused by tiling error is greater for a compressor consisting of grating tiles with flat wavefront (R_{80} changes from 2.6 μm to 4.2 μm) than for that consisting of grating tiles with non-flat wavefront (R_{80} changes from 7.3 μm to 7.7 μm).
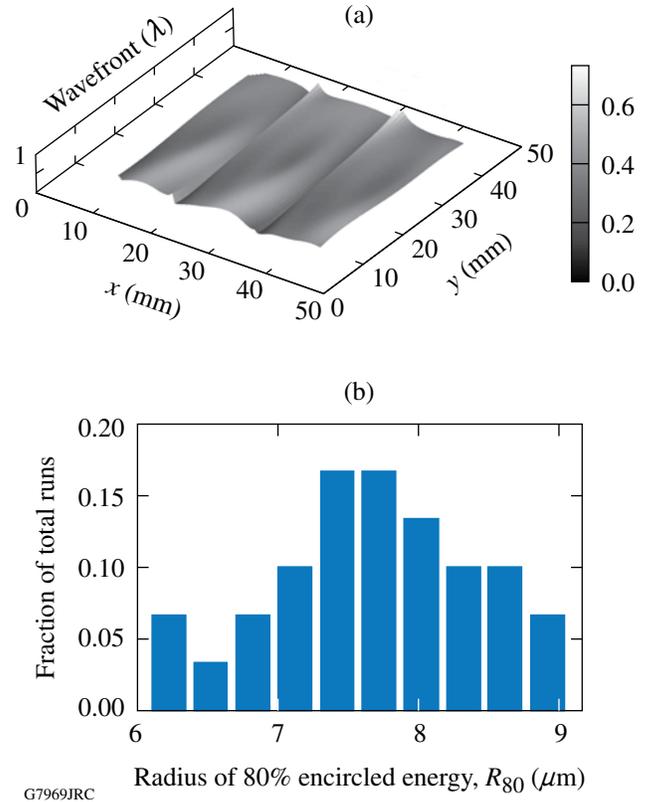
Figure 115.3

(a) The wavefront map of one compressor realization when there is no tiling error. (b) The histogram of R_{80} for 500 simulations when tiling error and grating-tile wavefront are taken into account.

Interferometric Tiling Technique in a Grating Compressor Chamber at Vacuum and the Performance of the Tiled TGA's

A 12-in.-aperture Fizeau interferometer was built for each compressor inside the grating compressor chamber (GCC) to tile individual TGA's at vacuum. The laser wavelength of the interferometer is 1053 nm. As shown in Fig. 115.4, the col-
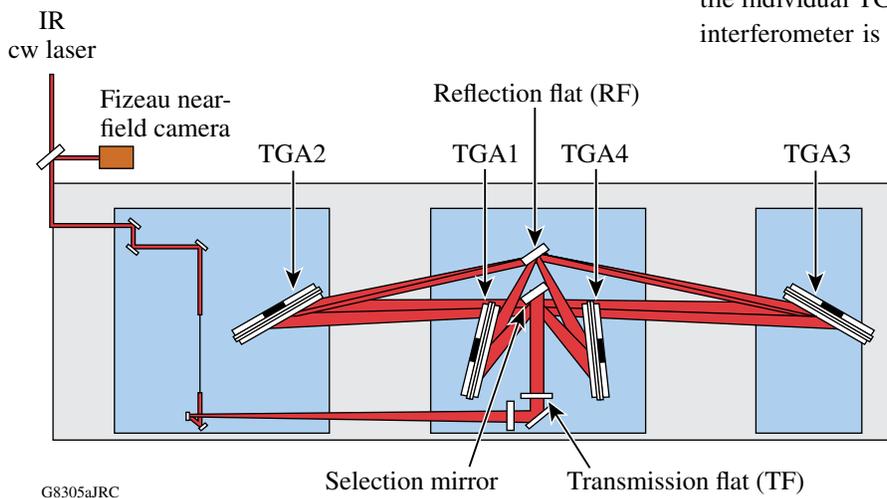
Figure 115.4

Optical layout for tiling each individual TGA with a Fizeau interferometer inside the GCC. The combined movement of the TGA selection mirror and RF makes it possible for the interferometer to see all of the gaps of the four TGA's, sequentially.

limated Fizeau beam is transmitted through the transmission flat and directed to two adjacent tiles of each one of the four TGA's by the selection mirror. The reflection flat (RF) is oriented to retroreflect the diffracted beam from each TGA at its working angle. Unique orientations of the TGA's, the selection mirror, and the RF were required to sequentially tile each of the eight gaps of four TGA's. The Fourier analysis of the resulting interferogram[9] was used to retrieve the phase of each tile and to calculate the differential tilt, tip, and piston between the central tile and an outboard tile. The differential values were used as feedback to control the tiling actuators to minimize the overall wavefront of the full TGA. This near-field tiling process has been automated.

To predict the focal-spot performance of a tiled-grating compressor, it is essential to obtain the overall wavefront and stability of a tiled TGA having three tiles. Before the TGA's were installed inside the GCC, a 24-in.-aperture Fizeau interferometer was used to tile each TGA and obtain the overall wavefront using an automated near-field method in a large-optics test facility.

Figures 115.5(a)–115.5(c) illustrate the automatic tiling process and show the phase map of the two tiles under alignment before, during, and at the end of the automatic tiling process, respectively. Minimized wavefront (rms wavefront = 0.0562 λ) of the two tiles was achieved after removing the angular and piston misalignment between the two tiles.

Figure 115.6(a) shows the overall rms wavefront of all tiled TGA's, which is under 0.08 λ. Figure 115.6(b) illustrates the typical tiling stability. The tiled wavefront of one of the eight TGA's was maintained below 0.09 λ for at least 12 h by tiling actuators in a closed control loop. The stability test was done during the night since there were many other integration activities around the interferometer area during the day. Please note: the grating compressor vacuum chamber provides a much more controlled environment.

After all of the eight TGA's were installed inside the GCC, they were retiled using the GCC interferometers. The differential angle between two adjacent tiles was measured for 12 h by the Fizeau interferometer. Figure 115.7 shows the typical

(a) rms = 0.4984 λ

(b) rms = 0.2259 λ

(c) rms = 0.0562 λ
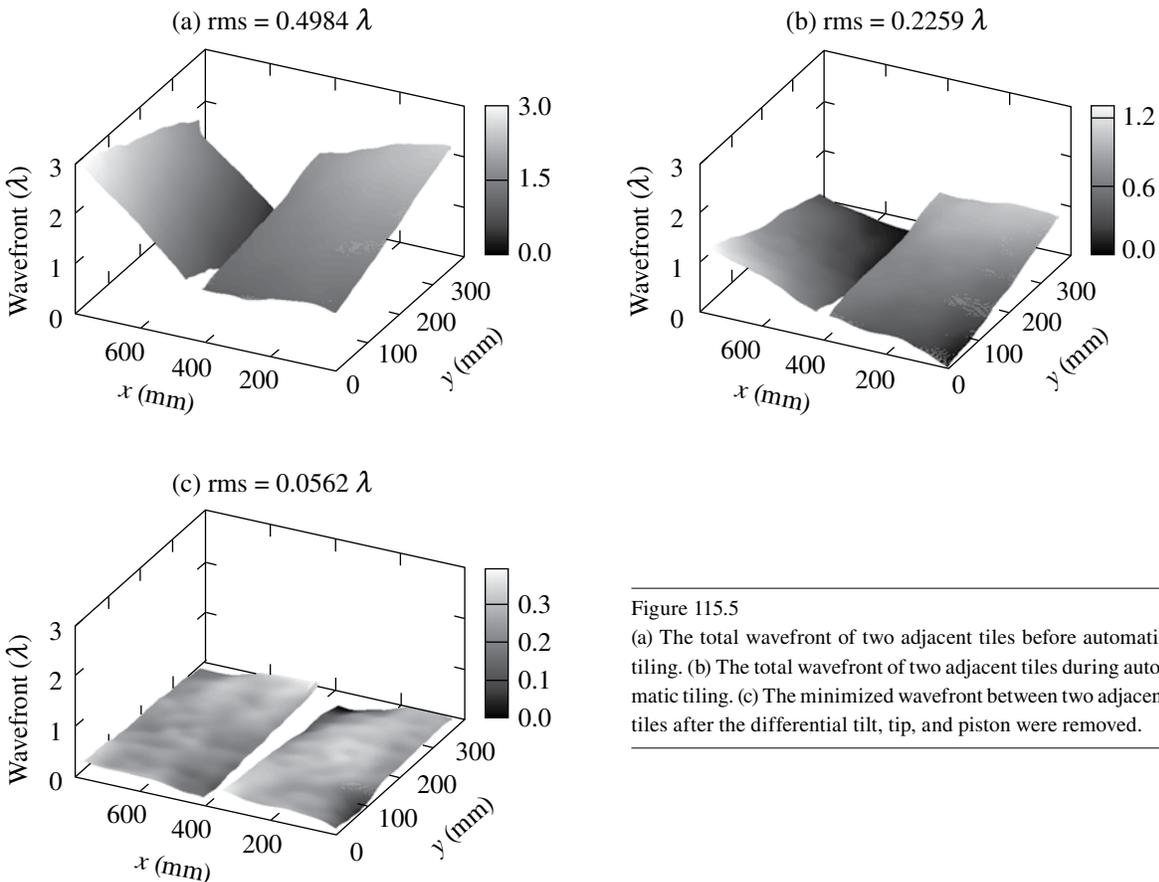
Figure 115.5
(a) The total wavefront of two adjacent tiles before automatic tiling. (b) The total wavefront of two adjacent tiles during automatic tiling. (c) The minimized wavefront between two adjacent tiles after the differential tilt, tip, and piston were removed.

E17011JR

(a)

(b)
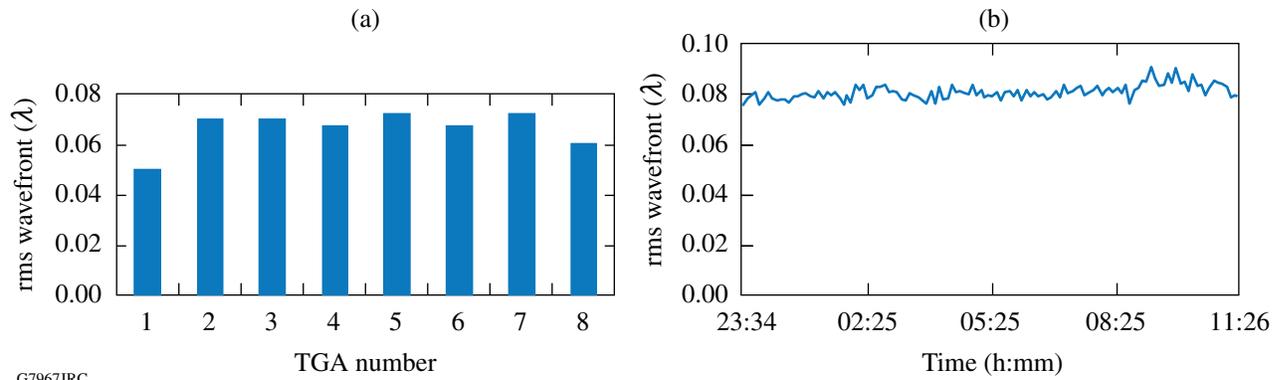
G7967JRC

Figure 115.6
(a) Root-mean-square (rms) tiled wavefronts of all eight TGA's; (b) typical wavefront stability of a tiled TGA.
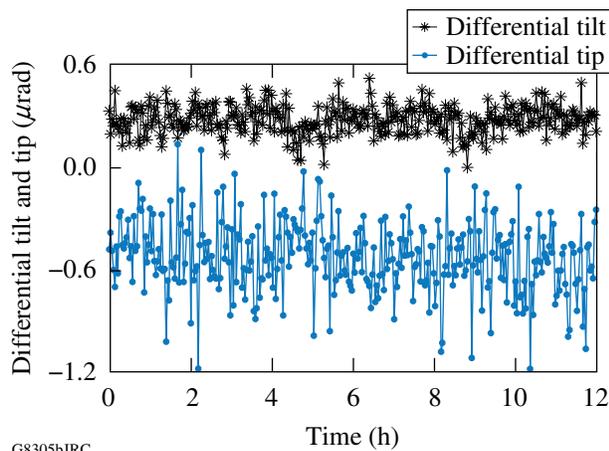
G8305bJRC

Figure 115.7
Angular tiling stability in the GCC at vacuum.

angular tiling stability in the GCC at vacuum. The standard deviation of the differential tilt (horizontal) and differential tip (vertical) is 0.1 μrad and 0.2 μrad, respectively.

Performance Characterization and Optimization of Tiled-Grating Compressors

After individual TGA tiling, the four TGA's were rotated to their previously aligned compressor position. Any residual tiling misalignment among the four outboard tiles (i.e., one tile per TGA) on the same side of the beam can be canceled using one of the tiles (see the highlighted tiles in Fig. 115.8). We chose to use the outboard tiles of TGA4 to compensate the cumulative tiling error. This was done by a far-field analysis. A tiling apodizer array with three different apertures was placed in the collimated tiling-beam space. The translation of the tiling-apodizer array limited the illumination of the compressor to one single tile, two adjacent tiles, or all three tiles at a time. The far-field pattern of two adjacent tiles is compared to that of the central tiles in order

to obtain angular misalignment and differential phase information, therefore providing feedback to drive the corresponding tiling actuators of TGA4 to remove the residual tiling error. After this tiling optimization, the three-tile apodizer is translated into the beam to evaluate the final tiling performance.

It is not possible to directly compare the focal-spot performance of the tiled-grating compressor having four sets of TGA's (a total of 12 tiles) to that of a compressor consisting of four monolithic gratings with the same aperture size due to the unavailability of the latter. To evaluate the effect of tiling on focal-spot degradation, we apodized the beam size along the tiling (horizontal) direction to construct a sub-aperture compressor consisting of only the four central tiles. The aperture-size ratio between the single-central-tile compressor and the triple-tile compressor is 1:2.95 and 1:1 along the horizontal and vertical directions, respectively. Since the two compressors have the same beam size along the vertical direction, the two vertical lineouts were compared to evaluate focal-spot degradation due to tiling. The two horizontal lineouts were compared to show the aperture ratio between the two configurations. Figures 115.9(a) and 115.9(b) show the focal spots of the single-central-tile compressor and the triple-tile compressor, respectively. Figure 115.9(c) shows a comparison between two horizontal and vertical lineouts. In these plots, f_x and f_y are the dimensions, in microradians, of the focal spot along the horizontal and vertical directions.

The full width at half maximum (FWHM) of the focal-spot lineout ratio between the single-central-tile sub-aperture compressor and the triple-tile full-aperture compressor is 3:1 and 1:1 for the horizontal and vertical directions, respectively. This is expected when comparing a sub-aperture compressor to a properly aligned full-aperture grating compressor with four monolithic gratings. The profiles of two vertical lineouts are comparable. We can conclude that tiling does not degrade the

spatial performance of the tiled-grating compressor. A triple-tile compressor delivers a tighter focal spot and three times the energy of a single-central-tile-only compressor.

After compressor alignment and grating tiling, temporal compression was optimized by changing the dispersion of the stretcher. The optical parametric chirped-pulse–amplification
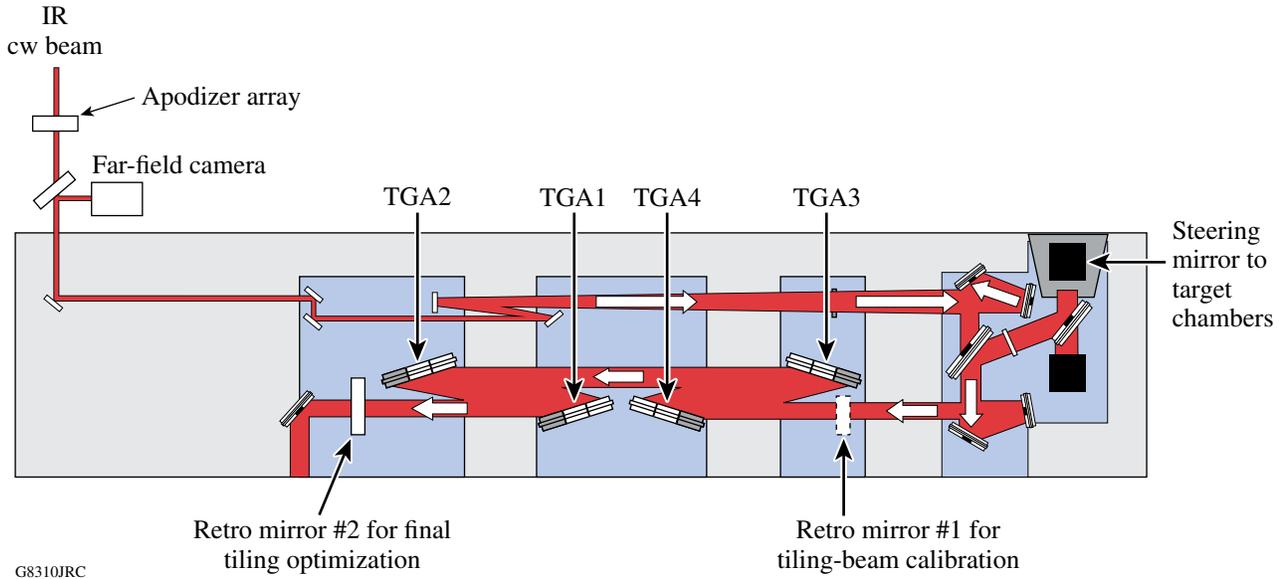
Figure 115.8
Optical layout for evaluating and optimizing overall tiling performance of the whole compressor. Before tiling optimization, retro mirror #1 was used to calibrate the far field of the tiling beam. During tiling optimization, this mirror was removed from the beam. The tiling beam went through the compressor and was reflected back by retro mirror #2. One of the four highlighted tiles was chosen to optimize the overall tiling performance.
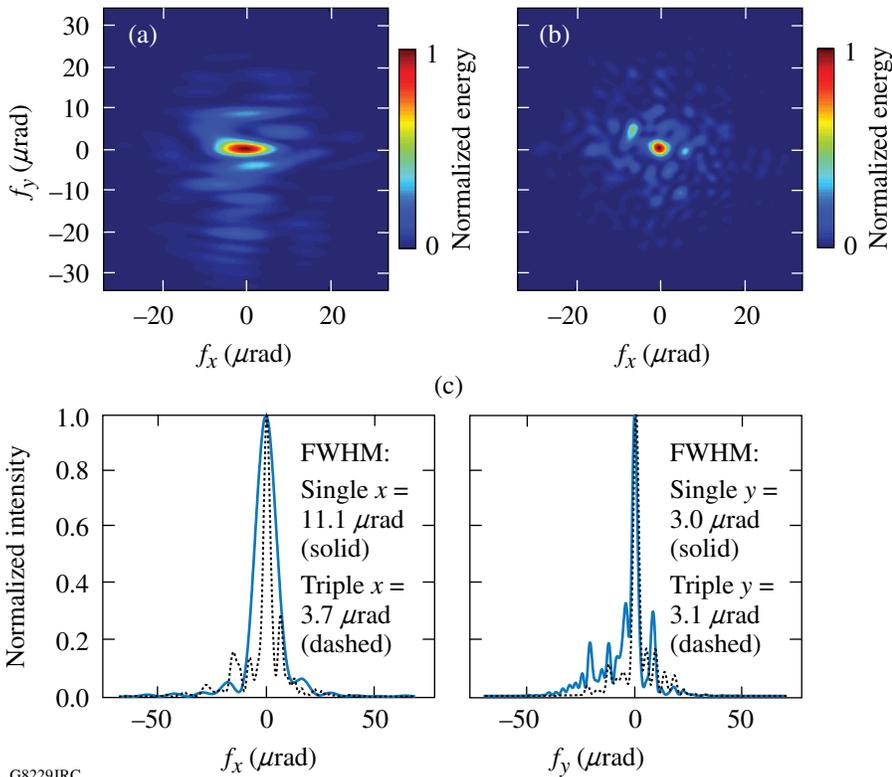
Figure 115.9
(a) Focal spot of the single-central-tile compressor; (b) focal spot of the triple-tile compressor; (c) comparison between the horizontal lineouts and vertical lineouts of the two focal spots.

(OPCPA) front end is operated at 5 Hz (Ref. 10). The autocorrelation of the output pulses was measured for both single-central-tile and triple-tile configurations for both OMEGA EP compressors. Figures 115.10(a) and 115.10(b) show the measured autocorrelations with a decorrelation factor of 1.34 (calculated from the measured spectrums). The pulse width is 630 fs for both the single-central-tile and triple-tile configurations of compressor 1. Similarly, we obtained a 600-fs pulse width for the single-central-tile and triple-tile configurations of compressor 2. The transform-limited pulse width is 400 fs and 410 fs for compressors 1 and 2, respectively. Single- and triple-tile configurations delivered the same pulse width. Therefore, there is no change in pulse duration due to tiling.
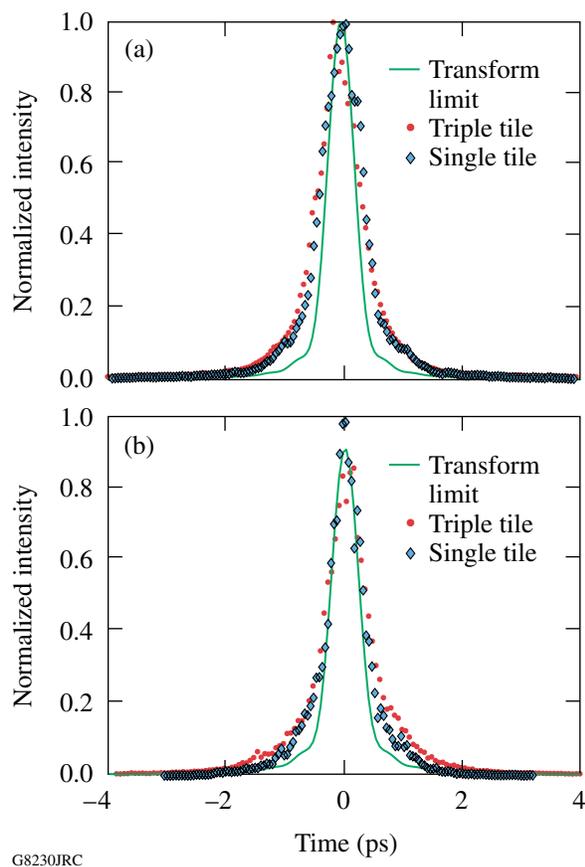
Figure 115.10

(a), (b) Autocorrelation scanning results for single-tile and triple-tile configurations for (a) compressor 1 and (b) compressor 2.

Conclusions

In conclusion, we have developed and built eight precision tiled-grating assemblies. Submicroradian tiling accuracy and stability have been achieved for all eight TGA's. A ray-tracing

model predicts that the static wavefront of the grating tiles dominates focal-spot degradations when submicroradian tiling accuracy is achieved. For the first time, we demonstrated pulse compression in two 1.5-m, large-aperture tiled-grating compressors for the OMEGA EP high-energy, petawatt-class laser system. Measurement of the tiled-grating compressors verified the model prediction and confirmed that the focal-spot degradation caused by tiling is minimal. Output-pulse autocorrelation measurements verified that both compressors achieved subpicosecond pulse widths and there is no pulse duration change due to tiling. This demonstration opens the path for constructing even larger tiled-grating compressors (multiple meters) for high-energy, high-power OPCPA systems.

REFERENCES

1. J. H. Kelly, L. J. Waxer, V. Bagnoud, I. A. Begishev, J. Bromage, B. E. Kruschwitz, T. J. Kessler, S. J. Loucks, D. N. Maywar, R. L. McCrory, D. D. Meyerhofer, S. F. B. Morse, J. B. Oliver, A. L. Rigatti, A. W. Schmid, C. Stoeckl, S. Dalton, L. Folnsbee, M. J. Guardalben, R. Jungquist, J. Puth, M. J. Shoup III, D. Weiner, and J. D. Zuegel, J. Phys. IV France **133**, 75 (2006).

2. J. A. Britten *et al.*, in *Laser-Induced Damage in Optical Materials: 2003*, edited by G. J. Exarhos *et al.* (SPIE, Bellingham, WA, 2004), Vol. 5273, pp. 1–7.

3. T. Zhang, M. Yonemura, and Y. Kato, Opt. Commun. **145**, 367 (1998).

4. Y. Zuo *et al.*, Opt. Lett. **32**, 280 (2007).

5. T. J. Kessler, J. Bunkenburg, H. Huang, A. Kozlov, and D. D. Meyerhofer, Opt. Lett. **29**, 635 (2004).

6. A. Cotel *et al.*, Opt. Express **15**, 2742 (2007).

7. J. Qiao, A. Kalb, M. J. Guardalben, G. King, D. Canning, and J. H. Kelly, Opt. Express **15**, 9562 (2007).

8. *LLE Review Quarterly Report* **100**, 242, Laboratory for Laser Energetics, University of Rochester, Rochester, NY, LLE Document No. DOE/SF/19460-578, NTIS Order No. PB2006-106672 (2004). (Copies may be obtained from the National Technical Information Service, Springfield, VA 22161.)

9. M. Takeda, H. Ina, and S. Kobayashi, J. Opt. Soc. Am. **72**, 156 (1982).

10. V. Bagnoud, I. A. Begishev, M. J. Guardalben, J. Puth, and J. D. Zuegel, Opt. Lett. **30**, 1843 (2005).

Fast-Ignition Target Design and Experimental-Concept Validation on OMEGA

Introduction

The fast-ignitor concept for inertial confinement fusion[1,2] has shown significant promise due to successful small-scale integrated experiments.[3,4] It makes it possible to use lower driver energies than conventional hot-spot ignition[5] and has the potential for higher gains. The fast-ignitor concept separates the fuel assembly and fuel heating by using an ultrafast laser in addition to a driver that compresses the fuel to high density. The ultrafast laser produces relativistic electrons with high efficiency (up to 50% has been reported[6]) that heat the fuel. Options for the compression driver are laser or heavy-ion-beam–heated hohlraums or laser direct drive.[7]

Many challenges remain for the fast-ignitor concept. The first is to demonstrate the required compression of the fuel to areal densities required for ignition. The conversion efficiency from ultrafast laser to energetic electrons must be high at ignition-relevant intensities, energies, and pulse lengths. The energy distribution of the hot electrons must be compatible with the areal density of the compressed core to ensure that the electrons deposit most of their energy into a hot spot of at least 0.3 g/cc cm (Ref. 8). Another challenge is the transport of relativistic electrons from the critical-density region ($n_e \sim 10^{21}$ cm^{-3} for a typical 1-μm laser), where the ultrafast laser is absorbed and converted into electrons, to the compressed fuel—a distance that can be hundreds of microns in an ignition-scale target. For an electron-beam divergence of $\sim$20°, the overlap between the electron beam originating from a small focal spot ($\sim$10-μm radius) and the dense core with a diameter of <50 μm would be very small.[9,10] Two solutions have been proposed to minimize this standoff distance: a channeling beam to bore a hole in the plasma atmosphere around the core,[2,11] which would allow the ultrafast laser to be absorbed closer to the core, and a re-entrant cone to keep the path of the ultrafast laser free of plasma and bring it as close as possible to the dense core.[3,12] The cone-in-shell concept, while advantageous with respect to the electron transport, breaks the symmetry of the spherical fuel assembly, which could limit the fuel areal density that can be achieved with a given driver energy. Another issue for cone-in-shell targets is plasma filling the inside of the cone from the

shock wave that the high-pressure core plasma sends through the gold cone. Self-generated electromagnetic fields from the propagation of the electron beam in plasma will modify both the transport and the energy-deposition characteristics. The transport and energy deposition of the fusion alpha particles in near-ignition plasma conditions could significantly change the plasma conditions in the assembled fuel.

All of these physics areas will be experimentally accessible with the combined OMEGA/OMEGA EP Facility at LLE. OMEGA EP[13] provides two short-pulse ($\sim$1 ps to 100 ps), high-energy laser beams with an energy of up to 2.6 kJ per beam at 1.053 μm, integrated into the existing OMEGA[14] Laser Facility (60 beam, 30 kJ at 0.35 μm). The OMEGA EP beams can be combined collinearly and coaxially and routed to either the existing OMEGA target chamber or the new OMEGA EP target chamber. The combined beams allow the channeling approach to fast ignition (FI) to be studied under realistic conditions for the first time, whereas only one beam is required for cone-in-shell experiments. The OMEGA/OMEGA EP Facility will be best suited to perform integrated fast-ignition experiments because of OMEGA's unique ability to compress cryogenic D$_2$ and DT targets.[15,16] To study alpha transport under realistic conditions, the areal density of the compressed core must be of the order of the hot-spot areal density of an ignition target, $\sim$0.3 g/cm^2 (Ref. 8), which could be achieved in high-performance cryogenic-DT implosions on OMEGA.[17]

This article describes several important components of LLE's comprehensive scientific program to investigate the physics of the fast-ignitor concept. The following sections (1) introduce the OMEGA/OMEGA EP integrated laser facility; (2) describe hydrodynamic experiments on high-areal-density implosion and fuel assembly with cone-in-shell targets; (3) discuss experiments that measure the conversion efficiency from laser light into energetic electrons and the development of a coherent transition radiation diagnostic to investigate the hot-electron transport; (4) summarize simulations of integrated fast-ignitor physics experiments on OMEGA EP and full-scale, high-gain, fast-ignition experiments; and (5) provide a short summary of the information presented.

Laser System

The OMEGA EP Laser Facility is housed in a structure on the south side of the existing OMEGA laser building (see Fig. 115.11). The OMEGA EP target chamber is due east of the existing OMEGA target chamber. The OMEGA Laser System delivers up to 30 kJ of UV light in 60 beams arrayed in a "soccer ball" symmetry for uniform illumination of spherical implosion targets.[14] OMEGA has an elaborate pulse-shaping system, which can provide up to ~4-ns-long, highly shaped pulses with a contrast of up to 100. The individual OMEGA beams are smoothed by distributed phase plates (DPP's),[18] two-dimensional smoothing by spectral dispersion[19] with 1-THz bandwidth in the UV, and polarization smoothing.[20]

The four new OMEGA EP beamlines are located to the south of the compression chamber and the new target chamber. The beamlines use a folded beam path similar to the architecture[21] of the National Ignition Facility (NIF)—an upper level that includes a 7-disk booster amplifier and a transport spatial filter, and a lower level that includes an 11-disk main amplifier, a cavity spatial filter, a plasma-electrode Pockels cell (PEPC),[22] and a deformable mirror. A second polarizer is inserted between the PEPC and the cavity spatial filter to protect the laser system against IR light reflected from the target when the beamline is operated in short-pulse mode. Two of the beams can be compressed using four 141-cm × 41-cm diffraction-grating units, with each unit consisting of three multilayer-dielectric–grating tiles.[23,24] A deformable mirror placed after the last grating unit provides further wavefront correction in each beamline. The beams are either combined before leaving the compression chamber and propagate coaxially through evacuated tubes to the OMEGA or OMEGA EP target chamber, or they can be directed into the OMEGA EP

chamber on separate paths in an orthogonal configuration. An *f*/2 off-axis parabola focuses the short-pulse beam to provide a small focal spot even with the expected phase-front distortions in such a large-scale, high-energy laser system. The beams are synchronized to each other and to the OMEGA laser pulse to better than 10-ps rms. A comprehensive set of laser diagnostics measures the laser energy, pulse duration, and, for the first time on a high-energy petawatt system, the focal-spot intensity distribution at full energy. All four beams can be used as long-pulse beams and converted into the third harmonic at 351 nm (<10 ns, up to 6.5 kJ). These beams propagate only to the OMEGA EP target chamber. The long-pulse beams are focused with *f*/6.5 lenses onto the target and are arrayed in a square with a 23° angle to their common centerline. DPP's for beam shaping will be available in 2009.

Fuel-Assembly Experiments

High fuel compression and high areal densities have been achieved on OMEGA, both with cryogenic targets[25] and room-temperature targets,[26] using highly shaped pulses that put the target on a low adiabat (ratio of the shell pressure to the Fermi-degenerate pressure). It has been shown that the areal density ρR depends primarily on the adiabat α of the target and the laser energy E:[27]

$$(\rho R)_{max} = 2.6 \Big/ \alpha^{0.54} E_{MJ}^{0.33}. \qquad (1)$$

The cryogenic targets are 10-μm-thick, ~430-μm-outer-radius CD shells, filled with D_2 to form a 95-μm-thick layer at the inside of the CD shell at cryogenic temperatures.

The pulse shape for the cryogenic target (Fig. 115.12) uses a decaying-shock-adiabat shaping picket[28] and a slowly rising

OMEGA target chamber

OMEGA EP target chamber

Main amplifiers

Beam 1 2 3 4

Booster amplifiers

OMEGA Laser Bay

Compression chamber

G6957nJRC
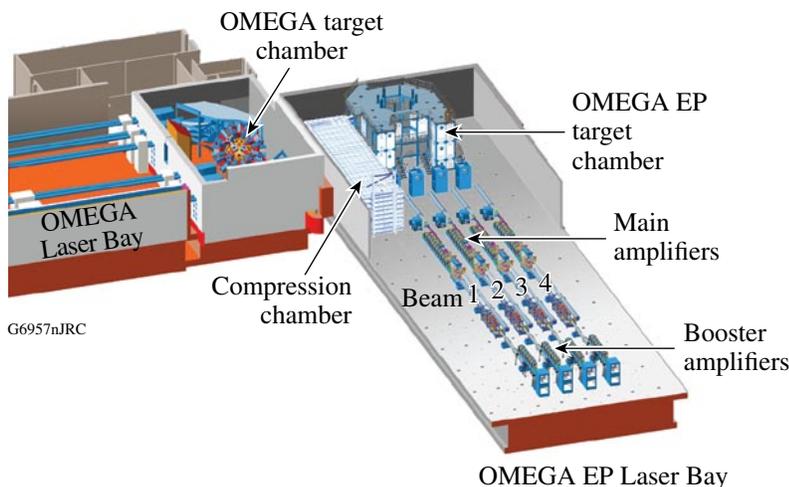
OMEGA EP Laser Bay

Figure 115.11
Schematic of the expanded OMEGA Laser Facility. The new OMEGA EP laser adjacent to the existing 60-beam OMEGA facility includes four NIF-like beamlines, a compression chamber, and a new target chamber. Two of the four beams can be run in short-pulse mode and can be directed into either target chamber. All four beams can be converted into UV and used in the OMEGA EP target chamber.

main pulse to put the cryogenic D_2 fuel on an adiabat of $\alpha \sim$ 2. The areal density of the imploded targets is inferred from the energy downshift in the secondary proton spectrum.[29] These protons are created by D^3He fusion reactions, which are secondary reactions in D_2 fuel. Figure 115.13 shows a measured secondary proton spectrum from the cryogenic target compared to 1-D *LILAC*[30] simulations.[25] An areal density of ~200 mg/cm^2 can be inferred from the spectrum, which is more than 80% of the clean 1-D predictions. The density of the compressed D_2 approaches ~100 g/cm^3—a 500-fold
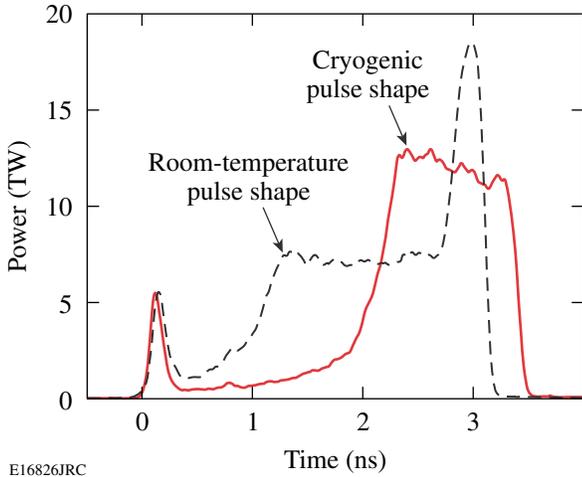
compression of the original D_2-ice density. In the room-temperature experiments, 40-μm-thick, 430-μm-outer-radius plastic shells coated outside with a 0.1-μm layer of aluminum and filled with D_2 gas with pressure ranging from 8 to 25 atm were imploded using relaxation adiabat-shaping, ~16- to 20-kJ UV laser pulses.[26,31,32] A typical experimental pulse shape that puts the room-temperature plastic targets on an adiabat of $\alpha \sim 1.5$ is shown in Fig. 115.12. A picket at the beginning of the pulse and a spike at the end of the pulse were used to optimize the implosion for high yield and high areal density. The room-temperature targets also showed areal densities of up to ~200 mg/cm^2 and densities of the order of 100 g/cm^3, which translates into a 100-fold compression.

Fuel assembly in direct-drive cone-in-shell targets has been investigated using experiments on OMEGA in both indirect-[33] and direct-drive[34] geometries, including the achievable areal densities and filling the cone with plasma. Gas-tight targets were developed for the direct-drive experiments to be able to fill the targets with D_2 or D^3He, which makes it possible to use nuclear diagnostics to measure the areal density achieved in the implosion. The targets were 24- to 40-μm-thick CH shells of ~870-μm outer diameter, with a hollow gold cone with an opening angle of 70° or 35° inserted through a hole in the shell (Fig. 115.14).[34] A step on the cone defines the distance between the cone tip and the center of the shell, typically 30±10 μm. The cone has a thickness of ~100 μm outside the shell and 10 μm inside the shell and ends in a 30-μm-thick hyperbolic-shaped tip. For some experiments the cone tip was

E16826JRC

Figure 115.12
Laser pulse shapes used in the low-adiabat OMEGA cyrogenic (solid) and room-temperature (dashed) target implosions.

TC8044JRC

Figure 115.13
Measured secondary-proton spectrum (solid line) for the cryogenic target. The dashed line shows the calculated spectrum from the 1-D hydrocode.

TC7487aJR
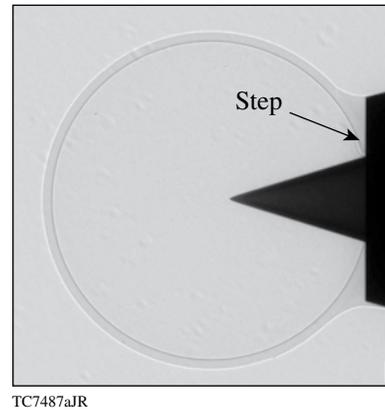
Figure 115.14
Radiograph of a gas-tight, fast-ignitor cone-in-shell target. A gold cone with an opening angle of 35° is inserted through a hole in a 24-μm-thick CH shell of ~870-μm outer diameter. A step on the cone defines the location of the cone tip at a distance of 30±10 μm to the center of the shell. It also provides a convenient interface to apply enough glue to make the assembly gas tight.

cut off to form a 15-μm-thick flat tip. Most experiments used 54 of the 60 OMEGA beams, at 351-nm wavelength, with a 1-ns square pulse and ~21 kJ of total energy or a highly shaped pulse of ~3-ns duration and ~20-kJ energy. For some experiments, 15 beams with a total energy of ~6 kJ were diverted to a backlighter foil and focused to a spot size of 600 μm. The target was irradiated using 35 of the remaining beams with ~11 kJ of laser energy.

X-ray framing cameras[35] were used to acquire backlit images of the fuel assembly around the cone tip. Figure 115.15 shows a backlit image of a cone-in-shell target (lower half) irradiated with a 1-ns square pulse at peak density compared to a 2-D *DRACO*[36] hydrodynamic simulation (upper half). The image shows a dense core ~100 μm from the cone tip, with lower-density plasma in between. An areal density of ~70 mg/cm^2 was measured for a 35° cone target using nuclear diagnostics—more than 60% of what a 1-D simulation predicts for an equivalent full sphere.[34] Mixing does not seem to be an issue in these direct-drive cone experiments,[34] and the hydro-efficiency penalty from the cone is not very big. A streaked optical pyrometer (SOP)[37] was used to investigate the filling of the inside of the cone. The high-pressure core plasma sends a shock wave through the gold cone that creates a plasma inside the cone when it breaks out. This could significantly increase the electron propagation distance. SOP uses an optical system that images the inside of the tip of the cone onto the slit of the streak camera with an ~10-μm spatial resolution and a 500-μm field of view. The breakout of the shock driven by the pressure from the core produces a short burst of light.

Figure 115.16 shows a lineout through the center of the SOP trace from a 35° cone target with a 15-μm-thick flat tip irradiated by a highly shaped pulse at 20-kJ energy, as well as the areal density of the compressed core as predicted by the 2-D hydrocode *DRACO* and the drive-laser pulse shape. The shock signal starts just after the time of peak compression as calculated by *DRACO*. The absolute timing uncertainty of SOP is estimated to be ~100 ps. This shows that with the current designs the inside of the cone is free of plasma at the time when the short-pulse laser would propagate. Since the projected range for a 1-MeV electron in gold is of the order of ~50 μm (Ref. 38), the gold tip must be as thin as possible to avoid excessive energy loss of the fast electrons. In an optimized cryogenic capsule, the core would produce a lower pressure on the cone due to the lower average ionization of hydrogenic plasma compared to CH plasma.

E16828JRC
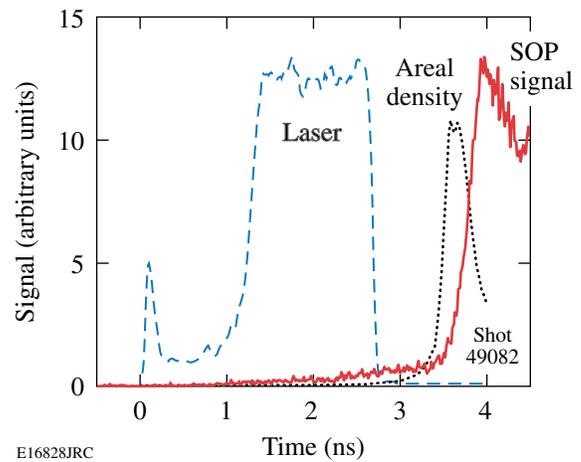
Figure 115.16
Lineout through the center of the SOP signal (solid line) of a cone-in-shell target with a 35° opening angle irradiated by a shaped pulse at 20 kJ. The dashed line shows the laser pulse power, and the dotted line represents the calculated evolution of the areal density.

TC7959JRC

Figure 115.15
Backlit framing-camera image from a target filled with 10 atm of D$_2$ and imploded using a 1-ns square pulse at 11-kJ laser energy, compared to a 2-D *DRACO* radiation hydrodynamic code simulation.

Short-Pulse Experiments and Diagnostics

The conversion efficiency from laser energy into energetic electrons $\eta_{L \to e}$ has been measured using K-shell spectroscopy of reduced-mass Cu targets.[39] It has been shown that the normalized fast-electron–induced K$_\alpha$ yield from reduced-mass targets is approximately constant above 10^{18} W/cm^2 and can be readily used to infer $\eta_{L \to e}$ (Refs. 40 and 41). The heating of these reduced-mass targets is sufficient to affect the inner-shell fluorescence probabilities.[41] Ionization of the outer shells of copper at high temperature affects the M $\longrightarrow$ K and the L $\longrightarrow$ K transition probabilities and causes a deviation in the ratio of the emitted

number of K_β and K_α photons. This is used to infer the electron temperature of the target and allows the conversion efficiency $\eta_{L\to e}$ to be inferred independently from the absolute K_α yield by using a model for the equation of state of copper.[41]

The experiments have been performed on both the Rutherford Appleton Laboratory PW facility[42] and the Multi-Terawatt (MTW) laser at LLE.[43] The Vulcan PW laser delivers up to 500 J of energy with a pulse duration as short as 0.5 ps at a wavelength of 1.054 μm, focused by an *f*/3 off-axis parabola onto the target. Roughly 30% of the laser energy is contained in a 7-μm full width at half maximum (FWHM) spot. The MTW laser delivered 1- to 5-J, 1-ps pulses at a wavelength of 1.053 μm and was focused by an *f*/2 off-axis parabola at normal incidence to the target. The focal spot has an FWHM between 4 to 6 μm containing ~50% of the laser energy, with a peak intensity of 2×10^{19} W/cm^2.

Copper foils ranging between $20 \times 20 \times 2$ μm^3 and $500 \times 500 \times 50$ μm^3 were used as targets. They were mounted by using either a 17-μm-diam silicon carbide stalk or, in the case of the smallest targets, a pair of 1-μm-diam spider silk threads.

The K-shell line radiation was measured using a single-photon–counting spectrometer[44] based on an SI 800-145 x-ray back-illuminated, charge-coupled device (CCD).[45] Various copper filters between 75 to 150 μm were used to optimize the signal-to-background ratio of the K-shell emission. Figure 115.17(a) (Ref. 39) shows the measured conversion

efficiency of laser energy into K_α photons emitted from $500 \times 500 \times 20$-μm^3 copper targets as a function of the laser intensity. The K_α photon yield increases up to intensities of 10^{18} W/cm^2 and stays constant at higher intensity. The data from Fig. 115.17 are compared to a model of K_α photon production, which assumes an exponentially distributed fast-electron spectrum $f(E) = \exp(-E/T_e)$, where T_e is calculated from the laser intensity through the ponderomotive scaling.[46]

$$T_e\,[\text{MeV}] = 0.511\left[\left(1 + I_{18}\lambda_{\mu m}^2/1.37\right)^{0.5} - 1\right], \quad (2)$$

where E is the electron energy, T_e is the electron temperature, I_{18} is the laser intensity in units of 10^{18} W/cm^2, and $\lambda_{\mu m}$ is the laser wavelength in microns. The energy loss of the fast electrons is calculated using the continuous slowing down for cold approximation solid-density copper.

The model assumes that all electrons are reflected at the target boundaries from electrostatic sheath fields[47,48] and deposit all their energy in the target (refluxing). Relativistic corrections to the copper K-shell ionization cross section[49] are included, and the only free parameter in the model is the conversion efficiency $\eta_{L\to e}$. A laser-to-electron energy-conversion efficiency $\eta_{L\to e} = (20\pm10)\%$ can be inferred by comparing the experimental data with the predictions of this model. The discrepancies in the observed K_α yield at lower laser intensities are most likely due to the assumption of ponderomotive scaling, which breaks down at a laser irradiance below 10^{18} W/cm^2 μm^2 (Ref. 46).
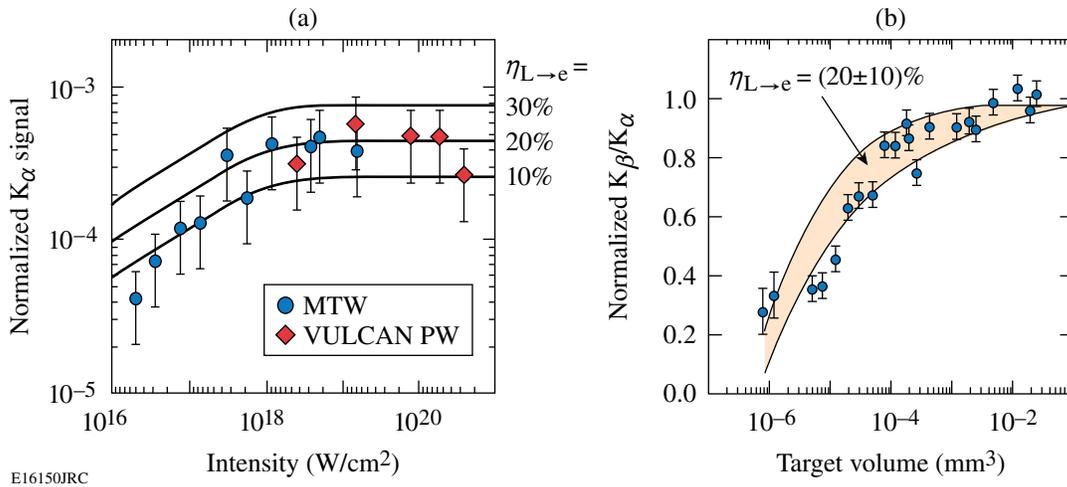
Figure 115.17
(a) Energy in K_α photons (normalized to the laser energy) emitted by a $500 \times 500 \times 20$-μm^3 copper target as a function of laser intensity. The curves correspond to the total calculated K_α yield at a given laser-to-electron-energy-conversion efficiency $\eta_{L\to e}$. (b) Ratio of the number of K_β to K_α photons (normalized to the cold material value) as a function of target volume. Numerical calculations of K_β/K_α are shown as a function of target volume caused by target heating, assuming $\eta_{L\to e} = (20\pm10)\%$.

Figure 115.17(b) (Ref. 39) shows the measurement of the change in the ratio of the number of emitted K_β and K_α photons $\left(K_\beta/K_\alpha\right)$ normalized to the cold material value as a function of the target volume at a constant laser intensity of 2×10^{19} W/cm^2. Numerical target-heating calculations using the implicit-hybrid particle-in-cell code *LSP*[50] infer the energy content of the fast electrons from the reduction in the ratio of K_β/K_α (Ref. 41). The collisional-radiative code *PrismSPECT*[51] was used to determine the target's ion-population distribution. Assuming a conversion efficiency of $\eta_{L \to e} = (20\pm10)\%$, the calculation reproduces the observed variation in the ratio $\left(K_\beta/K_\alpha\right)$ with target volume, which is consistent with the efficiencies inferred from the absolute K_α yield. This technique can be readily extended to laser energies on the multikilojoule level and pulse durations >10 ps on OMEGA EP, much closer to the fast-ignitor laser conditions as in the present small-scale experiments.

A promising technique that provides information about the transport of the energetic electrons generated in the short-pulse laser–plasma interaction is the measurement of transition radiation (TR).[52] TR is emitted when a charged particle passes through a refractive-index interface[53]—in this case, energetic electrons exiting the target into vacuum. The emit-

ted electromagnetic energy is very small for a single electron. However, the laser-generated energetic-electron distribution typically has a highly correlated longitudinal electron-density structure, which leads to a considerable coherent enhancement, producing coherent transition radiation (CTR).[54] The two dominant electron-acceleration processes produce structures at different frequencies: resonance absorption[55] accelerates electrons into the target once every optical cycle, whereas the $\vec{v} \times \vec{B}$ force[46] accelerates electrons twice every optical cycle, generating a CTR signal at the first or second harmonic of the laser frequency, respectively. The spatial-intensity distribution and spectrum of the CTR emission measured at the backside of the target provide information about the electron transport, especially the spatial distribution and divergence of the coherent part of the electron distribution exiting the target and the slope or temperature of the longitudinal energy distribution.

A transition radiation diagnostic (TRD)[56] has been developed to acquire high-resolution images of the target's rear-side optical emission at the second harmonic ($\lambda \sim 527$ nm) for experiments conducted on the MTW laser. The optical design is shown in Fig. 115.18(a) (Ref. 56). A commercial 20× infinity corrected objective[57] collects the optical emission from the target's rear

E16194JRC
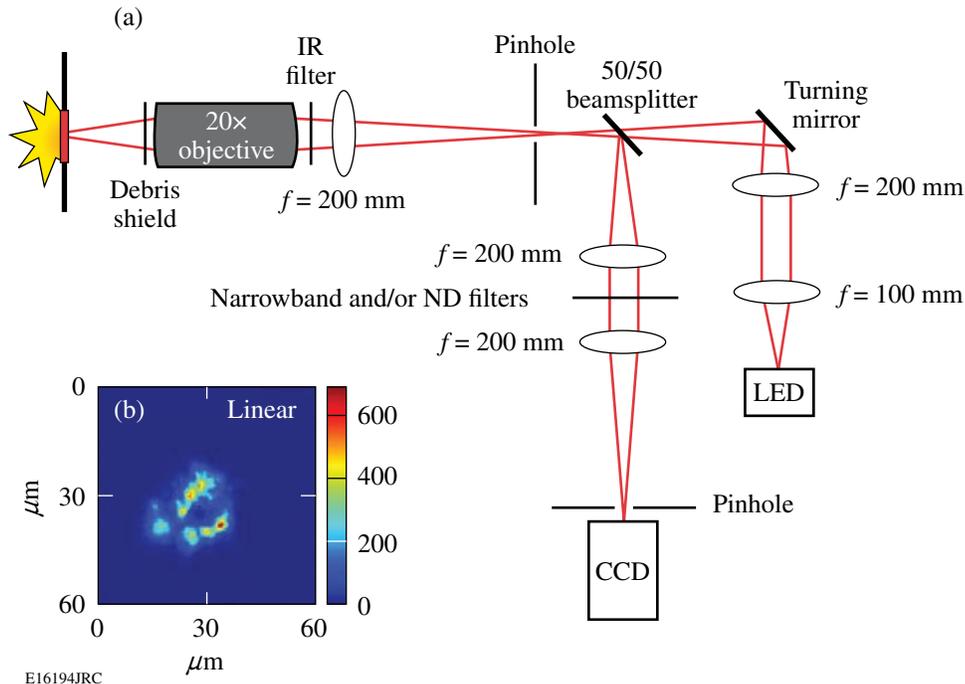
Figure 115.18
(a) Optical design of the transition radiation detector. A high-quality microscope objective and an optical system of three lenses image the rear surface of the target onto a CCD detector. Filters and pinholes are used to minimize background contributions. The right arm of the system is used for pre-shot focusing. (b) Image of the rear-side optical CTR emission from a 20-μm-thick aluminum foil. The scale is logarithmic and the intensity is expressed in arbitrary units. A number of ~2-μm-diam filaments are contained within a 15-μm-diam emission region.

surface. A sacrificial 150-μm-thick glass microscope protects the objective from target debris. The objective is mounted on a high-resolution (20-nm step), motorized, 1-D linear actuator. Filters prevent 1ω laser light from propagating and narrow the spectral acceptance of the optical system to a 24-nm band centered on $\lambda = 529$ nm. An optical system of three 200-mm-focal-length achromatic lenses and a 50/50 beam splitter transports the light to a CCD camera. This Spectral Instruments (SI) 800-series CCD uses a front-illuminated chip with 1024 × 1024, 13.5-μm × 13.5-μm pixels, thermo-electrically cooled to –40°C to minimize the dark current.[45] To obtain consistent high-resolution images of the target's rear-surface emission, the microscope objective must be positioned with ~1-μm precision relative to the rear surface of the target since its depth of focus is only 1.6 μm. The second arm of the optical system sends light from an ultrabright green LED (light-emitting diode) through the beam splitter and collection optics onto the target. The light reflected off small-scale surface features on the rear surface of the target is imaged onto the CCD camera. These features are used to obtain the best focus position for the objective. Extensive tests have shown that the optical resolution of the TRD in the optimum focus position is limited only by the CCD pixel size to ~1.4 μm over the full field of view.[56] The pinholes shown in Fig. 115.18(a) minimize the propagation of stray light through the system. The background from hard x rays is minimized by folding the optical system through 90° so that the detector can be shielded behind a 10-cm-thick lead brick wall. An additional 2-mm-thick lead shield is placed around the CCD camera to minimize single hits by scattered x rays arriving from the rear and top sides. This shielding reduces the background by more than an order of magnitude on the CCD detector.

The TRD has been used in several experiments to diagnose electron transport in solid materials. Figure 115.18(b) shows a coherent transition radiation image from the rear side of a 30-μm aluminum foil. A 5-J, 500-fs pulse from the MTW laser was focused to an ~4-μm-radius spot on the target, corresponding to a laser intensity of ~10^{19} W/cm^2. The diameter of the rear-side coherent optical emission is less than 20 μm. Structures, indicative of electron-beam filaments, superimposed on a ring-like feature are clearly visible in this region with a spatial full width at half maximum of ~2 μm. These structures are indicative of electron-beam filamentation.[58]

This instrument will be used extensively on the MTW to study the divergence and potential breakup of the electron flow through the target and to infer the slope temperature of the longitudinal electron temperature.[54] Based on the experience with this TRD on the MTW, a detector suitable for OMEGA EP is being designed.

Simulations

To understand the interaction of the electron beam with the target and its effect on the neutron production in both integrated FI experiments on OMEGA EP and high-gain FI targets, the 2-D axisymmetric radiation hydrocode DRACO was coupled with the 2-D/3-D hybrid particle-in-cell code LSP.[50] DRACO simulates the target implosion and the hydrodynamic reaction of the target to the fast-electron heating, using a realistic tabular equation of state, radiation transport, and α-particle transport in DT targets. LSP is used to simulate hot-electron transport including self-generated electromagnetic fields. The laser–plasma interaction that creates the energetic electrons is not modeled in LSP; a hot-electron distribution is created by promoting background electrons to higher energy according to a theoretical prescription such as Wilks's scaling law[46] and a constant conversion efficiency. The transport of hot electrons is currently modeled in LSP only from the end of the cone tip for cone-in-shell targets to the dense core, where the hot-electron energy is absorbed; the cone itself and the electron transport in the cone are not simulated.

The LSP part of the simulation starts when the high-energy, short-pulse laser is injected using the hydrodynamic profiles predicted by DRACO. LSP runs for a short time (~1 ps) during which the hydrodynamic evolution is minimal, and it generates a time history of hot-electron energy deposition. DRACO then runs for the same time, using the energy deposition calculated by LSP as an additional energy source in the temperature equation. The hydrodynamic profiles in LSP are updated according to the DRACO results, while the hot-electron distributions and the electromagnetic fields in LSP are left unchanged. DRACO and LSP are run together for the duration of the high-energy petawatt pulse. The hydrodynamic reaction of the target after the high-energy petawatt pulse is simulated by DRACO.

The first simulations of integrated fast-ignitor experiments planned for the combined OMEGA/OMEGA EP Laser System used 40-μm-thick CD shells of ~870-μm outer diameter, a gold cone with an opening angle of 35° and a tip thickness of 15 μm, irradiated by a highly shaped laser pulse of ~3-ns duration and ~20-kJ energy. Currently, radiation transport is not included in the hydro simulation, which leads to an overestimate of the compressed target density. The OMEGA EP laser is assumed to deliver 2.6 kJ in a 10-ps pulse into the cone, which is translated into a hot-electron distribution assuming a 30% conversion efficiency and a slope temperature according to the Wilks scaling. The hot electrons are given a Gaussian profile in the radial direction with a diameter of 20 μm (FWHM) and an angular spread of 20° (half-angle, FWHM). Figure 115.19 shows results

from these simulations as 2-D maps of (a) the plasma density, (b) hot-electron density, and (d) the azimuthal magnetic field in the r–z plane 6 ps after the beginning of the hot-electron pulse. Figure 115.19(c) shows the total plasma-temperature increase caused by the heating from hot electrons at the end of the laser pulse. The hot electrons are seen to be well collimated by the resistive magnetic field generated by the electron beam despite the high initial divergence. The maximum temperature increase in the core is of the order of 1 keV.

This *LSP/DRACO* code combination scheme was also used to perform integrated high-gain, fast-ignition simulations. An optimized spherically symmetric target imploded with a highly shaped 300-kJ compression pulse[7] was used, and the electron beam was injected 125 μm from the target center. The electron beam had a square profile in time with a duration of 10 ps and a Gaussian profile in the radial direction with a diameter of 30 μm (FWHM). A Maxwellian distribution was assumed for the electrons with a mean energy of 2 MeV and an angular spread of 20° (half-angle, FWHM). In contrast to the simulations of the experiments on OMEGA EP, these simulations show what is believed to be resistive filamentation, similar to observations in the hybrid simulations of Honrubia and Meyer-ter-Vehn.[59] For the given parameters, 43 kJ of energetic electrons were required for ignition, resulting in a gain of ~100. When the effect of the magnetic field on beam electrons was artificially suppressed, the minimum electron-beam energy required for ignition increased to 96 kJ, demonstrating the beneficial effect of the resistive magnetic field.

Summary

A comprehensive scientific program is being pursued at LLE to investigate the fast-ignitor concept for inertial confinement fusion. The combined OMEGA/OMEGA EP Laser Facility provides the experimental infrastructure for these investigations. The OMEGA EP laser was completed in April 2008. Two of the four OMEGA EP beamlines can operate in short-pulse mode, with up to 2.6 kJ each at a 10-ps pulse duration. These beams can be routed into either the OMEGA EP chamber or combined collinearly into the existing OMEGA target chamber for integrated fast-ignitor experiments. Fuel-assembly experiments on OMEGA with both room-temperature and cryogenic targets have achieved high fuel-areal densities of ~200 mg/cm^2, sufficient to stop the MeV electrons produced by the short-pulse laser. Experiments on the fuel assembly of cone-in-shell targets showed only a small deterioration of achievable areal density. The measured areal density was more than 60% of what a 1-D simulation predicts for an equivalent full sphere. The conversion efficiency from laser energy to fast electrons was measured using two independent experimental methods on both LLE's MTW laser and the RAL Vulcan Petawatt and found to be ~20% at intensities >10^{18} W/cm^2. A high-resolution (1.4-μm) TRD measures the coherent transition radiation from the rear side of a solid target, providing insight into the hot-electron transport. Simulation of both full-scale fast-ignition experiments and near-term integrated experiments on OMEGA, using a combination of a radiation hydrocode (*DRACO*) and a hybrid particle-in-cell code (*LSP*), shows the beneficial effects of the resistive magnetic fields generated by the propagation of the
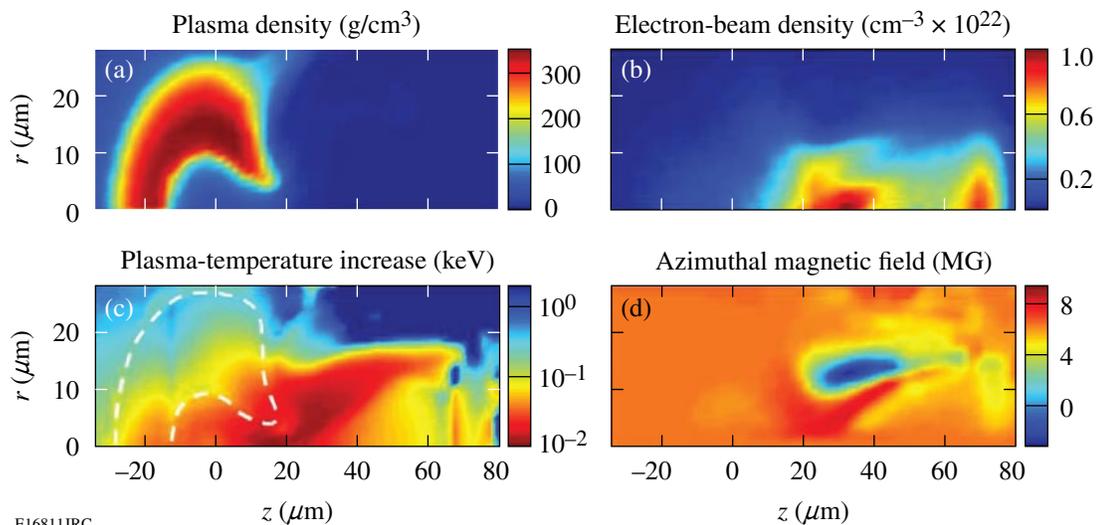
Figure 115.19
Snapshots of the (a) plasma density, (b) hot-electron density, and (d) the azimuthal magnetic field 6 ps after the beginning of the hot-electron pulse, for near-term, integrated fast-ignitor experiments on OMEGA. The maximum increase in plasma temperature (c) at the end of the pulse is ~1 keV

energetic electron into the high-density core. A decrease of the energy required to ignite a target imploded by a 300-kJ UV laser from ~100-kJ electron energy to ~40-kJ electron energy due to the magnetic fields was observed in simulations of full-scale fast-ignition targets. Simulations of fast-ignitor experiments with room-temperature cone-in-shell targets on OMEGA EP showed a temperature increase of up to 1 keV in the core with the short-pulse-laser–produced energetic electrons heating the target. Integrated experiments with room-temperature targets on the combined OMEGA/OMEGA EP Laser Facility are scheduled for the summer of 2008.

ACKNOWLEDGMENT

REFERENCES

1. N. G. Basov, S. Yu. Gus'kov, and L. P. Feokistov, J. Sov. Laser Res. **13**, 396 (1992).

2. M. Tabak *et al.*, Phys. Plasmas **1**, 1626 (1994).

3. R. Kodama *et al.*, Nature **412**, 798 (2001).

4. R. Kodama *et al.*, Nature **418**, 933 (2002).

5. J. D. Lindl, R. L. McCrory, and E. M. Campbell, Phys. Today **45**, 32 (1992).

6. K. Yasuike *et al.*, Rev. Sci. Instrum. **72**, 1236 (2001).

7. R. Betti, K. Anderson, J. Knauer, T. J. B. Collins, R. L. McCrory, P. W. McKenty, and S. Skupsky, Phys. Plasmas **12**, 042703 (2005).

8. J. Nuckolls *et al.*, Nature **239**, 139 (1972).

9. C. K. Li and R. D. Petrasso, Phys. Rev. E **70**, 067401 (2004).

10. R. B. Stephens *et al.*, Phys. Rev. E **69**, 066414 (2004).

11. Y. Kitagawa *et al.*, Phys. Plasmas **9**, 2202 (2002).

12. P. A. Norreys *et al.*, Phys. Plasmas **7**, 3721 (2000).

13. L. J. Waxer, D. N. Maywar, J. H. Kelly, T. J. Kessler, B. E. Kruschwitz, S. J. Loucks, R. L. McCrory, D. D. Meyerhofer, S. F. B. Morse, C. Stoeckl, and J. D. Zuegel, Opt. Photonics News **16**, 30 (2005).

14. T. R. Boehly, D. L. Brown, R. S. Craxton, R. L. Keck, J. P. Knauer, J. H. Kelly, T. J. Kessler, S. A. Kumpan, S. J. Loucks, S. A. Letzring, F. J. Marshall, R. L. McCrory, S. F. B. Morse, W. Seka, J. M. Soures, and C. P. Verdon, Opt. Commun. **133**, 495 (1997).

15. C. Stoeckl, C. Chiritescu, J. A. Delettrez, R. Epstein, V. Yu. Glebov, D. R. Harding, R. L. Keck, S. J. Loucks, L. D. Lund, R. L. McCrory, P. W. McKenty, F. J. Marshall, D. D. Meyerhofer, S. F. B. Morse, S. P. Regan, P. B. Radha, S. Roberts, T. C. Sangster, W. Seka, S. Skupsky, V. A. Smalyuk, C. Sorce, J. M. Soures, R. P. J. Town, J. A. Frenje, C. K. Li, R. D. Petrasso, F. H. Séguin, K. Fletcher, S. Padalino, C. Freeman, N. Izumi, R. Lerche, and T. W. Phillips, Phys. Plasmas **9**, 2195 (2002).

16. T. C. Sangster, R. Betti, R. S. Craxton, J. A. Delettrez, D. H. Edgell, L. M. Elasky, V. Yu. Glebov, V. N. Goncharov, D. R. Harding, D. Jacobs-Perkins, R. Janezic, R. L. Keck, J. P. Knauer, S. J. Loucks, L. D. Lund, F. J. Marshall, R. L. McCrory, P. W. McKenty, D. D. Meyerhofer, P. B. Radha, S. P. Regan, W. Seka, W. T. Shmayda, S. Skupsky, V. A. Smalyuk, J. M. Soures, C. Stoeckl, B. Yaakobi, J. A. Frenje, C. K. Li, R. D. Petrasso, F. H. Séguin, J. D. Moody, J. A. Atherton, B. D. MacGowan, J. D. Kilkenny, T. P. Bernat, and D. S. Montgomery, Phys. Plasmas **14**, 058101 (2007).

17. P. W. McKenty, V. N. Goncharov, R. P. J. Town, S. Skupsky, R. Betti, and R. L. McCrory, Phys. Plasmas **8**, 2315 (2001).

18. Y. Lin, T. J. Kessler, and G. N. Lawrence, Opt. Lett. **21**, 1703 (1996).

19. S. Skupsky and R. S. Craxton, Phys. Plasmas **6**, 2157 (1999).

20. T. R. Boehly, V. A. Smalyuk, D. D. Meyerhofer, J. P. Knauer, D. K. Bradley, R. S. Craxton, M. J. Guardalben, S. Skupsky, and T. J. Kessler, J. Appl. Phys. **85**, 3444 (1999).

21. G. H. Miller, E. I. Moses, and C. R. Wuest, Opt. Eng. **43**, 2841 (2004).

22. M. A. Rhodes *et al.*, Appl. Opt. **34**, 5312 (1995).

23. B. W. Shore *et al.*, J. Opt. Soc. Am. A **14**, 1124 (1997).

24. T. J. Kessler, J. Bunkenburg, H. Huang, A. Kozlov, and D. D. Meyerhofer, Opt. Lett. **29**, 635 (2004).

25. T. C. Sangster, V. N. Goncharov, P. B. Radha, V. A. Smalyuk, R. Betti, R. S. Craxton, J. A. Delettrez, D. H. Edgell, V. Yu. Glebov, D. R. Harding, D. Jacobs-Perkins, J. P. Knauer, F. J. Marshall, R. L. McCrory, P. W. McKenty, D. D. Meyerhofer, S. P. Regan, W. Seka, R. W. Short, S. Skupsky, J. M. Soures, C. Stoeckl, B. Yaakobi, D. Shvarts, J. A. Frenje, C. K. Li, R. D. Petrasso, and F. H. Séguin, Phys. Rev. Lett. **100**, 185006 (2008).

26. W. Theobald, R. Betti, C. Stoeckl, K. S. Anderson, J. A. Delettrez, V. Yu. Glebov, V. N. Goncharov, F. J. Marshall, D. N. Maywar, R. L. McCrory, D. D. Meyerhofer, P. B. Radha, T. C. Sangster, W. Seka, D. Shvarts, V. A. Smalyuk, A. A. Solodov, B. Yaakobi, C. D. Zhou, J. A. Frenje, C. K. Li, F. H. Séguin, R. D. Petrasso, and L. J. Perkins, Phys. Plasmas **15**, 056306 (2008).

27. V. N. Goncharov, T. C. Sangster, P. B. Radha, R. Betti, T. R. Boehly, T. J. B. Collins, R. S. Craxton, J. A. Delettrez, R. Epstein, V. Yu. Glebov, S. X. Hu, I. V. Igumenshchev, J. P. Knauer, S. J. Loucks, J. A. Marozas, F. J. Marshall, R. L. McCrory, P. W. McKenty, D. D. Meyerhofer, S. P. Regan, W. Seka, S. Skupsky, V. A. Smalyuk, J. M. Soures, C. Stoeckl, D. Shvarts, J. A. Frenje, R. D. Petrasso, C. K. Li, F. Séguin, W. Manheimer, and D. G. Colombant, Phys. Plasmas **15**, 056310 (2008).

28. V. N. Goncharov, J. P. Knauer, P. W. McKenty, P. B. Radha, T. C. Sangster, S. Skupsky, R. Betti, R. L. McCrory, and D. D. Meyerhofer, Phys. Plasmas **10**, 1906 (2003).

29. C. K. Li, D. G. Hicks, F. H. Séguin, J. A. Frenje, R. D. Petrasso, J. M. Soures, P. B. Radha, V. Yu. Glebov, C. Stoeckl, D. R. Harding, J. P. Knauer, R. L. Kremens, F. J. Marshall, D. D. Meyerhofer, S. Skupsky, S. Roberts, C. Sorce, T. C. Sangster, T. W. Phillips, M. D. Cable, and R. J. Leeper, Phys. Plasmas **7**, 2578 (2000).

30. J. Delettrez, R. Epstein, M. C. Richardson, P. A. Jaanimagi, and B. L. Henke, Phys. Rev. A **36**, 3926 (1987).

31. K. Anderson and R. Betti, Phys. Plasmas **11**, 5 (2004).

32. C. D. Zhou, W. Theobald, R. Betti, P. B. Radha, V. A. Smalyuk, D. Shvarts, V. Yu. Glebov, C. Stoeckl, K. S. Anderson, D. D. Meyerhofer, T. C. Sangster, C. K. Li, R. D. Petrasso, J. A. Frenje, and F. H. Séguin, Phys. Rev. Lett. **98**, 025004 (2007).

33. R. B. Stephens *et al.*, Phys. Rev. Lett. **91**, 185001 (2003).

34. C. Stoeckl, T. R. Boehly, J. A. Delettrez, S. P. Hatchett, J. A. Frenje, V. Yu. Glebov, C. K. Li, J. E. Miller, R. D. Petrasso, F. H. Séguin, V. A. Smalyuk, R. B. Stephens, W. Theobald, B. Yaakobi, and T. C. Sangster, Phys. Plasmas **14**, 112702 (2007).

35. D. K. Bradley *et al.*, Rev. Sci. Instrum. **66**, 716 (1995).

36. P. B. Radha, T. J. B. Collins, J. A. Delettrez, Y. Elbaz, R. Epstein, V. Yu. Glebov, V. N. Goncharov, R. L. Keck, J. P. Knauer, J. A. Marozas, F. J. Marshall, R. L. McCrory, P. W. McKenty, D. D. Meyerhofer, S. P. Regan, T. C. Sangster, W. Seka, D. Shvarts, S. Skupsky, Y. Srebro, and C. Stoeckl, Phys. Plasmas **12**, 056307 (2005).

37. J. A. Oertel *et al.*, Rev. Sci. Instrum. **70**, 803 (1999).

38. P. K. Gupta *et al.*, Appl. Phys. Lett. **39**, 32 (1981).

39. P. M. Nilson, W. Theobald, J. Myatt, C. Stoeckl, M. Storm, O. V. Gotchev, J. D. Zuegel, R. Betti, D. D. Meyerhofer, and T. C. Sangster, Phys. Plasmas **15**, 056308 (2008).

40. W. Theobald, K. Akli, R. Clarke, J. Delettrez, R. R. Freeman, S. Glenzer, J. Green, G. Gregori, R. Heathcote, N. Izumi, J. A. King, J. A. Koch, J. Kuba, K. Lancaster, A. J. MacKinnon, M. Key, C. Mileham, J. Myatt, D. Neely, P. A. Norreys, H.-S. Park, J. Pasley, P. Patel, S. P. Regan, H. Sawada, R. Shepherd, R. Snavely, R. B. Stephens, C. Stoeckl, M. Storm, B. Zhang, and T. C. Sangster, Phys. Plasmas **13**, 043102 (2006).

41. J. Myatt, W. Theobald, J. A. Delettrez, C. Stoeckl, M. Storm, T. C. Sangster, A. V. Maximov, and R. W. Short, Phys. Plasmas **14**, 056301 (2007).

42. C. N. Danson *et al.*, Nucl. Fusion **44**, S239 (2004).

43. V. Bagnoud, I. A. Begishev, M. J. Guardalben, J. Puth, and J. D. Zuegel, Opt. Lett. **30**, 1843 (2005).

44. C. Stoeckl, W. Theobald, T. C. Sangster, M. H. Key, P. Patel, B. B. Zhang, R. Clarke, S. Karsch, and P. Norreys, Rev. Sci. Instrum. **75**, 3705 (2004).

45. Spectral Instruments, Tucson, AZ 85745.

46. S. C. Wilks *et al.*, Phys. Rev. Lett. **69**, 1383 (1992).

47. A. J. Mackinnion *et al.*, Phys. Rev. Lett. **88**, 215006 (2002).

48. Y. Sentoku *et al.*, Phys. Rev. Lett. **90**, 155001 (2003).

49. H. Kolbenstvedt, J. Appl. Phys. **38**, 4785 (1967).

50. D. R. Welch *et al.*, Nucl. Instrum. Methods Phys. Res. A **464**, 134 (2001).

51. Prism Computational Sciences, Inc., Madison, WI 53711.

52. S. D. Baton *et al.*, Phys. Rev. Lett. **91**, 105001 (2003).

53. V. L. Ginzburg, Phys.-Usp. **39**, 973 (1996).

54. J. Zheng *et al.*, Phys. Plasmas **10**, 2994 (2003).

55. W. L. Kruer, *The Physics of Laser Plasma Interactions*, Frontiers in Physics (Westview Press, Boulder, CO, 2003), pp. 39–43.

56. M. Storm, C. Guo, D. D. Meyerhofer, J. Myatt, T. C. Sangster, and C. Stoeckl, "Relativistic Electron-Beam Transport Measurements," to be published in Review of Scientific Instruments.

57. K. Miyamoto, *Plasma Physics for Nuclear Fusion*, Revised (MIT Press, Cambridge, MA, 1989).

58. L. Gremillet, G. Bonnaud, and F. Amiranoff, Phys. Plasmas **9**, 941 (2002).

59. J. J. Honrubia and J. Meyer-ter-Vehn, Nucl. Fusion **46**, L25 (2006).

A Focal-Spot Diagnostic for On-Shot Characterization of High-Energy Petawatt Lasers

Introduction

Knowledge of the laser focus is an essential part of accurately controlling and interpreting target experiments using petawatt-class lasers.[1–9] Large-scale lasers present significant challenges for the development of focal-spot diagnostics. Their focal spots can be highly structured due to the complexity of systems containing hundreds of optical surfaces. Furthermore, high-energy petawatt lasers typically require adaptive and tiled optics that must be configured correctly for a successful target shot.[10–12] Focal-spot characterization on each full-energy shot is a necessity and the only way to capture effects such as thermally induced aberrations in the amplifiers.

Depending on the target experiment, the quantity of interest may range from the focal-spot width to an analysis of encircled energy at a given plane, to a full characterization of the focal volume along an extended interaction region. Direct measurement of the focus at full energy without interfering with the target experiment is impractical, if not impossible, due to the extreme intensities at focus. One option is to precharacterize the near-field wavefront after propagation through focus, from which the focal volume is obtained using a diffraction calculation.[13] This article demonstrates a simplified near-field approach that does not rely on wavefront sensing in the target chamber and is therefore more suited to the complexity of high-energy petawatt lasers. Results are reported for an on-shot focal-spot diagnostic (FSD) for OMEGA EP, a high-energy petawatt-class laser that was recently activated at LLE.[1] The following three sections describe (1) the FSD, (2) the experiments used to qualify the FSD by comparison to direct measurement at low energy, and (3) results for high-energy target shots.

Diagnostic Concept and Design

1. Focal-Spot Diagnostic (FSD)

The FSD characterizes full-energy shots using high-resolution measurements of the near-field wavefront and fluence. The time-integrated focal spot at the target is calculated numerically from these measurements using standard diffraction theory.[14] Direct measurements of the full beam without interfering with the target shot are not practical due

to its high energy (up to 2.6 kJ on target) and large size (400×400 mm^2). The FSD, like the other on-shot laser diagnostics, measures a lower-energy sample of the main beam that is attenuated and down-collimated to a more convenient beam size (12×12 mm^2). Careful calibration is necessary to ensure that measurements made on the sample beam reflect the main beam at focus. Therefore, a critical part of the FSD is the cross-calibration of the wavefront sensor measurements to a reference surface centered on the target location, from which the optical fields are numerically propagated.

Figure 115.20 shows a schematic of one of the short-pulse beamlines in OMEGA EP, necessary for understanding how the FSD was implemented and qualified. The front end of the laser system uses an optical parametric chirped-pulse amplifier (OPCPA) to produce stretched pulses (250 mJ, square 8-nm spectrum, 5 Hz).[15] For target shots, these pulses are amplified using a multipass Nd:glass amplifier. A tiled-grating compressor (three tiles per grating, four gratings) is used to compress the pulses. A deformable mirror corrects compressor aberrations and pre-corrects aberrations in the transport and the off-axis parabolic (OAP) focusing mirror ($f = 1.046$ m, $f/2$). A diagnostic pickoff mirror reflects 99% of the compressed pulse energy toward the target chamber as the main beam and transmits the remainder as a sample beam for the laser diagnostics package. The wavefront sensor (WFS) used by the FSD for each compressor is one of more than a dozen laser diagnostics used to characterize the on-shot beam.

The WFS chosen for OMEGA EP is a Shack–Hartmann sensor,[16] which is positioned at an image plane conjugate to the fourth compressor grating. It has a 133×133-lenslet array with a 14×14-mm^2 charge-coupled-device (CCD) sensor.[17] A local wavefront gradient as high as 15 mrad can be measured. The accuracy of the defocus term was measured to be better than 0.01 waves at 1.053 μm, and the relative error in astigmatism was less than 2%. The accuracy of measuring higher-order aberrations was studied using sinusoidal phase plates (one-wave peak-to-valley). Wavefront measurements up to 25% of the maximum spatial frequency were confirmed to have less

than 1% discrepancy with interferometric measurements of the phase plates. Measurements at higher spatial frequencies were limited by the maximum slope capability of the WFS.

The FSD must be calibrated to numerically transfer the sample-beam measurement at the sensor to a spherical reference surface in the target chamber that is centered on the intended focal-spot location. One part of this calibration is to precisely measure the amount of demagnification during the four down-collimation and imaging stages from the diagnostic mirror to the WFS. Another part is to measure the difference between (a) sample-beam aberrations that are artifacts in the on-shot measurement that must be subtracted and (b) aberrations in the main beam path that are after the diagnostic mirror and so must be added to the on-shot measurement. This difference, the

transfer wavefront (ΔW_{trans}), is applied to correct the on-shot measurement before calculating the focal spot.

The transfer wavefront is measured by using two separate laser sources to probe the back end of the laser system, as shown in Fig. 115.21. The sample path from the WFS to an actuated compressor alignment mirror (CAM) and back is characterized using a laser source that is included in the diagnostics. The measured wavefront is

$$W_1 = W_{S0} + 2W_S,\qquad(1)$$

where W_{S0} is the measured source wavefront and W_S is the single-pass aberration in the sample path to the CAM. The path from the target focus back to the WFS is characterized
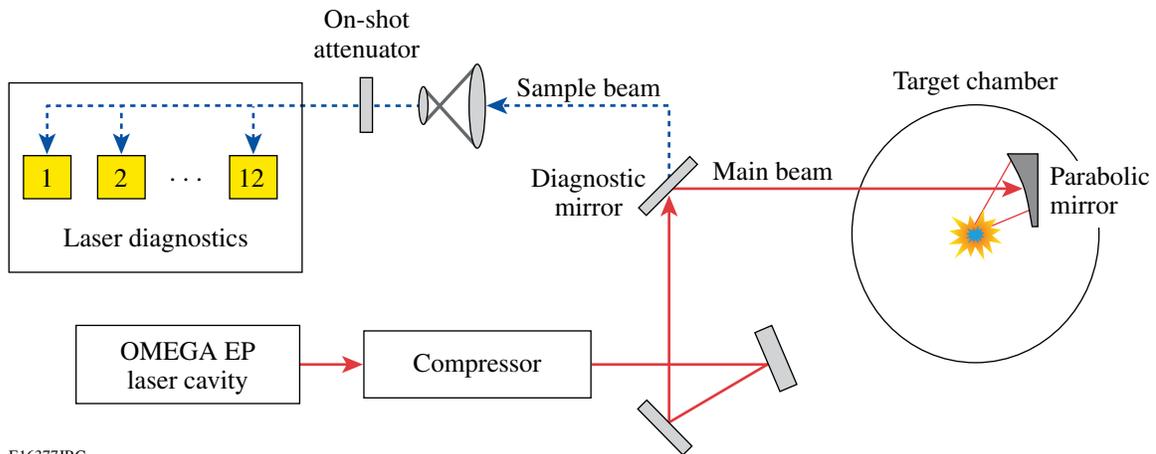
Figure 115.20
Overview of OMEGA EP, showing the relative location of the main laser beam and the sample beam used by diagnostics for on-shot measurement of the laser properties. The focal-spot diagnostic wavefront sensor is one of many laser diagnostics that characterize the sample beam.
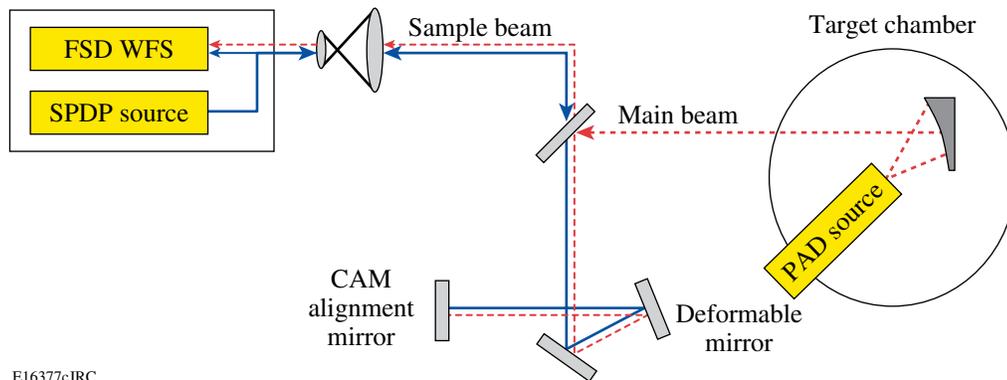
Figure 115.21
Schematic showing probe lasers used to calibrate the FSD.

using a back-propagating point source positioned at the desired focal-spot location. On OMEGA EP, the parabola alignment diagnostic (PAD) provides this point source. The measured wavefront is

$$W_2 = T^{-1}(W_{M0}) + W_M + W_S, \qquad (2)$$

where W_{M0} is the measured point-source wavefront and W_M represents the main-path aberrations to the CAM. The inverse transformation $T^{-1}(\dots)$ may be necessary to account for geometric distortion T produced by the focusing element, such as that due to low-f-number OAP's.[18] The transfer wavefront is given by

$$\Delta W_{\text{trans}} = W_M - W_S = W_1 - W_2 + W_{S0} - T^{-1}(W_{M0}). \quad (3)$$

Results from the transfer wavefront measurement for the OMEGA target chamber are shown in Fig. 115.22.

In principle, other approaches could be used to measure ΔW_{trans}. For example, one could use a single laser source and add a second WFS to measure the wavefront of the converging beam directly in the target chamber.[13] In this case additional steps would be needed to ensure that the resulting measurements were correctly scaled and registered before calculating ΔW_{trans}. With this single WFS approach, W_1 and W_2 are automatically registered in transverse alignment and in the image plane that is conjugate to the sensor. Furthermore, for a system as complex as OMEGA EP, it is simpler to produce a backward-propagating point source inside a target chamber than it is to provide accurate, high-resolution wavefront measurements of a forward-propagating, focusing probe beam.

After a shot, the field measured at the wavefront sensor is calibrated to a spherical reference surface centered on the target location by adding ΔW_{trans}. This field is numerically propagated to the target plane. If the f number of the OAP exceeds unity, a scalar field approximation is sufficient[18] and the diffraction calculation reduces to a two-dimensional Fourier transformation. One advantage of this field-based approach is that the irradiance can be calculated at any plane relative to the target by changing the diffraction calculation. Once the irradiance is calculated, it is straightforward to calculate the encircled energy as a function of radius.

One limitation of this approach is that it is strictly valid only if there is no chromatic variation of the transfer or on-shot wavefronts. The wavefront reported by a Shack–Hartmann sensor is a spectrally weighted average. Effects such as longitudinal chromatic aberration that has not been fully compensated[19] or angular dispersion from stretcher or compressor misalignment,[12] once quantified using independent techniques, can be included in the post-shot calculation.[20]

2. Focal-Spot Microscope for Direct Measurement at Low Energies

A custom focal-spot microscope (FSM) was built to validate the accuracy of the FSD. It provides a direct measurement of the focus in the OMEGA target chamber with spatial resolution of 0.36 μm per pixel and sufficient dynamic range to capture the diffuse low-intensity spray around the main focal spot that, when integrated, can represent a significant fraction of the total energy. Although not able to be used on a full-energy shot, the FSM has enough internal attenuation (6.0 OD) to safely measure focused pulses produced by the OMEGA EP front end,

(a) W_1 (b) W_2 (c) ΔW_{trans}

E16886JRC
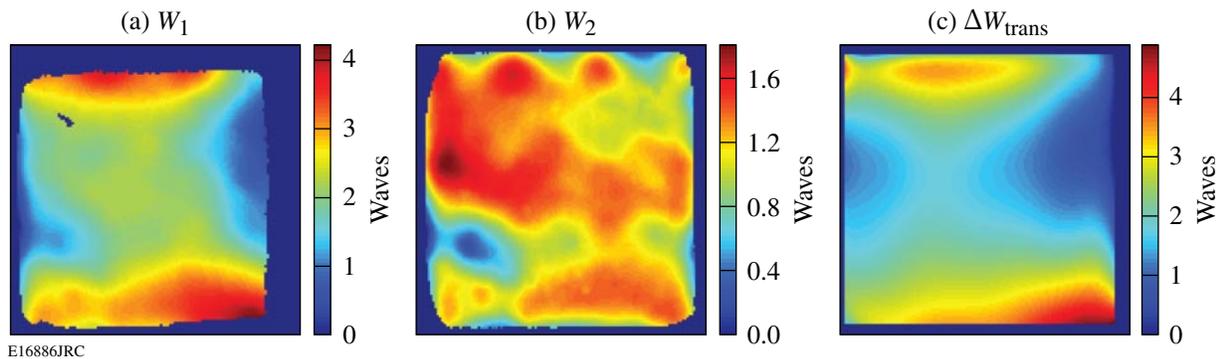
Figure 115.22
Measured transfer wavefront (in units of waves) obtained using two probe sources. (a) W_1, with the target chamber source (PAD), (b) W_2, with the diagnostic package source, and (c) ΔW_{trans}, transfer wavefront after source errors have been subtracted and a Legendre modal fit has been used to extrapolate to an extended pupil region.

with sufficient energy available after the diagnostic mirror for the FSD WFS to make a simultaneous measurement.

Figure 115.23 shows a schematic of the FSM that was installed in the OMEGA target chamber, using the ten-inch manipulator (TIM) that opposed the OAP. The microscope objective was optimized for near-infrared (10×, N.A. = 0.26, f = 20 mm), with a damage threshold of 20 mJ/cm^2 and a long working distance (30 mm), making it suitable for laser focus characterization. When combined with the 660-mm-focal-length tube lens, the total magnification of the system was 33×. Between the objective and tube lens were a wedged vacuum window, a pair of neutral-density filters with a total optical density (OD) of 4.0, and a beam splitter at 45° that was also made from neutral-density filter glass (2.0 OD). The scientific-grade camera used a one-megapixel, front-illuminated CCD chip cooled to –20°C, giving a read-noise limited dynamic range of 14.5 bits. The entire FSM was contained in an air bubble to permit its use with the target chamber at vacuum. Care was taken with internal surface preparations and baffling to minimize stray light and scattering within the FSM that could reduce the instrument's dynamic range.

The FSM was aligned to the intended focus location using the same techniques as used with the PAD point source. First, a reflective sphere was aligned precisely so that it was centered on the desired focal-spot location. Then, a collimated fiber-fed beam at 1053 nm was focused by the FSM objective onto the surface of the sphere. The FSM position was adjusted so that the focusing beam was normal to the sphere surface, at which point the FSM focal plane was coincident with the intended focus location. Under these conditions light reflected back off the sphere into the FSM appears tightly focused at the CCD. Coarse positioning was done using the TIM; fine positioning was achieved using the piezo and mechanical actuators of a motion-control system.

FSD Qualification Results

The focal-spot diagnostic was qualified using a sequence of experiments designed to compare measurements made by the FSD and FSM. The laser source for these experiments was the front-end system for OMEGA EP after propagation through the entire beamline and compression chamber into the OMEGA target chamber. Gain narrowing by the Nd:glass amplifiers during a full-energy shot reduces the square 8-nm spectrum to a 3.3-nm-wide Gaussian-like spectrum. Therefore, the impact of any chromatic aberrations and angular dispersion on the focal spot, which could in principle be present during a shot, would have been exaggerated during these low-energy tests. Wave-plate throttles were set so that 400 μJ of the 100-mJ front end were focused in the target chamber. This provided enough energy per pulse for the FSD wavefront sensor after transmission through the diagnostic mirror (0.5%) and yet was not too high for the FSM due to its internal attenuation (6.0 OD). Data acquisition by the FSD and FSM was synchronized so that each measurement represented the same OPCPA pulse.

Figure 115.24 shows an example of data measured by the FSD wavefront sensor. The raw 2-K × 2-K image contains Shack–Hartmann spots formed by the 133 × 133-lenslet array, from which is calculated both the wavefront and fluence at the input to the wavefront sensor. The image plane for this sensor is the last of the four tiled-grating assemblies inside

Beam splitter (2.0 OD on transmission)
Attenuator pair (4.0 OD)
Tube lens
Fiber collimator
Microscope objective (0.26 N.A.)
12 in.
16-bit CCD camera

E16887JRC
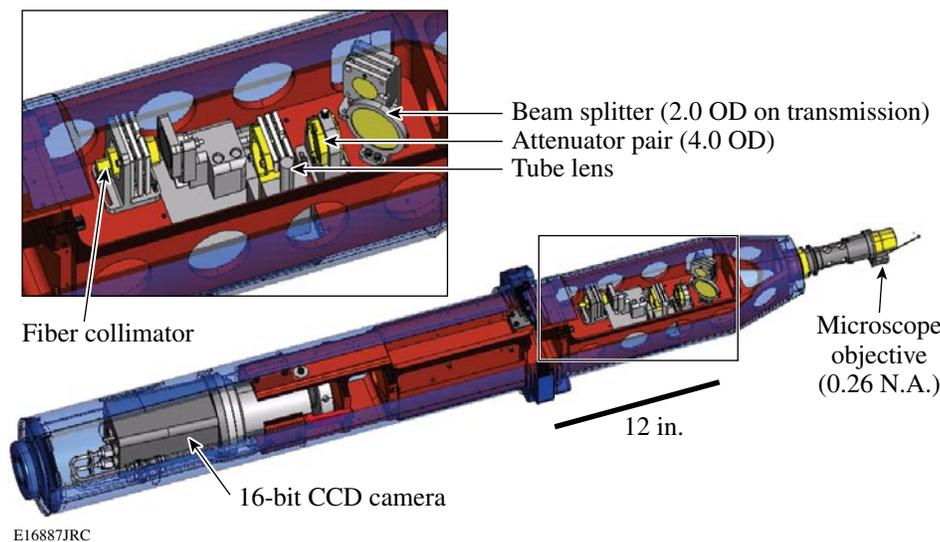
Figure 115.23
Focal-spot microscope (FSM) used for direct, low-energy measurements of the OMEGA EP focal spot in the OMEGA target chamber.

the compressor. The gaps between grating tiles are apodized within the main beamline to minimize diffraction effects that would otherwise result from each tile edge. As a result, the OPCPA beam is divided into three sub-beams, each of which is reduced separately. Separate measurements of the tiled-grating compressor were made to ensure the gratings were correctly

aligned and tiled;[12] therefore it was assumed that there was no significant residual angular dispersion or differential piston error between the tiles.

Figure 115.25 shows a direct comparison of a focal spot measured indirectly by the FSD and directly by the FSM,

E16888JRC
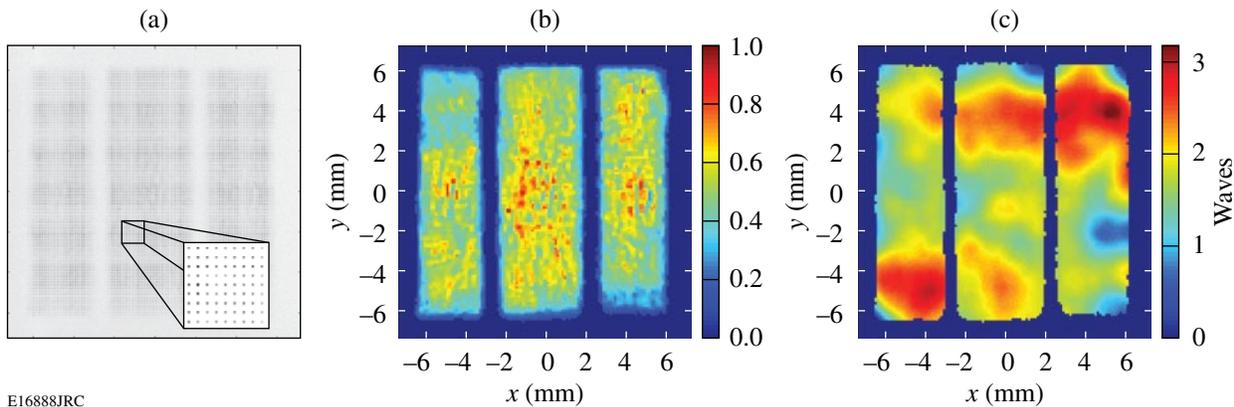
Figure 115.24
FSD measurements using the OPCPA front end. (a) Raw Shack–Hartmann image with inset showing the spots formed by each lenslet, (b) fluence (normalized), (c) wavefront (in units of waves).

E16889JRC
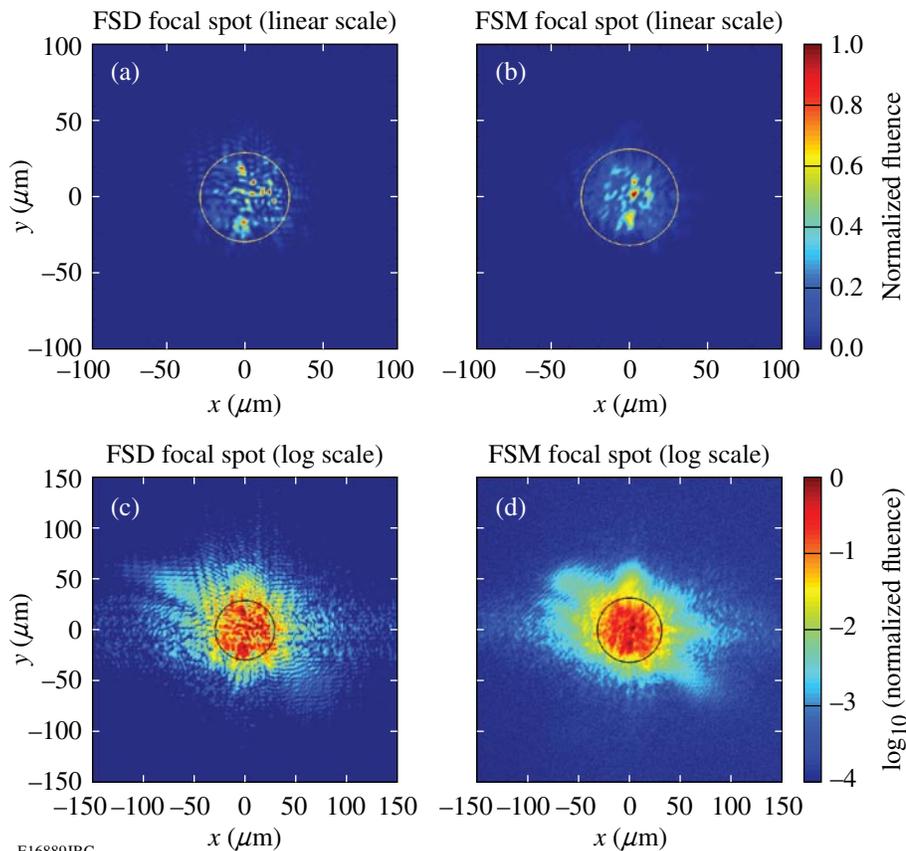
Figure 115.25
Same-shot measurements of focal spot by the FSD and FSM. (a),(b) Linear scale plots; (c),(d) logarithmic scale plots. Circles contain 80% of the energy.

on both linear and logarithmic scales. The FSD results were calculated using the transfer wavefront shown in Fig. 115.22(c) and the OPCPA measurements in Fig. 115.24. Agreement is reasonable, on both linear and logarithmic scales. The only fitting parameter used when calculating the FSD image was 25 μm of defocus between the PAD position used when measuring ΔW_{trans} and the FSM focal plane. This is reasonable given the precision of setting the axial position of one TIM-based diagnostic relative to another. The encircled energy curves calculated for both measurements are in good agreement up to the 70% encircled energy radius (see Fig. 115.26). Beyond this, FSD encircled energy values are larger than those measured by the FSM for the same radius by up to 4%. This trend has been seen consistently in a number of our experiments, both on OMEGA EP and smaller-scale test beds using continuous-wave sources.[19] Possible explanations include optical scattering from the FSM optics and within the CCD chip that could scatter light from the main spot, thereby reducing the inferred measurement of encircled energy at a given radius. Alternatively, the finite spatial resolution of the FSD wavefront sensor (133 × 133 lenslets) will not capture high spatial frequencies present in the wavefront to some degree, and these frequencies may contribute significantly to scattering to regions far from the main spot.

Figure 115.27
Comparison of FSD and FSM measurements for strongly aberrated focal spots (logarithmic scale). Circles contain 80% of the energy.

Figure 115.26
Encircled energy curves derived from Fig. 115.25.

To further test the validity of FSD measurements, we used a deformable mirror to severely distort the focal spot. The FSD and FSM measurements for distorted focal spots are shown in Figs. 115.27 and 115.28. Again, agreement is reasonably good, even down to four orders of magnitude below the maximum fluence.
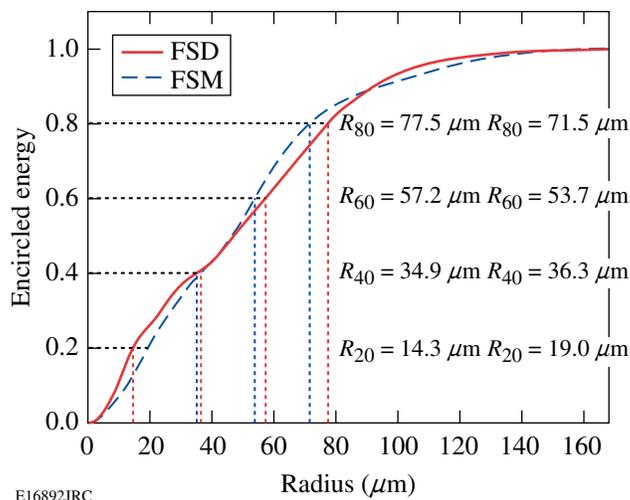
Figure 115.28
Encircled energy curves for the strongly aberrated focal spots shown in Fig. 115.27.

FSD Results for High-Energy Shots

A series of high-energy OMEGA EP target shots were taken in April 2008 to qualify the new laser system. Included in this qualification was an on-shot measurement by the FSD of the focal spot at the target. The following figures show results for one of the target shots (#3053), which was a 10-ps, 440-J shot to a planar target in the OMEGA target chamber.

Figure 115.29 shows the FSD measurement of the calibrated fluence and wavefront (i.e., after ΔW_{trans} was added). The diagnostic showed that there were ~3.3 waves of astigmatism and

defocus due in part to thermally induced aberrations within the amplifiers. This type of on-shot information makes it possible to further improve the system, for example, by adjusting OAP alignment or optimizing the beamline adaptive optics system. The corresponding focal spot is shown in Fig. 115.30, in the form of a transverse scan through the focal volume along the axial direction of the beam, obtained by numerically propagating the field to each plane. The flexibility of this approach makes it possible to calculate the focal spot at an arbitrary plane. For example, the target for this shot was a Au-coated plastic ($500 \times 500 \times 10 \ \mu m^3$) set at 45° to the beam, so the

E16893JRC
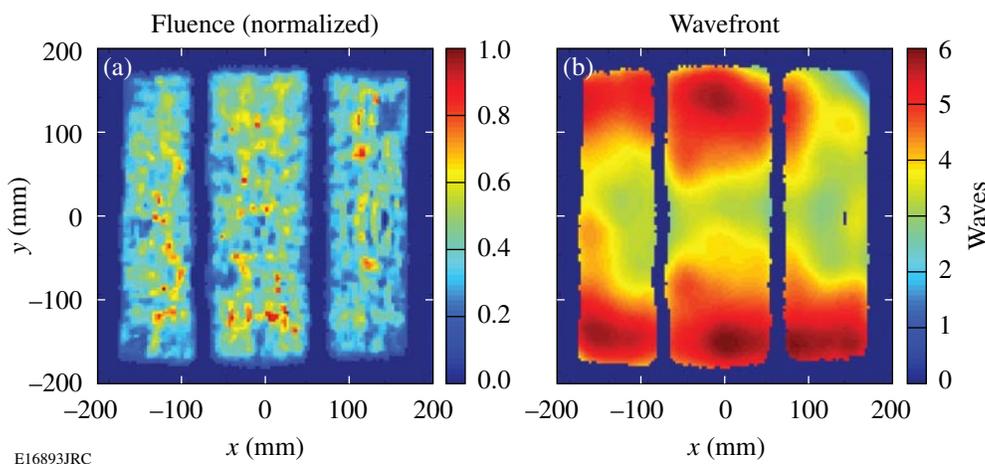
Figure 115.29
(a) On-shot fluence (normalized) and (b) wavefront (in units of waves), calibrated by adding ΔW_{trans}.
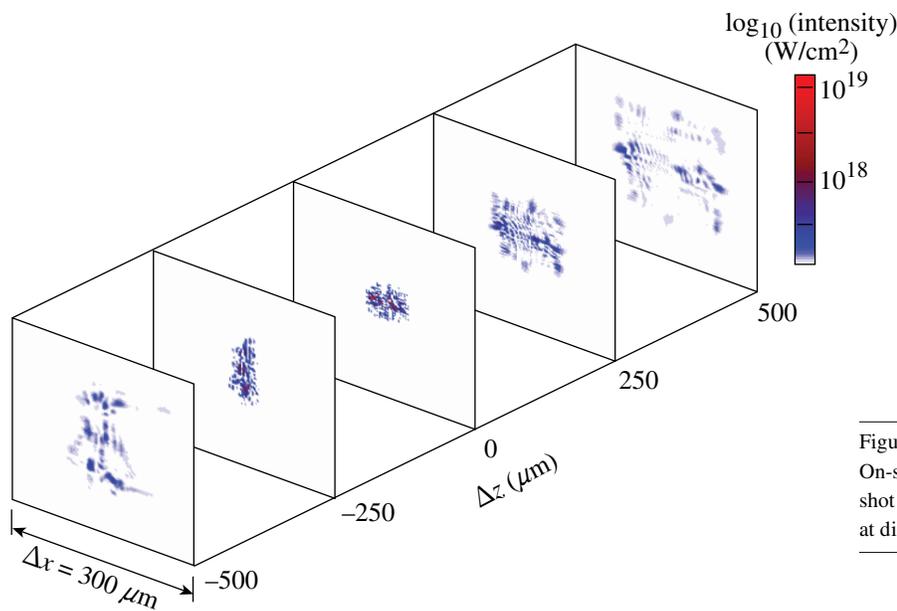
E16843JRC

Figure 115.30
On-shot focal volume for a 10-ps, 440-J OMEGA EP target shot to the OMEGA chamber. Images show the focal spot at different planes, plotted on a logarithmic scale.

focal spot on the target surface can be obtained despite the oblique angle of incidence. Figure 115.31 shows the focal spot on a logarithmic scale along with the corresponding encircled energy curve.
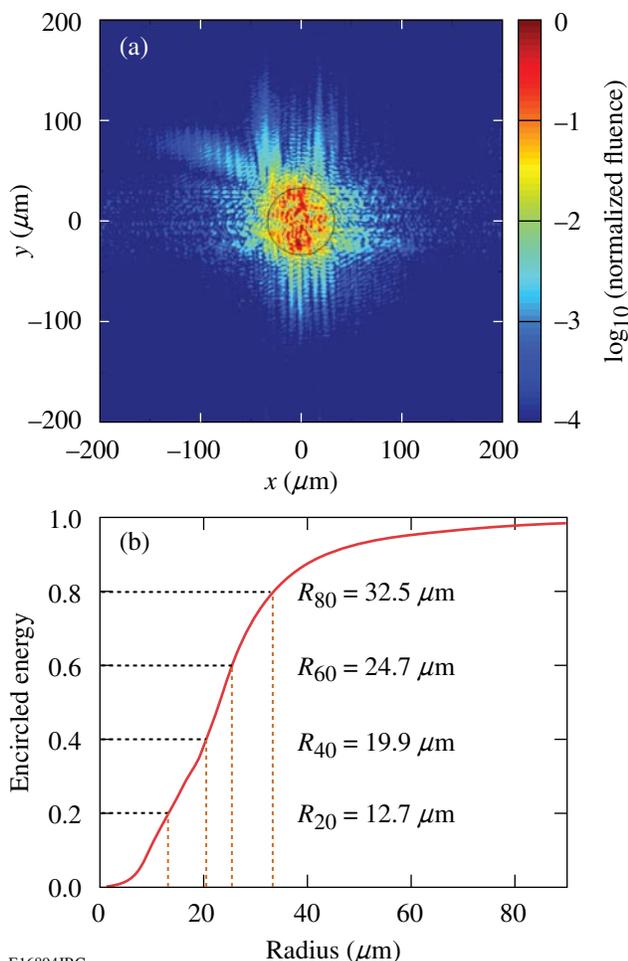
Figure 115.31
(a) Focal spot normalized fluence (logarithmic scale) and (b) encircled energy for a 10-ps, 440-J target shot.

Conclusions

A new focal-spot diagnostic suitable for characterizing high-energy petawatt-class lasers at full energy has been presented. The diagnostic was developed and demonstrated at LLE and is currently deployed as a facility laser diagnostic on the OMEGA EP Laser System. Accurate measurements at full energy are made using high-resolution wavefront sensing in combination with techniques to calibrate on-shot measurements made on a low-energy sample beam. The diagnostic was

validated at low energy using a custom focal-spot microscope to directly measure the focus in the target chamber. Measurements at full energy are also shown for 10-ps, 450-J target shots taken as part of the campaign to activate OMEGA EP to the OMEGA target chamber.

REFERENCES

1. L. J. Waxer, M. J. Guardalben, J. H. Kelly, B. E. Kruschwitz, J. Qiao, I. A. Begishev, J. Bromage, C. Dorrer, J. L. Edwards, L. Folnsbee, S. D. Jacobs, R. Jungquist, T. J. Kessler, R. W. Kidder, S. J. Loucks, J. R. Marciante, D. N. Maywar, R. L. McCrory, D. D. Meyerhofer, S. F. B. Morse, A. V. Okishev, J. B. Oliver, G. Pien, J. Puth, and A. L. Rigatti, presented at CLEO/QELS 2008, San Jose, CA, 4–9 May 2008 (Paper JThB1).

2. L. J. Waxer, D. N. Maywar, J. H. Kelly, T. J. Kessler, B. E. Kruschwitz, S. J. Loucks, R. L. McCrory, D. D. Meyerhofer, S. F. B. Morse, C. Stoeckl, and J. D. Zuegel, Opt. Photonics News **16**, 30 (2005).

3. C. P. J. Barty *et al.*, Nucl. Fusion **44**, S266 (2004).

4. N. Blanchot *et al.*, in *Topical Problems of Nonlinear Wave Physics*, edited by A. M. Sergeev (SPIE, Bellingham, WA, 2006), Vol. 5975, p. 59750C.

5. C. Le Blanc *et al.*, in *Inertial Fusion Sciences and Applications 2003*, edited by B. A. Hammel, D. D. Meyerhofer, J. Meyer-ter-Vehn, and H. Azechi (American Nuclear Society, La Grange Park, IL, 2004), pp. 608–611.

6. C. N. Danson *et al.*, Nucl. Fusion **44**, S2396 (2004).

7. K. Mima *et al.*, Fusion Sci. Technol. **47**, 662 (2005).

8. V. Yanovsky *et al.*, Opt. Express **16**, 2109 (2008).

9. M. Martinez *et al.*, in *Laser-Induced Damage in Optical Materials: 2005*, edited by G. J. Exarhos *et al.* (SPIE, Bellingham, WA, 2006), Vol. 5991, p. 59911N.

10. R. A. Zacharias *et al.*, Opt. Eng. **43**, 2873 (2004).

11. T. J. Kessler, J. Bunkenburg, H. Huang, A. Kozlov, and D. D. Meyerhofer, Opt. Lett. **29**, 635 (2004).

12. J. Qiao, A. Kalb, M. J. Guardalben, G. King, D. Canning, and J. H. Kelly, Opt. Express **15**, 9562 (2007).

13. S.-W. Bahk, P. Rousseau, T. A. Planchon, V. Chvykov, G. Kalintchenko, A. Maksimchuk, G. A. Mourou, and V. Yanovksy, Opt. Lett. **29**, 2837 (2004).

14. J. W. Goodman, *Introduction to Fourier Optics* (McGraw-Hill, New York, 1968).

15. L. J. Waxer, V. Bagnoud, I. A. Begishev, M. J. Guardalben, J. Puth, and J. D. Zuegel, Opt. Lett. **28**, 1245 (2003).

16. B. C. Platt and R. Shack, J. Refractive Surg. **17**, S573 (2001).

17. Imagine Optic, 91400 Orsay, France.

18. S.-W. Bahk, P. Rousseau, T. A. Planchon, V. Chvykov, G. Kalintchenko, A. Maksimchuk, G. Mourou, and V. Yanovsky, Appl. Phys. B **80**, 823 (2005).

19. T. J. Kessler, H. Huang, and D. Weiner, in *International Conference on Ultrahigh Intensity Laser Development, Science and Emerging Applications 2006* (ICUIL, Cassis, France, 2006), pp. 126–128.

20. S.-W. Bahk, J. Bromage, J. D. Zuegel, and J. R. Fienup, presented at CLEO/QELS 2008, San Jose, CA, 4–9 May 2008 (Paper JThB6).

Suprathermal Electrons Generated by the Two-Plasmon-Decay Instability in Gas-Filled Hohlraums

Inertial confinement fusion (ICF) occurs when a spherical shell target containing thermonuclear fuel (i.e., deuterium and tritium) is imploded to produce energy gain.[1,2] Energy gain is predicted to be achieved with megajoule (MJ)-class lasers, such as the 192-beam, 351-nm, 1.8-MJ National Ignition Facility (NIF) being constructed at the Lawrence Livermore National Laboratory.[3] The implosion is driven by the ablation of material from the outer shell surface with intense laser beams (direct drive)[1] or with x rays produced in a high-Z enclosure or hohlraum (indirect drive).[2] Ignition will be first explored on the NIF with indirect-drive ICF. The NIF laser beams are arranged in two cones around the poles of the spherical target chamber to irradiate both sides of the cylindrical hohlraum through the laser entrance holes (LEH's). The laser beams irradiate the inner high-Z wall (i.e., Au, U) of the hohlraum, and the resulting high-Z plasma radiates x rays that are trapped and re-radiated by the opaque hohlraum wall and uniformly ablate the implosion capsule.[2,4] Ignition requires high-compression implosions (convergence ratio ~30), which places strict requirements on the irradiation-nonuniformity level of the x-ray drive on the capsule (<1% to 2% rms) and on the compressibility of the DT fuel. The required drive symmetry is more likely to be achieved if the hohlraum is filled with a low-Z gas fill, which minimizes the motion of the laser-deposition region.[2] A thin (0.5-μm) polyimide window covering each LEH is required to initially contain the gas fill. High compressibility requires that the DT fuel remain close to Fermi degenerate throughout the implosion. This requires control of irreversible heating of the DT fuel, leading to precise pulse shaping to minimize shock heating of the fuel.[2,5] Any additional irreversible heating sources such as suprathermal or hot electrons ($T_{\rm hot} > 20$ keV) produced by laser–plasma interactions need to be understood and controlled. This article reports, for the first time, evidence of hot-electron production during the early-time burnthrough of the LEH window, which, if not properly controlled, could lead to unacceptably large hot-electron preheat of the DT fuel in an ignition capsule.

The experimental signature of suprathermal-electron generation is the hard x-ray bremsstrahlung emission from small angle scattering of the hot electrons in the high-Z wall of the hohlraum target.[6] The possible sources of hot-electron generation are parametric processes that produce electron-plasma waves, such as two-plasmon-decay ($2\omega_{\rm pe}$) instability[7,8] and stimulated Raman scattering (SRS).[8,9] The $2\omega_{\rm pe}$ instability occurs near quarter-critical density when the phase-matching conditions are satisfied for the laser light to decay into two electron-plasma waves or plasmons. SRS involves the decay of a laser photon into a plasmon and a scattered photon in the visible spectrum. Wave–particle interactions (e.g., Landau damping, trapping, and wave breaking) can generate hot electrons.[8] In addition to hard x rays, an experimental signature of $2\omega_{\rm pe}$ instability is significant $3/2\omega$ emission, which is Thomson scattering of the laser drive from the plasmons.

This article shows, for the first time, that gas-filled hohlraums driven with 13.5 kJ of 351-nm laser light produce two bursts of suprathermal electrons that are clearly resolved with the shaped laser pulse drive having a lower-intensity foot pulse followed by a higher-intensity main drive. The first burst from the two-plasmon-decay ($2\omega_{\rm pe}$) instability in the exploding LEH window produces up to 20 J of hot electrons with $T_{\rm hot}$ ~ 75 keV. It has a sharp laser-intensity threshold when the overlapped beam intensity is around 0.5×10^{15} W/cm^2. The $2\omega_{\rm pe}$ instability has been observed in direct-drive ICF;[10] however, this is the first observation of the $2\omega_{\rm pe}$ instability for indirect-drive ICF using 351-nm laser light. The second pulse with $T_{\rm hot}$ ~ 20 keV coincides with the SRS during the main laser drive. Previous hard x-ray experiments were not sensitive to the production of window hot electrons because they were time integrated.[6] Window hot electrons were also not observed using an x-ray spectroscopic technique.[11] Only a single burst of hard x rays is observed from a vacuum hohlraum because it does not have a gas fill contained by an LEH window.

Gas-filled Au hohlraums were irradiated on the OMEGA Laser System[12] with 40 beams arranged in three cones and smoothed with phase plates.[13] The thickness of the Au hohlraum wall ranged from 2 to 5 μm, and the hohlraum length varied from 2.3 to 2.55 mm. The inside diameter was 1.6 mm and

the LEH diameter varied from 1.07 to 1.2 mm. Figure 115.32 shows a computer rendering of the hohlraum and the energy-deposition regions of the cone 1, cone 2, and cone 3 beams having angles of incidence to the hohlraum axis of 21.4°, 42.0°, and 58.8°, respectively. Best focus of all the beams occurred at the LEH. Cone 2 and cone 3 beams were pointed to the center of the LEH and contributed to the peak overlapped laser intensity. Cone 1 beams were pointed slightly outside the center of the LEH and did not overlap the other beams at the LEH. All of the hohlraums, except for the vacuum ones, had a 0.6-μm-thick polyimide window, which is close to the 0.5-μm LEH window thickness of the NIF target. As shown in Table 115.I, the initial fully ionized electron density n_e of the hohlraum gas fill was varied by changing the gas fill, where the critical density is given as $n_{cr} = 1.1 \times 10^{21} / \lambda_{\mu m}^2 \, cm^{-3} = 9.0 \times 10^{21} \, cm^{-3}$. The measured laser power of the shaped laser pulse drive (PS26) is shown in Fig. 115.33. The total on-target laser energy E_{UV} was 13.5 kJ. The peak foot power was adjusted to vary the overlapped laser intensity at the LEH window from 0.5 to 1.5 × 10^{15} W/cm^2. The laser burned through the LEH window with

the lower-intensity foot and produced peak radiation temperatures of ~190 eV during the higher-intensity main drive.

The hard x-ray diagnostic (HXRD) has four high-pass energy channels recording time-resolved measurements along a line of sight 42° to the hohlraum axis.[14] The channels have the following lower-energy cutoffs: $h\nu > 20$ keV (HXRD1), $h\nu > 40$ keV (HXRD2), $h\nu > 60$ keV (HXRD3), and $h\nu > 80$ keV (HXRD4). The HXRD has a 120-ps rise time and a 1/e decay time of 1.2 ns. The absolute time scale was established using the hard x rays emitted from a Au spherical target irradiated with an ~200-ps

E16297JRC

Figure 115.32
Computer rendering of a gas-filled Au hohlraum irradiated with 40 laser beams. The beams are arranged in three cones and have elliptical phase plates. The energy-deposition regions of cone 1, cone 2, and cone 3 beams are shown on the inner wall of the hohlraum. A shaped laser pulse delivers 13.5 kJ of 351-nm light.

E16298JR
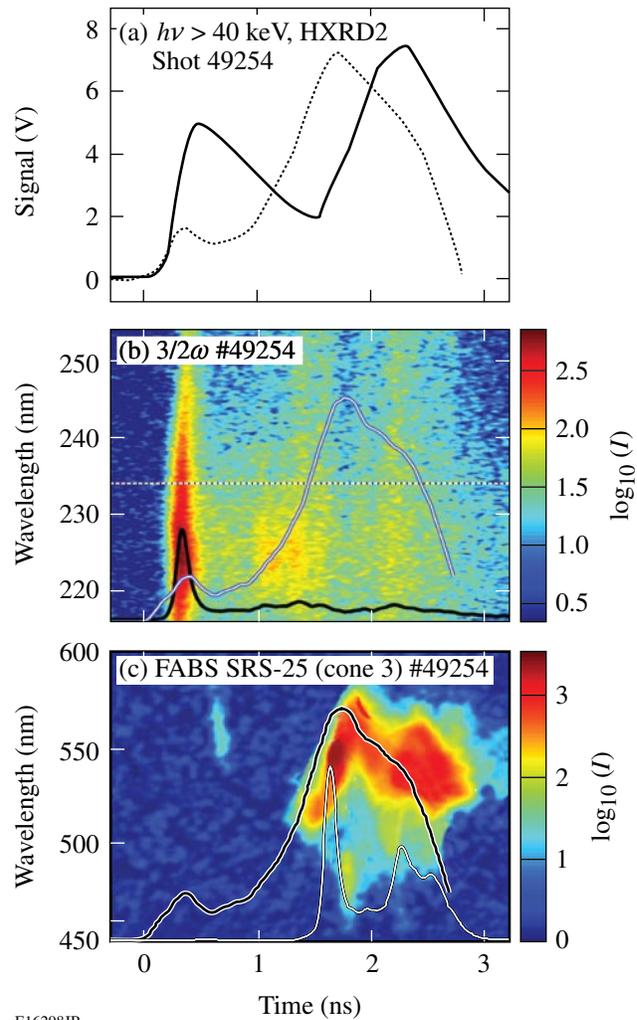
Figure 115.33
(a) Time history of HXRD2 ($h\nu > 40$ keV) (solid curve) compared with laser power (dotted curve). (b) Time-resolved spectral measurement of 3/2ω emission compared with measured laser pulse (white/black curve). Spectrally integrated time history is superposed (white curve). (c) Time-resolved FABS SRS with spectrally integrated time history (white curve) and laser power (white/black curve) superposed.

Table 115.I: Hohlraum specifications.

Gas Fill	Pressure (atm)	Initial Fully Ionized n_e
100% CH$_4$	0.9	0.02 n_{cr}
76% CH$_4$ + 24% C$_5$H$_{12}$	0.9	0.04 n_{cr}
100% C$_5$H$_{12}$	0.9	0.1 n_{cr}

Gaussian laser pulse. The fraction f_{hot} of laser energy E_{UV} coupled to hot electrons (i.e., $E_{hot} = f_{hot} E_{UV}$) and the temperature characterizing the Maxwellian distribution of hot electrons T_{hot} were inferred from the HXRD measurements using the thick-target bremsstrahlung radiation approximation

$$\frac{dI}{d\nu d\Omega} = \frac{5 \times 10^{11}}{4\pi} E_{hot} \frac{Z}{79} \exp\left(1 - \frac{h\nu}{T_{hot}}\right) \text{keV/keV/sr},$$

where Z is the atomic number of the hohlraum wall material.[6] The attenuation of the lower-energy hard x rays by the Au hohlraum wall was included in the analysis. An *in-situ* calibration was performed on the HXRD using the hard x-ray emission spectrum from a vacuum Au hohlraum irradiated with an 18-kJ, 1-ns square laser pulse. The calibration relied on earlier hohlraum hard x-ray measurements taken on the NOVA laser: the hard x-ray emission from a vacuum Au hohlraum was measured with the filter fluorescer experiment diagnostic,[6] and a Maxwellian distribution of hot electrons with $T_{hot} = 30$ keV and $f_{hot} = 0.3\%$ to 1.0% was inferred from the hard x-ray measurements.[15] The calibration of the HXRD on OMEGA used $T_{hot} = 30$ keV and $f_{hot} = 1\%$; therefore, the estimates of E_{hot} reported in this article represent upper limits. The uncertainty in the absolute value of E_{hot} does not affect the scaling of hot-electron production with the overlapped laser intensity on the window nor the inferred values of T_{hot}. The $3/2\omega$ emission from the LEH was recorded with a 100-ps temporal resolution and a 0.5-nm spectral resolution.[16] The SRS scattered directly back into the OMEGA lens of a cone 3 beam was recorded with a full-aperture backscatter station (FABS).[16]

The time history of HXRD2 (solid curve) recorded on shot number 49254 for a gas-filled Au hohlraum is compared with the PS26 laser pulse (dotted curve) in Fig. 115.33(a). The peak overlapped foot intensity was $\sim 1.2 \times 10^{15}$ W/cm^2 and the initial fully ionized n_e of the gas fill was 0.1 n_{cr}. The first burst of hard x rays occurs around the time of peak laser foot power, while the second burst of hard x rays occurs around the time of peak laser power. The long decay times of the HXRD measurements are instrumental; nevertheless, the diagnostic has enough temporal resolution to resolve the two bursts of hard x-ray emission. The x-ray fluences of the first and second hard x-ray pulses were calculated for each of the four energy channels, and T_{hot} and f_{hot} were quantified using a least-squares-fitting routine. The time-resolved $3/2\omega$ spectrum is shown in Fig. 115.33(b) and the time-resolved FABS SRS in Fig. 115.33(c). Overplotted on the streaked spectra in Figs. 115.33(b) and 115.33(c) are the laser power and the spectrally integrated scattered-light signals. As

can be seen in Fig. 115.33, the first x-ray pulse correlates with the $3/2\omega$ emission during the foot of the laser drive, and the second x-ray pulse correlates with the FABS SRS during the main drive.

The dependence of hot-electron production on the initial hohlraum n_e was investigated, with the peak overlapped foot intensity at the LEH around 1.2×10^{15} W/cm^2. As n_e was increased from 0.02 n_{cr} to 0.1 n_{cr}, f_{hot} for the first hard x-ray pulse increased from 0.005% to 0.1% and T_{hot} increased from 50 to 75 keV. As n_e was increased from 0 to 0.1 n_{cr}, f_{hot} for the second hard x-ray pulse increased from 0.1% to 5% and T_{hot} remained constant around 20 keV. The difference in T_{hot} for the first and second hard x-ray pulses is due to the higher phase velocity of the electron-plasma waves generated by the $2\omega_{pe}$ instability compared to those created by SRS.

The overlapped laser intensity on the LEH was varied from 0.5 to 1.5×10^{15} W/cm^2, and the intensity scaling of hot-electron generation in the exploding LEH window was investigated. The results are shown in Fig. 115.34(a) for E_{hot} with a very sharp threshold just above 0.5×10^{15} W/cm^2. The circles and triangles represent the lower ($n_e = 0.04$ n_{cr}) and higher ($n_e = 0.1$ n_{cr}) electron densities, respectively. The total energy in hot electrons, E_{hot}, is approximately 20 J with the higher n_e and an overlapped LEH laser intensity of $\sim 1.2 \times 10^{15}$ W/cm^2. The production of window hot electrons for the NIF-like density ($n_e = 0.04$ n_{cr}) with the high overlapped intensity is between 2 and 5 J. The scaling of T_{hot} with the overlapped LEH intensity is shown in Fig. 115.34(b). The hohlraums with $n_e = 0.1$ n_{cr} and the highest overlapped intensity have $T_{hot} \sim 75$ keV. More scatter in T_{hot} (40 keV $< T_{hot} <$ 80 keV) is observed for the hohlraums with $n_e = 0.04$ n_{cr} and the highest overlapped intensity. The measurements with the lowest overlapped intensity show a decrease in T_{hot} to ~ 30 keV. The OMEGA experiment is an excellent surrogate for the production of window hot electrons on the NIF ignition hohlraum: 2-D simulations from the radiation hydrodynamics code *HYDRA*[17] show that the window burnthrough phase of the gas-filled OMEGA hohlraum is hydrodynamically similar to that of an ignition hohlraum.

The linear theory of Simon *et al.* for the $2\omega_{pe}$ instability[7] predicts the threshold and growth rate of the instability, as well as the hot-electron temperature T_{hot} of electrons trapped in the plasmons; however, it does not predict the total energy in the trapped electrons. This requires determining the amplitude of the plasma waves, the trapping rate of electrons in the waves, and the competition between trapping and other wave saturation mechanisms, such as collisions. For the simulated
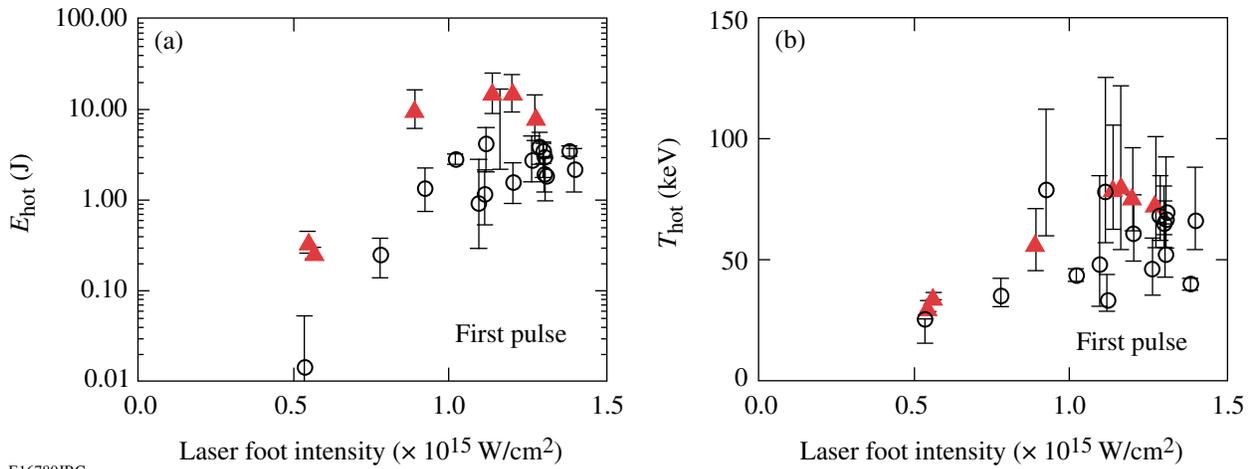
E16780JRC

Figure 115.34
Scaling of (a) E_{hot} and (b) T_{hot} with the peak overlapped laser intensity on the LEH window for $n_e = 0.04\ n_{cr}$ (circles) and $n_e = 0.1\ n_{cr}$ (triangles).

electron temperatures in the exploding window of an OMEGA hohlraum, the linear theory of the $2\omega_{pe}$ instability predicts $T_{hot} \geq 70$ keV, which is consistent with measurements during the early part of the laser pulse.

The $2\omega_{pe}$ instability occurs only in the vicinity of plasma at $n_e = 0.25\ n_{cr}$. The threshold intensity for the $2\omega_{pe}$ instability, $I_{thresh} \propto T_e/\lambda L$, is a function of the laser wavelength λ, electron temperature T_e, and density gradient scale length in the direction of the laser beam, $L = n_e(\partial n_e/\partial x)^{-1} = (n_{cr}/4)(\partial n_e/\partial x)^{-1}$. Motivated by recent direct-drive experiments,[10] the overlapped beam intensity is used in the threshold formula rather than the intensity of a single beam. This lower threshold is likely due to cooperative excitation of a common forward-directed plasma wave and/or to effects, such as swelling in intensity and increased interaction length for incident light waves that turn near the quarter-critical density.

Using 2-D radiation hydrodynamic simulations from the code *HYDRA*, it is possible to determine the laser power P_{pass} that passes the $n_e = 0.25\ n_{cr}$ surface with intensity above the threshold. The energy at risk of scattering into two plasmons is then given by

$$E_{risk} = \int_t \max(0, P_{pass} - P_{thresh})dt$$
$$= \int_t dt \sum_N P_{ray} \max\left(0, \frac{I_{pass} - I_{thresh}}{I_{thresh}}\right).$$

Here, $P_{pass} - P_{thresh}$ is the laser power with intensity $I > I_{thresh}$ and P_{ray} is the power of each of the N computed laser rays as it

crosses the $n_e = 0.25\ n_{cr}$ surface. In *HYDRA*, the average intensity, defined as the amount of power traversing a zone, is used to represent the overlap intensity I. This expression does not predict E_{hot} since it does not include the efficiency at which the $2\omega_{pe}$ instability generates hot electrons; however, the threshold given above can qualitatively explain the observed scalings of E_{hot} with hohlraum gas-fill density and laser intensity.

The two factors that determine the energy at risk for the $2\omega_{pe}$ instability are the fraction of the laser flux that crosses a surface of density $n_e = 0.25\ n_{cr}$ and the intensity of the laser at that surface. When the laser beams initially ablate the 0.6-μm-thick polyimide LEH window, they launch a shock wave. As the window plasma expands to low density, the laser-energy–deposition rate drops. The shock wave becomes unsupported and transits into the gas plasma behind the window as a hemispherical blast wave. When the blast wave expands below $n_e = 0.25\ n_{cr}$ everywhere, the risk of the $2\omega_{pe}$ instability in the LEH region is gone.

For hohlraums with an initial gas plasma density of $n_e = 0.04\ n_{cr}$, *HYDRA* simulations show that the blast-wave density is below $n_e = 0.25\ n_{cr}$ as soon as it enters the gas region. For the $n_e = 0.10\ n_{cr}$ hohlraums, the blast-wave peak density remains above $n_e = 0.25\ n_{cr}$ for about 0.1 ns after the blast wave enters the gas plasma. *HYDRA* simulations predict that E_{risk} should drop by a third between $n_e = 0.10\ n_{cr}$ and $n_e = 0.04\ n_{cr}$, which is consistent with the upper range of the points in Fig. 115.34(a). Post-processed *HYDRA* simulations confirm that E_{risk} decreases with intensity; however, this predicted scaling is too slow to explain the rapid drop in E_{hot} observed for intensities below 10^{15} W/cm^2. Presumably, the observed

drop is due to a decrease in the efficiency of trapping and accelerating electrons in the plasmons, which is not modeled in the expression for E_{risk}.

The observed threshold for the window hot electrons can be exploited to mitigate the hot-electron production as the LEH window burns through in gas-filled hohlraums. Specifications for the NIF ignition target restrict E_{hot} to less than 8 J for $T_{hot} = 70$ keV and to less than 38 J for $T_{hot} = 30$ keV; otherwise, pre-heat of the implosion capsule could jeopardize hot-spot ignition. As a result of this research, the initial overlapped laser intensity incident on the LEH window of an ignition target for the NIF has been set below the measured intensity threshold to retain ignition margin by staggering the turn-on time of the inner and outer cones of beams.

Two bursts of suprathermal electrons are observed from gas-filled hohlraums driven with 351-nm laser light. The $2\omega_{pe}$ instability in the exploding LEH window appears to produce up to 20 J of hot electrons with $T_{hot} \sim 75$ keV at early times and has a sharp laser-intensity threshold around 0.5×10^{15} W/cm^2. The observed threshold can be exploited to mitigate the hot-electron production in hohlraums. Simulations using a 2-D radiation hydrodynamics code and a linear theory of the $2\omega_{pe}$ instability show qualitative agreement with the experimental results. The second pulse produced by SRS during the main laser drive has more energy, but significantly lower $T_{hot} \sim 20$ keV.

REFERENCES

1. R. L. McCrory, D. D. Meyerhofer, R. Betti, R. S. Craxton, J. A. Delettrez, D. H. Edgell, V. Yu Glebov, V. N. Goncharov, D. R. Harding, D. W. Jacobs-Perkins, J. P. Knauer, F. J. Marshall, P. W. McKenty, P. B. Radha, S. P. Regan, T. C. Sangster, W. Seka, R. W. Short, S. Skupsky, V. A. Smalyuk, J. M. Soures, C. Stoeckl, B. Yaakobi, D. Shvarts, J. A. Frenje, C. K. Li, R. D. Petrasso, and F. H. Séguin, Phys. Plasmas **15**, 055503 (2008).

2. J. D. Lindl *et al.*, Phys. Plasmas **11**, 339 (2004).

3. J. A. Paisner, E. M. Campbell, and W. J. Hogan, Fusion Technol. **26**, 755 (1994); G. H. Miller, E. I. Moses, and C. R. Wuest, Opt. Eng. **43**, 2841 (2004).

4. J. Schein *et al.*, Phys. Rev. Lett. **98**, 175003 (2007); O. S. Jones *et al.*, Phys. Plasmas **14**, 056311 (2007).

5. M. C. Herrmann, M. Tabak, and J. D. Lindl, Nucl. Fusion **41**, 99 (2001); R. Betti, K. Anderson, V. N. Goncharov, R. L. McCrory, D. D. Meyerhofer, S. Skupsky, and R. P. J. Town, Phys. Plasmas **9**, 2277 (2002).

6. R. P. Drake *et al.*, Phys. Rev. A **40**, 3219 (1989); J. W. McDonald *et al.*, Rev. Sci. Instrum. **75**, 3753 (2004); J. W. McDonald *et al.*, Phys. Plasmas **13**, 032703 (2006).

7. D. W. Phillion *et al.*, Phys. Rev. Lett. **49**, 1405 (1982); D. M. Villeneuve, R. L. Keck, B. B. Afeyan, W. Seka, and E. A. Williams, Phys. Fluids **27**, 721 (1984); C. Rousseaux *et al.*, Phys. Fluids B **4**, 2589 (1992); W. Seka, R. E. Bahr, R. W. Short, A. Simon, R. S. Craxton, D. S. Montgomery, and A. E. Rubenchik, Phys. Fluids B **4**, 2232 (1992); C. S. Liu and M. N. Rosenbluth, Phys. Fluids **19**, 967 (1976); A. Simon, R. W. Short, E. A. Williams, and T. Dewandre, Phys. Fluids **26**, 3107 (1983); A. B. Langdon, B. F. Lasinski, and W. L. Kruer, Phys. Rev. Lett. **43**, 133 (1979); B. F. Lasinski and A. B. Langdon, Lawrence Livermore National Laboratory, Livermore, CA, Report UCRL-50021-77, 4-49 (1978); B. B. Afeyan and E. A. Williams, Phys. Plasmas **4**, 3827 (1997); B. B. Afeyan and E. A. Williams, Phys. Plasmas **4**, 3845 (1997).

8. W. L. Kruer, *The Physics of Laser–Plasma Interactions,* Frontiers in Physics, Vol. 73, edited by D. Pines (Addison-Wesley, Redwood City, CA, 1988), Chap. 4, pp. 37–43.

9. J. W. Shearer *et al.*, Phys. Rev. A **6**, 764 (1972); K. Estabrook, W. L. Kruer, and B. F. Lasinski, Phys. Rev. Lett. **45**, 1399 (1980); K. Estabrook and W. L. Kruer, Phys. Fluids **26**, 1892 (1983); A. A. Offenberger *et al.*, Phys. Rev. Lett. **49**, 371 (1982); T. P. Hughes, *Plasmas and Laser Light* (Wiley, New York, 1975); B. J. MacGowan *et al.*, Phys. Plasmas **3**, 2029 (1996).

10. C. Stoeckl, R. E. Bahr, B. Yaakobi, W. Seka, S. P. Regan, R. S. Craxton, J. A. Delettrez, R. W. Short, J. Myatt, A. V. Maximov, and H. Baldis, Phys. Rev. Lett. **90**, 235002 (2003).

11. S. H. Glenzer *et al.*, Phys. Rev. Lett. **81**, 365 (1998).

12. T. R. Boehly, D. L. Brown, R. S. Craxton, R. L. Keck, J. P. Knauer, J. H. Kelly, T. J. Kessler, S. A. Kumpan, S. J. Loucks, S. A. Letzring, F. J. Marshall, R. L. McCrory, S. F. B. Morse, W. Seka, J. M. Soures, and C. P. Verdon, Opt. Commun. **133**, 495 (1997).

13. *LLE Review Quarterly Report* **112**, 212, Laboratory for Laser Energetics, University of Rochester, Rochester, NY, LLE Document No. DOE/SF/19460-790 (2007).

14. C. Stoeckl, V. Yu. Glebov, D. D. Meyerhofer, W. Seka, B. Yaakobi, R. P. J. Town, and J. D. Zuegel, Rev. Sci. Instrum. **72**, 1197 (2001).

15. R. L. Kauffman, Lawrence Livermore National Laboratory, private communication (2008).

16. W. Seka, D. H. Edgell, J. P. Knauer, J. F. Myatt, A. V. Maximov, R. W. Short, T. C. Sangster, C. Stoeckl, R. E. Bahr, R. S. Craxton, J. A. Delettrez, V. N. Goncharov, I. V. Igumenshchev, and D. Shvarts, Phys. Plasmas **15**, 056312 (2008).

17. M. M. Marinak *et al.*, Phys. Plasmas **8**, 2275 (2001).

Effectiveness of Silicon (Si) as a Laser Shinethrough Barrier for 351-nm Light

Introduction

In direct-drive inertial confinement fusion (ICF), energy from many individual high-power laser beams is delivered to a spherical target, causing a spherically symmetric implosion.[1] Current ignition designs for direct-drive targets require a layer of condensed D_2 or DT fuel that adheres to the inner surface of a spherical plastic-shell ablator. The laser ionizes the target shell's surface, forming a plasma that surrounds the target. This coronal plasma governs any further interaction of the laser and the target, and the critical surface within the plasma prevents further direct transmission of light into the target's interior. The laser energy is absorbed in the subcritical underdense plasma and transported by the electrons through the overdense plasma to the ablation front. The ablation pressure drives the fuel layer inward, compressing both it and the gaseous fuel at the target's center. The drive pressure is varied in time such that the fuel density is compressed (up to ~1000× solid density for ignition designs) while remaining close to Fermi degenerate. Shock waves resulting from the drive-pressure history, along with compressive work, heat the central gaseous-core "hot spot" to the high temperatures needed to initiate burning of the fuel.

Asymmetry-induced hydrodynamics can reduce the performance of ICF targets to well below that predicted by 1-D modeling.[2] The hydrodynamic instability of most concern is Rayleigh–Taylor instability (RTI).[3,4] Imperfections in the spherical symmetry of both the target structure and the laser illumination act as seeds for the RTI. The nonlinear growth of this instability on the inner surface of the target mixes the cold compressed fuel layer with the hot-spot fuel vapor and/or shell, reducing fusion yield or preventing ignition.[5–8] Ignition requirements impose severe constraints on the illumination uniformity and the sphericity of the target.[9]

It has long been known[10,11] that very early during laser irradiation, before the coronal plasma density reaches critical density, the target is transparent to the laser light and laser energy can penetrate into the target. Deposition of this laser "shinethrough" energy within the target can severely degrade target performance even though the total energy is small. Absorption of shinethrough laser light can transmit nonuniformities in the illumination due to power imbalance or imprint into the target's interior. These asymmetries are made worse by filamentation of the penetrating laser power inside the target, which has been observed to leave permanent damage tracks.[10] The nonuniform deposition of energy in the interior of the target can create density perturbations that seed the RTI.

Shinethrough-seeded RTI has been identified as the likely cause of anomalous results in "burnthrough" mass-ablation-rate experiments.[12,13] In these experiments, a high-Z tracer layer was embedded within a target as a diagnostic, and the onset time of characteristic x-ray radiation from that layer during an implosion was used to infer the burnthrough ablation rates. The measured ablation rates were far greater than predicted by 1-D modeling. The spatial distribution of the characteristic x rays was found to be emitted from many localized spots.[13] The addition of an opaque barrier layer on the target surface was shown to bring the characteristic x-ray onset time in line with the 1-D predictions.[12]

A thin barrier layer of UV opaque material on the outer surface of the target forces breakdown to occur at the outer surface, effectively eliminating the deleterious effects of shinethrough. The conventional material used for shinethrough barriers is aluminum (Al). Barrier layers of Al have been shown to block shinethrough light and improve implosion performance. A thin barrier layer of 200 Å of Al eliminated all signs of filamentation damage tracks in laser-illuminated targets.[10] Deuterium-filled glass targets with a 500-Å Al barrier imploded using the original 24-beam OMEGA Laser System[14] showed a clear yield improvement over uncoated targets.[11]

For direct-drive cryogenic targets on OMEGA, a suitable shinethrough barrier material must be opaque to the 351-nm UV laser light *and* be compatible with the standard cryogenic target fabrication techniques of permeation filling, infrared (IR) layering, and optical characterization. The common Al barrier material is unsuitable in this context in all respects. In

the past, silicon (Si) has been identified as a potential barrier material for cryogenic direct-drive targets.[15] Its transmission characteristics are sufficient for optical characterization at 627 nm (Fig. 115.35) and laser-assisted cryogenic layering at 3.16 μm, and it is suitable for permeation filling.

At the laser wavelength (351 nm) the Si barrier is almost opaque and its opacity increases with laser intensity due to the easy formation of free electrons in Si. Silicon thus appears to be an excellent candidate for a shinethrough barrier material.
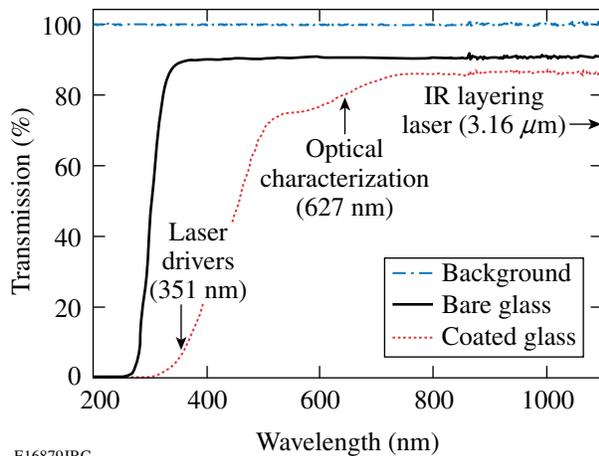
Figure 115.35
Transmission of light through uncoated glass and through glass coated with ~1100 Å of Si. The silicon-coating transmission is low at the UV laser driver wavelength (351 nm) and high at the ice-layer optical characterization wavelength (627 nm).

In this article we experimentally verify the suitability of Si as a shinethrough barrier material for 351-nm direct-drive laser-fusion experiments. The following sections (1) report the successful permeation filling, IR layering, and optical characterization of Si barrier–coated cryogenic targets; (2) experimentally verify the performance of Si as a shinethrough barrier; (3) determine a minimum acceptable barrier thickness; and (4) discuss our conclusions.

Cryogenic Target Fabrication with Si Barriers

Cryogenic targets for OMEGA are permeation filled with either D_2 or DT at room temperature at approximately 1000 atm in the Fill/Transfer Station (FTS).[16] The targets are deuterated polystyrene shells of 3- to 10-μm wall thickness suspended in a beryllium "C-mount" using four submicron threads of spider silk. Once filled, the targets are cooled slowly (~0.1 K/min) to below their fuel triple point, forming rough ice layers inside the targets.[16]

The rough ice layers are subsequently smoothed using volumetric heating just below the triple point, which leads to a sublimation/condensation redistribution of the ice mass toward an inner surface that is smoother, more uniform, and closer to an isotherm. Volumetric heating naturally occurs in DT and T_2 fuels that self-heat due to tritium beta decay.[17,18] For D_2 fuel, the infrared heating technique[19] deposits energy volumetrically in the ice by pumping an IR collisionally induced vibration–rotation band of deuterium. The wavelength of the IR heating laser employed at LLE is 3.16 μm.

LLE uses optical backlit shadowgraphy to characterize OMEGA cryogenic target ice layers.[20,21] A 627-nm, red-light–emitting diode (LED) provides the backlighting. A shadowgram records the image of the light rays passing through a backlit target. The rays are reflected and refracted at the shell wall and ice-layer surfaces, forming characteristic rings in the shadowgram. The most-prominent ring or "bright ring" results from a single internal reflection off the inner solid/vapor interface of the ice layer. The position of the bright ring in the shadowgram is directly correlated with the position of the inner surface of the ice layer and makes it possible to characterize the nonuniformity of the inner surface. A 3-D reconstruction of the inner ice surface can be built from multiple shadowgrams from different views. Details can be found in Refs. 20 and 21.

To test the suitability of Si as a shinethrough barrier material, standard cryogenic target shells were coated with Si, then permeation filled, layered, and characterized using the standard procedures. Several typical OMEGA cryogenic shells were coated with Si using a room-temperature radio-frequency sputter coater. The Si thickness was estimated by a quartz crystal monitor, and the coating thickness was verified offline using reflected-light interferometry. The shells were affixed to a substrate with a weak adhesive and coated from above. The targets were flipped over at midpoint in the coating process to expose the other side. This single "roll-over" method produced some low-mode nonuniformity in the coating thickness, but the coverage was sufficiently uniform to test permeation filling, IR layering, or optical characterization of the Si-coated cryogenic targets. If Si barriers become common for spherical direct-drive targets, they will require a more-uniform coating technique than the roll-over method used here.

The optical shadowgrams of two Si barrier–coated cryogenic targets shown in Fig. 115.36 are proof that permeation filling and optical characterization through a Si barrier are possible. The shells, one coated with 500 Å of Si and the other with 1000 Å, were cooled to below the triple point for D_2

(18.73 K). Sufficient IR heating laser power kept the liquid layer in Fig. 115.36 from freezing. The shadowgrams in Fig. 115.36 show that both targets could be optically characterized.

A shadowgram and intensity lineout showing the ice layer of a DT permeation-filled target coated with 750 Å of Si are displayed in Fig. 115.37. The bright ring is very strong and two of the fainter inner rings are also clearly visible. A Fourier-mode power spectrum for the bright ring is shown in Fig. 115.38. The Si barrier did not significantly affect optical characterization
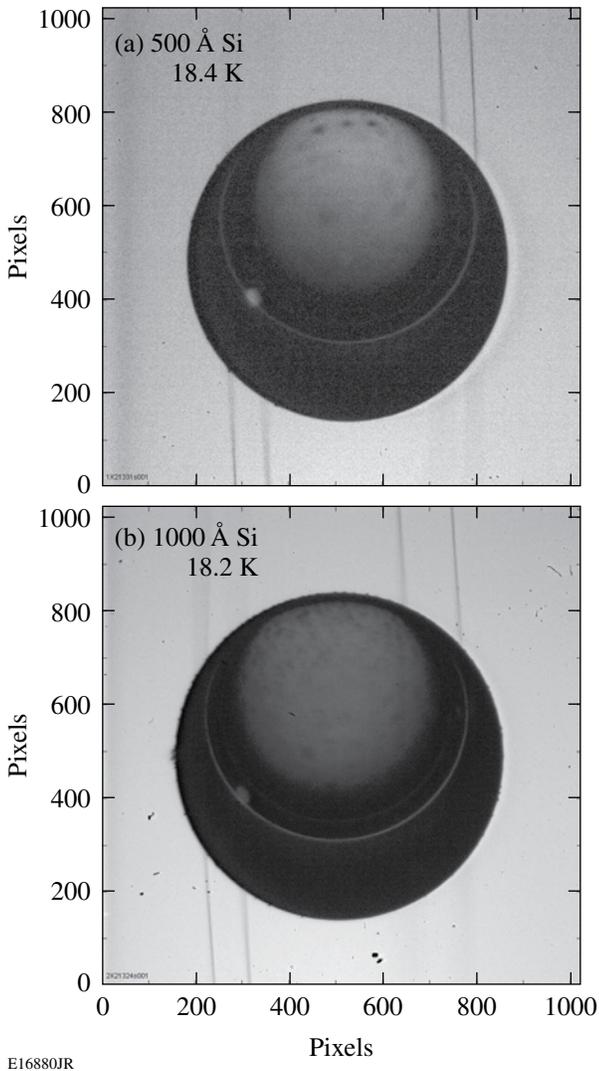
Figure 115.36

Backlit shadowgrams of permeation-filled cryogenic deuterium targets with Si shinethrough barrier coatings of (a) 500-Å and (b) 1000-Å thickness. The layering sphere temperatures are below the D_2 triple point, yet the fuel is still liquid. The off-center circular rings inside the target are the result of light internally reflecting off the vapor/liquid interface of the "bubble" inside the target.
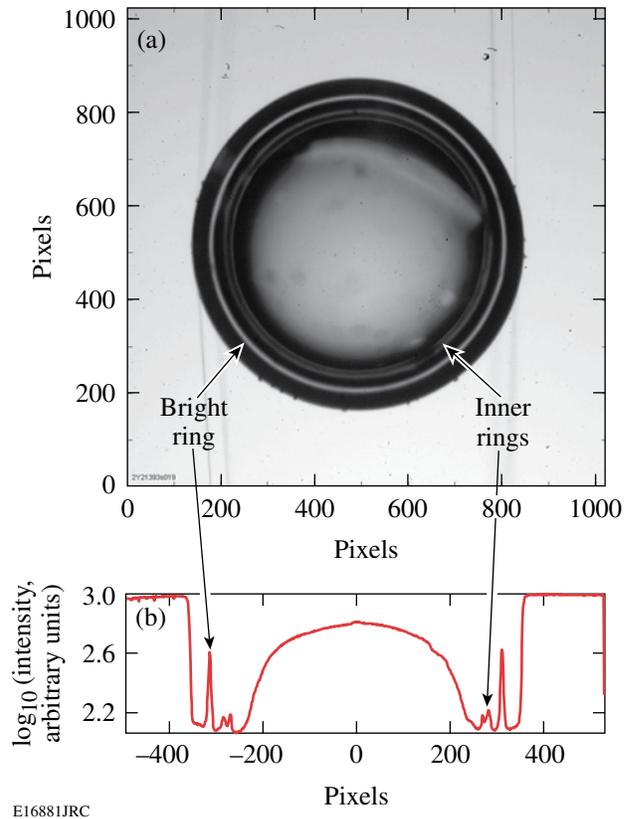
Figure 115.37

(a) Shadowgram of a Si-coated (750 Å), DT-filled cryogenic target and (b) a horizontal lineout through the target of the logarithm of the shadowgram intensity. Both the bright ring and two fainter inner rings are clearly visible through the Si barrier.
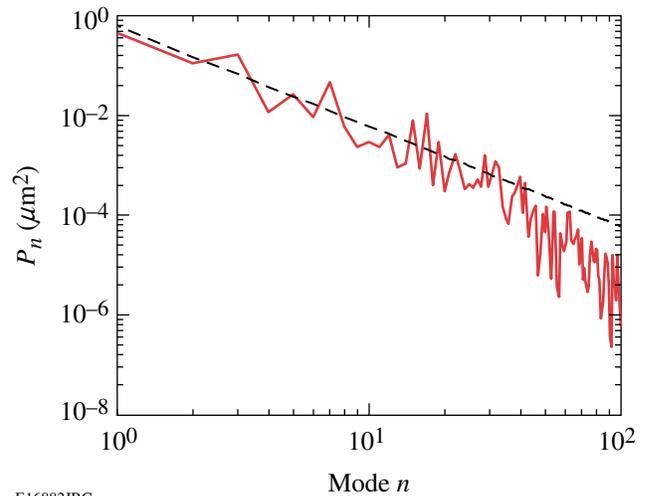
Figure 115.38

The Fourier-mode power spectrum of the bright ring (solid line) from Fig. 115.37 compared to the specification for direct-drive–ignition targets (dashed line).[9] The ice-surface rms for this view is 0.94 μm for all modes and for mode numbers 10 and above. This view is within the specification.

nor did the Si barrier inhibit beta layering of DT cryogenic targets. The surface-averaged rms (root mean square) of the ice-layer thickness for the target shown in Fig. 115.37 was 0.91 μm, one of the best layers produced to date for OMEGA.

The IR-layered, Si-coated D_2 cryogenic targets do not meet ignition specifications. Both targets shown in Fig. 115.36 showed large asymmetries when frozen with surface-averaged ice-layer-thickness nonuniformities of 6.2 μm (rms) for a 500-Å coating of Si and 11.6 μm (rms) for a 1000-Å coating of Si. While IR-layered D_2 targets typically have larger ice-layer asymmetries than DT targets, these values are among the worst in recent years and the target with the thickest Si barrier was more asymmetric. Determining whether these poor D_2 layers were statistical aberrations or were directly related to the Si coating will require further investigation.

Effectiveness of Si as a Shinethrough Barrier

Planar-target experiments were performed to verify the efficacy of Si and to determine the minimum effective thickness of Si as a shinethrough barrier material. Previous studies[11] have shown that the amount of shinethrough energy transmitted by an uncoated glass surface before a critical plasma forms is very low and is very insensitive to the incident laser intensity. The experiments were performed using a single beam at low energy (<1.5 J). The targets survived the experiments and clearly exhibited permanent shinethrough damage where there was no shinethrough barrier. Figure 115.39 shows filamentation damage streaks along the laser beam path behind an uncoated
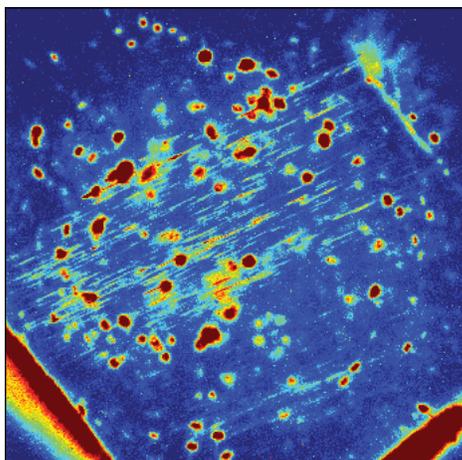
E16883JRC

Figure 115.39
Post-shot close-up image of a glass-cube target ($4 \times 4 \times 4$ mm^3) showing filamentation tracks along the laser beam path through the target behind an uncoated region.

region of a glass target after exposure to a low-energy pulse (200 ps, 1.5 J).

The target in this experiment was a 6-mm $\times$ 6-mm $\times$ 1-mm glass slide constructed as detailed in Fig. 115.40(a). The target front was illuminated by a laser pulse of 200-ps duration and 0.7 J of energy. An examination of the target shows a distinctive "hourglass" hole burnt into the Al coating on the back of the target corresponding to the uncoated regions on the front of the target exposed to the beam. The Al backing is intact behind both the Al and Si shinethrough barrier squares on the front of the target. This is qualitative evidence that Si was as effective at blocking shinethrough as the conventional Al barriers.

A series of experiments using VISAR (velocity interferometry system for any reflector)[22,23] tested the efficacy of Si as a shinethrough barrier during a pulse. VISAR detects a Doppler shift of a probe beam reflected off a moving surface. The interference between two paths of the probe laser, one reflected off a surface and one direct to the detector, produces fringes whose displacements are proportional to the velocity of the surface. The effect of shinethrough light on an opaque surface can be detected using VISAR. Any shinethrough energy will heat the opaque layer, causing it to expand and resulting in movement of the VISAR fringes. If the heating is sufficient to vaporize the layer, the expanding material will disrupt the VISAR fringes and blank out this fringe pattern.

For these studies, the rear surfaces of several planar glass targets were covered with 1000 Å of Al to provide a reflective surface suitable for observation by VISAR. Half of the front (laser-facing) side was coated with a Si barrier. The low-power laser beam was centered on the interface between the Si-coated and uncoated portions of the target. The VISAR probe beam was pointed at the rear of the target to sample a line across the coated/uncoated interface. The results are summarized in Fig. 115.41. The VISAR fringes behind unprotected regions are blanked out promptly at the start of the illumination pulse, indicating an ablation of the rear surface by shinethrough energy. Note that in Fig. 115.41(b) this blanking is not seen because VISAR is observed behind only the Si barrier–protected region due to error in VISAR pointing, target alignment, or target metrology. The correct timing of the VISAR image with the laser pulse has been verified using the laser timing fiducial pulses (the dots visible along the top and bottom of each VISAR image). The VISAR fringes behind portions of the targets protected by 750-Å, 300-Å, and 200-Å Si barriers [Figs. 115.41(a)–115.41(c)] are unaffected by shinethrough, indicating no detectable motion or heating of the rear surfaces
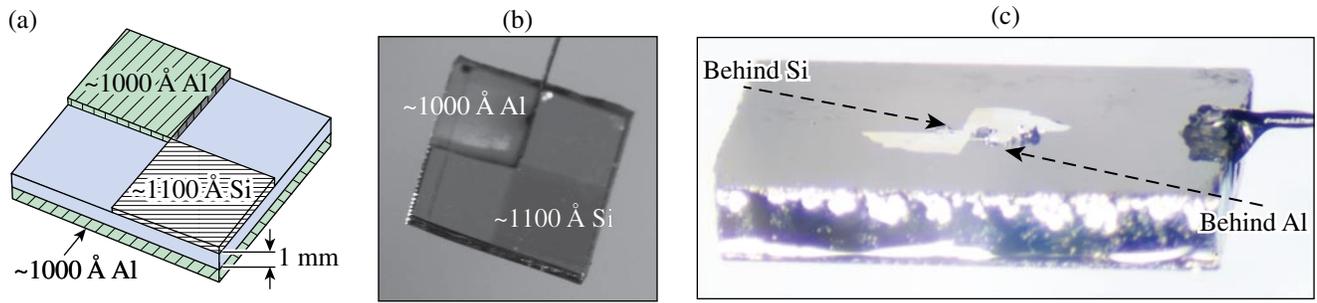
E16884JRC

Figure 115.40
Glass-slide planar target of dimensions roughly $6 \times 6 \times 1$ mm^3. (a) Design specifications: The back side of the target was coated with 1000 Å of Al. The front (laser-facing) side of the target was 1/4 coated with 1000 Å of Al, 1/4 coated with 1100 Å of Si, and 1/2 uncoated. (b) Pre-shot photograph of target front. (c) Post-shot photograph of back of target.
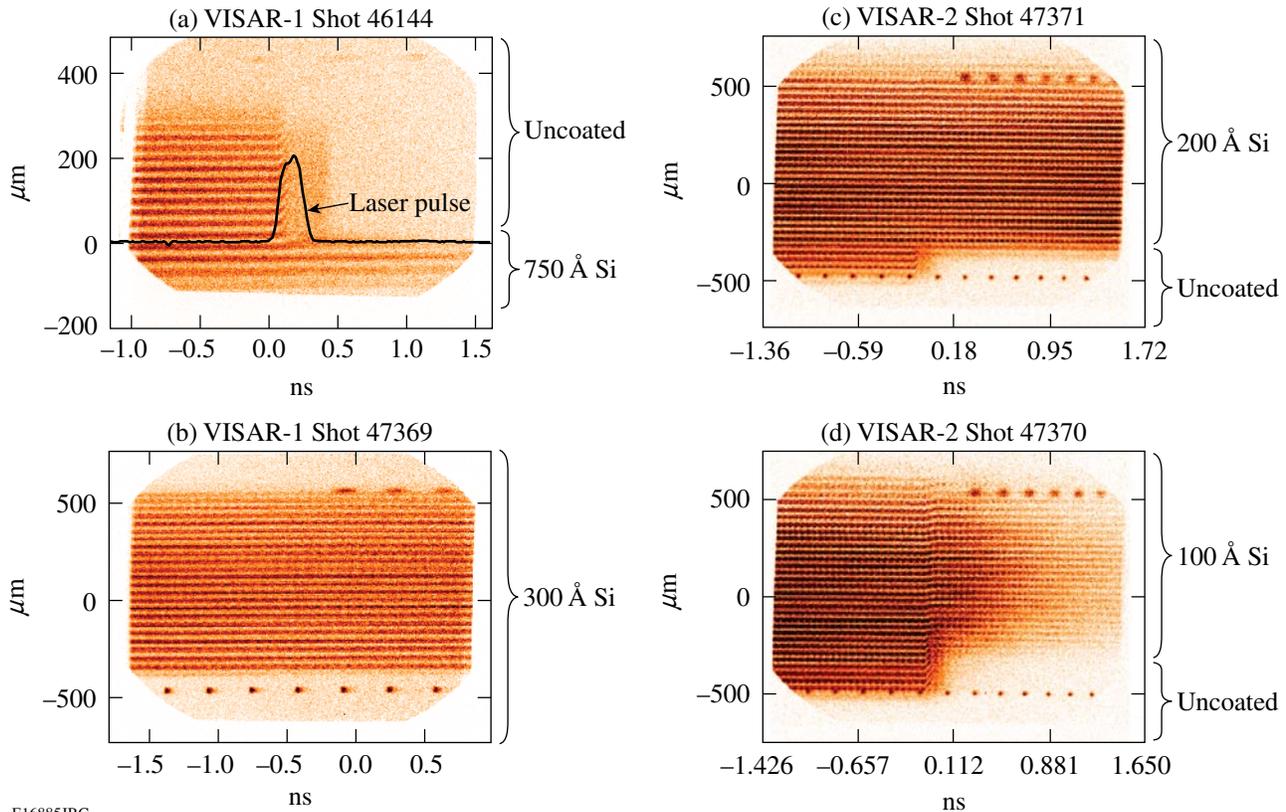
E16885JRC

Figure 115.41
VISAR fringes for four targets half coated with different thicknesses of Si: (a) 750 Å of Si, (b) 300 Å of Si, (c) 200 Å of Si, and (d) 100 Å of Si. The back surface behind the uncoated front is clearly ablated off by shinethrough at the start of the laser pulse [shown, for example, in (a) by the black line], blanking the VISAR signal wherever these unprotected sections are observed. The sections of the target protected by Si are unaffected except for the thinnest barrier layer in (d), where there is evidence of fringe motion behind the Si barrier–protected region, indicating motion/heating of the rear surface.

behind these barriers. Because the damage-threshold fluence for CH plastic is twice that for Al (Ref. 24), we conclude that these barrier thicknesses would have prevented shinethrough damage to an ICF plastic-shell target. In Fig. 115.41(d), however, the VISAR fringes show a slight motion of the surface behind a 100-Å Si barrier at the start of the pulse, clearly proving that some shinethrough energy has penetrated the Si barrier. From this VISAR data we conclude that a 100-Å Si coating is inadequate as a shinethrough barrier. A barrier layer of 200 Å of Si should be sufficient to block shinethrough light for 351-nm-laser–driven, direct-drive ICF plastic-shell targets. As previous studies[11] have shown that the total shinethrough energy transmitted before a critical surface forms in the coronal plasma is insensitive to the incident energy or intensity, this thickness should not need to be scaled for other experimental conditions. A 200-Å Si barrier should be sufficient to block shinethrough energy during the earliest part of the laser pulse before the coronal plasma reaches critical density in ICF and ignition experiments.

Discussion

These experiments have shown that direct-drive ICF cryogenic targets coated with up to 1000 Å of Si as a shinethrough barrier can be successfully permeation filled, beta-layered, and characterized. However, to minimize the effects of the barrier on these processes (such as the attenuation of light used to characterize the ice layer), we recommend using the minimum effective shinethrough barrier thickness of 200 Å of Si. This minimum thickness may also alleviate the possible difficulties with IR layering D_2 targets found in this study's limited sample set.

REFERENCES

1. J. Nuckolls *et al.*, Nature **239**, 139 (1972).

2. D. D. Meyerhofer, J. A. Delettrez, R. Epstein, V. Yu. Glebov, V. N. Goncharov, R. L. Keck, R. L. McCrory, P. W. McKenty, F. J. Marshall, P. B. Radha, S. P. Regan, S. Roberts, W. Seka, S. Skupsky, V. A. Smalyuk, C. Sorce, C. Stoeckl, J. M. Soures, R. P. J. Town, B. Yaakobi, J. D. Zuegel, J. Frenje, C. K. Li, R. D. Petrasso, D. G. Hicks, F. H. Séguin, K. Fletcher, S. Padalino, C. Freeman, N. Izumi, R. Lerche, T. W. Phillips, and T. C. Sangster, Phys. Plasmas **8**, 2251 (2001).

3. Lord Rayleigh, Proc. London Math Soc. **XIV**, 170 (1883).

4. G. Taylor, Proc. R. Soc. London Ser. A **201**, 192 (1950)

5. V. Lobatchev and R. Betti, Phys. Rev. Lett. **85**, 4522 (2000).

6. M. C. Herrmann, M. Tabak, and J. D. Lindl, Phys. Plasmas **8**, 2296 (2001).

7. R. Betti, K. Anderson, V. N. Goncharov, R. L. McCrory, D. D. Meyerhofer, S. Skupsky, and R. P. J. Town, Phys. Plasmas **9**, 2277 (2002).

8. R. P. J. Town and A. R. Bell, Phys. Rev. Lett. **67**, 1863 (1991).

9. P. W. McKenty, V. N. Goncharov, R. P. J. Town, S. Skupsky, R. Betti, and R. L. McCrory, Phys. Plasmas **8**, 2315 (2001).

10. J. E. Balmer, T. P. Donaldson, W. Seka, and J. A. Zimmermann, Opt. Commun. **24**, 109 (1978).

11. D. K. Bradley, T. Boehly, D. L. Brown, J. Delettrez, W. Seka, and D. Smith, in *Laser Interaction and Related Plasma Phenomena*, edited by H. Hora and G. Miley (Plenum Press, New York, 1991), Vol. 9, pp. 323–334.

12. J. Delettrez, D. K. Bradley, P. A. Jaanimagi, and C. P. Verdon, Phys. Rev. A **41**, 5583 (1990).

13. M. Nishikino *et al.*, Bull. Am. Phys. Soc. **46**, 142 (2001).

14. J. M. Soures, J. Fusion Energy **10**, 295 (1991).

15. Y. Fisher, T. R. Boehly, D. K. Bradley, D. R. Harding, D. D. Meyerhofer, and M. D. Wittman, Bull. Am. Phys. Soc. **43**, 1784 (1998).

16. D. R. Harding, T. C. Sangster, D. D. Meyerhofer, P. W. McKenty, L. D. Lund, L. Elasky, M. D. Wittman, W. Seka, S. J. Loucks, R. Janezic, T. H. Hinterman, D. H. Edgell, D. Jacobs-Perkins, and R. Q. Gram, Fusion Sci. Technol. **48**, 1299 (2005).

17. J. K. Hoffer and L. R. Foreman, Phys. Rev. Lett. **60**, 1310 (1988).

18. A. J. Martin, R. J. Simms, and R. B. Jacobs, J. Vac. Sci. Technol. A **6**, 1885 (1988).

19. D. N. Bittner *et al.*, Fusion Technol. **35**, 244 (1999).

20. D. H. Edgell, W. Seka, R. S. Craxton, L. M. Elasky, D. R. Harding, R. L. Keck, and M. D. Wittman, Fusion Sci. Technol. **49**, 616 (2006).

21. D. H. Edgell, R. S. Craxton, L. M. Elasky, D. R. Harding, S. J. Verbridge, M. D. Wittman, and W. Seka, Fusion Sci. Technol. **51**, 717 (2007).

22. L. M. Barker and R. E. Hollenbach, J Appl. Phys. **43**, 4669 (1972).

23. P. M. Celliers, D. K. Bradley, G. W. Collins, D. G. Hicks, T. R. Boehly, and W. J. Armstrong, Rev. Sci. Instrum. **75**, 4916 (2004).

24. T. R. Boehly, Y. Fisher, D. D. Meyerhofer, W. Seka, J. M. Soures, and D. K. Bradley, Phys. Plasmas **8**, 231 (2001).

Elimination of Self-Pulsations in Dual-Clad, Ytterbium-Doped Fiber Lasers

Introduction

High-power, high-beam-quality, stable continuous-wave (cw) fiber lasers are desired in sensing, ranging, telecommunications, and spectroscopy.[1,2] Although high-output powers have been achieved in many high-power fiber laser systems,[3] self-pulsing often occurs in cw fiber lasers under specific pumping and cavity conditions.[4] Generally, self-pulsing in fiber lasers can be classified as sustained self-pulsing (SSP) and self-mode-locking (SML). SSP is the periodic emission of optical pulses at a repetition rate corresponding to the relaxation oscillation frequency of the inversion and photon populations. SML is the periodic emission of optical pulses with a rate corresponding to the cavity-round-trip time.[5] Both of the regimes can be described by the interaction of the photon population and the population inversion.[6]

Although the self-pulsations typically occur at the lower end of the pump power range, the pulses caused by these instabilities carry sufficient optical energy to cause catastrophic damage to the fiber laser, particularly when they are allowed to occur for extended periods of time. For this reason, there have been intensive investigations on self-pulsation suppression in cw fiber lasers. Electronic feedback has been used on the pump laser to shift the gain and phase to minimize relaxation oscillations.[7] Auxiliary pumping near the lasing wavelength sustains the population inversion in the gain medium, thereby preventing rapid gain depletion and minimizing the relaxation oscillations.[8] The fast saturable gain of a semiconductor optical amplifier included within the fiber-laser cavity prevents large signal buildup in the fiber laser and suppresses the self-pulsing behavior.[9] The narrow passband of a $\lambda/4$-shifted fiber Bragg grating (FBG) structure in a ring cavity limits the number of longitudinal cavity modes and suppresses self-pulsations.[10] In this article, increasing the round-trip time in the cavity by inserting a long section of passive fiber is shown to change the relaxation oscillation dynamics and make it possible to completely eliminate self-pulsations at all pumping levels. This technique is much simpler to implement than the alternative methods described above.

Experimental Results

The experimental setup is shown in Fig. 115.42. The 25-W pump light at a wavelength of 915 nm is delivered by the pump coupling fiber, which has a 200-μm core diameter and 0.22 numerical aperture (N.A.) with aspheric lenses of focal lengths 27 mm and 13.5 mm. The overall pump coupling efficiency is 75%. The laser gain medium is a 20-m, dual-clad, ytterbium-doped, single-mode fiber with an absorption rate of 0.5 dB/m at 915 nm. This ytterbium-doped fiber has a 130-μm cladding diameter with an N.A. of 0.46. The fiber has a core diameter of 5 μm with an N.A. of 0.12. One end of the fiber is spliced into an FBG having a 3-dB bandwidth of 0.36 nm and >99% reflectivity at a center wavelength of 1080 nm. The other end of the active fiber is cleaved perpendicularly, providing a 4% reflection at the fiber–air interface. A dichroic mirror is inserted between the aspheric lenses to couple the laser output signal into a 2-GHz-bandwidth optical detector and a 600-MHz-bandwidth oscilloscope to measure laser dynamics. Three additional configurations are characterized in this experiment. In these alternate configurations, three long sections of passive fiber (329 m, 1329 m, and 2329 m) are spliced into the laser cavity between the active fiber and the FBG. The four lasers are designated as laser 1 (20-m cavity), laser 2 (349-m cavity), laser 3 (1349-m cavity), and laser 4 (2349-m cavity).
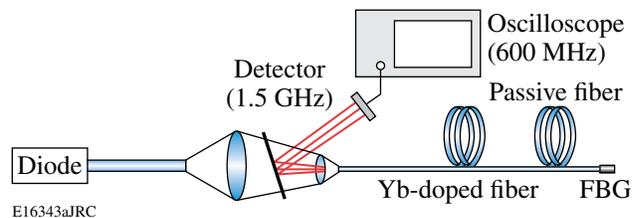
Figure 115.42
Schematic diagram of the ytterbium-doped fiber laser. FBG is the fiber Bragg grating.

The lasing properties of the four configurations have been characterized. The four lasers have about the same pump threshold of 0.75 W. At maximum pump power, the difference in output power between the four lasers is less than 9% due to the scattering loss of the passive fiber sections. Both SSP and SML have been observed in laser 1. A cw optical output is observed with low pump powers. As the injected pump power is increased beyond 2.0 W, quasi-periodic optical pulses, induced by undamped relaxation oscillations, are observed in the SSP regime. Figure 115.43 shows an example of such pulsations when the pump power is 3.2 W. The pulse period is around 20 μs, which agrees with the calculated relaxation oscillation frequency of the laser. As the pump power is tuned higher to 6.6 W, SML pulsing at a rate corresponding to a cavity-round-trip time is observed. This regime occurs because the gain medium is pumped hard enough to recover the population inversion in a single-cavity-round-trip time. Figure 115.44 shows an example
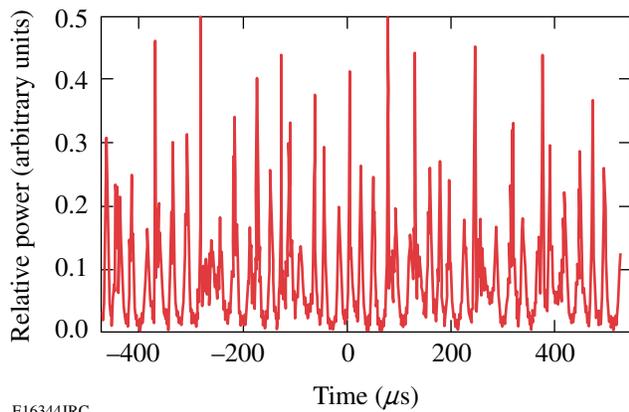
Figure 115.43
The self-pulsing dynamics of laser 1 when the pump power is 3.2 W.
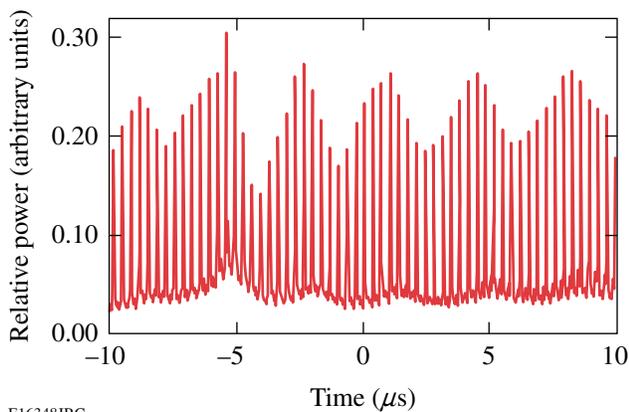
of such pulsations when the pump power is 7.2 W. The measured pulse period of 290 ns corresponds to the round-trip time of the laser cavity. As the pump power is further increased beyond 7.5 W, the laser once again operates in the cw regime because the gain is replenished more rapidly than the time it takes for the pulse to complete a round-trip through the laser cavity.

Analysis

The physics underscored here implies that when the pumping rate is sufficiently fast compared to the relaxation oscillation dynamics, the gain will always be replenished before a pulse can build up in the cavity. The dynamics in the SSP regime are dependent on the cavity length such that the relaxation oscillation frequency becomes smaller with increasing cavity length, as governed by conventional laser theory. The dynamics in the SML regime are directly dependent on the cavity length since the laser mode locks to the cavity-round-trip time. Therefore, by sufficiently increasing the cavity length, all self-pulsation dynamics can be slowed down compared to the pumping rate and all self-pulsations will be eliminated.

The modulation depth of the pulsations, defined as the ratio of the peak-to-valley value of the modulation to the peak value, indicates the competition between self-pulsing and cw working regimes. Figure 115.45 shows the modulation depth as a function of pump power for the four laser cavities. As predicted by fiber-laser rate equations,[11] the modulation depth decreases as the fiber-laser cavity length is increased, indicating a stronger tendency toward cw operation. In addition, the pump range where self-pulsations occur also decreases drastically with increasing cavity length. Laser 2 has an instability range that is less than 19% of that of laser 1, while laser 3 has an instabil-

Figure 115.44
The self-pulsing dynamics of laser 1 when the pump power is 7.2 W.
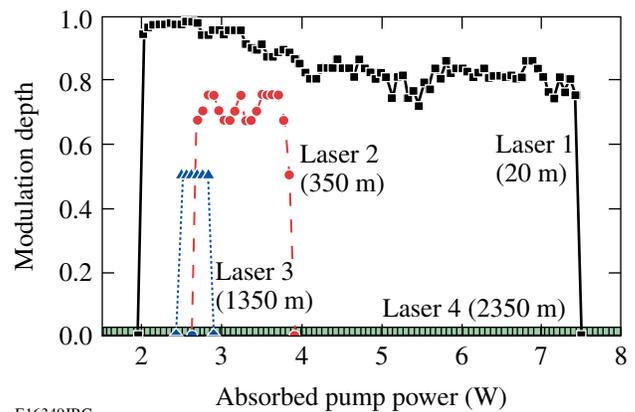
Figure 115.45
The self-pulsing characteristics of the fiber lasers with four different cavity lengths. The active fiber length is 20 m in all four cases

ity range that is less than 7% of that of laser 1. For laser 4, the instability range reduces to zero and no self-pulsations occur over the entire pump range.

For fiber lasers having long cavity lengths such as in laser 4, stimulated Raman scattering (SRS) can occur at high-power levels. In the experiments described above, no SRS spectra above the noise floor were observed, but SRS can be induced at higher pump levels. For example, a laser with a 1-km cavity length has an SRS threshold of about 5 W. SRS can be mitigated with appropriate filters, such as wavelength-division multiplexers, in-line short-pass filters, or hole-assisted single-polarization fibers.[12] Large-mode-area fiber can also be used to suppress SRS in long fiber lasers. For example, higher-order-mode (HOM) fiber with a mode-field diameter of 86 μm (Ref. 13) can increase the nonlinear threshold by a factor of 200 compared to normal single-mode fiber. By inserting a 1-km passive HOM delay fiber into the laser cavity, the effective fiber length that contributes to the nonlinearity is about 5 m, mitigating the SRS impairment of such a long-cavity fiber laser.

Using long lengths of passive fiber to suppress self-pulsing has many advantages over other methods. No active components or electronics are required, resulting in reduced system complexity. This method does not require free-space alignment and can be easily integrated into existing laser systems. Even though our demonstration was in an ytterbium-doped fiber laser, the technique can be applied to any rare-earth-doped fiber laser (e.g., erbium). Additionally, the laser output power degrades only a few percent due to the scattering loss so that high-efficiency performance can be maintained.

Conclusion

In conclusion, suppression and elimination of self-pulsing in a watt-level, dual-clad, ytterbium-doped fiber laser have been demonstrated. Self-pulsations are caused by the dynamic interaction between the photon population and the population inversion. The addition of a long section of passive fiber in the laser cavity makes the gain recovery faster than the self-pulsation dynamics, allowing only stable continuous-wave lasing. This scheme provides a simple and practical method requiring no active devices for eliminating self-pulsations in fiber lasers at all pumping levels.

REFERENCES

1. L. Qiu *et al.*, IEEE Photonics Technol. Lett. **16**, 2592 (2004).

2. W. Guan and J. R. Marciante, Electron. Lett. **43**, 558 (2007).

3. Y. Jeong *et al.*, Opt. Express **12**, 6088 (2004).

4. A. Hideur *et al.*, Opt. Commun. **186**, 311 (2000).

5. F. Brunet *et al.*, J. Lightwave Technol. **23**, 2131 (2005).

6. M. Dinand and Ch. Schütte, J. Lightwave Technol. **13**, 14 (1995).

7. V. Mizrahi *et al.*, J. Lightwave Technol. **11**, 2021 (1993).

8. L. Luo and P. L. Chu, Opt. Lett. **22**, 1174 (1997).

9. H. Chen *et al.*, Appl. Opt. **41**, 3511 (2002).

10. A. Suzuki *et al.*, IEEE Photonics Technol. Lett. **19**, 1463 (2007).

11. M. Ding and P. K. Cheo, IEEE Photonics Technol. Lett. **8**, 1151 (1996).

12. D. A. Nolan *et al.*, Opt. Lett. **29**, 1855 (2004).

13. S. Ramachandran *et al.*, Opt. Lett. **31**, 1797 (2006).

Resolving Dark Pulses from Photon Pulses in NbN Superconducting Single-Photon Detectors

Introduction

Fast and reliable single-photon detectors (SPD's) have become a highly sought after technology in recent years.[1] Some of the most interesting applications for SPD's, which include quantum communications and quantum key distribution,[2] as well as satellite communications, require devices that can successfully operate at telecommunication wavelengths, namely 1310 nm and 1550 nm. Another desirable feature for an ideal SPD is its photon-number resolution (PNR) capability.[3,4] InGaAs avalanche photodiodes work at telecommunication wavelength and are commercially available; they do, however, suffer from severe after-pulsing and require time gating, which limits their maximum count rate. Presently, they also lack the PNR capability.[5,6]

It has already been established that nanostructured, NbN superconducting single-photon detectors (SSPD's) operate based on hotspot formation and bias current redistribution in ultrathin (4 nm), narrow (100- to 120-nm), and long (~0.5-mm) meandering NbN superconductive stripes.[1] NbN SSPD's have been shown to have counting rates exceeding 250 MHz, with reported quantum efficiencies (QE's) up to 57% (Ref. 7) at 1550-nm wavelength and very low dark-count rates, ~10 Hz to 10 kHz, depending on the operation bias point.[8]

Typically, the SSPD's are kept at temperatures between 4.2 and 1.7 K (far below the NbN critical temperature T_c), and biased at currents I_{bias} close to the meandering stripe critical current I_c. Once a photon is absorbed by the NbN nanostripe, it breaks a Cooper pair, and, subsequently, a large number of quasiparticles are generated through the electron–electron and electron–phonon interactions, creating a local hotspot where superconductivity is suppressed or even destroyed. The hotspot expels the supercurrent from its volume and forces it to flow near the stripe edges, where it can exceed the I_c value, leading to the generation of phase-slip centers and the eventual formation of a resistive region across the width of the stripe.

When the device is directly connected to a transmission line with the characteristic impedance Z_0 equal to, e.g., 50 Ω,

the above-mentioned resistive region, which is >50 Ω, forces the bias current to redistribute from the SSPD into the load, which means that the amplitude of the SSPD voltage response is always simply the $Z_0 I_{bias}$ product. The above conclusion is true even if the SSPD were illuminated by several photons and, consequently, several hotspots were simultaneously generated at various points along the meander. Thus, in the above typical experimental arrangement, the SSPD photoresponse is insensitive to the number and energy of incoming photons.

We need to stress that a biased SSPD can generate output electrical pulses even when the input light is completely blocked and there are no photons incident upon the device. The dark-count pulses are transient voltage signals, spontaneously generated in a current-biased, long, superconducting nanostripe, and their amplitude, when the device is connected to a 50-Ω line, is also close to $Z_0 I_{bias}$, despite the fact that their physical origin is different from the photon counts. In the case of dark counts, the transient resistive state across the SSPD stripe is, actually, due to the current-induced vortex–antivortex generation.[9,10]

The goal of this work is to show that, with our proposed new readout scheme, which implements a low-noise cryogenic amplifier and a high-load resistor next to the detector, we are able to resolve the difference between dark counts and photon counts in our devices. The same readout approach also leads to the photon-number–resolving and energy-resolving capabilities in our standard SSPD's,[11] making the SSPD a PNR-type and/ or an energy-sensitive photon sensor.

Device Description and Experimental Setup

SSPD's are patterned from epitaxial-quality NbN films, deposited by dc reactive magnetron sputtering onto sapphire substrates.[12] The films are characterized by a sheet resistance between 400 and 500 Ω/sq at room temperature, with T_c between 10 and 11 K, and the critical current density $J_c \approx 10^6$ A/cm^2. The meander patterning is done by e-beam lithography and reactive ion etching. The films were deposited at the Moscow State Pedagogical University and patterned at Delft University of Technology. Perhaps because of the slight

differences in geometry, or slight patterning technique differences, the SSPD's in this work had three to four times lower I_c's (~5 to 10 μA) than the typical Moscow fabricated and patterned devices.[12] The QE's, however, were on par with the standard 10×10-μm^2 SSPD's, with the devices measured in this work having QE $\approx$ 4% at $\lambda = 800$ nm.

The standard SSPD operation setup is shown in Fig. 115.46(a). The device is wire bonded to a 50-Ω microstrip transmission line, coupled to a multimode optical fiber, and immersed into liquid helium.[13] The microstrip is then connected to a semirigid coaxial cable and at room temperature connected to a wideband bias-tee (0.08- to 26-GHz bandwidth). The bias-tee makes it possible to simultaneously amplify the transient photoresponse signal using a tandem of two broadband amplifiers (0.08- to 8.5-GHz bandwidth, 22-dB gain) and bias the SSPD by a stable low-noise dc voltage source. The amplified output signals, corresponding to photon counts and/or dark counts, are recorded by using either a Tektronix TDS 6604 digital single-shot (6-Ghz-bandwidth) oscilloscope or a pulse counter. As a single-photon source, we use a tunable Ti:sapphire mode-locked laser, heavily attenuated. For dark-count measurements, the detector was blocked from all incoming radiation, i.e., shielded inside the dewar by a metallic enclosure.

An equivalent electrical model of the SSPD photoresponse is shown in Fig. 115.46(b). Kinetic inductance L_k is in series with a parallel arrangement of a hotspot resistance R_{hs} and a switch S represents the photodetection (switching) event in the SSPD. The detector is then connected to a dc bias source and a readout circuit, which consists in this case of a trans-

mission line and amplifier with input impedance $Z_0 = 50$ Ω. In the simulations, which will be presented later, a bandpass filter representing the amplifier bandwidth is added. Finally, V_{out} is the experimentally observed transient voltage pulse during photodetection.
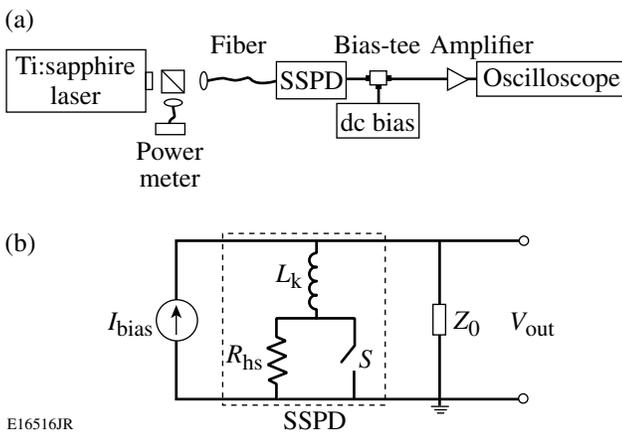
Initially, the switch is closed, and there is no voltage drop. Once a photon is absorbed by our nanostripe, the switch opens, and as R_{hs} grows to a value much larger than Z_0, most of the current redistributes into Z_0, and the resultant voltage pulse amplitude is simply $V_{out} \approx GI_{bias}Z_0$, where G is the amplifier gain. Thus, independent of the number or energy of the absorbed incident photons, V_{out} always has the same value for a given I_{bias} for the circuit shown in Fig. 115.46.

The new readout scheme presented here implements a high-electron-mobility transistor (HEMT) amplifier, operated cryogenically and mounted next to (on the same board) the SSPD. Because the HEMT input impedance is very high, a 500-Ω load (or shunt) resistor R_L is utilized in parallel with the detector and the HEMT, as shown in Fig. 115.47, which presents the circuit schematics. By applying the detector transient response to the gate of the HEMT, one can read out the amplified drain voltage, which should, ideally (for $R_L \gg R_{hs}$), be proportional to the hotspot resistance and equal to $V_{out} \approx GI_{bias}R_{hs}$. If the number of photons simultaneously absorbed in the SSPD meander happens to be larger than 1, the photons are very likely to form separate hotspots and their resistances will add up in series. The HEMT output voltage in this case should be $V_{out} \approx GI_{bias}nR_{hs}$, where n is the number of absorbed photons per pulse (actually, the number of created hotspots).

Figure 115.46
(a) Experimental setup and (b) standard electrical photoresponse model of an SSPD.
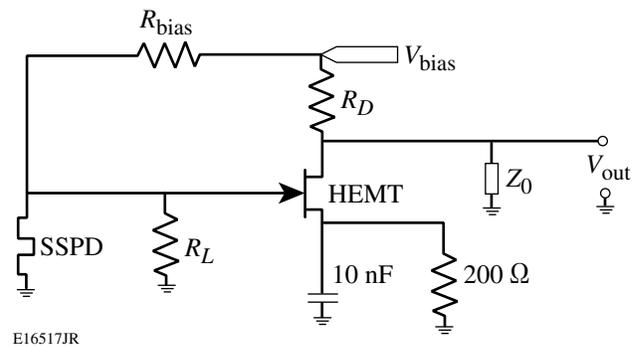
Figure 115.47
Circuit schematics implementing an HEMT amplifier and a 500-Ω load resistor R_L. The 10-nF capacitor sets the maximum ac gain and the 200-Ω resistor sets the dc current for the HEMT; R_{bias} and R_D are the biasing and pull-up resistors, respectively.

Thus, for relatively small n's, and $nR_{hs} < R_L$, the output pulse height of our setup is proportional to n, effectively leading to PNR.[11]

The HEMT setup should also enable one to distinguish pulses generated in response to either a single-photon absorption event (photon count) or a spontaneous voltage transient (dark count). In the case of dark counts, one can expect only a single localized resistive region, created due to the vortex–antivortex motion across the stripe, but its effective resistance should be different than R_{hs}, resulting in a somewhat different value of V_{out}.

Figure 115.48 compares photon-count time traces for the SSPD connected according to the standard scheme (Fig. 115.46) and the one with HEMT (Fig. 115.47). Even from this very short time trace, one can clearly see that with the standard-technique pulse amplitudes do not vary as much as those where the HEMT is utilized.

Results and Discussion

In the experiments reported here, 700-nm-wavelength photons were used to compare time traces of photon events with dark-count events. Figure 115.49 shows histograms that compare pulse-amplitude distributions of the dark-count [Fig. 115.49(a)] and photon-count events [Figs. 115.49(b) and 115.49(c)] at two different laser intensities. All data were taken at the same bias current $I_{bias} = 0.9\,I_c$.

Figure 115.48
Comparison of real-time oscilloscope time-domain traces for (a) a traditional scheme (50-Ω load line) and (b) an HEMT readout scheme, taken at similar laser intensities, such that $n \leq 1$ (HEMT is an inverting amplifier; therefore, the pulses are negative). The repetition rate of the laser was 82 MHz.
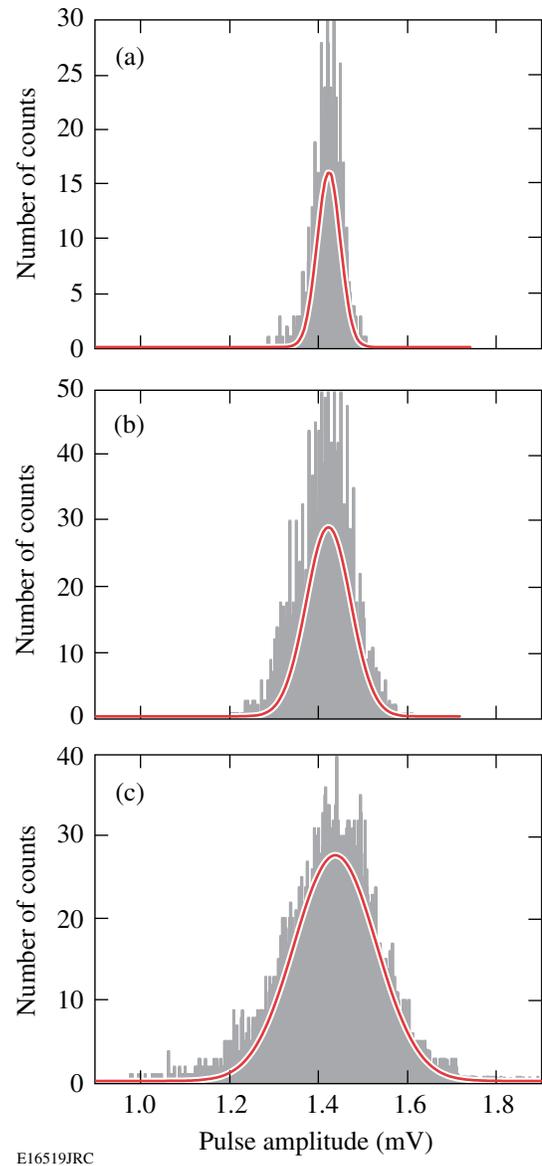
Figure 115.49
(a) Pulse-amplitude histograms of dark counts, (b) photon counts in the single-photon regime, $n \ll 1$, and (c) multiphoton regime, $n \geq 1$. All measurements performed at 4.2 K and at $I_{bias} = 0.9\,I_c$. The SSPD output voltage amplitudes (x axis) are divided by the amplifier gain.

All histograms can be fit with a simple Gaussian function, and it is quite obvious from Fig. 115.49(a) that the dark counts have the narrowest distribution. It was shown previously[10] that, when the detector is blocked from all incoming radiation and placed in liquid helium shielded by a metallic enclosure, the spontaneous transient voltage pulses, or dark counts, are most likely due to topological excitations. The NbN film thickness of our devices is 4 nm, which puts the SSPD nanowire in a two-dimensional (2-D) superconductor regime because its thickness is smaller than the NbN Ginzburg–Landau coherence length. In 2-D systems in general, true long-range superconducting order is not possible, and in an ultrathin film, topological excitations come in the form of vortex–antivortex pairs (VAP's).[14] VAP's are superconducting analogous to electron-hole excitations in semiconductors.[15] At the typical SSPD operating temperature, and in the absence of I_{bias}, all VAP's are bound and there is no dissipation in the NbN film. Once I_{bias} is applied, it exerts a Lorentz force on the VAP's, and at I_{bias} close to I_c, this force is strong enough to exceed the VAP binding energy and break them. The latter effect creates free vortices (analog to excited carriers in semiconductors) and allows vortices and antivortices to move in opposite directions toward the edges of the NbN stripe, causing dissipation, and, in turn, the resistive state and Joule heating. The dark-counting rate in SSPD's falls off quasi-exponentially with the biasing current.[10]

The photon-count amplitude distributions shown in Figs. 115.49(b) and 115.49(c), collected when the detector was irradiated by 700-nm photons, are clearly wider than that corresponding to the dark counts, even in the single-photon regime [Fig. 115.49(b)], when the average number of photons per pulse in the optical beam incident upon the SSPD is $n \ll 1$ (e.g., 0.01 photons per pulse). When the laser intensity was increased such that $n \geq 1$, we can see that the full width at half maximum (FWHM) of the distribution shown in Fig. 115.49(c) became over two times wider than that in Fig. 115.49(a).

The correlation between the beam intensity (average number of photons per pulse) incident upon the detector and the distribution FWHM of the response signals was very reproducible, and, as presented in Fig. 115.50, it depended on the SSPD bias current. One can clearly see that the dark-count signals (open squares) exhibit overall the narrowest distribution, which, in addition, is independent of the bias current.

For photon counts, the general trend is that the distribution width increases somewhat with increasing I_{bias}, and there is a wide jump between FWHM's corresponding to the multiphoton ($n \geq 1$, closed triangles) and single-photon ($n < 1$, closed circles and open triangles) illumination. However, for $n \ll 1$ (closed circles), as I_{bias} approaches I_c, the dark counts start to dominate over the photon counts and the amplitude distribution width starts to drop around $I_{bias} = 0.83\ I_c$, eventually overlapping with open squares at $I_{bias} > 0.9\ I_c$. The latter behavior agrees very well with our earlier observation that the rate of photon and dark counts depends on the I_{bias}/I_c ratio, as shown in the inset of Fig. 115.50.

When the laser intensity is set so that $n \geq 1$ (closed triangles in Fig. 115.50), one can observe the widest distribution width of the SSPD response pulse. We believe that this behavior is related to the non-perfect fabrication of SSPD's, resulting in some variations in the width or even the thickness of an NbN


E16520JR
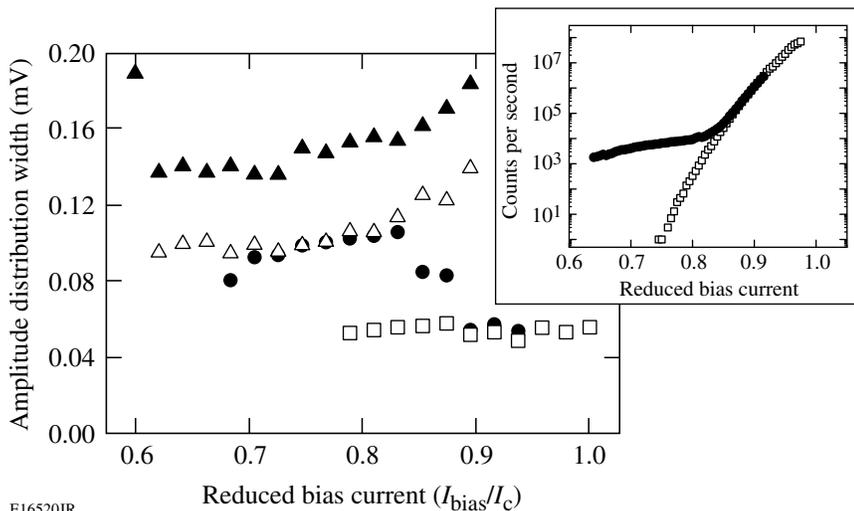
Figure 115.50
Amplitude distribution width (FWHM of Gaussian fits) for dark counts (open squares), $n \ll 1$ (closed circles), $n \leq 1$ (open triangles), and $n \geq 1$ (closed triangles). The inset shows the counting rate as a function of bias current for dark counts (open squares) and $n \ll 1$ (closed circles).

meander stripe. Since the device I_c is determined by the narrowest and thinnest section(s) of the stripe, fluctuations in the stripe width must lead to variations of the final hotspot resistance, which in turn correspond to the broadened amplitude distributions of the photon-count responses. When light intensity is increased ($n \geq 1$), more sections of the SSPD meander with, and apparently, different widths are activated, leading to enhanced fluctuations in the response pulse amplitudes and, finally, to the largest value of the distribution FWHM.

Electrical Model and PSpice Simulations

If the electrical model only is considered, the difference in amplitude, for different hotspot resistances, stems from the time it takes for the current that initially biases the device to redistribute into the readout circuit. In other words, for a given R_L, current redistribution time decreases with increasing R_{hs}. For the hotspot to stop growing, and the cooling mechanism to take over, the current through the device must drop to a value below $\sim 0.23\, I_c$ (Ref. 16). When the SSPD photoresponse is modeled such that R_{hs} is a simple resistor, then the fall and rise time constants of the transient V_{out} are simply $\tau_{fall} = L_k / (R_{hs} + R_L)$ and $\tau_{rise} = L_k / R_L$ (Ref. 17), respectively. Unfortunately, this latter behavior is undesired if we want to observe PNR since, for a given R_L, the current redistribution time for two hotspots, which follows $\tau_{fall} = L_k / (2R_{hs} + R_L)$ occurs faster than that for a single hotspot.

For PSpice modeling, the value of R_L was chosen to be 500 Ω, even though it was suspected that this value might be lower than the hotspot resistance. The reason is that higher R_L values can lead to an underdamped circuit because, as can be seen in Fig. 115.47, there is a large inductor ($\sim$400-nH kinetic inductance of the SSPD) in parallel with R_L. In addition, in our readout circuit there is always a small parasitic capacitance estimated to be around 2 to 3 pF (coming from a circuit board, as well as other components). Figure 115.51(a) shows the PSpice simulated pulses for different values of R_L, and as can be seen, even for R_L = 500 Ω (gray solid curve), the circuit is already slightly underdamped, as there is a small oscillation following the main pulse. Figure 115.51(b) shows the experimental (solid curve), as well as simulated (dashed curve), voltage pulses for our HEMT readout approach. The broader, more-damped oscillation behind the measured main pulse is likely due to some second-order effects from the amplifier and/or stainless steel coaxial line. Critical damping yielded R_L = 270 Ω [dashed curve in Fig. 115.51(a)], which is actually a smaller value than the estimated hotspot resistance.
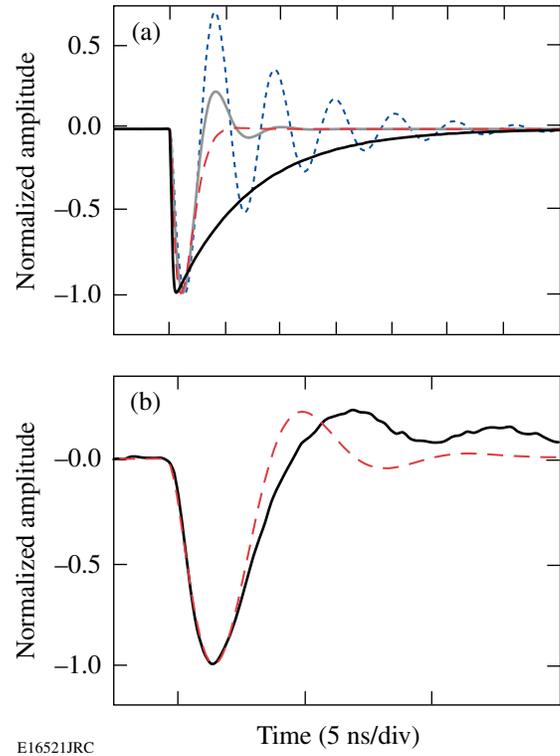
Figure 115.51
(a) PSpice simulations of voltage transients at different values of R_L: 50 Ω (black solid curve), 270 Ω (dashed curve), 500 Ω (gray solid curve), and 2 kΩ (short-dashed curve); (b) measured photoresponse (solid curve) and simulated photoresponse (dashed curve), for R_L = 500 Ω.

Finally, it must be mentioned that in order to fully model the behavior of an SSPD integrated with an HEMT readout, it is not enough to simply use the above electrical model, as there are many processes at play simultaneously. The Joule heating occurs in parallel with the cooling process and current redistribution,[18] so, ultimately, a more-complex physical model must be used, which is outside the scope of this work.

Toward Photon-Number Resolution

As mentioned before and presented in Ref. 11, the integrated, cryogenic HEMT readout not only allows one to distinguish dark counts from photon counts, but it should also allow one to achieve PNR in SSPD's. For large R_L's, the SSPD transient output pulse resulting from photodetection should be proportional in amplitude to the number of photons absorbed or, equivalently, the number of hotspots created in the SSPD. Unfortunately, it was shown by Ref. 18, in typical SSPD biased close to I_c, the R_{hs} can be as large as 5.5 kΩ, mainly due to Joule

heating. Even if it were possible to find a cryogenic amplifier with such large input R_L, the readout scheme would not work because the current would not be able to redistribute into the load fast enough before a runaway heating effect, and the device would simply latch.

Our devices, as mentioned before, have much lower than typical I_c's, although they still operate quite well. With our $I_{bias} \approx 5~\mu A$, we estimate R_{hs} to be between 600 and 1000 Ω, so our selected $R_L = 500~\Omega$ is reasonable and should make it possible, in principle, to distinguish between the single- and multiphoton events.

Indeed, when the laser intensity and I_{bias} were increased so that the detector started to register nearly every incident light pulse, while the dark counts were still low, we observed that, in time-domain traces, some response pulses exhibited visibly higher amplitudes than the rest. Figure 115.52 shows an example of such a time trace, which is quite convincing, but, of course, it is impossible to conclude that these large pulses were indeed due to double-photon events, instead of, e.g., a single-photon event arriving close in time to a dark-count event, or even resulting from inhomogeneities of our meander stripe and resulting longer current redistribution time. It was therefore very useful to look at the statistics of the pulse-amplitude distributions once again. This time, most of our measurements were done by varying the intensity of our laser pulses (mode-locked and twice up-converted light to get $\lambda = 267$ nm) and I_{bias}, and collecting amplitudes of several thousand pulses at each value of the laser intensity and I_{bias}.
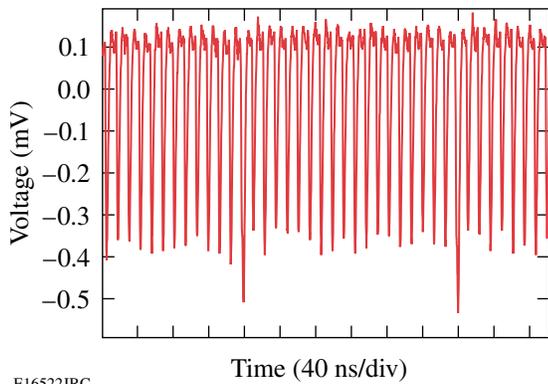
The results are presented in Fig. 115.53. When $I_{bias} \approx 0.7~I_c$, the amplitude distribution could be easily fit with a simple Gaussian function, as shown in Figs. 115.53(a) and 115.53(b). However, once I_{bias} reached 0.9 I_c, as shown in Figs. 115.53(c) and 115.53(d), we started to see a clear second peak at lower amplitudes, and the distribution now had to be fit with two Gaussians. The latter can be easily explained by the varying width (nonuniformity) of the NbN stripe: at higher I_{bias}, more (wider) sections of the SSPD meander were activated for photodetection, giving rise to the second Gaussian peak. This peak is expected to be centered at lower amplitudes, because Joule heating in the wider sections should give rise to lower R_{hs}, as in those sections we should expect a better heat dissipation into the substrate than that in the narrower sections.

When the data shown in Figs. 115.53(c) and 115.53(d) were plotted on a semi-log scale, as presented in Figs. 115.53(e) and 115.53(f), respectively, it became quite clear that in the $n \leq 1$ regime [Fig. 115.53(f)] there was, actually, a third small peak centered around 0.8 mV. This peak was completely absent in the $n \ll 1$ regime [Fig. 115.53(e)] and when I_{bias} was below 0.78 I_c. At present, we have no clear interpretation for the existence of this third peak. It cannot be related to the dark counts since they fall off exponentially with I_{bias} and are nearly zero below 0.85 I_c. Thus, the most-reasonable, tentative explanation is that it is indeed due to the SSPD detection of multiphoton events. Further analysis and calculations are needed to either support or disprove this conclusion.

Conclusion

We were able to resolve the difference between dark counts and photon counts in our NbN SSPD by utilizing an HEMT amplifier readout technique and examining pulse-amplitude distribution widths. The dark-count distribution width is very narrow for a given bias current, while that for photon counts is up to 2.5 times wider and is clearly related to the incident photon flux upon the SSPD (the average number of photons per pulse). The latter demonstrates that the HEMT readout is a promising approach in the future for PNR measurements.

E16522JRC

Figure 115.52
Real-time oscilloscope trace-domain trace, showing higher pulse amplitudes of some pulses.
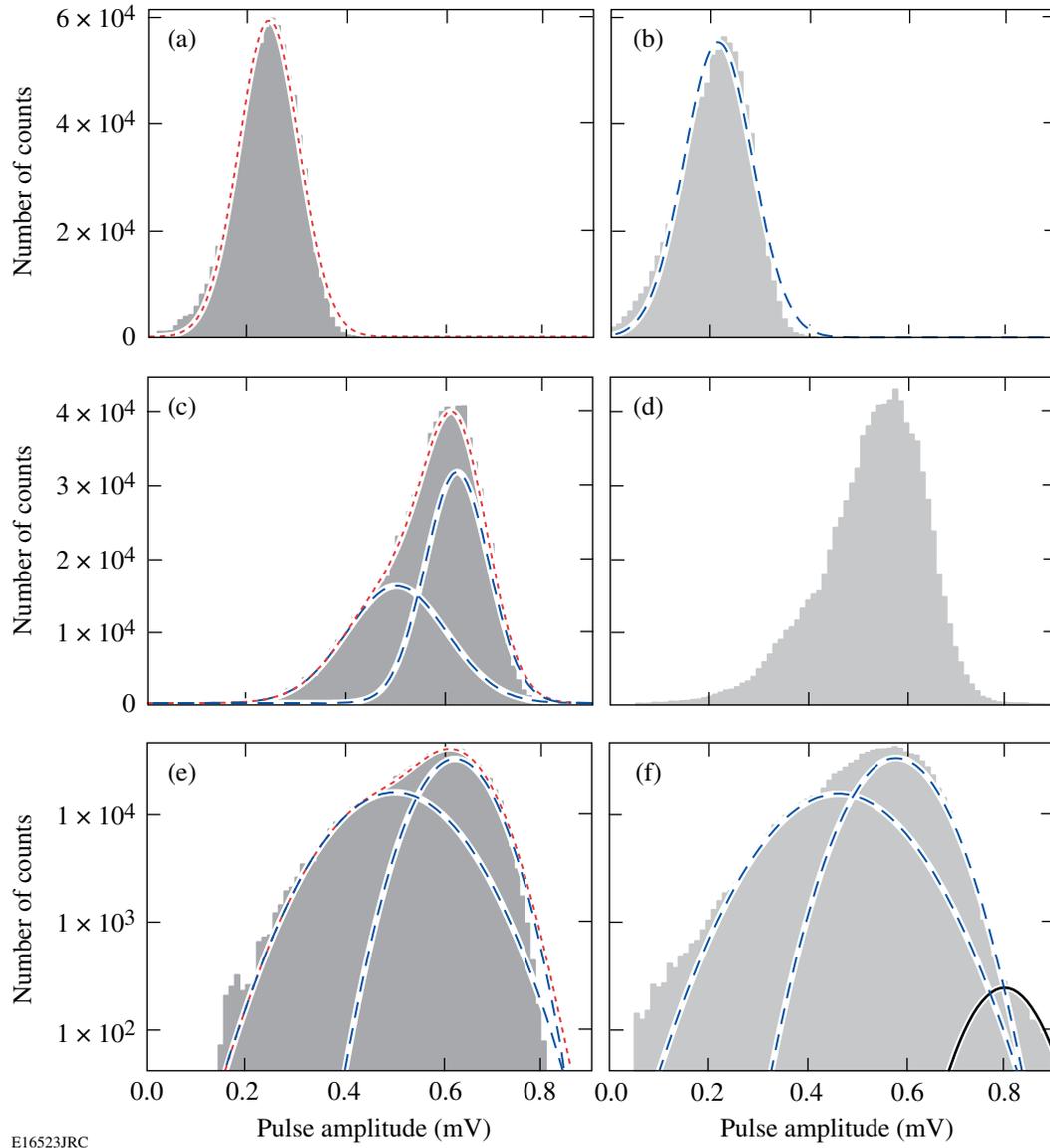
Figure 115.53

Pulse-amplitude histograms for (a) $n \ll 1$, $I_{bias} = 0.7\ I_c$, (b) $n \leq 1$, $I_{bias} = 0.7\ I_c$, (c) $n \ll 1$, $I_{bias} = 0.9\ I_c$, (d) $n \leq 1$, $I_{bias} = 0.9\ I_c$, (e) semi-log plot of (c), (f) semi-log plot of (d) (dark gray histograms indicate the same incident photon flux for the $n \ll 1$ regime; light gray histograms indicate the same incident photon flux for the $n \leq 1$ regime).

REFERENCES

1. W. Słysz, M. Węgrzecki, J. Bar, P. Grabiec, M. Górska, V. Zwiller, C. Latta, P. Böhi, A. J. Pearlman, A. S. Cross, D. Pan, J. Kitaygorsky, I. Komissarov, A. Verevkin, I. Milostnaya, A. Korneev, O. Minayeva, G. Chulkova, K. Smirnov, B. Voronov, G. N. Gol'tsman, and R. Sobolewski, J. Mod. Opt. **54**, 315 (2007).

2. C. Bennett and G. Brassard, in *International Conference on Computers, Systems, and Signal Processing* (IEEE Computer Society, IEEE Circuits and Systems Society, and Indian Institute of Science, Bangalore, India, 1984), pp. 175–179.

3. E. Waks, A. Zeevi, and Y. Yamamoto, Phys. Rev. A **65**, 052310 (2002); G. Brassard *et al.*, Phys. Rev. Lett. **85**, 1330 (2000).

4. E. Knill, R. Laflamme, and G. J. Milburn, Nature **409**, 46 (2001).

5. Y. Kang *et al.*, Appl. Phys. Lett. **85**, 1668 (2004).

6. G. Ribordy *et al.*, J. Mod. Opt. **51**, 1381 (2004).

7. K. M. Rosfjord *et al.*, Opt. Express **14**, 527 (2006).

8. J. Kitaygorsky, J. Zhang, A. Verevkin, A. Sergeev, A. Korneev, V. Matvienko, P. Kouminov, K. Smirnov, B. Voronov, G. Gol'tsman, and R. Sobolewski, IEEE Trans. Appl. Supercond. **15**, 545 (2005).

9. A. Engel *et al.*, Phys. Stat. Sol. C **2**, 1668 (2005).

10. J. Kitaygorsky, I. Komissarov, A. Jukna, D. Pan, O. Minaeva, N. Kaurova, A. Divochiy, A. Korneev, M. Tarkhov, B. Voronov, I. Milostnaya, G. Gol'tsman, and R. Sobolewski, IEEE Trans. Appl. Supercond. **17**, 275 (2007).

11. M. G. Bell *et al.*, IEEE Trans. Appl. Supercond. **17**, 289 (2007).

12. G. N. Gol'tsman, K. Smirnov, P. Kouminov, B. Voronov, N. Kaurova, V. Drakinsky, J. Zhang, A. Verevkin, and R. Sobolewski, IEEE Trans. Appl. Supercond. **13**, 192 (2003).

13. W. Słysz, M. Węgrzecki, J. Bar, P. Grabiec, M. Górska, V. Zwiller, C. Latta, P. Böhi, I. Milostnaya, O. Minaeva, A. Antipov, O. Okunev, A. Korneev, K. Smirnov, B. Voronov, N. Kaurova, G. Gol'tsman, A. Pearlman, A. Cross, I. Komissarov, A. Verevkin, and R. Sobolewski, Appl. Phys. Lett. **88**, 261113 (2006).

14. J. E. Mooij, in *Percolation, Localization, and Superconductivity*, edited by A. M. Goldman and S. A. Wolf, NATO ASI, Series B, Vol. 109 (Plenum Press, New York, 1984), pp. 325–370.

15. A. M. Kadin, J. Appl. Phys. **68**, 5741 (1990).

16. A. VI. Gurevich and R. G. Mints, Rev. Mod. Phys. **59**, 941 (1987).

17. A. J. Kerman *et al.*, Appl. Phys. Lett. **88**, 111116 (2006).

18. J. K. W. Yang IEEE Trans. Appl. Supercond. **17**, 581 (2007).

Optimizing Electron–Positron Pair Production on kJ-Class High-Intensity Lasers for the Purpose of Pair-Plasma Creation

Introduction

The creation of a relativistically hot electron–positron plasma in the laboratory is an ambitious experimental challenge that has yet to be realized. Electron–positron pair plasmas are theoretically interesting because of the mass symmetry between the plasma components. For example, this symmetry results in the absence of both acoustic modes and Faraday rotation.[1,2] Waves and instabilities in electron–positron plasmas differ significantly from asymmetric electron–ion plasmas and have been discussed theoretically in Refs. 1 and 2. Electron–positron plasmas are important in astrophysical settings;[3] new insights into astrophysical phenomena such as black holes, pulsar magnetospheres, active galactic nuclei, bipolar outflows (jets), and gamma-ray bursts (GRB) may be gained by appropriate laboratory investigations.[4]

The main difficulty in creating an electron–positron plasma arises because terrestrial positron sources are typically very weak; e.g., source rates of $\sim 10^6$ positrons s^{-1} are obtained using radioactive sources[5,6] and (10^8 to 10^9) positrons s^{-1} using accelerator-based sources.[7] To date, classical single-component, positron-plasma charge clouds have been created and confined, with cloud sizes slightly exceeding the Debye length, by storing and cooling positrons created through radioactive decay in electrostatic Penning traps.[5,6,8] Penning traps cannot, however, simultaneously confine significant numbers of both positive and negative species.[2] In principle, the simultaneous confinement of electrons and positrons in non-neutral stellarators[9] or mirror machines[10] appears possible, but it has yet to be achieved. An alternative to the above schemes is proposed that uses ultra-intense laser pulses as an intense positron source.[11–17] The first step toward producing a pair plasma is to optimize the pair-production rate. Calculations in this article indicate that source rates approaching 10^{24} positrons s^{-1} are attainable with the generation of petawatt laser systems either recently completed, such as OMEGA EP,[18] or currently under construction, e.g., NIF-ARC.[19] Such source rates are shown to be high enough that the density of pairs approaches that required for the formation of a pair plasma.

The following sections of this article (1) present calculations of the direct and indirect yield as a function of laser intensity and target geometry; (2) analyze the results, optimizing the yields, and the production rates; (3) estimate the likelihood of pair–plasma production; and (4) summarize our conclusions.

Calculation of Positron Yield in Laser–Target Interactions

High-energy petawatt lasers, such as LLE's recently completed OMEGA EP Laser Facility,[18] deliver kilojoules of laser energy at focused laser intensities of $I_0 \lesssim 10^{20}$ W/cm². Such intensities are still several orders of magnitude below the level required to create electron–positron pairs from the vacuum.[20–22] However, laser–matter interaction at intensities $I_0 \gtrsim 10^{18}$ W/cm² efficiently produce hot electrons with characteristic energies in the MeV range,[23] which may be approximated by the ponderomotive (Wilks) scaling for the hot-electron "temperature"[24]

$$\Theta_{\text{hot}} = 0.511 \left[\left(1 + I_{18} \lambda_{\mu m}^2 \big/ 1.37 \right)^{1/2} - 1 \right] \text{MeV}, \quad (1)$$

where I_{18} is the laser intensity in units of 10^{18} W/cm² and $\lambda_{\mu m}$ is the laser wavelength in μm (= 1.053 μm for OMEGA EP). This scaling predicts temperatures ranging from $\Theta_{\text{hot}} \sim 1$ MeV at $I_L = 1 \times 10^{19}$ W/cm² to $\Theta_{\text{hot}} \sim 15$ MeV at $I_L = 1 \times 10^{21}$ W/cm². Electrons with kinetic energies exceeding the threshold value, $T_{\text{th,e}} \approx 2 m_e c^2 = 1.022$ MeV (neglecting the small correction due to recoil of the nucleus), have a finite probability of creating an electron–positron pair in matter. A significant uncertainty exists in the scaling of hot-electron temperature with laser intensity. An alternative scaling, the so-called Beg scaling,[25] has been proposed $\left[\Theta_{\text{hot}} = 0.46 \left(I_{19} \lambda_{\mu m}^2 \right)^{1/3} \text{MeV} \right]$, which seems to give better agreement with a certain class of high-contrast experiments.[26] The Beg scaling predicts significantly lower temperatures for a given laser intensity leading to less-favorable pair-production rates.

Several mechanisms lead to the production of pairs: Pairs can be created directly (trident process) by energetic electrons interacting with the Coulomb field of the atomic nucleus (or with the field of an atomic electron) or pairs can be created indirectly.

Indirect production first requires the production of a bremsstrahl-ung photon followed by pair production by the photon in the nuclear (or atomic-electron) field (photo-pair production). The reaction rate for direct production in the nuclear (electron) field is of the order of $Z^2 n_{hot} n_i \alpha^2$ ($n_{hot} n_e \alpha^2$), while bremsstrahlung is of the order of $Z^2 n_{hot} n_i \alpha$ and pair production is $Z^2 n_\gamma n_i \alpha$. Here, $\alpha \approx 1/137$ is the fine-structure constant, Z is the atomic number, and n_{hot}, n_i, n_e, and n_γ are the hot-electron, atomic, atomic-electron, and photon number densities, respectively. Two-photon-pair production is the lowest-order process in α (zeroth), but it can be ignored because the (bremsstrahlung) photon density is orders of magnitude lower than the hot-electron number density. The reverse of this process, pair annihilation, is expected to occur and will provide a characteristic annihilation radiation signature of back-to-back photons at ~511 keV, which can be used to diagnose the presence of pairs.[27,28]

The ratio of the cross sections for direct and photoproduc-tion, with energy dependence, has been given in Ref. 29:

$$\frac{\sigma_T}{\sigma_{\gamma \rightarrow e^+e^-}} = \frac{\alpha}{\pi}\left[\log\left(\frac{E_0}{m_e c^2}\right)\log\left(\frac{E_0}{2.137\, m_e c^2 Z^{-1/3}}\right)\right.$$

$$\left. +\frac{1}{3}\log^2\left(2.137\, Z^{-1/3}\right)\right], \qquad (2)$$

where E_0 is the total energy of the incident electron (photons are assumed to have the same energy), m_e is the electron mass, and c is the speed of light. From this expression it can be seen that pair production is more efficient (at 5 MeV the ratio is $\sigma_T / \sigma_{\gamma \rightarrow e^+e^-} = 0.017$), but there is an additional inef-ficiency associated with first creating the hard bremsstrahlung photons. In the following subsections, the efficiencies of each process are carefully computed. The cross sections (per atom) for both direct production σ_T and photon-pair production $\sigma_{\gamma \rightarrow e^+e^-}$ are proportional to Z^2. The production efficiency will be greatest using a target material that optimizes the prod-uct of Z^2 and the atomic number density n_i. In this article we assume the target to be Au ($Z = 79$), which is close to optimal $\left(Z^2 n_i = Z^2 \rho N_A / A \sim 3.66 \times 10^{26}\ \text{cm}^{-3}\right)$, where A is the atomic weight, ρ is the mass density, and N_A is the Avogadro number.

The threshold kinetic energy for the production of muons is $T_{th,\mu} = 212$ MeV and $T_{th,\pi} \approx 280$ MeV for pions.[30] It is unlikely that muons or pions can be created with any significant effi-ciency with the current generation of petawatt-class lasers.

1. Direct Pair Production by Electrons (Trident Production)

Trident production[(a),29,31,32] of electron–positron pairs by fast electrons colliding with the Coulomb field of an atomic nucleus has been approximated by either the Bhabha cross section[29] or various forms valid at high energy.[33] The Bhabha cross section is not entirely satisfactory since the uncertainties over the range of electron energies considered here (ranging roughly from threshold to a few tens of MeV) are hard to determine.[11] More recently Gryaznykh[34] numerically evaluated the integrals arising from the three lowest-order diagrams that have been computed by Baĭer *et al.*[35] Reference 34 provides a fitting formula for the total cross section σ_T, which is valid from threshold to ~100 MeV,

$$\sigma_T = 5.22\, Z^2 \log^3\left[\frac{2.30 + T_0\,(\text{MeV})}{3.52}\right]\mu\text{b}, \qquad (3)$$

together with limiting forms near threshold

$$\sigma_T = \frac{7\, Z^2 r_0^2 \alpha^2}{2304} \frac{\left(T_0 - 2m_e c^2\right)^3}{\left(m_e c\right)^3}, \qquad (4)$$

and at high energies

$$\sigma_T = \frac{28\pi Z^2 r_0^2 \alpha^2}{27} \log^3\left(\frac{T_0}{m_e c^2}\right). \qquad (5)$$

Here, T_0 is the kinetic energy of the incident electron, $r_0 \equiv e^2/m_e c^2 = 2.82 \times 10^{-13}$ cm^2 is the classical electron radius, and e is the elementary charge. In an infinite target, the trident yield $Y_{+,T}$ can be computed for a given probability distribution of incident electron kinetic energies, $f_0(T_0)$, by integrating along the electron path, running down in kinetic energy from the initial value T_0 assuming the continuous slowing-down approximation (CSDA),

$$Y_{+,T} = \eta_r N_e \int_0^\infty dT_0 f_0(T_0) \int_0^{T_0} dT n_i \sigma_T(T) \left|\frac{dT}{ds}\right|^{-1}$$

$$= \eta_r N_e \int_0^\infty dT_0 f_0(T_0) \int_0^{s(T_0)} ds' n_i \sigma_T\left[T(T_0, s')\right]. \quad (6)$$

[(a)]In general, "trident" and "quartets" refer to the production of lepton pairs by virtual photons in the Coulomb fields of nuclei and atomic electrons, respec-tively. "Pairs" and "triplets" refer to the corresponding process induced by real photons.

Here N_e is the total number of hot electrons, s' is the path length variable for an electron of initial kinetic energy T_0 of CSDA range $s(T_0)$, and $\eta_r = 1$. The yield in a thin target, significantly thinner than the hot-electron practical range, can be estimated by introducing the "refluxing efficiency" $\eta_r \lesssim 1$ (Ref. 36). The refluxing efficiency represents the fraction of hot electrons that are trapped by the space charge of the target relative to the total number, which can be close to unity for a range of target interaction conditions.[36,37] The electron stopping power $-(dT/ds)$, from which $T(T_0, s) = T_0 + \int_0^s ds'(dT/ds')$ is computed, has been taken from Ref. 38.

The yield computed according to Eq. (6), per kJ of hot electrons, is shown as the dashed line in Fig. 116.1 for a range of hot-electron temperatures, perfect refluxing efficiency $\eta_r = 1$, and an exponential hot-electron energy distribution function $f_0(T_0) = (1/\Theta_{hot})\exp(-T_0/\Theta_{hot})$. The average positron kinetic energy $\overline{T}_+$ for an incident electron of energy T_0 is calculated by the formula $\overline{T}_+ = T_0\{1/3 - b\log[T_0/(3m_ec^2)]\}$. The dimensionless parameter $b (= 0.0565)$ has been found in Ref. 34 by fitting to the results of numerical computation of the integrals. The average positron energy produced for a distribution of hot electrons, $f_0(T_0)$, can be estimated by
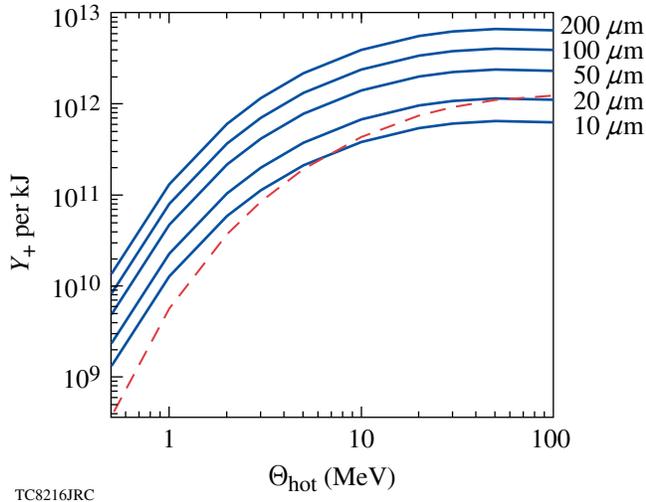
TC8216JRC

$$\langle T_+ \rangle_T = \int_0^\infty dT_0 f_0(T_0) \frac{1}{\Xi(T_0)}$$

$$\times \int_0^{s(T_0)} ds' \overline{T}_+[T(T_0, s')] \sigma_T[T(T_0, s')], \qquad (7)$$

where $\Xi(T_0) \equiv \int_0^{s(T_0)} ds' \sigma_T$.

2. Indirect Photo-Pair Production

a. Hard x-ray production. To compute the indirect yield, one must first calculate the hard component of the bremsstrahlung. This can be estimated using the Bethe–Heitler cross section[39]

$$\sigma_\gamma(E_0, k)dk = Z^2 r_0^2 \alpha \frac{dk}{kE_0^2}\left\{\left(E_0^2 + E^2\right)\left[\phi_1(\gamma) - \frac{4}{3}\log Z\right]\right.$$

$$\left. - \frac{2}{3}EE_0\left[\phi_2(\gamma) - \frac{4}{3}\log Z\right]\right\}. \qquad (8)$$

This represents the cross section for an incident electron of total energy $E_0 = (T_0 + m_ec^2)$ to produce a bremsstrahlung photon, in the field of an atomic nucleus, with energy between k and $k + dk$ (the scattered electron has energy $E = E_0-k$). The screening factors $\phi_1(\gamma)$ and $\phi_2(\gamma)$ have their usual definitions,[40] with the screening parameter γ given by $\gamma = 100\, m_ec^2 k/(E_0 EZ^{1/3})$.

The photon energy spectrum, differential in photon energy, produced by electrons with an initial energy spectrum $f_0(T_0)$ that run down their energy completely in the target is given by

$$N_\gamma(k)dk = (\eta_r N_e)\int_0^\infty dT_0 f_0(T_0)$$

$$\times \int_0^{T_0} dTn_i \sigma_\gamma(E, k)dk\left|\frac{dT}{ds}\right|^{-1}$$

$$= (\eta_r N_e)\int_0^\infty dT_0 f_0(T_0)$$

$$\times \int_0^{s(T_0)} ds' n_i \sigma_\gamma[E(E_0, s')k]dk. \qquad (9)$$

The energy contained in bremsstrahlung photons, ϵ_γ, may be computed by multiplying Eq. (9) by photon energy k and integrating, to give

$$\epsilon_{\gamma\{0,>\}} = (\eta_r N_e) \int_0^\infty dT_0 f_0(T_0) T_0 Y_{\{0,>\}}(T_0), \quad (10)$$

where $Y_{\{0,>\}}$ has the definition

$$Y_{\{0,>\}}(T_0) \equiv \frac{n_i}{T_0} \int_{\{0,2mc^2\}}^\infty dk k \sigma_\gamma \left[E(T_0, s') k \right]. \quad (11)$$

In the above definitions of ϵ_γ and Y, the symbol "0" or ">" in the subscript indicates if the photon energy k in the k integration is either unrestricted or restricted to be greater than the threshold for pair production, $k > 2m_e c^2$ (= 1.022 MeV), respectively. The quantity Y_0 is the usual "radiation yield."[38] This is the fraction of an incident electron's kinetic energy T_0 that is converted into radiation as the electron thermalizes within an infinite medium of a given material. Likewise, $Y_>$ measures the fraction of this energy that is above threshold for pair production. For convenience, the "bremsstrahlung efficiency" $\eta_{\gamma,\{0,>\}} \equiv \epsilon_{\gamma,\{0,>\}} / (N_e \Theta_{hot})$ has been introduced. It is defined as the ratio of bremsstrahlung energy to hot-electron kinetic energy for hot electrons described by the probability distribution $f_0(T_0)$.

Figure 116.2 shows a plot of the bremsstrahlung efficiency $\eta_{\gamma,0}$, radiation yield Y_0, and a comparison with the Koch and Motz scaling,[39]
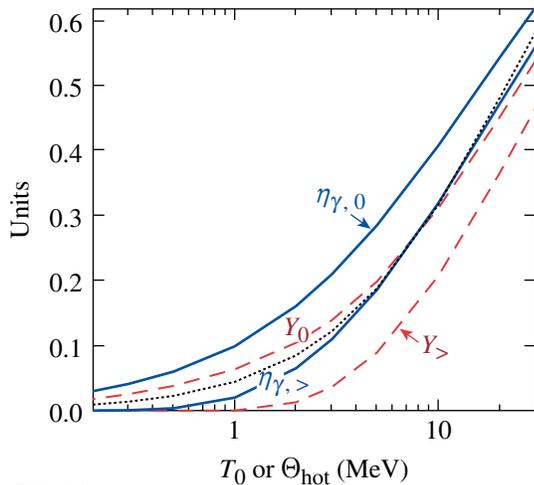
Figure 116.2
Solid curves show the bremsstrahlung efficiency $\eta_{\gamma,0} \equiv \epsilon_{\gamma,0} / (N_e \Theta_{hot})$ and bremsstrahlung efficiency above threshold $\eta_{\gamma,>}$ as functions of hot-electron temperature from Eq. (10). The dashed curves show the radiation yield Y_0 and radiation yield above threshold $Y_>$ [Eq. (11)] as functions of electron kinetic energy. The dotted curve is the Koch and Motz thick-target bremsstrahlung scaling.[39]

$$(Y_0)_{K-M} = 3 \times 10^{-4} Z T_0' \Big/ \left(1 + 3 \times 10^{-4} Z T_0' \right),$$

where T_0' is the electron kinetic energy in mass units, $T_0' \equiv T_0 / m_e c^2$. The quantities $\eta_{\gamma,>}$ and $Y_>$ are also shown. In these calculations the best-available tabulated differential bremsstrahlung cross sections have been used (from Ref. 41) rather than the Bethe–Heitler expression [Eq. (8)].

Two important loss mechanisms preclude the *extraction* of an amount of bremsstrahlung energy equal to the radiation yield in practical laser–foil interaction experiments. These are (a) the escape of high-energy electrons from the foil (i.e., $\eta_r <$ 1) and (b) the self-absorption of a portion of the bremsstrahlung generated in the foil. In this application, however, self-absorption is desired—the dominant contribution to the attenuation coefficient being pair production for photon energies $\gtrsim 5$ MeV (Ref. 42). High refluxing efficiency $\eta_r \sim 1$ is observed in experiments conducted at laser energies $E_L \sim 500$ J (Refs. 37 and 43). Future experiments are planned to test the extrapolation to kJ laser energies.[37] Another potentially important consideration for higher target energy densities is target expansion caused by the hot-electron pressure.[44] This represents an additional energy sink for the hot electrons.

b. Pair production. If the bremsstrahlung energy spectrum $N_\gamma(k)$ is known, either experimentally[23] or as computed by Eq. (9), the resulting photo-pair yield is readily computed assuming isotropy and homogeneity of the bremsstrahlung emission. In a foil where Compton scattering is negligible, the number of photo-produced positrons in the (total) energy range $E_+ + dE_+$, produced in a foil of thickness d, is given by

$$N_e + (E_+) dE_+ = \frac{N_A}{A} \int_0^\infty dk \int d\Omega \left(\int_0^d \rho dt \left\{ \int_0^t ds \frac{1}{|\cos\theta|} \right. \right.$$

$$\times n_\gamma^-(k,t,\theta) \exp\left[-\mu(k) \frac{(t-s)}{|\cos\theta|} \right]$$

$$+ \int_t^d ds \frac{1}{|\cos\theta|} n_\gamma^+(k,t,\theta)$$

$$\left. \left. \times \exp\left[-\mu(k) \frac{(s-t)}{|\cos\theta|} \right] \right\} \right)$$

$$\times \sigma_{\gamma \to e^+e^-}(k,E_+) dE_+, \quad (12)$$

TC8217JRC

where E_+ is the (total) positron energy and $\mu(k) = n_i \sigma_{\text{tot}}(k)$ is the linear attenuation coefficient for x rays of energy k.[b] The total cross section σ_{tot} has contributions from coherent and incoherent Compton scattering, photo-electric absorption, pair production, and photo-nuclear absorption, $\sigma_{\text{tot}} = \sigma_{\text{scat}} + \sigma_{p-e} + \sigma_{\gamma \to e^+e^-} + \sigma_{p-n}$. For photon energies $k \gtrsim 5$ MeV, pair production dominates, while close to threshold, $k \sim 1$ MeV, pair production competes with Compton scattering, $\sigma_{\gamma \to e^+e^-} \sim \sigma_{\text{scat}}$. In gold at solid density, the Compton-scattering cross section $\sigma_{\text{scat}} \lesssim 10$ barns translates into a probability of ~ 0.06 scattering events mm^{-1}. Since it will be verified *a posteriori* that optimal target thicknesses will not exceed the millimeter scale, the assumptions leading to Eq. (12) are justified. In Eq. (12), a new quantity $n_\gamma^\pm(k,t,\theta)dk\,dt\,d\Omega$, has been introduced. It represents the number of photons of energy between k and $k + dk$ that are born with a propagation direction falling into the solid angle between Ω and $\Omega + d\Omega$, originating at a depth between t and $t + dt$ in the target, and propagating in the forward/backward $(+/-)$ direction. The simplifying assumption that bremsstrahlung photons are isotropic and produced homogeneously throughout the foil volume, perhaps as a result of hot-electron refluxing,[37,43] allows $n_\gamma^\pm$ to be written simply in terms of $N_\gamma(k)$, i.e.,

$$n_\gamma^\pm(k,t,\theta)dk\,dt\,d\Omega = \frac{1}{2}N_\gamma(k)dk\left(\frac{dt}{d}\right)\left(\frac{d\Omega}{2\pi}\right)H[\pm\cos(\theta)],$$

where H is the Heaviside step function. Equation (12) becomes

$$N_{e^+}(E_+)dE_+ = \frac{N_A}{A}\int_0^\infty dk\,N_\gamma(k)\sigma_{\gamma \to e^+e^-}(k,E_+)dE_+$$

$$\times \int \frac{d\Omega}{4\pi}(\rho L)_{\text{eff}}, \tag{13}$$

where $(\rho L)_{\text{eff}}$ is an "effective depth" in the target (in g/cm^2) for photons of energy k with birth angle θ. This can be written as the product of the average depth in the absence of attenuation, $\rho d/(2|\cos\theta|)$, and an attenuation correcting factor C,

$$(\rho L)_{\text{eff}} = \frac{\rho d}{2|\cos\theta|} \cdot C\left[\frac{\mu(k)d}{|\cos\theta|}\right], \tag{14}$$

where $C(w) = 2/w^2\,[\exp(-w)-(1-w)]$. This correction factor ranges from unity, when attenuation along the path w is small, to $C \sim 2|\cos\theta|/(\mu d)$ when the attenuation is large, giving $(\rho L)_{\text{eff}} \approx \rho/\mu$.

For solid-density gold, $\rho/\mu = (19.3)(0.79) = 15.3$ g/cm^2 at threshold photon energy ($k = 1.022$ MeV). The angle-average effective depth for photons of energy k required by Eq. (13) becomes

$$\langle\rho L\rangle_\Omega \equiv \frac{1}{4\pi}\int d\Omega(\rho L)_{\text{eff}} \tag{15}$$

$$= \rho d\int_0^1 dx\,\min\left\{\frac{1}{2x}C\left(\frac{\mu d}{x}\right),\frac{r}{d}\right\}. \tag{16}$$

The replacement of $(\rho L)_{\text{eff}}$ by $(\rho L)_{\text{eff}} \longrightarrow \min\{(\rho L)_{\text{eff}},\rho r\}$ takes into account the effect of finite target radius r (transverse dimensions). The integral in Eq. (16) can be readily performed, yielding

$$\langle\rho L\rangle_\Omega = \frac{1}{2}\frac{\rho}{\mu}\left[1 + \left(1 - \frac{1}{\mu d}\right)\left(1 - e^{-\mu d}\right) - \mu d\,Ei(-\mu d)\right]$$

$$- \frac{x^*}{2}\frac{\rho}{\mu}\left[1 + \left(1 - \frac{x^*}{\mu d}\right)\left(1 - e^{-\mu d/x^*}\right) - \frac{\mu d}{x^*}\right.$$

$$\left. \times Ei\left(-\frac{\mu d}{x^*}\right)\right] + x^*\rho r, \tag{17}$$

where $Ei(x)$ is the "exponential integral"[45] and x^* is given by the solution to $x^*/(\mu d)(1 - e^{-\mu d/x^*}) = 1 x^*\mu r$, if $r < 1/\mu$, or $x^* = 0$ otherwise. In the case of most interest to experiment, that of weak attenuation $d < r \ll 1/\mu$, Eq. (17) can be approximated as

$$\langle\rho L\rangle_\Omega \approx \frac{\rho d}{2}\log\left(\frac{2.516}{\mu d}\right), \quad \mu d \ll 1, \mu r \geq 1 \tag{18}$$

$$\langle\rho L\rangle_\Omega \approx \frac{\rho d}{2}\log\left(5.437\frac{r}{d}\right), \quad \mu d \ll 1, \mu r \ll 1 \tag{19}$$

In the case of strong attenuation, Eq. (17) can be approximated as

$$\langle\rho L\rangle_\Omega \approx \frac{\rho}{\mu}, \quad \mu d \gg 1, r > d/2. \tag{20}$$

Intermediate cases $\mu d \lesssim 1$ and $\mu r \lesssim 1$ require the numerical evaluation of Eq. (17). The origin of the logarithmic dependence on either foil radius r or absorption $1/\mu$ in Eqs. (18) and (19) is because these serve to regularize the otherwise logarithmically divergent integral, Eq. (16).

---

[b]Usually called the mass attenuation coefficient when expressed in cm^2/g.

With the above results, the positron energy spectrum is given by

$$N_{e^+}(E_+)dE_+ = \frac{N_A}{A}\int_0^\infty dk N_\gamma(k)$$
$$\times \sigma_{\gamma \to e^+e^-}(k,E_+)dE_+ \langle\rho L\rangle_\Omega, \quad (21)$$

and the total photo-produced positron yield is given by $Y_{+,\gamma} = \int_{mc^2}^\infty N_{e^+}(E_+)dE_+$. The yield can be computed directly from the *total* pair cross section

$$\sigma_{\gamma \to e^+e^-}(k) = \int dE_+ \sigma_{\gamma \to e^+e^-}(k,E_+),$$

(the tabulated total cross section is more readily available) according to

$$Y_{+,\gamma} = \frac{N_A}{A}\int_0^\infty dk N_\gamma(k)\sigma_{\gamma \to e^+e^-}(k)\langle\rho L\rangle_\Omega. \quad (22)$$

In Eq. (21), the bremsstrahlung spectrum $N_\gamma(k)$ is given by Eq. (9) and the angle-average effective depth $\langle\rho L\rangle_\Omega$ by Eq. (17), while the differential pair cross-section[41] $\sigma_{\gamma \to e^+e^-}(k,E_+)$ is obtained from the bremsstrahlung cross section [Eq. (8)]. This is achieved by making the substitution $E_0 \longrightarrow -E_+$, $E \longrightarrow E_-$, $k \longrightarrow -k$ and multiplying by $E_+^2 dE_+/(k^2 dk)$ to take care of the change in density of final states (general substitution rule[46]), where E_- is the energy of the pair electron. In general, this expression for the cross section is accurate only for high energies, so we normalize this differential expression to yield a total cross section $\sigma_{\gamma \to e^+e^-}(k)$ that agrees with those tabulated by Hubbell *et al.*[42] The total cross sections of Hubbell *et al.* represent the most-recent systematic computations and tabulations. The same reference provides the mass attenuation coefficient.

Analysis of the Positron-Yield Calculations

1. Dependence of Positron Yield and Positron Spectrum on Interaction Conditions

Figure 116.1 shows the photo-produced positron yield $Y_{+,\gamma}$ per kilojoule of hot-electron energy as a function of hot-electron temperature for foil thicknesses ranging between 10 μm and 200 μm and a radius $r = 1$ mm. Photo-produced pairs dominate over trident pairs for targets of thickness $d \gtrsim 20$ μm for hot-electron temperatures $0.5 \lesssim \Theta_{hot} \lesssim 100$ MeV. For pair production in "showers,"[30] it is known that production by virtual photons becomes negligible compared with production by real photons if the target thickness is much more than 1/25 of a radiation length (i.e., for $d \gtrsim 135$ μm in Au). Hot-electron refluxing is responsible for the dominance of photo-produced pairs in thinner-than-expected targets. Refluxing leads to higher photon production for a given foil thickness, i.e., it is the difference between thin- and thick-target bremsstrahlung yields.[37,43]

Figure 116.3 shows the average positron kinetic energy $\langle T_+\rangle_\gamma$ and the average hot-electron kinetic energy Θ_{hot} as a function of laser intensity I_L. In Fig. 116.3, the hot-electron temperature corresponding to a particular laser intensity has been determined by two different scalings: the ponderomotive scaling [Eq. (1)] and the Beg intensity scaling.[25] Unlike transformed Eq. (8), the cross section $\sigma_{\gamma \to e^+e^-}$ is asymmetric in the energy distribution of the pair for high-Z elements near threshold.[40] Accounting for this effect would lead to a slightly higher positron temperature by an amount of the order of the binding energy, which is considered to be negligible.

For a fixed target thickness, the pair creation efficiency (Fig. 116.1) increases with hot-electron temperature, with energetic efficiencies of $E_{e^+}/E_{hot} \sim 1.6 \times 10^{-4}$ achieved for $\Theta_{hot} \sim 2$ MeV. The optimal hot-electron temperature for the creation of pairs by the Bethe–Heitler process is $(\Theta_{hot})_{opt} \approx 50$ MeV, corresponding to an optimal laser intensity of $(I_L)_{opt} \sim 10^{22}$ W/cm^2, based on the ponderomotive scaling, or $(I_L)_{opt} \sim 10^{25}$ W/cm^2 for the Beg scaling. This enormous variation in optimal laser intensity reflects the degree of uncertainty of the hot-electron temperature scaling with laser intensity in the regime $I_L \gtrsim 10^{21}$ W/cm^2. The


TC8218JRC
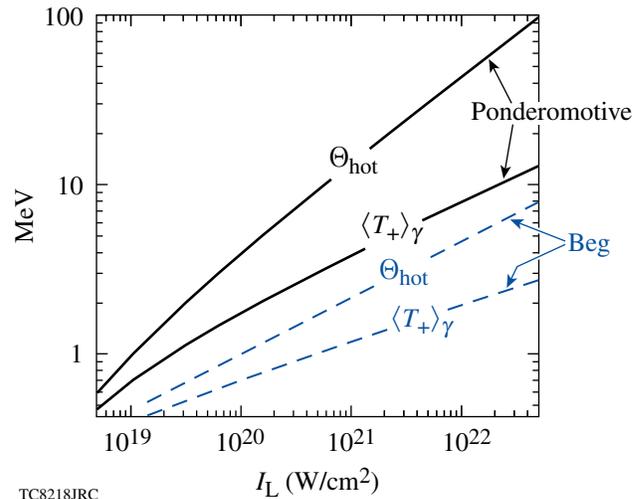
Figure 116.3

The solid curves show the hot-electron temperature (upper curve) and mean positron kinetic energy $\langle T_+\rangle_\gamma$ (lower curve), resulting from the energy spectrum computed in Eq. (21) as functions of laser intensity, assuming the ponderomotive scaling. The dashed curves show the same quantities, but for Beg intensity scaling.

scalings used in Fig. 116.3 have been extrapolated beyond the tested regime $10^{18} \lesssim I_L \lesssim 10^{21}$ W/cm². The Beg scaling, which predicts far fewer energetic electrons, was originally based on experiments in the intensity range $I_L \lesssim 10^{19}$ W/cm² (Ref. 25). For higher hot-electron temperatures $\Theta_{hot} \gtrsim 50$ MeV, the positron production efficiency $Y_{+,\gamma}$, expressed per kJ of hot-electron energy, decreases ($E_{hot} = N_e \Theta_{hot}$ is the energy content of the hot electrons) because the bremsstrahlung spectrum becomes too hard. The pair-production cross section has a very weak energy dependence above photon energies of $k \sim 10$ MeV, and, as far as maximizing the number of pairs is concerned, it is more efficient to have two photons at half the energy.

For a given laser intensity and small x-ray attenuation μd, the production efficiency increases with target thickness by Eq. (18) or Eq. (19), depending on the ratio of the target radius to the photon linear attenuation length μr. For $\mu d \gg 1$, the efficiency is independent of target thickness and $Y_{+,\gamma} \approx \rho/\mu \int dk N_\gamma(k) \sigma_{\gamma \to e^+ e^-}(k)$. The attenuation length varies weakly over the photon energy range of $1 < k < 100$ MeV and has the approximate value $1/\mu \leq 0.8$ cm.

2. Optimized Useful Positron Yield

The long-term goal of this work is to create a pair plasma in the space surrounding the foil target where one can conduct experiments, and not in its interior. The "useful" pair yield (i.e., the number of pairs able to escape the target per kJ of hot-electron energy) must therefore be optimized. For a given laser intensity it might seem that the target should be made as thick as possible, up to an x-ray attenuation length $d \sim 1/\mu \sim 0.8$ cm. The target thickness is more tightly constrained, however, since only positrons within a range $r_0(E_+)$ of the surface will be able to escape and the positron range is typically much less than the x-ray attenuation length $r_0 \ll 1/\mu$. The optimal target thickness $d = d_{opt}(\langle T_+ \rangle)$ is a function of the positron energy, determined by the hot-electron spectrum and depends on the scaling of the hot-electron temperature with laser intensity. Unfortunately, the latter represents a source of considerable uncertainty because such scalings are imprecisely known and are extrapolated from significantly smaller laser systems $E_L \lesssim 500$ J.

Figure 116.4 shows an estimate for the optimal target thickness d_{opt} as a function of average positron energy $\langle T_+ \rangle$. Taken with Fig. 116.3, Fig. 116.4 allows one to estimate the optimal target thickness to be made for a given incident laser intensity. This estimate has been obtained by setting the target thickness d equal to the thickness that is known, experimentally, to trans-
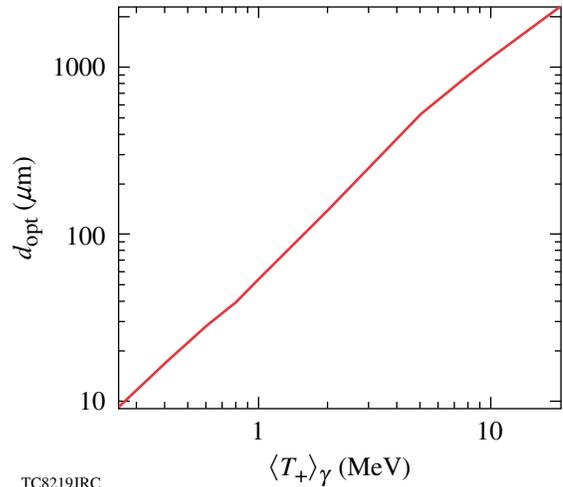
Figure 116.4
The solid curve shows an estimate for the optimal target thickness d_{opt} in μm as a function of average positron energy $\langle T_+ \rangle$ in MeV (positron energy is shown as a function of incident laser intensity in Fig. 116.3).

mit only 50% of a normally incident monoenergetic electron beam of energy T, where T is set to the average positron energy $T = \langle T_+ \rangle$. This thickness is substantially less than the CSDA range due to the path-length straggling caused by multiple scattering of electrons (and positrons) in the Coulomb field of high-Z nuclei (such as Au). This calculation provides a useful "rule of thumb" that will be refined by future detailed Monte Carlo modeling for a more-precise optimization. For a given thickness d, the transmission $Tr(T,Z,d)$ is computed from the "empirical transmission equation" $Tr(T,Z,d) = \exp\left[-\alpha(d/R_{ex})^\beta\right]$ of Ebert et al.,[47] where T is the incident electron energy (the differences between electron and positron stopping and scattering in matter are neglected). The "extrapolated range" R_{ex} is approximated by $R_{ex} = 0.565 [125/(Z + 112)] T - 0.423 [175/(Z + 162)]$ g/cm², where $\alpha = (1-1/\beta)^{1-\beta}$ and the parameter β is given by $\beta = [387 T/Z (1 + 7.5 \times 10^{-5} ZT^2)]^{0.25}$, with T in MeV. The regime of validity for this expression for $Tr(T,Z,d)$ has been expanded from 4 MeV $< T <$ 12 MeV (Ref. 47) to $T \sim$ 0.25 MeV by using the extrapolated ranges of Tabata et al.[48] in the regime 0.25 MeV $< T <$ 4 MeV.

Figure 116.5 shows the "optimized useful yield" as a function of laser intensity for both Beg and ponderomotive scalings. It is apparent that at intensities of $I_L \sim 5 \times 10^{19}$ W/cm²,(c) there is an uncertainty in the pair yield of almost two orders of magnitude. This is a result of the strong temperature dependence of the yield for electron temperatures close to the threshold
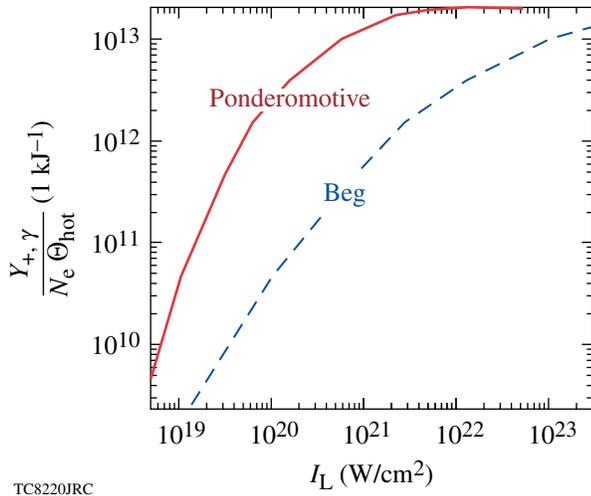
TC8220JRC

Figure 116.5
The solid curve shows the optimum pair yield per kJ of hot electrons $Y_{+,\gamma}/(N_e \Theta_{hot})$ as a function of incident laser intensity I_L, assuming ponderomotive scaling. The dashed curve shows the same quantity, but for Beg intensity scaling.

for pair production, $\Theta_{hot} \sim 1$ MeV, and the current uncertainty in hot-electron energy scaling with laser intensity. At $I_L = 5 \times 10^{19}$ W/cm², the Beg scaling predicts a hot-electron temperature of $\Theta_{hot} \approx 0.8$ MeV and an optimized yield of $Y_{+,\gamma} = 1.5 \times 10^{10}$ pairs per kJ of hot electrons, achieved with a foil of thickness $d = 40\ \mu$m. At the same laser intensity, the ponderomotive scaling predicts $T_{hot} = 2.5$ MeV and a yield of $Y_{+,\gamma} = 1 \times 10^{12}$ per kJ at $d = 200\ \mu$m. This extreme sensitivity will make measurements of the pair yield a good diagnostic for hot-electron temperature in the regime of importance for advanced inertial confinement fusion (ICF) designs, such as fast ignition.[49,50]

A reasonable upper bound for the optimized pair yield on OMEGA EP, and similar future laser systems, can be determined: Assuming the ponderomotive scaling [Eq. (1)], which is more consistent with experiments with significant pre-plasma,[26] a laser energy of $E_L = 2.5$ kJ delivered at an intensity of $I_L = 5 \times 10^{19}$ W/cm², a hot-electron conversion efficiency of $\eta_{L\to e} = 0.2$ (Ref. 51), and perfect refluxing efficiency $\eta_r = 1$ (Refs. 37, 43, and 51), the expected yield is $Y_{+,\gamma} = 5 \times 10^{11}$ pairs. This corresponds to 0.4×10^{10} pairs per steradian, assuming isotropic emission.

3. Optimized Pair-Production rates
The pair-production rate $\dot{Y}_{+,\gamma}$ is estimated by $\dot{Y}_{+,\gamma} \approx Y_{+,\gamma}/\tau^*$, where τ^* is the characteristic production time. Here, τ^* is the time required for the initial hot-electron distribution $f_0(T)$ to slow down so that the relative fraction of particles above threshold,

$$\phi_>(t) \equiv \int_{T_{th,e}}^{\infty} \mathrm{d}T\, f(T,t) \Big/ \int_{T_{th,e}}^{\infty} \mathrm{d}T\, f_0(T),$$

has fallen by $1/e$, i.e., $\phi_>(\tau^*) = 1/e$. The slowing-down distribution at time t, $f(T,t)$ is computed according to the CSDA approximation: $f(T,t) = f_0(T + \Delta T)$, where $\Delta T = -c \int_{t_0}^{t} \mathrm{d}t\, \beta(T)\, |\mathrm{d}t/\mathrm{d}s|$, $\beta = (1-1/\gamma^2)^{1/2}$, and $\gamma = 1 + T/(m_e c^2)$. This assumes that the production time τ^* is longer than the laser pulse duration. If this is not the case, it must be factored into the calculation.

Figure 116.6 shows the pair-production rate $\dot{Y}_{+,\gamma}$ as a function of laser intensity, for both Beg and ponderomotive scalings. For the case of ponderomotive scaling, the production rate rises rapidly for intensities around $I_L \sim 1 \times 10^{19}$ W/cm² ($\Theta_{hot} = 0.96$ MeV) and reaches a maximum at $(I_L)_{max} = 1.5 \times 10^{21}$ W/cm² ($\Theta_{hot} = 16.4$ MeV). The maximum-achievable production rate of $\dot{Y}_{+,\gamma} \approx 10^{24}\,\mathrm{s}^{-1}\,\mathrm{kJ}^{-1}$ greatly exceeds any known terrestrial source; indeed, such a high rate is normally encountered only in astrophysical and cosmological settings.[3]

The maximum in pair-production rate is very broad, with 50% of the maximum value achieved at the moderate intensity of $I_L = 1 \times 10^{20}$ W/cm² ($\Theta_{hot} = 3.9$ MeV). This implies that highly useful experiments can be conducted at $I_L \ll (I_L)_{max}$. High production rates can be obtained by virtue of the large available energy $E_L \sim 5$ kJ on currently available systems (OMEGA EP) with the practical possibility of high-intensity short-pulse lasers with $E_L \sim 100$ kJ in the near future (e.g., the
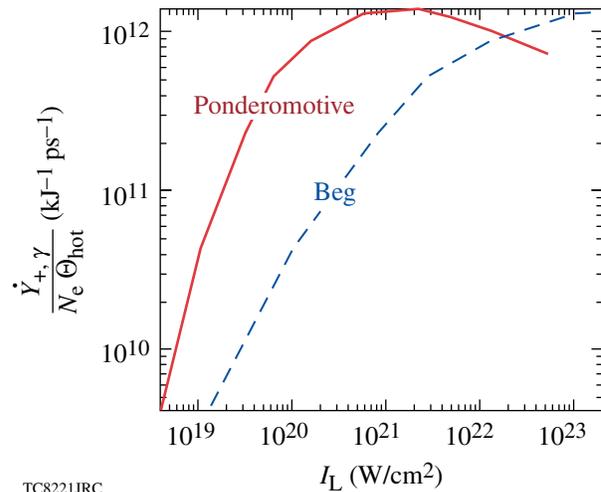
TC8221JRC

Figure 116.6
The solid curve shows the optimized pair-production rate per kJ of hot electrons $\dot{Y}_{+,\gamma}/(N_e \Theta_{hot})$ as a function of laser intensity for the ponderomotive scaling. The dashed curve shows the same quantity for the Beg intensity scaling.

proposed "HiPER" facility[52,53]). The corresponding intensities for Beg scaling are easily obtained from ponderomotive intensities by making the approximate transformation

$$(I_{20})_{\text{Beg}} \approx 87.9 (I_{20})_{\text{pond}}^{3/2}$$

$$\times \left[1 - 0.35(I_{20})_{\text{pond}}^{-1/2} + 0.08(I_{20})_{\text{pond}}^{-1} - ... \right],$$

which is useful for $(I_{20})_{\text{pond}} \gtrsim 1$. Here, I_{20} is the laser intensity I_L expressed in units of 10^{20} W/cm^2.

4. Relativistic Pair-Plasma Production

As shown in Fig. 116.3, the expanding cloud of pair particles will have a temperature characteristic of the hot electrons and γ rays that created it. Unless confined, the relativistic electron–positron pairs will expand into the space surrounding the target at approximately the speed of light.

Although, in general, the expansion into the vacuum can be expected to be quite complicated,[d] the expected plasma parameters can be estimated by assuming free expansion at the speed of light from an infinitesimal source, starting at time $t = 0$, combined with a constant source rate $\dot{Y}_{+,\gamma}$. On this basis, the positron density n_+ at radius r and time t is

$$n_+(r,t) = \frac{1}{4\pi r^2} \frac{\dot{Y}_{+,\gamma}}{c} \quad \text{for } c(t - \tau^*) < r < ct ; \quad (23)$$

$$\text{otherwise,} \quad n_+(r,t) = 0. \quad (24)$$

This gives in practical units

$$n_+(r,t) \approx 0.7 \times 10^{16} \left(\frac{0.03 \text{ cm}}{r}\right)^2$$

$$\times \frac{\dot{Y}_{+,\gamma}}{10^{12} \text{ kJ}^{-1} \text{ ps}^{-1}} \frac{E_{\text{hot}}}{2.5 \text{ kJ}} \text{ cm}^{-3}. \quad (25)$$

The Coulomb coupling parameter $\Gamma_+ = e^2 / \left(a \langle T_+ \rangle_\gamma\right)$, where the ion-sphere radius $a = (4\pi n_+/3)^{-1/3}$ expresses the ratio of Coulomb energy of the particles to their thermal energy. This parameter is much less than unity,

$$\Gamma_+ = 5 \times 10^{-8} \left(n_+ / 10^{16} \text{ cm}^{-3}\right)^{1/3} \left(\langle T_+ \rangle_\gamma / 1 \text{ MeV}\right)^{-1} \ll 1,$$

because the particles are dilute and their temperature is high. The number of particles in a Debye sphere $N_D = (3\Gamma_+)^{-3/2}$ is correspondingly high,

$$N_D = 1.7 \times 10^{10} \left(n_+ / 10^{16} \text{ cm}^{-3}\right)^{-1/2} \left(\langle T_+ \rangle_\gamma / 1 \text{ MeV}\right)^{3/2}.$$

The expanding cloud may appear to be a classical weakly coupled plasma.[54] For collective excitation to be supported, however, the cloud size must exceed the Debye length,

$$\lambda_D = \sqrt{4\pi n_+ e^2 / \langle T_+ \rangle_\gamma} \approx 7.4 \times 10^3$$

$$\times \left(n_+ / 10^{16} \text{ cm}^{-3}\right)^{-1/2} \left(\langle T_+ \rangle_\gamma / 1 \text{ MeV}\right)^{1/2} \text{ cm}.$$

The ratio of density scale length $L_n = \left| d \log n_+ / dr \right|^{-1}$ to the Debye length, for the expansion given by Eq. (23), is

$$\frac{L_n}{\lambda_D} = \frac{1}{2} \left(\frac{\dot{Y}_{+,\gamma} e^2}{c \langle T_+ \rangle_\gamma}\right)^{1/2}. \quad (26)$$

This ratio is independent of r, assuming that the expansion is isothermal,

$$\frac{L_n}{\lambda_D} = 1.7 \left(\frac{\dot{Y}_{+,\gamma}}{10^{12} \text{ ps}^{-1} \text{ kJ}^{-1}}\right)^{1/2} \left(\frac{E_{\text{hot}}}{2.5 \text{ kJ}}\right)^{1/2} \left(\frac{\langle T_+ \rangle_\gamma}{1 \text{ MeV}}\right)^{-1/2}. \quad (27)$$

Adiabatic expansion would give a more favorable ratio for larger radii.

From the above estimate [Eq. (27)], the rate of positron production $\dot{Y}_{+,\gamma}$ is probably insufficient to guarantee the production of a pair plasma for laser energies of several kJ. The chances for success can be greatly improved, however, by limiting the expansion of the cloud.

Confinement of the pairs, such as might be obtained in a magnetic mirror,[10] is not necessary. Radial confinement of the order of 100 μm with free expansion in the remaining dimension will lead to a cloud that is several tens of Debye lengths in size[55]

---

[d]Electrostatic sheath fields and large-scale, self-generated dc magnetic fields will modify the expansion.

and has many particles in a Debye sphere; i.e., the cloud will form a classical weakly coupled plasma. Radial confinement may be obtained in several ways, e.g., by using one of the OMEGA EP beams to magnetize the positron-generation foil using a "magnetic trap" target,[55] or by the application of an externally generated magnetic field of the type used in the Magneto-Inertial Fusion Electrical Discharge System (MIFEDS).[56]

Summary

The yield of electron–positron pairs caused by both direct and indirect processes resulting from the interaction of laser-accelerated hot electrons with target atoms has been calculated. Indirect production is the dominant process for practical target interaction conditions.

Calculation of the indirect yield required two steps: First, an expression for the hard x-ray spectrum and yield was obtained [Eqs. (9) and (10)]. This was computed in the limit in which the majority of fast electrons are confined to the target by space-charge effects (the so-called "refluxing limit"). Second, convenient expressions were obtained for the pair spectrum [Eq. (21)] and pair yield [Eq. (22)]. These are given in terms of the photon spectrum $N_\gamma(k)$ and an angle-average effective depth for photons $\langle \rho L \rangle_\Omega$, which is dependent on the photon energy and target geometry [Eqs. (17–20)]. Predictions of bremsstrahlung yield [Eq. (10)] and spectrum [Eq. (9)] are experimentally verifiable and might prove useful for other applications.

For a given target thickness, the efficiency of pair creation (pairs per kJ of hot electrons) was shown to increase with the temperature Θ_{hot} of the laser-excited electrons, with maximum production efficiency obtained at a hot-electron temperature of Θ_{hot} = 50 MeV. Energetic efficiencies of ~1.6×10^{-4} are shown to be achievable at Θ_{hot} = 2 MeV. The corresponding laser intensity for optimal yield could optimistically be as low as $I_L \sim 10^{22}$ W/cm^2.

The optimal "useful" yield is limited by the range of the pairs in the target material. It has been maximized by matching the target thickness to the expected penetration distance of the pairs as a function of laser intensity and Θ_{hot} scaling (see Fig. 116.5). It was demonstrated that a yield of $Y_{+,\gamma} = 5 \times 10^{11}$ pairs might be generated on OMEGA EP, provided that the hot-electron temperature is consistent with the ponderomotive scaling. More unfavorable yields are obtained with Beg scaling.

Pair-production rates were calculated and shown to have a very broad maximum of $\dot{Y}_{+,\gamma} = 1 \times 10^{24}$ s^{-1} kJ^{-1}, obtained at $I_L = 1.5 \times 10^{21}$ W/cm^2 (Θ_{hot} = 16.4 MeV), which is a significantly lower Θ_{hot} than that required for maximizing the yield. The rate displays little sensitivity to the hot-electron temperature over a wide range. This implies that, as far as production rates are concerned, increasing laser intensities above the currently attainable levels is less important than increasing available laser energy, which does not rely on further technological advances.

An estimate of plasma parameters, assuming free expansion of the pairs into the vacuum, indicates that current kJ-class, high-intensity lasers may come close to producing a pair plasma with a physical size similar to, or slightly smaller than, the Debye length. A successful demonstration will probably require efforts to confine or limit the expansion of the expanding pairs. Possible confinement schemes, such as externally applied magnetic fields, are suggested. The yields, production rates, and energy spectra that have been computed in this article will be useful for particle-in-cell (PIC) or implicit-hybrid PIC calculations of the dynamics of expansion and pair-plasma production.

REFERENCES

1. V. Tsytovich and C. B. Wharton, Comments Plasma Phys. Control. Fusion **4**, 91 (1978).

2. G. P. Zank and R. G. Greaves, Phys. Rev. E **51**, 6079 (1995).

3. M. L. Burns, A. K. Harding, and R. Ramaty, eds. *Positron-Electron Pairs in Astrophysics, AIP Conference Proceedings 101* (American Institute of Physics, New York, 1983).

4. B. A. Remington *et al.*, Science **284**, 1488 (1999).

5. C. M. Surko, M. Leventhal, and A. Passner, Phys. Rev. Lett. **62**, 901 (1989).

6. C. M. Surko and T. J. Murphy, Phys. Fluids B **2**, 1372 (1990).

7. T. Kurihara *et al.*, Nucl. Instrum. Methods Phys. Res. B **171**, 164 (2000).

8. C. M. Surko *et al.*, Nucl. Instrum. Methods Phys. Res. B **171**, 2 (2000).

9. T. S. Pedersen *et al.*, J. Phys. B **36**, 1029 (2003).

10. G. Gibson, W. C. Jordan, and E. J. Lauer, Phys. Rev. Lett. **5**, 141 (1960).

11. J. W. Shearer *et al.*, Phys. Rev. A **8**, 1582 (1973).

12. E. P. Liang, S. C. Wilks, and M. Tabak, Phys. Rev. Lett. **81**, 4887 (1998).

13. D. A. Gryaznykh, Ya. Z. Kandiev, and V. A. Lykov, JETP Lett. **67**, 257 (1998).

14. T. E. Cowan *et al.*, in *High-Field Science*, edited by T. Tajima, K. Mima, and H. Baldis (Kluwer Academic, New York, 2000), pp. 145–156.

15. C. Gahn *et al.*, Appl. Phys. Lett. **77**, 2662 (2000).

16. K. Nakashima and H. Takabe, Phys. Plasmas **9**, 1505 (2002).

17. S. C. Wilks *et al.*, Astrophys. Space Sci. **298**, 347 (2005).

18. L. J. Waxer, D. N. Maywar, J. H. Kelly, T. J. Kessler, B. E. Kruschwitz, S. J. Loucks, R. L. McCrory, D. D. Meyerhofer, S. F. B. Morse, C. Stoeckl, and J. D. Zuegel, Opt. Photonics News **16**, 30 (2005).

19. M. H. Key, Phys. Plasmas **14**, 055502 (2007).

20. J. Schwinger, Phys. Rev. **82**, 664 (1951).

21. E. Brezin and C. Itzykson, Phys. Rev. D **2**, 1191 (1970).

22. H. Nitta *et al.*, Phys. Rev. Lett. **93**, 180407 (2004).

23. S. P. Hatchett, C. G. Brown, T. E. Cowan, E. A. Henry, J. S. Johnson, M. H. Key, J. A. Koch, A. B. Langdon, B. F. Lasinski, R. W. Lee, A. J. MacKinnon, D. M. Pennington, M. D. Perry, T. W. Phillips, M. Roth, T. C. Sangster, M. S. Singh, R. A. Snavely, M. A. Stoyer, S. C. Wilks, and K. Yasuike, Phys. Plasmas **7**, 2076 (2000).

24. S. C. Wilks *et al.*, Phys. Rev. Lett. **69**, 1383 (1992).

25. F. N. Beg *et al.*, Phys. Plasmas **4**, 447 (1997).

26. M. G. Haines, Imperial College, private communications (2008).

27. T. E. Cowan, M. Roth, J. Johnson, C. Brown, M. Christl, W. Fountain, S. Hatchett, E. A. Henry, A. W. Hunt, M. H. Key, A. MacKinnon, T. Parnell, D. M. Pennington, M. D. Perry, T. W. Phillips, T. C. Sangster, M. Singh, R. Snavely, M. Stoyer, Y. Takahashi, S. C. Wilks, and K. Yasuike, Nucl. Instrum. Methods Phys. Res. A **455**, 130 (2000).

28. H. Chen *et al.*, Rev. Sci. Instrum. **77**, 10E703 (2006).

29. H. J. Bhabha, Proc. R. Soc. Lond. A, Math. Phys. Sci. **152**, 559 (1935).

30. Y.-S. Tsai, Rev. Mod. Phys. **46**, 815 (1974).

31. G. Racah, Nuovo Cimento **14**, 93 (1937).

32. B. B. Rossi, *High-Energy Particles*, Prentice-Hall Physics Series (Prentice-Hall, New York, 1952).

33. T. Murota, A. Ueda, and H. Tanaka, Prog. Theor. Phys. **16**, 482 (1956).

34. D. A. Gryaznykh, Phys. At. Nucl. **61**, 394 (1998).

35. V. N. Baĭer and V. S. Fadin, Sov. Phys.-JETP **34**, 253 (1972).

36. J. Myatt, W. Theobald, J. A. Delettrez, C. Stoeckl, M. Storm, T. C. Sangster, A. V. Maximov, and R. W. Short, Phys. Plasmas **14**, 056301 (2007).

37. P. M. Nilson, W. Theobald, J. F. Myatt, C. Stoeckl, M. Storm, J. D. Zuegel, R. Betti, D. D. Meyerhofer, and T. C. Sangster, "Bulk Heating of Dense Plasma High-Intensity Laser-Plasma Interactions," submitted to Physical Review E.

38. H. O. Wyckoff, *ICRU Report*, **37**, International Commission on Radiation Units and Measurements, Inc., Bethesda, MD (1984).

39. H. W. Koch and J. W. Motz, Rev. Mod. Phys. **31**, 920 (1959).

40. H. A. Bethe and J. Ashkin, in *Experimental Nuclear Physics*, edited by E. Sergrè (Wiley, New York, 1953), Vol. I, pp. 166–357.

41. S. M. Seltzer and M. J. Berger, Nucl. Instrum. Methods Phys. Res. B **12**, 95 (1985).

42. J. H. Hubbell, H. A. Gimm, and I. Øverbø, J. Phys. Chem. Ref. Data **9**, 1023 (1980).

43. S. D. Baton *et al.*, High Energy Density Phys. **3**, 358 (2007).

44. M. Tabak, Bull. Am. Phys. Soc. **52**, 284 (2007).

45. M. Abramowitz and I. A. Stegun, eds. *Handbook of Mathematical Functions with Formulas, Graphs, and Mathematical Tables*, Applied Mathematics Series 55 (U.S. Government Printing Office, Washington, DC, 1964).

46. J. D. Bjorken and S. D. Drell, *Relativistic Quantum Mechanics*, International Series in Pure and Applied Physics (McGraw-Hill, New York, 1964).

47. P. J. Ebert, A. F. Lauzon, and E. M. Lent, Phys. Rev. **183**, 422 (1969).

48. T. Tabata, R. Ito, and S. Okabe, Nucl. Instrum. Methods **103**, 85 (1972).

49. N. G. Basov, S. Yu. Gus'kov, and L. P. Feokistov, J. Sov. Laser Res. **13**, 396 (1992).

50. M. Tabak *et al.*, Phys. Plasmas **1**, 1626 (1994).

51. P. M. Nilson, W. Theobald, J. Myatt, C. Stoeckl, M. Storm, O. V. Gotchev, J. D. Zuegel, R. Betti, D. D. Meyerhofer, and T. C. Sangster, Phys. Plasmas **15**, 056308 (2008).

52. M. Dunne, Nat. Phys. **2**, 2 (2006).

53. S. Atzeni *et al.*, Phys. Plasmas **15**, 056311 (2008).

54. S. Ichimaru, *Statistical Plasma Physics. Volume I, Basic Principles*, Frontiers in Physics (Addison-Wesley, Redwood City, CA, 1992).

55. J. Myatt, A. V. Maximov, R. W. Short, and D. D. Meyerhofer, Bull. Am. Phys. Soc. **52**, 66 (2007).

56. O. V. Gotchev, N. W. Jang, J. P. Knauer, M. D. Barbero, R. Betti, C. K. Li, and R. D. Petrasso, J. Fusion Energy **27**, 25 (2008).

Neutron Yield Study of Direct-Drive, Low-Adiabat Cryogenic D$_2$ Implosions on OMEGA

Introduction

As a viable path to energy production, inertial confinement fusion (ICF) has been actively pursued over the past decades.[1] In a standard ICF design, a thin-shell capsule containing a solid DT (ice) layer and low-density DT gases is imploded as symmetrically as possible, either directly driven by high-energy lasers[2] or indirectly driven by x rays in a hohlraum.[3] The high-speed, inward-moving shell compresses the low-density DT gases, thereby creating a "hot spot" during the stagnation of the implosion. Thermonuclear reactions in this high-temperature hot spot can trigger a burn wave that ignites the assembled, surrounding high-density fuel. To obtain energy gain, the imploding DT fuel must be compressed to thousands of times its solid density.[4] On one hand, a properly created hot spot, with certain density and temperature, provides the alpha (α) particles for subsequent heating of the assembled, surrounding high-density, low-temperature fuels. On the other hand, the fuel areal density (ρR) must be high enough to stop the heating particles for efficient burn-wave propagation. It is clear that proper hot-spot formation and high-density fuel assembly must be attained simultaneously to guarantee a successful ignition. Any target perturbations can grow exponentially via Rayleigh–Taylor (RT) instability[5–9] to disrupt the hot-spot formation as well as the high-density fuel assembly.

Cryogenic implosions with high adiabats of $\alpha \geq 4$ (α is defined as the ratio of fuel pressure to the Fermi-degenerate pressure) have been previously investigated in OMEGA experiments[10] and simulations.[11] To efficiently compress ICF targets to high densities, the fuel must maintain a low adiabat of $\alpha \simeq 2$ during a direct-drive implosion.[12] Low-adiabat implosions are very sensitive, however, to RT instability growth. Mitigation of RT growth has been proposed and conducted using a laser picket in front of the main pulse, which shapes the fuel adiabat to be low at the back surface and high at the ablation front.[13,14] A series of such shaped low-adiabat ($\alpha \simeq 2$ to 3) cryogenic targets have been imploded at the OMEGA Laser Facility.[15–17] Since efficient diagnostic methods for ρR measurement of DT implosions are not yet fully implemented, most cryogenic implosions on OMEGA are currently performed

with D$_2$ targets. For D$_2$ implosions, the compression has been successfully measured up to $\rho R \sim 200$ mg/cm^2 by secondary proton scattering.[15–17] As discussed above, assembly of high-density fuels is extremely crucial, but getting the predicted fusion yield from the formed hot spot is equally important to the success of ICF; after all, it provides the "trigger" for ignition burn propagation to occur. A variety of perturbations can significantly reduce the fusion yield. This article is devoted to understanding the perturbation sources and how they affect the neutron yield in low-adiabat cryogenic D$_2$ implosions conducted on OMEGA.

The next two sections give a brief description of the two-dimensional (2-D) numerical simulations and experimental basics, respectively. Subsequent sections (1) present simulation results that examine in detail the effects of both individual and combined perturbation sources on the implosion yield degradation; (2) discuss the absolute experimental neutron yield and neutron rate measurements, when compared to our modelings; and (3) summarize our results.

Two-Dimensional *DRACO* Simulations

The 2-D radiation hydrodynamics code *DRACO* has been developed at LLE for both implosion and planar target simulations.[18] *DRACO* can be run in either Lagrangian, Eulerian, or Arbitrary–Lagrangian–Eulerian (ALE) mode, but this study uses only the ALE version. For spherical implosion simulations, the *DRACO* coordinates are defined by the cylindrical axis z and radius R, with the assumption of azimuthal symmetry. The laser absorption of plasmas through inverse bremsstralung is implemented by three-dimensional (3-D) ray tracing with the exact port geometry of OMEGA.[19] Although *DRACO* has the option of using different equations of state (EOS's) in hydrosimulations, the *SESAME* EOS table[20] is used throughout this study. The *SESAME* EOS of direct-drive ICF shell material has recently been verified by compressibility measurements.[21,22] Agreements were found for a variety of drive conditions related to direct-drive ICF. The radiation transport in *DRACO* has used the multigroup diffusion model, in which the Astrophysics Opacity Table (AOT)[23] is applied.

Since the laser energy absorbed near the critical-density region must be transported to the ablation surface by electrons, the thermal-transport model in direct-drive ICF is crucial for properly simulating the target drive. There has been a long history of using flux-limited Spitzer thermal conductivity in laser–plasma fluid modelings.[24] Previous experiments with both planar and spherical targets[25,26] have shown that a flux limiter of $f = 0.06$ works well for low/middle laser intensities (up to ~6×10^{14} W/cm^2) of square pulses; however, there was also evidence that a time-dependent flux limiter[27] or a nonlocal heat-transport model[16] is required to better simulate implosions driven by high-intensity lasers and/or sophisticated pulse shapes. In principle, we can perform our 2-D simulations with a time-dependent flux limiter, which partially accounts for the nonlocal effects. However, since the purpose of this study is to explore the perturbation effects on the neutron-yield degradation of implosions, we have confined our simulations to those shots that are insensitive to the heat-transport model. Namely, we have studied mostly cryogenic D_2 implosions with low/middle laser intensities ranging from 2.5 to 6×10^{14} W/cm^2. For those implosions, the local and nonlocal 1-D *LILAC*[28] simulations show less sensitivity to shock timing; therefore, a normal flux limiter of $f = 0.06$ was adopted for these studies.

DRACO's capability to simulate Rayleigh–Taylor instability growth has recently been demonstrated with intense laser-driving planar-target experiments on OMEGA.[29] For low-mode perturbations similar to those investigated here, the code properly predicts their growth rate at the relevant laser-intensity range. Generally, we have examined an ice-layer roughness mode up to $\ell = 12$. The higher modes of ice-layer perturbations are found to be less important to yield degradation in thin-shell (~5-μm) implosions.

D_2 Implosion Experiments on OMEGA

The 60-beam OMEGA Laser Facility delivers up to 30-kJ, 351-nm UV energies on target.[30] A typical laser pulse used for low-adiabat D_2 implosions is shown in Fig. 116.7(b), in which the Gaussian-like laser picket is used to shape the target adiabat.[13,14] Each laser beam, coming from ports in 3-D geometry, is equipped with an SG-4 phase plate. Standard beam-smoothing techniques were used, including distributed phase plates,[31] polarization smoothing,[32] and smoothing by spectral dispersion (SSD).[33] The power imbalance (PI) among beams has an rms (root mean square) of ~2.6%, while the mistiming (MT) is typically within ~12-ps rms. The mispointing of each beam has an uncertainty of ~12-μm rms. All of these low-mode laser nonuniformities have been implemented in our 3-D ray-tracing laser-absorption package. We have separately

examined the effect of each of these nonuniformities and their combined effects on the performance of a uniform target. The simulation results are summarized in Table 116.I. Compared to the uniform irradiation, it was found that mistiming among beams is the dominant effect to the total yield-over-clean (YOC) degradation, while other low-mode laser perturbations change the YOC only a few percent around that of the symmetric implosion. The "clean" yield is defined as the neutron yield from a 2-D simulation with uniform laser irradiation and
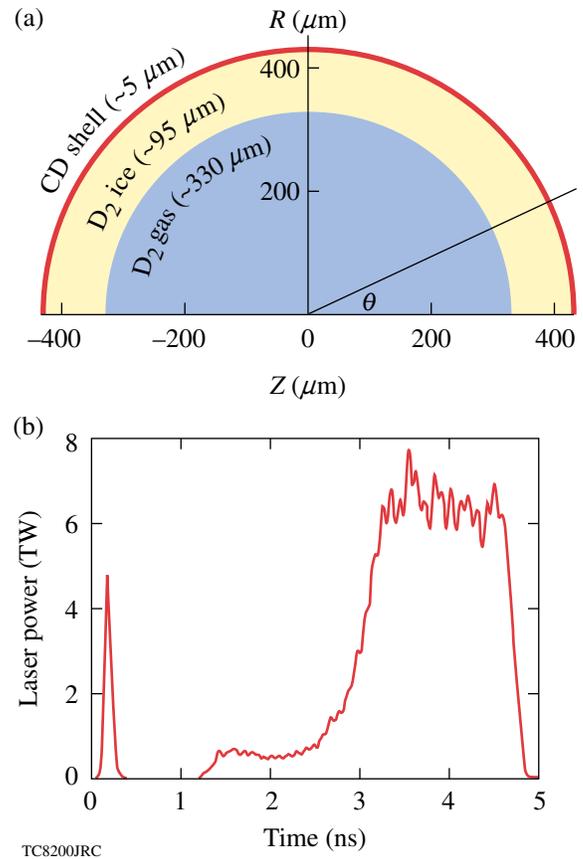
Figure 116.7
(a) The schematic diagram of a typical thin-shell cryogenic D_2 target imploded on OMEGA; (b) the shaped low-adiabat ($\alpha \simeq 2$ to 3) laser pulse with a picket.

Table 116.I: YOC dependence on low-mode laser nonuniformities.

Low-mode laser nonuniformity	YOC$_{2\text{-D}}$
3-D port geometry only	96.7%
Geometry + mispointing (~12 μm)	98.0%
Geometry + power imbalance (~2.6%)	102%
Geometry + mistiming (~12 ps)	82.2%
Full nonuniformity (including all)	83.3%

a symmetric target. It shows that all of these combined illumination nonuniformities reduce the YOC to a level of ~83% for a uniform target. All of the following studies have included these low-ℓ-mode laser nonuniformities since they are always present in OMEGA experiments.

Detailed descriptions of cryogenic targets formed for OMEGA implosions can be found in Refs. 34 and 35. Basically, the targets are D$_2$ filled, with a CD shell having an outer diameter of ~860 μm and a shell thickness of 5 to 10 μm. The targets are permeation filled with high-pressure D$_2$ gas and cooled to below the triple point (~18.7 K). They are then transported to a characterization station for layer formation and finally to the OMEGA target chamber for implosion. The ice-layer roughness is measured in experiment before implosion. The actual low-mode spectrum of ice roughness is used in our simulations.

A typical target [shown schematically in Fig. 116.7(a)] has an ice layer of ~95-μm thickness. Figure 116.8 illustrates the irradiation nonuniformity in the case of non-zero target offset. The target offset is caused by oscillation when the shroud is pulled before implosion. This initial target offset is measured through an x-ray pinhole camera image at the beginning of corona plasma formation.[10] The fusion yield is measured by a combination of activation, scintillation, and track recorder. When compared to the predicted symmetric implosion yield, the YOC provides a direct measurement of target performance.

The low-adiabat cryogenic implosion campaign conducted on OMEGA used a wide range of peak laser intensities up to ~10^{15} W/cm^2. For high intensities near ~10^{15} W/cm^2, the compression is somewhat degraded with respect to the standard 1-D prediction due to different mechanisms.[15,16,36] Thus, this study of neutron-yield degradation will focus on those low- to mid-intensity shots that obtained $\langle \rho R \rangle_{exp}$ better than 60% of the standard 1-D prediction. They are generally in the range of $\langle \rho R \rangle_{exp} \simeq 100$ to 200 mg/cm^2.

Results and Discussions

Using the laser pulse shown in Fig. 116.7(b) throughout this general study, we will first address, separately, the effects induced by pure offset and pure ice roughness on the YOC degradation. We then discuss their combined effects on reducing the neutron yield. Finally, we compare the simulation results to experiments. The absolute neutron yields and rates from *DRACO* simulations are also compared with measurements for individual shots. Note that the laser nonuniformities discussed above have been included in all of the following studies since they are always present in OMEGA experiments.

1. Pure Offset

For the target and pulse shape characterized in Fig. 116.7, we simulated implosions with different initial target offsets but no ice roughness present (symmetric target). The offset is along the positive z axis, thereby leading to more irradiation on the "left" side than on the "right" side of the target. This can be
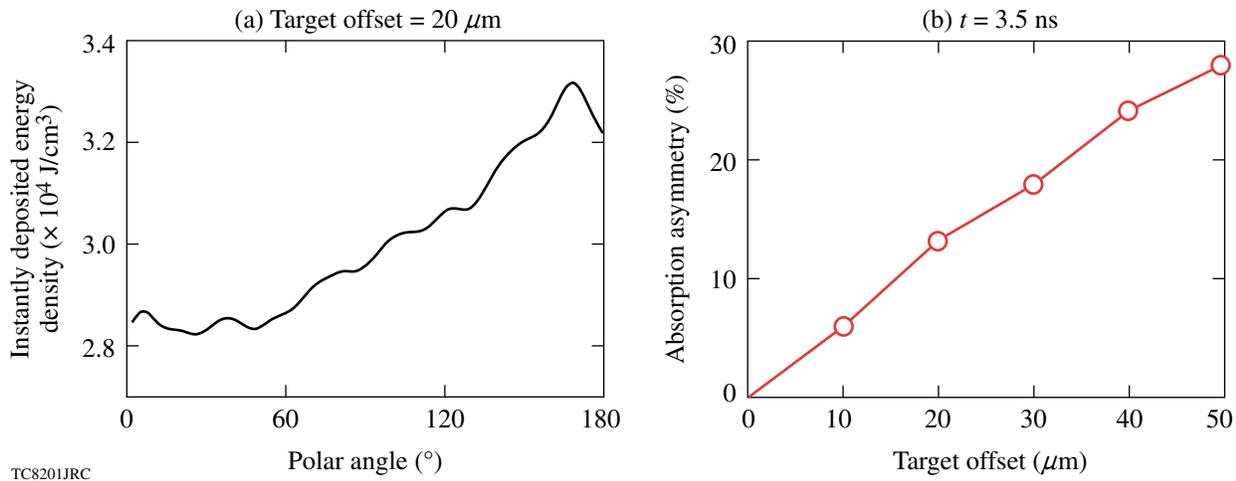

Figure 116.8

(a) The deposited energy density at $t = 3.5$ ns versus the angle θ (relative to the $+z$ axis) for a target offset of 20 μm; (b) the absorption asymmetry plotted as a function of target offset.

seen in Fig. 116.8(a) for the case of a 20-μm offset, in which is plotted the instantly absorbed laser energy density (ED) at time $t = 3.5$ ns as a function of the polar angle θ [defined in Fig. 116.7(a)]. The $\theta = 0°$ line is along the positive z axis, while $\theta = 180°$ is for the negative z axis. The absorption asymmetry is defined as

$$\text{absorption symmetry} = \frac{\text{ED}_{max} - \text{ED}_{min}}{\text{ED}_{avg}}, \quad (1)$$

where ED_{max}, ED_{min}, and ED_{avg} are the temporal maximum, minimum, and averaged energy-density depositions in the full range of polar angle θ. For the case of zero offset, the symmetric illumination gives no absorption asymmetry, while it reaches to ~13% at a 20-μm offset. In Fig. 116.8(b), the absorption asymmetry is plotted at $t = 3.5$ ns as a function of the initial target offset. Approximately 30% more laser absorption is seen on the left side than on the right side of the target in the case of a 50-μm offset. The uneven drive compresses the target asymmetrically, thereby reducing the final hot-spot temperature and density, which leads to neutron-yield degradation. As examples, the density contours are plotted at the peak compression time ($t = 4.9$ ns) for the cases of 20-μm and 40-μm offset in Figs. 116.9(a) and 116.9(b) and the neutron rates as a function of time in Fig. 116.9(c). It can be seen that the larger the offset, the more asymmetric the compression. Consequently, the hot-spot ion temperature and density decrease from $T_i \simeq$ 1.8 keV and $\rho \simeq 9$ g/cm^3 to $T_i \simeq 1.5$ keV and $\rho \simeq 7$ g/cm^3 as the target offset increases from 20 μm [Fig. 116.9(a)] to 40 μm [Fig. 116.9(b)]. Compared to the symmetric case, a non-zero target offset has caused the "burn" to truncate early and has resulted in a relatively lower peak rate, thereby leading to an overall reduction in neutron yield, as shown in Fig. 116.9(c). The resulting YOC$_{2\text{-D}}$ decreases from 43% to 13.8% for these two cases, respectively.

Figure 116.10 explores the detailed hydrodynamics of how the offset affects hot-spot formation. Density snapshots at different times of (a) $t = 4.55$ ns, (b) $t = 4.65$ ns, (c) $t = 4.75$ ns, and (d) $t = 4.85$ ns are shown during shell stagnation for the case of 20-μm offset. Since the absorption on the target's left side is constantly higher, the shock from the left side is stronger than that from the right side. The asymmetric shock converges and shifts to the right side, away from the core center. At $t = 4.55$ ns, the asymmetrically converged shock starts to bounce back. As evidence of the bounced shock asymmetry, the unevenly formed high-pressure region on the inner surface of the right side of the target is indicated by Fig. 116.10(b). This asymmetrically bounced shock acting with a continuously uneven drive makes the target convergence unequal from both sides.
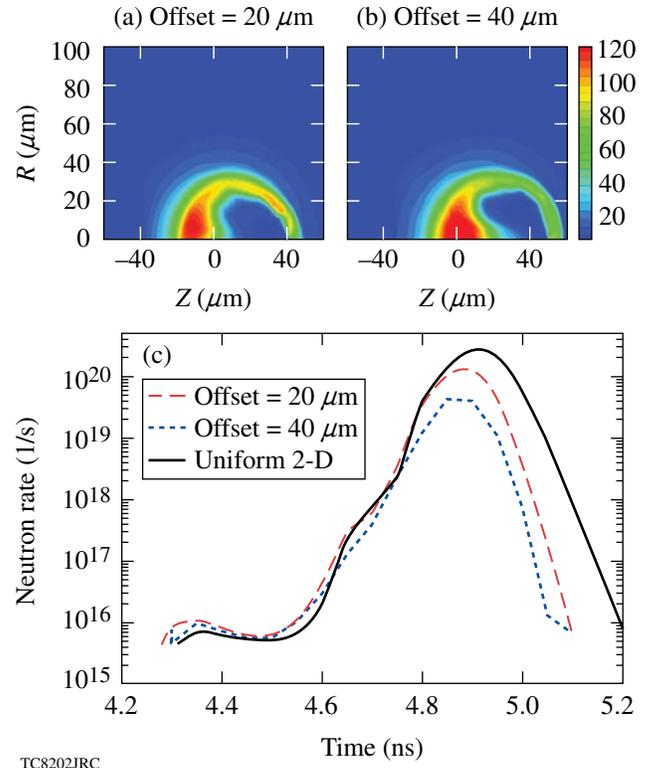
Figure 116.9
The density contour plots at peak compression for target offset of (a) 20 μm and (b) 40 μm. The corresponding neutron rates are plotted in (c) for the two offset situations as well as the symmetric case.

As time goes on, convergence is stronger on the left side of the target (opposite to the initial target offset direction), thereby leading to high compression along that side. All these features are presented in the simulations in Fig. 116.10.

Pure-offset simulations up to 50 μm have been performed with the pulse shape and uniform target characterized in Fig. 116.7; the results are summarized in Fig. 116.11. It is noted that at zero offset the laser illumination nonuniformities degrade the YOC$_{2\text{-D}}$ to ~83%, as was addressed above. Overall, the YOC$_{2\text{-D}}$ monotonically decreases as the offset increases. For a target offset of 20 μm, the simulation gives a YOC ~40%, which is three to four times higher than experimental observations. Thus, the target offset alone cannot explain the YOC degradation in experiments.

2. Ice Roughness Only
   The ice-layer roughness has been characterized in experiments.[34] As an example, the low-ℓ-mode spectrum of ice roughness for a typical cryogenic D_2 target is shown in Fig. 116.12, with $\sigma_{rms} \simeq 3.2$ μm. Approximating the ice-layer

TC8202JRC

TC8203JRC
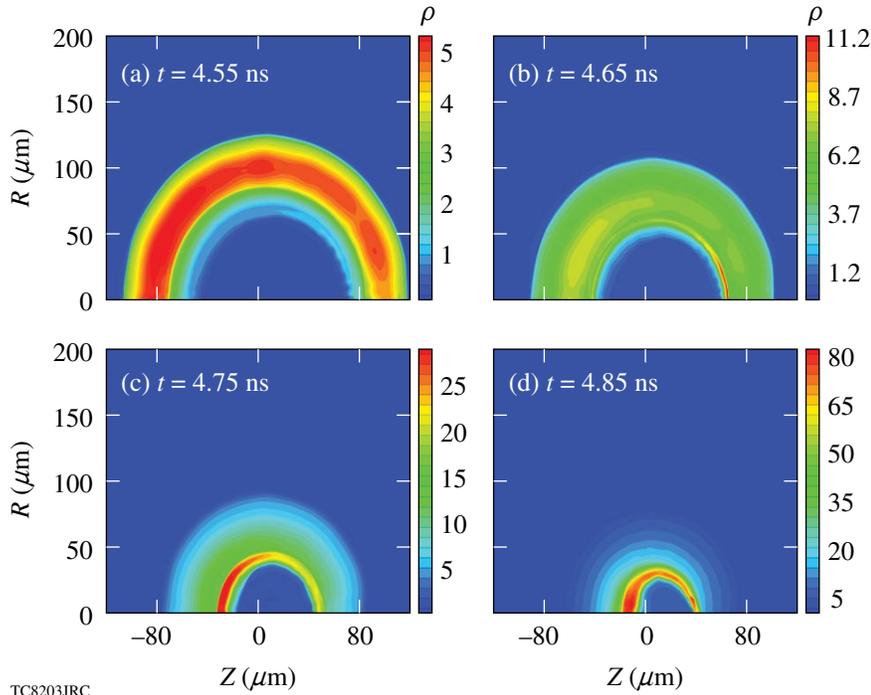
Figure 116.10
The density contour plots of a uniform target implosion with 20-μm offset, during the deceleration phase at times (a) $t = 4.55$ ns, (b) $t = 4.65$ ns, (c) $t = 4.75$ ns, and (d) $t = 4.85$ ns.

TC8204JRC
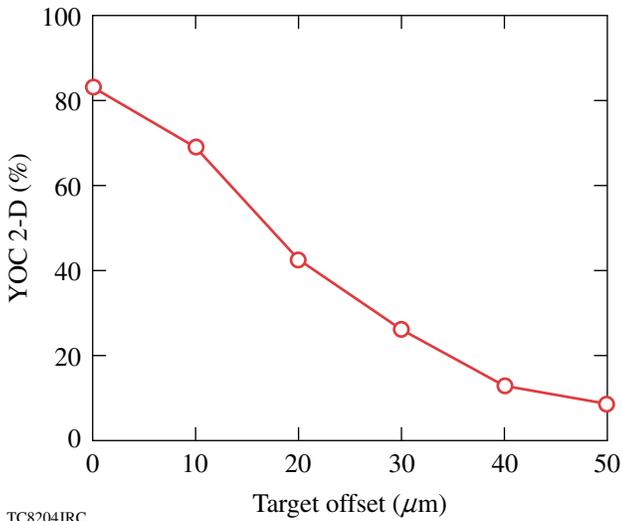
Figure 116.11
The YOC$_{2\text{-}D}$ as a function of target offset only.

TC8205JRC
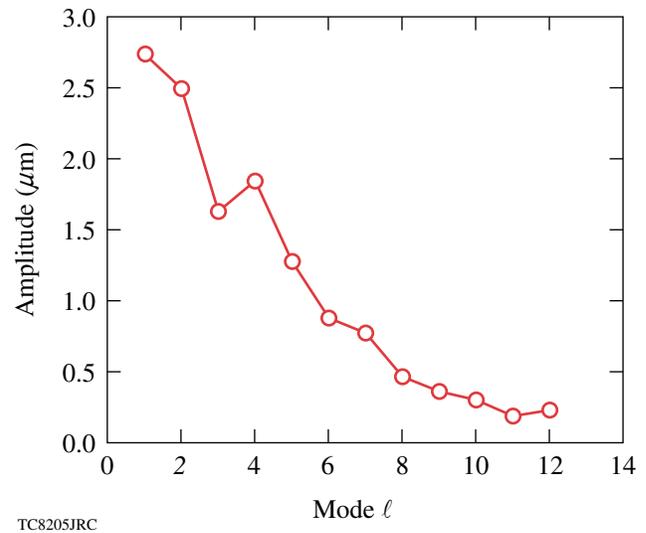
Figure 116.12
The low-ℓ-mode spectrum of ice-layer roughness for a typical cryogenic D$_2$ target imploded on OMEGA.

perturbation as a sum of *cosine* modes, we construct the ice-layer thickness (ΔR) for our *DRACO* simulations. Namely,

$$\Delta R(\theta) = \Delta R_0 + \sum_{\ell=1}^{n} \pm A_\ell \cos(\ell\theta), \qquad (2)$$

where ΔR_0 is the average thickness of the ice layer and A_ℓ is the perturbation amplitude of the ℓth mode. Due to the

hydro-boundary conditions imposed in *DRACO*, the phase among different modes can only be either 0 or π radian. This gives a plus (+) or minus (–) sign in the superposition of each mode. Different combinations of these signs provide various phases of the ice layer, which give different perturbed shell thicknesses along the polar angle θ. For instance, three such phases are drawn in Fig. 116.13. We mark the shell thickness at

$\theta = 0°$, $\theta = 90°$, and $\theta = 180°$ for each target condition. For the phase-1 target shown in Fig. 116.13(a), the thinnest ice layer is along the $\theta = 0°$ axis, while the thickest portion is at $\theta = 90°$. Figures 116.13(b) and 116.13(c) indicate the other two cases, of which the thinnest ice layer is along $\theta = 90°$, but different conditions are indicated along the z axis.

Without target offset, simulations were performed for these three target conditions characterized in Fig. 116.13. The simulated results are presented in Figs. 116.14(a)–116.14(c) for density contours at peak compression and in Fig. 116.14(d) for neutron rates. Depending on which part is the thinnest ice layer, the shock will first break out there. For example, the shock breaks out early from the right side ($\Delta R = 90$ μm at $\theta = 0°$) of the target in the phase-1 condition. The asymmetrically converged shock will push the core toward the left side (along the $\theta = 180°$ direction). For targets in phases 2 and 3, the thinnest ice layer is along the $\theta = 90°$ direction. When the shock breaks out early from there, it makes the final hot spot more elongated along the z axis as illustrated in Figs. 116.14(b) and 116.14(c). Consequently, we observe that the compressed core of the phase-1 target shifts to $z \simeq -10$ μm at stagnation, while the center of mass moves roughly to $z \simeq +10$ μm for phases 2 and 3. The phase-1 target gives a better performance than the other two targets. The YOC$_{2\text{-D}}$ is about 31% on average and varies within ~3% for these three phases. The yield performance is not sensitive to different phases in the case of zero offset, but this observation can be largely changed when combined to nonzero target offset. Even though an ice roughness of $\sigma \simeq 3.2$ μm could significantly reduce the YOC$_{2\text{-D}}$ to a level of ~30%, these simulations indicate that the ice roughness alone cannot explain the experimental YOC measurements. They are generally two to
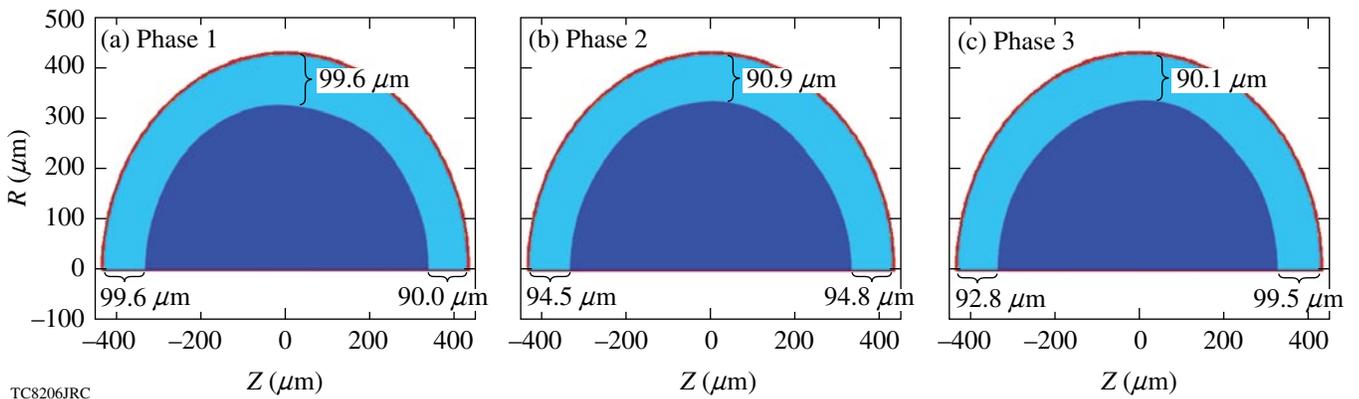
Figure 116.13
Different target conditions depending on the phases among low modes of the ice-layer roughness.
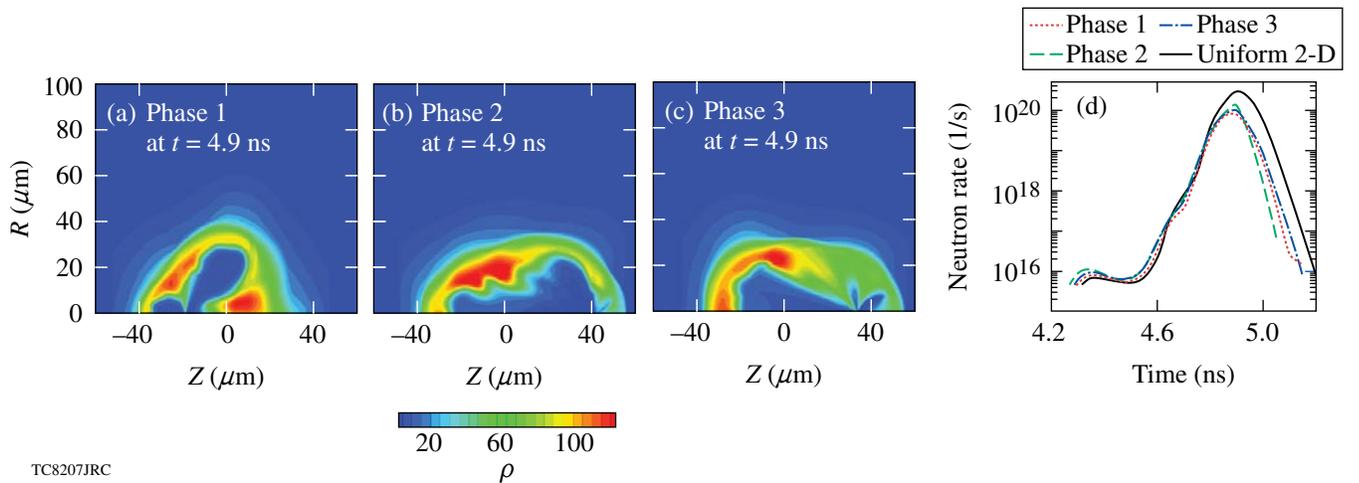
Figure 116.14
The density plots at peak neutron production, respectively, for the three different target conditions [(a), (b), and (c)] in Fig. 116.13. The corresponding neutron rates are shown in (d).

three times higher than the experimental YOC measurements, which have both ice roughness and nonzero target offset.

3. Combination of Target Offset and Ice Roughness

From here on, we examine the combined perturbation effects of both the target offset and the ice-layer roughness on the neutron-yield degradation of D$_2$ target implosions. Numerical examples are shown in Fig. 116.15 in the case of a 30-μm offset for the target ice-layer conditions illustrated in Fig. 116.13. In these figures, the density contours are plotted at the time of their peak neutron production. Overall, the offset acts like a dominant $\ell = 1$ mode that compresses the shell more on the left side (e.g., along the "anti-offset" direction). However, the detailed core configurations vary significantly for different phases of ice roughness. As seen in Fig. 116.14(a), the pure ice roughness in phase 1 gives a final compressed core shifted to $Z = -10$ μm, referred to here as the "equivalent offset" to the ice roughness. This equivalent offset is opposite the real target offset, which is set along the positive z direction. Namely, the two perturbation effects are "out of phase" as the hard-driven side (along $\theta = 180°$) encounters a thicker ice layer [see Fig. 116.13(a)], so that the shocks breaking out from both sides are somewhat more balanced in phase 1. Thus, when combining the real target offset of $z = +30$ μm with the phase-1 ice roughness, the final compressed core moves roughly to $z \simeq +30–10 \simeq 20$ μm as indicated by Fig. 116.15(a). It therefore gives a better performance and results in more neutron production, shown as the thick, solid curve in Fig. 116.15(d). While for phases 2 and 3, the ice-roughness effect is "in phase" with the target offset perturbation. In other words, both perturbations constructively cause the target to perform less satisfactorily. Figures 116.15(b) and

116.15(c) show that the final cores shift to distances larger than their initial target offset of 30 μm; therefore, both cases perform less satisfactorily than the phase-1 target. With the extra perturbation of offset, the target performance is now more sensitive to the phase of ice roughness. The final target performance actually depends on whether the target offset is in phase or out of phase with the ice roughness. We have also explored other phases and found that phases 1 and 2 shown here are the two extremes.

To characterize the hot-spot condition, the quantity of $\rho^2 T_i^4$ is plotted in Fig. 116.16 for the three cases shown in Fig. 116.15, where ρ and T_i are the D$_2$ density and the ion temperature, respectively. Since the fusion rate is proportional to this quantity,[1] these plots indicate where neutrons are probably generated and what portion of the core volume contributes to neutron production during peak compression. Bearing in mind the azimuthal symmetry imposed in *DRACO*, one can see from Fig. 116.16 that the core condition of the phase-1 target is much better (having more volume with higher $\rho^2 T_i^4$) than the other two cases, which is consistent with the higher neutron production from the phase-1 target.

By varying the target offset and the ice roughness, the effects of different combinations of the two on the implosion neutron yield have been numerically examined. The results are summarized in Fig. 116.17, which plots the YOC$_{2\text{-D}}$ versus the initial target offset for ice roughnesses of $\sigma_{\text{rms}} = 1.0$ μm and $\sigma_{\text{rms}} = 3.2$ μm. All phases explored for each point have been averaged; also indicated is the YOC$_{2\text{-D}}$ range that each target phase could possibly reach. Figure 116.17 shows that, as the
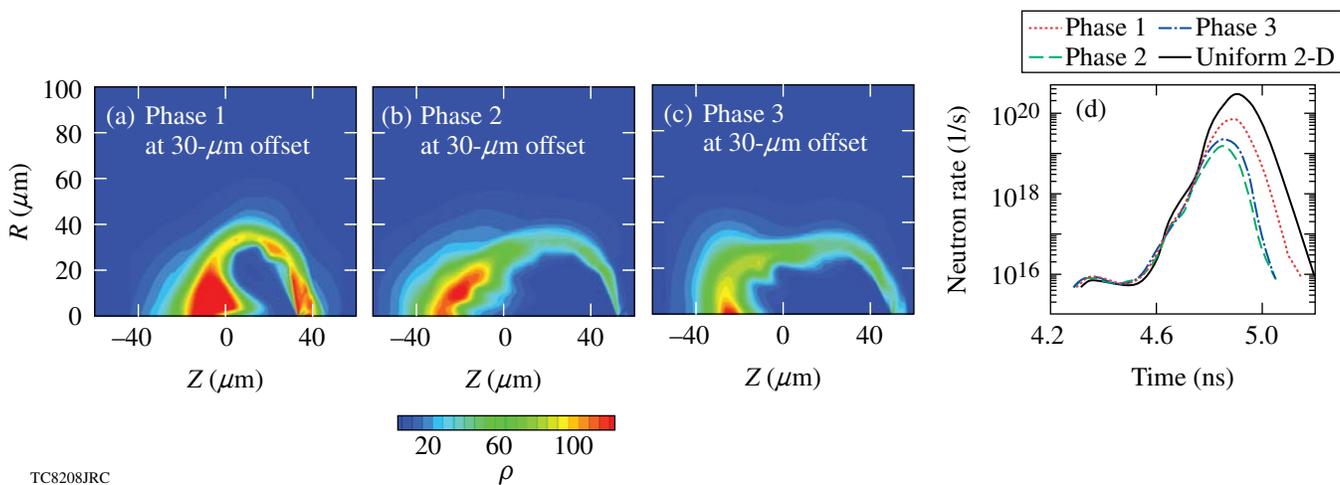
Figure 116.15
Similar to Fig. 116.14, but the targets are now offset by 30 μm.

TC8208JRC
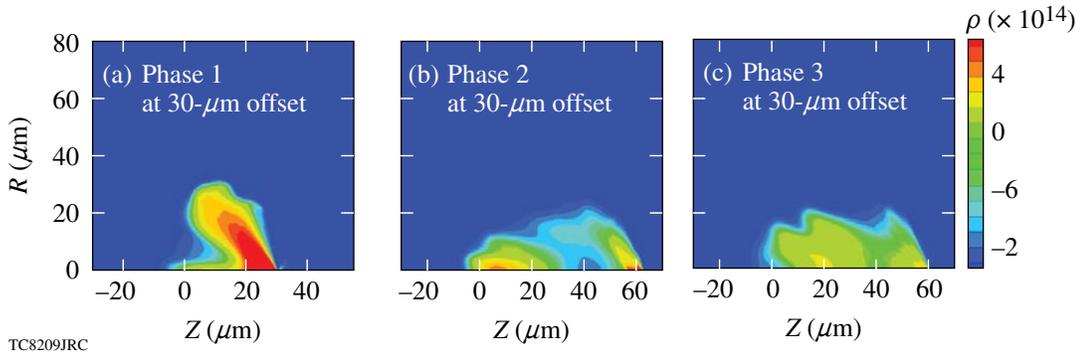
Figure 116.16
The contour plots of $\rho^2 T_i^4$ on the z–r plane, for the corresponding cases [(a), (b), and (c)] in Fig. 116.15. The images indicate where most of the neutrons are probably generated, as the fusion cross section is proportional to $\rho^2 T_i^4$.
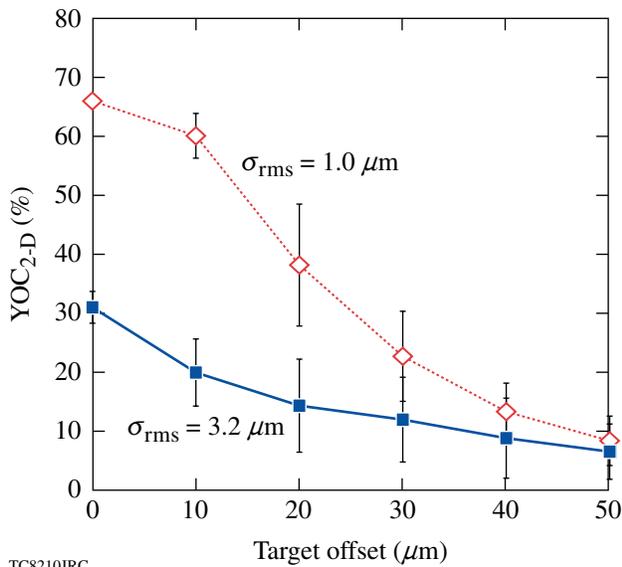
Figure 116.17
$YOC_{2\text{-D}}$ versus target offset for ice roughnesses $\sigma_{rms} = 1.0\ \mu m$ and $\sigma_{rms} = 3.2\ \mu m$. The points are obtained by averaging different phases, where the possible $YOC_{2\text{-D}}$ range is also marked for each condition.

target offset increases beyond ~10 μm, the $YOC_{2\text{-D}}$ drops more dramatically in the case of $\sigma_{rms} = 1\ \mu m$ than that of $\sigma_{rms} = 3.2\ \mu m$. For both cases, the phase-dependent YOC range is significant at a target offset of 20 to 40 μm. When the target offset increases to 50 μm, it becomes the dominant effect and the yield is no longer sensitive to the ice roughness.

4. Comparison to Experiments

In this subsection, we first compare the overall YOC performance as a function of target offset and ice roughness. Secondly, we focus on individual shots by using the actual experimental conditions in our simulations.

The general studies presented in Fig. 116.17 were performed for the case of low-adiabat, thin-CD-shell (5-μm) D_2 implosions. Similar-condition experiments have been conducted on OMEGA.[15–17] Shots that resulted in a compression of $\langle\rho R\rangle_{exp}/\langle\rho R\rangle_{1\text{-}D} \geq 60\%$ are plotted in comparison with our *DRACO* simulations ($\sigma_{rms} = 3.2\ \mu m$) in Fig. 116.18. The shots are divided into two groups according to their target ice roughness, i.e., $\sigma_{rms} < 3.5\ \mu m$ (circles) and $\sigma_{rms} > 3.5\ \mu m$ (triangles). We find reasonably good agreement between our *DRACO* simulation and experiments at an ice-roughness level of $\sigma_{rms} \sim 3\ \mu m$. Shots with a larger ice roughness ($\sigma_{rms} > 3.5\ \mu m$) constantly give a lower YOC, which is reasonably below our simulations of $\sigma_{rms} = 3.2\ \mu m$.
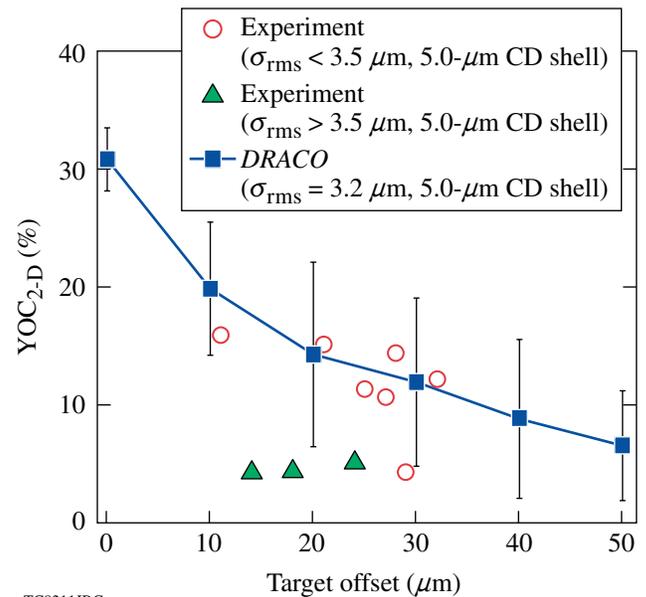
Figure 116.18
A comparison of simulated $YOC_{2\text{-D}}$ with experimental measurements for low-adiabat ($\alpha \simeq 2$ to 3), thin-shell (~5-μm) D_2 implosions on OMEGA.

D_2 targets having thick (~10-μm) CD shells were also imploded with the shaped pulse indicated in Fig. 116.19(a). For the thick-shell targets that we studied, the ice layer had a thickness of ~95 μm. The peak laser intensity now increases to ~5×10^{14} W/cm^2. In this case, the laser continuously ablates the CD shell during the entire implosion, and there is no ablation transition from CD to D_2. Compared to the thin-shell implosions, the 10-μm-thick-shell targets give a constantly lower YOC $\leq$ 7%. To understand the yield performance in thick-shell implosions, a general study was also performed through low-ℓ-mode *DRACO* simulations. The comparison is

made in Fig. 116.19(b). The numerical prediction of YOC$_{2-D}$ from low-ℓ-mode *DRACO* simulations is higher overall than the experimental measurements by a factor of ~3. In contrast to the thick-shell situation, high-ℓ-mode perturbation growth in thin-shell implosions is probably stabilized when the laser ablation transits into D_2 (high ablation velocity). We speculate that for thick-shell targets, high-mode perturbations such as laser imprinting[37,38] may become more important since the high-density CD shell stays intact at the ablation surface during the laser irradiation. To that end, we performed simulations to resolve high modes up to $\ell_{max} \simeq 200$. The results indicate that a factor of 2 reduction is observed, which brings the high-ℓ-mode simulation results close to experimental measurements for thick-shell implosions.

To get a sense of how YOC degrades when ice roughness increases, we have collected those shots with usual target offsets between ~10 μm and ~40 μm. The results are plotted in Fig. 116.20 and compared with low-ℓ-mode *DRACO* simulations. For thin-shell (5-μm) targets, our simulations are performed with an average target offset of 25 μm. The numerical results provide an upper limit for these experiments. The overall trend of YOC degradation with increased ice roughness is reasonably well reproduced by *DRACO* simulations. The 10-μm-thick-shell targets consistently give a lower YOC
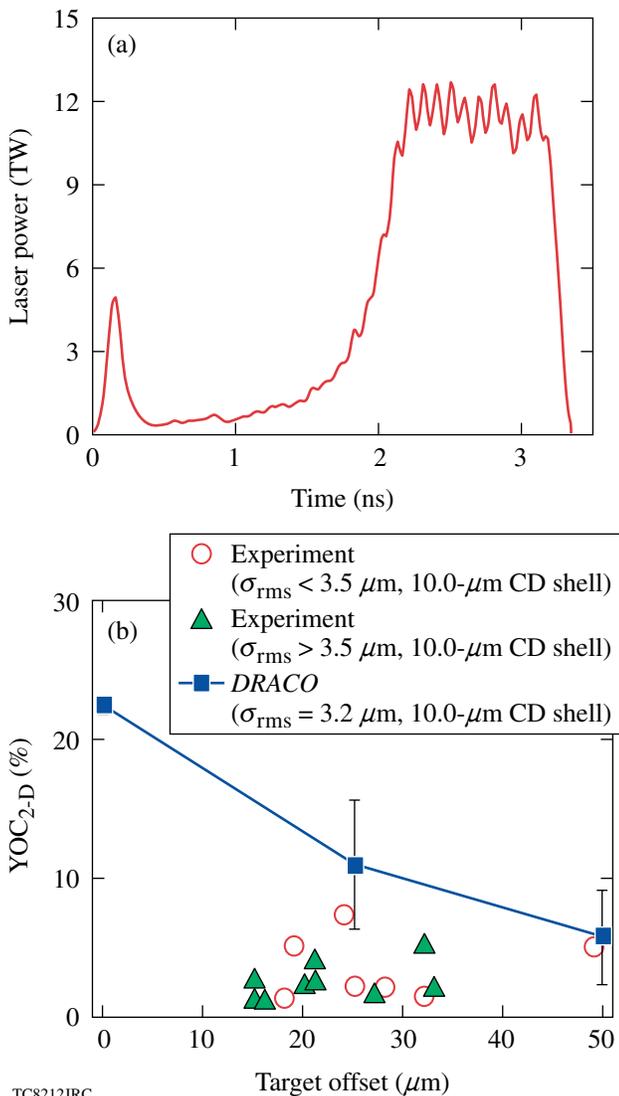
Figure 116.19
(a) A shaped pulse for low-adiabat ($\alpha \simeq 2$ to 3), thick-shell (~10-μm) D_2 implosions on OMEGA; (b) low-ℓ-mode *DRACO* simulated YOC compared with experimental measurements.
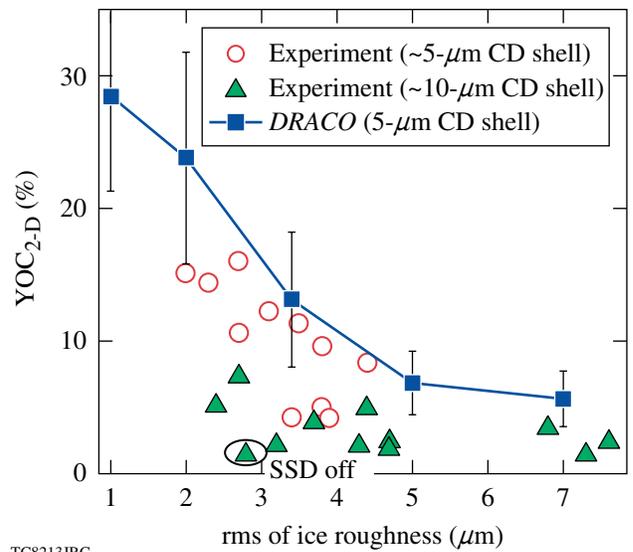
Figure 116.20
The simulated thin-shell YOC$_{2-D}$ as a function of the ice roughness σ_{rms} at a target offset of 25 μm, which is compared to experimental YOC measurements for both 5-μm- and 10-μm-CD-shell implosions at an offset range of 10 to 40 μm. The laser peak intensity (2.5 to 6.0×10^{14} W/cm^2) and pulse shape vary for different experimental shots.

than thin-shell targets. One shot with SSD off is marked in the figure, which shows a very low YOC level.

Finally, we discuss *DRACO* simulations for several individual shots in different conditions. The measured absolute neutron yields, which span two orders of magnitude, are plotted in comparison with *DRACO* simulations in Fig. 116.21. Different low-adiabat pulse shapes are used for these shots with peak intensities varying from 2.5×10^{14} W/cm^2 to $\sim 6 \times 10^{14}$ W/cm^2. For most thin-shell (5-μm) targets, the simulated neutron yields reasonably track the measurements (within a factor of 2). One shot (46864) labeled "shock timing" in Fig. 116.21 has shown a big difference between simulation and experiment. Our constant flux-limiter ($f = 0.06$) simulation gives three-to-four-times-higher neutron yield. For this shot, we noticed that the laser pulse has a higher picket so that the yield and compression performance was sensitive to the thermal transport modeling. Shock timing has played a significant role in target performance. There is also significant discrepancy between the low-ℓ-mode *DRACO* simulation and the experiment for a 10-μm-thick-shell implosion, which is also labeled in Fig. 116.21. Again, high-ℓ-mode perturbations not included in simulations may have further degraded the neutron yield in experiments.

Besides the total neutron yield, we have also compared the calculated time-resolved neutron rates to those observed in thin-shell experiments. Examples of such comparisons are illustrated in Fig. 116.22. The simulated neutron rate has been

broadened somewhat to account for the time dispersion (due to thermal broadening and/or 3-D effects) in experiments. Good agreement is reached when the Gaussian broadening is done with a width of $\sigma \simeq 100$ ps. We noticed that the thermal broadening contributes only to $\sigma \sim 40$ ps; it is not yet clear about other sources of broadening, although 3-D effect may be the major player. For the low-intensity ($\sim 3 \times 10^{14}$ W/cm^2) shot (50267) in which the simulated total yield agrees with the experiment, the measured neutron rate is reproduced by a *DRACO* simulation with a broadening of ~ 100 ps, as shown in Fig. 116.22(a). While, for the mid-intensity ($\sim 6 \times 10^{14}$ W/cm^2) shot (49937) illustrated by Fig. 116.22(b), the simulated neutron rate is wider and higher than measurement, the total neutron

Figure 116.22
The neutron-rate comparison between experiments (circles) and simulations (lines) for (a) low-intensity ($\sim 3 \times 10^{14}$ W/cm^2) shot 50267 and (b) mid-intensity ($\sim 6 \times 10^{14}$ W/cm^2) shot 49937.

Figure 116.21
The absolute neutron yields are compared between experiments and *DRACO* simulations. Different phases are explored in the simulations. The two shots that are labeled are sensitive to either shock timing or thick-shell implosion for which high-ℓ-mode nonuniformities may be important.

yield in the 2-D simulation is larger than the experimental value by almost a factor of 2. We believe that such a discrepancy may be within the uncertainties that the approximation of a 2-D code may cause in approaching the 3-D reality.

Conclusion

Using 2-D *DRACO* simulations, we have systematically investigated low-ℓ-mode perturbation effects on the neutron-yield degradation of direct-drive, low-adiabat ($\alpha \simeq 2$ to 3) cryogenic D$_2$ implosions on OMEGA. Despite the limitation of reduced dimensionality, our 2-D simulations show that for thin-shell (5-μm) targets, the yield degradation can be reasonably explained by the combined perturbations from the target offset, the low-ℓ-mode ice roughness, and low-ℓ-mode laser illumination nonuniformities. In terms of YOC, thick-shell targets generally do not perform as well as thin-shell targets using similar pulse shapes. We show that high-ℓ-mode perturbations such as laser imprinting may play a role in further reducing neutron yields in thick-shell cryogenic implosions. Besides the total neutron yield, the broadened neutron rates from 2-D simulations are also reasonably comparable to measurements, especially for low-intensity and thin-shell implosions. It should also be important to directly carry out such studies for DT implosions because extrapolating these D$_2$ results to the DT case is not straightforward since shock timing may play a different role. So far fewer DT shots have been conducted on OMEGA than D$_2$ shots. For these reasons, we leave such a similar investigation of DT implosions for future studies.

REFERENCES

1. S. Atzeni and J. Meyer-ter-Vehn, *The Physics of Inertial Fusion: Beam Plasma Interaction, Hydrodynamics, Hot Dense Matter*, International Series of Monographs on Physics (Clarendon Press, Oxford, 2004); J. D. Lindl, *Inertial Confinement Fusion: The Quest for Ignition and Energy Gain Using Indirect Drive* (Springer-Verlag, New York, 1998).

2. S. E. Bodner *et al.*, Phys. Plasmas **7**, 2298 (2000).

3. J. D. Lindl, Phys. Plasmas **2**, 3933 (1995).

4. P. W. McKenty, V. N. Goncharov, R. P. J. Town, S. Skupsky, R. Betti, and R. L. McCrory, Phys. Plasmas **8**, 2315 (2001).

5. S. E. Bodner, Phys. Rev. Lett. **33**, 761 (1974); H. Takabe *et al.*, Phys. Fluids **28**, 3676 (1985); H. J. Kull and S. I. Anisimov, Phys. Fluids **29**, 2067 (1986); A. B. Bud'ko and M. A. Liberman, Fluids B **4**, 3499 (1992); V. V. Bychkov, S. M. Goldberg, and M. A. Liberman, Phys. Plasmas **1**, 2976 (1994); J. Sanz, Phys. Rev. Lett. **73**, 2700 (1994); J. G. Wouchuk and A. R. Piriz, Phys. Plasmas **2**, 493 (1995).

6. R. Betti, V. N. Goncharov, R. L. McCrory, P. Sorotokin, and C. P. Verdon, Phys. Plasmas **3**, 2122 (1996); R. Betti, V. N. Goncharov, R. L. McCrory, and C. P. Verdon, Phys. Plasmas **5**, 1446 (1998); V. N. Goncharov, P. McKenty, S. Skupsky, R. Betti, R. L. McCrory, and C. Cherfils-Clérouin, Phys. Plasmas **7**, 5118 (2000).

7. B. A. Remington *et al.*, Phys. Rev. Lett. **73**, 545 (1994); K. Shigemori *et al.*, Phys. Rev. Lett. **78**, 250 (1997); S. G. Glendinning, S. N. Dixit, B. A. Hammel, D. H. Kalantar, M. H. Key, J. D. Kilkenny, J. P. Knauer, D. M. Pennington, B. A. Remington, R. J. Wallace, and S. V. Weber, Phys. Rev. Lett. **78**, 3318 (1997); M. M. Marinak *et al.*, Phys. Rev. Lett. **80**, 4426 (1998); C. J. Pawley *et al.*, Phys. Plasmas **6**, 565 (1999).

8. D. L. Tubbs, C. W. Barnes, J. B. Beck, N. M. Hoffman, J. A. Oertel, R. G. Watt, T. Boehly, D. Bradley, P. Jaanimagi, and J. Knauer, Phys. Plasmas **6**, 2095 (1999); C. Cherfils *et al.*, Phys. Rev. Lett. **83**, 5507 (1999).

9. V. A. Smalyuk, T. R. Boehly, D. K. Bradley, V. N. Goncharov, J. A. Delettrez, J. P. Knauer, D. D. Meyerhofer, D. Oron, and D. Shvarts, Phys. Rev. Lett. **81**, 5342 (1998); J. P. Knauer, R. Betti, D. K. Bradley, T. R. Boehly, T. J. B. Collins, V. N. Goncharov, P. W. McKenty, D. D. Meyerhofer, V. A. Smalyuk, C. P. Verdon, S. G. Glendinning, D. H. Kalantar, and R. G. Watt, Phys. Plasmas **7**, 338 (2000); O. Sadot, V. A. Smalyuk, J. A. Delettrez, D. D. Meyerhofer, T. C. Sangster, R. Betti, V. N. Goncharov, and D. Shvarts, Phys. Rev. Lett. **95**, 265001 (2005); H. Azechi *et al.*, Phys. Rev. Lett. **98**, 045002 (2007).

10. F. J. Marshall, R. S. Craxton, J. A. Delettrez, D. H. Edgell, L. M. Elasky, R. Epstein, V. Yu. Glebov, V. N. Goncharov, D. R. Harding, R. Janezic, R. L. Keck, J. D. Kilkenny, J. P. Knauer, S. J. Loucks, L. D. Lund, R. L. McCrory, P. W. McKenty, D. D. Meyerhofer, P. B. Radha, S. P. Regan, T. C. Sangster, W. Seka, V. A. Smalyuk, J. M. Soures, C. Stoeckl, S. Skupsky, J. A. Frenje, C. K. Li, R. D. Petrasso, and F. H. Séguin, Phys. Plasmas **12**, 056302 (2005).

11. P. W. McKenty, T. C. Sangster, M. Alexander, R. Betti, R. S. Craxton, J. A. Delettrez, L. Elasky, R. Epstein, A. Frank, V. Yu. Glebov, V. N. Goncharov, D. R. Harding, S. Jin, J. P. Knauer, R. L. Keck, S. J. Loucks, L. D. Lund, R. L. McCrory, F. J. Marshall, D. D. Meyerhofer, S. P. Regan, P. B. Radha, S. Roberts, W. Seka, S. Skupsky, V. A. Smalyuk, J. M. Soures, K. A. Thorp, M. Wozniak, J. A. Frenje, C. K. Li, R. D. Petrasso, F. H. Séguin, K. A. Fletcher, S. Padalino, C. Freeman, N. Izumi, J. A. Koch, R. A. Lerche, M. J. Moran, T. W. Phillips, G. J. Schmid, and C. Sorce, Phys. Plasmas **11**, 2790 (2004).

12. R. Betti, K. Anderson, J. Knauer, T. J. B. Collins, R. L. McCrory, P. W. McKenty, and S. Skupsky, Phys. Plasmas **12**, 042703 (2005); J. P. Knauer, K. Anderson, R. Betti, T. J. B. Collins, V. N. Goncharov, P. W. McKenty, D. D. Meyerhofer, P. B. Radha, S. P. Regan, T. C. Sangster, V. A. Smalyuk, J. A. Frenje, C. K. Li, R. D. Petrasso, and F. H. Séguin, Phys. Plasmas **12**, 056306 (2005).

13. V. N. Goncharov, J. P. Knauer, P. W. McKenty, P. B. Radha, T. C. Sangster, S. Skupsky, R. Betti, R. L. McCrory, and D. D. Meyerhofer, Phys. Plasmas **10**, 1906 (2003).

14. K. Anderson and R. Betti, Phys. Plasmas **10**, 4448 (2003).

15. T. C. Sangster, V. N. Goncharov, P. B. Radha, V. A. Smalyuk, R. Betti, R. S. Craxton, J. A. Delettrez, D. H. Edgell, V. Yu. Glebov, D. R. Harding, D. Jacobs-Perkins, J. P. Knauer, F. J. Marshall, R. L. McCrory, P. W. McKenty, D. D. Meyerhofer, S. P. Regan, W. Seka, R. W. Short, S. Skupsky, J. M. Soures, C. Stoeckl, B. Yaakobi, D. Shvarts, J. A. Frenje, C. K. Li, R. D. Petrasso, and F. H. Séguin, Phys. Rev. Lett. **100**, 185006 (2008).

16. V. N. Goncharov, T. C. Sangster, P. B. Radha, R. Betti, T. R. Boehly, T. J. B. Collins, R. S. Craxton, J. A. Delettrez, R. Epstein, V. Yu. Glebov, S. X. Hu, I. V. Igumenshchev, J. P. Knauer, S. J. Loucks, J. A. Marozas, F. J. Marshall, R. L. McCrory, P. W. McKenty, D. D. Meyerhofer, S. P. Regan, W. Seka, S. Skupsky, V. A. Smalyuk, J. M. Soures, C. Stoeckl, D. Shvarts, J. A. Frenje, R. D. Petrasso, C. K. Li, F. Séguin, W. Manheimer, and D. G. Colombant, Phys. Plasmas **15**, 056310 (2008).

17. R. L. McCrory, D. D. Meyerhofer, R. Betti, R. S. Craxton, J. A. Delettrez, D. H. Edgell, V. Yu Glebov, V. N. Goncharov, D. R. Harding, D. W. Jacobs-Perkins, J. P. Knauer, F. J. Marshall, P. W. McKenty, P. B. Radha, S. P. Regan, T. C. Sangster, W. Seka, R. W. Short, S. Skupsky, V. A. Smalyuk, J. M. Soures, C. Stoeckl, B. Yaakobi, D. Shvarts, J. A. Frenje, C. K. Li, R. D. Petrasso, and F. H. Séguin, Phys. Plasmas **15**, 055503 (2008).

18. P. B. Radha, T. J. B. Collins, J. A. Delettrez, Y. Elbaz, R. Epstein, V. Yu. Glebov, V. N. Goncharov, R. L. Keck, J. P. Knauer, J. A. Marozas, F. J. Marshall, R. L. McCrory, P. W. McKenty, D. D. Meyerhofer, S. P. Regan, T. C. Sangster, W. Seka, D. Shvarts, S. Skupsky, Y. Srebro, and C. Stoeckl, Phys. Plasmas **12**, 056307 (2005); D. Keller, T. J. B. Collins, J. A. Delettrez, P. W. McKenty, P. B. Radha, B. Whitney, and G. A. Moses, Bull. Am. Phys. Soc. **44**, 37 (1999).

19. J. A. Marozas, F. J. Marshall, R. S. Craxton, I. V. Igumenshchev, S. Skupsky, M. J. Bonino, T. J. B. Collins, R. Epstein, V. Yu. Glebov, D. Jacobs-Perkins, J. P. Knauer, R. L. McCrory, P. W. McKenty, D. D. Meyerhofer, S. G. Noyes, P. B. Radha, T. C. Sangster, W. Seka, and V. A. Smalyuk, Phys. Plasmas **13**, 056311 (2006).

20. B. I. Bennett *et al.*, Los Alamos National Laboratory, Los Alamos, NM, Report LA-7130 (1978).

21. S. X. Hu, V. A. Smalyuk, V. N. Goncharov, J. P. Knauer, P. B. Radha, I. V. Igumenshchev, J. A. Marozas, C. Stoeckl, B. Yaakobi, D. Shvarts, T. C. Sangster, P. W. McKenty, D. D. Meyerhofer, S. Skupsky, and R. L. McCrory, Phys. Rev. Lett. **100**, 185003 (2008).

22. R. Cauble *et al.*, Phys. Rev. Lett. **80**, 1248 (1998).

23. W. F. Huebner *et al.*, Los Alamos National Laboratory, Los Alamos, NM, Report LA-6760-M (1977).

24. R. C. Malone, R. L. McCrory, and R. L. Morse, Phys. Rev. Lett. **34**, 721 (1975).

25. S. P. Regan, R. Epstein, V. N. Goncharov, I. V. Igumenshchev, D. Li, P. B. Radha, H. Sawada, W. Seka, T. R. Boehly, J. A. Delettrez, O. V. Gotchev, J. P. Knauer, J. A. Marozas, F. J. Marshall, R. L. McCrory, P. W. McKenty, D. D. Meyerhofer, T. C. Sangster, D. Shvarts, S. Skupsky, V. A. Smalyuk, B. Yaakobi, and R. C. Mancini, Phys. Plasmas **14**, 056305 (2007).

26. T. R. Boehly, E. Vianello, J. E. Miller, R. S. Craxton, T. J. B. Collins, V. N. Goncharov, I. V. Igumenshchev, D. D. Meyerhofer, D. G. Hicks, P. M. Celliers, and G. W. Collins, Phys. Plasmas **13**, 056303 (2006).

27. A. Sunahara, J. A. Delettrez, C. Stoeckl, R. W. Short, and S. Skupsky, Phys. Rev. Lett. **91**, 095003 (2003).

28. J. Delettrez, Can. J. Phys. **64**, 932 (1986); J. Delettrez, R. Epstein, M. C. Richardson, P. A. Jaanimagi, and B. L. Henke, Phys. Rev. A **36**, 3926 (1987).

29. V. A. Smalyuk, S. X. Hu, V. N. Goncharov, D. D. Meyerhofer, T. C. Sangster, D. Shvarts, C. Stoeckl, B. Yaakobi, J. A. Frenje, and R. D. Petrasso, Phys. Rev. Lett. **101**, 025002 (2008); V. A. Smalyuk, S. X. Hu, V. N. Goncharov, D. D. Meyerhofer, T. C. Sangster, C. Stoeckl, and B. Yaakobi, Phys. Plasmas **15**, 082703 (2008).

30. T. R. Boehly, D. L. Brown, R. S. Craxton, R. L. Keck, J. P. Knauer, J. H. Kelly, T. J. Kessler, S. A. Kumpan, S. J. Loucks, S. A. Letzring, F. J. Marshall, R. L. McCrory, S. F. B. Morse, W. Seka, J. M. Soures, and C. P. Verdon, Opt. Commun. **133**, 495 (1997).

31. Y. Lin, T. J. Kessler, and G. N. Lawrence, Opt. Lett. **20**, 764 (1995).

32. T. R. Boehly, V. A. Smalyuk, D. D. Meyerhofer, J. P. Knauer, D. K. Bradley, R. S. Craxton, M. J. Guardalben, S. Skupsky, and T. J. Kessler, J. Appl. Phys. **85**, 3444 (1999).

33. S. Skupsky, R. W. Short, T. Kessler, R. S. Craxton, S. Letzring, and J. M. Soures, J. Appl. Phys. **66**, 3456 (1989); J. E. Rothenberg, J. Opt. Soc. Am. B **14**, 1664 (1997); S. P. Regan, J. A. Marozas, J. H. Kelly, T. R. Boehly, W. R. Donaldson, P. A. Jaanimagi, R. L. Keck, T. J. Kessler, D. D. Meyerhofer, W. Seka, S. Skupsky, and V. A. Smalyuk, J. Opt. Soc. Am. B **17**, 1483 (2000).

34. D. H. Edgell, W. Seka, R. S. Craxton, L. M. Elasky, D. R. Harding, R. L. Keck, and M. D. Wittman, Fusion Sci. Technol. **49**, 616 (2006).

35. T. C. Sangster, R. Betti, R. S. Craxton, J. A. Delettrez, D. H. Edgell, L. M. Elasky, V. Yu. Glebov, V. N. Goncharov, D. R. Harding, D. Jacobs-Perkins, R. Janezic, R. L. Keck, J. P. Knauer, S. J. Loucks, L. D. Lund, F. J. Marshall, R. L. McCrory, P. W. McKenty, D. D. Meyerhofer, P. B. Radha, S. P. Regan, W. Seka, W. T. Shmayda, S. Skupsky, V. A. Smalyuk, J. M. Soures, C. Stoeckl, B. Yaakobi, J. A. Frenje, C. K. Li, R. D. Petrasso, F. H. Séguin, J. D. Moody, J. A. Atherton, B. D. MacGowan, J. D. Kilkenny, T. P. Bernat, and D. S. Montgomery, Phys. Plasmas **14**, 058101 (2007).

36. V. A. Smalyuk, D. Shvarts, R. Betti, J. A. Delettrez, D. H. Edgell, V. Yu. Glebov, V. N. Goncharov, R. L. McCrory, D. D. Meyerhofer, P. B. Radha, S. P. Regan, T. C. Sangster, W. Seka, S. Skupsky, C. Stoeckl, B. Yaakobi, J. A. Frenje, C. K. Li, R. D. Petrasso, and F. H. Séguin, Phys. Rev. Lett. **100**, 185005 (2008).

37. D. H. Kalantar, M. H. Key, L. B. Da Silva, S. G. Glendinning, B. A. Remington, J. E. Rothenberg, F. Weber, S. V. Weber, E. Wolfrum, N. S. Kim, D. Neely, J. Zhang, J. S. Wark, A. Demir, J. Lin, R. Smith, G. J. Tallents, C. L. S. Lewis, A. MacPhee, J. Warwick, and J. P. Knauer, Phys. Plasmas **4**, 1985 (1997); M. Nakai *et al.*, Phys. Plasmas **9**, 1734 (2002); V. A. Smalyuk, O. Sadot, J. A. Delettrez, D. D. Meyerhofer, S. P. Regan, and T. C. Sangster, Phys. Rev. Lett. **95**, 215001 (2005); V. A.

Smalyuk, V. N. Goncharov, K. S. Anderson, R. Betti, R. S. Craxton, J. A. Delettrez, D. D. Meyerhofer, S. P. Regan, and T. C. Sangster, Phys. Plasmas **14**, 032702 (2007).

38. R. J. Taylor, A. L. Velikovich, J. P. Dahlburg, and J. H. Gardner, Phys. Rev. Lett. **79**, 1861 (1997); A. L. Velikovich *et al.*, Phys. Plasmas **5**, 1491 (1998); V. N. Goncharov, S. Skupsky, T. R. Boehly, J. P. Knauer, P. McKenty, V. A. Smalyuk, R. P. J. Town, O. V. Gotchev, R. Betti, and D. D. Meyerhofer, Phys. Plasmas **7**, 2062 (2000); P. B. Radha, V. N. Goncharov, T. J. B. Collins, J. A. Delettrez, Y. Elbaz, V. Yu. Glebov, R. L. Keck, D. E. Keller, J. P. Knauer, J. A. Marozas, F. J. Marshall, P. W. McKenty, D. D. Meyerhofer, S. P. Regan, T. C. Sangster, D. Shvarts, S. Skupsky, Y. Srebro, R. P. J. Town, and C. Stoeckl, Phys. Plasmas **12**, 032702 (2005).

Al 1*s*–2*p* Absorption Spectroscopy of Shock-Wave Heating and Compression in Laser-Driven Planar Foil

Introduction

A physical understanding of the shock-wave heating, radiative heating, and heating by energetic electrons in direct-drive inertial confinement fusion (ICF) is required to control the pressure in the main fuel layer.[1] A direct-drive hot-spot ignition ICF target consists of a spherical cryogenic fuel shell of deuterium and tritium surrounded by a thin plastic layer.[2] It is illuminated by symmetrically arranged intense laser beams having a temporal laser shape of a low-intensity foot followed by the gradual increase to a high-intensity main drive. The foot intensity launches a weak shock into the target, and the ramp of the laser intensity launches multiple shock waves with increasing strengths (compression wave) to isentropically compress the shell and implode the target to form a central hot spot with sufficient fuel areal density and temperature for ignition. The shell entropy or adiabat (α), defined as the ratio of the pressure in the fuel layer to the Fermi pressure, relates to the ICF target performance and the stabilization of Rayleigh–Taylor (RT) hydrodynamic instabilities.[3] The minimum energy required for ignition scales to $E_{ig} \sim \alpha^{1.88}$, while the ablation velocity that stabilizes the RT growth is proportional to $V_a \sim \alpha^{3/5}$ (Ref. 3). Therefore, a successful direct-drive ICF implosion design with energy gain creates an adiabat in the shell that strikes a balance between the laser-energy requirement and the target stability.

The shock wave launched by laser ablation is the dominant heating mechanism that sets the shell adiabat. After a coronal plasma is formed, the ablation process is driven by the energy flow via electron thermal transport from the critical density and the ablation surface (conduction zone). The incident laser can propagate into the plasma up to the critical density where the laser frequency is equal to the plasma frequency $\left(n_c = 1.1 \times 10^{21}/\lambda_{\mu m}^2\right)$. The laser energy that is absorbed near the critical-density surface is thermally transported by electrons to the ablation surface where the outer surface of the target is ablated and a shock wave is launched inward. The shell accelerates via the rocket effect. Modeling of electron thermal transport in the conduction zone is challenging because the steep temperature gradient in the plasma causes the classical Spitzer–Härm thermal conductivity[4] to break down. The

1-D hydrodynamics code *LILAC*[5] uses a flux-limited thermal transport model[6] to calculate the heat flux. It takes the minimum value of the heat flux calculated with either the classical Spitzer–Härm thermal conductivity ($q_{SH} = \kappa \nabla T_e$, where κ is the Spitzer conductivity)[4] or an artificially inhibited, free-streaming heat flux ($q_{FS} = n_e T_e v_{th}$, where v_{th} is the thermal electron velocity) [i.e., $q = \min (q_{SH}, f \bullet q_{FS})$, where f is the empirically determined flux limiter]. The typical value of f for simulations of direct-drive experiments is $0.04 < f < 0.1$. Although simulations with a constant flux limiter and experiments agree well, simulations with the same value of f do not consistently match to the all experimental data.[7] For instance, shock-velocity measurements in CH foils on OMEGA[8] agree with the simulation with $f = 0.06$, while the Richtmyer–Meshkov-growth measurements are in agreement with $f = 0.1$ (Ref. 9). A nonlocal electron-transport model developed by Goncharov[10] has shown consistent agreement between these two experiments and the simulations.[9] The nonlocal model acts like a time-dependent flux limiter and includes the transport of high-energy electrons in the tail of the electron-velocity distribution. X-ray radiation from the corona and suprathermal (energetic) electrons generated from two-plasmon-decay (TPD) instability[11] have been identified as possible target-heating sources.[12] These mechanisms could preheat the target before the shock-wave heating occurs. This preheating could increase the shell adiabat, reduce the compressibility of the fuel, and lead to a degradation of the ICF target performance.

The plasma conditions of a direct-drive, shock-wave–heated, compressed target are predicted to be in a warm-dense-matter (WDM)[13] regime where the degree of degeneracy and the electron–electron coupling parameter[14] are of the order of unity and the ion–ion coupling parameter exceeds 1 (Ref. 15). The electron–electron coupling parameter Γ_{ee} is defined as the ratio of Coulomb potential between free electrons to the average kinetic energy of the free electrons [$\Gamma_{ee} = e^2/dk_B T_e$, where $d = (3/4\pi n_e)^{1/3}$ is the average interparticle spacing]. The degree of degeneracy Θ is the ratio of the Fermi temperature to the electron temperature $\left(\Theta = T_F/T_e\right)$. Diagnostic techniques to probe plasma conditions in the WDM regime are limited

because the electron temperature of the plasma is too low for it to emit x rays and its density (above solid density) is too high to be probed with optical lasers for Thomson-scattering measurements.[16] These extreme conditions have been diagnosed with x-ray scattering[17,18] and x-ray absorption spectroscopy.[19,20] Spectrally resolved x-ray scattering has been demonstrated to probe these plasmas created with radiative heating[17,21] and direct-drive, shock-wave heating.[22] Scattering experiments require a relatively large amount of matter to scatter a sufficient number of incident x rays, limiting its spatial resolution. Although it requires a buried mid-Z tracer layer in the shock-wave–heated foil, x-ray absorption spectroscopy measurements can provide time-resolved local measurements. The temporal and spatial resolution of the time-resolved x-ray absorption spectroscopy is sufficient to resolve the shock-wave heating from heat-front penetration.

Local plasma conditions during shock-wave heating and compression, as well as the timing of heat-front penetration, are diagnosed with time-resolved Al 1s–2p absorption spectroscopy of planar plastic foils with a buried tracer layer of Al. Plastic foils are surrogates for cryogenic fuel layers. The objective of this article is to test electron-thermal-transport models in *LILAC* by comparing the predicted shock-wave–heated plasma conditions with measurements and to determine if additional heating due to energetic electrons or x-ray radiation from the coronal plasma is significant. The CH/Al/CH drive foil was directly irradiated with peak intensities of 10^{14} to 10^{15} W/cm^2 and probed with a point source of Sm backlighter irradiated with laser intensities of ~10^{16} W/cm^2 (Ref. 19). The measured Al 1s–2p spectra were analyzed with the atomic physics code *PrismSPECT*[23] to infer T_e and ρ in the buried Al layer, assuming uniform plasma conditions during the shock-wave heating and compression, and to determine when the heat front penetrated the Al layer. Strong shock waves and isen-

tropic compression were studied. This is the first observation of plasma conditions created with a compression wave.[24] The level of shock-wave heating and timing of heat-front penetration inferred from the experiments were compared with the post-processed *LILAC* simulations using the time-dependent atomic physics code *Spect3D*.[25] The shock-wave heating and heat-front penetration predicted by *LILAC* using $f = 0.06$ or the nonlocal model agree with experimental results for times when the shock is transiting the foil. At late times in the drive, observed discrepancies between the predicted and measured plasma conditions in the Al layer are attributed to reduced radiative heating due to lateral heat flow in the corona. Therefore, preheat due to energetic electrons near the end of the laser drive could not be resolved in this experiment.

The following sections of this article (1) describe the setup of the x-ray absorption spectroscopy experiment on OMEGA; (2) present 1-D *LILAC* simulations and absorption spectra calculated from the post-processed *LILAC* using *Spect3D*; (3) present measured streak spectra and analyses of Al 1s–2p absorption spectra with *PrismSPECT*; (4) discuss and present results for square and shaped laser drives; (5) briefly mention future work; and (6) summarize results.

Experiment

The experiment consists of three main components: a point-source Sm backlighter, a CH/Al/CH drive foil, and a Bragg crystal spectrometer, with a schematic (not drawn to scale) shown in Fig. 116.23. The relative alignment of these three components is crucial for the success of the experiment. A 50-μm planar CH foil with a 1- or 2-μm buried Al layer was irradiated with up to 21 OMEGA laser beams[8] that were smoothed with distributed phase plates (DPP's),[26] 1-THz, 2-D smoothing by spectral dispersion (SSD),[27] and polarization smoothing (PS).[28] The overlapped intensity was uniform
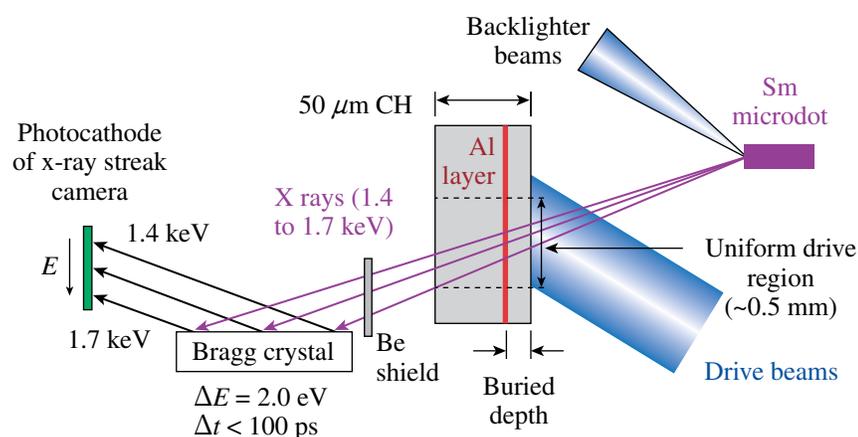

Figure 116.23
A schematic of the Al 1s–2p absorption spectroscopy experiment showing a point-source Sm backlighter, a plastic drive foil with a buried Al layer, a Be blast shield, and a Bragg crystal spectrometer coupled to an x-ray streak camera.

E16525aJRC

over a 0.5-mm-diam spot and peak intensities in the range of 10^{14} to 10^{15} W/cm^2. The overall thickness of the drive foil was chosen based on competing considerations of hydrodynamic instabilities and transmission of the target to ~1.5-keV x rays. Hydrodynamic instabilities due to target acceleration could compromise the spatial resolution of the measurement by mixing the Al layer with the CH.[29] Since the acceleration phase is delayed as the target thickness is increased, thicker targets are less susceptible to hydrodynamic instabilities than thinner ones; however, thicker targets attenuate the x-ray backlighter more than thinner ones. Choosing a drive foil with a 50-μm thickness was a good compromise. The buried depth of the layer was varied to probe the plasma conditions in different regions of the target. Al 1s–2p absorption spectroscopy of the drive foil was performed with a point-source Sm microdot backlighter irradiated with six tightly focused (~100-μm spot) laser beams having an overlapped intensity of ~10^{16} W/cm^2. This creates the well-defined Bragg reflection geometry necessary for this experiment. Source broadening can degrade the spectral resolution of the measurement. In contrast to the point-source Sm backlighter, the CH coronal plasma of the drive foil having an ~1-mm diameter does not create a well-defined Bragg reflection geometry. The coronal plasma emission contributes a background signal that degrades the contrast of the absorption features. The size of the Sm backlighter source was monitored with an x-ray framing camera and found to be less than 100 μm. The Sm M-shell emission provided a relatively smooth continuous spectrum in the 1.4- to 1.7-keV range, which overlaps the Al 1s–2p absorption features around 1.5 keV and probes the uniformly driven portion of the target (see Fig. 116.23).[20] The transmitted spectrum was recorded with an x-ray streak camera[30] outfitted with a Bragg crystal spectrometer that used a flat RbAP crystal[31] to disperse the spectrum onto a low-density (fluffy) CsI photocathode.[32] Each of the three components was positioned independently to ensure that the driven portion of the target was being probed with the Al 1s–2p absorption spectroscopy. Since alignment of the experiment was based on mechanical references, it was extremely reproducible. In a contrast measurement calibration using a Pb slit plate on the x-ray photocathode of the streaked x-ray spectrometer, a spectral resolution of 2.0 eV ($E/dE \sim 750$) was estimated from the sharpness of the measured step function.[33] The dynamic range of the x-ray streak camera was measured to be ~50. The relative time axis of the x-ray streak spectra was established using the UV timing fiducial on OMEGA. The x-ray streak camera has a uniform streak speed with an average speed of 115 ps/mm.[34] It uses a microchannel-plate (MCP)[35] image intensifier, and the streaked spectrum is recorded on Kodak TMAX 3200 film. The film is converted from optical density to a linear intensity

scale using the step wedge imprinted on each roll of film. The frequency-dependent transmission of a shocked Al layer was obtained from the ratio of transmitted Sm spectra through CH drive foils with and without an Al tracer layer.

One-Dimensional Simulations

Direct-drive plastic foils with a buried Al tracer layer were simulated with the 1-D hydrodynamics code *LILAC*[5] using either a flux-limited[6] or a nonlocal thermal transport model.[10] A flux-limited transport model calculates heat flux with either the classical Spitzer thermal conduction ($q_{SH} = \kappa \nabla T_e$) or a fraction of free-streaming flux ($q_{FS} = n_e T_e v_{th}$). The Spitzer transport model is valid only when the mean free path of electrons (λ_e) is much shorter than the electron-temperature scale length $\left[L_T = T_e \big/ (dT_e / dx)\right]$. When λ_e is comparable to L_T such as in a conduction zone with a steep temperature gradient, a flux-limited free-streaming flux ($q = f \bullet q_{FS}$) is used to model the heat flux. The flux limiter was either 0.06 (lower heat flux) or 0.1 (higher heat flux) in these simulations. A higher flux limiter in the model allows more energy to flow from the critical density to the ablation surface, producing a stronger shock wave compared to a flux limiter with a lower value. A nonlocal model developed by Goncharov[10] does not require a flux limiter to calculate heat flux. It solves a simplified Boltzmann equation using the Krook collision model and calculates heat flux using a convolution with the Spitzer heat flux and a delocalization kernel. This nonlocal treatment of the thermal transport includes time dependence of a reduced heat flux from the Spitzer model in plasmas with a steep temperature gradient and nonlocal preheat due to long-range electrons from the coronal plasma. Details of the nonlocal electron-transport model are described in Refs. 10 and 36. The radiation transport is modeled in *LILAC* with multigroup diffusion using the Los Alamos National Laboratory astrophysical tables[37] for the opacities. The equation of state (EOS) is modeled using the *SESAME* tables[38] for both CH and Al. The serial numbers of *SESAME* EOS used in *LILAC* for these experiments are 7593 for CH and 3720 for Al.

Figure 116.24 shows the 1-D spatial profiles of the electron temperature and mass density predicted by *LILAC* in a drive foil during shock-wave heating and heat-front penetration using a flux limiter of 0.06. As the shock wave launched by laser ablation propagates through the Al layer, it compresses the layer and creates uniform plasma conditions in the target behind the shock wave [Fig. 116.24(a)]. The predicted electron temperatures due to shock-wave heating in the experiment are in the range of 10 eV to 40 eV. The uniform plasma approximation is valid until the ablation surface reaches the Al. Once the

heat front penetrates into the Al layer, it creates strong gradients of T_e and ρ as shown in Fig. 116.24(b). The *LILAC* predictions are post-processed with *Spect3D*[25] to simulate the Al 1s–2p absorption spectral line shapes. Both *Spect3D* and the atomic physics code *PrismSPECT*[23] use level populations of detailed configuration accounting (DCA) to compute absorption spectra. The Stark-broadened line shapes are calculated using the Multi-Electron Radiator Line Shape (MERL) code.[39] MERL uses the adjustable parameter exponential approximation (APEX)[40] for ion microfield calculation and a quantum-mechanical relaxation approximation for electron broadening.[41] Figures 116.24(c) and 116.24(d) show Al absorption spectra post-processed *LILAC* profiles of uniform conditions and strong gradients shown in Figs. 116.24(a) and 116.24(b). The spatial profiles of the electron temperature and density from *LILAC* simulations are taken into account in calculating the Al absorption spectra. As shown in

Fig. 116.24(c), a few absorption features (F-like, O-like, and N-like features) are created in the uniform condition, while the strong T_e gradient in the Al creates a wide range of 1s–2p absorption features from F-like to Li-like in Fig. 116.24(d). Both synthetic and measured absorption spectra were analyzed with *PrismSPECT* to infer T_e and ρ during the shock-wave heating and to establish a range of upper and lower limits of T_e during heat-front penetration, as described in the next section.

Analysis of Measured Absorption Spectra

Figure 116.25 shows examples of the x-ray streak images recorded from CH targets (a) with and (b) without an Al layer (shot 48232 and 48233, respectively). The drive and backlighter beams were co-timed at $t = 0$ ns. The drive foil was irradiated with a shaped laser pulse having a foot intensity of 3×10^{14} W/cm^2 and a peak intensity of 8×10^{14} W/cm^2. The time
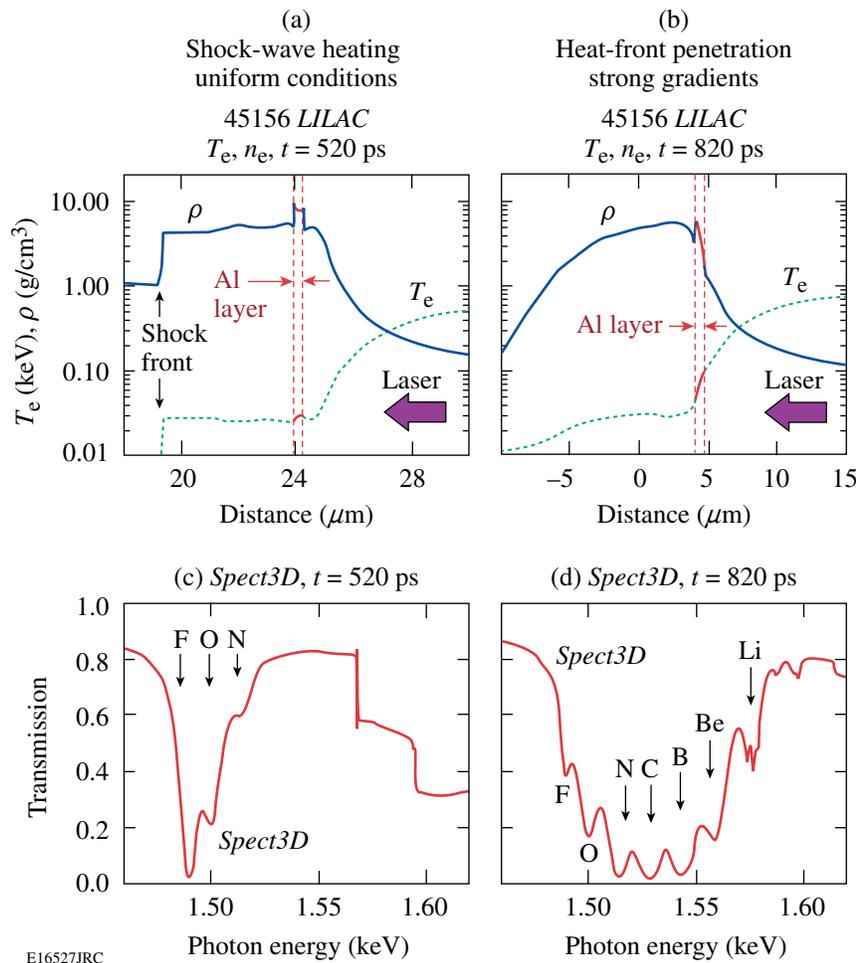

Figure 116.24
Simulated spatial profiles of electron temperature (dotted) and mass density (solid) during (a) shock-wave heating and (b) heat-front penetration. The Al absorption spectra simulated by post-processing *LILAC* with *Spect3D* are shown in (c) and (d). The prominent Al 1s–2p absorption features are identified.

axis of the streak images was established based on the average measured sweep speed (115 ps/mm) of the x-ray streak camera. The time $t = 0$ ns represents the time on the rising edge of the x-ray intensity when each measured streak reached 2% of the peak intensity. The absolute timing of the measured x-ray streak was established by synchronizing the measured onset of shock-wave heating in the buried Al layer with that predicted by the *LILAC* simulation. The experimental signature of shock-wave heating in the Al layer is a shift in the photon energy of the Al K edge at 1.56 keV. If the electron temperature is above

CH[10]Al[1]CH[40]

CH[50]

Figure 116.25
Measured streak images from (a) a CH foil with a buried Al layer and (b) a pure CH foil driven by the $\alpha = 3$ drive with a peak intensity of 8×10^{14} W/cm^2.

E16526JRC

~10 eV, the shifting K edge is accompanied by the appearance of the F-like Al 1s–2p absorption. In this experiment, the shifting K edge was used as a timing fiducial in the measured spectra for synchronization with the *LILAC* simulations. The difference in shock timings predicted by *LILAC* using $f = 0.06$ and $f = 0.1$ is less than the experimental temporal resolution of 60 ps. A good timing fiducial around $t = 0$ in the x-ray streak does not exist for most of the drive conditions studied because the initial x-ray emission from the coronal plasma of the drive foil is usually below detection threshold of the streaked x-ray spectrometer. The spectral dispersion for the streak data was calibrated using the K-shell emission from a point-source Mg backlighter. Shortly after the laser irradiates the drive foil, the shock heats and compresses the buried Al layer. As shown in Fig. 116.25(a), the experimental signature of the shock-wave heating is the appearance of the Al 1s–2p, F-like absorption feature and a blue shift in the Al K edge. When the heat front penetrates the Al layer, a wide range of the higher charge states up to the Be-like feature appears as seen after 1.0 ns. None of these features appear in Fig. 116.25(b) since the CH drive foil does not have an Al layer. The streak images were temporally binned and averaged over a temporal resolution of 60 ps. The apparent absorption-like feature observed at 1.58 keV is an artifact caused by a portion of the photocathode with low sensitivity for this particular shot.

An *in-situ* calibration of the x-ray streak spectrometer was performed to eliminate contamination of background light from the measured intensity signals. An examination of the measured cold Al K edge at 1.56 keV from an undriven CH/Al/CH foil showed a degradation in contrast compared to the modeled contrast of the cold Al K edge.[42] Since there is no coronal plasma emission from the undriven target and the dynamic range of the detector (~50) does not limit the measured contrast, the cause of the degraded contrast was attributed to secondary fluorescence that occurs when intense x rays interact with a Bragg crystal or device parts of the spectrometer.[43,44] The fluorescence level was assumed to be proportional to a fraction of peak x-ray intensity and to contribute a constant background across the x-ray photocathode. This background light must be subtracted from the measured signals to calculate the transmission of the CH/Al/CH drive foil. There are two sources of background light for a driven target shot: x-ray fluorescence of the Bragg crystal and x-ray emission from the coronal plasma of the drive foil. For a driven target shot, the level of background was estimated prior to the shock arrival at the buried Al layer based on corrections of the measured contrast at the K edge. After the shock propagated through the Al layer, the total background level from the coronal plasma and x-ray fluorescence was estimated based

on comparisons of measured Al 1s–2p absorption to *LILAC/Spect3D* predictions. A constant background was subtracted for both the absorption and the incident spectra.

The measured spectra with background corrections were fit with *PrismSPECT*[23] assuming uniform conditions for various combinations of T_e and ρ. *PrismSPECT* is a nonlocal-thermodynamic-equilibrium (NLTE), collisional-radiative code that calculates the absorption spectrum assuming a uniform slab plasma for a given T_e, ρ, and ΔL. The product of ρ and ΔL (areal density) for an Al layer is assumed to be conserved throughout the planar experiment. Figure 116.26 shows measured spectra fit with *PrismSPECT* at (a) t = 360 ps during shock-wave heating and (b) t = 1224 ps during heat-front penetration for shot 48232 shown in Fig. 116.25. The best fit to the measured spectra during shock-wave heating was determined based on a least-squares-fitting routine, which inferred T_e and ρ simultaneously. The plasma condition inferred from the fit in Fig. 116.26(a) is 22 eV ($\pm$2 eV) and 6 g/cm^3 ($\pm$3 g/cm^3). The ionization caused by shock-wave heating and compression can be obtained with different combinations of electron temperature and density; therefore, the inference of electron temperature is limited by the uncertainty in compressed density. The error estimates from the spectral-fitting routine were determined by doubling the minimum χ-squared value.[45] The uncertainty of the inference of T_e due to background subtraction has been considered by varying the estimated background levels for the drive intensity of 1×10^{14} W/cm^2 (Ref. 33). The uncertainties in the T_e and ρ inferences in this experiment were estimated to be ~10% and ~20% to 50%, respectively.

The experimental signature of heat-front penetration is the onset of absorption from a wide range of higher charge states of Al. The measured spectra at the time of the heat-front penetration were qualitatively compared to the product of two calculated spectra as shown in Fig. 116.26(b). Because of the strong gradients in T_e and ρ when heat front penetrates, the absorption spectrum cannot be fit by a calculated spectrum with a single T_e and ρ. Spatially resolved measurements of electron-temperature and density profiles in the conduction zone are challenging. To identify the time of heat-front penetration, it was assumed that the Al layer has two regions that determine a range of the plasma conditions: (1) a lower-density and higher-temperature region characteristic of matter ablated into the conduction zone, and (2) a higher-density and lower-temperature region characteristic of the shock-heated and compressed matter. The inferred ranges of T_e and ρ from the measured spectrum shown in Fig. 116.26(b) are 47 eV < T_e < 70 eV and 2.5 g/cm^3 < ρ < 3.5 g/cm^3. The initial areal density ($\rho\Delta L$) was equally divided into two parts. The total spectrum is a product of the calculated transmission spectra from each region and can be compared with the overall shape of measured spectra to roughly deter-

(a) Shock heating; t = 360 ps

T_e = 22 eV
ρ = 6.0 g/cm^3

(b) Heat-front penetration; t = 1223 ps

T_e = 47 eV
ρ = 3.5 g/cm^3
ΔL = 0.38 μm

T_e = 70 eV
ρ = 2.5 g/cm^3
ΔL = 0.53 μm

E17056JRC
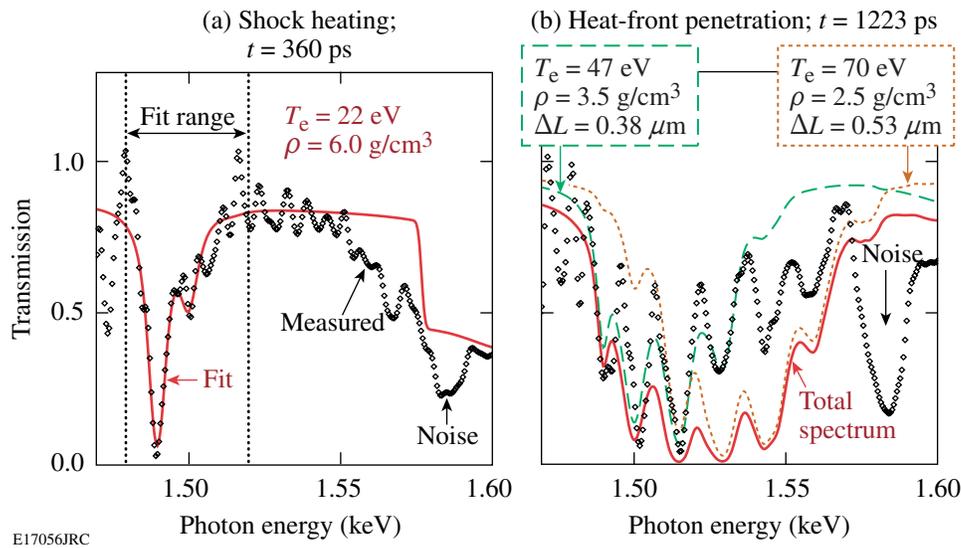
Figure 116.26

(a) A measured spectrum during shock-wave heating (diamond) and fit (thick black curve) obtained in a least-squares-fitting routine to infer T_e of 22 eV and ρ of 6.0 g/cm^3. (b) A measured spectrum during heat-front penetration and spectral analysis using two calculated spectra to determine upper and lower limits of T_e for shot 48232. The modeled spectra are calculated with T_e = 47 eV and ρ = 3.5 g/cm^3 for the lower limit (thin dashed black curve) and T_e = 70 eV and ρ = 2.5 g/cm^3 for the upper limit (thin dotted black curve). The total modeled spectrum (thick solid black curve) is obtained by the product of the two spectra.

mine the upper and lower limits of T_e. Although this is not a quantitative fitting, the procedure satisfies the experimental objective to identify the time of heat-front penetration by finding when a wide range of temperatures (greater than the shock-heated temperature) exists in the Al layer.

Results and Discussion

Time-resolved electron temperatures inferred from the experiments during shock-wave heating and heat-front penetration were compared with post-processed *LILAC* simulations using a nonlocal thermal-transport model,[10] as well as flux-limited models[5] with $f = 0.06$ and $f = 0.1$. The laser pulse shapes used in the experiment—1 ns square (1×10^{15} W/cm^2 and 4×10^{14} W/cm^2), 3 ns square (1×10^{14} W/cm^2), $\alpha = 3$ (peak intensities of 8×10^{14} W/cm^2 and 1×10^{15} W/cm^2), and $\alpha = 2$ pulses—are shown in Fig. 116.27. The target adiabat in this experiment is predicted to be $1.5 < \alpha < 5$. Square laser pulses launch a single shock wave through a CH/Al/CH foil, and a shell adiabat of 5 is created by the 1-ns square pulse with a peak intensity of 1×10^{15} W/cm^2. A shaped laser pulse drive with a low-intensity foot pulse that gradually increases to a constant high-intensity main drive produces a lower adiabat in the target. The adiabat of a CH/Al/CH foil driven with a shaped pulse is set by the foot intensity. The slowly rising intensity of the main drive produces a series of hydrodynamic waves as the drive pressure slowly increases (i.e., a compression wave).

Ideally, isentropic target compression is achieved with a shaped laser pulse. The observation of plasma conditions created with a weak shock and a compression wave in direct-drive planar targets is presented in this section. The laser pulse shape and the number of drive beams were selected to achieve a desired target adiabat α and peak intensity. The buried depth of the Al tracer layer was varied to probe different portions of the target.

1. Plasma Conditions Achieved with Square Laser Pulses

Peak laser intensities of 1×10^{14} W/cm^2, 4×10^{14} W/cm^2, and 1×10^{15} W/cm^2 were generated for the square laser pulses using either a 1-ns or 3-ns square laser pulse shape. *LILAC* predicted that the pressures of the single shock wave launched by these drive intensities were 15, 40, and 70 Mbar, respectively. The Sm backlighter target was irradiated with the same pulse shape as the CH/Al/CH drive foil. The absorption spectra recorded just after shock-wave heating are compared with the fitted line shapes in Fig. 116.28. The Al layer was buried at 10 μm for each of these shots. The lowest-intensity shot had an Al thickness of 2 μm and the other shots had an Al thickness of 1 μm. This improved the signal-to-noise ratio of the absorption spectra recorded with the lowest-intensity drive. As drive intensity is increased, the shock-wave pressure increases and higher Al charge states are observed in $1s$–$2p$ absorption. Only the F-like charge state was recorded for the lowest drive intensity (1×10^{14} W/cm^2), while F-like, O-like, N-like, and C-like charge states are observed for
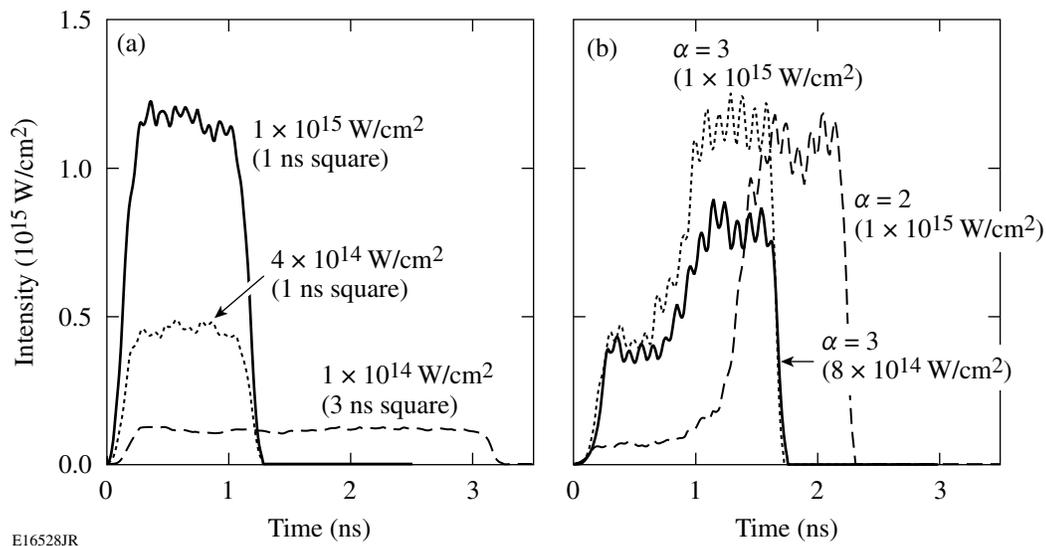
Figure 116.27

Laser pulse shapes for (a) square pulse shapes (1 ns square and 3 ns square) and (b) shaped pulse shapes ($\alpha = 3$ and $\alpha = 2$). The peak intensities for the square laser pulses are 1×10^{14} W/cm^2 (dashed), 4×10^{14} W/cm^2 (dotted), and 1×10^{15} W/cm^2 (solid). For the $\alpha = 3$ drives, the peak intensities are 8×10^{14} W/cm^2 (solid) and 1×10^{15} W/cm^2 (dotted); for the $\alpha = 2$ drives, peak intensity is 1×10^{15} W/cm^2 (dashed curve).
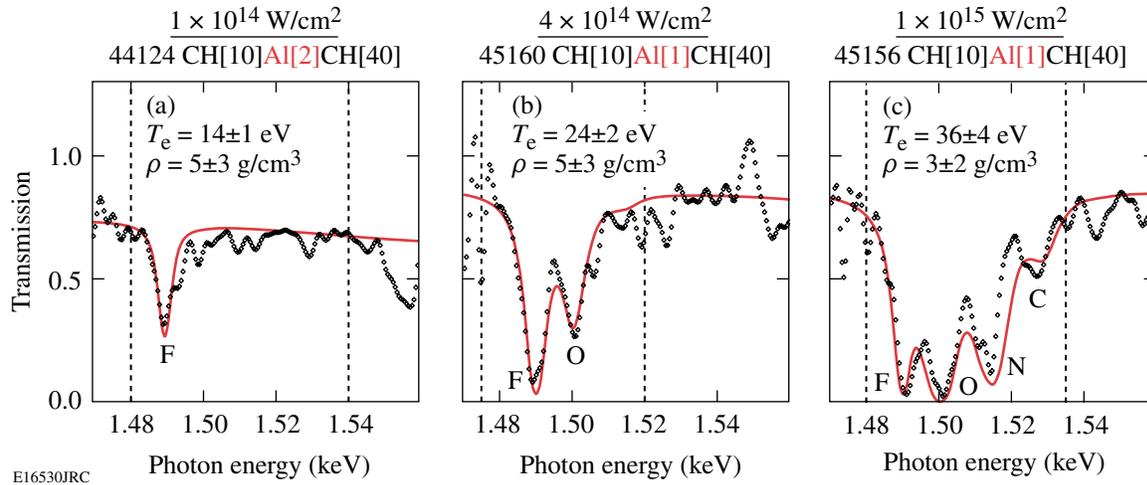
Figure 116.28
Measured Al absorption spectra (diamonds) and fits (solid curve) during shock heating and compression for the square laser pulse drives having intensities of (a) 1×10^{14} W/cm^2, (b) 4×10^{14} W/cm^2, and (c) 1×10^{15} W/cm^2. The buried depth of an Al layer was 10 μm for all three targets. The inferred condition from the fit is shown in each figure.

the highest drive intensity (1×10^{15} W/cm^2). Consequently, the inferred electron temperature increased from 14 eV to 24 eV to 36 eV (with 10% errors) as the drive intensities increased from 1×10^{14} W/cm^2 to 4×10^{14} W/cm^2 to 1×10^{15} W/cm^2. The mass densities inferred from measured spectra for the square laser pulses were ~5 g/cm^3 ($\pm$~2 g/cm^3).

Three buried depths—5, 10, and 15 μm—of the Al layer were studied for the 1-ns square pulse drive with a peak intensity of 1×10^{15} W/cm^2. A time history of the electron tempera-

ture in the Al layer inferred from the absorption spectroscopy for each of these buried depths is plotted in Fig. 116.29. The experimental data are presented with a single symbol during shock-wave heating and with a vertical line connecting two symbols that represent the range of upper and lower limits of inferred T_e after the heat front penetrates. Figure 116.29 also shows the *LILAC* simulations using $f = 0.06$, $f = 0.1$, and the nonlocal model. The post-processed electron temperatures were calculated as described in the previous section. The shock-breakout time from the rear surface of the target ($t = 0.72$ ns),
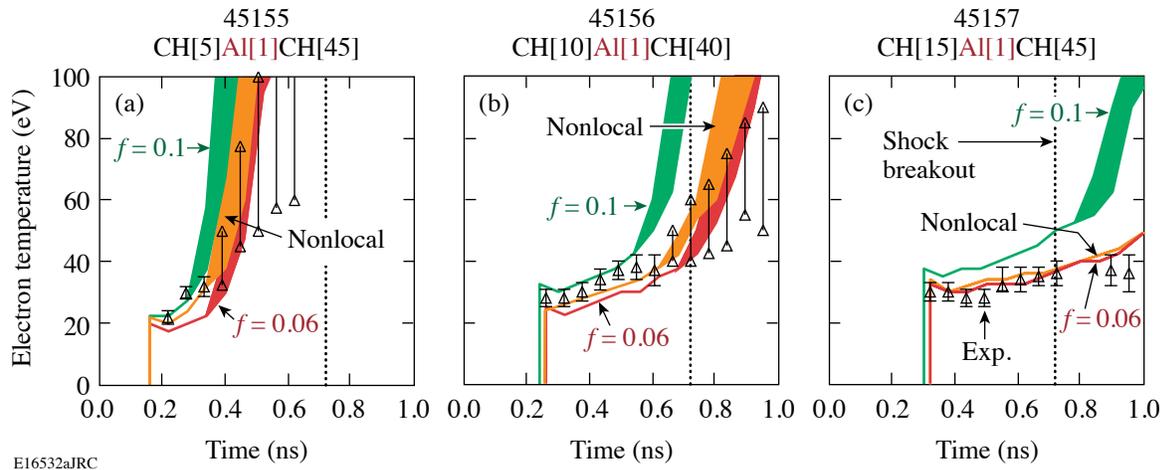
Figure 116.29
Time-resolved electron temperatures in the buried Al layer inferred from the experiment (triangles) for a 1-ns square laser drive with an intensity of 1×10^{15} W/cm^2 compared with the *LILAC* simulations using $f = 0.06$ (dark gray), $f = 0.1$ (black), and the nonlocal model (light gray). The depth of the buried Al layer was (a) 5 μm, (b) 10 μm, and (c) 15 μm. The shock-breakout time from the rear surface of the target ($t = 0.72$ ns), calculated with the nonlocal model for this drive intensity, is indicated by the dotted vertical line in each figure.

calculated with the nonlocal model for this drive intensity, is indicated by the dotted vertical line in each figure. The drive foil begins to accelerate and decompress after the shock wave breaks out of the rear surface of the target. An examination of Fig. 116.29 reveals the experimental delay in the onset of shock-wave heating as the buried depth of the Al layer is increased. A similar trend is observed for heat-front penetration. The simulation with the higher flux limiter predicts more shock-wave heating and an earlier penetration of the heat front than the other models. While the shock wave is transiting the drive foil (i.e., for times earlier than the shock-breakout time at $t = 0.72$ ns), the *LILAC* predictions using the nonlocal model agree with the experimental results for the 5-μm, 10-μm, and 15-μm buried depths. The nonlocal prediction is closer to the $f = 0.1$ prediction for the 5-μm buried depth, but it is similar to the $f = 0.06$ prediction for the deeper depths. This shows the time-dependent nature of the nonlocal heat transport.[46] For the 5-μm and 10-μm buried depths, the measured timing of heat-front penetration occurs before or around the predicted shock-breakout time. The prediction using the nonlocal model or $f = 0.06$ agrees with the measured heat-front penetration of the 5-μm and 10-μm buried depths. After the shock-wave breakout there are some minor discrepancies between the models and the measurements. The measured electron temperature for the 15-μm buried depth remains constant in time, while the prediction shows it should increase with time although it is close to the uncertainties. This discrepancy is likely due to the 2-D effects discussed in the next section. The $f = 0.1$ predictions do not agree with the measured heat-front penetration in the 10-μm- and 15-μm-buried-depth cases.

Two buried depths—5 and 10 μm—of the Al layer were studied for the 1-ns square pulse drive with a peak intensity of 4×10^{14} W/cm^2. A time history of the electron temperature in the Al layer inferred from the absorption spectroscopy for each of these buried depths is plotted in Fig. 116.30. The experimental data are presented with a single symbol during shock-wave heating and with a vertical line connecting two symbols that represent the range of upper and lower limits of inferred T_e after the heat front penetrates. Figure 116.30 also shows the *LILAC* simulations using $f = 0.06$, $f = 0.1$, and the nonlocal model. The post-processed electron temperatures were calculated as described in the previous section. The shock-breakout time from the target's rear surface ($t = 0.88$ ns) is calculated with the nonlocal model for this drive intensity and is indicated by the dotted vertical line in each figure. It occurs very late in the pulse. Timing of shock-wave heating and heat-front penetration on the buried depth is similar to Fig. 116.29. Nonlocal predictions are similar to those using
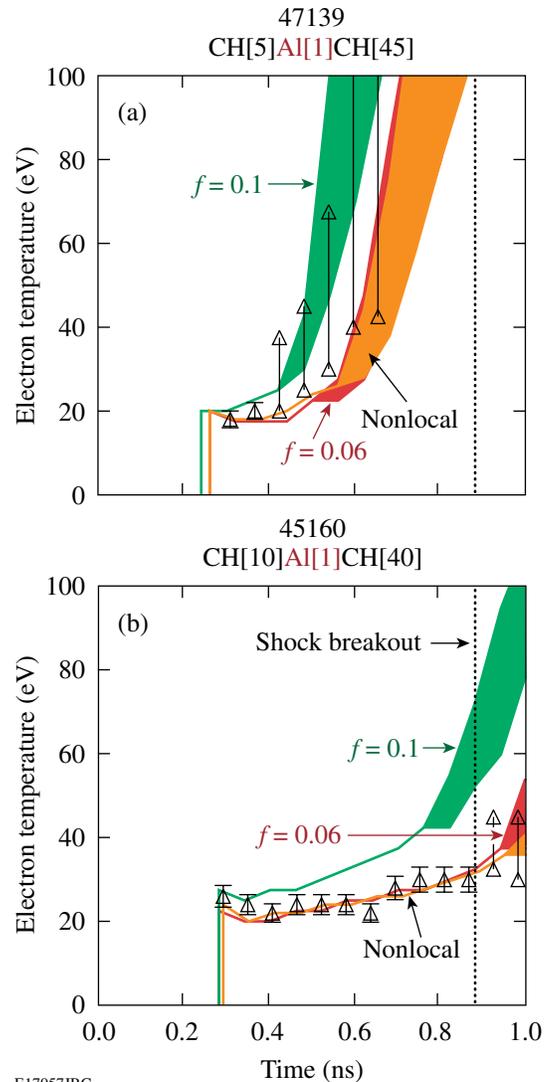

Figure 116.30
Time-resolved electron temperatures in the buried Al layer inferred from the experiment (triangles) for a 1-ns square laser drive with an intensity of 4×10^{14} W/cm^2 for (a) 5-μm and (b) 10-μm buried depths. The data are compared with *LILAC* simulations using $f = 0.06$ (dark gray), $f = 0.1$ (black) and the nonlocal model (light gray). The shock-breakout time from the rear target surface ($t = 0.88$ ns) is calculated with the nonlocal model for this drive intensity and is indicated by the dotted vertical line in each figure.

$f = 0.06$. The simulation with the higher flux limiter predicts more shock-wave heating and an earlier penetration of the heat front than the other models. *LILAC* predictions using the nonlocal model or the $f = 0.06$ model agree with the experimental results for the 10-μm buried depth throughout the pulse. The initial level of shock-wave heating agrees with all three models for the 5-μm buried depth; however, the $f = 0.1$ model is closest to the heat-front penetration for this shallow depth. The advanced penetration of the heat front for the 5-μm

buried depth may be caused by spatial nonuniformities in the laser irradiation profile.

Two buried depths—5 and 10 μm—of the Al layer were studied for the 3-ns square pulse drive with a peak intensity of 1×10^{14} W/cm^2. The 2-D SSD system was not employed for this experiment to match the drive conditions used for the spectrally resolved x-ray scattering measurement presented in Ref. 22. Smoothing by spectral dispersion smoothes the spatial nonuniformities in the laser irradiation profile on a time scale that is short compared to the hydrodynamic time scales. The disadvantage of turning off 2-D SSD is an increase in the level of the laser irradiation nonuniformities. A time history of the electron temperature in the Al layer inferred from the absorption spectroscopy for each of these buried depths is shown in Fig. 116.31. The experimental data are presented with a single symbol during shock-wave heating and with a vertical line connecting two symbols that represent the range of upper and lower limits of inferred T_e after the heat front penetrates. Figure 116.31 also shows the *LILAC* simulations using $f = 0.06$, $f = 0.1$, and the nonlocal model. The post-processed electron temperatures were calculated as described in the previous section. The shock-breakout time ($t = 1.37$ ns) calculated with the nonlocal model for this drive intensity is indicated by the dotted vertical line in each figure. All of the models have similar predictions. The *LILAC* predictions agree with the experimental results for the 10-μm buried depth throughout the pulse [Fig. 116.31(b)]. This drive appears to be insensitive to the reduction of radiative heating caused by 2-D effects. The coronal plasma temperature predicted with *LILAC* remains relatively low (~2 keV) after shock-breakout time; consequently, the level of radiative heating is negligible. The initial level of shock-wave heating for the 5-μm buried depth is below detection threshold until just after $t = 0.4$ ns. The heat-front penetration for this shallow depth is much earlier than the *LILAC* predictions [Fig. 116.31(a)] and is most likely caused by the higher level of laser irradiation nonuniformities with the 2-D SSD turned off. The 10-μm buried depth does not appear to be influenced by this effect. Plasma smoothing of the laser irradiation nonuniformities reduces nonuniformities in the drive at the ablation surface.[47] Since the heat-front penetration time is delayed as the buried depth is increased, the 10-μm buried depth has more time to form a coronal plasma. Consequently, the plasma smoothing is more effective and early heat-front penetration is not observed for the 10-μm case. Further investigation to understand the cause of the early heat-front penetration for this drive condition is needed. The measured level of shock-wave heating of ~13 eV for the 3-ns square pulse drive with a peak intensity of 1×10^{14} W/cm^2 is
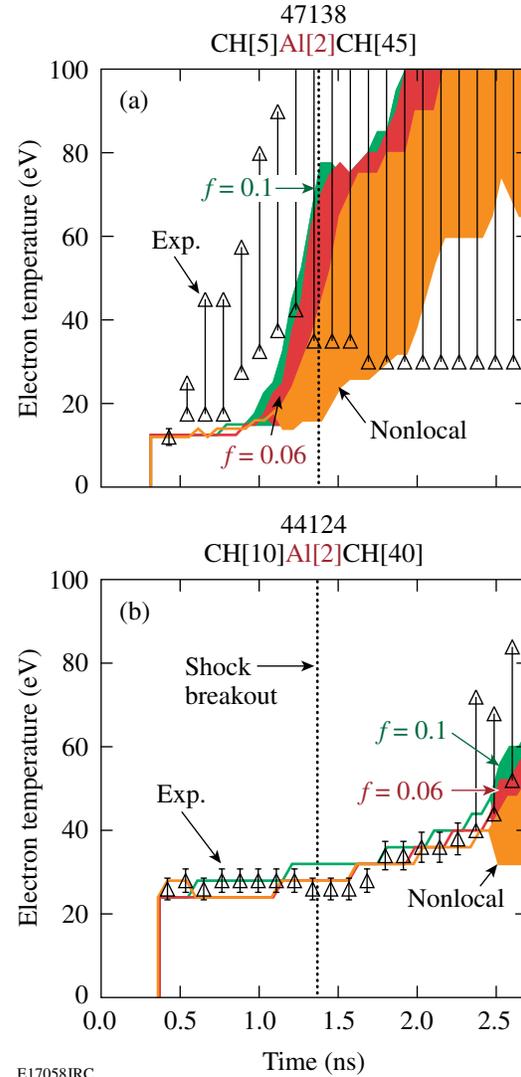
Figure 116.31
Comparisons of time-resolved electron temperatures in the buried Al layer inferred from the experiment (triangles) for a 3-ns square laser drive with an intensity of 1×10^{14} W/cm^2 with the *LILAC* simulations using $f = 0.06$ (dark gray), $f = 0.1$ (black), and the nonlocal model (light gray) for (a) 5-μm and (b) 10-μm buried depths. The shock-breakout time ($t = 1.37$ ns) calculated with the nonlocal model for this drive intensity is indicated by the dotted vertical line in each figure.

close to the simulations. This is consistent with the results from noncollective spectrally resolved x-ray scattering experiment on OMEGA using the same drive condition.[22]

2. Plasma Conditions Achieved with Shaped Laser Pulses

High target compression can be achieved in ICF using a shaped laser pulse drive that launches a weak shock wave dur-

ing the foot pulse through the target followed by a compression wave during the rise to the main pulse. Three shaped laser drives were investigated using the following laser pulse shapes: $\alpha = 3$ drive with a peak intensity of 8×10^{14} W/cm², $\alpha = 3$ drive with a peak intensity of 1×10^{15} W/cm², and $\alpha = 2$ drive with a peak intensity of 1×10^{15} W/cm² [see Fig. 116.27(b)]. To realize the full effect of the compression wave on the buried Al layer in a planar target, the shock-breakout time needs to occur after the shaped laser pulse reaches peak intensity. The buried depth should be deep enough to avoid heat-front penetration until after the compression wave has propagated through the Al layer. This section demonstrates how higher target compression can be achieved with a shaped laser drive compared to a square laser drive.

The peak intensity of the $\alpha = 3$ drive was increased from 8×10^{14} W/cm² to 1×10^{15} W/cm² to investigate preheat of the buried Al layer by energetic electrons. The higher peak intensities were achieved by increasing the number of drive beams from 15 to 21. In the TPD instability,[11] the incident laser decays into two electron-plasma waves (plasmons) around the quarter-critical-density region, producing energetic electrons.[48] Preheat caused by these electrons usually occurs during the main drive of the shaped laser pulse.[49] Hard x-ray signals produced by the energetic electrons have been observed to increase exponentially with the overlapped laser intensities in the range from 0.5 to 1.0×10^{15} W/cm² range (Ref. 49). This experiment was designed to increase the energetic electron production by varying the peak intensity of the $\alpha = 3$ drive. The hard

x-ray signals were monitored with the four-channel hard x-ray detector recording x-ray energies greater than 20 keV, 40 keV, 60 keV, and 80 keV (Ref. 49). In the absorption spectroscopy experiment, hard x rays can be produced in the coronal plasmas of the backlighter and the drive foil. Hard x-ray measurements of the drive foil alone are not available.

TPD is expected to occur for most of the drives under consideration based on the threshold parameter[48] given as $I_{14} \times L_{\mu m}/(230 \times T_c)$, where I_{14} is the incident laser intensity at the quarter-critical density in units of 10^{14} W/cm², $L_{\mu m}$ is the density scale length in microns at the quarter-critical density, and T_c is the electron temperature at the quarter critical density in keV. When the threshold parameter is above 1, laser light from the drive may decay into two electron-plasma waves around the quarter-critical density. The predicted density scale length in a planar target is longer than in a spherical implosion with the same overlapped laser intensity, resulting in more-energetic electron production. The higher-intensity $\alpha = 3$ drive exceeds a threshold parameter of 1 at $t = \sim 0.8$ ns, while the threshold parameter for the lower-intensity drive exceeds 1 around $t = 1.0$ ns.

Three buried depths—10, 15, and 20 μm—of the Al layer were studied for the $\alpha = 3$ drive with peak intensity of 8×10^{14} W/cm². A time history of the electron temperature in the Al layer inferred from the absorption spectroscopy for each of these buried depths is plotted in Fig. 116.32. The experimental data are presented with a single symbol during shock-wave
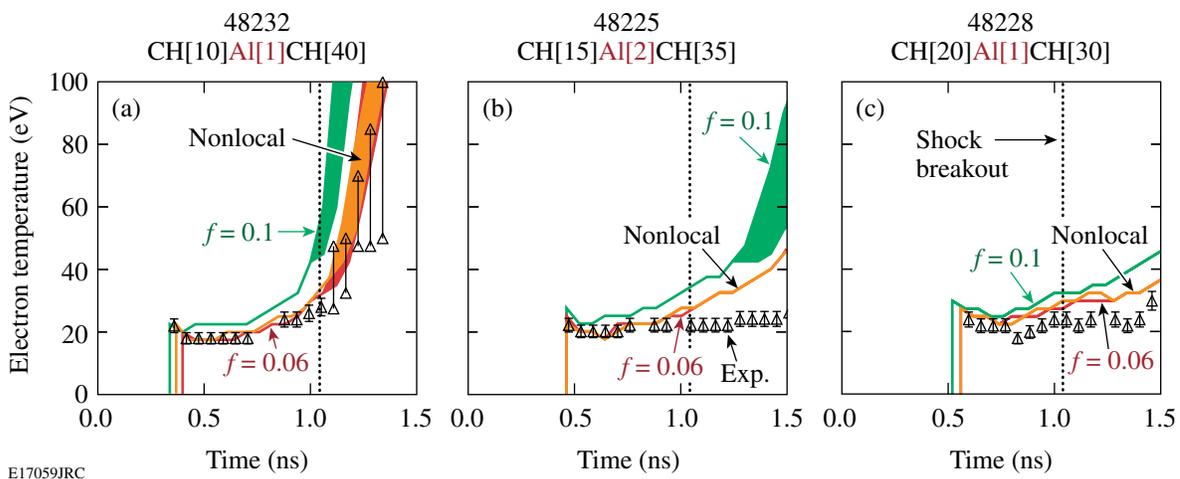
Figure 116.32
Comparisons of the measured electron temperatures in the buried Al layer (triangles) for the $\alpha = 3$ drive with peak intensity of 8×10^{14} W/cm² with the *LILAC* simulations using $f = 0.06$ (dark gray), $f = 0.1$ (black), and the nonlocal model (light gray) for (a) 10-μm, (b) 15-μm, and (c) 20-μm buried depths. The shock-breakout time ($t = 1.04$ ns) calculated with the nonlocal model for this drive intensity is indicated by the dotted vertical line in each figure.

heating and with a vertical line connecting two symbols that represent the range of upper and lower limits of inferred T_e after the heat front penetrates. Figure 116.32 shows the *LILAC* simulations using $f = 0.06$, $f = 0.1$, and the nonlocal model. The post-processed electron temperatures were calculated as described in the previous section. The timing of shock-wave heating and heat-front penetration is delayed as the buried depth of the Al layer is increased. The shock-breakout time ($t = 1.04$ ns) calculated with the nonlocal model for this drive intensity is indicated by the dotted vertical line in each figure. As can be seen in Fig. 116.27(b) the rising edge of the main drive of the $\alpha = 3$ drive with a peak intensity of 8×10^{14} W/cm^2 ends at 1.2 ns, which is after the shock-breakout time ($t = 1.04$ ns). While the shock wave is transiting the drive foil (i.e., for times earlier than the shock-breakout time at $t = 1.04$ ns), *LILAC* predictions using the nonlocal model or the $f = 0.06$ model agree with the experimental results for the 10-μm, 15-μm, and 20-μm buried depths. The $f = 0.1$ prediction is higher than the electron temperature inferred from the experiment during shock heating, and the predicted heat-front penetration occurs earlier than the experimental results. In Fig. 116.32(a) the *LILAC* predictions using the nonlocal model or the $f = 0.06$ model agree with the measured timing of heat-front penetration that occurs just after the shock-breakout time. The late time discrepancies observed in Figs. 116.32(b) and 116.32(c) are likely due to 2-D effects discussed below.

Similar plasma conditions were inferred in CH/Al/CH targets driven with the $\alpha = 3$ drive with a higher peak intensity of 1×10^{15} W/cm^2. The time-resolved electron temperatures in the Al layer inferred are presented in Fig. 116.33 for buried depths of 15 μm and 20 μm. The 10-μm depth was not studied with the higher drive intensity because the Al layer is ablated before peak compression is achieved in the target. The experimental data and the *LILAC* simulations in Fig. 116.33 are presented in a format similar to Fig. 116.32. The shock-breakout time ($t = 1.02$ ns) calculated by the nonlocal model for this drive intensity is indicated by the dotted vertical line in each figure. While the shock wave is transiting the drive foil (i.e., for times earlier than the shock-breakout time at $t = 1.02$ ns), *LILAC* predictions using the nonlocal model or the $f = 0.06$ model are close to the experimental results for the 15-μm and 20-μm buried depths. Prior to the shock-breakout time, however, the higher-intensity drive with the 20-μm buried depth shows slightly more discrepancy between simulation and measurement [see Fig. 116.33(b)] than the same case with the lower-intensity drive [see Fig. 116.32(c)]. The electron temperature predicted with $f = 0.1$ is higher than that measured for all times.
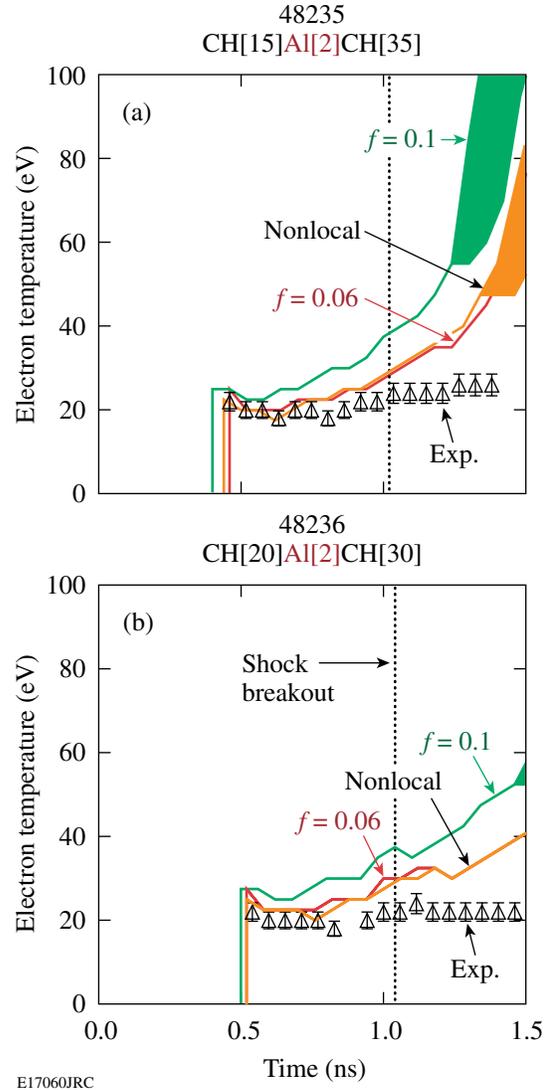

Figure 116.33
Comparisons of the measured electron temperatures in the buried Al layer (triangles) for the $\alpha = 3$ drive with a peak intensity of 1×10^{15} W/cm^2 with the *LILAC* simulations using $f = 0.06$ (dark gray), $f = 0.1$ (black), and the nonlocal model (light gray) for (a) 15-μm and (b) 20-μm buried depths. The shock-breakout time ($t = 1.02$ ns) calculated with the nonlocal model for this drive intensity is indicated by the dotted vertical line in each figure.

After the shock wave breaks out of the rear surface of the target, the *LILAC* simulation does not accurately predict the experimental results. This can be seen in Figs. 116.32(b), 116.32(c), 116.33(a), and 116.33(b). Although rising electron temperatures are predicted for 15- and 20-μm depths due to radiative heating, the experimental data remain at a constant value of ~20 eV. Measured and simulated absorption spectra are examined for times before and after the shock-wave breakout time in Fig. 116.34.

$\alpha = 3$ $(1 \times 10^{15}$ W/cm^2)
48236 CH[20]Al[2]CH[30]
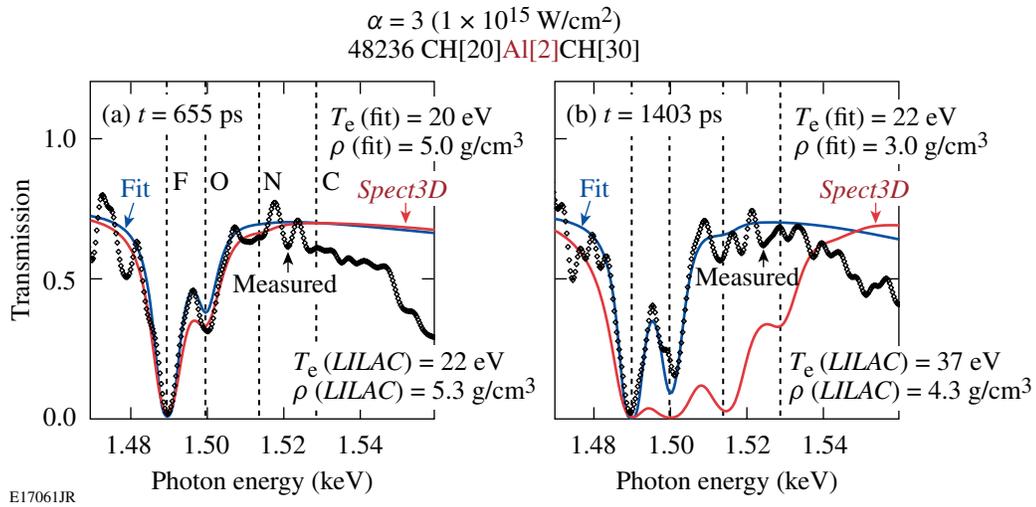
Figure 116.34
Measured (diamonds) and simulated Al absorption spectra before and after the shock-breakout time for the $\alpha = 3$ drives with a peak intensity of 1×10^{15} W/cm^2 (shot 48236). The fitted spectra assuming uniform conditions are shown in gray and *LILAC/Spect3D* spectra in black.

The simulated spectra are calculated using *LILAC* and *Spect3D* as described in **One-Dimensional Simulations** (p. 187). The spectral fitting calculated with *PrismSpect* is also shown. The simulated absorption spectrum is close to the measured one before shock breakout, for the $\alpha = 3$ drive with peak intensity of 1×10^{15} W/cm^2 [Fig. 116.34(a)], but after shock breakout, the measured spectrum has virtually no N-like and C-like absorption features indicating a lower electron temperature than the simulated one [Fig. 116.34(b)]. Quantitatively, the T_e and ρ inferred from the spectral fitting are 20 eV and 5.0 g/cm^3 and compare favorably to the predicted conditions of 22 eV and 5.3 g/cm^3. After the shock breakout, the T_e and ρ inferred from the spectral fitting are 22 eV and 3.0 g/cm$^3$ and are lower than the predicted conditions of 37 eV and 4.3 g/cm^3. If the mass density in the fits were increased, the peak of the O-like absorption is predicted to increase in transmission. Therefore, the differences between the simulated and measured spectra can be explained only by a lower measured electron temperature compared to the prediction.

The significant discrepancies between the measured and predicted plasma conditions in the Al layer after the shock wave breaks out of the rear surface of the foil are attributed to 2-D effects in the planar experimental geometry. The laser drive does not produce a planar shock front. The spatial-intensity profile of the laser drive incident on the target is defined by the single-beam super-Gaussian profile[50] and the overlap of beams having an angle of incidence up to ~60°. It causes the ablation front to have curvature and it creates a coronal plasma with lateral gradients in the temperature and density profiles, leading to a lateral heat flow. The resulting lower coronal plasma temperatures reduce the radiated x-ray power of the corona compared to the case with only radial gradients (i.e., the 1-D prediction). As a consequence the radiative heating of the Al layer is reduced. Nonuniform acceleration of the drive foil can bow the target, further enhancing the 2-D effects.

A 2-D hydrodynamic simulation *DRACO*[51] was performed to estimate the amount of lateral heat flow caused by 2-D effects. Figure 116.35 shows the simulated mass-density contours from *DRACO* for the $\alpha = 3$ with a peak intensity of 1×10^{15} W/cm^2 at (a) $t = 0$ ns, (b) $t = 0.6$ ns, and (c) $t = 1.4$ ns. The calculation was performed with cylindrical symmetry around the horizontal axis and the laser is incident on the target from the right. The vertical axis corresponds to the radial dimension of the target. The Al 1s–2p absorption spectroscopy probes radial locations up to 200 μm, which corresponds to the uniform drive region. The 2-D simulation includes the experimental configuration of beam angles and the single-beam intensity profiles. At $t = 0.6$ ns, curvature in the shock front and deformation of the shocked planar target are evident. The curvature becomes more pronounced at $t = 1.4$ ns. This creates 2-D gradients in the temperature and density profile in the coronal plasma, leading to a lateral heat flow. Figure 116.36 compares 1-D *LILAC* and 2-D *DRACO* simulations for (a) the maximum corona plasma temperatures and (b) the electron temperatures in the Al layer along with the measurement. The 2-D simulation shows a lower corona plasma temperature by ~1 keV and a lower electron temperature in the

buried Al layer by ~10 eV than the 1-D simulation at the 1-D predicted time of shock breakout ($t = 1.02$ ns). The minimum and maximum temperatures in the Al layer predicted by the 2-D simulation are closer to the experimental results than the 1-D prediction as shown in Fig. 116.36(b).

Preheat by energetic electrons is expected to be observed in the drive foil having the Al layer buried at 20 μm and driven with the $\alpha = 3$ drive with a peak intensity of 1×10^{15} W/cm^2 [Fig. 116.34(b)]. The 1-D *LILAC* prediction does not simulate the TPD instability; therefore, evidence of preheat would be an
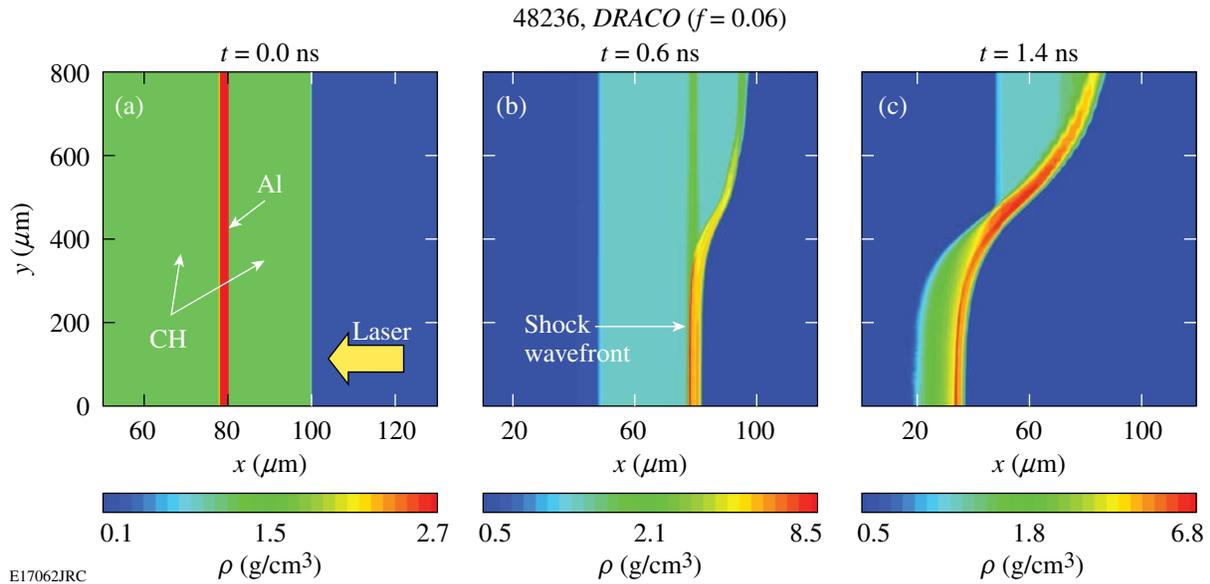
Figure 116.35
Mass-density contours of the driven CH/Al/CH planar target simulated with 2-D hydrodynamics code *DRACO* for shot 48236 at (a) $t = 0$, (b) $t = 0.6$ ns, and (c) $t = 1.4$ ns. The calculation was performed with cylindrical symmetry around the horizontal axis and the laser is incident on the target from the right.
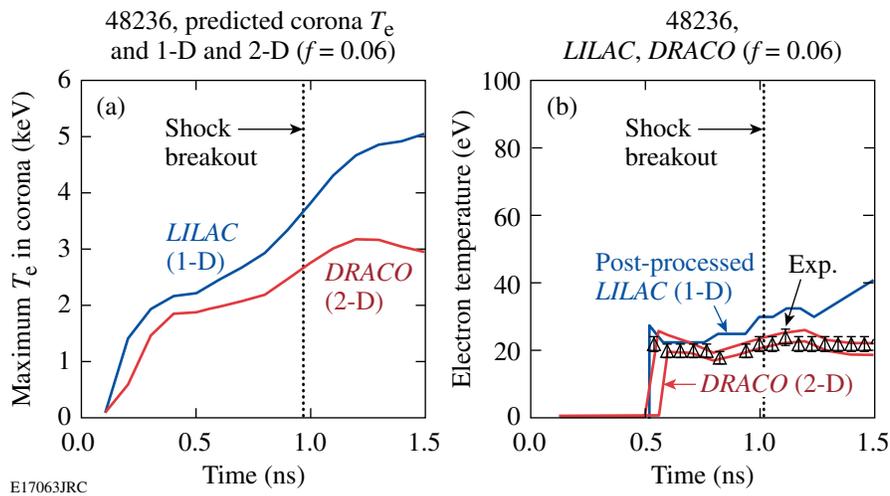
Figure 116.36
(a) A comparison of the maximum coronal plasma temperatures predicted by 1-D and 2-D simulations for a planar CH/Al/CH target driven with the $\alpha = 3$ drive with a peak intensity of 1×10^{15} W/cm^2. (b) Time histories of predicted electron temperatures in the Al layer using *LILAC* and *DRACO* compared with the experimental data for shot 48236. The 1-D, post-processed T_e is shown in black, and the minimum and maximum predicted temperatures with *DRACO* are shown in gray.

inferred electron temperature in the Al layer that is higher than 1-D prediction. The 2-D effects, however, cause the electron temperature in the Al layer to be less than the 1-D prediction after the shock-breakout time ($t = 1.04$ ns). The 2-D effects mask any signature of increased electron temperature due to preheat from energetic electrons late in the drive pulse. Therefore, the evidence for preheat due to energetic electrons is inconclusive in this experiment.

Three buried depths—10, 15, and 20 μm—of the Al layer were studied for the $\alpha = 2$ drive with a peak intensity of 1×10^{15} W/cm^2. A time history of the electron temperature in the Al layer inferred from the absorption spectroscopy for each of these buried depths is plotted in Fig. 116.37. The experimental data are presented with a single symbol during shock-wave heating and with a vertical line connecting two symbols that represent the range of upper and lower limits of inferred T_e after the heat front penetrates. The foot intensity of the $\alpha = 2$ drive pulse was ~4×10^{13} W/cm^2 [Fig. 116.27(b)], producing ~8-Mbar pressure in the Al layer. The shock-wave strength was too weak to increase the T_e in the Al layer enough to generate F-like Al; however, a shifting spectral position of the Al K edge was observed. The absolute timing of the measurement could be established with the shifting Al K edge. The observed Al 1s–2p absorption lines appeared as the electron temperature in the Al layer increased due to radiative heating during the main laser drive and the compression wave. Figure 116.37 shows *LILAC* simulations using $f = 0.06$, $f = 0.1$, and the nonlocal model. The post-processed electron temperatures were calculated as

described in the previous section. The timing of shock-wave heating and heat-front penetration are delayed as the buried depth of the Al layer is increased. The shock-breakout time ($t = 1.6$ ns) calculated with the nonlocal model for this drive intensity is indicated by the dotted vertical line in each figure. As can be seen in Fig. 116.27 the rising edge of the main drive of the $\alpha = 2$ drive with a peak intensity of 1×10^{15} W/cm^2 ends at 1.5 ns, which is just before the shock-breakout time ($t = 1.6$ ns). The predicted peak compression of the Al occurs at 1.5 ns. *LILAC* simulations with different thermal-transport models are close to each other for this drive condition. The *LILAC* simulations accurately model the experimental data before shock-breakout time of 1.6 ns. The inferred mass density from the Stark-broadened spectrum at the peak compression is 11 g/cm^3 (±5 g/cm^3). As described before, the 2-D effects lower the electron temperature in the coronal plasma, reducing the radiative heating of the Al. The 2-D predictions for 15- and 20-μm depths are in good agreement with the measurements before the shock-breakout times, but lower than the measurements by ~5 eV after the shock breakout. The TPD threshold parameter for the $\alpha = 2$ drive exceeds 1 at $t = 1.3$ ns, indicating that the difference between the measured and 2-D predicted temperatures in the Al at late time of the drive could be heating due to energetic electrons from the TPD instability. Further work is required to identify the level of preheating and to include the nonlocal electron thermal transport model in the 2-D simulations for a consistent explanation of the experimental results for the square and shaped laser drives after the shock-breakout time.
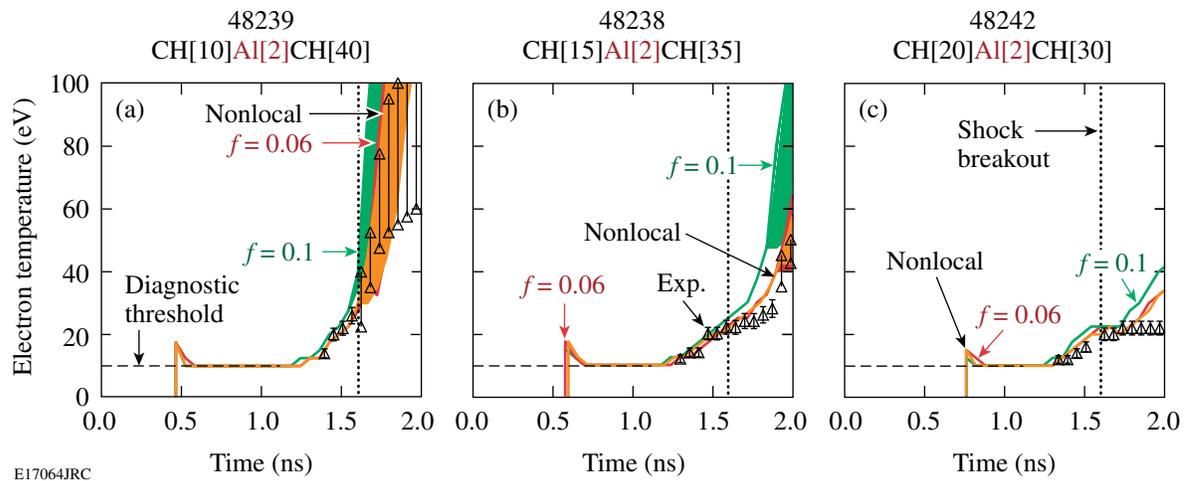
Figure 116.37

Comparisons of the measured electron temperatures in the buried Al layer for the $\alpha = 2$ drive with *LILAC* simulations using $f = 0.06$ (dark gray), $f = 0.1$ (black), and the nonlocal model (light gray) for (a) 10-μm, (b) 15-μm, and (c) 20-μm buried depths. The shock-breakout time ($t = 1.6$ ns) calculated with the nonlocal model for this drive intensity is indicated by the dotted vertical line in each figure.

Higher target compression has been achieved with a shaped laser pulse drive compared to a square laser pulse drive. A single shock wave launched by the square laser pulse creates a nearly constant mass density in the shocked Al. The shaped laser pulse launches a shock wave by the foot laser intensity and multiple hydrodynamic waves coalescing to form a compression wave with increasing pressure during the ramp of the laser intensity. A mass density of 11 g/cm^3 ($\pm$5 g/cm^3) and an electron temperature of 20 eV were created in the buried Al layer with the $\alpha = 2$ drive. Figure 116.38 presents a comparison of Al 1s–2p absorption spectra for two drive conditions. Both spectra have F-like and O-like absorption features. This is the first measurement of the plasma temperature and density in a direct-drive target created by multiple shock waves (i.e., a weak shock and a compression wave).[24] The best fit to each spectrum is represented by the black curve. The mass densities inferred are between 5 and 7 g/cm^3 for the 1-ns square laser pulse [Fig. 116.38(a)] and between 6 and 16 g/cm^3 for the $\alpha = 2$ drives [Fig. 116.38(b)]. The simulated spectra for the upper and lower limits of the mass density are plotted in Fig. 116.38. The predicted mass density of 14 g/cm^3 is consistent with the measured density of 11 g/cm^3 at the peak compression for the shaped laser pulse. The lower predicted mass density of 8 g/cm^3 for the 1-ns square pulse is consistent with the lower inferred value of 6 g/cm^3. Although the difference in the mass densities is just resolved with the Al 1s–2p absorption spectroscopy, this experiment shows that higher target compression is achieved with the shaped laser pulse drive compared with the square laser pulse drive.

Future Work and Application

The experimental results presented here demonstrate the diagnostic capability of measuring shock-wave heating and timing of heat-front penetration using the time-resolved Al 1s–2p absorption spectroscopy of a direct-drive, shock-wave–heated and compressed planar plastic foil for a wide range of drive conditions. Understanding electron thermal transport in a spherical geometry is the ultimate goal of this research. A spherical or hemispherical CH target with a buried Al layer will be investigated. Shifting to a spherical geometry eliminates the 2-D effects observed in the planar geometry and would pave the way for a conclusive preheat experiment. The CH foil is a surrogate for a deuterium–tritium (DT) cryogenic layer for a direct-drive ICF capsule. Measurements of plasma conditions in a shock-wave–heated planar DT or DD cryogenic layer with x-ray absorption spectroscopy will be a next step to understanding the shell condition of a laser-driven cryogenic ICF target. The target development will be challenging since a direct-drive, cryogenic deuterium planar experiment using x-ray absorption spectroscopy will require an Al foil in a liquid deuterium.

(a)
1 ns square (4×10^{14} W/cm^2)
$t = 0.35$ ns

T_e (*LILAC*) = 20 eV
ρ (*LILAC*) = 8 g/cm^3

$T_e = 24$ eV
$\rho = 6$ g/cm^3
$\rho = 7$ g/cm^3
$\rho = 5$ g/cm^3

(b)
$\alpha = 2$ (1×10^{15} W/cm^2)
$t = 1.47$ ns

T_e (*LILAC*) = 19 eV
ρ (*LILAC*) = 14 g/cm^3

$T_e = 20$ eV
$\rho = 11$ g/cm^3
$\rho = 16$ g/cm^3
$\rho = 6$ g/cm^3

E16535JRC
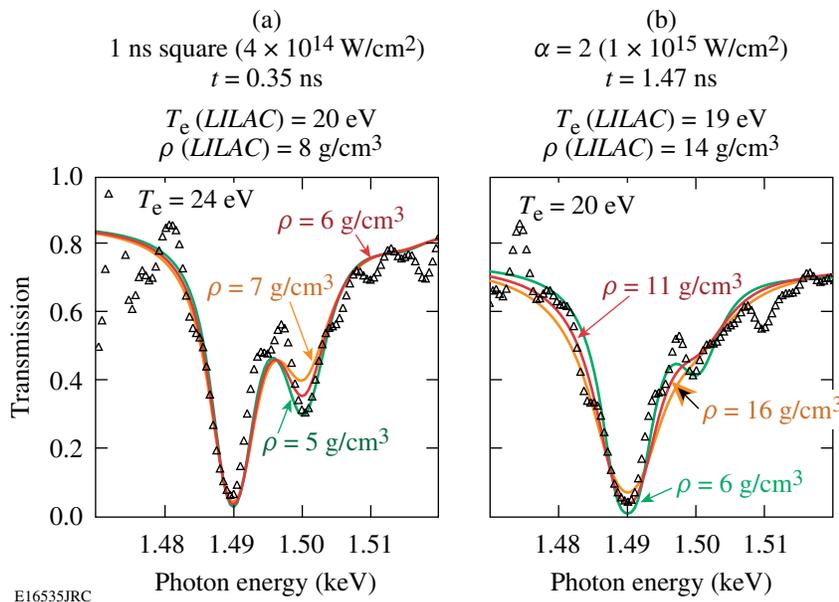
Figure 116.38
Spectral fits to the measured spectra for (a) a square laser pulse (4×10^{14} W/cm^2) taken at $t = 0.35$ ns and (b) shaped laser pulse ($\alpha = 2$ drive) taken at 1.47 ns. Inferred mass densities from fitting the Stark-broadened Al 1s–2p absorptions are between 5 g/cm^3 (light gray) and 7 g/cm^3 (dark gray) for the square laser pulse and between 6 g/cm^3 (light gray) and 16 g/cm^3 (dark gray) for the shaped laser pulse. The modeled spectra for the best fit are shown in black.

Conclusion

The plasma conditions of a direct-drive, shock-wave–heated and compressed planar target comprising warm dense matter[13] were diagnosed using time-resolved Al $1s$–$2p$ absorption spectroscopy. A 50-μm planar CH foil with a buried tracer layer of Al was irradiated with intensities of 10^{14} to 10^{15} W/cm^2, and ~1.5 keV x rays from a point-source Sm backlighter were transmitted through the drive foil. Local shell conditions of T_e and ρ during the shock-wave heating and heat-front penetration were inferred from the measured absorption spectra analyzed with *PrismSPECT*, assuming uniform conditions in the Al layer. The drive foil was simulated with the 1-D hydrodynamic code *LILAC* using flux-limited ($f = 0.1$ and $f = 0.06$) or a nonlocal thermal transport model. The experimental results showed that 1-D simulations using the nonlocal model or $f = 0.06$ accurately predict the timing of heat-front penetration and the level of shock-wave heating for square and shaped laser pulses while the shock transits the target. The accuracy of the electron temperatures inferred from the experiments was sufficient to distinguish between the two flux-limited hydrodynamics predictions. The predicted plasma conditions of a shocked Al layer using the nonlocal model were similar to the ones using $f = 0.06$ in this experiment. Significant discrepancies between measured and predicted shock-wave heating were observed at late times in the drive, which can be explained by reduced radiative heating due to lateral heat flow in the corona. An early burnthrough observed for 5-μm buried depth could be caused by high laser irradiation nonuniformity levels without laser-beam smoothing with 2-D SSD. Preheat experiments of the buried Al layer due to energetic electron production by the two-plasmon-decay instability were inconclusive since the 2-D effects masked any experimental signature of preheat.

REFERENCES

1. J. Nuckolls *et al.*, Nature **239**, 139 (1972); J. D. Lindl, R. L. McCrory, and E. M. Campbell, Phys. Today **45**, 32 (1992); R. L. McCrory, J. M. Soures, C. P. Verdon, F. J. Marshall, S. A. Letzring, S. Skupsky, T. J. Kessler, R. L. Kremens, J. P. Knauer, H. Kim, J. Delettrez, R. L. Keck, and D. K. Bradley, Nature **335**, 225 (1988); R. L. McCrory, S. P. Regan, S. J. Loucks, D. D. Meyerhofer, S. Skupsky, R. Betti, T. R. Boehly, R. S. Craxton, T. J. B. Collins, J. A. Delettrez, D. Edgell, R. Epstein, K. A. Fletcher, C. Freeman, J. A. Frenje, V. Yu. Glebov, V. N. Goncharov, D. R. Harding, I. V. Igumenshchev, R. L. Keck, J. D. Kilkenny, J. P. Knauer, C. K. Li, J. Marciante, J. A. Marozas, F. J. Marshall, A. V. Maximov, P. W. McKenty, J. Myatt, S. Padalino, R. D. Petrasso, P. B. Radha, T. C. Sangster, F. H. Séguin, W. Seka, V. A. Smalyuk, J. M. Soures, C. Stoeckl, B. Yaakobi, and J. D. Zuegel, Nucl. Fusion **45**, S283 (2005).

2. P. W. McKenty, V. N. Goncharov, R. P. J. Town, S. Skupsky, R. Betti, and R. L. McCrory, Phys. Plasmas **8**, 2315 (2001); P. W. McKenty, T. C. Sangster, M. Alexander, R. Betti, R. S. Craxton, J. A. Delettrez, L. Elasky, R. Epstein, A. Frank, V. Yu. Glebov, V. N. Goncharov, D. R. Harding, S. Jin, J. P. Knauer, R. L. Keck, S. J. Loucks, L. D. Lund, R. L. McCrory, F. J. Marshall, D. D. Meyerhofer, S. P. Regan, P. B. Radha, S. Roberts, W. Seka, S. Skupsky, V. A. Smalyuk, J. M. Soures, K. A. Thorp, M. Wozniak, J. A. Frenje, C. K. Li, R. D. Petrasso, F. H. Séguin, K. A. Fletcher, S. Padalino, C. Freeman, N. Izumi, J. A. Koch, R. A. Lerche, M. J. Moran, T. W. Phillips, G. J. Schmid, and C. Sorce, Phys. Plasmas **11**, 2790 (2004).

3. M. C. Herrmann, M. Tabak, and J. D. Lindl, Phys. Plasmas **8**, 2296 (2001); R. Betti, K. Anderson, V. N. Goncharov, R. L. McCrory, D. D. Meyerhofer, S. Skupsky, and R. P. J. Town, Phys. Plasmas **9**, 2277 (2002).

4. L. Spitzer, Jr. and R. Härm, Phys. Rev. **89**, 977 (1953).

5. J. Delettrez, R. Epstein, M. C. Richardson, P. A. Jaanimagi, and B. L. Henke, Phys. Rev. A **36**, 3926 (1987); J. Delettrez, Can. J. Phys. **64**, 932 (1986).

6. R. C. Malone, R. L. McCrory, and R. L. Morse, Phys. Rev. Lett. **34**, 721 (1975).

7. S. P. Regan, R. Epstein, V. N. Goncharov, I. V. Igumenshchev, D. Li, P. B. Radha, H. Sawada, W. Seka, T. R. Boehly, J. A. Delettrez, O. V. Gotchev, J. P. Knauer, J. A. Marozas, F. J. Marshall, R. L. McCrory, P. W. McKenty, D. D. Meyerhofer, T. C. Sangster, D. Shvarts, S. Skupsky, V. A. Smalyuk, B. Yaakobi, and R. C. Mancini, Phys. Plasmas **14**, 056305 (2007).

8. T. R. Boehly, D. L. Brown, R. S. Craxton, R. L. Keck, J. P. Knauer, J. H. Kelly, T. J. Kessler, S. A. Kumpan, S. J. Loucks, S. A. Letzring, F. J. Marshall, R. L. McCrory, S. F. B. Morse, W. Seka, J. M. Soures, and C. P. Verdon, Opt. Commun. **133**, 495 (1997).

9. O. Gotchev, V. N. Goncharov, J. P. Knauer, T. R. Boehly, T. J. B. Collins, R. Epstein, P. A. Jaanimagi, and D. D. Meyerhofer, Phys. Rev. Lett. **96**, 115005 (2006).

10. V. N. Goncharov, O. V. Gotchev, E. Vianello, T. R. Boehly, J. P. Knauer, P. W. McKenty, P. B. Radha, S. P. Regan, T. C. Sangster, S. Skupsky, V. A. Smalyuk, R. Betti, R. L. McCrory, D. D. Meyerhofer, and C. Cherfils-Clérouin, Phys. Plasmas **13**, 012702 (2006).

11. W. L. Kruer, *The Physics of Laser−Plasma Interactions*, Frontiers in Physics, Vol. 73, edited by D. Pines (Addison-Wesley, Redwood City, CA, 1988).

12. B. Yaakobi, C. Stoeckl, T. Boehly, D. D. Meyerhofer, and W. Seka, Phys. Plasmas **7**, 3714 (2000); B. Yaakobi, T. R. Boehly, T. C. Sangster, D. D. Meyerhofer, B. A. Remington, P. G. Allen, S. M. Pollaine, H. E. Lorenzana, K. T. Lorenz, and J. A. Hawreliak, Phys. Plasmas **15**, 062703 (2008).

13. National Research Council (U.S.) Committee on High Energy Density Plasma Physics, *Frontiers in High Energy Density Physics: The X-Games of Contemporary Science* (National Academies Press, Washington, DC, 2003), p. 84.

14. S. Ichimaru, Rev. Mod. Phys. **54**, 1017 (1982).

15. A. Ng *et al.*, Laser Part. Beams **23**, 527 (2005).

16. S. H. Glenzer *et al.*, Phys. Plasmas **6**, 2117 (1999).

17. O. L. Landen *et al.*, J. Quant. Spectrosc. Radiat. Transf. **71**, 465 (2001).

18. S. H. Glenzer *et al.*, Phys. Rev. Lett. **90**, 175002 (2003).

19. T. R. Boehly, J. A. Delettrez, J. P. Knauer, D. D. Meyerhofer, B. Yaakobi, R. P. J. Town, and D. Hoarty, Phys. Rev. Lett. **87**, 145003 (2001).

20. D. J. Hoarty *et al.*, J. Quant. Spectrosc. Radiat. Transf. **99**, 283 (2006).

21. S. H. Glenzer *et al.*, Phys. Rev. Lett. **98**, 065002 (2007).

22. H. Sawada, S. P. Regan, D. D. Meyerhofer, I. V. Igumenshchev, V. N. Goncharov, T. R. Boehly, R. Epstein, T. C. Sangster, V. A. Smalyuk, B. Yaakobi, G. Gregori, S. H. Glenzer, and O. L. Landen, Phys. Plasmas **14**, 122703 (2007).

23. Prism Computational Sciences, Inc., Madison, WI 53711.

24. S. P. Regan, H. Sawada, V. N. Goncharov, D. Li, P. B. Radha, R. Epstein, J. A. Delettrez, S. X. Hu, V. A. Smalyuk, B. Yaakobi, T. C. Sangster, D. D. Meyerhofer, R. L. McCrory, and R. C. Mancini, "Spectroscopic Observations of Fermi-Degenerate Aluminum Compressed and Heated to Four Times Solid Density and 20 eV," submitted to Physical Review Letters.

25. J. J. MacFarlane *et al.*, High Energy Density Phys. **3**, 181 (2006).

26. T. J. Kessler, Y. Lin, J. J. Armstrong, and B. Velazquez, in *Laser Coherence Control: Technology and Applications*, edited by H. T. Powell and T. J. Kessler (SPIE, Bellingham, WA, 1993), Vol. 1870, pp. 95−104.

27. S. Skupsky, R. W. Short, T. Kessler, R. S. Craxton, S. Letzring, and J. M. Soures, J. Appl. Phys. **66**, 3456 (1989).

28. T. R. Boehly, V. A. Smalyuk, D. D. Meyerhofer, J. P. Knauer, D. K. Bradley, R. S. Craxton, M. J. Guardalben, S. Skupsky, and T. J. Kessler, J. Appl. Phys. **85**, 3444 (1999).

29. J. P. Knauer, R. Betti, D. K. Bradley, T. R. Boehly, T. J. B. Collins, V. N. Goncharov, P. W. McKenty, D. D. Meyerhofer, V. A. Smalyuk, C. P. Verdon, S. G. Glendinning, D. H. Kalantar, and R. G. Watt, Phys. Plasmas **7**, 338 (2000).

30. D. H. Kalantar *et al.*, in *22nd International Congress on High-Speed Photography and Photonics*, edited by D. L. Paisley and A. M. Frank (SPIE, Bellingham, WA, 1997), Vol. 2869, pp. 680−685.

31. B. L. Henke, E. M. Gullikson, and J. C. Davis, At. Data Nucl. Data Tables **54**, 181 (1993).

32. B. L. Henke, J. P. Knauer, and K. Premaratne, J. Appl. Phys. **52**, 1509 (1981).

33. H. Sawada, "Experimental Investigation of a Direct-Drive Shock Wave Heated and Compressed Planar Target Relevant to ICF," Ph.D. thesis, University of Rochester, 2008.

34. S. P. Regan, Laboratory for Laser Energetics, private communication (2008).

35. D. K. Bradley, P. M. Bell, J. D. Kilkenny, R. Hanks, O. Landen, P. A. Jaanimagi, P. W. McKenty, and C. P. Verdon, Rev. Sci. Instrum. **63**, 4813 (1992).

36. V. N. Goncharov, T. C. Sangster, P. B. Radha, R. Betti, T. R. Boehly, T. J. B. Collins, R. S. Craxton, J. A. Delettrez, R. Epstein, V. Yu. Glebov, S. X. Hu, I. V. Igumenshchev, J. P. Knauer, S. J. Loucks, J. A. Marozas, F. J. Marshall, R. L. McCrory, P. W. McKenty, D. D. Meyerhofer, S. P. Regan, W. Seka, S. Skupsky, V. A. Smalyuk, J. M. Soures, C. Stoeckl, D. Shvarts, J. A. Frenje, R. D. Petrasso, C. K. Li, F. Séguin, W. Manheimer, and D. G. Colombant, Phys. Plasmas **15**, 056310 (2008).

37. W. F. Huebner *et al.*, Los Alamos National Laboratory, Los Alamos, NM, Report LA-6760-M (1977).

38. S. P. Lyon and J. D. Johnson, Los Alamos National Laboratory, Los Alamos, NM, Report LA-UR-92-3407 (1992).

39. R. C. Mancini *et al.*, Comput. Phys. Commun. **63**, 314 (1991).

40. C. A. Iglesias, J. L. Lebowitz, and D. MacGowan, Phys. Rev. A **28**, 1667 (1983).

41. D. A. Haynes, Jr., D. T. Garber, C. F. Hooper, Jr., R. C. Mancini, Y. T. Lee, D. K. Bradley, J. Delettrez, R. Epstein, and P. A. Jaanimagi, Phys. Rev. E **53**, 1042 (1996).

42. B. L. Henke, E. M. Gullikson, and J. C. Davis, At. Data Nucl. Data Tables **54**, 181 (1993).

43. P. A. Jaanimagi, Laboratory for Laser Energetics, private communication (2008).

44. C. I. Szabó, *et al.*, Radiat. Phys. Chem. **75**, 1824 (2006).

45. P. R. Bevington, *Data Reduction and Error Analysis for the Physical Sciences* (McGraw-Hill, New York, 1969), p. 53.

46. A. Sunahara, J. A. Delettrez, C. Stoeckl, R. W. Short, and S. Skupsky, Phys. Rev. Lett. **91**, 095003 (2003).

47. S. E. Bodner, J. Fusion Energy **1**, 221 (1981).

48. A. Simon, R. W. Short, E. A. Williams, and T. Dewandre, Phys. Fluids **26**, 3107 (1983).

49. C. Stoeckl, R. E. Bahr, B. Yaakobi, W. Seka, S. P. Regan, R. S. Craxton, J. A. Delettrez, R. W. Short, J. Myatt, A. V. Maximov, and H. Baldis, Phys. Rev. Lett. **90**, 235002 (2003).

50. S. P. Regan, J. A. Marozas, J. H. Kelly, T. R. Boehly, W. R. Donaldson, P. A. Jaanimagi, R. L. Keck, T. J. Kessler, D. D. Meyerhofer, W. Seka, S. Skupsky, and V. A. Smalyuk, J. Opt. Soc. Am. B **17**, 1483 (2000).

51. P. B. Radha, V. N. Goncharov, T. J. B. Collins, J. A. Delettrez, Y. Elbaz, V. Yu. Glebov, R. L. Keck, D. E. Keller, J. P. Knauer, J. A. Marozas, F. J. Marshall, P. W. McKenty, D. D. Meyerhofer, S. P. Regan, T. C. Sangster, D. Shvarts, S. Skupsky, Y. Srebro, R. P. J. Town, and C. Stoeckl, Phys. Plasmas **12**, 032702 (2005).

A Measurable Lawson Criterion and Hydro-Equivalent Curves for Inertial Confinement Fusion

Introduction

In inertial confinement fusion[1,2] (ICF), a shell of cryogenic deuterium and tritium ice is imploded at high velocities (~2 to 4×10^7 cm/s) and low entropy to achieve high central temperatures and high areal densities. The final fuel assembly consists of a relatively low density (~30 to 80 g/cc), high-temperature (~4 to 8 keV) core (the hot spot) surrounded by a dense (~300 to 1000 g/cc), cold (~100 eV) fuel layer (the compressed shell). The Lawson criterion[3] determining the onset of thermonuclear ignition is usually expressed through the product $p\tau > 10$ atm $\times$ s, where p is the plasma pressure in atm and τ is the energy confinement time in seconds. In magnetic fusion devices, both the pressure and confinement time are routinely measured, and the performance of each discharge can be assessed by comparing the value of $p\tau$ with respect to the ignition value (10 atm $\times$ s). In inertial confinement fusion, both p and τ cannot be directly measured and the performance of sub-ignited ICF implosions cannot be assessed with respect to the ignition condition. Often, the Lawson criterion is extended to ICF by simply restricting its application to the hot spot and by replacing p with the ideal gas equation of state $p = 2\rho_h T_h / m_i$ (ρ_h is the hot-spot mass density, T_h is the hot-spot temperature, and m_i is the DT average ion mass) and τ with the sound wave's traveling time through the hot spot, $t \sim R_h / C_s$ (here R_h is the hot-spot radius and C_s is the hot-spot sound speed, $C_s \sim \sqrt{T_h}$). This leads to the hot-spot–ignition condition $(\rho_h R_h)\sqrt{T_h} >$ const, where $\rho_h R_h$ is the hot-spot areal density. Such a simple derivation creates two problems: (a) the confinement time is incorrect since it neglects the inertial confinement of the surrounding cold shell, and (b) the hot-spot areal density cannot be experimentally measured.

A more accurate form of the hot-spot–ignition condition is given in Refs. 1 and 4–6 with the alpha heating balancing all the hot-spot power losses (thermal conduction and radiation losses). Our approach to ignition is somewhat different than the one in Ref. 4. First, our ignition model is dynamic since it includes both the compression and expansion phases of the shell motion. Second, our ignition condition is given in terms of the total areal density rather than the hot-spot areal den-

sity. Third, the ignition condition is viewed as an instability of both the pressure and the temperature rather than only the temperature. This causes the heat conduction losses to enter the ignition condition in a fundamentally different way. A more detailed discussion of this point is provided in the next section. It is important to emphasize that the presence of a cold, dense shell surrounding the hot spot significantly alters the onset of the thermonuclear instability (a similar point is made in Refs. 4, 7, and 8). Since the heat conductivity is negligible in the cold shell, most of the heat leaving the hot spot is recycled back into the hot spot in the form of internal energy and pdV work of the plasma ablated off the inner shell surface. Much of the radiation losses are also recycled back through ablation since the cold shell is opaque to the low-energy portion of the x-ray bremsstrahlung spectrum (only the high-energy x rays can penetrate the dense shell). As argued in Ref. 7, the heat conduction and, to some extent, the radiation losses do not appreciably change the hot-spot pressure (i.e., energy). Instead, those losses raise the density and lower the temperature while keeping $p \sim \rho T$ approximately constant. The fusion rate scales as $n^2 \langle \sigma v \rangle$, where n is the ion density and $\langle \sigma v \rangle$ is the fusion reactivity. Since $\langle \sigma v \rangle \sim T^{3-4}$ for $T < 6$ to 8 keV and $\langle \sigma v \rangle \sim T^2$ for 6 to $8 < T < 25$ keV, it follows that the alpha self-heating is degraded by heat conduction and radiation losses only at low temperatures less than 6 to 8 keV but unchanged at high temperatures $T > 6$ to 8 keV. This occurs because at high temperatures, the fusion rates depend only on the hot-spot pressure $(n^2 \langle \sigma v \rangle \sim p^2)$, which is independent of the heat losses. While these recycling effects (described in details in Ref. 7) improve the ignition threshold, the expansion losses, which are often not included in the ignition condition, causes a transfer of internal energy to kinetic energy and degrade the ignition conditions. Since hot-spot expansion occurs against the dense shell, the ignition conditions depend on the inertia of the dense shell. Furthermore, the hot spot's internal energy comes from the shell's kinetic energy, which is also used to assemble the shell's areal density. As shown in Ref. 9, there is a direct correlation between the hot spot areal density and the shell's areal density. Thus one can expect that the ICF Lawson criterion depends on the shell's areal density.

In this article, we derive a form of the Lawson criterion that can be directly measured in ICF implosions and includes the confinement of the surrounding cold shell. One can use such a new criterion to assess how far current and future sub-ignited ICF implosions are from achieving ignition. Such a new ignition criterion depends on the only two measurable quantities in the ICF fuel assembly: the total areal density and the hot-spot ion temperature. Note that the total areal density comes mostly from the cold shell surrounding the hot spot and is directly related to the inertial confinement time. In cryogenic implosions, the total areal density can be measured through charged-particle spectroscopy or x-ray radiography. The ion temperature is measured with neutron time-of-flight (nTOF) diagnostics.[10] For instance, recent cryogenic implosions[11] of D_2 targets on the OMEGA laser[12] have achieved a fusion burn–averaged areal density exceeding 200 mg/cm^2 and burn-averaged ion temperature of 2 keV—the highest performance for a cryogenic implosion to date. The burn-averaged areal density has been measured through the energy downshift of the proton spectrum from secondary $D + He^3$ reactions.[13] The ion temperature was measured through the nTOF diagnostics. The ion temperature used in the ignition condition is computed without alpha-particle heating. Thus, our measurable Lawson criterion is applicable to D_2 surrogate targets and DT sub-ignited implosions. Obviously, ignited DT implosions do not need a theoretical ignition criterion to verify that ignition conditions have been achieved.

We also show that hydro-equivalent curves can be represented on the same $\left(\rho R_{tot}, T_i^h\right)$ plane. Hydro-equivalent curves are defined as curves with constant adiabat and implosion velocity. Since the laser energy is the only parameter varying along such curves, they can be used to predict how a given implosion would perform when scaled up to a larger laser. For example, any implosion carried out on OMEGA[12] is represented by a point on a hydro-equivalent curve. By increasing the laser energy and keeping the implosion hydro-equivalent, the point on the diagram moves along the hydro-equivalent curve. If that point ends up within the ignition region for NIF-like energies, one can then conclude that particular OMEGA implosion scales to one-dimensional ignition on the National Ignition Facility (NIF).[14]

The remaining sections of this article (1) describe the analytic ignition model and derive its initial conditions; (2) derive the ignition condition from the analytic model and compare it with the results of one-dimensional hydrodynamic simulation; (3) discuss the assumptions concerning the alpha-particle confinement and compare with previous forms of ignition con-

dition; and (4) derive the hydro-equivalent curves and discuss them in the conclusions.

Dynamic Model of Thermonuclear Ignition

The dynamic model described in this section includes standard energy losses and sources (heat conduction, radiation losses, alpha heating) as well as compression and expansion dynamics of a hot spot surrounded by a dense shell. The model describes the assembly phase of the hot spot up to ignition. It does not include the propagation of the burn wave or the disassembly of the ignited fuel. As such, energy gains are not calculated and the focus is restricted to the onset of thermonuclear instability in the hot spot (i.e., ignition).

In the derivation of ignition conditions, the hydrodynamic model of Refs. 7 and 8 is closely followed. During assembly of the hot spot, its temperature is high and the flow velocity is less than the hot spot's sound speed. Thus, the subsonic model of Refs. 7 and 8 is adopted and the kinetic energy with respect to the internal energy inside the hot spot is neglected. It is assumed that most of the alpha particles generated from the fusion reactions deposit their energy into the hot spot, requiring that the size of the hot spot exceeds the alpha particle's mean free path. This condition depends on the hot spot's areal density and temperature and is verified *a posteriori*. Energy losses in the hot spot include heat conduction and bremsstrahlung radiation. Conservation of the hot spot's energy including the *pdV* work of the shell, the alpha-particle heating, and the conduction and radiation energy losses, can be written in the following simple form:

$$\frac{\partial}{\partial t}\left(\frac{p}{\gamma-1}\right) + \nabla \times \left[\vec{u}\left(\frac{\gamma p}{\gamma-1}\right)\right] = \nabla \times \kappa(T) \nabla T$$
$$+ \frac{\theta\rho^2}{4m_i^2}\langle\sigma v\rangle\varepsilon_\alpha - \nabla \cdot \vec{F}, \quad (1)$$

where $\rho(r,t)$, $p(r,t)$, $\vec{u}(r,t)$ are the hot-spot density, pressure, and velocity, respectively. Here γ is the ratio of specific heats or adiabatic index ($\gamma = 5/3$) and $\kappa(T) = \kappa_0 T^\nu$ is the Spitzer thermal conductivity with $\nu = 5/2$. The second term on the right-hand side of Eq. (1) represents the alpha particle's energy deposition, with θ being the absorbed alpha-particle fraction depending on the hot spot's areal density and temperature, m_i the ion mass for DT, $\varepsilon_\alpha = 3.5$ MeV the alpha-particle energy from DT reactions, and $\langle\sigma v\rangle$ the fusion reaction rate as a function of the ion temperature T. The last term is the bremsstrahlung radiation. The radiation flux $\vec{F}$ is the first moment of the radiation field over angle[15] integrated over all frequencies. The radiation flux $\vec{F}$ depends on

both the bremsstrahlung radiation and absorption processes. The bremsstrahlung emission[1,16] for the hot-spot plasma is expressed in terms of its pressure and temperature as $j = C_1 p^2 T^{-3/2}$, where $C_1 \approx 3.88 \times 10^{-29} Z^3/(1 + Z)^2$ in m $\times$ J$^{5/2}$ $\times$ s^{-1} $\times$ N^{-2}, pressure p in N/m^2, temperature T in J, and j in W/m^3.

Inside the hot spot, the temperature is high and the plasma is optically thin. At the interface of the hot spot and the cold shell, the temperature drops significantly and much of the radiation energy escaping the hot spot is absorbed near the inner shell surface. The mean free path (l) of photons[1,16] with energy $h\nu$ in a DT plasma is

$$l \approx 2.25 \times 10^4 \frac{\sqrt{T} (h\nu)^3}{\rho^2}, \qquad (2)$$

where l is in μm, ρ is the plasma density in g/cm^3, T is the plasma temperature in keV, and $h\nu$ is in keV. Consider the free–free emission in a marginal's ignited hot spot of typical radius ~50 μm, temperature 5 keV, and density ~50 g/cm^3. Most of the radiation energy is carried by photons with energy below 5 keV. According to Eq. (2), the mean free path of 5-keV photons ($l \sim$ 2500 μm) is much longer than the size of the hot spot. Therefore, typical hot spots are transparent to bremsstrahlung radiation. On the contrary, a 5-keV photon has a very short mean free path in the cold shell surrounding the hot spot. For typical compressed shell densities of ~600 g/cm^3 and temperatures of ~200 eV, the mean free path of a 5-keV photon is only 3.5 μm, much shorter than the typical dense shell thickness of 50 μm. This shows that in the fuel assembly of typical ICF implosions, the hot spot is optically thin and the opacity increases sharply near the shell's inner surface, resulting in a narrow absorption zone with strong attenuation at the hot spot/shell interface.

For typical ICF plasmas near stagnation, the hot-spot temperature is high enough that its sound speed exceeds the flow velocity. The fuel assembly develops an isobaric configuration,[7,8,17] and the hot spot has a flat pressure profile with $p \approx p(t)$. The temperature of the high-density shell is much less than that of the low-density hot spot. By neglecting the radiation energy, a self-similar solution for the hot-spot temperature[7] is obtained as $T = T_0 \hat{T}(\hat{r})$, where T_0 is the central temperature in the hot spot and $\hat{r}$ is the radius r normalized to the hot-spot radius R_h as $\hat{r} = r/R_h$,

$$\hat{T} \approx (1 - \hat{r}^2)^{2/5}/(1 - 0.15\hat{r}^2). $$

This profile indicates $T(\hat{r} = 1) \to 0$ at the boundary between the hot spot and the shell. The radiation flux reaching the hot-spot boundary is

$$F(R_h) = \int_0^{R_h} jr^2 \, \mathrm{d}r = C_1 p^2 T_0^{-3/2} R_h^3 \int_0^1 \hat{T}^{-3/2} \hat{r}^2 \, \mathrm{d}\hat{r}. $$

This radiation flux is absorbed and recycled back into the hot spot with the ablated material at the shell's inner surface. As the heat conduction losses are also recycled back into the hot spot via the ablated shell material, both effects alter the hot-spot temperature's evolution without appreciably changing the pressure.

After integrating Eq. (1) from 0 to the hot-spot radius $R_h(t)$, the heat conduction and radiation terms vanish since, as stated above, most of the heat and radiation fluxes are absorbed near the shell's inner surface; thus, the volume integral of the energy in Eq. (1) yields

$$\frac{1}{2}\dot{p}R_h^3 + \frac{5}{2}pR_h^2 u(R_h, t) = \frac{p^2 R_h^3}{(1 + Z)^2} \int_0^1 \hat{r}^2 \frac{\theta \varepsilon_\alpha \langle \sigma v \rangle}{4T^2} \mathrm{d}\hat{r}, \quad (3)$$

where $\dot{p}$ is the time derivative of the pressure and $u(R_h, t)$ is the flow velocity at the shell's inner surface. The shell material is ablated into the hot spot as a result of the heat and radiation energy deposited at the shell's inner surface. The flow velocity resulting from the combination of the inner surface motion and the ablative flow is

$$u(R_h, t) = \dot{R}_h - V_a, \qquad (4)$$

where V_a is the ablation velocity and $\dot{R}_h$ scales with the implosion velocity. Since $V_a \ll \dot{R}_h$, the ablation velocity can be neglected and Eq. (3) can be rewritten as

$$\frac{\mathrm{d}}{\mathrm{d}t}(pR_h^3) + 2pR_h^2 \dot{R}_h = \frac{2p^2 R_h^3}{(1 - Z)^2} f(T). \qquad (5)$$

Notice that pR_h^3 is proportional to the total internal energy of the hot spot and $pR_h^2 \dot{R}_h$ to the pdV work. The function $f(T)$, defined as $f(T) \equiv (\theta \varepsilon_\alpha / 4) \int_0^1 \hat{r}^2 (\langle \sigma v \rangle / T^2) \mathrm{d}\hat{r}$ represents the alpha-particle heating with the fusion reactivity being a function of the temperature T. Observe that $f(T)$ is constant if $\langle \sigma v \rangle$ is approximated with a quadratic power-law dependence on the temperature.

Some of the points made here about the recycling of the heat-conduction losses into the hot spot were also highlighted in Refs. 7, 8, and 17. In Ref. 17, it was also argued that a similar effect applies to the alpha particles leaving the hot spot. That is, the alpha particles leaving the hot spot are efficiently stopped by the dense shell within a narrow layer, thus causing the dense shell material to ablate into the hot spot. The ablated material would recycle the alpha particle's energy back into the hot spot in the form of internal energy of the ablated material. As argued

in Ref. 17, similarly to the heat conduction, alpha-particle losses do not lead to a lower hot-spot energy (i.e., pressure) but only to a lower temperature. In this optimistic scenario, the parameter θ in Eq. (1) would be close to unity since all the alpha-particle energy is retained within the hot spot. In our model, we set $\theta \approx 1$ and verify *a posteriori* whether or not the hot spot's areal density is large enough to confine most of the alphas (see the **Alpha-Particle Confinement** section, p. 213).

To simplify the analysis, we use a simple numerical fit of $f(T)$ as a power of the temperature $f(T) = \left(\varepsilon_\alpha T_*^\sigma / 4c_k^2 + \sigma \right) C_0 \hat{T}^\sigma$ after integration over the hot-spot volume, where $c_k = 1.6 \times 10^{-16}$ J/keV, $\varepsilon_\alpha = 5.6 \times 10^{-13}$ J, $C_0 \approx 2.6 \times 10^{-26}$ m^3 × keV^{-3} × s^{-1} for $\sigma = 1$ and T_* in J is defined later in Eq. (8). A comparison between the numerical fit and the accurate values of the fusion-reaction rate from Ref. 18 is shown in Fig. 116.39 for temperatures in the range of 3 to 8 keV. It is important to notice that the fusion reactivity follows a T^3 power law for temperatures $3 < T < 8$ keV and a T^2 power law for $8 < T < 25$ keV. To accurately capture the onset of the thermonuclear instability, we use a T^3 fit that is more accurate near the ignition threshold temperatures below 8 keV. Using the power-law dependence of fusion reactivity also helps to define the onset of the ignition process. In the power-law model, the thermonuclear instability does not saturate since the fusion burn continues until the fuel is depleted. This causes the solution of the ignition model to develop an explosive instability or mathematical singularity. It follows
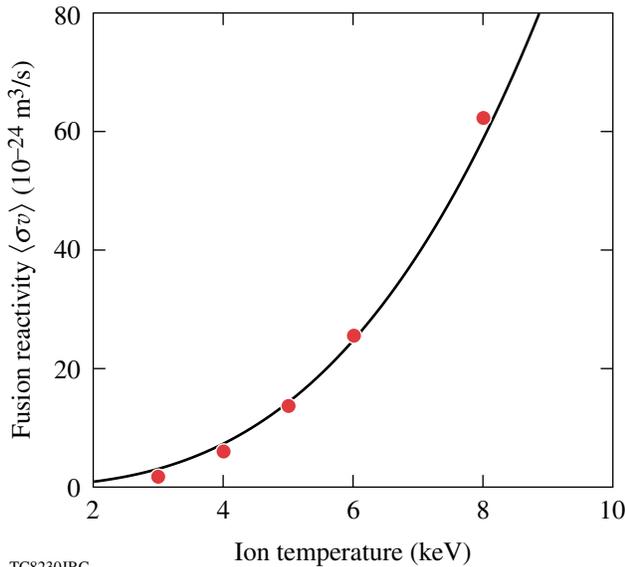

TC8230JRC

Figure 116.39
Fusion reactivity $\langle \sigma v \rangle$ is plotted as T^3 (solid curve). The dots are data taken from Ref. 18.

that one can identify the onset of ignition with the development of mathematical singularity. This can be easily explained by observing that in the absence of plasma motion $\left(\dot{R}_h = 0 \right)$ and T^2 dependence of the reactivity, Eq. (5) reduces to

$$\frac{dp}{dt} = C_\alpha p^2, \tag{6}$$

where the right-hand side represents alpha-particle heating and $C_\alpha > 0$. Equation (6) yields the explosive solution for $t > t_0$,

$$p(t) = \frac{p(t_0)}{1 - C_\alpha p(t_0)(t - t_0)}. \tag{7}$$

If ignition occurs, our model develops an explosive solution even in the presence of energy losses. Equation (6) also helps to explain the difference in the heat-conduction treatment in Ref. 17 as compared to our model. Reference 17 makes the same argument made here (and in Ref. 7), that the heat conduction losses do not cause a net energy loss (p is not dependent on heat conduction) but do lead to a loss of temperature. Since in Ref. 17 ignition is defined as the condition for dT/d$t > 0$ [Eq. (26) of Ref. 17], the heat losses do enter into the ignition condition; however, the authors of Ref. 17 also realize that ignition can occur when dT/d$t < 0$. In this case, the temperature initially decreases but eventually reverses its course and increases rapidly. This form of ignition [which is not included in Eq. (26) of Ref. 17] can be included by defining ignition in terms of pressure increase (dp/d$t > 0$) rather than temperature increase (dT/d$t > 0$) as the pressure can increase even if the temperature decreases. Since our ignition model is dynamic, all the different paths to ignition are included with both pressure and temperature explosive growth.

It is useful to rewrite Eq. (5) in dimensionless form by defining the following normalization factors:

$$\tau = \frac{V_i t}{R_s}, \hat{p}(\tau) = \frac{p}{p_s}, \hat{R}(\tau) = \frac{R_h}{R_s},$$

$$\hat{T}(\tau) = \frac{T_0}{T_*}, T_* = \left(\frac{25 \mu_1}{48 \pi \kappa_0} p_s R_s V_i \right)^{2/7}, \tag{8}$$

where p_s and R_s are the hot-spot pressure and radius at stagnation and V_i is the implosion velocity. As will be shown in the **Solution of the Ignition Model and Marginal Ignition Condition** section (p. 209), T_* represents the stagnation temperature resulting from an adiabatic compression of the hot spot (in the absence of alpha heating and radiation losses). Here

T_* has the units of J with $\mu_1 \approx 0.55$ and $\kappa_0 = 3.7 \times 10^{69}$ m$^{-1} \times$ s$^{-1} \times$ J$^{-5/2}$ for ln$\Lambda \approx 5$. For typical ICF implosion parameters, $T_*^{\mathrm{keV}} \equiv T_*/c_k$ falls in the range of 5 ~ 8 keV.

Using the power-law fit for $\langle \sigma v \rangle$ in Eq. (5) and substituting the dimensionless variables leads to the following simplified form of the energy equation:

$$\frac{d}{d\tau}\left(\hat{p}\hat{R}^5\right) = \gamma_\alpha \hat{p}^2 \hat{R}^5 \hat{T}^\sigma, \tag{9}$$

where $\gamma_\alpha = \left(\varepsilon_\alpha C_0 p_s R_s / 2(1+Z)^2 c_k^{2+\sigma} V_i\right) T_*^\sigma$ is a parameter related to the initial shell condition at the beginning of the deceleration phase (see the **Initial Conditions** section, p. 209). Notice that Eq. (9) indicates that as long as the fusion reactivity $\langle \sigma v \rangle$ is proportional to ~T^2 and the alpha heating rate depends only on the pressure ($n^2 \langle \sigma v \rangle \sim p^2$), the temperature does not enter into the ignition condition. This is not the case for $\langle \sigma v \rangle \sim T^{3-4}$ since the fusion-reaction rate will depend on pressure *and* temperature ($n^2 \langle \sigma v \rangle \sim p^2 T^{1-2}$). Here, an additional equation describing the evolution of the temperature is required.

Since the pressure is determined by the *pdV* work and the alpha-particle heating, one can use mass conservation and the equation of state to evaluate the temperature. The evolution of the hot-spot density depends on the mass ablation rate off the shell. This was first calculated in Refs. 7 and 8 and later in Ref. 19. The ablation rate can be determined by integrating the energy in Eq. (1) across the hot-spot boundary. All divergent-free terms vanish as both temperature and radiation flux approach zero at the hot-spot boundary. A straightforward integration leads to

$$\frac{5}{2A}\dot{m}_a T_0 R_h^2 = \frac{6}{5}\kappa_0 T_0^{\nu+1} R_h + \mu_0 C_1 p^2 T_0^{-3/2} R_h^3, \tag{10}$$

where the ablative mass rate is $\dot{m}_a = \rho V_a = Ap V_a/T$, $A = m_i/(1+Z)$, and $\mu_0 = \int_0^1 \hat{r}^2 \hat{T}^{-3/2} d\hat{r} \approx 0.85$. Notice that Eq. (10) is derived by approximating the temperature profile with a step function, the correct limit of a $\nu \gg 1$ expansion. Equation (10), accurate to order $1/\nu$, describes the energy flux balance at the hot-spot boundary where the radiation and conduction energy flows are recycled back by the ablated material.

The total hot-spot mass can be expressed as

$$M_{\mathrm{hs}} = \int_0^{R_h} 4\pi \rho r^2 dr = 4\pi \mu_1 Ap R_h^3/T_0,$$

where $\mu_1 \approx 0.55$ is the value of the integral $\mu_1 = \int_0^1 \hat{r}^2/\hat{T} d\hat{r}$ and T_0 is the hot spot's central temperature. Due to mass conservation, the change of the hot spot's mass is caused by mass abla-

tion off the shell, $dM_{\mathrm{hs}}/dt = 4\pi R_h^2 \dot{m}_a$. Substituting the above results into Eq. (10) yields

$$\frac{d}{dt}\left(\frac{pR_h^3}{T_0}\right) = \frac{12\kappa_0}{25\mu_1}R_h T_0^{5/2} + \frac{2\mu_0 C_1}{5\mu_1}\frac{p^2 R_h^3}{T_0^{5/2}}. \tag{11}$$

Notice that this equation governs the hot-spot temperature. Terms on the right-hand side represent heat conduction and radiation effects on the hot-spot temperature.

After a straightforward manipulation, the dimensionless form of the temperature equation can be written as

$$\frac{d}{d\tau}\left(\frac{\hat{p}\hat{R}^3}{\hat{T}}\right) = \hat{R}\hat{T}^{5/2} + \beta \frac{\hat{p}^2 \hat{R}^3}{\hat{T}^{5/2}}, \tag{12}$$

where $\beta = 2\mu_0 C_1 p_s^2 T_*^{-3/2} R_s/5\mu_1 p_s V_i$. Notice that β is proportional to the ratio between the total radiation energy emitted from the hot spot and the imploding shell's kinetic energy. The radiation energy is proportional to $C_1 p_s^2 T_s^{-3/2} R_s^3 \tau_c$ and the shell's kinetic energy is proportional to the hot spot's internal energy $MV_i^2 \sim p_s R_s^3$. As shown below, the time $\tau_c \sim R_s/V_i$ represents the confinement time of the hot spot surrounded by a dense shell imploded with velocity V_i. Ignited ICF capsules require that the radiation energy be smaller than the compression work so that high temperatures can be reached in the hot spot. Furthermore, the bremsstrahlung losses are also smaller than the heat-conduction losses and do not appreciably alter the temperature profile, which is determined mostly by heat conduction.

The third and last equation of our ignition model governs the conservation of momentum of the thin shell surrounding the hot spot. The thin-shell approximation (discussed in Ref. 7) assumes that the entire shell kinetic energy is transferred to the internal energy of the hot spot upon stagnation. Even though the thin-shell model overestimates the stagnation energy, it yields the correct ignition scaling. This is shown in Ref. 8 where a more accurate shell model, the so-called "thick-shell" model, is compared with the "thin-shell" one. In the thick-shell model, the shell is treated as a finite-thickness, compressible gas, including the presence of a return shock driven by the rapid increase of the hot-spot pressure. A similar model was also later adopted in Ref. 19. While the thick shell is a more realistic (but more complicated) model than the thin-shell one, the ignition scaling is virtually the same. Furthermore, we will use the results of Refs. 9 and 20 to heuristically limit the transfer of kinetic energy from the shell to the hot spot, which, in the

thin-shell model, is overestimated (100% transfer). Within the frame of the thin-shell model, the shell compresses the hot spot like a spherical piston and the equation of motion for the shell is simply the shell Newton's law $M_s\ddot{R} = 4\pi pR^2$. In dimensionless form, this equation can be rewritten using Eq. (8) as

$$\frac{d^2\hat{R}}{d\tau^2} = \hat{p}\hat{R}^2. \tag{13}$$

The shell Newton's law shows that the shell confinement time at stagnation scales as $\tau_c \sim \sqrt{M_s/p_s R_s}$. Since $M_s V_i^2 \sim p_s R_s^3$, the confinement time can be rewritten as $\tau_c \sim R_s/V_i$. During this time the hot spot's hydrodynamic pressure is at its peak value (in the absence of alpha heating). The shell's confinement time should not be confused with the burn time that depends on the shell's areal density (Ref. 1).

Equations (9), (12), and (13) represent a dynamic model of thermonuclear ignition. The next step is to determine the relevant set of initial conditions for the system of equations.

Initial Conditions

Based on the definition of the dimensionless variables, the initial condition of the thin-shell model requires that $\hat{R}(0) = R(0)/R_s$, $\dot{\hat{R}}(0) = -1$, $\hat{p}(0) = p(0)/p_s$, and $\hat{T}(0) = T_0(0)/T_*$, where $R(0)$, $p(0)$, $T_0(0)$ are the values of the radius, pressure, and central temperature at the beginning of the deceleration phase ($\tau = 0$) when the shell is imploding inward with its maximum velocity [$dR/dt(0) = -V_i$]. The stagnation values R_s and p_s can be defined through the energy conservation and adiabatic compression in the absence of alpha heating and radiation losses. In this case, energy conservation requires that $(1/2)M_s V_i^2 = (4\pi/3)p_s R_s^3$, while adiabatic compression requires that $p_s V_s^{5/3} = p(0)V(0)^{5/3}$ or $p_s R_s^5 = p(0)R(0)^5$. Using these relations, the initial conditions for the dimensionless variables can be rewritten as $\hat{R}(0) = \varepsilon_0^{-1/2}$, $\dot{\hat{R}}(0) = -1$, and $\hat{p}(0) = \varepsilon_0^{-5/2}$, where $\varepsilon_0 \equiv (1/2)M_s V_i^2/(4\pi/3)p(0)R(0)^3$ is the ratio between the shell's kinetic energy and the hot spot's internal energy at the beginning of the deceleration phase. Notice that $\varepsilon_0 \gg 1$ in typical ICF implosions where the hot spot's energy is amplified many times during the deceleration of the shell. The initial condition for the temperature requires a special treatment. We start by integrating in Eq. (12) from the beginning of the deceleration phase ($\tau = 0$) to stagnation (τ_s). The stagnation values for the dimensionless variables are $\tau_s = \varepsilon_0^{1/2}$, $\hat{p}(\tau_s) = 1$, $\hat{R}(\tau_s) = 1$, and $\hat{T}(\tau_s) = 1$. The initial temperature $\hat{T}(0)$ can be inferred from an analysis of the temperature in Eq. (12). At the beginning of the deceleration phase, both pressure and temperature are small and the radiation losses can be neglected

with respect to heat losses. Neglecting the alpha-particle heating during the hot-spot assembly phase (that is, $\gamma_\alpha = 0$) results in the adiabatic compression of the hot spot, leading to $\hat{p}\hat{R}^5 = 1$. Thus, the temperature defined in Eq. (12) can be rewritten as

$$\frac{d\hat{\phi}}{d\tau} = \hat{\phi}^{-5/2}\hat{R}^{-4}, \tag{14}$$

where $\hat{\phi} \equiv \hat{p}\hat{R}^3/\hat{T}$. The solution of Eq. (14) is

$$\hat{\phi}(\tau)^{7/2} = \hat{\phi}(0)^{7/2} + (7/2)\int_0^\tau \hat{R}^{-4} d\tau.$$

For large $\varepsilon_0 \gg 1$, one expects the stagnation temperature to be independent of its value at the beginning of the deceleration phase (as long as the initial value is much smaller than the stagnation value). Thus, one requires that $I \equiv (7/2)\int_0^\tau \hat{R}^{-4} d\tau \gg \hat{\phi}(0)^{7/2}$. Defining $\dot{\hat{R}} = d\hat{R}/d\tau$, the integral I can be rewritten as $I = (7/2)\int_0^\infty \hat{R}^{-4}\dot{\hat{R}}^{-1} d\hat{R}$. Notice that most of the contribution to the integral I comes from the stagnation values $\hat{R} \approx \hat{R}(\tau_s) = 1$ and $\dot{\hat{R}} \approx \dot{\hat{R}}(\tau_s) \approx 0$. By using the shell Newton's law [Eq. (13)], one finds that $\ddot{\hat{R}}(\tau_s) \approx 1$ and the shell velocity $\dot{\hat{R}}$ can be approximated by $\dot{\hat{R}} \approx \sqrt{2(\hat{R}-1)}$ near stagnation. Substituting into I and integrating over $\hat{R}$ yields $I = (5\pi/16\sqrt{2})$. At the beginning of the deceleration phase, the initial value of $\hat{\phi}$ is $\hat{\phi}(0) = \hat{p}(0)\hat{R}(0)^3/\hat{T}(0) = [\varepsilon_0\hat{T}(0)]^{-1}$. To guarantee a stagnation temperature independent of its initial value, one needs to choose $\varepsilon_0^{-1} \ll \hat{T}(0) \ll 1$. Any value of $\hat{T}(0) = \varepsilon_0^\omega$ with $-1 < \omega < 0$ satisfies this condition, and the resulting solution of the ignition model is independent of ε_0 and ω as long as $\varepsilon_0 \rightarrow \infty$. Here we choose $\omega = 1/2$ and $\hat{T}(0) = \varepsilon_0^{-1/2} \ll 1$.

Solution of the Ignition Model and Marginal Ignition Condition

Our ignition model consists of the three equations [(9), (12), and (13)] representing mass, momentum, and energy conservation, with the initial conditions derived in the **Initial Conditions** section (p. 209). For convenience, the equations and initial conditions are summarized below:

$$\frac{d}{d\tau}\left(\hat{p}\hat{R}^5\right) = \gamma_\alpha \hat{p}^2 \hat{R}^5 T^\sigma$$

$$\frac{d}{d\tau}\left(\frac{\hat{p}\hat{R}^3}{\hat{T}}\right) = \hat{R}\hat{T}^{5/2} + \beta\frac{\hat{p}^2\hat{R}^3}{\hat{T}^{5/2}}$$

$$\frac{d^2\hat{R}}{d\tau^2} = \hat{p}\hat{R}^2 \tag{15}$$

$$\hat{p}(0) = \varepsilon_0^{-5/2}, \hat{T}(0) = \varepsilon_0^{-1/2}, \hat{R}(0) = \varepsilon_0^{1/2}, \dot{\hat{R}}(0) = -1.$$

Equations (15) are numerically solved up to the stagnation time $\tau \sim \tau_s = \varepsilon_0^{1/2}$ for a large value of $\varepsilon_0 \gg 1$, and $\sigma = 1$ is used in the computation. The solution develops an explosive instability when the parameter γ_α exceeds a critical value for a preset value of β. Here, we are interested in the asymptotic value of γ_α for $\varepsilon_0 \to \infty$ (we use $\varepsilon_0 = 10^4$ in the numerical integration). Physically, this instability corresponds to the onset of ignition. The critical values of γ_α and β are obtained through a series of numerical solutions of the system of Eqs. (15) and shown in Fig. 116.40, where each dot represents a single pair of γ_α and β such that the solution of the equations turns singular for both pressure and temperature. The ignition curve in Fig. 116.40 can be accurately fitted by the following simple formula:

$$\gamma_\alpha = 1.12 + \beta^2 + 0.28\beta^3. \tag{16}$$

Within the frame of the thin-shell model, the shell thickness is negligible. The effects of finite thickness can be included, however, by noticing that only a fraction of the shell's kinetic energy is converted into hot-spot internal energy. That fraction is related to the ratio of the hot spot and shell volume at stagnation and can be written as $(1 + A^{-1})^{-3}$, where A is the aspect ratio defined as the hot-spot radius R_h over the shell thickness Δ, $A = R_h/\Delta$. The total mass is expressed as $M = 4\pi(\rho\Delta)R_s^2\Sigma(A)$ (Ref. 20) with the volume factor Σ defined as $\Sigma(x) = 1 + (1/x) + 1/(3x^2)$.


TC8231JRC
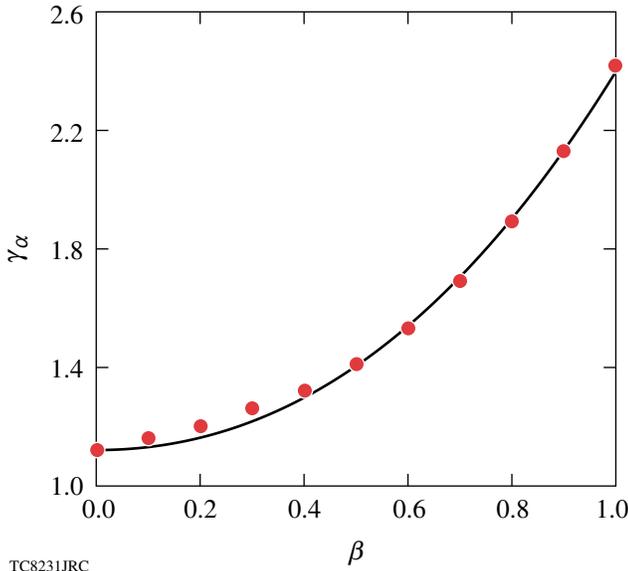
Figure 116.40
Relation between γ_α and β. Each dot represents a single pair of γ_α and β such that the solution of Eqs. (15) turns singular. The solid curve is the fitting formula $\gamma_\alpha(\beta)$ in Eq. (16).

Thus, the important parameter γ_α in the ignition condition can be rewritten as

$$\gamma_\alpha = \frac{\varepsilon_\alpha C_0 T_*^\sigma}{2(1+Z)^2 c_k^{2+\sigma}} \frac{\sqrt{M}\sqrt{MV_i^2/(1+A^{-1})^3}}{4\pi R_s^2}$$

$$= \frac{\varepsilon_\alpha C_0 T_*^\sigma}{2(1+Z)^2 c_k^{2+\sigma}} \frac{\Sigma(A)}{(1+A^{-1})^{3/2}}(\rho\Delta)V_i. \tag{17}$$

Similarly, the temperature normalization factor T_* can be written as

$$T_* = \left(\frac{25\mu_1}{48\pi\kappa_0} \times \frac{M_s V_i^3}{R_s^2}\right)^{2/7}$$

$$= \left(\frac{25\mu_1}{12\kappa_0} \times \frac{\Sigma(A)(\rho\Delta)V_i^3}{(1+A^{-1})^{9/2}}\right)^{2/7}. \tag{18}$$

For typical ICF implosions, the stagnation aspect ratio A usually falls within the range of $1 < A < 4$ (Ref. 20). Within this interval, the function $\Sigma(A)/(1+A^{-1})^{9/2}$ can be approximated by the power law, $\Sigma(A)/(1+A^{-1})^{9/2} \approx 0.12A^{1.045}$. Since the stagnation aspect ratio scales with the implosion velocity and shell adiabat as $A \approx 8.2 \times 10^{-6}V_i^{0.96}/\alpha^{0.19}$ (Ref. 9), the function $\Sigma(A)$ can be approximated as

$$\Sigma(A)/(1+A^{-1})^{9/2} \approx \delta_0 V_i/\alpha^{0.2},$$

with the constant $\delta_0 = 5.7 \times 10^{-7}$ s/m. Substituting into Eq. (18) and solving for the implosion velocity yields

$$V_i = \left(\frac{12\kappa_0}{25\mu_1\delta_0}\right)^{1/4}\alpha^{0.05}(\rho\Delta)^{-1/4}T_*^{7/8}. \tag{19}$$

Notice that the adiabat dependence is very weak, so it is neglected in the following derivation. Furthermore, the aspect ratio's dependence in Eq. (17) can be approximated with a constant, $\Sigma(A)/(1+A^{-1})^{3/2} \approx 0.85$ for $1 < A < 4$. Substituting this result and Eq. (19) into Eq. (17), one finds the γ_α dependence on the areal density $\rho\Delta$ and temperature T_*:

$$\gamma_\alpha = \frac{0.85\varepsilon_\alpha C_0}{2(1+Z)^2 c_k^{2+\sigma}}\left(\frac{12\kappa_0}{25\mu_1\delta_0}\right)^{1/4}(\rho\Delta)^{3/4}T_*^{\sigma+7/8}. \tag{20}$$

The parameter β can be expanded in the same manner as above. Notice that $\beta/\gamma_\alpha \sim T_*^{-\sigma-3/2}$ and β can be written in the following form:

$$\beta = \frac{0.34\,\mu_0 C_1}{\mu_1}\left(\frac{12\kappa_0}{25\mu_1\delta_0}\right)^{1/4}(\rho\Delta)^{3/4}T_*^{-5/8}. \qquad (21)$$

In both Eqs. (20) and (21), the units of $\rho\Delta$ and T_* are in kg/m² and J, respectively. To express T_* in keV in these equations, γ_α and β can be rewritten as

$$\gamma_\alpha = C_3(\rho\Delta)^{3/4}\left(T_*^{\mathrm{keV}}\right)^{15/8},$$

$$C_3 = \frac{0.85\,\varepsilon_\alpha C_0}{2(1+Z)^2 c_k^{9/8}}\left(\frac{12\kappa_0}{25\mu_1\delta_0}\right)^{1/4},$$

$$\qquad\qquad\qquad\qquad\qquad\qquad\qquad (22)$$

$$\beta = C_4(\rho\Delta)^{3/4}\left(T_*^{\mathrm{keV}}\right)^{-5/8},$$

$$C_4 = \frac{0.34\,\mu_0 C_1}{\mu_1 c_k^{5/8}}\left(\frac{12\kappa_0}{25\mu_1\delta_0}\right)^{1/4},$$

where $Z = 1$ for DT plasma, $\varepsilon_\alpha = 3500$, $c_k = 5.6\times10^{-13}$ J, $C_0 = 2.6\times10^{-26}$ m³ × keV⁻³ × s⁻¹, $\mu_0 = 0.85$, $\mu_1 = 0.55$, $\kappa_0 = 3.7\times1069$ m⁻¹ × s⁻¹ × J⁻⁵/², $\delta_0 = 5.7\times10^{-7}$ m⁻¹ × s. Using $C_1 = 9.7\times10^{-30}$ m × J⁵/² × s⁻¹ × N⁻² for $Z = 1$ leads to $C_4 \approx 0.327$ keV⁵/⁸ m³/² × kg⁻³/⁴, and the parameter $\beta \leq 1$ for typical values of areal density and temperature. Using $C_0 \approx 2.6\times10^{-26}$ m³ × keV⁻³ × s⁻¹ into the first equation of (22) yields $C_3 \approx 7.6\times10^{-3}$ keV⁻¹⁵/⁸ × m³/² × kg⁻³/⁴ for DT fuel.

The next step is to relate the parameter T^* to the maximum temperature in the absence of alpha heating $\left(T_{\max}^{\mathrm{no}\,\alpha}\right)$. Such a temperature is approximately equal to the temperature measured in D₂ targets or sub-ignited DT implosions where the self-heating plays a negligible role in the hot-spot energy balance. A more detailed discussion of the validity of $T_{\max}^{\mathrm{no}\,\alpha}$ as a measurable parameter is included in the **Conclusions** (p. 216). The value of $T_{\max}^{\mathrm{no}\,\alpha}$ is found by setting $\gamma_\alpha = 0$ and by solving Eq. (15) for various values of β. The maximum of the solution for $\hat{T}$ corresponds to $T_{\max}^{\mathrm{no}\,\alpha}/T_*$. A series of numerical solutions lead to the following relations between the parameter β and the maximum hot-spot temperature $\hat{T}_{\max}^{\mathrm{no}\,\alpha}$ without alpha heating:

$$\hat{T}_{\max}^{\mathrm{no}\,\alpha} = \frac{T_{\max}^{\mathrm{no}\,\alpha}}{T_*} = \frac{0.78}{\Pi(\beta)}, \qquad (23)$$

$$\Pi(\beta) = 1 + 0.42\beta^{0.9} + 1.7\times10^{-3}\beta^{1.8},$$

as shown in Fig. 116.41. Using Eq. (23) and the definitions of γ_α and β in Eqs. (22), one can easily rewrite the ignition condition as

$$(\rho\Delta)\left(T_{\max}^{\mathrm{no}\,\alpha}\right)^{5/2} = 33.5\,\frac{\left[\gamma_\alpha(\beta)\right]^{4/3}}{\Pi(\beta)^{5/2}}, \qquad (24)$$

where $\rho\Delta$ is in g/cm², $T_{\max}^{\mathrm{no}\,\alpha}$ is in keV, γ_α is given in Eq. (16), and β can be determined in terms of $T_{\max}^{\mathrm{no}\,\alpha}$ from the following equation:

$$\frac{\beta\,\Pi(\beta)^{5/2}}{\lambda_\alpha(\beta)}\left[\frac{3.4}{T_{\max}^{\mathrm{no}\,\alpha}}\right]^{5/2}. \qquad (25)$$

Notice that for large temperatures $T_{\max}^{\mathrm{no}\,\alpha} \gg 3.4$ keV, β is small and the ignition condition reduces to

$$(\rho\Delta)\left(T_{\max}^{\mathrm{no}\,\alpha}\right)^{5/2} = 33.5\,\mathrm{g}/\mathrm{cm}^2\mathrm{keV}^{2.5}.$$

Numerically solving Eq. (25) for various $T_{\max}^{\mathrm{no}\,\alpha}$ in the range $2.5 < T_{\max}^{\mathrm{no}\,\alpha} < 8$ keV to find β and substituting $\beta\left(T_{\max}^{\mathrm{no}\,\alpha}\right)$ into


TC8232JRC
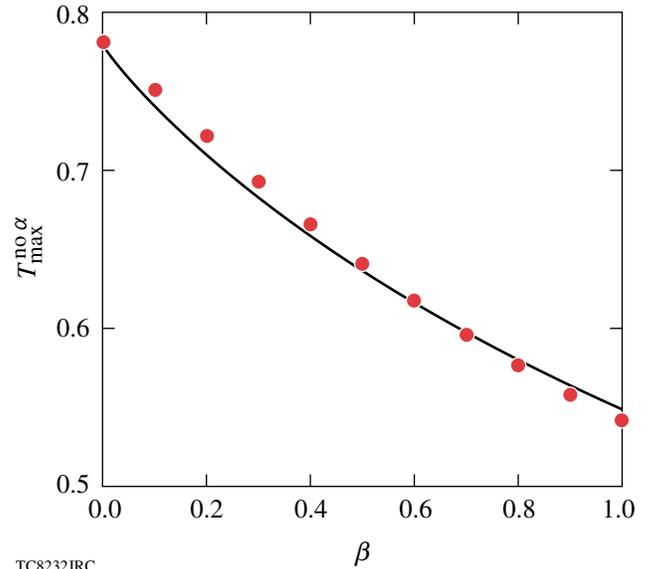
Figure 116.41
Relation between $\hat{T}_{\max}^{\mathrm{no}\,\alpha}$ and β. Each dot represents a single pair of $\hat{T}_{\max}^{\mathrm{no}\,\alpha}$ and β by solving Eqs. (15) with $\gamma_\alpha = 0$ for various β. $\hat{T}_{\max}^{\mathrm{no}\,\alpha}$ is the maximum value of $\hat{T}$ in the solution. The solid curve is the fitting formula $\hat{T}_{\max}^{\mathrm{no}\,\alpha}(\beta)$ in Eq. (23).

Eq. (24) yields the ignition condition in terms of the two measurable parameters $\rho\Delta$ and $T_{max}^{no\,\alpha}$. Figure 116.42 shows the ignition condition in the $\rho\Delta$, $T_{max}^{no\,\alpha}$ plane. A simple fit of the ignition condition, accurate to within $\pm10\%$ in the range $4 < T_{max}^{no\,\alpha} < 8$, is given by

$$(\rho\,\Delta) \approx \frac{2.5}{\left(T_{max}^{no\,\alpha}\right)^{1.18}\left[1 - \left(\frac{3}{T_{max}^{no\,\alpha}}\right)^{2.5}\right]} \ . \tag{26}$$

The solid curve in Fig. 116.42 shows the numerical fit in relation to the exact numerical solution of the ignition model (dots). Notice that Eq. (26) exhibits a singularity for $T_{max}^{no\,\alpha} \approx 3$ keV, indicating that at such low temperatures, ignition requires very large areal densities. The areal density in Eq. (26) refers to the shell's areal density without including the hot spot's contribution. The hot spot's contribution to the areal density is typically small except for marginally ignited targets at high temperatures. As shown in Fig. 116.42, when the $T_{max}^{no\,\alpha}$ temperatures increase, the shell's areal density required for marginal ignition falls below 0.5 g/cm². At such low values, the areal densities of both the shell and the hot spot are of the same order and the hot spot's contribution is a significant portion of the total areal density. In the next section, the total areal density from a set of hydrodynamic simulations is used to generate an ignition

TC8233JRC

Figure 116.42
Relation between $\rho\Delta$ and $T_{max}^{no\,\alpha}$ according to the ignition model of Eq. (15). Each dot represents a single pair of $\rho\Delta$ and $T_{max}^{no\,\alpha}$ from the solution of Eqs. (24) and (25) for $4 < T_{max}^{no\,\alpha} < 8$. The solid curve is the fitting formula in Eq. (26) and represents the marginal ignition condition.

curve similar to the one in Fig. 116.42. Therefore, significant discrepancies between the theoretical and numerical results are expected at high ignition temperatures. A detailed discussion of the validity of Eq. (26) and a comparison with the results of numerical simulations are the subjects of the next section.

Hydrodynamic Simulations

About 20 marginally ignited direct-drive targets have been simulated with the one-dimensional Lagrangian radiation-hydrodynamic code *LILAC*.[21] *LILAC* is routinely used for ICF target design studies at the Laboratory for Laser Energetics. It includes *SESAME*[22] equation-of-state tables, flux-limited Spitzer thermal conduction (the value of the flux limiter is set at $f = 0.06$), multigroup radiation transport, multigroup alpha-particle transport, and 3-D laser ray tracing. The targets used in the simulations were spherical shells consisting of a single DT-ice layer or two layers of wetted-foam [(DT)$_6$CH] and pure-DT ice. All targets were filled with 1 atm of DT gas at 2.1×10^{-4} g/cm³, and the initial aspect ratio of the targets varied from 2.0 to 5.5. The relaxation (RX) adiabat shaping[23] technique was used to design most of the laser pulse shapes for these implosions. The relaxation (RX) laser pulse consisted of a prepulse followed by an interval of laser shut-off and the main pulse. Such a laser pulse is used to shape the adiabat in the ablator. In these simulations, the UV driver energy varies from 35 kJ to 10 MJ, adiabat from 0.7 to 4, and implosion velocity from 1.75 to 5.3×10^7 cm/s. These targets are designed to achieve marginal ignition with minimum laser energy. In the simulations, marginal ignition is defined as gain = 1 (fusion energy = laser energy on target). These implosions are also simulated without alpha energy deposition to compute the areal density and the no-alpha ion temperature used in the ignition condition (previous section).
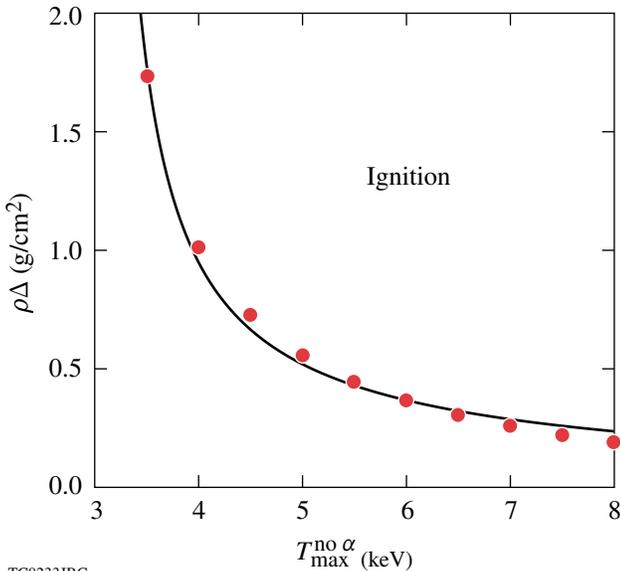
Each dot in Figs. 116.43 and 116.44 shows the areal density and ion temperature of each marginally ignited target. Figure 116.43 shows the maximum total areal density and the maximum hot-spot-volume–averaged, no-alpha ion temperature (the volume average is carried out over the hot-spot volume). Observe that all the points lie on a curve (i.e., the ignition curve). The latter can be accurately approximated (Fig. 116.43) by the following fitting formula:

$$\rho R_{max} \approx \frac{33.5}{\langle T^{no\,\alpha}\rangle_v^{5/2}\left[1 - \left(\frac{1.2}{\langle T^{no\,\alpha}\rangle_v}\right)^{5/2}\right]^{4/3}} \ , \tag{27}$$

where ρR_{max} is in g/cm² and $T^{no\,\alpha}$ is in keV. Similarly, Fig. 116.44 shows the ignition points in terms of the burn-
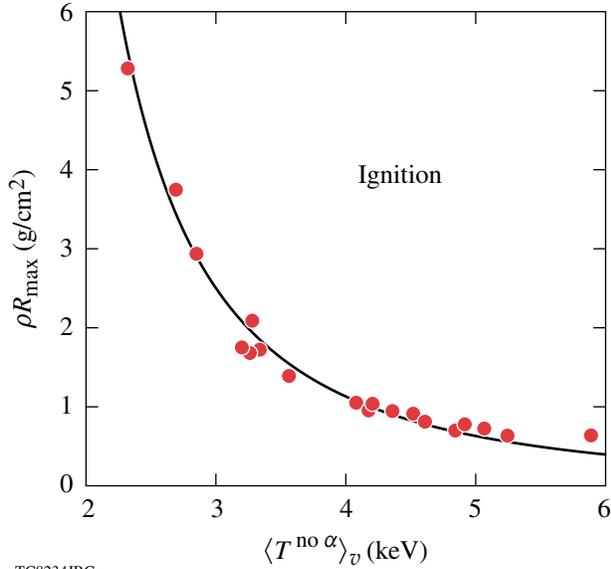
Figure 116.43
Relation between the maximum total areal density (ρR_{max}) and the maximum hot-spot volume-averaged, no-alpha ion temperature $\left(\langle T^{\text{no }\alpha}\rangle_v\right)$ for marginally ignited targets. Each dot represents a single simulation from the 1-D hydrocode *LILAC*. The solid curve is the fitting formula in Eq. (27).
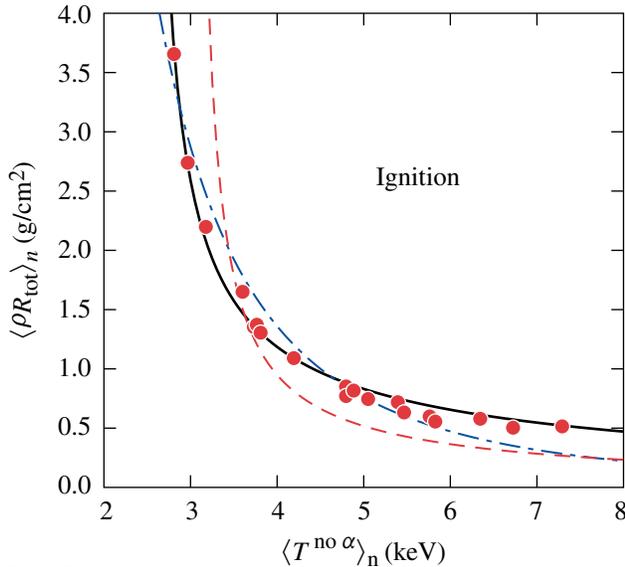
Figure 116.44
Relation between neutron-averaged, no-alpha temperature $\left(\langle T_i^{\text{no }\alpha}\rangle_n\right)$ and neutron-averaged total areal density $\left(\langle\rho R_{tot}\rangle_n\right)$ for marginally ignited targets. Each dot represents a single simulation from 1-D hydrocode. The solid curve is the fitting formula in Eq. (28). The dashed–dotted curve is the approximation of the ignition curve in Eq. (29). The dashed curve is the ignition model given in Eq. (26) of the **Solution of the Ignition Model and Marginal Ignition Condition** section (p. 209).

averaged areal density and the burn-averaged ion temperature. The burn-averaged areal density is defined as the total areal density weighted in time with the neutron rate. The burn-averaged temperature is the temperature weighted in time and space with the fusion reaction rate. Even in the $\langle\rho R_{tot}\rangle_n$, $\langle T_i^{\text{no }\alpha}\rangle_n$ plane the simulated marginal ignition points lie on an ignition curve. This curve is of particular importance since $\langle\rho R_{tot}\rangle_n$, $\langle T_i^{\text{no }\alpha}\rangle_n$ are the only two measurable parameters of the fuel assembly in an ICF implosion. The burn-averaged total areal density can be inferred from the downshift of the spectrum of charged fusion products,[13] and the burn-averaged ion temperature can be measured with the neutron time-of-flight diagnostics (nTOF's).[10] One can argue that the measurements give $\langle T_i\rangle_n$ instead of $\langle T_i^{\text{no }\alpha}\rangle_n$. The two parameters are virtually identical, however, for D_2 surrogate implosions or sub-ignited DT implosions with gain $\ll 1$. The ignition curve in Fig. 116.44 can also be approximated with a simple fitting formula

$$\langle\rho R_{tot}\rangle_n = \frac{3.4}{\langle T^{\text{no }\alpha}\rangle_n^{0.97}\left[1-\left(\frac{2.5}{\langle T^{\text{no }\alpha}\rangle_n}\right)^{2.5}\right]^{0.79}}, \tag{28}$$

where $\langle\rho R_{tot}\rangle_n$ is in g/cm^2 and $\langle T^{\text{no }\alpha}\rangle_n$ is in keV. Equation (28), plotted as the solid curve in Fig. 116.44, is the most useful form of the ignition condition that can be directly measured. A rough approximation of the ignition curve can be cast into a simple power law

$$\langle\rho R_{tot}\rangle_n \times \langle T_i^{\text{no }\alpha}\rangle_n^{2.6} > 50 \text{ g}\times\text{cm}^{-2}\times\text{keV}^{2.6}. \tag{29}$$

The dashed–dotted line in Fig. 116.44 shows the simple fit [Eq. (29)] in relation to the simulation results (dots). To compare the ignition condition from the analytic model in the previous section with the simulation results, we plot Eq. (26) in the $\langle\rho R_{tot}\rangle_n$, $\langle T_i^{\text{no }\alpha}\rangle_n$ plan of Fig. 116.44. The dashed curve in Fig. 116.44 shows the ignition model results as given in Eq. (26). This suggests that in spite of its simplicity, the ignition model captures the essential physics and the ignition condition [Eq. (26)] is in reasonable agreement with the simulation results. Notice that, as expected, the model prediction (dashed curve) falls below the simulation results at high temperatures since the hot-spot areal density is not accounted for.

Alpha-Particle Confinement

An important assumption used in the analytic model in the **Solution of the Ignition Model and Marginal Ignition Condition** section (p. 209) concerns the alpha-particle confinement. The assumption was made that most of the alpha particles slow down within the hot spot, and that the alpha-particle energy

deposited inside the hot spot is close to 100% ($\theta \approx 1$). Since the alpha-energy deposition in the hot spot depends on its areal density and temperature,[24] we have computed the hot-spot areal densities and hot-spot temperature for the marginal ignited targets in our simulation database. Figure 116.45 shows the hot-spot areal density and temperature at marginal ignition from the 1-D simulations discussed in the previous section. Observe that all the marginally ignited targets have a hot-spot areal density above the critical value of 0.3 g/cm^2 often cited in the literature.[1,2] To estimate the fraction of absorbed alpha particles (θ), we use the results of Ref. 24 to find that

$$\theta = \frac{3\tau}{2} - \frac{4}{5}\tau^2, \tau \leq \frac{1}{2};$$

$$\theta = 1 - \frac{1}{4\tau} + \frac{1}{160\tau^2}, \tau \geq \frac{1}{2}; \tag{30}$$

$$\tau \approx 92 (\rho R)_{\text{hs}} \Big/ T_h^{3/2},$$

where $(\rho R)_{\text{hs}}$ is the hot-spot areal density in g/cm^2 and T_h is the hot-spot temperature in keV. Substituting the areal densities and temperatures from Fig. 116.45 into Eq. (30) shows that the fraction of alpha energy deposited within the hot spot ranges from about 87% to 99% ($0.87 < \theta < 0.99$). Thus, our assumption that $\theta \approx 1$ seems to be satisfied at marginal ignition. It is also
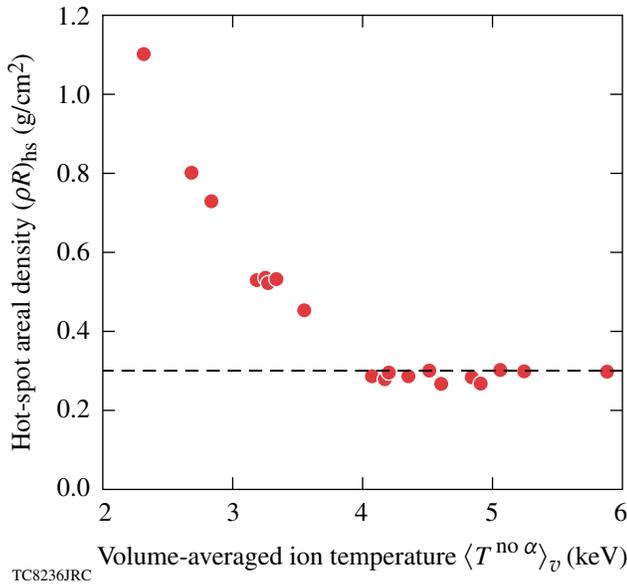
interesting to observe that, as shown in Fig. 116.45, ignition at no-alpha temperatures $\langle T_h^{\text{no }\alpha} \rangle$ below 4 keV requires a hot-spot areal density well above the 0.3-g/cm^2 critical value.

For large hot-spot areal densities and low hot-spot temperatures, a significant fraction of the bremsstrahlung radiation and conductive heat flux is absorbed within the hot spot, thus preventing a severe temperature degradation. For these targets, the only confinement issue is with the hydrodynamic disassembly of the surrounding shells. Since high hot-spot areal densities are correlated with high shell areal densities,[9] the inertial confinement of such shells is very long and ignition can occur at very low no-alpha temperatures, as shown in Fig. 116.45.

Comparison with the HTL Ignition Condition

To test the validity of the ignition condition derived in this article, we compare it to the ignition criterion derived by Herrmann *et al.* in Ref. 25. We refer to the criterion of Ref. 25 as the Herrmann–Tabak–Lindl (HTL) ignition condition. The HTL condition is a more accurate extension of the ignition scaling of Levedahl and Lindl,[26] and it correlates the minimum shell kinetic energy required for ignition with the implosion velocity, shell adiabat, and ablation pressure. Since all our simulations are for direct-drive targets with maximum intensity around 10^{15} W/cm^2, we will use the form of the HTL condition rewritten in terms of laser energy on target rather than the shell kinetic energy as shown in Eq. (53) of Ref. 9. The relation between laser energy and kinetic energy is $E_{\text{L}} = E_\kappa / \eta$, where η is the overall hydrodynamic efficiency. For intensities of 10^{15} W/cm^2, our 1-D hydrodynamic simulations show an ablation pressure close to 200 Mbar at the end of the acceleration phase in spherical implosions. Using $I_{15} = 1$ and $P_L = 200$ Mbar into Eq. (53) of Ref. 9, we find the following modified HTL ignition criterion:

$$E_{\text{L}} \approx 5.9 \times 10^2 \alpha_{\text{if}}^{1.9} \left(\frac{3 \times 10^7}{V_i} \right)^{6.6}, \tag{31}$$

where the laser energy E_{L} is in kJ and the implosion velocity V_i in cm/s. Since our ignition criterion uses the areal density and the ion temperature, a relation between these variables and those in Eq. (31) is required. For simplicity, we will consider the simplest (and the least accurate) form of our criterion, $\langle T^{\text{no }\alpha} \rangle_n^{2.6} \times \langle \rho R \rangle_n > 50$ keV$^{2.6} \times$ g/cm^2. The scaling relations derived in Ref. 9 provide accurate formulas relating the maximum areal density and the maximum volume-averaged, no-alpha temperature to the laser energy, shell adiabat, and implosion velocity. We will use the same scaling relation in Ref. 9 and simply adjust the proportionality constant to fit the neutron-averaged quantities in our ignition criterion. A simple fit of the numerical results from our implosion database leads to

TC8236JRC

Figure 116.45
Hot-spot areal density $[(\rho R)_{\text{hs}}]$ and volume-averaged, no-alpha hot-spot ion temperature $(\langle T^{\text{no }\alpha} \rangle_v)$. Each dot represents a single simulation from 1-D hydrocode. The dashed line marks the hot-spot areal density of 0.3 g/cm^2.

$$\langle \rho R \rangle_n (E_L) = \frac{0.78}{\alpha_{if}^{0.54}} \left(\frac{V_i}{3 \times 10^7} \right)^{0.06} \left(\frac{E_L}{100} \right)^{0.33}$$

(32)

$$\left\langle T_i^{no\,\alpha} \right\rangle_n (E_L) = \frac{3.5}{\alpha_{if}^{0.15}} \left(\frac{V_i}{3 \times 10^7} \right)^{1.25} \left(\frac{E_L}{100} \right)^{0.07}.$$

Figures 116.46 and 116.47 compare the results of the simulations with the above fitting formulas. Substituting Eq. (32) into our ignition criterion yields the minimum energy required for

$$E_L (kJ) > 5.9 \times 10^2 \alpha_{if}^{1.8} \left(\frac{3 \times 10^7}{V_i} \right)^{6.5}.$$

(33)

Notice that the power indices and the proportionality constants in Eq. (33) are virtually identical to those in Eq. (31). This shows that our ignition criterion reproduces the HTL scaling quite accurately.


TC8237JRC
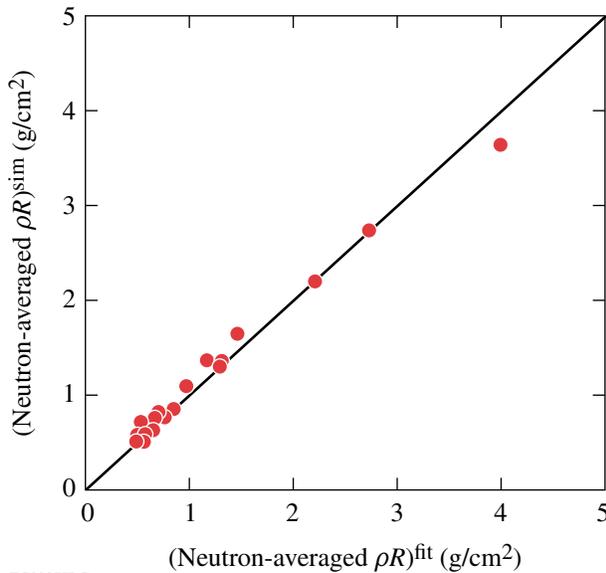
Figure 116.46
Neutron-averaged areal density $\langle \rho R \rangle_n$ from simulations (dots) compared to the numerical fit in Eq. (32) (solid line).

Hydro-Equivalent Curves

In this section we introduce the concept of hydro-equivalency and hyro-equivalent curves in the ρR, T_i plane. ICF targets with similar in-flight hydrodynamic variables, but different driver energy and gain, are considered hydrodynamically equivalent. Hydro-equivalent targets are expected to exhibit the same hydrodynamic behavior with respect to their hydro-


TC8238JRC
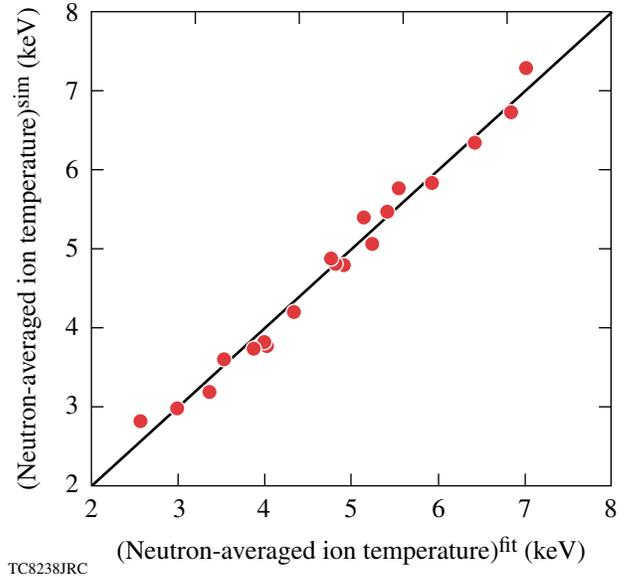
Figure 116.47
Neutron-averaged, no-alpha ion temperature $\left\langle T_i^{no\,\alpha} \right\rangle_n$ from simulation (dots) compared to the numerical fit in Eq. (32) (solid line).

dynamic performance not only in 1-D but also in 3-D. Here, we relate the hydrodynamic performance to the peak pressure of the stagnating core and to the hydrodynamic stability of the implosion. If a set of targets is scaled in mass (M), radius (R), thickness (Δ), adiabat (α), implosion velocity (V_i), laser intensity (I), and energy (E_L) according to the simple scaling $M \sim E_L$, $R \sim E_L^{1/3}$, $\Delta + E_L^{1/3}$, $I \sim$ constant, $\alpha \sim$ constant, and $V_i \sim$ constant, then the target implosions yield the same peak pressure and the same hydrodynamic stability properties. The latter is related to the magnitude of the in-flight aspect ratio (IFAR), which depends on the implosion velocity, adiabat, and laser intensity (Ref. 9). Assuming the same relative size of the initial perturbations on targets, hydro-equivalent targets have the same Rayleigh–Taylor (RT) growth factor (Ref. 9) and the same RT amplitude with respect to their thicknesses. As shown in Eqs. (32) (and in Ref. 9), due to the dependence on the laser energy E_L, hydro-equivalent targets will produce different areal densities and slightly different no-alpha temperatures. Obviously, targets imploded by larger drivers (larger E_L) will achieve greater ρR and T_i.

Using Eqs. (32), one can easily plot hydro-equivalent curves on the $\langle \rho R \rangle_n$, $\langle T^{no\,\alpha} \rangle_n$ ignition plane, by fixing α and V_i in Eqs. (32) and letting E_L vary. In Fig. 116.48, we plot two hydro-equivalent curves for the direct-drive NIF point design[27] and the current best-performing cryogenic D_2 implosion on OMEGA to date.[11] The direct-drive NIF point design

TC8239JRC
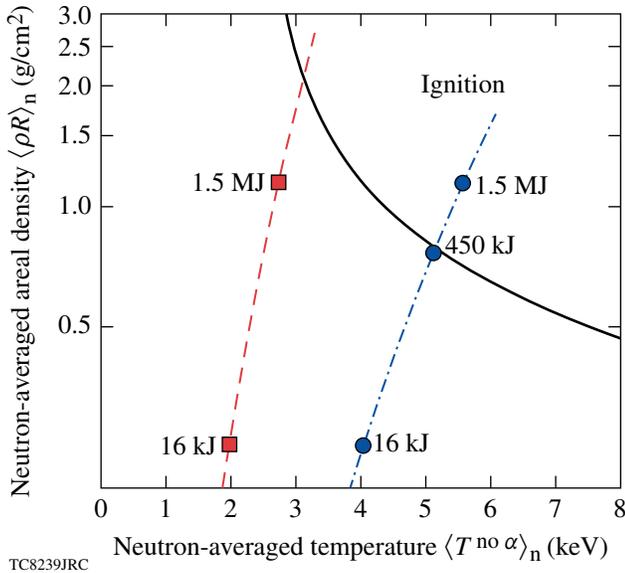
Figure 116.48
Hydro-equivalent curves in the $\left(\langle\rho R\rangle_n, \langle T^{no\,\alpha}\rangle_n\right)$ plane. The solid curve is the ignition condition in Eq. (28). The dashed curve is the hydro-equivalent curve for implosions with $\alpha_{if} = 2.5$, $V_i = 2.4 \times 10^7$ cm/s in Eq. (32). The lower square represents an implosion at 16 kJ and the upper one at 1.5 MJ. The dashed–dotted curve is the hydro-equivalent curve for implosions with $\alpha_{if} = 2.7$, $V_i = 4.25 \times 10^7$ cm/s. The three dots are implosions at 16 kJ, 450 kJ, and 1.5 MJ, respectively.

has an in-flight adiabat of 2.7 and implosion velocity of 4.25×10^7 cm/s. The hydro-equivalent curve for such values of α_{if} and V_i is the dashed–dotted curve in Fig. 116.48. The bottom dot on such a curve is the hydro-equivalent point for a 16-kJ implosion. The areal density and no-alpha temperature corresponding to that point are $\langle\rho R\rangle_n \approx 0.25$ g/cm² and $\langle T^{no\,\alpha}\rangle_n \approx 4.1$ keV, respectively. The top dot on the same curve represents the same implosion scaled up to NIF-like energies of 1.5 MJ. The middle dot is the same implosion scaled up to 450 kJ. Notice that the 450-kJ implosion is right on the 1-D marginal ignition curve (the solid curve in Fig. 116.48). This shows that the full NIF energy of 1.5 MJ is approximately three times larger than required for 1-D marginal ignition. The plots in Fig. 116.48 mainly imply that if a 16-kJ cryogenic implosion is carried out on OMEGA to achieve areal densities and temperatures as indicated on the bottom point, then one can use such a result to theoretically conclude that the same implosion scaled up to the NIF will have three times more energy as required by the 1-D Lawson criterion. While this is not absolute proof that such a target will ignite on the NIF, it will establish some confidence in the achievement of ignition.

The point representing the highest areal density cryogenic implosion on the OMEGA laser to date is the bottom square on the dashed curve. The point represents a neutron-averaged areal density slightly exceeding 0.2 g/cm² and neutron-averaged temperature of 2 keV. The corresponding implosion had an in-flight adiabat of about 2.5 and implosion velocity of about 2.4×10^7 cm/s. The upper square on that hydro-equivalent curve is below the marginal ignition curves and represents the same implosion scaled up to the full NIF energy of 1.5 MJ. Obviously, such an implosion would fail to ignite. This is explained by the relatively low implosion velocity ($V_i \approx 2.4 \times 10^7$ cm/s) and by the sensitivity on V_i of the minimum energy required for ignition [see Eq. (33)]. Current OMEGA cryogenic targets are massive shells (430-μm outer diam) with a 95-μm-thick cryogenic layer and a 10-μm-thick plastic ablator used to study high compression while reducing the effect of hydrodynamic instabilities. A point worth making is that current OMEGA targets have been imploded with ignition-relevant adiabats that are even slightly below the value required for the direct-drive point design.

In summary, hydro-equivalent curves plotted on the ρR, T_i ignition plane are useful in predicting 1-D performance for different laser energies. An immediate conclusion is that OMEGA-size capsules will have to be imploded at higher implosion velocities (for the same adiabat) to achieve a hydro-equivalent demonstration of ignition.

Conclusions
Equation (28) provides an accurate representation of a measurable Lawson criterion for inertial confinement fusion with DT fuel. Such an ignition condition is found using an analytical dynamic model of ignition, and it is confirmed by the results of one-dimensional simulations of marginally ignited direct-drive targets (gain $\approx$ 1). A simple fit of the ignition condition can be written as

$$\left\langle T_i^{no\,\alpha}\right\rangle_n^{2.6} \times \langle\rho R_{tot}\rangle_n > 50 \; \text{keV}^{2.6} \times \text{g}/\text{cm}^2. \qquad (34)$$

This ignition condition is given in terms of the only two measurable parameters of the compressed fuel: (1) the burn-averaged total areal density $\langle\rho R_{tot}\rangle_n$, and (2) the neutron-averaged hot-spot ion temperature $\langle T_i^{no\,\alpha}\rangle_n$ without accounting for the α-particle energy deposition. The burn-averaged total areal density can be measured through the detection of the spectrum of fusion products such as protons from secondary reactions.[13] The neutron-averaged temperature is measured through the neutron time-of-flight diagnostic.[10] In our ignition

condition, the neutron-averaged ion temperature is computed without the contribution of the fusion alpha particles. This is done to avoid using the actual temperature that undergoes extremely large and sudden variations when the compressed fuel assembly approaches the ignition condition. The so-called no-alpha temperature $T^{no\,\alpha}$ used in this article is a slowly varying hydrodynamic parameter that is well suited to measure the implosion performance with respect to the ignition condition. The only drawback for using $T^{no\,\alpha}$ rather than T is that $T^{no\,\alpha}$ is not always equal to the actual measurable temperature. The no-alpha temperature and the real temperature are virtually identical for cryogenic implosions with surrogate fuel (such as D_2) and for sub-ignited DT implosions with gains much less than unity. In both cases, the fusion self-heating is negligible and $T^{no\,\alpha} \approx T$. For DT implosions approaching ignition (gains ≥ 0.1), the alpha heating plays an important role in determining the hot-spot temperature and our form of the Lawson criterion cannot be used. In this case, however, the neutron-yield measurement alone is sufficient to determine that the implosion is approaching ignition. Because of the large excursion in neutron yield of a target approaching ignition (commonly referred to as the "ignition cliff"), the neutron yield rather than a formula like Eq. (34) is a much better indicator of target performance.

The measurable Lawson criterion, Eq. (34), favorably compares with the Herrmann–Tabak–Lindl ignition scaling when the areal density and temperature are rewritten in terms of the implosion velocity, in-flight adiabat, and driver energy by using the conversion formulas Eqs. (32) (also from Ref. 9). Furthermore, hydro-equivalent curves [Eqs. (32)] are plotted on the ignition diagram to show how hydro-equivalent implosions would perform with respect to the ignition condition when scaled up in laser energy.

It is worth mentioning that the ignition model presented here could be modified according to the results in Ref. 28 to include the effects of hydrodynamic instabilities developing at the hot-spot/shell interfaces. Such an extension of the ignition model could lead to a more accurate ignition condition that is valid in multidimensions.

ACKNOWLEDGMENT

REFERENCES

1. S. Atzeni and J. Meyer-ter-Vehn, *The Physics of Inertial Fusion: Beam Plasma Interaction, Hydrodynamics, Hot Dense Matter*, International Series of Monographs on Physics (Clarendon Press, Oxford, 2004).

2. J. D. Lindl, *Inertial Confinement Fusion: The Quest for Ignition and Energy Gain Using Indirect Drive* (Springer-Verlag, New York, 1998).

3. J. D. Lawson, Proc. Phys. Soc. Lond. **B70**, 6 (1957).

4. S. Atzeni and A. Caruso, Phys. Lett. A **85**, 345 (1981).

5. S. Yu. Gus'kov, O. N. Krokhin, and V. B. Rozanov, Nucl. Fusion **16**, 957 (1976).

6. R. Kishony, E. Waxman, and D. Shvarts, Phys. Plasmas **4**, 1385 (1997).

7. R. Betti, M. Umansky, V. Lobatchev, V. N. Goncharov, and R. L. McCrory, Phys. Plasmas **8**, 5257 (2001).

8. R. Betti, K. Anderson, V. N. Goncharov, R. L. McCrory, D. D. Meyerhofer, S. Skupsky, and R. P. J. Town, Phys. Plasmas **9**, 2277 (2002).

9. C. D. Zhou and R. Betti, Phys. Plasmas **14**, 072703 (2007).

10. V. Yu. Glebov, D. D. Meyerhofer, C. Stoeckl, and J. D. Zuegel, Rev. Sci. Instrum. **72**, 824 (2001).

11. T. C. Sangster, V. N. Goncharov, P. B. Radha, V. A. Smalyuk, R. Betti, R. S. Craxton, J. A. Delettrez, D. H. Edgell, V. Yu. Glebov, D. R. Harding, D. Jacobs-Perkins, J. P. Knauer, F. J. Marshall, R. L. McCrory, P. W. McKenty, D. D. Meyerhofer, S. P. Regan, W. Seka, R. W. Short, S. Skupsky, J. M. Soures, C. Stoeckl, B. Yaakobi, D. Shvarts, J. A. Frenje, C. K. Li, R. D. Petrasso, and F. H. Séguin, Phys. Rev. Lett. **100**, 185006 (2008).

12. T. R. Boehly, D. L. Brown, R. S. Craxton, R. L. Keck, J. P. Knauer, J. H. Kelly, T. J. Kessler, S. A. Kumpan, S. J. Loucks, S. A. Letzring, F. J. Marshall, R. L. McCrory, S. F. B. Morse, W. Seka, J. M. Soures, and C. P. Verdon, Opt. Commun. **133**, 495 (1997).

13. J. A. Frenje, C. K. Li, F. H. Séguin, J. Deciantis, S. Kurebayashi, J. R. Rygg, R. D. Petrasso, J. Delettrez, V. Yu. Glebov, C. Stoeckl, F. J. Marshall, D. D. Meyerhofer, T. C. Sangster, V. A. Smalyuk, and J. M. Soures, Phys. Plasmas **11**, 2798 (2003).

14. E. M. Campbell and W. J. Hogan, Plasma Phys. Control. Fusion **41**, B39 (1999).

15. D. Mihalas and B. Weibel-Mihalas, *Foundations of Radiation Hydrodynamics* (Oxford University Press, New York, 1984).

16. Ya. B. Zel'dovich and Yu. P. Raizer, in *Physics of Shock Waves and High-Temperature Hydrodynamic Phenomena*, edited by W. D. Hayes and R. F. Probstein (Dover Publications, Mineola, NY, 2002).

17. S. Atzeni and A. Caruso, Nuovo Cimento B **80**, 71 (1984).

18. H.-S. Bosch and G. M. Hale, Nucl. Fusion **32**, 611 (1992).

19. Y. Saillard, Nucl. Fusion **46**, 1017 (2006).

20. R. Betti and C. Zhou, Phys. Plasmas **12**, 110702 (2005).

21. M. C. Richardson, P. W. McKenty, F. J. Marshall, C. P. Verdon, J. M. Soures, R. L. McCrory, O. Barnouin, R. S. Craxton, J. Delettrez, R. L. Hutchison, P. A. Jaanimagi, R. Keck, T. Kessler, H. Kim, S. A. Letzring, D. M. Roback, W. Seka, S. Skupsky, B. Yaakobi, S. M. Lane, and S. Prussin, in *Laser Interaction and Related Plasma Phenomena*, edited by H. Hora and G. H. Miley (Plenum Publishing, New York, 1986), Vol. 7, pp. 421–448.

22. S. P. Lyon and J. D. Johnson, Los Alamos National Laboratory, Los Alamos, NM, Report LA-UR-92-3407 (1992).

23. K. Anderson and R. Betti, Phys. Plasmas **11**, 5 (2004).

24. O. N. Krokhin and V. B. Rozanov, Sov. J. Quantum Electron. **2**, 393 (1973).

25. M. C. Herrmann, M. Tabak, and J. D. Lindl, Nucl. Fusion **41**, 99 (2001).

26. W. K. Levedahl and J. D. Lindl, Nucl. Fusion **37**, 165 (1997).

27. P. W. McKenty, V. N. Goncharov, R. P. J. Town, S. Skupsky, R. Betti, and R. L. McCrory, Phys. Plasmas **8**, 2315 (2001).

28. J. Sanz *et al.*, Phys. Plasmas **12**, 112702 (2005).

Pulsed-THz Characterization of Hg-Based, High-Temperature Superconductors

Introduction

Superconductivity is still regarded as a very promising technology to be applied in high-performance electronics (e.g., Josephson junction digital circuits, ultrasensitive magnetometers) and optoelectronics (broadband x-ray-to-visible-light photodetectors, optical single-photon and photon-number–resolving detectors). The discovery of high-temperature superconductors (HTS's)[1] made those applications technically easier to achieve, at least from the cryogenics point of view, since most HTS's require only liquid nitrogen cooling. Among them, the $HgBa_2Ca_{n-1}Cu_nO_{2n+2+\delta}$ (HBCCO, Hg-based) compound, with its record high superconducting critical temperature T_c of 134 K at ambient pressure,[2] has attracted special attention. However, it is a very complicated system and its complete understanding from the physics, chemistry, and materials science points of view is needed in order to overcome the technological barriers facing HBCCO, and HTS's in general, in their quest for widespread applications.

This work presents comprehensive studies of time-resolved dynamics of Cooper pairs and quasiparticles in Hg-based superconductors. Our experiments implement a femtosecond optical system to perform the time-domain spectroscopy (TDS), using either pulses with 1-THz bandwidth for transmission measurements or the ultrafast optical-pump THz-probe (OPTP) characterization method. In the case of the transmission-type THz-TDS experiments, our sample is put into the path of a subpicosecond-in-duration, THz radiation burst and the transmitted electric-field waveform is measured. After performing the fast Fourier transform (FFT) of the time-domain transient, the frequency-dependent magnitude and phase components of the signal are obtained. By comparing the obtained data to the reference signal collected without the sample present in the system, either the frequency-dependent complex index of refraction $n(\omega)$ or conductivity $\sigma(\omega)$ of the sample's material can be deduced without resorting to Kramers–Kronig analysis. Since various pairing theories predict the different temperature behavior of the complex $\sigma = \sigma_{re} - i\sigma_{im}$ in HTS's,[3] by measuring the temperature- and frequency-dependent components of σ (σ_{re} and σ_{im}), we are able to provide insight on the intrinsic relaxation dynamics of quasiparticles in the HBCCO material.

Sample Fabrication and Experimental Setup

1. Sample Fabrication

Our Hg-based thin films were synthesized from 200 to 600-nm-thick Re-Ba-Ca-Cu-O precursor films, rf-magnetron sputtered at the room temperature on $LaAlO_3$ substrates, then followed by an *ex-situ* mercuration process in a sealed, evacuated quartz ampoule, using an un-reacted (Hg, Re)-1223 pellet as the source of mercury, prepared by a sol-gel method. The ampoule was placed inside a furnace, kept at 800°C for 5 h, and later cooled at a rate of 120°C/h to the ambient temperature.[4]

The x-ray-diffraction analyses demonstrated that our films were predominantly composed of a *c*-axis–oriented Hg-1212 phase, together with a Hg-1223 phase. Four-point resistance measurements of chemically etched, 20-μm-wide microbridges, showed that the samples used in this study exhibited the onset of the superconducting transition $T_{c,on}$ at ~122 K and the zero-resistance $T_{c,0}$ at ~110 K.[4]

2. Experimental Setup

Figure 116.49 shows our experimental setup. A 1-kHz, 800-nm-wavelength, 50-fs-duration commercial Ti:sapphire amplifier system was used as a laser source with a total output of ~500 mW. The output from the laser was split into three beams: one beam was used to optically pump the Hg-based sample and generate photoexcited quasiparticles; the second beam was used to generate THz radiation via optical rectification in a ZnTe emitter; and the third one (very weak) detected the THz transmission signal via a free-space, electro-optic sampling in a ZnTe sensor. The generated THz transient was formed and focused on the HBCCO sample (marked by an arrow in Fig. 116.49) using two sets of metallic parabolic mirrors. The sample was mounted on a cold finger inside an optical, continuous-flow, liquid-helium cryostat with the temperature controlled between 8 K and 293 K. The computer-based data-acquisition system monitored current flow through two balanced photodetectors using a lock-in amplifier. The
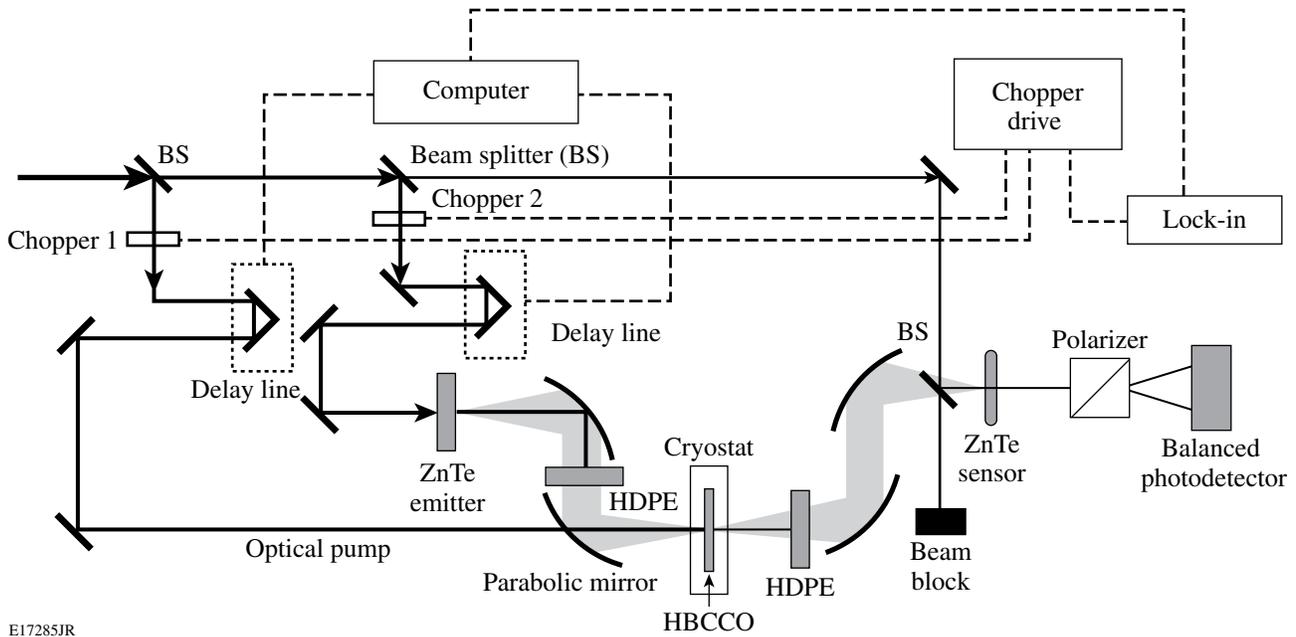
E17285JR

Figure 116.49
THz-TDS/OPTP experimental setup.

same setup was used for both the transmission THz-TDS and OPTP measurements, but, of course, the optical pump beam was blocked when performing transmission THz-TDS experiments. Further technical details of the experimental setup and OPTP spectroscopy can be found in Ref. 5.

Experimental Results and Discussion

1. THz-TDS Experiments

The transmission THz-TDS experiments were performed in the temperature range between 8 K and 293 K on both the HBCCO thin film and the bare LaAlO$_3$ substrate. Figure 116.50 shows the transmitted THz signals for a nominally (before annealing) 500-nm-thick HBCCO film at different temperatures. The THz transient amplitude decreases and the peak position slightly shifts as the temperature drops below T_c, indicating that Cooper pairs contribute to both the increased reflectivity and the phase shift via the imaginary component of the conductivity. We stress that the observed temperature-related changes in the THz transient are solely due to the change in the HBCCO superconducting properties since the reference THz-TDS studies performed on the bare LaAlO$_3$ did not reveal any changes, indicating no substrate absorption. The refractive index of LaAlO$_3$ remained constant and was ~4.85 for frequencies below 1 THz, which agrees with the results reported by Zhang.[6] As shown in the inset in Fig. 116.50, above T_c, the amplitude of the transmitted electric field decreased slowly with
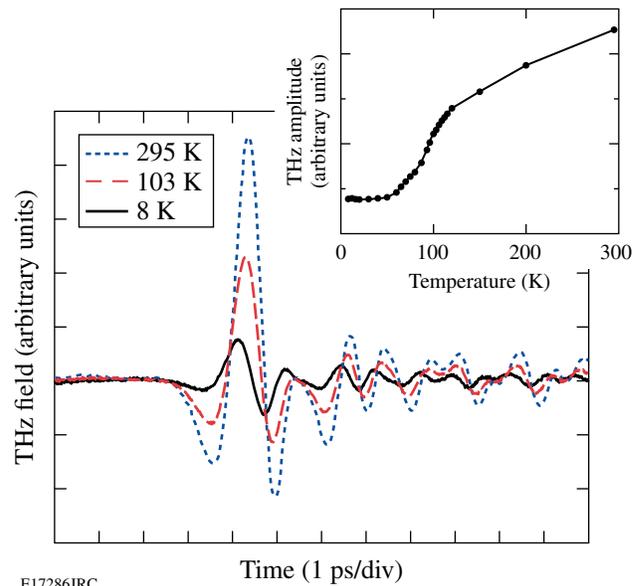
E17286JRC

Figure 116.50
Transmitted THz field through a HBCCO film at different temperatures. The inset shows temperature dependence of the THz field amplitude.

the temperature decrease, due to the progressive increase of the film's conductivity. When the temperature crossed T_c, there was a sharp drop in the THz transmission, as we will show later, directly related to the strong increase in σ_{im}.

2. THz-TDS Experiments—Complex Conductivity Analysis

Our HBCCO film on the LaAlO$_3$ substrate was put in the experimental THz optical path at the normal incidence to the THz beam as is schematically illustrated in Fig. 116.51(a). Therefore, the transmitted waveform can be expressed as

$$E_{sam+sub} = Et(\omega)t_{31}\exp[in_3(\omega/c)d_3],\qquad(1)$$

with the transmission coefficient t of the air/HBCCO/LaAlO$_3$ system equal to[7]

$$t(\omega) = \frac{t_{12}t_{23}\exp[in_2(\omega/c)d_2]}{1 + r_{12}r_{23}\exp[2in_2(\omega/c)d_2]},\qquad(2)$$

where $t_{ij} = 2n_i/(n_i+n_j)$, $r_{ij} = (n_i-n_j)/(n_i+n_j)$, E is the incident THz field, d_2 and d_3 are thicknesses of the thin film and the substrate, respectively, and n_i and n_j are complex refraction indexes. In general, we should consider a Fabry–Pérot effect due to multiple reflections from the interferences.[8] However, the thickness of LaAlO$_3$ is ~0.5 mm, so even the first-reflection signal is going to be outside the time window of interest associated with the transmitted signal; therefore, reflections can be ignored.

In the case of the bare LaAlO$_3$ substrate illuminated with the Thz radiation [Fig. 116.51(b)], the transmitted waveform can be expressed as

$$E_{air+sub} = Et_{13}t_{31}\exp[in_3(\omega/c)d_3]\exp[i(\omega/c)d_2].\qquad(3)$$

(a)

(b)

E17287JR
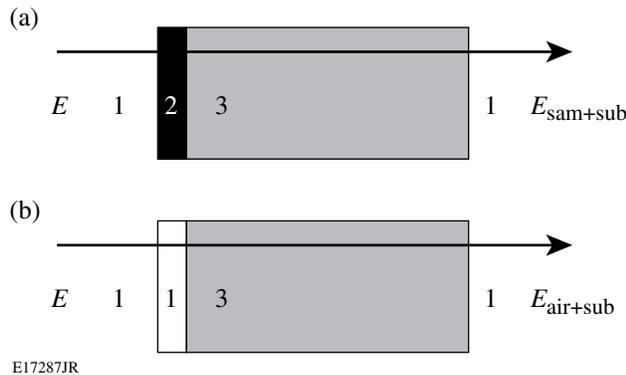
Figure 116.51
Schematic of THz wave transmission through (a) an HBCCO thin-film sample + LaAlO$_3$ substrate (sam+sub) and (b) air + a bare LaAlO$_3$ substrate (air+sub). The numbers 1, 2, and 3 correspond to air, HBCCO sample, and LaAlO$_3$ substrate, respectively.

Thus, dividing Eqs. (1) and (3), we get

$$\frac{E_{sam+sub}}{E_{air+sub}} = t(\omega)\big/\{t_{13}\exp[i(\omega/c)d_2]\}$$

$$= A(\omega)\exp[i\phi(\omega)],\qquad(4)$$

where $A(\omega)$ is the frequency-dependent magnitude of $E_{sam+sub}$ divided by that of $E_{air+sub}$, and $\varphi(\omega)$ is the frequency-dependent phase of $E_{sam+sub}$ subtracted by that of $E_{air+sub}$. Since, in our case, $|n_2(\omega/c)d|\ll1$, and $|n_2|\gg n_3\gg1$, therefore[7]

$$\frac{1+n_3}{1+n_3Z_0d_2\sigma(\omega)} = A(\omega)\exp\{i[\phi(\omega)+\omega d_2/c]\},\qquad(5)$$

where Z_0 is the impedance of free space. Equation (5) shows that now we can directly relate the experimentally measured THz-TDS spectra given by Eq. (4) to the tested complex $\sigma(\omega)$ of our sample.

The complex $\sigma(\omega)$ of superconductors can be described by the two-fluid model[1] and is composed of two parts: (1) an imaginary part that is dominant below T_c and related to the superfluid fraction f_s of electrons and (2) a Drude component proportional to the quasiparticle (normal electron) fraction f_n (Ref. 3):

$$\sigma(\omega,T) = \sigma_{re} + i\sigma_{im} = \frac{ne^2}{m^*}\left[\frac{f_n(T)}{\tau(\omega,T)^{-1}-i\omega} - \frac{f_s(T)}{i\omega}\right],\quad(6)$$

where $f_n + f_s = 1$ and $\tau(\omega,T)$ is the quasiparticle scattering time.

The temperature dependences of σ_{re} and σ_{im} are presented in Fig. 116.52. Figure 116.52(a) shows that σ_{re} increases with the decrease of temperature, exhibits a small cusp at ~T_c, and reaches the main peak below T_c, which is due to a competition of the quasiparticle density decrease and simultaneous increase of their scattering rate. The main σ_{re} peak [see Fig. 116.52(a)] shifts to lower temperatures with lower frequencies, and its amplitude becomes larger. On the other hand, Fig. 116.52(b) demonstrates that the σ_{im} component increases dramatically below T_c, which is due to the presence and increase of the superconducting condensate (Cooper pairs). There is a small nonzero σ_{im} in the normal state, apparently due to a residual kinetic-inductive effect. The latter can be speculated as evidence of the pseudogap state, but more systematic studies are needed.
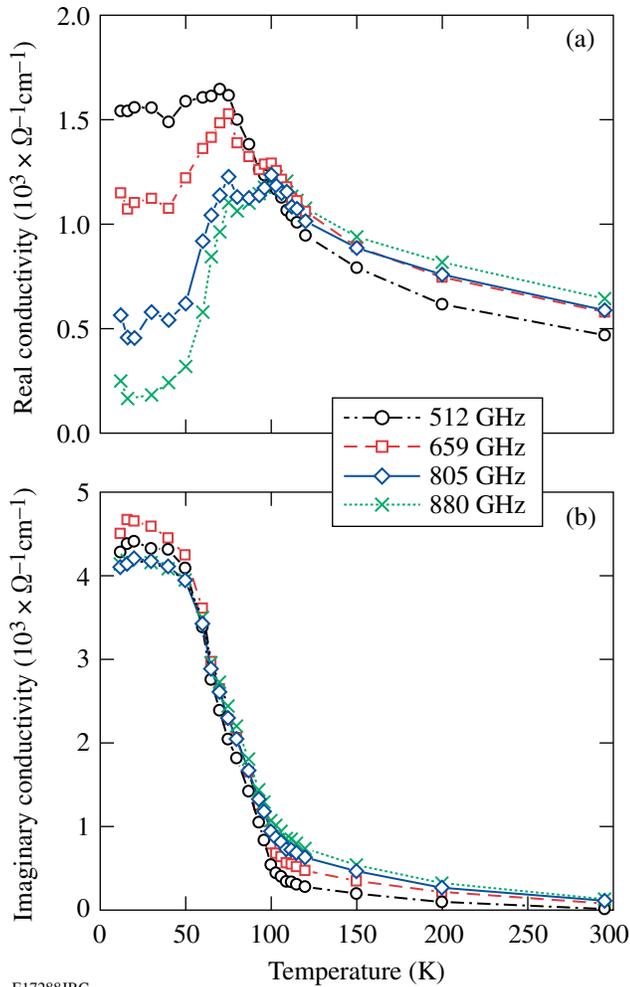
E17288JRC

Figure 116.52

(a) Temperature-dependent real conductivity at different frequencies; (b) temperature-dependent imaginary conductivity at different frequencies.

3. Time-Resolved OPTP Experiments

Optical excitation of a superconductor induces $\Delta\sigma_{re}$ and $\Delta\sigma_{im}$ changes, which result in a change of the transmitted transient THz electric field $\Delta E(t)$. As we mentioned before, the $\Delta\sigma_{im}$ component contains information about the superconducting condensate density, while the quasiparticle (normal electron) density is probed by $\Delta\sigma_{re}$. In our OPTP measurements, optical excitation increases the amplitude of the transient THz signal. Thus, we can fix the THz-probe-signal optical-delay line at the position where the positive, maximum peak of the THz electric-field waveform occurs [$\Delta E(t = t_{max})$] and, subsequently, vary the arrival time of the femtosecond optical excitation pump pulse (see Fig. 116.49). This way we can obtain the time-resolved $\Delta\sigma(t)$ dynamics and the corresponding quasiparticle dynamics.

Figure 116.53 shows our OPTP results at different temperatures below T_c with an optical fluence of the pump beam equal to 2 μJ/cm^2. The measured THz $\Delta E(t)$ transients have their decay times of the order of 2 ps and represent the quasiparticle relaxation (Cooper-pair formation) dynamics. We note that the above observation is contrary to the common, slow relaxation process in photoinduced superconductors, typical for conventional (e.g., metallic) superconductors, where the quasiparticle relaxation speed is limited by the acoustic-phonon escape time for the film to the substrate. The latter is called the phonon-bottleneck effect[9] and is due to the secondary pair-breaking by the acoustic phonons emitted during the process of two-quasiparticle recombination into a Cooper pair. The corresponding phonon escape time is in the nanosecond range, depending linearly on the superconductor thickness. In HBCCO superconductors, 2Δ is estimated to be in the 50- to 70-meV range and the acoustic phonons predominantly relax enharmonically; thus, they are decoupled from the carriers, resulting in the direct intrinsic quasiparticle recombination process. According to Fig. 116.53, far below T_c, our HBCCO material relaxes back to the fully superconducting (equilibrium) state in less than 2 ps. The latter observation is in direct agreement with our earlier, all-optical, pump–probe spectroscopy studies[10] and confirms that, far below T_c, thermal (phonon) contribution is negligible in the relaxation dynamics of the nonequilibrium HBCCO superconductors.
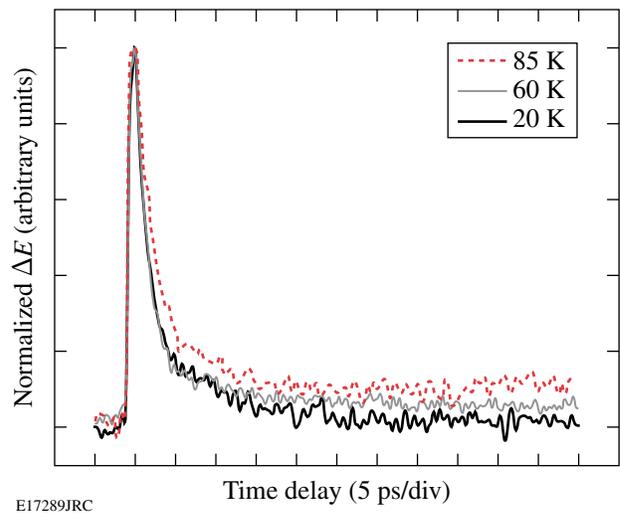
E17289JRC

Figure 116.53

Normalized transient transmitted electrical field signals at different temperatures below T_c obtained from OPTP experiments.

Conclusion

We presented our complex conductivity studies of HBCCO HTS thin films using the THz-TDS and OPTP techniques. THz studies are the volume measurements; thus, they are insensitive to the sample roughness or granularity, which are much smaller in size compared to the THz radiation wavelength. The latter is important in the case of our *ex-situ*-grown HBCCO films, which have a rough surface and are to some extent multi-phased specimens. From the transient THz transmission measurements, one observed that $\Delta\sigma_{re}$ shows a peak below T_c, which shifts to lower temperatures with lower frequencies. At the same time, $\Delta\sigma_{im}$ has a sharp increase below T_c due to the increase in Cooper-pair density and formation of a superconducting condensate. Both findings are in general agreement with the complex conductivity model for low-energy excitations (far below the material's 2Δ) in superconductors. The time-resolved quasiparticle relaxation of HBCCO, measured directly by the OPTP techniques, exhibits an intrinsic single-picosecond dynamics with no phonon bottleneck, or a substantial bolometric signal plateau, which is a unique feature among both LT and HT nonequilibrium superconductors, and makes this material very promising for ultrafast photodetector applications.

REFERENCES

1. See, e.g., M. Tinkham, *Introduction to Superconductivity*, 2nd ed., International Series in Pure and Applied Physics (McGraw-Hill, New York, 1996), pp. 108–381.

2. C. W. Chu, Chin. J. Phys. **34**, 166 (1996).

3. R. D. Averitt *et al.*, J. Opt. Soc. Am. B **17**, 327 (2000).

4. Š. Chromik, M. Valeriánová, V. Štrbík, Š. Gaži, P. Odier, X. Li, Y. Xu, R. Sobolewski, F. Hanic, G. Plesch, and Beňačka, Appl. Surf. Sci. **254**, 3638 (2008).

5. P. D. Cunningham and L. M. Hayden, J. Phys. Chem. **112**, 7928 (2008).

6. Z. M. Zhang *et al.*, J. Opt. Soc. Am. B **11**, 2252 (1994).

7. T.-R. Tsai, C.-C. Chi, and S.-F. Horng, Physica C **391**, 281 (2003).

8. L. Duvillaret, F. Garet, and J.-L. Coutaz, IEEE J. Sel. Top. Quantum Electron. **2**, 739 (1996).

9. A. Rothwarf and B. N. Taylor, Phys. Rev. Lett. **19**, 27 (1967).

10. X. Li, Y. Xu, Š. Chromik, V. Štrbík, P. Odier, D. De Barros, and R. Sobolewski, IEEE Trans. Appl. Supercond. **15**, 622 (2005).

LLE's Summer High School Research Program

During the summer of 2008, 15 students from Rochester-area high schools participated in the Laboratory for Laser Energetics' Summer High School Research Program. The goal of this program is to excite a group of high school students about careers in the areas of science and technology by exposing them to research in a state-of-the-art environment. Too often, students are exposed to "research" only through classroom laboratories, which have prescribed procedures and predictable results. In LLE's summer program, the students experience many of the trials, tribulations, and rewards of scientific research. By participating in research in a real environment, the students often become more excited about careers in science and technology. In addition, LLE gains from the contributions of the many highly talented students who are attracted to the program.

The students spent most of their time working on their individual research projects with members of LLE's technical staff. The projects were related to current research activities at LLE and covered a broad range of areas of interest including experimental diagnostic development and analysis, computational modeling of implosion hydrodynamics and radiation physics, database development, materials science, cryogenic target characterization, target vibration analysis, and engineering device development (see Table 116.II).

The students attended weekly seminars on technical topics associated with LLE's research. Topics this year included laser physics, fusion, holography, fiber optics, optical manufacturing, the physics of music, and electronic paper. The students also received safety training, learned how to give scientific presentations, and were introduced to LLE's resources, especially the computational facilities.

The program culminated on 27 August with the "High School Student Summer Research Symposium," at which the students presented the results of their research to an audience including parents, teachers, and LLE staff. The students' written reports will be made available on the LLE Web site and bound into a permanent record of their work that can be cited in scientific publications.

Two hundred and thirty three high school students have now participated in the program since it began in 1989. This year's students were selected from approximately 50 applicants.

At the symposium LLE presented its 12th annual William D. Ryan Inspirational Teacher Award to Ms. Jane Bowdler, a mathematics teacher at Brockport High School. This award is presented to a teacher who motivated one of the participants in LLE's Summer High School Research Program to study science, mathematics, or technology and includes a $1000 cash prize. Teachers are nominated by alumni of the summer program. Ms. Bowdler was nominated by Priya Rajasethupathy, a participant in the 2000 Summer Program. Priya recognized Ms. Bowdler as an exceptional teacher who inspired and nurtured her intellectual curiosities: "She is able to bring structure into a classroom and make a difficult subject more manageable… She understands her students and their needs and is able to provide individualized attention… She goes beyond the call of duty by leading the math club and constantly innovating ways to recruit students and sustain their interest in math… Her unbounded patience toward students is one of her unique qualities." Mr. Glen Levandowski, principal of Brockport High School, added: "Her knowledge of math is outstanding and she has the ability to make it interesting and fun to all students, even those who may not generally favor the subject. Overall, Jane is an outstanding educator and serves as a wonderful role model for her students."

Table 116.II: High School Students and Projects—Summer 2008.

Name	High School	Supervisor	Project Title
Jay Amin	Rush-Henrietta	C. Dorrer	Development of an Optical Pulse Characterization Device Based on Spectral Shearing Interferometry
Chris Baldwin	Honeyoye Falls-Lima	R. W. Kidder	Exploring Metadata for Laser Diagnostics and Control Systems
Husain Bawany	Brighton	R. Janezic	Development of the Cryogenic Target Information System
Krysta Boccuzzi	Mercy	E. Kowaluk	Investigation of the Causes of and Possible Remedies for Damage to Sensors Used on the OMEGA Laser System
David Brummond	Honeyoye Falls-Lima	C. Stoeckl	Controlling a PC-Based Data Acquisition System with Java
Nicholas Hensel	Fairport	D. Jacobs-Perkins	High-Speed Measurements of Target-Support Vibrations Using Linescan Cameras
Rachel Kurchin	Harley	R. S. Craxton, M. D. Wittman	Characterization of a Cryogenic Target in a Transparent Cylindrical Hohlraum
Alexis Kurmis	Greece Arcadia	T. C. Sangster, T. Duffy	Counting System for the Carbon Activation Diagnostic
Mangala Patil	Pittsford Mendon	K. L. Marshall	Contamination-Resistant Sol-Gel AR Coatings by Vapor-Phase Silylation
Angela Ryck	Fairport	R. S. Craxton	Optimization of Cone-in-Shell Implosions
Collin Sowinski	Penfield	W. T. Shmayda	Minimization of the Tritium Contamination of Surfaces
Jack Stokes	Fairport	S. Ingraham, D. J. Lonobile	Investigation of Brushless dc Motor Commutation Techniques
James Tsay	Phillips	R. Epstein	K-Shell Emission-Line Backlighter Source Optimization
Brian Wang	Webster Thomas	J. F. Myatt, P. Jaanimagi	The Effects of Space Charge on Electron Pulse Broadening in Streak Cameras
Bradley Wideman	Fairport	F. J. Marshall	Automated Determination of Crystal Reflectivity in the X-Ray Laboratory

FY08 Laser Facility Report

OMEGA Laser Facility

During FY08 the OMEGA Laser Facility conducted 1169 target shots on OMEGA and 85 target shots on OMEGA EP for a variety of users (see Table 116.III). A total of 50 D_2 and 8 DT low-adiabat cryogenic target implosions were performed. Double- and triple-picket pulse-shaping developments highlighted the ongoing development of direct-drive cryogenic implosion capability. The OMEGA Availability and Experimental Effectiveness averages for FY08 were 91.3% and 96.1%, respectively. Highlights of other achievements for FY08 include the following:

Pulse-shaping capability has evolved to meet the demands of producing double- and triple-picket shaped pulses for cryogenic experiments (see Fig. 116.54). The picket-generation hardware has been upgraded to allow for the creation and independent timing/amplitude control of three picket channels. Pulse-shape measurement diagnostics and analysis software have also become more sophisticated to accurately predict picket energies and UV pulse shapes.

A new harmonic energy detector (HED) system was designed and installed to replace the legacy system that was based on aging CCD technology and controlled by dated software.
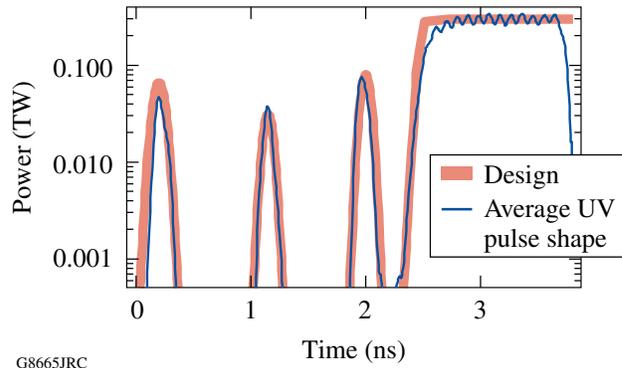

Figure 116.54
OMEGA average pulse shape from cryogenic target implosions (shot 53066) using pulse shape SG3801T.

The Fiducial Laser System has been upgraded to solid-state, diode-pumped regenerative amplifier technology with increased capacity for fiducial signal outputs. This upgrade improves fiducial pulse stability, provides greater reliability, and requires less maintenance than the dated technology that it replaced. Additionally, the fourth-harmonic UV fiducial repetition rate increased from once every 10 min to rates as high as 0.1 Hz, resulting in more-efficient timing of experimental diagnostics.

Table 116.III: The OMEGA target shot summary for FY08.

Laboratory	Planned Number of Target Shots	Actual Number of Target Shots	IDI NIC	DDI NIC	Total NIC	Non-NIC
LLE	607	600	145	409	554	46
LLNL	221	237	117	0	117	120
NLUF	114	125	0	0	0	125
LANL	85	85	22	0	22	63
LBS	50	51	0	0	0	51
CEA	35	39	0	0	0	39
AWE	30	32	0	0	0	32
Total	1142	1169	284	409	693	476

All rod amplifier power-conditioning-unit control systems were upgraded with improved trigger boards. These upgrades mitigate the recently observed increased failure rates associated with the aging control system hardware.

A new Target Viewing System (TVS) was installed on the OMEGA target chamber in June of this year, greatly enhancing target-viewing performance and capability. The new TVS features real-time image processing, up to a 50-mm field of view, up to 2000-frames/s data collection, cryogenic target imaging improvements, remote focus capability, and target detection improvements.

New environmental controls were added to the pulse-generation room (PGR) and the driver electronics room (DER) to improve temperature and humidity stability. The thermal stability improvements resulted in better stability for both the temporal pulse shape and spatial profile.

OMEGA EP Laser Facility
The OMEGA EP Laser Facility completed the integration to target of two short-pulse beamlines and two long-pulse UV beamlines. A total of 85 target shots were taken. Beamline 1 was activated in short-pulse mode to the OMEGA EP target chamber via both the backlighter and sidelighter paths as well as to the OMEGA target chamber. Beamline 2 was activated in short-pulse mode to the OMEGA EP target chamber via the backlighter path and to the OMEGA target chamber.

Beamlines 3 and 4 were activated to the OMEGA EP target chamber in long-pulse UV mode. On 16 September 2008, an OMEGA EP beamline provided greater than 1.3 kJ of infrared light to target in a 10-ps laser pulse. This energy to target is more than a factor of 2 higher than has ever been achieved with a high-energy, short-pulse laser system.

Two additional ten-inch manipulators (TIM's) were commissioned on the OMEGA EP target chamber, bringing the total to three. A suite of initial target diagnostics have been qualified for use, including

- NRL − Dual-Crystal Spectrometer
- LLE − Yaakobi X-Ray Spectrometer
- LLE − Ultrafast X-Ray Streak Camera
- LLE − X-Ray Monitor and Neutron Time-of-Flight Detectors
- LLNL − Proton Film Pack
- CEA − Static Penumbral Imager and Fixed Activation Devices
- LLNL − High-Energy Radiography Imager for OMEGA EP

A NIF preamplifier module (PAM) was installed in the Laser Sources Bay. Preliminary engineering of a 2-D SSD module improvement as well as connection and diagnostic hardware necessary to seed Beamline 4 with the PAM has been accomplished.

National Laser Users' Facility and External Users' Programs

During FY08, a governance plan was implemented to formalize the scheduling of the OMEGA Laser Facility as an NNSA User Facility. Under this plan, OMEGA shots are allocated by campaign. The majority of the FY08 target shots were allocated to the National Ignition Campaign (NIC), and integrated experimental teams from LLNL, LANL, SNL, and LLE conducted a variety of NIC-related experiments primarily at the OMEGA Laser Facility. Shots were also allocated in FY08 to the high-energy-density (HED) physics programs from LLNL and LANL.

Under the governance plan, 25% of the facility shots are allocated to Basic Science experiments. Roughly half of these are dedicated to University Basic Science under the National Laser Users' Facility program, and the remaining shots are allotted to Laboratory Basic Science, comprising peer-reviewed basic science experiments conducted by the national laboratories and LLE/FSC.

The OMEGA Facility is also being used for several campaigns by teams from the Commissariat à l'Énergie Atomique (CEA) of France and AWE of the United Kingdom. These programs are conducted at the facility on the basis of special agreements put in place by DOE/NNSA and the participating institutions.

The external users during this year included six collaborative teams participating in the National Laser Users' Facility (NLUF) program; many collaborative teams from the national laboratories conducting experiments for the National Ignition Campaign (NIC); investigators from LLNL and LANL conducting experiments for HED physics programs; and scientists and engineers from CEA of France and AWE of the United Kingdom.

In this section, we briefly review all the external user activity on OMEGA during FY08, including NLUF programs and experiments conducted by users from LLNL, LANL, CEA, and AWE.

NLUF Program

In FY08, the Department of Energy (DOE) issued a solicitation for NLUF grants for the period of FY09–FY10.

A total of 13 proposals were submitted to DOE for the NLUF FY09–FY10 program. An independent DOE Technical Evaluation Panel comprised of Dr. Steven Batha (LANL), Dr. Gilbert (Rip) Collins (LLNL), Dr. Ramon Leeper (SNL), Prof. Howard Milchberg (University of Maryland), and Prof. Donald Umstadter (University of Nebraska, Lincoln) reviewed the proposals on 18 April 2006 and recommended that 11 of the proposals receive DOE funding and shot time on OMEGA in FY09–FY10. Table 116 IV lists the successful proposals.

FY08 NLUF Experiments

FY08 was the second of a two-year period of performance for the NLUF projects approved for the FY07–FY08 funding and OMEGA shots. Six of these NLUF projects were allotted OMEGA shot time and received a total of 125 shots on OMEGA in FY08. Some of this work is summarized in this section.

Experimental Astrophysics on the OMEGA Laser

Principal Investigator: R. P. Drake (University of Michigan)
Co-investigators: D. Arnett (University of Arizona); T. Plewa (Florida State University); A. Calder (University of Chicago); J. Glimm, Y. Zhang, and D. Swesty (State University of New York–Stony Brook); M. Koenig (LULI, École Polytechnique, France); C. Michaut (Observoratorie de Paris, France); M. Busquet (France); J. P. Knauer and T. R. Boehly (LLE); P. Ricker (University of Illinois); and B. A. Remington, H. F. Robey, J. F. Hansen, A. R. Miles, R. F. Heeter, D. H. Froula, M. J. Edwards, and S. H. Glenzer (LLNL)

The OMEGA laser, with its ability to produce pressures greater than 10 Mbars, can create conditions of very high energy density that are relevant to astrophysical phenomena. This project explores two such issues: the contribution of hydrodynamic instabilities to the structure in supernovae and the dynamics of radiative shock waves. The study of radiative shock dynamics is a continuation of successful campaigns at LLE that have employed x-ray radiography to quantify the average shock velocity and the structure of the dense, shocked matter. Of primary importance to understanding the role played

Table 116.IV: FY09–FY10 NLUF Proposals.

Principal Investigator	Affiliation	Proposal Title
F. Beg	University of California, San Diego	Systematic Study of Fast Electron Transport and Magnetic Collimation in Hot Plasmas
R. P. Drake	University of Michigan	Experimental Astrophysics on the OMEGA Laser
R. Falcone	University of California, Berkeley	Detailed *In-Situ* Diagnostics of Multiple Shocks
U. Feldman	ARTEP, Inc.	EP-Generated X-Ray Source for High Resolution 100–200 keV Point Projection Radiography
Y. Gupta	Washington State University	Ramp Compression Experiments for Measuring Structural Phase Transformation Kinetics on OMEGA
P. Hartigan	Rice University	Dynamics of Shock Waves in Clumpy Media
R. Jeanloz	University of California, Berkeley	Recreating Planetary Core Conditions on OMEGA, Techniques to Produce Dense States of Matter
K. Krushelnick	University of Michigan	Intense Laser Interactions with Low Density Plasmas Using OMEGA EP
R. Mancini	University of Nevada, Reno	Three-Dimensional Studies of Low-Adiabat Direct-Drive Implosions at OMEGA
M. Meyers	University of California, San Diego	Response of BCC Metals to Ultrahigh Strain Rate Compression
R. D. Petrasso	Massachusetts Institute of Technology	Monoenergetic Proton and Alpha Radiography of Laser-Plasma-Generated Fields and of ICF Implosions

by radiation in the shock dynamics is the electron temperature throughout the shocked material. We have used x-ray Thomson scattering to make such temperature measurements.

In the experiment, ten OMEGA laser beams irradiate a Be drive disk with UV light for 1 ns. The beams deposit a total energy of ~3.8 KJ, giving an average irradiance of ~4.8×10^{14} W/cm^2, corresponding to an ablation pressure of ~46 Mbar in the Be drive disk. The enormous pressure first launches shocks and then accelerates the Be material, which in turn drives a shock into a cylinder filled with Ar gas. The shock moves through the Ar with an average velocity of the order of ~150 km/s, which is fast enough that radiative effects play a significant role in the shock dynamics. An additional eight OMEGA laser beams irradiate a Mn foil for 1 ns to create the x rays needed to probe the shocked Ar system. The x rays are scattered through an average angle of 100° before being spectrally resolved by a crystal spectrometer and then detected by a four-strip gated microchannel plate.

Figure 116.55 shows some of the resulting data. The probe for these data was offset from the drive beams by 15 ns, placing the measurement in the precursor region of the shock. Additional measurements were made at different times, cor-

responding to different regions in the shock system. The signal includes two peaks produced by elastic scattering from tightly bound electrons and a broad red-shifted feature expected from


U828JRC
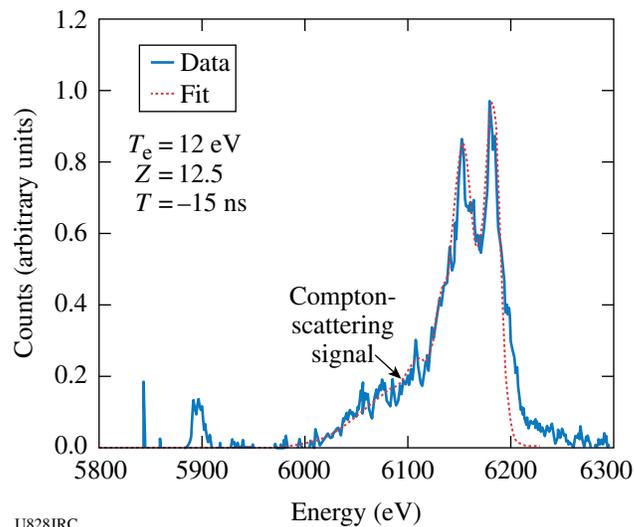
Figure 116.55

Spectrum of x-ray Thomson-scattered light from the precursor region of radiative shock, showing peaks from elastic scattering and a shifted feature from free electrons.

photons that are Compton scattered from the free electrons. By fitting a theoretical line to the observed signal, the electron temperature and average ionization can in principle be deduced. The fit shown is preliminary.

Laboratory Experiments of Supersonic Astrophysical Flows Interacting with Clumpy Environments

Principal Investigator: P. Hartigan (Rice University)
Co-investigators: R. Carver and J. Palmer (Rice University); J. Foster, P. Rosen, and R. Williams (AWE); B. Wilde and M. Douglas (LANL); A. Frank (University of Rochester); and B. Blue (General Atomics)

Strong shock waves occur in many astrophysical systems, and the morphology of the emission lines that occur from the hot gas behind these shocks is often highly clumpy. The objective of this sequence of NLUF experiments is to develop scaled laboratory experiments to study the hydrodynamics of clumpy supersonic flows. The laboratory work complements new astrophysical images from the Hubble Space Telescope (HST) that were motivated by the results of the NLUF program.

Our work in the past year has concentrated first on developing and implementing an experimental design that could follow the destruction of a single clump by the passage of a strong shock and then expanding this work to include two clumps that are close enough that shadowing significantly affects the dynamics of the interactions. A sample of the results from these successful experiments appears in Fig. 116.56. Upper panels (a) and (b) show how a single clump flattens and the bow shock widens as time progresses in the interaction. Remarkably, we have now seen this exact phenomenon in our most-recent image of one of the knots in a Herbig–Haro object (HH 2). The bottom panels show H_α images obtained with HST in 1994, 1997, and 2007. The new bow shock clearly expands as a result of the strong wind that passes from right to left in the figure.

A large complex region of multiple clumps within HH 2 shown in the figure appears to have significant morphological changes. In several cases significant differential motions exist between adjacent clumps, and it now appears that shadowing and merging are probably common in such flows. We see
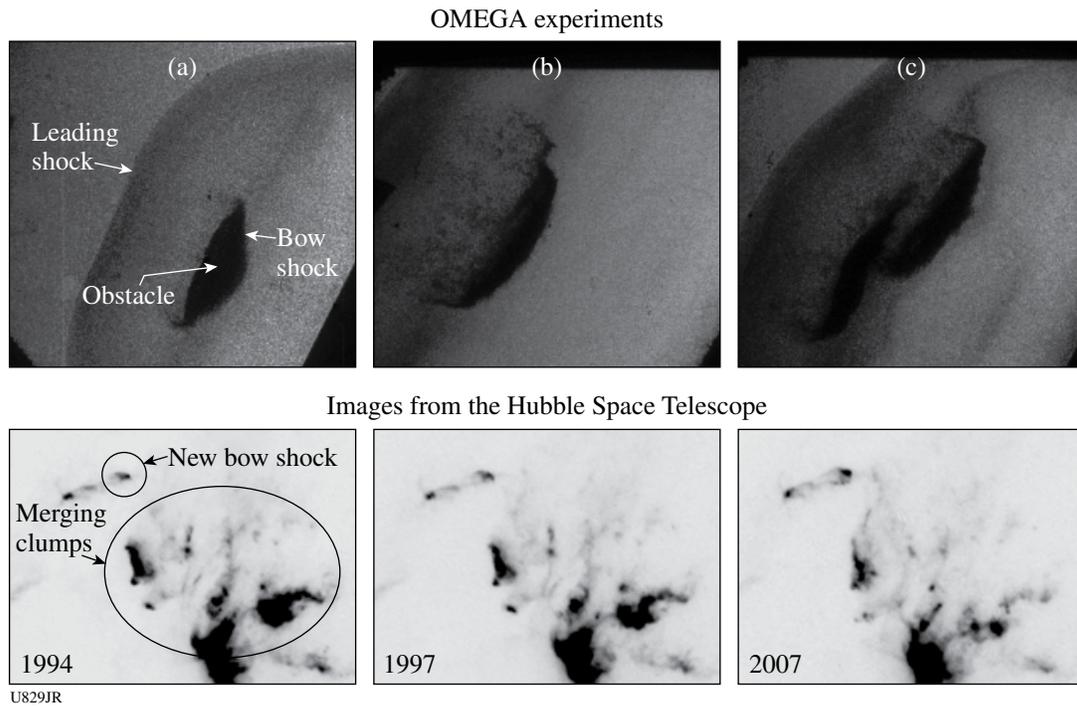

Figure 116.56
OMEGA experiments (top) and three astronomical images (bottom) of shock waves around single and multiple clumps. The experimental images (a) and (b) show how a shock wave flattens and tears apart an obstacle. Analogous behavior has just been observed unambiguously for the first time with a third-epoch Hubble Space Telescope image of shocks in HH 2 (bottom). Note how the new bow shock widens in the most-recent 2007 image. The third experimental image (c) shows how shadowing affects two clumps. Multiple clump interactions also occur in HH 2.

analogous behavior in the laboratory experiment labeled (c) where shadowing effects have created a bumpy bow shock around two closely spaced obstacles in the flow. In the coming year we will be evolving this design to address shocked flow through a medium with dozens of small clumps. Two additional third-epoch HST images will complement the experimental work in the coming year.

Multiview Tomographic Study of OMEGA Direct-Drive-Implosion Experiments

Principal Investigators: R. Mancini (University of Nevada, Reno), R. Tommasini (LLNL)
Co-investigators: N. Izumi (LLNL); I. E. Golovkin, (Prism Computational Sciences); D. A. Haynes and G. A. Kyrala (LANL); and J. A. Delettrez, S. P. Regan, and V. A. Smalyuk (LLE)

The determination of the spatial structure of inertial confinement fusion implosion cores is an important problem of high-energy-density physics. To this end, three identical multimonochromatic x-ray imagers (DDMMI's), designed and built as part of this project, are currently being used in direct-drive OMEGA implosion experiments to perform simultaneous observations along three quasi-orthogonal lines of sight (LOS). The implosions are driven with 60 OMEGA beams using high- and low-adiabat laser pulses, and the targets are gas-filled plastic shells. At the collapse of the implosion, the hot and dense core plasma achieves temperatures in the 1-keV to 2-keV range and electron number densities in the 1×10^{24} cm^{-3} to 3×10^{24} cm^{-3} range. X-ray K-shell line emission from a tracer amount of argon added to the deuterium fuel is a suitable spectroscopy diagnostic for this temperature and density range. In addition, x-ray absorption from a titanium tracer layer embedded in the plastic yields information about the compressed shell.

Core images recorded by DDMMI instruments are formed by a large array of 10-μm-diam pinholes, with an ~100-μm separation between pinholes, and are reflected off a depth-graded WB$_4$C multilayer mirror with an average bilayer thickness of 15 Å. The instrument is equipped with 10-cm-long mirrors that permit the observation of narrowband x-ray images over a 3-keV to 5-keV photon energy range. They have a magnification of 8.5, provide spatial resolution of approximately 10 μm, and record gated (framed) images characteristic of a 50-ps time interval. The broad photon energy range, afforded by the use of long mirrors, covers the K-shell line emission from argon ions as well as the K-shell line absorption from titanium L-shell ions. As an illustration

of the data recorded by DDMMI instruments, Fig. 116.57 displays gated argon Ly$_\beta$ ($1s$ ^2S–$3p$ ^2P, $h\nu$ = 3936 eV) narrowband core images observed simultaneously along three quasi-orthogonal LOS: TIM-3, TIM-4, and TIM-5. These images are taken close to the state of maximum compression of the core. The photon energy range of these narrowband images is given by the (mainly) Stark-broadening widths of the line shape, which for the plasma conditions achieved in these cores is in the 60-eV to 70-eV range. The multiview data recorded with DDMMI instruments make it possible to study the three-dimensional structure of the implosion core. It is interesting to observe the differences in distribution of brightness associated with the Ly$_\beta$ core images along different LOS, which depends on both temperature and density conditions in the core. In addition to differences in intensity distributions, there are differences in shapes: the image observed along TIM-4 is the most-elongated one (i.e., oval of largest eccentricity), while the shapes observed along TIM-3 and TIM-5 are less elongated. Argon Ly$_\alpha$ ($1s$ ^2S–$2p$ ^2P, $h\nu$ = 3320 eV) and He$_\beta$ ($1s^2$ ^1S–$1s3p$ ^1P, $h\nu$ = 3684 eV) images are also recorded, thus providing data that will determine the temperature and density distribution in the core. Several analysis methods initially developed and tested for single LOS data analysis are now being extended to consider the analysis of data simultaneously observed along three LOS for a three-dimensional reconstruction of the spatial structure in the core.


U830JRC
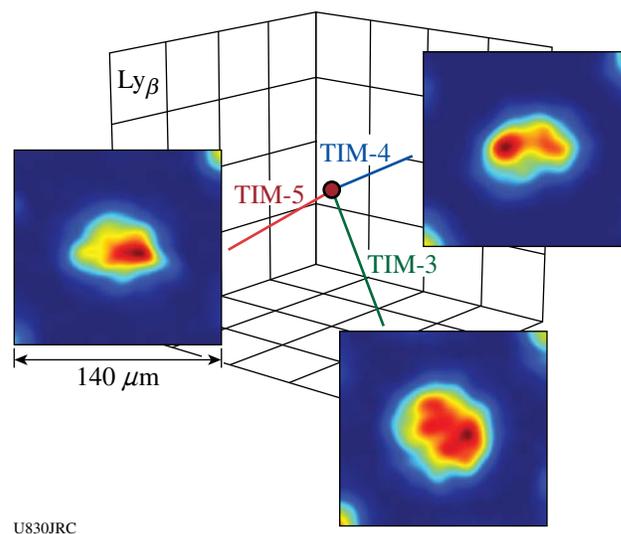
Figure 116.57
Gated argon Ly$_\beta$ narrowband images of the implosion core simultaneously recorded by DDMMI instruments along three quasi-orthogonal lines of sight: TIM-3, TIM-4, and TIM-5 for OMEGA shot 49956.

Monoenergetic Proton Radiography of ICF Implosions

Principal Investigators: R. D. Petrasso and C. K. Li (Massachusetts Institute of Technology)
Co-investigators: F. H. Séguin and J. A. Frenje (MIT); J. P. Knauer and V. A. Smalyuk (LLE); and J. R. Rygg and R. P. J. Town (LLNL)

MIT's NLUF program has continued an ongoing series of experiments using monoenergetic charged-particle radiography in the study of plasmas and transient electromagnetic fields generated by the interactions of OMEGA laser beams with plastic foils and ICF target capsules. This work, involving novel studies of field instabilities, magnetic reconnection, ICF implosion dynamics, and self-generated electromagnetic fields in ICF implosions, has already resulted in many publications, including four in Physical Review Letters[1–4] and one in Science,[5] as well as several invited talks at conferences.[6–9]

Figure 116.58 shows the basic experimental setup for imaging of implosions (see Ref. 10 for more general details of the radiography method). Up to 40 OMEGA laser beams interact with a target capsule, which has a spherical plastic shell with or without a gold cone inserted for "fast-ignition" studies. A radiographic image of the imploded capsule is made by using a special backlighter and a matched imaging detector. The backlighter is a glass-shell ICF capsule filled with D^3He gas and imploded by ~20 OMEGA laser beams, producing D^3He protons (14.7 MeV) and other fusion products. CR-39 nuclear track detectors are used in conjunction with appropriate filters and processing techniques to record individual charged particles and their energies in the detector plane. Since the burn duration of the D^3He implosion is short (~130 ps) relative to the nanosecond-scale duration of the capsule illumination (1 ns) and subsequent evolution, and since the relative timing of the backlighter and
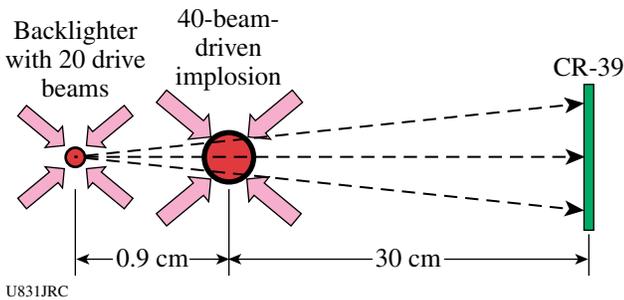
the capsule illumination was adjustable, it is possible to record images at different times during implosions.

The experiments resulted in the discovery and characterization of two distinctly different types of electromagnetic configurations in ICF implosions (Fig. 116.59), as well as the measurement of capsule radius and areal-density (ρR) temporal evolution (Fig. 116.60).[4,5] Proton radiography reveals field structures through deflection of proton trajectories. The two field structures evident in Fig. 116.59 consist of (1) many radial filaments with complex striations and bifurcations, permeating the entire field of view, of magnetic field magnitude 60 T; and (2) a coherent, centrally directed electric field of the order of 10^9 V/m within the capsule, leading to the central concentration of protons in Fig. 116.59(b). Figure 116.60 shows the values of capsule radius and ρR at various times during the implosions of spherical capsules studied in images similar to those in Fig. 116.59.[4] The size was inferred from the spatial structure of the images, while ρR was determined from the energy loss of the imaging protons while passing through the capsule center.
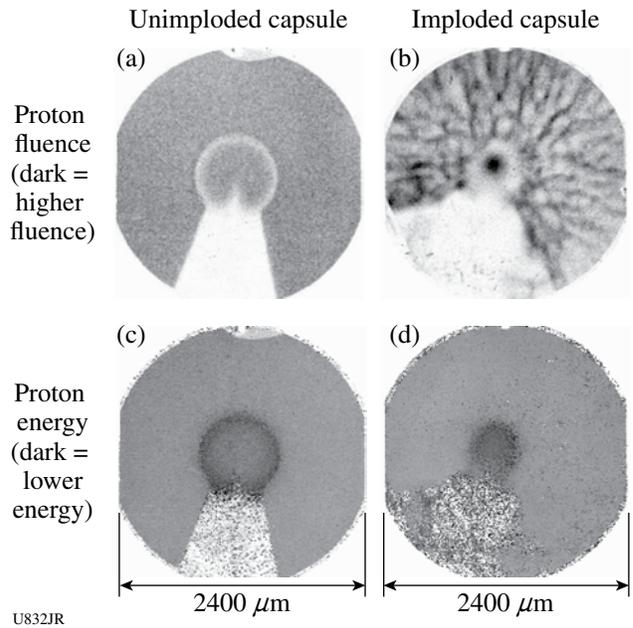
Figure 116.59
Images of a 430-μm-radius spherical CH capsule with attached gold cone, before and during implosion. Images (a) and (c) show the unimploded capsule used in OMEGA shot 46531. Images (b) and (d) show a capsule at 1.56 ns after the onset of the laser drive (shot 46529). In (a) and (b) dark areas correspond to regions of higher proton fluence, while in (c) and (d) dark areas correspond to regions of lower proton energy. The energy image values in the region shadowed by the cone are mostly noise since very few protons were detected in that region.


Figure 116.58
Experimental setup with proton backlighter, subject implosion, CR-39 imaging detector, and laser beams. The subject implosion shown here has a spherical plastic shell, but images were also made with "cone-in-shell" capsules (see Fig. 116.59).
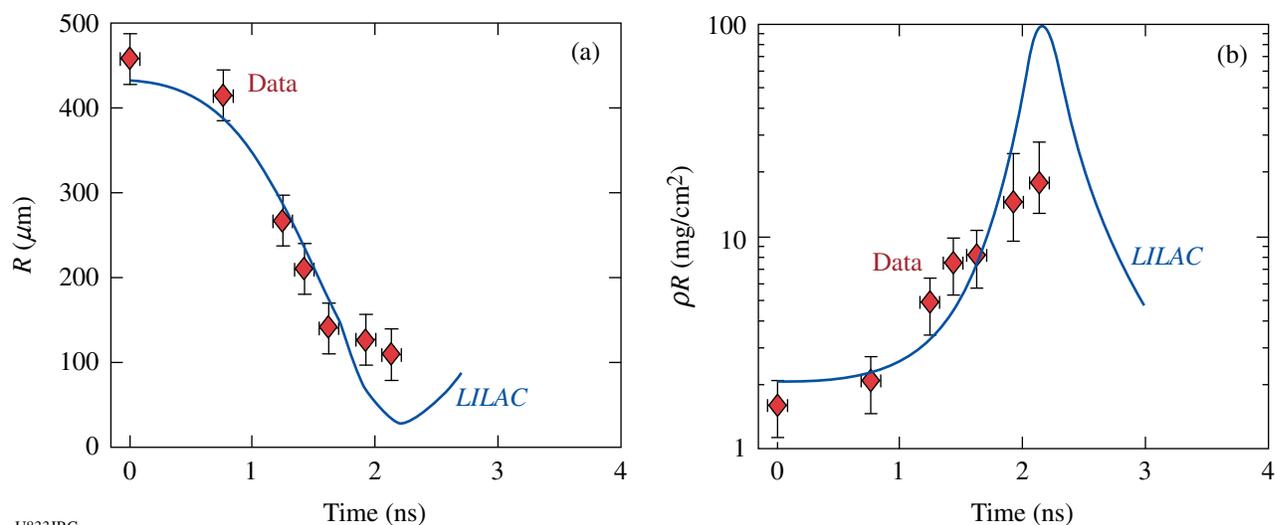
Figure 116.60
Measured capsule radius (a) and ρR (b) as a function of time,[4] from a series of images of spherical implosions (40 drive beams in a 1-ns flat-top pulse). The curves show *LILAC* 1-D simulations.

The relationship of the measured sizes and ρR's to predictions of the 1-D code *LILAC* are also shown.

X-Ray Thomson-Scattering Spectra
in Shock-Compressed Beryllium
Principal Investigators: R. Falcone and H. J. Lee (University of California, Berkeley), P. Neumayer and S. H. Glenzer (LLNL)

Direct measurement of the exact thermodynamic and physical properties of dense matter is of great interest to test dense plasma modeling and to address fundamental physics questions such as the equation of state and the structure of dense matter. Powerful laser-produced x-ray sources have been used to probe dense matter, which has enabled a quantitative *in-situ* diagnostic of densities and temperatures using x-ray Thomson scattering measurements.[11] We have continued x-ray scattering experi-

ments in shock-compressed beryllium to measure the electron temperature and density for varying drive-beam conditions.

Two types of planar targets coupled with Mn backlighters were deployed for the x-ray Thomson-scattering measurements of 25° and 90° scattering angles on the OMEGA laser. A 250-μm-thick beryllium foil was driven by 12 beams smoothed with distributed phase plates (SG-4) overlapped in a ~1-mm-diam focal spot. Laser intensities of 10^{14} W/cm$^2 < I < 10^{15}$ W/cm^2 in a 4-ns-long constant or 5-ns shaped pulse were applied. Radiation-hydrodynamic calculations performed using Helios[12] indicate that under these irradiation conditions, a strong shock wave is launched in the solid target, compressing it homogeneously at pressures in the range of 20 to 60 Mbar. Twelve additional focused beams (~200-μm spot) illuminate a Mn foil to produce ~6.18-keV He$_\alpha$ x rays for 25° scattering (17 backlighter beams are used for 90° scattering). Figures 116.61(a) and 116.61(b)
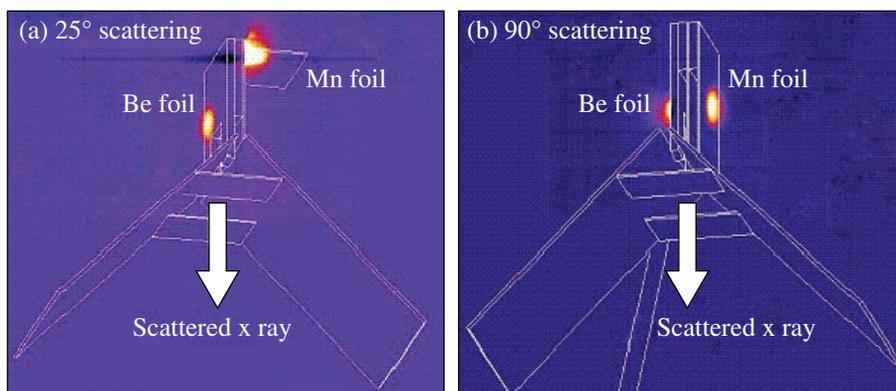
Figure 116.61
Time-integrated images for $E > 2$ keV show the emission produced by heater and probe beams for (a) 25° scattering and (b) 90° scattering.

present time-integrated images showing the emission by drive and backlighter beams. A highly oriented pyrolytic graphite (HOPG) crystal spectrometer coupled to a gated microchannel plate detector in TIM-3 has been used as a spectrometer and a detector. The scattered photon fraction is determined by the product $n_e \sigma_{TS} l$, where σ_{TS} is the Thomson-scattering cross section and l is the length of the scattering volume.

Figures 116.62(a) and 116.62(b) show the scattering spectra (solid lines) and fits (dotted lines) for a 25° and a 90° scattering angle from 4-ns-long constant drive beams, which give a pressure of 30 Mbar. Two small plasmon features in addition to the two elastic peaks from the 6.18-keV Mn He$_\alpha$ line and the 6.15-keV intercombination line are measured at a 25° scattering angle, indicating a collective scattering regime with a scattering parameter $\alpha = 1/k\lambda_s = 1.56$ and λ_s being the screening length and k the scattering vector with

$k = 4\pi (E_0/hc) \sin g(\theta/2) = 1.36$ Å^{-1}. The frequency shift of the plasmon is determined by the frequency of plasma oscillations. Calculated spectra using the theoretical form factor indicate that the solid beryllium is compressed by a factor of 3 with 7×10^{23} cm^{-3} < n_e < 8×10^{23} cm^{-3}.

The Compton-scattering spectrum measured at a scattering angle of $\theta = 90°$ accessing the noncollective scattering regime with $\alpha = 0.5$ and $k = 4.4$ Å^{-1} shows a parabolic spectrum downshifted in energy from the incident radiation by the Compton effect; the shift is determined by the Compton energy $E_C = h^2 k^2/2m_e = 74$ eV. The theoretical fit to the measured spectrum indicates the same densities and temperatures as obtained for collective scattering. Details may be found in Ref. 13.

To generate higher compression, the intensity of nanosecond laser beams was shaped to have (1) a 4-ns-long step-like foot,
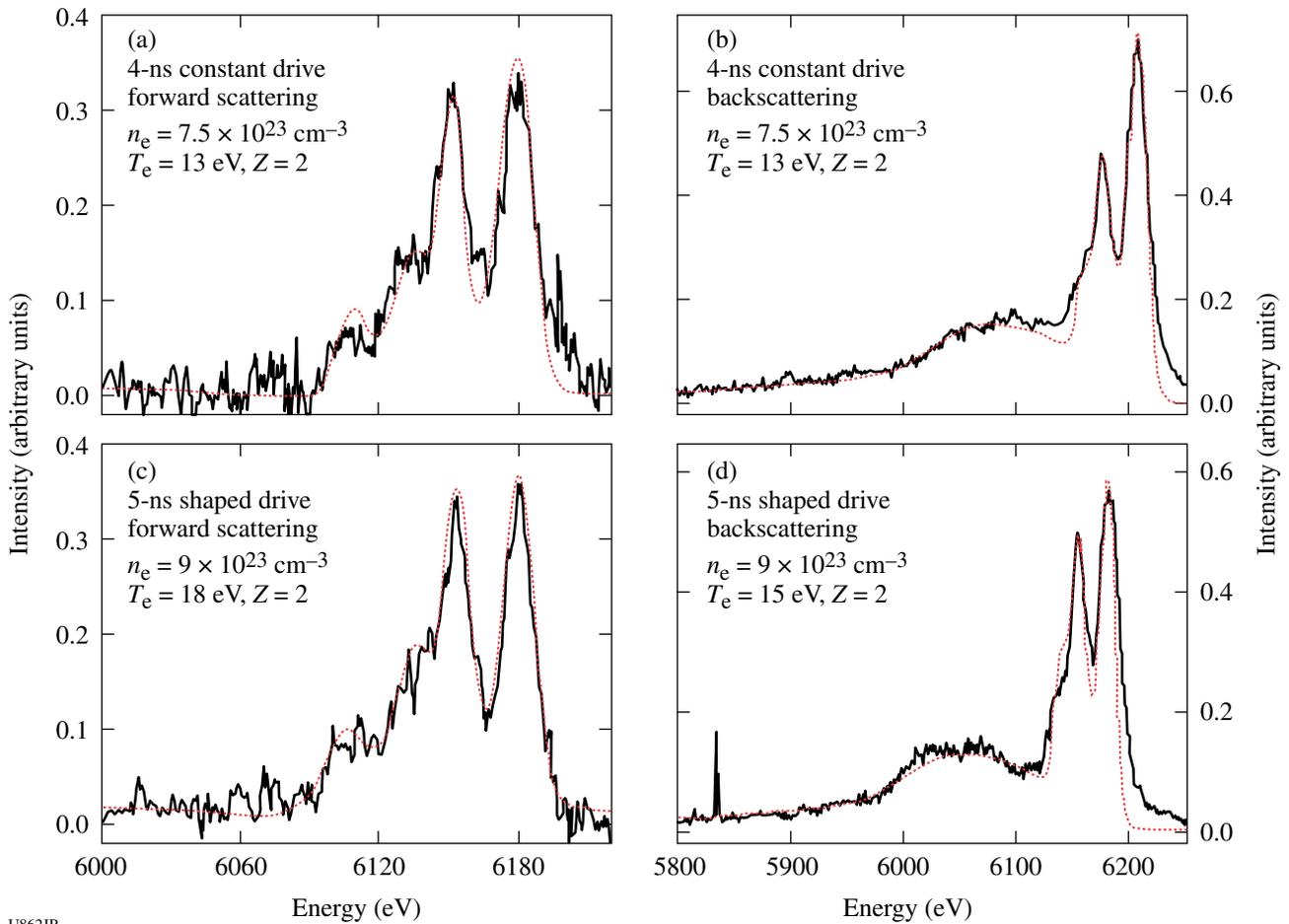

Figure 116.62
X-ray scattering data (solid lines) and fits (dotted lines) of 25° forward scattering [(a) and (c)] and 90° backscattering [(b) and (d)] with different driving beams.

with a 2-ns first foot at 8×10^{13} W/cm^2 and a 2-ns second foot at 1.6×10^{14} W/cm^2 and (2) a 1-ns-long peak at 4.8×10^{14} W/cm^2 following a 4-ns step-like foot. Radiation-hydrodynamic simulations show that the three shock waves from each step merge at about 6 ns after the beginning of drive beams and compress the target by more than a factor of 3.5.

Figures 116.62(c) and 116.62(d) show the experimental scattering spectra (solid lines) at a 25° and a 90° scattering angle and fits (dotted lines) from 5-ns-long shaped drive beams that drive a strong shock reaching ~60 Mbar. The calculated spectrum with $n_e = 9 \times 10^{23}$ cm^{-3}, $T_e = 15$ eV, and $Z = 2$ gives a best fitting to the Compton-scattering data. The parameters from the fit to the data in the collective scattering regime are in good agreement with the ones from the noncollective scattering data within error bars of ±20% in temperature. Theoretical x-ray scattering spectra have been calculated in a random phase approximation for the free-electron feature and density-functional theory for the ion feature.

Through this campaign, we have successively accomplished the measurement of the Compton and plasmon resonance on shock-compressed Be. In addition to the accurate measurement within ±7% in density, we have demonstrated that we can characterize multiply shocked matter by changing the drive pulse shape and intensity. This opens up the possibility of obtaining a compression of $n_e > 1.0 \times 10^{24}$ cm^{-3} by co-propagating and counter-propagating the geometry of driving beams. In future research, the Thomson-scattering method will be used to investigate the equation of state in the multiple-shock-compressed matter.

FY08 LLNL OMEGA Experimental Programs

In FY08, Lawrence Livermore National Laboratory (LLNL) led 238 target shots on the OMEGA Laser System. Approximately half of these experiments were dedicated to the National Ignition Campaign (NIC); the other half were dedicated to supporting the high-energy-density stewardship experiments (HEDSE's).

Objectives of the LLNL-led NIC campaigns on OMEGA included the following:

- *Laser–plasma interaction studies of physical conditions relevant for the National Ignition Facility (NIF) ignition targets*

- *Studies of the x-ray flux originating from the laser entrance hole (LEH) window of a hohlraum, which might impact the performance of a fusion capsule*

- *Characterization of the properties of warm dense matter—specifically radiatively heated Be*

- *Studies of the physical properties of capsules based on Cu-doped Be, high-density carbon, and conventional plastics, including new high-resolution shock-velocimetry measurements*

- *Determining ablator performance during the implosion of NIC-candidate ablators*

- *Experiments to study the physical properties (thermal conductivity) of shocked fusion fuels*

- *High-resolution measurements of velocity nonuniformities created by microscopic perturbations in NIF ablator materials*

- *Demonstration of T_r = 100-eV foot-symmetry tuning using a re-emission sphere*

- *Demonstration of T_r = 100-eV foot-symmetry tuning using a backlit thin-shell capsule*

- *Quantification of x-ray foot preheat caused by laser–window interaction*

The LLNL HEDSE campaigns included the following:

- *Quasi-isentropic [isentropic compression experiment (ICE)] drive used to study material properties such as strength, equation of state, phase, and phase-transition kinetics under high pressure*

- *Development of long-duration, point-apertured, point-projection x-ray backlighters*

- *Development of an experimental platform to study non-local thermodynamic equilibrium (NLTE) physics using direct-drive implosions*

- *Opacity studies of high-temperature plasmas under LTE conditions*

- *Development of multikilovolt x-ray sources using under-dense NLTE plasmas for x-ray source applications*

- *Studies of improved hohlraum heating efficiency using cylindrical hohlraums with foam walls*

- *Laser-driven dynamic-hohlraum (LDDH)-implosion experiments*

- *High-speed hydrodynamic jets for code validation*

1. NIC Experiments

Laser–Plasma Interactions: The laser–plasma interaction experiments continued to emulate the plasma conditions expected along the laser-beam path in inertial confinement fusion designs. An interaction beam (beam 30) aligned along the axis of a gas-filled hohlraum is used to study laser-beam propagation. Figure 116.63 shows the results of laser–plasma interaction experiments that were performed to study the propagation of laser light through high-density $\left(N_e/N_{cr} > 10\%\right)$, millimeter-long, high-temperature ($T_e > 2.5$ keV) plasmas. These results provide limits on the intensity of the inner-cone beams to maintain stimulated Raman scattering (SRS) backscatter below the 5% requirements for ignition on the NIF.

Figure 116.64
Instantaneous SRS reflectivities measured 700 ps after the rise of the heater beams in a 11.5% N_{cr} plasma. Experiments without polarization smoothing (squares) show a threshold (reflectivity of 5%) for SRS at an intensity of 4.5×10^{14} W/cm^2 and a corresponding gain of 11. Adding polarization smoothing increases this threshold to an intensity of 6.8×10^{14} W/cm^2, which corresponds to an SRS gain of 17. *pf3D* simulations performed prior to the experiments are shown (open symbols) and predicted the main results of these experiments. The gains are calculated by post-processing hydrodynamic simulations using *LIP*.

for SRS by a factor of 1.5, which was predicted by *pf3D* code simulations completed prior to these experiments.

Prior work on stimulated Brillouin scattering (SBS) mitigation was documented and published in Refs. 14 and 15.

X-Ray Preheat from an LEH Window: The NIF ignition hohlraum was gas filled with polyimide windows over the laser entrance holes. During the early part of the laser pulse, the beams had to burn through the windows and fill-gas before reaching the hohlraum walls. As a result, the x rays generated during window burnthrough occured ~300 ps before the hohlraum x rays. There was concern that the resultant early deposition of energy at the capsule poles could have generated an asymmetric pressure wave, or that asymmetric preheat could have seeded instabilities in crystalline Be. Initial *LASNEX* calculations predicted that x-ray production would not be high enough to significantly perturb the capsule, but an extrapolation of existing experimental data suggested that *LASNEX* might have underestimated the flux from the windows. A short series of OMEGA shots were carried out to measure the absolute x-ray spectrum generated during burnthrough of polyimide windows of various thicknesses, and


Figure 116.63
Measured time-integrated backscatter as a function of density in a high-temperature millimeter-long plasma at three interaction-beam intensities: 10×10^{14} W/cm^2 (squares), 5×10^{14} W/cm^2 (diamonds), and 2.5×10^{14} W/cm^2 (circles). For densities above 10%, the backscatter is dominated by stimulated Raman scattering (SRS); the measured time-integrated stimulated Brillouin scattering (SBS) is less than 1%.

These experiments also quantified the effect of polarization smoothing in high-density plasmas where SRS dominates, providing further guidance for the design of a low-backscatter, indirect-drive ICF experiment. Figure 116.64 shows that adding polarization smoothing increases the intensity threshold

the inner- to outer-beam cone delay and intensities spanning those expected to be used on the NIF. The primary diagnostic on these shots was the Dante x-ray diode array.

Figure 116.65 shows the measured flux from Channel 5 (centered from 600 to 800 eV) for a series of five shots, together with *LASNEX* simulations for each shot. The results showed that in all cases the measured flux integrated over the first nanosecond was ~2× lower than predicted by *LASNEX*. The x-ray flux scaled as expected—approximately linearly with window thickness.

Channel 5

355:862 TW/cm   200 ps
355:862 TW/cm^2 400 ps
355:862 TW/cm^2 0 ps
507:1014 TW/cm^2 200 ps
507:1014 TW/cm^2 600 ps

LASNEX simulations

1.5-μm-thick foil

Dante data

Solid = data
Dashed = sim.

U869JRC
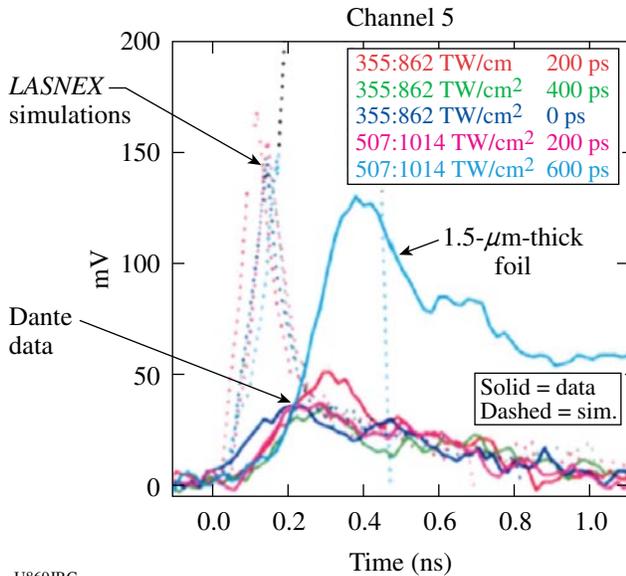
Figure 116.65
A measured signal from Dante Channel 5 for the window preheat shots. The legend shows an intensity of cone-1 beams in TW/cm^2 (first number), cone-2 intensity (second number), and the delay between beams (third number). The indicated curve depicts a 1.5-μm-thick foil; all others have 0.5-μm thickness.

Since no adverse effect was expected on the capsule even with nominal x-ray production, the low measured x-ray flux indicated that the ignition point design was robust to perturbations imposed on the capsule during window burnthrough.

Symmetry Diagnosis by a Re-emission Sphere: The NIC proposes to set the first 2 ns of hohlraum radiation symmetry by observing the instantaneous soft x-ray re-emission pattern from a high-Z sphere in place of the ignition capsule.[16] To assess this technique under NIC conditions, we used the OMEGA Laser Facility to image the re-emission of Bi-coated spheres with 200-ps temporal, 50- to 100-μm spatial, and 30% spectral resolution. The sphere was driven by 70% NIC-scale vacuum Au hohlraums heated to $T_r = 100$ eV using two cones/side laser-beam illumination (Fig. 116.66). The laser beams smoothed with SG4 phase plates using 1-ns square pulses generated intensities at the hohlraum wall that were similar to the foot of the NIF ignition design.

Good re-emit images were acquired at 100- to 115-eV NIF foot temperatures for both 900- and 1200-eV energy bands (see Fig. 116.67). The re-emission patterns at 900 eV and 1200 eV were consistent with each other, but their sensitivity ratio was greater than expected; this will be confirmed in FY09. We also demonstrated the expected P_2/P_0 dependence to the laser-cone power ratio (Fig. 116.67). The experiments demonstrated the required accuracies of $<5 (7\%)$ P_2/P_0 (P_4/P_0) Legendre mode-flux asymmetry at both 900-eV and 1200-eV re-emission photon energies.

Viewfactor calculations were in agreement with the experimentally measured hohlraum radiation flux and re-emit images when assuming 50% inner-beam and 95% outer-beam coupling


Gated x-ray imager
azimuthal asymmetry

Filter

d = 70/30 μm
pinhole array

Outer beams

Gated x-ray imager
4 MCP strips,
16 images

v = 25 cm

u = 12.5 cm

Inner beams

$M = 2\times$

Dante 37.4°
T_{rad}
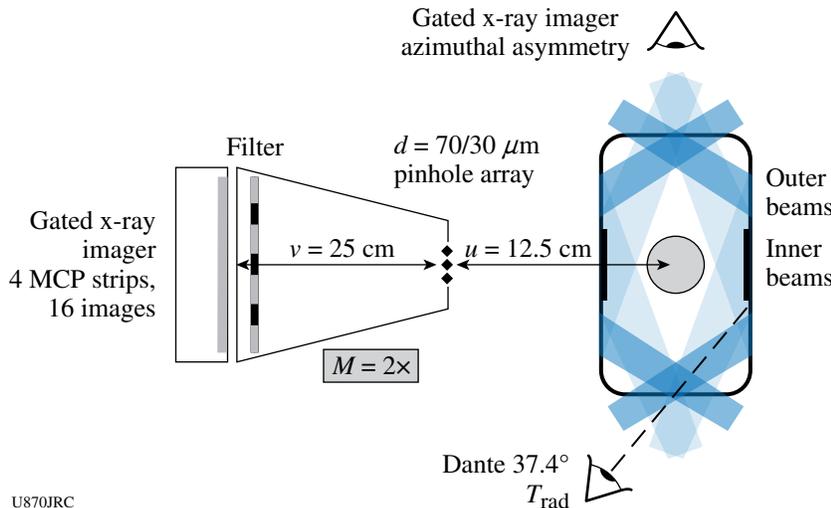
U870JRC

Figure 116.66
The re-emit experimental setup for the NIF and OMEGA.
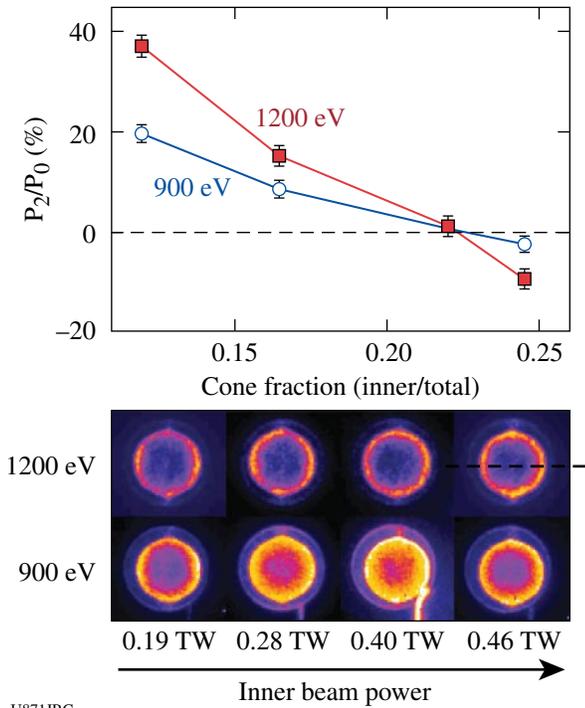
Figure 116.67
Re-emit images measured at 0.8 ns at 900-eV and 1200-eV energy bands for constant 0.28-TW outer-beam power and variable inner-beam power, and the corresponding measured re-emitted P_2/P_0 versus laser-cone power fraction.

Figure 116.68
Simulated viewfactor versus measured re-emit images for different inner-beam powers (outer beams: 0.28 TW/beam).

into x rays at the hohlraum wall (Fig. 116.68). Radiation-hydrodynamic simulations used to design the NIC ignition target confirm the lower inner-beam coupling to within 10%, as do the thin-walled shell experiments described below.

Symmetry Diagnosis by Thin Shell: Should it prove necessary to further optimize the symmetry during the second and third shocks to obtain maximum yield, the shape of a thin-shell capsule in flight can be measured during this time period by x-ray backlit imaging. The thin shell will be made of the ignition ablator mate-

rial with its thickness adjusted to optimize its sensitivity to drive at different times during the foot of the pulse. Recent experiments at the OMEGA Laser Facility demonstrated the viability of area backlit images of 0.6-scale Be capsules doped with 2% Cu under NIC foot conditions by using a 1-ns pulse shape for both drive and backlighter beams, as shown in Fig. 116.69.

To determine the drive symmetry during the foot of the pulse, a scale-0.6 hohlraum was illuminated with a 1.0-ns pulse, giving a drive peaking at 125 eV early in time. Sixteen high-precision images of the converged shell were then recorded on each shot with a 4.7-keV (Ti) foil backlighter, at times between 6.6 and 7.4 ns; an example is shown in Fig. 116.70.

The sensitivity of the measured P_2 distortions to changes in the fraction of the power in the inner and outer cones of beams confirmed the predictions of simulations, as shown in Fig. 116.71, albeit with an offset consistent with 10% less inner-cone absorption than predicted by this simulation. The
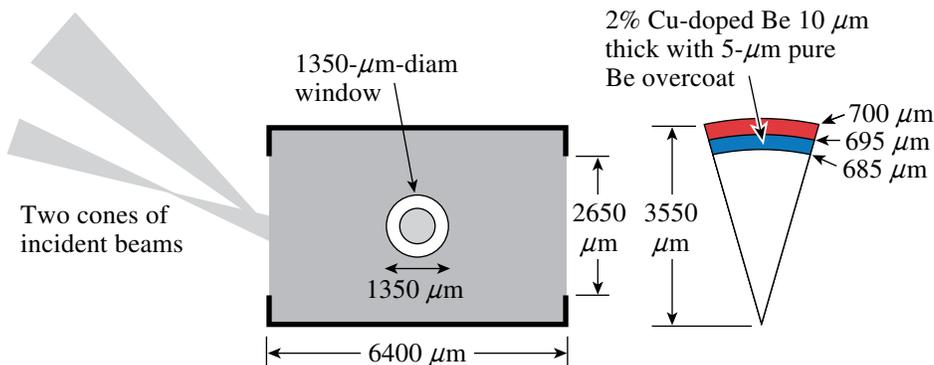

Figure 116.69
Schematic of the scale-0.6 NIC hohlraum and thin-shell capsule used on OMEGA to validate the plans to control the drive symmetry during the foot of the ignition pulse where $T_r \gtrsim 100$ eV. The obtained backlit images demonstrated that the measured ball distortion has the expected sensitivity to the $\ell = 2$ component of the drive and can measure the Legendre moments to the needed precision.
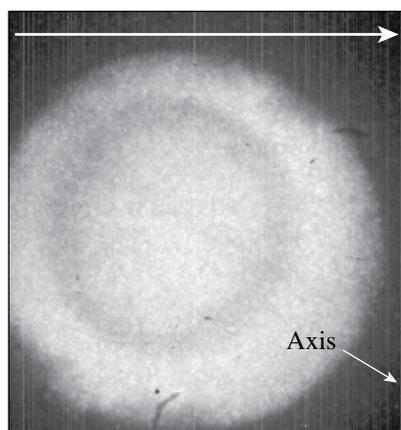
U874JR

Figure 116.70
Image of a thin shell converged to half its initial radius by a 125-eV x-ray drive in the NIC-like hohlraum.
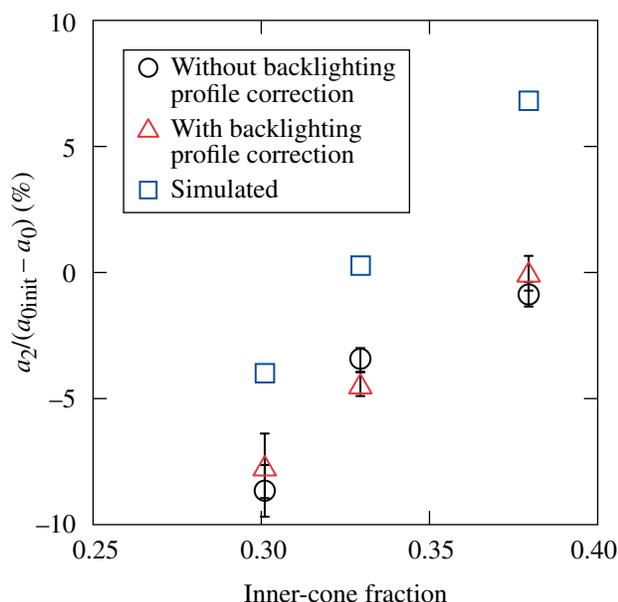

U875JRC

Figure 116.71
Measured versus simulated thin-shell P_2 relative to distance traveled versus cone fraction.

results verified that the overall measurement accuracy ($\pm 1\%$ in P_2, extrapolating to $\pm 0.3\%$ at full NIC scale and larger distance traveled) is sufficient to meet the $\pm 0.5\%$ P_2 requirement for foot symmetry control in the NIC.[17]

X-Ray Thomson Scattering (XRTS) Conductivity: The ultimate goal of this campaign was to measure the plasmon broadening in collective x-ray Thomson scattering (XRTS) to extract the plasma collisionality and, therefore, conductivity,

which is important to accurately model capsule performance on the NIF. For this purpose, 250-μm Be foils were driven at 3.5×10^{14} W/cm^2 over a total duration of 3 ns (see Fig. 116.72). From 1-D hydrodynamic simulations (*HELIOS*) we expected shock-compressed electron densities between 6 and 8×10^{23}/cc and electron temperatures in the range of 10 to 15 eV at times ≥ 4.25 ns after the start of the heater pulse at the Be rear surface. The Cl Ly-α line at 2.96 keV was employed to probe the plasma parameters. The scattered signal was dispersed by the GTS HOPG spectrometer in TIM-6 and recorded by XFRC4 coupled to the LLNL charge-coupled device (CCD).
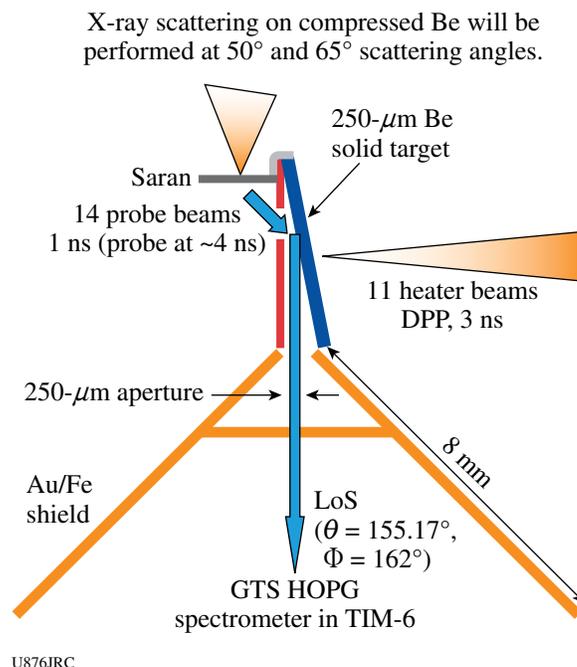

U876JRC

Figure 116.72
Schematic of the experimental configuration.

Figure 116.73 shows both the recorded spectrum from a 50° scattering shot fitted by a synthetically generated spectrum corresponding to a plasma density of $n_e = 1.5 \times 10^{23}$/cc and an electron temperature of 8 eV. We note that the shape of the red-shifted plasmon was sensitive to both n_e and T_e, and that T_e, on its own, was sensitive through detailed balance to the ratio of the blue- to red-shifted plasmon.

The density was $4\times$ to $5\times$ below the values predicted by the hydrodynamic simulations. This suggests that either the shock speed was slower than predicted, leaving an uncompressed, possibly preheated, region probed, or that a low-density blow-off plasma was generated at the back surface, delaying shock breakout. In either case, the 2.96-keV Cl Ly-α radiation was
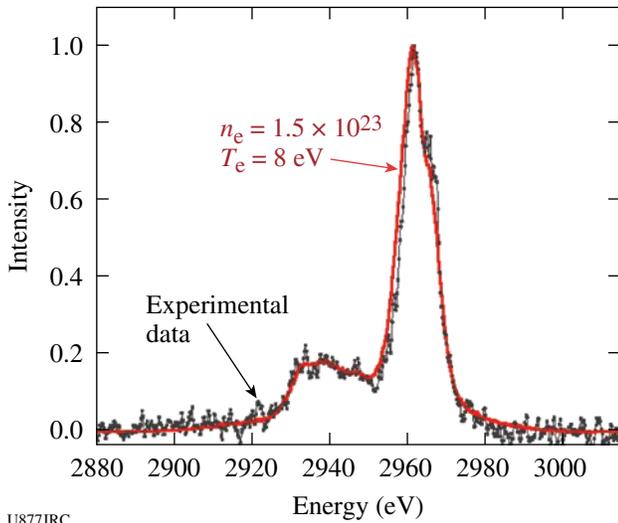
Figure 116.73
Experimental spectrum fitted to synthetic spectrum corresponding to $n_e = 1.5 \times 10^{23}$/cc and $T_e = 8$ eV.

Figure 116.74
Streaked radiograph showing a converging capsule leading up to bang time at 3.3 ns.

unable to penetrate to the shocked region and out of the target again. Future shots will optimize target and probe design.

Convergent Ablation: Determining ablator performance during an implosion was a critical part of the NIF tuning campaign. In particular, it was vital to have accurate, in-flight measurements of the velocity, areal density, and mass of the ablator. In tests on OMEGA, a new technique was developed that achieved time-resolved measurements of all these parameters in a single, area-backlit, streaked radiograph of an indirectly driven capsule (Fig. 116.74). Abel inverting the absorption profile to determine the density profile at each time step accomplished this. Results

showed a clear difference in ablated mass for Cu-doped Be-capsule implosions with different initial shell thicknesses, illustrating that this technique was suitably precise to be used as a remaining mass diagnostic for the NIF tuning campaign.

Deuterium Thermal Conductivity: Multiple shocks reverberating in a thin layer of liquid deuterium made it possible to attain quasi-isentropic compression of deuterium. Simultaneous measurements of velocity, reflectivity, and emissivity were used to investigate the transport properties of compressed deuterium. As seen in Fig. 116.75, the onset of a more highly reflective state at a temperature of 4000 K and pressure of 1.5 Mbar demonstrated a phase transition to a highly conductive, metal-like phase.
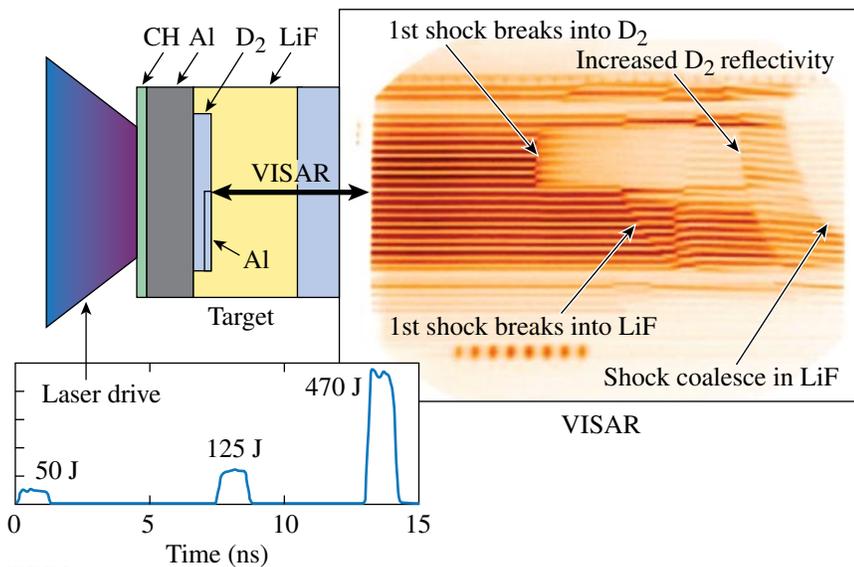
Figure 116.75
Experimental setup and VISAR record of shocked liquid D_2.

Capsule Instability Seeding by Shock Nonuniformity: The CAPSEED campaigns performed measurements of fluid-velocity nonuniformities created by microscopic perturbations in NIC ablator materials. Begun in FY07 and continued through FY08, these campaigns employed a newly commissioned instrument—the OMEGA high-resolution velocimeter (OHRV)—as the primary diagnostic. During FY08 we carried out a survey of the three candidate NIC ablators: Cu-doped Be, polycrystalline diamond, and Ge-doped CH. In addition, much progress was made on analyzing of the data sets and extracting quantitative results. The experiments in October 2007 focused on microcrystalline diamond samples, Be(Cu) targets with preimposed ripples, and sections of capsule shells made from both types of target. Analysis of the rippled Be(Cu) targets showed good agreement between the measured shock-ripple amplitude and simulations of the time evolution of the ripple perturbation (Fig. 116.76).

A surprising result was finding that the shock-front nonuniformities produced by diamond samples shocked below the melt transition were significantly higher than the nonuniformities produced by the same material shocked into the solid–liquid coexistence region (Fig. 116.77). Further experiments in February studied Be targets shocked into the solid–liquid coexistence region, on polycrystalline diamond samples with nanometer-sized grains and on CH(Ge) targets. A third campaign in

April continued to examine the three ablator candidates, with a particular focus on Be(Cu) flats constructed with the layered Cu-doping scheme that is specified in the NIC point design for Be capsules. Results from these campaigns are being used to assess the different ablator candidates.

2. High-Energy Stewardship Experiments

Material Properties: In FY08, the Materials Strength Experimental Team performed two types of experiments on OMEGA: vanadium Rayleigh–Taylor (VRT) strength measurements and ramped-drive-development experiments that use indirect x-ray illumination from a hohlraum.

The VRT experiment tested models of material strength by measuring the Rayleigh–Taylor (RT) growth factors on accelerated sinusoidally rippled samples of polycrystalline vanadium.[18] When driven, the amplitude of the rippled interface will grow via the RT hydrodynamic instability, with the amount of growth depending on the drive conditions and vanadium material strength at high pressures and strain rates. The amount of growth will be derived from face-on radiographs taken with the laser-driven x-ray backlighter. Our experiments were conducted to confirm the drive and growth-factor measurements of the previous experiments and to understand the results in terms of various material-strength models. The ripple sample had a period of 60 μm with an initial amplitude of

U880JRC
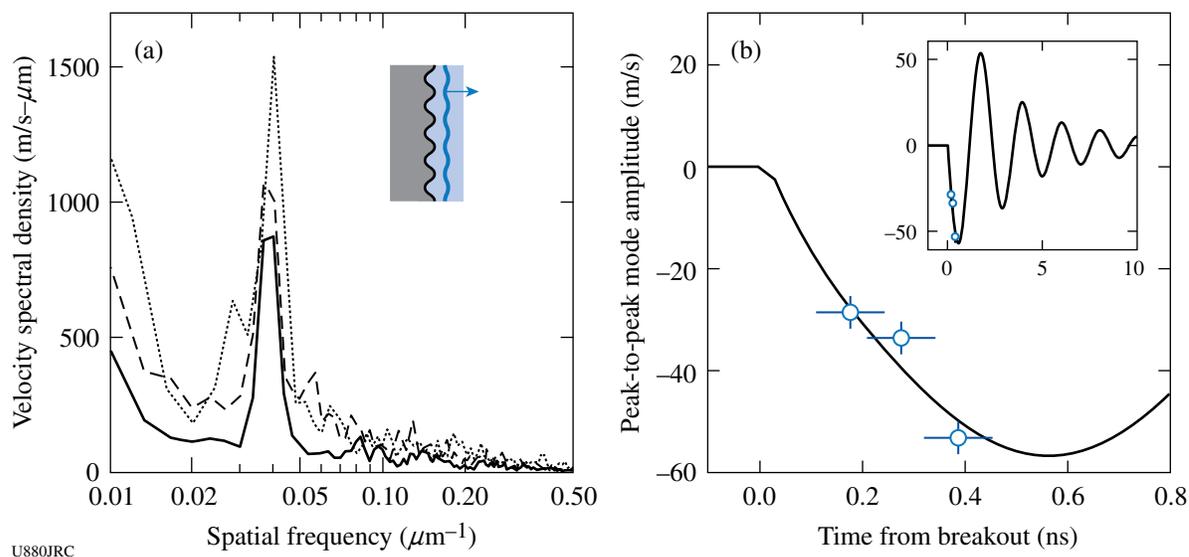
Figure 116.76

(a) Velocity spectra recorded at 180 ps (solid), 280 ps (dashed), and 390 ps (dotted) after shock breakout recorded from targets with a preimposed sinusoidal ripple of 25-μm wavelength and 125-nm initial amplitude at the interface between the Be(Cu) ablator and the PMMA indicator material. The 25-μm ripple mode occupies the spectral peak near a 0.04-μm^{-1} spatial frequency. (b) Velocity amplitude of the isolated ripple modes (symbols) compared to the prediction from a hydrodynamic simulation (curve). Inset: the same data on an expanded time scale.
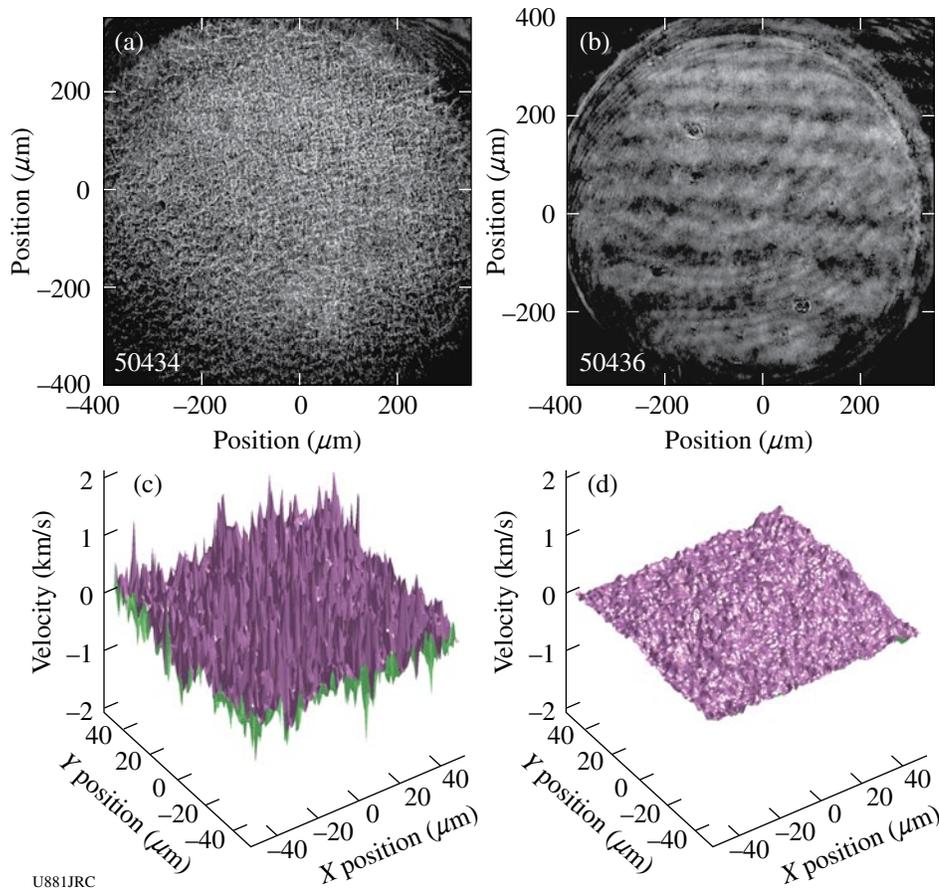
Figure 116.77

Intensity patterns of the probe beam reflected from shock fronts transmitted through polycrystalline diamond samples: (a) at ~300 GPa, which is below the melt, and (b) at ~800 GPa, which is in the solid–liquid coexistence region. Two-dimensional spatial-velocity fluctuations extracted from a $50 \times 50 \ \mu m^2$ region of these datasets are shown in (c) and (d), respectively.

0.6 μm. Figure 116.78 shows a radiograph of the ripples at 70 ns after the start of the drive using a vanadium He-α backlighter (~5.2 keV). From these data, we derived a measured growth factor of 12. Our data were compared with hydro simulations using three different strength models. The models we studied were Steinberg–Guinan (SG), Preston–Tonks–Wallace (PTW), and the new multiscale model that was developed at LLNL by Arsenlis and Becker. Figure 116.79 shows the results. We found that, in all cases, our measurements required modification to the model input parameters. With these modified input parameters, however, all three models were brought into agreement with the measurement. An experimental campaign over several different pressures and strain rates would now be required to distinguish between the models.

We performed three additional experiments that developed isentropic drives using hohlraums to drive a reservoir-gap-sample target package.[19] We employed an extended scale-2.5
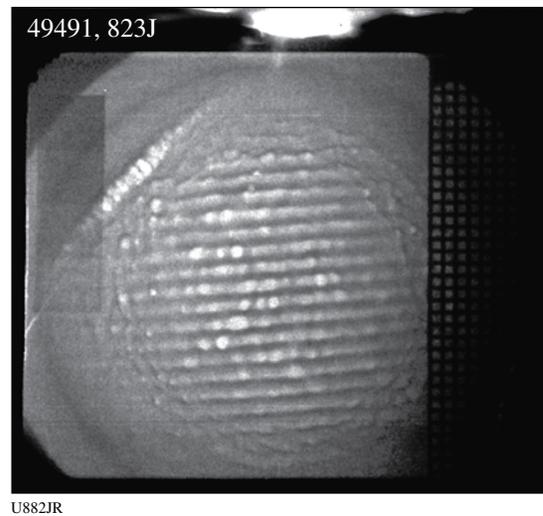

Figure 116.78

Vanadium Rayleigh–Taylor ripple-growth image taken 70 ns after the drive.
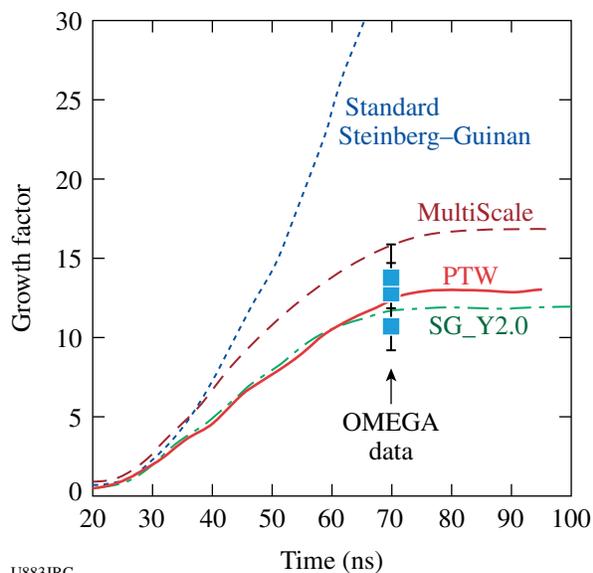
Figure 116.79
Experimental results (solid squares) of the vanadium ripple-growth factor versus the predictions from three different strength models. All models required changes to parameters to fit the data. Experiments at different pressure or strain rates will make it possible to distinguish the differences between the models.

Figure 116.80
A schematic of a quasi-isentropic drive target package mounted on a scale-2.5 hohlraum.

Figure 116.81
A VISAR image of the hohlraum-driven quasi-isentropic drive. The planarity yields resolution better than 150 ps across the 1-mm field of view.

hohlraum (7.0-mm length, 4.0-mm diam; and 2.4-mm-diam LEH) for the first time to create large enough planar regions to drive our samples in a ramp-loading configuration. We used the active shock breakout (ASBO) offset telescope that was specifically designed and commissioned to measure the pressure profile of samples mounted on the equator of the hohlraums. A schematic of our hohlraum package is shown in Fig. 116.80. The reservoir was a 75-μm-thick CH ablator glued to a 200-μm-thick 12% BrCH. An example of the resulting velocity interferometer for any reflector (VISAR) image from this hohlraum is shown in Fig. 116.81. Our measurements showed that the planarity in the measured data yielded resolution better than 150 ps across the entire 1-mm field of view. The peak radiation temperature (T_r) of 130 eV, measured by Dante, agreed well with the simulations. We also observed, however, unexpected second and third pressure rises and a late-time stagnation shock, as shown by the dashed–dotted curves in Fig. 116.82. Since our RT strength experiment requires taking radiographs at late times (>50 ns), these additional pressure waves and shock will cause undesirable increases in the growth factors. Our current understanding of these additional pressure rises is that they are caused by late-time hohlraum radiation, after the laser turns off. The experiments suggest that this late-time radiation (T_r) in the "tail" of the drive is ~15 eV higher than predicted by *LASNEX*.[20] This causes additional late-time ablation pressure, which recompresses the package

and launches additional pressure waves. The strong, late-time shock indicated by the "up" arrows is thought to occur because the ablated plasma from the ablator is flowing into a confined volume (the hohlraum), which fills up with plasma and exerts a back pressure, as opposed to flowing into an infinite vacuum, as modeled by *LASNEX* (solid curve in Fig. 116.82). This is called the stagnation shock. We artificially modified the simulated T_r profile so that it preserved the peak T_r, but increased the late-time T_r profile; the drive profile was roughly reproduced from this experiment.
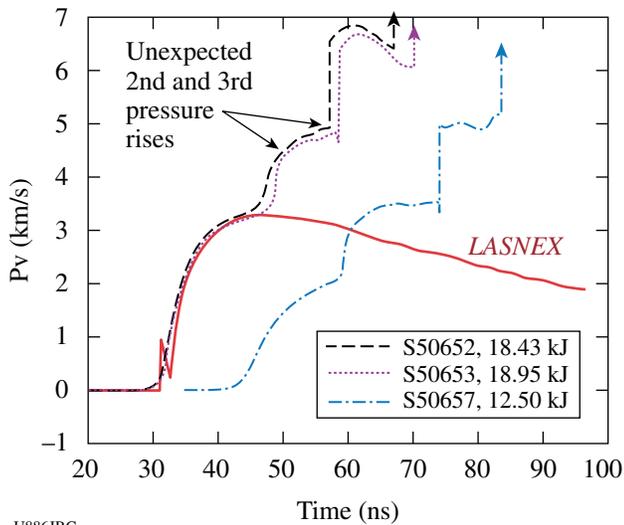
Figure 116.82
Drive profile from the hohlraum-driven ramped drive. The second and third rises are likely caused by late-time T_r that causes additional ablation pressure. We are now investigating the thin-walled hohlraums (<1-μm Au layer) to delay these late-time pushes.

We also tested a reservoir comprised of layers of high-density (1.98 g/cm^3 12% BrCH) to low-density (1.41 g/cm^3 4.3% BrCH) brominated plastic to test if hydrodynamic instabilities at the interfaces in the reservoir caused an unacceptable spatially nonuniform drive. The VISAR results showed that there is no spatial nonuniformity from these layers. We also tested quartz as a possible reservoir material. To reach very high pressure (>10 Mb), a high-density, high-sound-speed material will be needed as a part of the reservoir. These experiments will need to be performed on the NIF, where a high enough temperature can be achieved to generate the required plasma drive on release.

We studied a 500-mg/cm^3 foam layer that will be a part of the reservoir for the 5-Mb Ta strength experiment on the NIF. The low-density foam layers will make it possible for smoother loading of the initial ramp profile, thus mitigating the initial shock that may cause the sample to melt. It was demonstrated that the 500-mg/cm^3 CRF foam properly released into vacuum and did not display any spatial nonuniformity. The shock-breakout times from the foam, the release temperature, and arrival time across the gap matched the *LASNEX* predictions well.

In FY09, drive development will be continued using thin-walled hohlraums designed to lower the late-time T_r (Ref. 21). There are plans to perform Ta RT experiments using OMEGA EP's >20-keV backlighter capability.

Non-LTE Implosions: The goal of the nonlocal thermodynamic equilibrium (NLTE) campaign is to build a platform to study energy balance in implosions by measuring ion, electron, and radiation temperatures as a function of high-Z dopant concentration. In FY08 experiments, 60 beams of OMEGA were used for direct-drive implosions of thin (4-μm) glass capsules filled with 10 atm D^{3}He gas and 0.005 atm Kr gas as a spectroscopic tracer. The relative concentration of DD and ^{3}He was varied during the shots, and some capsules also contained as much as ~0.1 atm Xe. As a time-resolved electron-temperature (T_e) diagnostic, we fielded a mica conical crystal spectrometer coupled to a streak camera and viewed K-shell emission lines from the Kr dopant (see Fig. 116.83). Time-integrated spectra were also recorded with the HENEX spectrometer developed by NIST/NRL. We also fielded the direct-drive multispectral imager (DDMMI) to obtain 2-D images in the light of Li-like Kr lines. An increase in the DD/DT yield ratio with increasing DD concentration was observed, as well as an increase in the ion temperature, inferred from proton and neutron emission-time histories and spectra. The continuum emission spectra recorded from HENEX have been used to infer the time-integrated electron temperatures, which show a temperature decrease with an increase of dopant concentration. We used the time-resolved spectra from the conical crystal spectrometer to study the temporal evolution of the Kr He-β lines. The He-β2/He-β1 line ratio shows a peak in the central 50 ps of the Kr emission. Data analysis and comparison to simulations
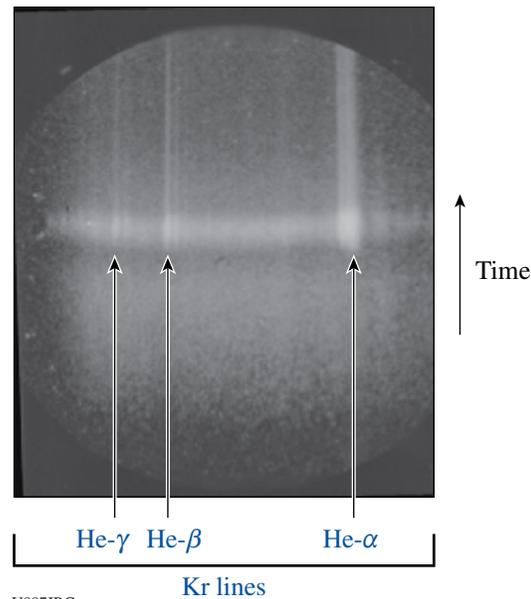
Figure 116.83
Typical time-resolved spectrum from the mica conical crystal spectrometer, for a capsule without Xe dopant.

is ongoing. For the next campaigns, we are building a Johann spectrometer, which will use the Doppler broadening of x-ray lines for measuring ion temperature (T_i), and a new multimonochromatic imager (MMI) designed for narrowband imaging in the 8- to 15-keV spectral region.

Long-Duration Backlighters: The long-duration backlighter campaign successfully demonstrated a pinhole-apertured point-projection backlighter lasting for 8 ns at both the Ni He-α-line energy (7.9 keV) and the Zn He-α-line energy (8.9 keV) (Ref. 22). Experiments on OMEGA used 20 beams with 1-ns square pulse shapes from P_7, with individual beams delayed such that the laser intensity on target was 2.6 to 2.9 × 10^{15} W/cm^2 for 7 ns, and 1.6 × 10^{15} W/cm^2 for an additional 1 ns. Beams irradiated either a zinc or nickel microdot, mounted on a 400-μm-thick high-density carbon substrate, centered over a 20-μm-diam pinhole or a 20-μm × 200-μm slot aperture in a 75-μm-thick tantalum substrate, with the target normal along the P_6–P_7 axis. The resulting x rays imaged a gold grid or wire array at 20× magnification on either a framing camera or streak camera in TIM-4. Diagnostics also monitored the emission spot, x-ray conversion efficiency, backscatter, and hard x-ray production.

Resolution studies on both gated and streaked diagnostics confirmed little-to-no pinhole closure over 8 ns for the nominal target and beam setup, which fired outer-cone beams first. Rearranging beams such that inner-cone beams fired first gave better conversion to x rays, which may have caused the pinhole to close

faster, but gave a dimmer overall signal late in time, resulting in dim images that could not be analyzed for source resolution. Early-time results on those shots showed very little pinhole closure. Figure 116.84 shows a streaked image of a wire array, illuminated with a nickel microdot emitter with a slot-apertured backlighter over 8 ns, and a lineout in time of the signal. Notice the signal varies some as beams turn on and off over the 8 ns. The laser intensity on target is relatively constant over the image, but beams closer to normal to the target's surface convert better to x rays. This can be seen by comparing the signal level early in time in the image, when 58° beams were on, to late times in the image, when the 21° beams fired.

Additionally, gated tests were done to purposefully cause quick pinhole closure, to match *LASNEX* models of closure time. The standoff distance between the microdot emitter and the pinhole was reduced to 250 μm, which was irradiated with a 3 × 10^{15}-W/cm^2 laser source for 5 ns by 21° and 42° beams. Resolution of grid wires and change in signal level through the pinhole show that the pinhole was closed to a 7±2-μm-diam source in 2.25 ns.

X-Ray-Source Applications: Bright, tunable x-ray sources are necessary for radiography applications, radiation-effects experiments, and as backlighters for high-energy-density experiments. LLNL's x-ray-source development campaign had one full day of shots during which three varieties of a multi-keV x-ray source were shot.[23] The x rays from the laser targets were characterized as a function of different
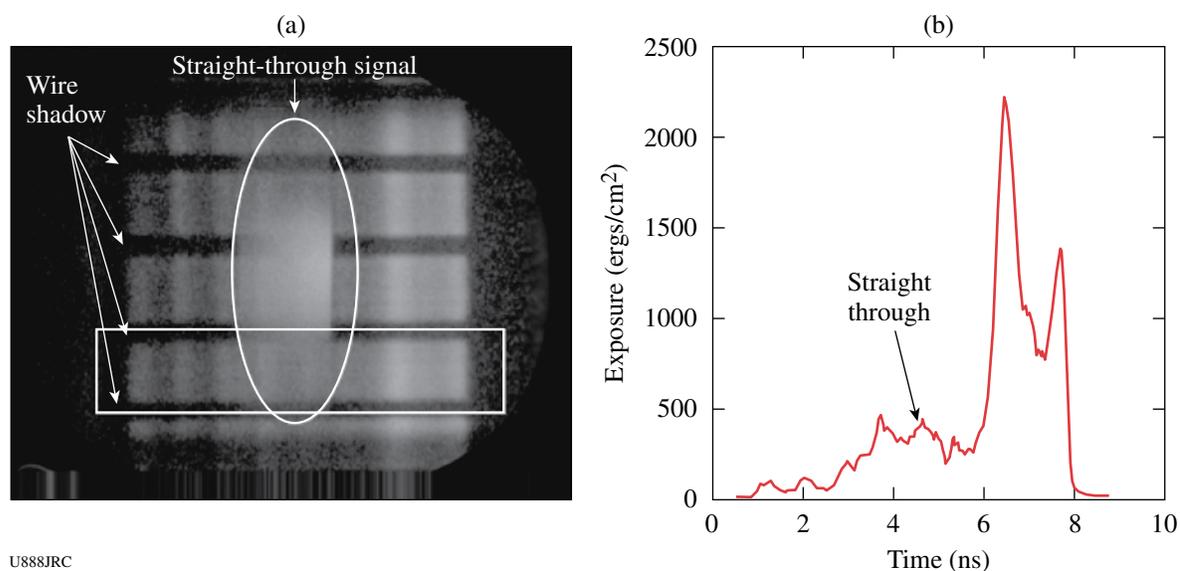

Figure 116.84
A streaked image of a wire array, illuminated with a slot-apertured backlighter over 8 ns with a nickel microdot emitter, and a lineout in time of the signal.

target geometries and volumes. Previous campaigns studied target yield as a function of laser intensity and target-plasma density. The x-ray sources were created by driving (using 20 kJ of laser energy) either ultralow-density (3- to 4-mg/cm^3) Ge-doped (20% atm) SiO_2 aerogels or Ge-foil-lined epoxy (CHNO) cavities. The laser-to-x-ray conversion efficiency in the 10- to 13-keV x-ray band was measured to be between 0.6% and 1.0% and in the 1.0- to 3.5-keV band between 35% and 40%. These shots compared output from aerogel targets that differed by 40% in volume and saw no difference in the measured x-ray yields. X-ray spectra and time-resolved images of the three types of targets are shown in Fig. 116.85. Analysis indicated that the laser-heated volume was the same in both targets, which resulted in the same number of emitting ions in the plasma. Similarly, and surprisingly, the foil-lined cavities produced measured yields, in all spectral bands, that did not differ from those of the aerogel targets. The measured yield for the foil-lined cavity target was consistent with trends observed with previous cavity targets, shot in 2007 by Commissariat à l'Énergie Atomique (CEA) researchers, that produced higher yields and had a better-optimized laser configuration. These experiments were conducted jointly with U.K.'s Atomic Weapons Establishment (AWE) Laboratory, Sandia National Laboratories, France's CEA, and the Department of Defense's (DoD) Missile Defense Agency and Defense Threat Reduction Agency. The x rays from these targets were applied to various test objects and the response was measured.

Dynamic Hohlraums: Earlier experiments showed that laser-driven dynamic hohlraums (LDDH's) emit very bright, spectrally smooth bursts of x rays up to 3.5 keV, suitable as broadband backlighters for absorption spectroscopy experiments (Fig. 116.86). These experiments also demonstrated that LDDH's are robust
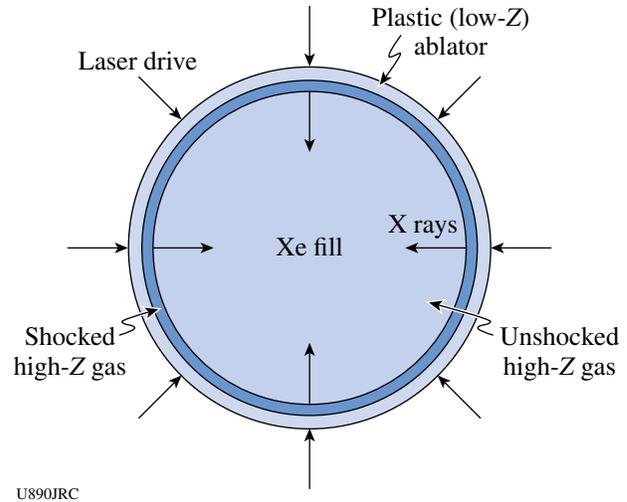
U890JRC

Figure 116.86
Concept of "dynamic hohlraum": shock-heated Xe gas forms a spherically converging shell that traps radiation inside. When the shell stagnates, radiation is released in a bright x-ray flash suitable as a backlighting source for opacity experiments. Data obtained of the converging dynamic hohlraum included x-ray streaked images of the self-emitted x rays, multiple x-ray images, and spectral data.

U889JRC

Figure 116.85
(a) Time-integrated x-ray pinhole-camera images, filtered for x rays above 3 keV, of the large and small aerogel targets shot on the x-ray source development day (8 May). (b) X-ray spectra reconstructed from data measured with the HENWAY spectrometer and the Dante diode array. Across the whole range shown, 35% to 45% of laser energy is converted into x rays.
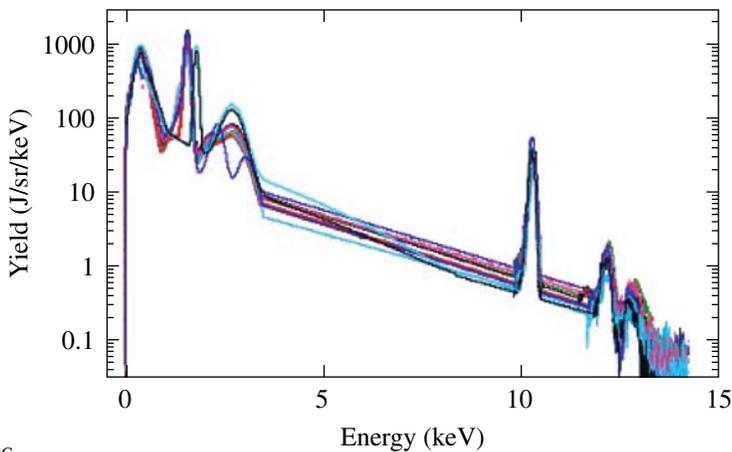
to the polar (nonspherically symmetric) laser configuration that will be used on the NIF as a continuum source backlighter. During FY08, these two aspects of LDDH's were combined in an experiment where a Xe-filled LDDH without an inner shell was driven by laser beams in a polar configuration and was used as a backlighter for absorption spectroscopy of heated Fe samples.[24] It was found that the LDDH emits a strong, 200-ps-long x-ray flash that is spectrally smooth from 4.5 keV to ~9 keV, enabling a significant expansion of the spectral range for future OMEGA and NIF opacity experiments. This year's LDDH experiments also completed a series of shots where capsules were filled with neopentane rather than xenon. These shots were experimentally difficult as the gaseous neopentane was near its boiling point just prior to the experiment and condensation had to be avoided. The successful completion of the experiment made it possible to measure the difference in yield and fuel density caused by the hohlraum effect (which is present in "standard" xenon-filled LDDH's but not in neopentane).

High-Speed Jets: The evolution of high-speed jets is an important benchmark for hydrodynamic simulations, e.g., the shape of the front of a jet penetrating into a surrounding medium can be either flat-topped or arrow-shaped, and this must be correctly predicted by simulations. An OMEGA experiment yielded a dramatic increase in the current data set of high-speed-jet images; the evolution of the jet was followed temporally ~2 to 2.5× longer than in previous experiments on OMEGA and in the NIF Early Light campaigns (see Fig. 116.87). A preliminary result from the experiment is the need to model foam material as two fluids in numerical simulations. A new
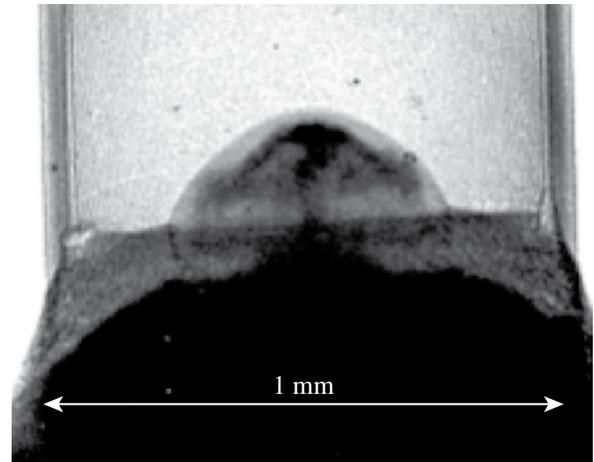
U891JR

Figure 116.87
X-ray radiograph of an aluminum jet driven into a 0.1-g/cm^3 carbon foam. The image is taken 35 ns after the start of the experiment, and the jet has evolved ~2× longer than in previous experiments of this type. The jet structure is clearly visible, as is the location and shape of the bow shock.

two-fluid model for foams is currently under development at LLNL. In the new model, foam is treated both with LEOS (used for undisturbed foam) tables and with an ideal gas (used for foam that has been "reflected" by the shock, i.e., cast out ahead of the shock by shock–foam interaction forces).

Enhanced Efficiency Hohlraums: The hohlraum development campaign investigated the behavior of gold-foam–walled halfraums ($\rho = 400$ mg/cm^3), comparing the flux levels and temperature to solid-gold halfraums.[25] The layout of the foam-walled halfraum is shown in Fig. 116.88. By optimizing the wall
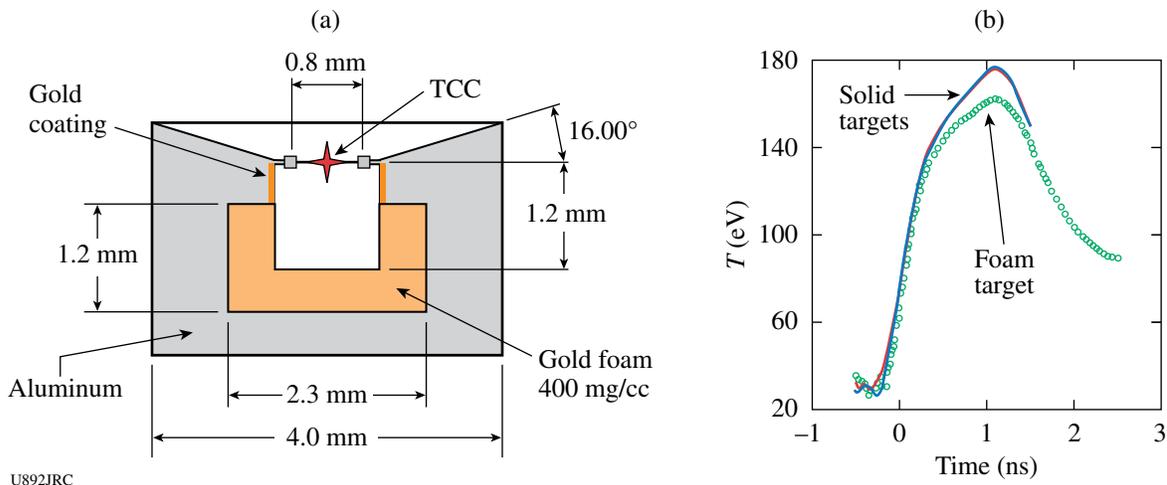
U892JRC

Figure 116.88
(a) Gold-foam–walled halfraum-target schematic. Beams hit a gold-coated plate near the LEH, while the rest of the cavity is lined with 400-mg/cm^3 foam. (b) Temperature as a function of time for two solid-gold targets and one foam target. Although lower-density gold was predicted to optimize target flux and temperature, the foam target had a lower temperature than the solid targets.

density for these hohlraums at temperatures near 200 eV, we expected to see an increase in flux by ~15%. These shots positioned the targets on the Dante axis and used 15 beams from the H16 direction, with the RR1001 reverse-ramp pulse shape and IDI-300 phase plates. Beams hit a 1200-μm-diam gold-coated solid surface near the 800-$\mu$m LEH on the foam targets, which hid the laser spots from the Dante view. The inner foam or solid surface was 1200 μm in diameter and 1200 μm in length. Dante measured flux while a soft x-ray camera in TIM-6 monitored the LEH. Over three shots, two solid targets were compared to one foam target. These shots showed a lower flux in the foam target than in the solid targets, contrary to our predictions [see Fig. 116.88(b)]. We are investigating whether the reverse-ramp pulse shape was the appropriate choice. Remaining targets will be used for future tests.

Opacity: In FY08, LLNL completed the development of a high-temperature laser-opacity platform. Thin-foil samples of co-mixed sodium chloride and titanium, tamped by plastic on all sides, were placed inside hohlraums, and heated to temperatures well above 100 eV in local thermodynamic equilibrium, or LTE, conditions. The samples were then backlit by two different broadband radiation sources. Separate shots used samples of co-mixed tantalum and titanium. The data in Fig. 116.89 show an edge-on view of the sample, backlit by a ten-beam Kr-filled dynamic hohlraum capsule backlighter, which was apertured down to 30 μm in one direction to improve the spatial resolution. The data are spectrally resolved in the horizontal direction using an MSPEC elliptical crystal spectrometer and a gated microchannel-plate detector. This was the first-ever laboratory measurement of a hot sample in the photon energy range above 4 keV. The expansion of the sample was consistent with pre-shot *LASNEX* simulations and established the sample density. The spectrum was well fit by the *VISTA* opacity code, using the known optical path length and measured density, at a temperature of 110±5 eV. Separate, nearly synchronous measurements were obtained in a 250- to 1600-eV spectral band using a variable-spaced grating spectrometer and a second backlighter. The latter data, including both absorption and self-emission spectra from the hot sample, provide detailed information on the sample's opacity in the spectral band contributing to the Rosseland mean opacity, which, in turn, controls the overall radiation flow through such a plasma. By simultaneously characterizing the sample's density, temperature, ionization balance, and Rosseland-band opacity, this new experimental platform makes possible detailed, photon-energy-specific investigations of the process of radiation transport in the hot plasmas found deep inside the sun and other stars.

U893JRC
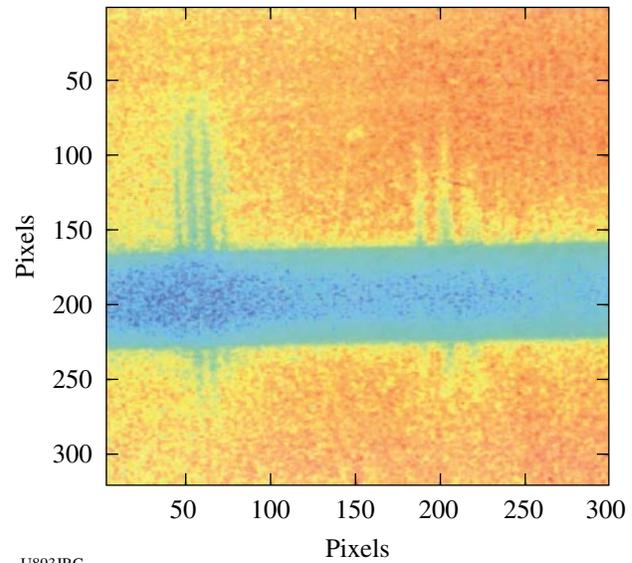
Figure 116.89
Gated space-resolved titanium absorption spectrum for photon energies around 5 keV. The horizontal bar is a gap between two strips on the detector. To the left are $n = 1$ to 2 absorption lines of F-like to C-like Ti. To the right are $n = 1$ to 3 lines of the same ions. The spatial expansion of the sample is determined by the vertical extent of the lines.

FY08 LANL OMEGA Experimental Programs

During FY08 Los Alamos National Laboratory (LANL) successfully fielded a range of experiments on OMEGA to study the physics relevant to inertial confinement fusion (ICF) and high-energy-density laboratory plasmas (HEDLP) in support of the national program. LANL conducted a total of 85 target shots on OMEGA. Collaborations with LLNL, LLE, MIT, and AWE remain an important component of LANL's program on OMEGA.

AGEX-EOS: The AGEX-EOS-09 campaign studies the role that radiative preheating plays in the Richtmyer–Meshkov mixing of a large-Atwood-number interface. The experiment uses a variant of the off-Hugoniot platform to produce a heated interface that is subsequently shocked. The resulting interface evolution is imaged radiographically.

The new platform, first tested in September 2008, employs an independently controlled shock and heating drive as well as a point-aperture pinhole backlighter configuration. The primary objectives for the September campaign were to exercise this new platform under every permutation of drive, identify sources of noise, and demonstrate the imaging viability of the experiment.

Figure 116.90 shows the target geometry and preliminary data obtained from shot 52215. The data clearly show the posi-

tion of the heated and shocked Teflon interface as well as the positions of the main and preheat-side shocks at 25 ns. Drawing from the success of September's experiment, a number of imaging improvements have been initiated, giving us high confidence for the physics experiments planned in February 2009.
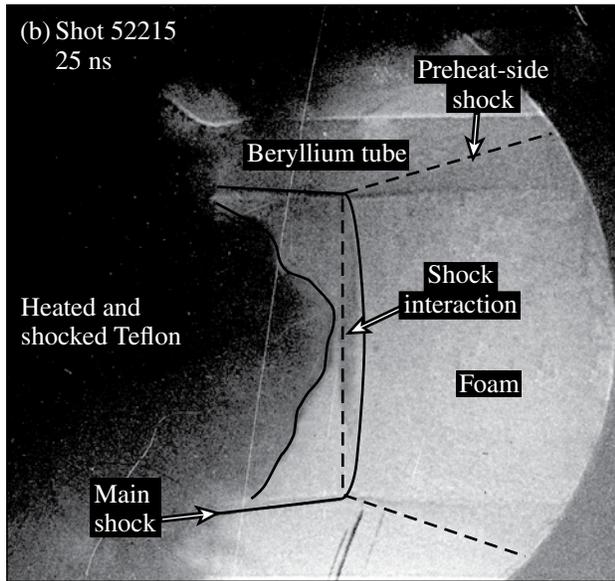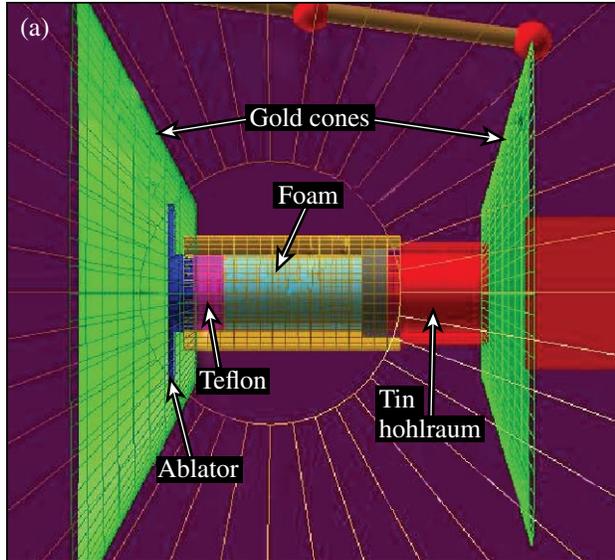

Figure 116.90
Overview of the (a) AGEX-EOS-09 target and the preliminary data from (b) shot 52215.

DTRat: In August 2008, LANL continued the *DT Ratio-³He Addition* campaign, imploding glass capsules filled with DT/³He using a 600-ps square laser pulse. Previous studies have looked at the effect of adding ³He to the D_2-filled capsules (as a

DT surrogate); this study is the first to look at the effect on DT. The use of DT also makes it possible to acquire high-quality reaction histories derived from the Gas Cherenkov Detector (GCD-1). From these reaction histories, it has been determined that the addition of ³He degrades the compression component of yield more than expected. This is consistent with the conclusions of the study conducted by MIT using $D_2/$³He-filled plastic capsules[26] and LANL's Hi-Z campaign utilizing glass capsules, also filled with $D_2/$³He (Ref. 27). Contrary to the MIT study, however, the shock component does not appear to be significantly affected.

Figure 116.91 shows the reaction histories for three concentrations of ³He addition. Overall, the measured neutron yield is ~37% of a clean calculation for *each* ³He concentration. However, when the histories are decomposed into Gaussian components representative of shock and compression yields, the measured compression component goes from being a factor of 3 lower than calculated at 0% ³He, to being a factor of 5 lower at 36% ³He. This agrees well with the MIT study as seen in Fig. 116.92 (the factor of 3 at 0% ³He is normalized out for the DTRat data set, whereas a factor of ~2.2 is normalized out for the "Rygg" data set). In contrast, the decomposed shock com-
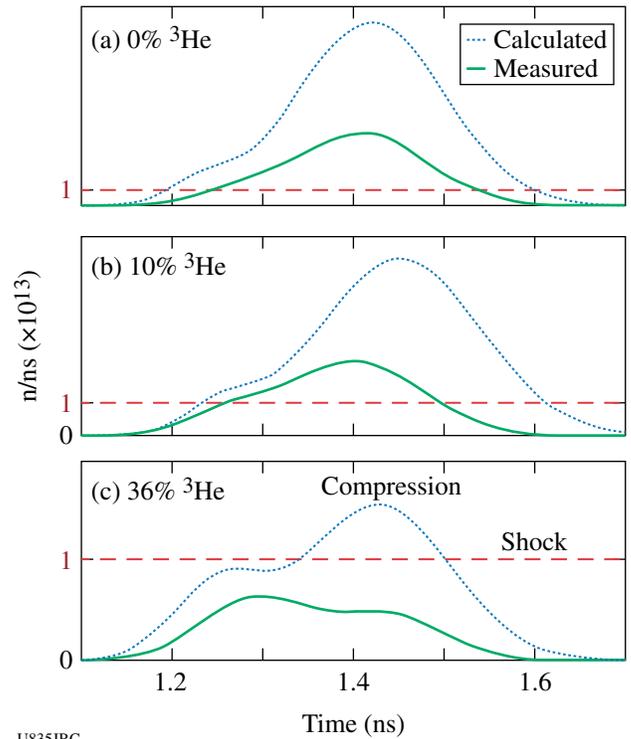
Figure 116.91
Calculated (convolved with residual instrument response) and measured (deconvolved GCD data) reaction histories for various ³He concentrations.
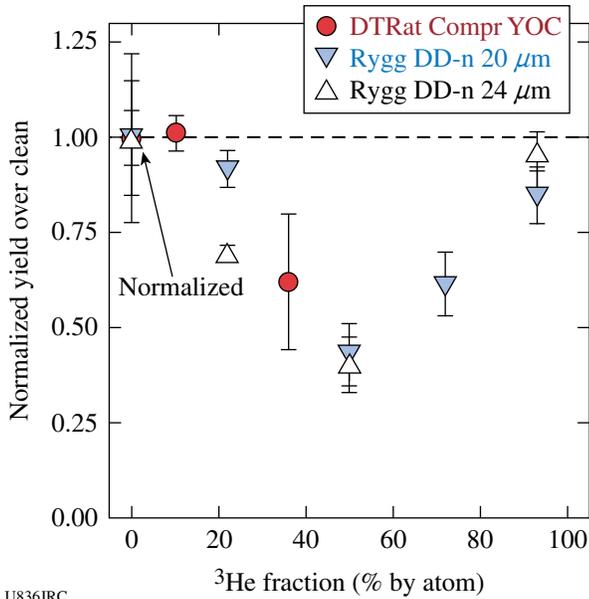
Figure 116.92
Scaled compression component of neutron yield normalized to 1 at 0% ^{3}He.

ponent from DTRat agrees quite well with the clean calculation for all three ^{3}He concentrations as shown in Fig. 116.93.

Shock-yield data for the 24-μm-wall-thickness capsules from MIT's "Rygg" study exhibit a parabolic dependence on ^{3}He fraction, with the minimum occurring near 50% ^{3}He,
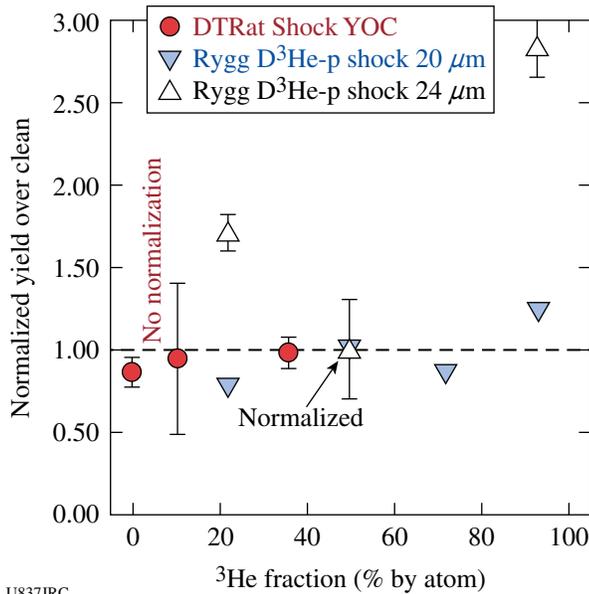
Figure 116.93
Scaled shock component of neutron yield normalized to 1 at 50% ^{3}He for "Rygg" data; no normalization for DTRat data.

similar to what was observed for the compression component. The data set for 20-μm-thick walls, however, does not appear to support this trend. We suspect the degraded yield anomaly arises only after the shock has reflected from the center and has hit the incoming shell. After such time, the shock yield is diminishing while the compression yield is rising. X-ray imaging and ρR data from DTRat, Hi-Z, and the MIT study support the hypothesis that capsules with ~50% ^{3}He are not as compressed at the time of peak neutron production rate during the compression phase as those without ^{3}He (or those with nearly pure ^{3}He from the MIT study). It is not understood at this time what is degrading the compression.

High-Z: The High-Z project successfully completed its planned experiments for FY08 at the OMEGA Laser Facility. These experiments investigated what effect the addition of He to ICF implosions has on fusion yield. The experiment used the standard glass-shell targets we have used in the past and varied the concentration of ^{3}He in the target and measured the resulting yield. These were done for three different concentrations of ^{3}He: 0%, 10%, and 50% by atomic fraction. The gas fills were also designed to be hydrodynamically equivalent to try to ensure similar hydrodynamic behavior. In addition, we also planned to measure the change in yield for two different laser pulse lengths. We first used our standard pulse length of 1.0 ns and then conducted a second series of experiments using a shorter pulse length of 0.6 ns. The shorter pulse length should emphasize the differences in the compression component of the yield where we believe the ^{3}He is causing a significant impact.

On 23 April 2008, we successfully fired eight shots on OMEGA with 1-ns laser pulses and varied the concentration of He in the capsules. The neutron-yield results from these experiments are shown in Fig. 116.94, along with the expected degradation caused by less deuterium in the target. One can see in the figure that the observed yield does fall below the expected yield as the He is increased. We also see little difference in the ion temperature for these shots, which varies from 6.9 keV to 7.4 keV and increases only slightly as the He concentration is increased.

We also did two additional shots on 23 April with 4.0-μm-thick glass shells. These targets contained 50% atom fraction of He, but one was ^{4}He instead of the usual ^{3}He. The yields for these two shots were 4.8×10 and 4.3×10, respectively—a difference of 10%, which is similar to our standard shot-to-shot variation. The ion temperature for these shots was higher, ~8.2 keV, consistent with thinner glass and a more rapid implosion.

Four additional shots were conducted on a separate half-day, 17 June; the results from those shots are shown in Fig. 116.95. The behavior is similar to what was observed for the 1-ns drive shots with one exception: the ion temperatures for these experiments varied greatly, from 5.3 keV for no He to 7.8 keV
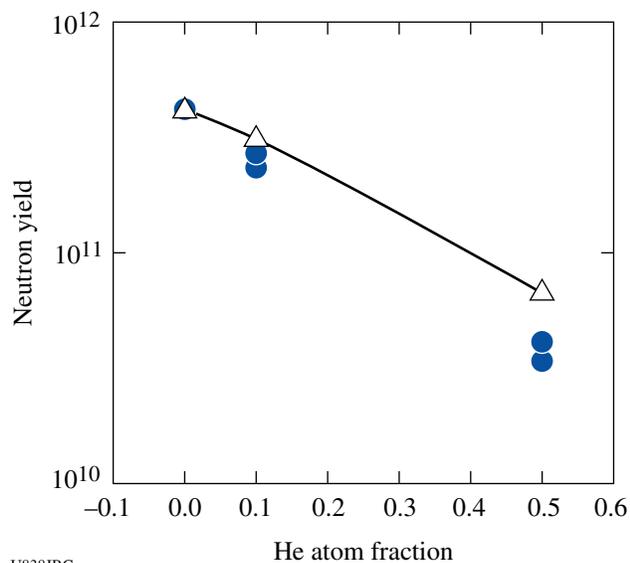
Figure 116.94
Neutron yield as a function of He atom fraction in the gas. The dots are data for a 1-ns pulse drive with 4.3-μm-thick walls and the curve represents the expected yield based on the deuterium concentration only.
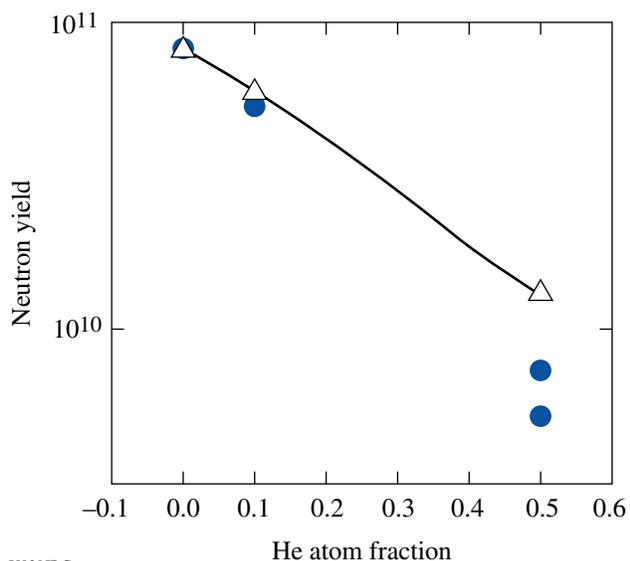
Figure 116.95
Neutron yield as a function of helium atom fraction in the gas. These experiments used 0.6-ns laser drive and the data are shown as dots. The curve represents the expected yield based on the deuterium concentration.

for 50% He and bring into question whether the implosions are hydrodynamically equivalent. This would be consistent with an even greater degradation of the compression burn, reducing its importance compared to the shock burn and effectively elevating the average burn temperature.

Overall, the results for doping the gas with ^{3}He were consistent with earlier results for Ar, Kr, and Xe, although a much larger atom fraction of ^{3}He was required to produce a similar effect.

NIF Platform #5: The NIF Platform #5 campaign continued experiments to develop diagnostic techniques for future NIF experiments. The FY08 experiments focused on backlighter source characterization and development as well as the successful execution of a new platform for the observation of absorption features due to heated materials.

One aspect of the backlighters that was examined was the conversion efficiency for L-shell and M-shell emitters. Over the course of the FY08 campaign, the studied laser irradiance varied from 10^{14} W/cm^2 up to nearly 10^{17} W/cm^2. The data obtained will assist in evaluating the expected photon fluxes at the NIF. An example of some of the data obtained from a CsI backlighter is shown in Fig. 116.96.

The platform for studying absorption spectroscopy is shown in Fig. 116.97. A Ti foil was heated inside a hohlraum. A CsI backlighter provided a quasi-continuum spectrum source, which passed through the sample and was recorded on by a spectrometer (Fig. 116.98). The recorded spectrum contains both the emission from the CsI backlighter and the absorption from the heated Ti foil. Although detailed analysis is still underway, these experiments provided valuable information on the absorption spectroscopy technique and have led to a number of improvements being implemented for future NIF experiments.

Symergy: We have used two cones of the OMEGA laser to irradiate a linear 0.7-scale NIF hohlraum to implode Be and CH capsules to measure the effect of beam phasing on the implosion symmetry. The vacuum hohlraums, with 2-mm-diam capsules, reached 105 eV using 1-ns laser pulses. The symmetry of the x-ray emission from the implosion was measured for both the CH and Be capsules. We were able to vary the symmetry at implosion time by varying the cone fraction or ratio of energy between the inner cones (21° or 42°) and the outer cone (59° beams) (Fig. 116.99). We found that the fraction where the best symmetry occurred was closest to those ratios that the re-emit
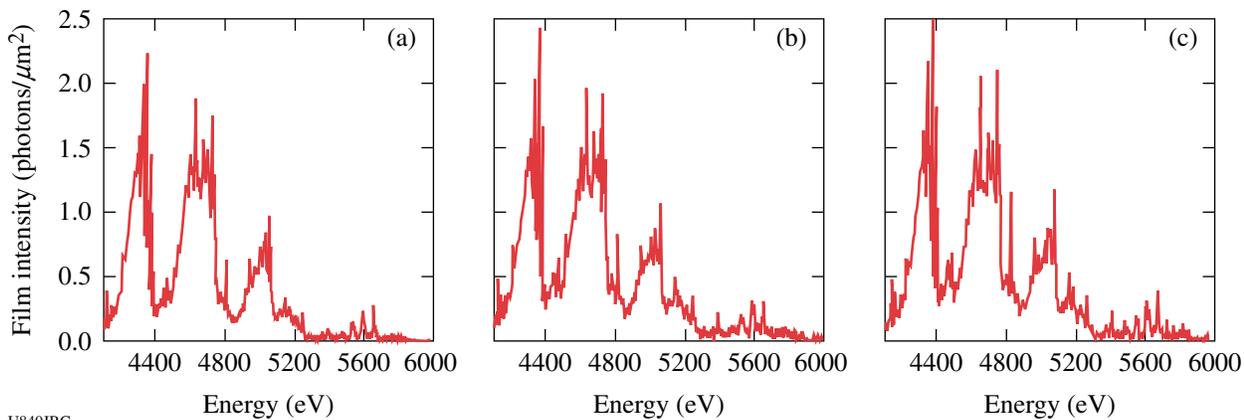
Figure 116.96
CsI spectra for (a) a nominal 600-, (b) nominal 400-, and (c) nominal 200-μm-diam spot. Note that although the laser irradiance spans an order of magnitude, the amount of emission stays essentially constant.
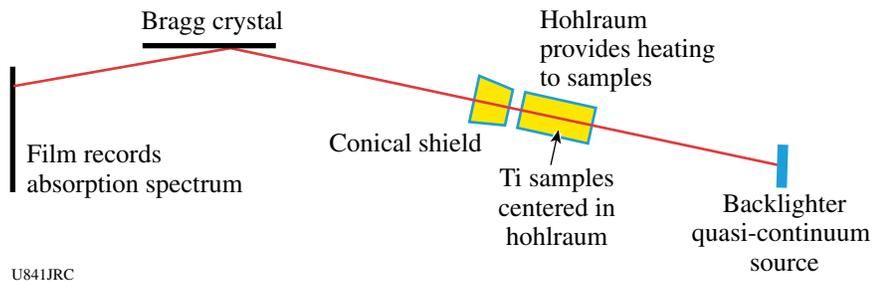
Figure 116.97
Schematic depicting the absorption spectroscopy configuration. Laser beams enter both sides of the hohlraum. A thin Ti foil sitting in the center of the hohlraum is then heated. The backlighter provides a quasi-continuum backlighter source, and its x rays pass through the Ti sample and are reflected off the Bragg crystal and recorded on film. Some of the backlighter emission is absorbed, depending on the temperature and density of the Ti. This schematic is not to scale.
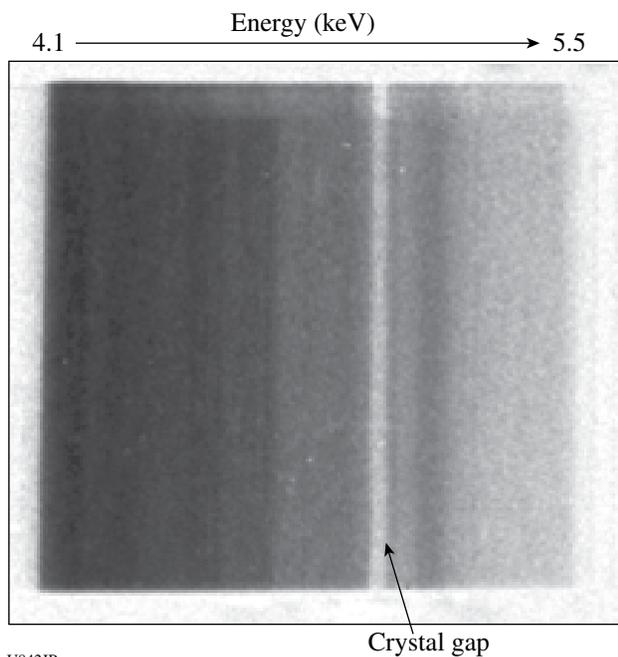
Figure 116.98
Spectrum containing the emission from a CsI backlighter and the absorption due to a thin, heated Ti foil.
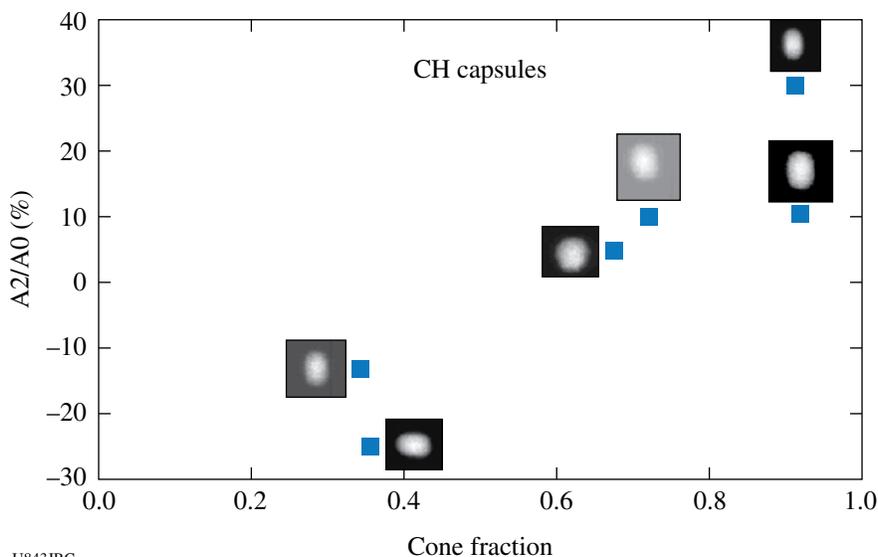
Figure 116.99
The measured second-order Legendre coefficient for the x-ray emission at the 30% level, measured at peak emission.

U843JRC

technique had found for the same pointing. When we replaced the 42° beams with the 21° beams and pointed to the same location in the hohlraum with the same laser irradiance, the hohlraum radiation was lower and the symmetry was affected, indicating some impaired propagation of the inner cone.

FY08 CEA OMEGA Experimental Programs

CEA conducted 39 target shots on the OMEGA Laser Facility in FY08. The CEA efforts included the following:

CEA Acquisition System and Software Developments for the OMEGA Facility: Since 1999 the development of specific CEA diagnostics for joint experiments with LLE, LANL, and LLNL on the OMEGA facility (for instance, DMX,[28] NIS,[29] or HRXI[30]) have used the same devices (single-shot oscilloscopes, CCD, HV supply, switches, fast triggering generators, electrical attenuators, etc.) to supply and record detectors placed inside the target chamber area. All these recording and control devices are quite sensitive to the radiative environment generated during the OMEGA high-yield neutron shots ($Y_n > 10^{13}$ n/4π) induced mainly by the hard x-ray components for every shot or the neutron and gamma ray flux for high-neutron-yield shots.[31] To protect these sensitive instruments, we decided to place them in a "quieter" radiative environment named "La Cave," located in the basement of the target chamber area and protected by 70 cm of concrete. Figure 116.100 shows FPE (Force de Projection d'Enregistrement)—the recording system installed in La Cave that presently includes

- fourteen high-bandwidth single-shot oscilloscopes (IN 7100 – 7 GHz)
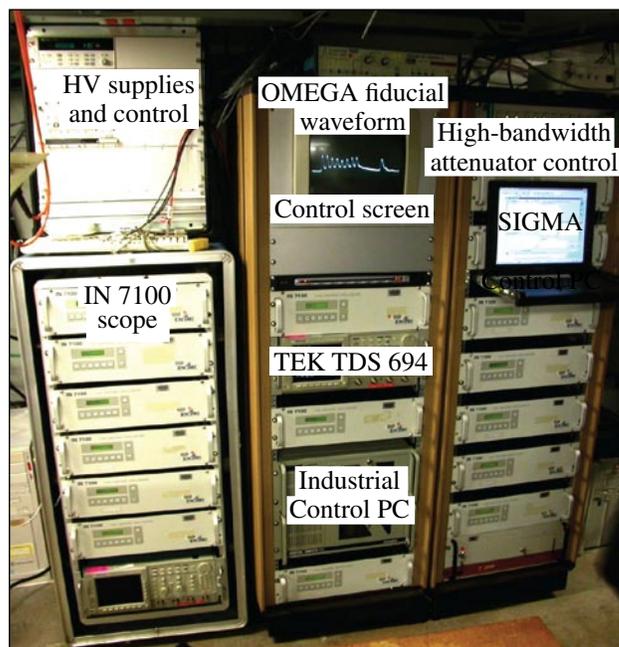
U852JRC

Figure 116.100
The CEA "FPE" acquisition system in the OMEGA "La Cave."

- two digital oscilloscopes (TEKTRONIX TDS694 – 3 GHz)

- some HV supplies (used for biasing our detectors) and a related voltmeter

- a control system for our DMX high-bandwidth remotely controlled electrical attenuators

- a fast triggering system (not shown at the rear side of these cabinets)

- an automated control/command system

The CEA FPE control/command system, described in detail in the next paragraph, is based on PC hardware and is specially designed to automatically control our devices during the shot sequence when access to La Cave is closed for safety reasons. During that time (from 10 min prior to the shot to a few minutes after, depending on the radiative decay), each specific "order" generated during the OMEGA countdown process (during the capacitor bank charge), from a few minutes before until a few seconds after the shot, is recognized and used to automatically trigger some specific action on each device remotely controlled by the software (HV on, oscilloscope or CCD armed, data transfer and storage process, HV off, etc.). These actions can also be manually triggered by an operator if needed during the setup and preparation of the diagnostic. This system can be also be seen (for controlling its correct automated operation during the shot sequence) by the OMEGA experimental team operators when the relevant diagnostic is included as a "facility diagnostic" (as done, for example, for DMX).

<u>"FPE-SIGMA" Command/Control System.</u> Most of the deployment and tuning of the measurement chains of each CEA diagnostic is done by a "mobile" team (present at the OMEGA facility only during main CEA experiments) that uses a specific tool to manage the acquisition devices and their controlling network of computers.

Developed and improved over a decade, the "SIGMA" software tool solves computing issues going from manual to fully automated experiments. A distributed architecture—which also downsizes to fit into a single computer—is controlled at one place by human interface. The tool supports the diagnostic design and improvement process by making it possible to describe the system in a smart graphical interface (the Microsoft Visio diagram editor is shown in Fig. 116.101). The targets, filters, and mirrors (the main components of DMX) appear at the left side of a schematic view in which the signal paths and delays also appear and can be documented. Thus the settings definition of each remote-controllable device is postponed after the definition of its use case. In fact, in an automated diagnostic, settings are sets of logical data that are selectively recalled into a static physical layer. The versatility of a physical layer increases with the remote controllability of its key components.

U853JRC
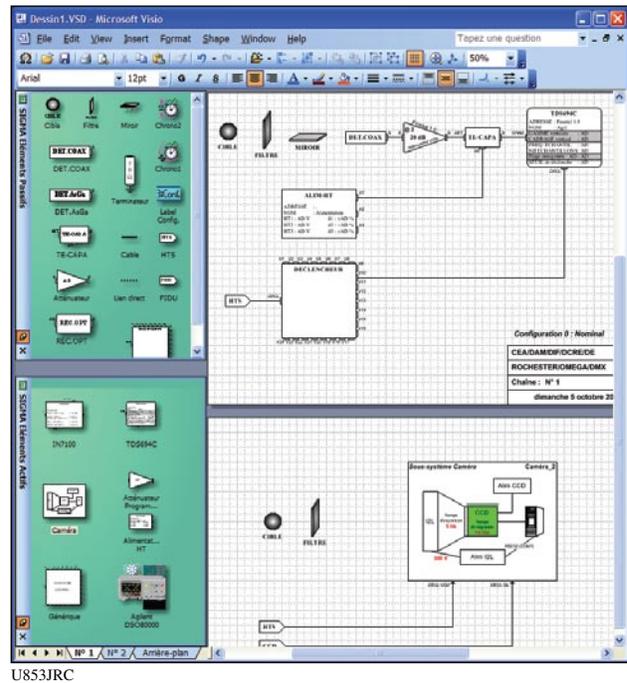
Figure 116.101
The diagnostic editor built over Microsoft Visio.

The underlying and hidden computing technologies include

- specific support of a few device drivers (GPIB controller, ISA/PCI imaging cards, USB devices)

- standard communication with serial ports, GPIB ports, TCP/IP connections, and ODBC databases

In addition, the complexity of some instrumental subsystems—e.g., based on more than one device connected to different ports, leading to advanced communication handshake or to advanced commands implementation—was hidden in high-level virtual device drivers that run on the device computers and expose a GPIB-like interface.

The supported classes of instruments come with a visual schematic footprint, an inline OCX front panel, a guarded OCX settings form, and a set of intrinsic commands provided by design. Intrinsic commands may generate specific event types that also come with their suite of *in-situ* viewers and commands.

Currently, the SIGMA software controls analog and digital oscilloscopes, power supplies, programmable attenuator banks, and neutronic imaging subsystems. At design time, the Visio multipage editor is fully automated to show the instrument settings according to the active configuration. At run time, the

configuration variable is also maintained and its value can be automatically affected in order to influence the conduct of operations. For example, the active configuration can be retrieved from a database each time a shot number is received.

Ten configurations are currently supported, each being freely labeled. At the instrument level, four sets of settings are freely associated to the ten configurations. Settings factorization across configurations simplifies diagnostic management. At the diagnostic level, a matrix determines the physical subsets (measurement chain) that are active with each configuration.

An experiment can be controlled manually, in a semi-automatic manner (triggering scripted sequences), or fully automatic [involving the internal scheduler or listening to a hierarchical uplink (supervisor)]. Supervisors can also be notified when selected error levels occur.

During a run time, the software builds a single chronology of time-stamped and typed events. Each event type shows a specific icon and comes with a set of tools that makes possible

inspection (texts, forms, curves, or pictures), event navigation, or procedure recall. Past-event inspection is possible at any time, as well as single command executions, script executions, and inspection/modification of instrument settings. The guarded variables cover every aspect of the system except the state of the user interface.

Recently, the SIGMA tool was qualified to be integrated into the OMEGA operations as the DMX diagnostic application controller. To make the startup and the stopdown of the diagnostic application easier, the tool was given a simplified alternate interface showing a strictly filtered set of notifications (Fig. 116.102). In addition, the non-specialist is guided from the first power up to the last shutdown thanks to a localized operator sheet (Fig. 116.103) and to the firing of some interactive checklists. In the meantime, the software monitors the presence of each component.

The SIGMA software developed and tested initially for OMEGA common experiments is also deployed at the LULI facility (Palaiseau, France) and the LIL facility (Cesta, France); CEA
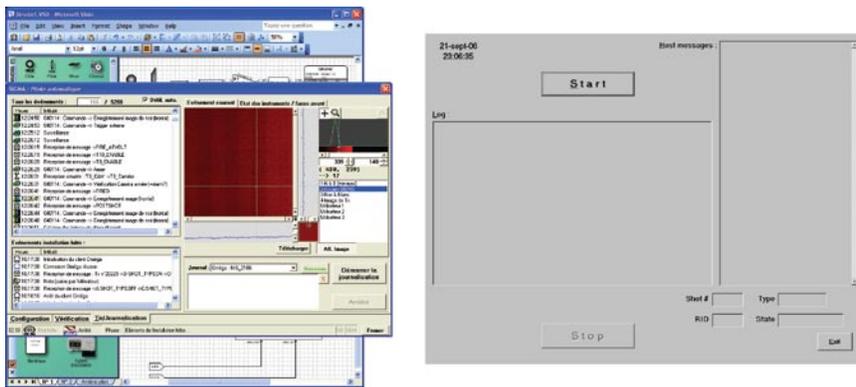

U854JRC

Figure 116.102
The complete versus the simplified run-time human interface.

U855JRC
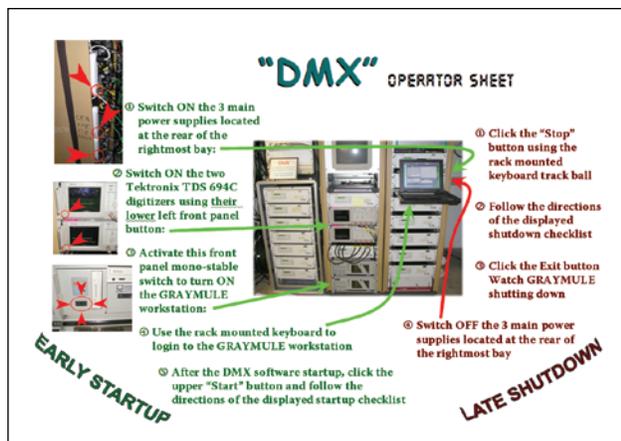
Figure 116.103
An operator sheet to properly start the minimum hardware and launch the checklist.

also uses it on its Gekko XII diagnostic (Osaka, Japan), justifying its given name of FPE for "Projected Force for Recording."

Monocrystalline CVD Diamond Detector: A Novel Tool for Neutron Yield and Duration Emission Measurement: Synthetic diamond detectors are now known to exhibit attractive characteristics to discriminate neutrons by the time-of-flight technique (nTOF), as well as to measure neutron bang time and ion temperature. Earlier work had, however, demonstrated how the quality of this material matters since the temporal properties of synthetic diamond devices (aiming to be in the 100-ps range) strongly differ from device to device and growth origins. For the record, sensitive CVD diamonds are usually too slow to be used for timing measurement, although such a development of sensitive and fast CVD diamonds would make it possible to perform simultaneously both neutron-yield and ion-temperature measurements, thus minimizing the number of nTOF detectors on the Laser Megajoule Facility.

More recently, and to complete the data acquired in 2007 (Ref. 32) for low-neutron-yield measurements, a new series of polycrystalline CVD diamonds (Element Six) and new monocrystalline CVD diamonds (CEA-LIST, Saclay) were implemented on the OMEGA Laser Facility during implosion experiments of DT capsules yielding 10^{13} to 10^{14} neutrons. These materials exhibited higher sensitivities. The goal was to determine how such novel materials could be relevant for neutron-yield, bang-time, and ion-temperature diagnostics.

On OMEGA, diamond detectors were inserted at distances of 30 cm, 1 m, and 2 m from the target chamber center using the TIM diagnostic insertion mechanisms. Other diamonds were placed outside the target chamber at 3.3 m from target chamber center (TCC). Distances and neutron-yield ranges provide the ability to probe the detectors' performances within two decades of the neutron flux (n/cm^2). The detectors exhibit a linear response over the dynamic range explored. To compare diamond materials, their sensitivities were normalized as a function of the sample volume: diamond sensitivity can often vary by several orders of magnitude, up to three decades previously observed. Table 116.V shows that the novel monocrystalline sample A260107B (from CEA-LIST) appears to be the most sensitive of all diamond material calibrated on OMEGA from the campaigns in 2007 and 2008.

Prior to the experiments, we had evaluated the temporal properties of these diamonds under 16-MeV electrons produced on a Linac accelerator at CEA (ELSA at Bruyères-le-Châtel). The pulse duration on ELSA is about 25 ps, making it possible to measure the main timing parameters. The monocrystalline diamond A260107B pulse shape has a 10% to 90% rise time that remains below 100 ps. Such temporal properties make this sensitive diamond a good candidate to measure the Doppler broadening of the neutron pulse along its propagation, thus enabling one to measure the ion temperature at bang time.

On OMEGA, the detector signal must propagate through 10 to 30 m of cable before it reaches the 7-GHz-bandwidth single-shot oscilloscope (IN7100). We have developed a software processing tool that makes it possible to deconvolve the pulse broadening produced by such a high cable length. It led to processed signals exhibiting rise times of 870 ps at 3.3 m from TCC with an ion temperature of 6.7 keV (Fig. 116.104). This signal rise time observed during DT implosions results from the 150-ps burn duration, convoluted with the temporal broadening induced by the DT ion's main energy at bang time.

Using the signal-processing technique already used in NTD diagnostics,[33] we can deduce the neutron pulse duration at 3.3 m from the target, which is mainly determined by the Doppler broadening produced by the ions. The resulting ion temperature and measured time duration are shown in the two last columns of Table 116.VI. The inferred ion temperatures from the CVD diamond signal are in good agreement with the standard OMEGA measurement performed at 5 m with a fast scintillator and an MCP photomultiplier and are presented for

Table 116.V: Diamond sensitivity measured under 14-MeV neutrons pulses.

CVD	Type	Thickness	Size	Gold Contact	High Voltage	Sensitivity ($C/n/cm^3$)
A260107B	Monocrystalline	500 μm	4×4 mm	3×3 mm	–1400 V	3.1×10^{-15}
A281103	Polycrystalline	260 μm	5×5 mm	4×4 mm	–360 V	1.8×10^{-15}
E6 300 μm	Polycrystalline	300 μm	ϕ 10 mm	ϕ 8 mm	–750 V	2.4×10^{-16}
E6 1 mm	Polycrystalline	1000 μm	ϕ 10 mm	ϕ 8 mm	–1000 V	1.3×10^{-16}
A270105	Polycrystalline	115 μm	5×5 mm	4×4 mm	–750 V	4.7×10^{-17}
A190106	Polycrystalline	450 μm	5×5 mm	4×4 mm	–500 V	4.9×10^{-18}
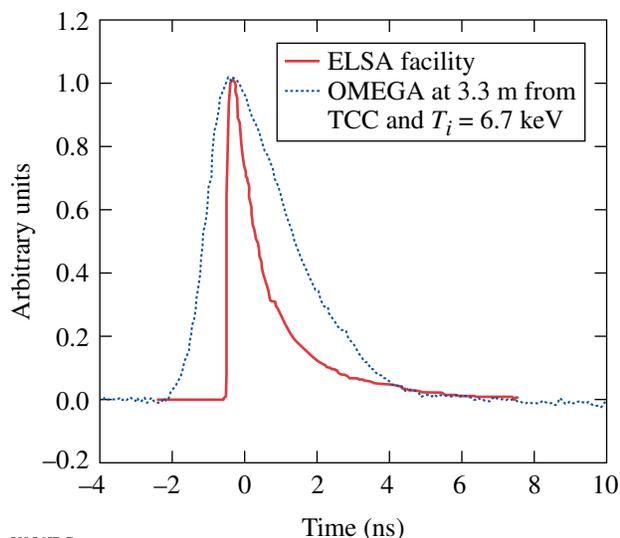
Figure 116.104
Comparison of a monocrystalline pulse shape measured on ELSA (solid curve) and OMEGA (dotted curve).

comparison in Table 116.VI. As predicted, monocrystalline CVD diamonds made by CEA-LIST (A260107B) are sensitive enough for neutron-yield measurements and fast enough for ion-temperature measurements.

Low-sensitivity diamonds are also required for neutron high-yield measurements. A polycrystalline diamond (A190106 from CEA-LIST) grown using a high level of nitrogen impurity was tested on OMEGA; it exhibited a very low sensitivity but also a very long pulse tail. A "black diamond" detector (from Applied Diamond) exhibiting high levels of "non-carbon impurities" was provided by V. Yu. Glebov of LLE. These two diamond samples were evaluated at the ELSA facility using 16-MeV electrons to compare their relative sensitivities and timing parameters (Fig. 116.105). Comparison with other diamonds tested on ELSA and OMEGA shows that those black diamonds are probably good "low-sensitivity" detectors for high neutron-yield measurements on MJ-class lasers.
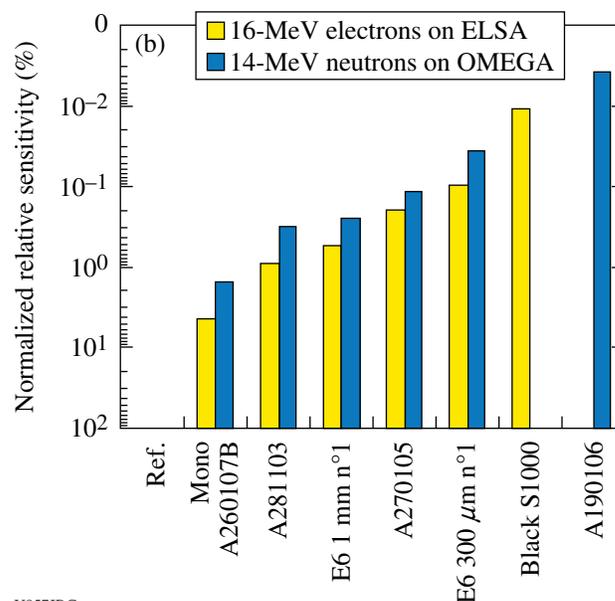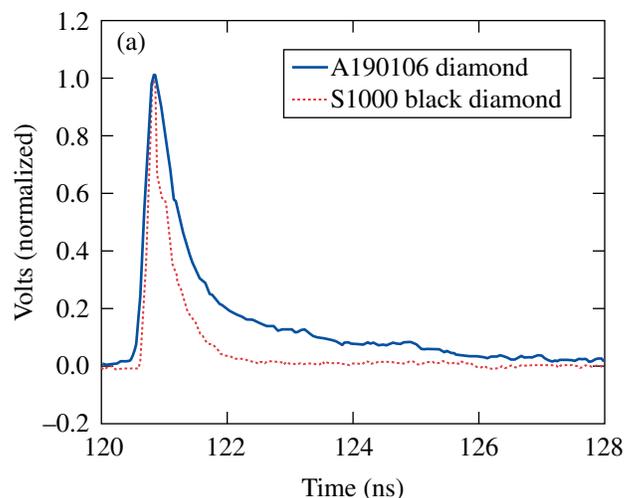
Figure 116.105
Comparison of pulse shape and electron–neutron relative sensitivity. Relative sensitivities are normalized to earlier measurements on one of the most-sensitive diamonds.

Table 116.VI: Ion-temperature measurement with monocrystalline CVD diamond at 3.3 m from TCC.

	OMEGA Measurement		CVD Diamond Measurement		
Shot	Ti LLE (±0.5 KeV)	Δt	CVD reference	Ti measured	Δt measured
51301	6.4 keV	992 ps	A260107B	6.7 keV	1016 ps
51305	5.3 keV	903 ps	A260107B	5.2 keV	893 ps
51314	3.6 keV	744 ps	A260107B	3.7keV	729 ps
51315	3.7 keV	754 ps	A260107B	3.6 keV	740 ps
51322	5.5 keV	919 ps	A260107B	5.6 keV	926 ps
51325	5.1 keV	885 ps	A260107B	5.1 keV	882 ps

The 2008 campaigns have therefore enabled us to identify families of materials that appear suitable according to measurement objectives. This development of faster high- and low-sensitivity CVD diamond detectors is still being investigated with CEA-LIST and LLE. A new challenge will now be to demonstrate that a large, sensitive CVD diamond is capable of measuring the downscattered neutron yield for ρR determination.

Neutron Imaging on OMEGA: For several years, CEA has obtained neutron-imaging measurements on OMEGA with an overall resolution of 20 μm (Refs. 29 and 34). The imaging system is based on a small aperture (a 2-mm-diam hole made in a 10-cm-thick tungsten cylinder) placed 260 mm from TCC.[35] The detector (80-mm diameter) is then set 8 m from the target. In this setup, aligning the aperture is very difficult due to the fact that any small misalignment entails a large displacement of the target image on the detector plane at 8 m. As shown with the penumbral aperture last year, there is also the influence of the source position inside the field of view, which is 200 μm for a source size of approximately 50-μm FWHM.[35,36]

In FY07 we presented the effects of misalignment on both calculated and experimental unfolded images obtained with a penumbral aperture. Distortions entailed on the image shape revealed that aperture-positioning tolerance is about 50 μm within the field of view to prevent any effects from misalignment on unfolded images. Briefly, our alignment technique uses a telescope and a beam splitter to view the target through the aperture and the detector, thus fixing the detector–target axis. Next, the aperture is aligned using picomotors on this axis. This technique is very accurate but quite long and fastidious. To meet OMEGA repetition rate and shot plan requirements, a new technique for coarse alignment was tested this year to earn time for setting up before shots. For fine alignment, the old technique is then performed. The new technique relies on a laser beam being injected inside the TIM by a single-mode optical fiber. The laser is sent in two collinear directions via a semitransparent plate, one through the aperture and one to the detector. The first allows us to be sure that we are well centered both on the target and the aperture, the second on the detector. Such a system permits us to be ready for a shot in about 1 h, compared to approximately 2.5 h in the past. We have thus obtained a usable image well centered on the detector on the first shot (51295, see Fig. 116.106).

For high SNR images, we use an annular aperture (see Fig. 116.107) to form neutron images.[34] This aperture is made with a biconical plug inserted in the penumbral aperture, but,
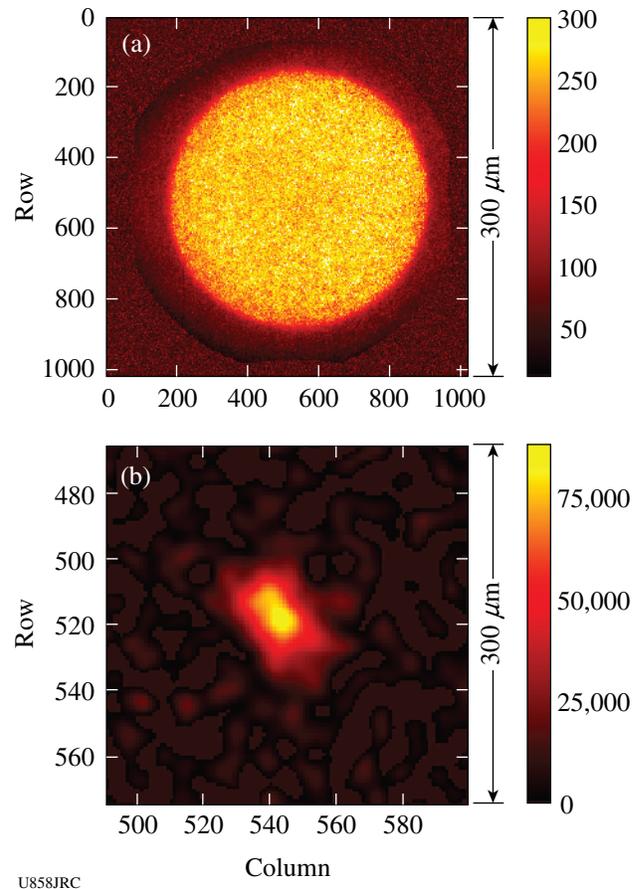
Figure 116.106
Image of DT implosion (shot 51295) yielding 4.0×10^{12} neutrons. (a) Raw image and (b) unfolded image using autocorrelation method[37] (SNR = 17).

in this case, there is no opportunity to send the laser through the aperture. Alignment precision then relies on the capability of reproducing two identical penumbral apertures that can be replaced with minimal misalignment. Aperture positioning tolerance and repeatability between these two apertures were quantified in our laboratory and verified during several campaigns on OMEGA. As for the penumbral aperture, this year (FY08) we studied image distortion as varying annular aperture alignment on OMEGA experiments. These results were compared to Monte Carlo calculations (Geant4)[38] and showed relatively good agreement with experimental results (see Fig. 116.108).

The oblate shape of Fig. 116.106(b) reveals that the aperture is not perfectly aligned; this image was ~200 μm off center. This misalignment was due to the TIM insertion/reinsertion cycle before the shot for adding tritium protection. Alignment control is impossible after tritium coverage addition. It was found that feedback springs on picomotors were not strong
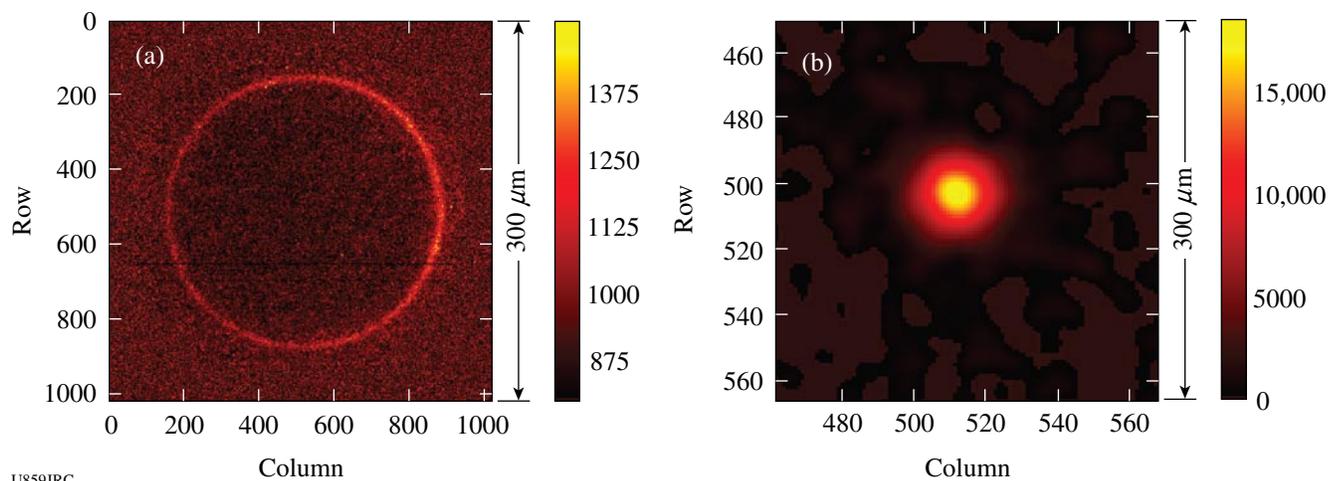
Figure 116.107
(a) Raw image of DT implosion (shot 51324) yielding 2.8×10^{13} neutrons. (b) Unfolded image using autocorrelation method[37] (SNR = 41).
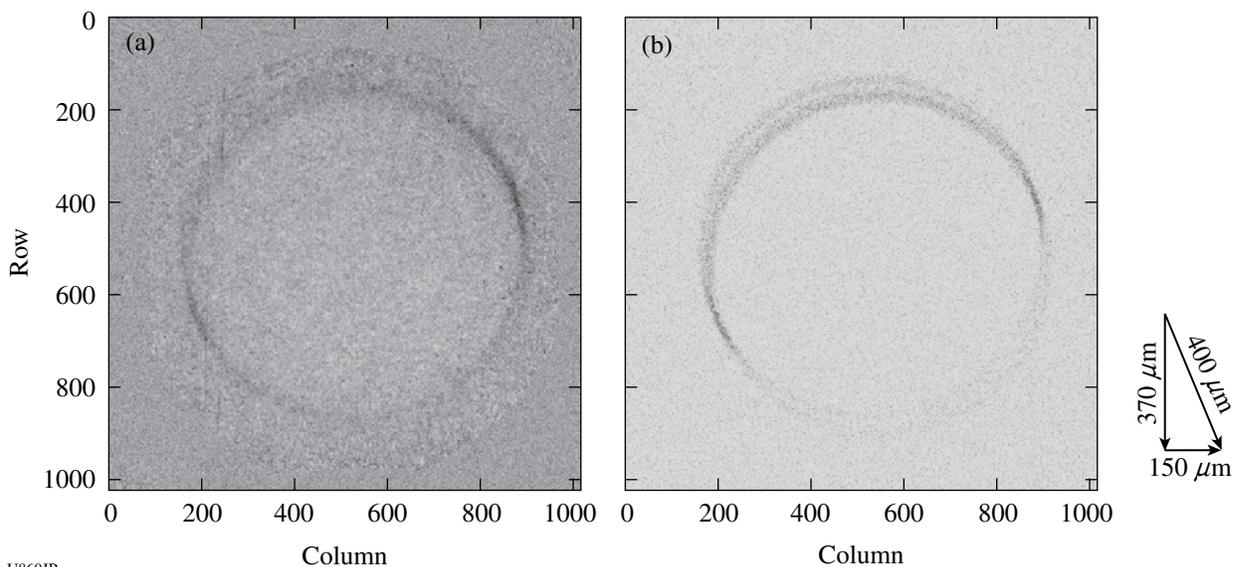
Figure 116.108
(a) Image of DT implosion (shot 51304) yielding 3.2×10^{13} neutrons. (b) Calculated image using Geant4 with 50-μm-diam neutron source off center by 400 μm (150 μm right and 370 μm down).

enough to recover the right position during insertion vibrations. Alignment technique was not responsible for this error.

The capability of being well aligned on a first shot is a crucial point for megajoule-class lasers with a 40-m line of sight. Misalignment contributors are now well known and can be reduced under acceptable values less than 50 μm. We are currently qualifying a 150-mm-diam camera for high-resolution measurements (down to 10 μm) that next year will be placed at 13 m from target.

FY08 AWE OMEGA Experimental Programs
Thirty-two target shots were taken for AWE-led experiments on OMEGA in FY08. Hohlraum symmetry was one of the principal topics of investigation.

Coupling laser energy into a hohlraum is a long-established method for generating a symmetric x-ray drive for high-convergence implosions. A number of studies of hohlraum symmetry have been undertaken to optimize the conditions for inertial confinement fusion;[39,40] therefore our codes are

relatively well validated in this regime. In certain situations, it is necessary to perturb the symmetry of the driver, for example, where beams are required for diagnostic purposes. To validate our simulations in such conditions, AWE has commenced a campaign to study the energetics of asymmetric hohlraums.

A laser-heated hohlraum was used (Fig. 116.109) and driven either from both ends ("symmetric drive") or from only one end ("asymmetric drive"). The OMEGA Dante diagnostic is used to measure temporal evolution of the radiation temperature. A capsule located at the center of the hohlraum is used as a diagnostic of the flux uniformity radiographed with a titanium area backlighter. Two classes of capsules with a nominal diameter of 600 μm were fielded on the first shot day (September 2008). A silicon aerogel sphere ($\rho \sim 325$ mg/cc) makes it possible to characterize the time-dependent drive as a function of angle via the steep x-ray transmission gradient just outside the converging ablation front. A plastic-coated, thin-shelled glass capsule provides a complementary measure of the angular variation in absorbed flux. The outer plastic layer serves to mitigate the backlighter attenuation from the ablated material, while the glass shell provides an opaque tracer layer for the radiography. For some targets a thin gold layer was applied over the diagnostic holes to maximize the albedo and reduce any azimuthal variation in the dynamics.

Figure 116.110 illustrates the late-time implosion dynamics of a thin-shell glass capsule driven from one side and synthetic radiographs produced from AWE's *NYM* radiation hydrocode. The experimental data indicate that the ablation is preferentially directed toward the laser spots, with a slightly reduced drive on axis adjacent to the laser entrance hole. This results in an inwardly propagating shock that converges on axis, driving a collimated jet ahead of the main shock front. The preliminary calculations of these targets qualitatively reproduce the macroscopic evolution of the implosion but overestimate the velocity of the shell. The radiographic images of the aerogel spheres show a clear departure from sphericity (Fig. 116.111). Contours of the backlighter transmission, coupled with the original location of the sphere, make a Legendre polynomial fit to the data possible. This indicates a significant P_1 mode resulting from the imposed drive imbalance within the hohlraum.
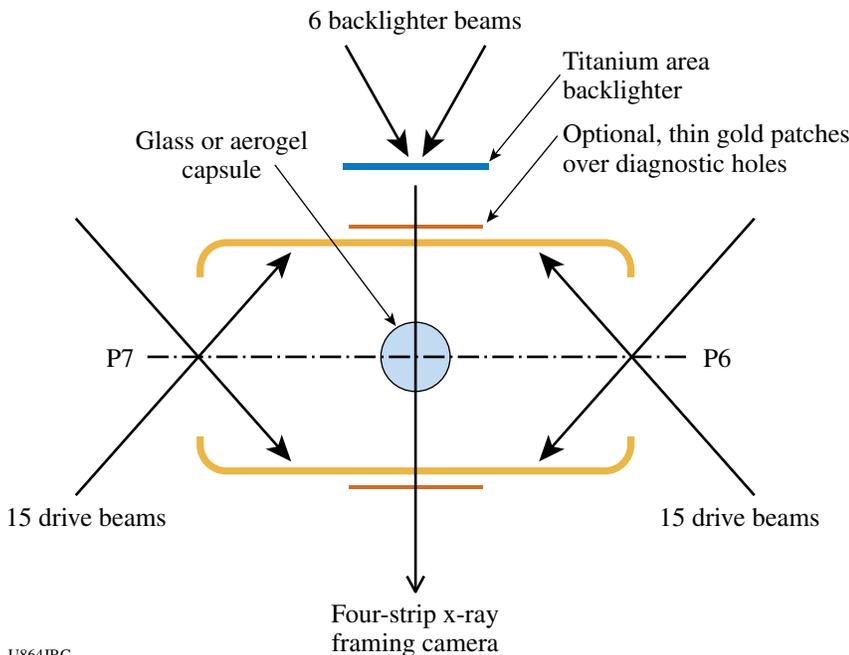
Figure 116.109
Schematic of the experiment to investigate the performance of an asymmetrically driven hohlraum. The 600-μm-diam spherical capsule is placed at the center of a 1.6-mm-diam hohlraum target that is heated through both laser entrance holes (symmetric-drive case) or through just one laser entrance hole (asymmetric-drive case). Radiographic measurements of the implosion are made using a titanium area backlighter and a four-strip x-ray framing camera.
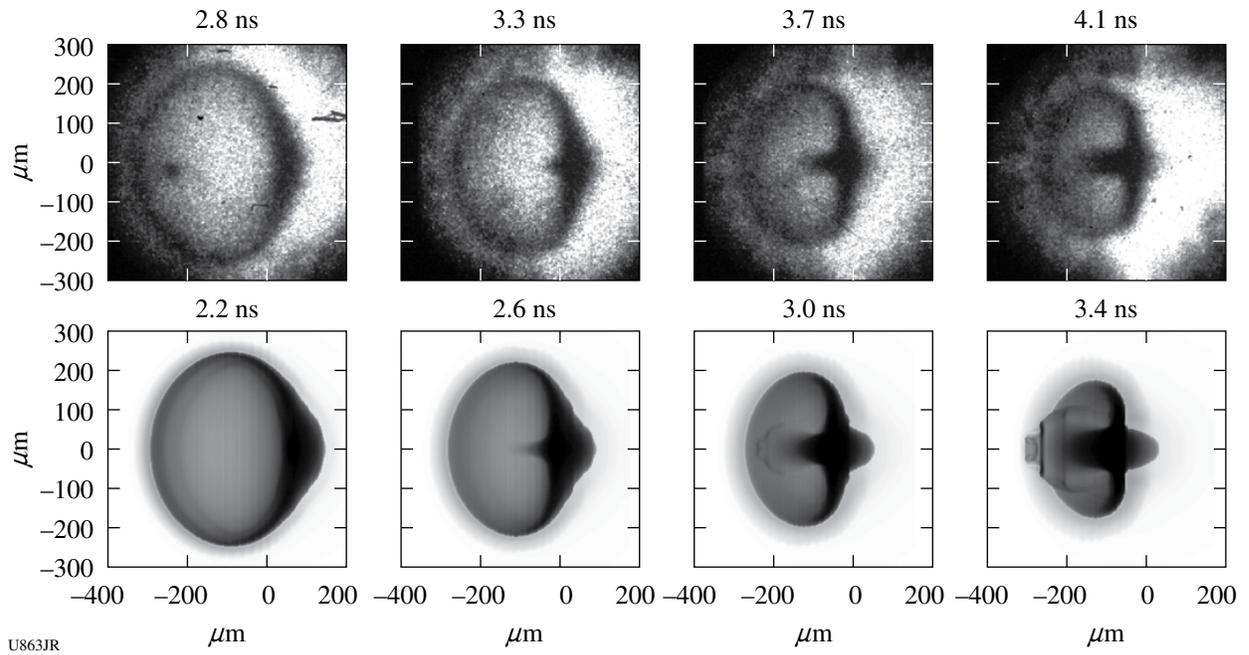
Figure 116.110
Radiographs of the capsule implosion (top) compared with synthetic radiographs (bottom) obtained by post-processing simulations using the AWE 2-D radiation hydrodynamics code *NYM*.
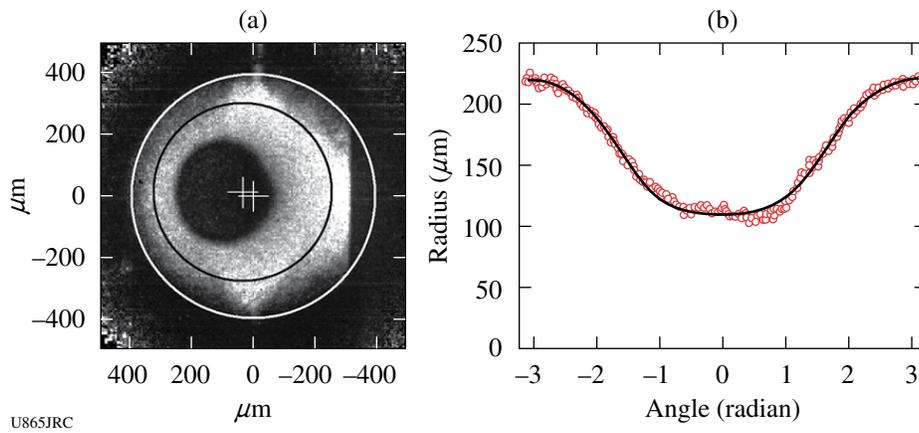
Figure 116.111
(a) Radiograph of an asymmetrically driven silica-aerogel sphere at 2.5 ns after onset of the radiation drive. The superimposed circles represent the initial positions of the aerogel sphere and diagnostic hole (the sphere and hole centers are shown by the crosses), and (b) Legendre-polynomial fit to the contour of transmitted backlighter intensity = 0.4. The inferred values of the first four Legendre coefficients are 156 μm (P_0), 62 μm (P_1), 4.3 μm (P_2), and 7.3 μm (P_3).

REFERENCES

1. C. K. Li, F. H. Séguin, J. A. Frenje, J. R. Rygg, R. D. Petrasso, R. P. J. Town, P. A. Amendt, S. P. Hatchett, O. L. Landen, A. J. Mackinnon, P. K. Patel, V. A. Smalyuk, T. C. Sangster, and J. P. Knauer, Phys. Rev. Lett. **97**, 135003 (2006).

2. C. K. Li, F. H. Séguin, J. A. Frenje, J. R. Rygg, R. D. Petrasso, R. P. J. Town, P. A. Amendt, S. P. Hatchett, O. L. Landen, A. J. Mackinnon, P. K. Patel, M. Tabak, J. P. Knauer, T. C. Sangster, and V. A. Smalyuk, Phys. Rev. Lett. **99**, 015001 (2007).

3. C. K. Li, F. H. Séguin, J. A. Frenje, J. R. Rygg, R. D. Petrasso, R. P. J. Town, O. L. Landen, J. P. Knauer, and V. A. Smalyuk, Phys. Rev. Lett. **99**, 055001 (2007).

4. C. K. Li, F. H. Séguin, J. R. Rygg, J. A. Frenje, M. Manuel, R. D. Petrasso, R. Betti, J. Delettrez, J. P. Knauer, F. Marshall, D. D. Meyerhofer, D. Shvarts, V. A. Smalyuk, C. Stoeckl, O. L. Landen, R. P. J. Town, C. A. Back, and J. D. Kilkenny, Phys. Rev. Lett. **100**, 225001 (2008).

5. J. R. Rygg, F. H. Séguin, C. K. Li, J. A. Frenje, M. J.-E. Manuel, R. D. Petrasso, R. Betti, J. A. Delettrez, O. V. Gotchev, J. P. Knauer, D. D. Meyerhofer, F. J. Marshall, C. Stoeckl, and W. Theobald, Science **319**, 1223 (2008).

6. C. K. Li, F. H. Séguin, J. A. Frenje, J. R. Rygg, R. D. Petrasso, R. P. J. Town, P. A. Amendt, S. P. Hatchett, O. L. Landen, A. J. Mackinnon, P. K. Patel, V. Smalyuk, J. P. Knauer, T. C. Sangster, and C. Stoeckl, Rev. Sci. Instrum. **77**, 10E725 (2006).

7. C. K. Li, F. H. Séguin, J. A. Frenje, M. Manuel, R. D. Petrasso, V. A. Smalyuk, R. Betti, J. Delettrez, J. P. Knauer, F. Marshall, D. D. Meyerhofer, D. Shvarts, C. Stoeckl, W. Theobald, J. R. Rygg, O. L. Landen, R. P. J. Town, P. A. Amendt, C. A. Back, and J. D. Kilkenny, Plasma Phys. Control. Fusion **51**, 014003 (2009).

8. R. Petrasso, Bull. Am. Phys. Soc. **52**, 97 (2007).

9. C. K. Li, Bull. Am. Phys. Soc. **53**, 20 (2008).

10. C. K. Li, F. H. Séguin, J. A. Frenje, J. R. Rygg, R. D. Petrasso, R. P. J. Town, P. A. Amendt, S. P. Hatchett, O. L. Landen, A. J. Mackinnon, P. K. Patel, V. Smalyuk, J. P. Knauer, T. C. Sangster, and C. Stoeckl, Rev. Sci. Instrum. **77**, 10E725 (2006).

11. S. H. Glenzer et al., Phys. Rev. Lett. **90**, 175002 (2003).

12. J. J. MacFarlane, I. E. Golovkin, and P. R. Woodruff, J. Quant. Spectrosc. Radiat. Transf. **99**, 381 (2006).

13. H. J. Lee et al., "X-Ray Thomson Scattering Measurements of Density and Temperature in Shock-Compressed Beryllium," to be published in Physical Review Letters.

14. D. H. Froula et al., Phys. Rev. Lett. **101**, 115002 (2008); D. H. Froula et al., Phys. Rev. Lett. **100**, 015002 (2008).

15. P. Neumayer et al., Phys. Rev. Lett. **100**, 105001 (2008); P. Neumayer et al., Phys. Plasmas **15**, 056307 (2008).

16. E. L. Dewald et al., Rev. Sci. Instrum. **79**, 10E903 (2008).

17. R. K. Kirkwood et al., Phys. Plasmas **16**, 012702 (2009).

18. H.-S. Park et al., "Experimental Tests of Vanadium Strength Models at High Pressures and High Strain Rates," International Journal of Plasticity (in preparation).

19. B. A. Remington et al., "A Path to Materials Science at Extreme Pressures," International Journal of Plasticity (in preparation).

20. S. Prisbrey et al., "3-D Hohlraum Simulations for an Indirect-Drive Strength Platform," International Journal of Plasticity (in preparation).

21. S. Pollaine et al., "Thin Walled Hohlraum Designs for High Pressure, Stagnation Free Loading," International Journal of Plasticity (in preparation).

22. A. B. Reighard et al., Rev. Sci. Instrum. **79**, 10E915 (2008).

23. K. B. Fournier et al., Absolute X-Ray Yields from Laser-Irradiated Ge-Doped Low-Density Aerogels," Physics of Plasmas (in preparation).

24. J. F. Hansen et al., Rev. Sci. Instrum. **79**, 013504 (2008).

25. P. E. Young et al., Phys. Rev. Lett. **101**, 035001 (2008).

26. J. R. Rygg, J. A. Frenje, C. K. Li, F. H. Séguin, R. D. Petrasso, J. A. Delettrez, V. Yu. Glebov, V. N. Goncharov, D. D. Meyerhofer, S. P. Regan, T. C. Sangster, and C. Stoeckl, Phys. Plasmas **13**, 052702 (2006).

27. D. C. Wilson, G. A. Kyrala, J. F. Benage Jr., F. J. Wysocki, M. A. Gunderson, W. J. Garbett, V. Yu. Glebov, J. Frenje, B. Yaakobi, H. W. Herrman, J. H. Cooley, L. Welser-Sherrill, C. J. Horsfield, and S. A. Roberts, J. Phys., Conf. Ser. **112**, 022015 (2008).

28. J. L. Bourgade et al., Rev. Sci. Instrum. **72**, 1173 (2001).

29. L. Disdier, A. Rouyer, A. Fedotoff, J.-L. Bourgade, F. J. Marshall, V. Yu. Glebov, and C. Stoeckl, Rev. Sci. Instrum. **74**, 1832 (2003).

30. J. L. Bourgade, P. Troussel, A. Casner, G. Huser, T. C. Sangster, G. Pien, F. J. Marshall, J. Fariaud, C. Redmond, D. Gontier, C. Chollet, C. Zuber, C. Reverdin, A. Richard, P. A. Jaanimagi, R. L. Keck, R. E. Bahr, W. J. Armstrong, J. Dewandel, R. Maroni, F. Aubard, B. Angelier, C. Y. Cote, and S. Magnan, Rev. Sci. Instrum. **79**, 10E904 (2008).

31. J. L. Bourgade, V. Allouche, J. Baggio, C. Bayer, F. Bonneau, C. Chollet, S. Darbon, L. Disdier, D. Gontier, M. Houry, H. P. Jacquet, J.-P. Jadaud, J. L. Leray, I. Masclet-Gobin, J. P. Negre, J. Raimbourg, B. Villette, I. Bertron, J. M. Chevalier, J. M. Favier, J. Gazave, J. C. Gomme, F. Malaise, J. P. Seaux, V. Yu. Glebov, P. Jaanimagi, C. Stoeckl, T. C. Sangster, G. Pien, R. A. Lerche, and E. Hodgson, Rev. Sci. Instrum. **75**, 4204 (2004).

32. *LLE Review Quarterly Report* **112**, 203, Laboratory for Laser Energetics, University of Rochester, Rochester, NY, LLE Document No. DOE/SF/19460-790 (2007).

33. R. A. Lerche, D. W. Phillion, and G. L. Tietbohl, Rev. Sci. Instrum. **66**, 933 (1995).

34. L. Disdier, A. Rouyer, I. Lantuéjoul, O. Landoas, J. L. Bourgade, T. C. Sangster, V. Yu. Glebov, and R. A. Lerche, Phys. Plasmas **13**, 056317 (2006).

35. *LLE Review Quarterly Report* **112**, 270, Laboratory for Laser Energetics, University of Rochester, Rochester, NY, LLE Document No. DOE/SF/19460-790 (2007).

36. M. C. Ghilea, T. C. Sangster, D. D. Meyerhofer, R. A. Lerche, and L. Disdier, Rev. Sci. Instrum. **79**, 023501 (2008).)

37. A. Rouyer, Rev. Sci. Instrum. **74**, 1234 (2003).

38. S. Agostinelli, *et al*., Nucl. Instrum. Methods Phys. Res. A **506**, 250 (2003); http://geant4.web.cern.ch/geant4.

39. S. G. Glendinning, P. Amendt, B. D. Kline, R. B. Ehrlich, B. A. Hammel, D. H. Kalantar, O. L. Landen, R. E. Turner, R. J. Wallace, T. J. Weiland, N. Dague, J.-P. Jadaud, D. K. Bradley, G. Pien, and S. Morse, Rev. Sci. Instrum. **70**, 536 (1999).

40. S. M. Pollaine *et al*., Phys. Plasmas **8**, 2357 (2001).

Publications and Conference Presentations

Publications

K. U. Akli, S. B. Hansen, A. J. Kemp, R. R. Freeman, F. N. Beg, D. C. Clark, S. D. Chen, D. Hey, S. P. Hatchett, K. Highbarger, E. Giraldez, J. S. Green, G. Gregori, K. L. Lancaster, T. Ma, A. J. MacKinnon, P. Norreys, N. Patel, J. Pasley, C. Shearer, R. B. Stephens, C. Stoeckl, M. Storm, W. Theobald, L. D. Van Woerkom, R. Weber, and M. H. Key, "Laser Heating of Solid Matter by Light-Pressure-Driven Shocks at Ultrarelativistic Intensities," Phys. Rev. Lett. **100**, 165002 (2008).

B. Ashe, C. Giacofei, G. Myhre, and A. W. Schmid, "Optimizing a Cleaning Process for Multilayer-Dielectric- (MLD) Diffraction Grating," in *Laser-Induced Damage in Optical Materials: 2007*, edited by G. J. Exarhos, A. H. Guenther, K. L. Lewis, D. Ristau, M. J. Soileau, and C. J. Stolz (SPIE, Bellingham, WA, 2007), Vol. 6720, p. 67200N.

B. Ashe, K. L. Marshall, D. Mastrosimone, and C. McAtee, "Minimizing Contamination to Multilayer Dielectric Diffraction Gratings Within a Large Vacuum System," in *Optical System Contamination: Effects, Measurements, and Control 2008*, edited by S. A. Straka (SPIE, Bellingham, WA, 2008), Vol. 7069, Paper 706902.

S.-W. Bahk, "Band-Limited Wavefront Reconstruction with Unity Frequency Response from Shack–Hartmann Slopes Measurements," Opt. Letters **33**, 1321 (2008).

S.-W. Bahk, J. Bromage, I. A. Begishev, C. Mileham, C. Stoeckl, M. Storm, and J. D. Zuegel, "On-Shot Focal-Spot Characterization Technique Using Phase Retrieval," Appl. Opt. **47**, 4589 (2008).

R. Betti, W. Theobald, C. D. Zhou, K. S. Anderson, P. W. McKenty, S. Skupsky, D. Shvarts, V. N. Goncharov, J. A. Delettrez, P. B. Radha, T. C. Sangster, C. Stoeckl, and D. D. Meyerhofer, "Shock Ignition of Thermonuclear Fuel with High Areal Densities," J. Phys., Conf. Ser. **112**, 022024 (2008).

T. R. Boehly, J. E. Miller, D. D. Meyerhofer, J. H. Eggert, P. M. Celliers, D. G. Hicks, and G. W. Collins, "Measurements of the Release of Alpha Quartz: A New Standard for Impedance-Matching Experiments," in *Shock Compression of Condensed Matter–2007*, edited by M. Elert, M. D. Furnish, R. Chau, N. Holmes, and J. Nguyen (American Institute of Physics, Melville, NY, 2007), Vol. 955, pp. 19–22.

A. M. Cok, R. S. Craxton, and P. W. McKenty, "Polar-Drive Designs for Optimizing Neutron Yields on the National Ignition Facility," Phys. Plasmas **15**, 082705 (2008).

A. S. Cross, D. Wang, G. Guarino, S. Wu, A. Mycielski, and R. Sobolewski, "Studies of Coherent Acoustic Phonons in CdMnTe Diluted-Magnetic Single Crystals," J. Phys., Conf. Ser. **92**, 012015 (2007).

J. E. DeGroote, A. E. Marino, J. P. Wilson, A. L. Bishop, and S. D. Jacobs, "The Role of Nanodiamonds in the Polishing Zone During Magnetorheological Finishing (MRF)," in *Optical Manufacturing and Testing VII*, edited by J. H. Burge, O. W. Faehnle, and R. Williamson (SPIE, Bellingham, WA, 2007), Vol. 6671, p. 66710Z.

J. E. DeGroote, A. E. Marino, J. P. Wilson, A. L. Bishop, J. C. Lambropoulos, and S. D. Jacobs, "Removal Rate Model for Magnetorheological Finishing of Glass," Appl. Opt. **46**, 7927 (2007).

C. Dorrer, "Analysis of Pump-Induced Temporal Contrast Degradation in Optical Parametric Chirped-Pulse Amplification," J. Opt. Soc. Am. B **24**, 3048 (2007).

C. Dorrer, "Effect of Jitter on Linear Pulse-Characterization Techniques," Opt. Express **16**, 6567 (2008).

C. Dorrer and J. Bromage, "Impact of High-Frequency Spectral Phase Modulation on the Temporal Profile of Short Optical Pulses," Opt. Express **16**, 3058 (2008).

C. Dorrer, J. Bromage, and J. D. Zuegel, "High-Dynamic-Range Single-Shot Cross-Correlator Based on an Optical Pulse Replicator," Opt. Express **16**, 13,534 (2008).

C. Dorrer and I. Kang, "Linear Self-Referencing Techniques for Short-Optical-Pulse Characterization," J. Opt. Soc. Am. B **25**, A1 (2008) (invited).

T. Duffy, W. T. Shmayda, R. Janezic, S. J. Loucks, and J. Reid, "LLE's High-Pressure DT-Fill-Process Control System," Fusion Sci. Technol. **54**, 379 (2008).

D. H. Edgell, W. Seka, R. E. Bahr, T. R. Boehly, and M. J. Bonino, "Effectiveness of Silicon as a Laser Shinethrough Barrier for 351-nm Light," Phys. Plasmas **15**, 092704 (2008).

M. C. Ghilea, T. C. Sangster, D. D. Meyerhofer, R. A. Lerche, and L. Disdier, "Aperture Tolerances for Neutron-Imaging Systems in Inertial Confinement Fusion," Rev. Sci. Instrum. **79**, 023501 (2008).

V. N. Goncharov, T. C. Sangster, P. B. Radha, R. Betti, T. R. Boehly, T. J. B. Collins, R. S. Craxton, J. A. Delettrez, R. Epstein, V. Yu. Glebov, S. X. Hu, I. V. Igumenshchev, J. P. Knauer, S. J. Loucks, J. A. Marozas, F. J. Marshall, R. L. McCrory, P. W. McKenty, D. D. Meyerhofer, S. P. Regan, W. Seka, S. Skupsky, V. A. Smalyuk, J. M. Soures, C. Stoeckl, D. Shvarts, J. A. Frenje, R. D. Petrasso, C. K. Li, F. Séguin, W. Manheimer, and D. G. Colombant, "Performance of Direct-Drive Cryogenic Targets on OMEGA," Phys. Plasmas **15**, 056310 (2008) (invited).

V. N. Goncharov, T. C. Sangster, P. B. Radha, R. Betti, J. A. Delettrez, R. Epstein, D. R. Harding, S. X. Hu, I. V. Igumenshchev, F. J. Marshall, R. L. McCrory, P. W. McKenty, D. D. Meyerhofer, S. P. Regan, W. Seka, D. Shvarts, S. Skupsky, V. A. Smalyuk, C. Stoeckl, J. A. Frenje, C. K. Li, and R. D. Petrasso, "Modeling High-Compression, Direct-Drive, ICF Experiments," J. Phys., Conf. Ser. **112**, 022002 (2008).

O. V. Gotchev, P. Brijesh, P. M. Nilson, C. Stoeckl, and D. D. Meyerhofer, "A Compact, Multiangle Electron Spectrometer for Ultraintense Laser-Plasma Interaction Experiments," Rev. Sci. Instrum. **79**, 053505 (2008).

O. V. Gotchev, N. W. Jang, J. P. Knauer, M. D. Barbero, R. Betti, C. K. Li, and R. D. Petrasso, "Magneto-Inertial Approach to Direct-Drive Laser Fusion," J. Fusion Energ. **27**, 25 (2008).

J. S. Green, V. M. Ovchinnikov, R. G. Evans, K. U. Akli, H. Azechi, F. N. Beg, C. Bellei, R. R. Freeman, H. Habara, R. Heathcote, M. H. Key, J. A. King, K. L. Lancaster, N. C. Lopes, T. Ma, A. J. MacKinnon, K. Markey, A. McPhee, Z. Najmudin, P. Nilson, R. Onofrei, R. Stephens, K. Takeda, K. A. Tanaka, W. Theobald, T. Tanimoto, J. Waugh, L. Van Woerkom, N. C. Woolsey, M. Zepf, J. R. Davies, and P. A. Norreys, "Effect of Laser Intensity on Fast-Electron-Beam Divergence in Solid-Density Plasmas," Phys. Rev. Lett. **100**, 015003 (2008).

W. Guan, Z. Jiang, and J. R. Marciante, "Specialty Fibers Shine as High-Power, High-Beam-Quality, Fiber Sources," Laser Focus World **43**, 105 (2007).

W. Guan and J. R. Marciante, "Pump-Induced, Dual-Frequency Switching in a Short-Cavity, Ytterbium-Doped Fiber Laser," Opt. Express **15**, 14,979 (2007).

M. J. Guardalben, "Littrow Angle Method to Remove Alignment Errors in Grating Pulse Compressors," Appl. Opt. **47**, 4959 (2008).

D. R. Harding, D. D. Meyerhofer, T. C. Sangster, S. J. Loucks, R. L. McCrory, R. Betti, J. A. Delettrez, D. H. Edgell, L. M. Elasky, R. Epstein, V. Yu. Glebov, V. N. Goncharov, S. X. Hu, I. V. Igumenshchev, D. Jacobs-Perkins, R. J. Janezic, J. P. Knauer, L. D. Lund, J. R. Marciante, F. J. Marshall, D. N. Maywar, P. W. McKenty, P. B. Radha, S. P. Regan, R. G. Roides, W. Seka, W. T. Shmayda, S. Skupsky, V. A. Smalyuk, C. Stoeckl, B. Yaakobi, J. D. Zuegel, D. Shvarts, J. A. Frenje, C. K. Li, R. D. Petrasso, and F. H. Séguin, "Cryogenic Target-Implosion Experiments on OMEGA," J. Phys., Conf. Ser. **112**, 022001 (2008).

S. X. Hu, "Heating of Frozen Rydberg Gases in a Strong Magnetic Field," J. Phys. B: At. Mol. Opt. Phys. **41**, 081009 (2008).

S. X. Hu, V. A. Smalyuk, V. N. Goncharov, J. P. Knauer, P. B. Radha, I. V. Igumenshchev, J. A. Marozas, C. Stoeckl, B. Yaakobi, D. Shvarts, T. C. Sangster, P. W. McKenty, D. D. Meyerhofer, S. Skupsky, and R. L. McCrory, "Studies of Plastic-Ablator Compressibility for Direct-Drive Inertial Confinement Fusion on OMEGA," Phys. Rev. Lett. **100**, 185003 (2008).

S. X. Hu, V. A. Smalyuk, V. N. Goncharov, S. Skupsky, T. C. Sangster, D. D. Meyerhofer, and D. Shvarts, "Validation of Thermal-Transport Modeling with Direct-Drive, Planar-Foil Acceleration Experiments on OMEGA," Phys. Rev. Lett. **101**, 055002 (2008).

I. V. Igumenshchev, "Magnetically Arrested Disks and the Origin of Poynting Jets: A Numerical Study," Astrophys. J. **677**, 317 (2008).

H. Irie, Q. Diduck, M. Margala, R. Sobolewski, and M. J. Feldman, "Nonlinear Characteristics of T-Branch Junctions: Transition from Ballistic to Diffusive Regime," Appl. Phys. Lett. **93**, 053502 (2008).

Z. Jiang and J. R. Marciante, "Impact of Transverse Spatial-Hole Burning on Beam Quality in Large-Mode-Area Yb-Doped Fibers," J. Opt. Soc. Am. B **25**, 247 (2008).

I. Kang, S. Chandrasekhar, L. Buhl, P. G. Bernasconi, X. Liu, C. R. Giles, C. Kazmierski, N. Dupuis, J. Decobert, F. Alexandre, C. Jany, A. Garreau, J. Landreau, M. Rasras, M. Cappuzzo, L. T. Gomez, Y. F. Chen, M. P. Earnshaw, J. Lee, A. Leven, and C. Dorrer, "A Hybrid Electroabsorption Modulator Device for Generation of High Spectral-Efficiency Optical Modulation Formats," Opt. Express **16**, 8480 (2008).

I. Kang, C. Dorrer, L. Zhang, M. Dinu, M. Rasras, L. L. Buhl, S. Cabot, A. Bhardwaj, X. Liu, M. A. Cappuzzo, L. Gomez, A. Wong-Foy, Y. F. Chen, N. K. Dutta, S. S. Patel, D. T. Neilson, C. R. Giles, A. Piccirilli, and J. Jaques, "Characterization of the Dynamical Processes in All-Optical Signal Processing Using Semiconductor Optical Amplifiers," IEEE J. Sel. Top. Quantum Electron. **14**, 758 (2008) (invited).

C. Kim, K. L. Marshall, J. U. Wallace, J. J. Ou, and S. H. Chen, "Novel Cholesteric Glassy Liquid Crystals Comprising Benzene Functionalized with Hybrid Chiral-Nematic Mesogens," Chem. Mater. **20**, 5859 (2008).

C. Kim, J. U. Wallace, S. H. Chen, and P. B. Merkel, "Effects of Dilution, Polarization Ratio, and Energy Transfer on Photoalignment of Liquid Crystals Using Coumarin-Containing Polymer Films," Macromolecules **41**, 3075 (2008).

C. Kim, J. U. Wallace, A. Trajkovska, J. J. Ou, and S. H. Chen, "Quantitative Assessment of Coumarin-Containing Polymer Film's Capability for Photoalignment of Liquid Crystals," Macromolecules **40**, 8924 (2007).

W. Manheimer, D. Colombant, and V. Goncharov, "The Development of a Krook Model for Nonlocal Transport in Laser Produced Plasmas. I. Basic Theory," Phys. Plasmas **15**, 083103 (2008).

K. L. Marshall, Z. Culakova, B. Ashe, C. Giacofei, A. L. Rigatti, T. J. Kessler, A. W. Schmid, J. B. Oliver, and A. Kozlov, "Vapor-Phase–Deposited Organosilane Coatings as 'Hardening' Agents for High-Peak-Power Laser Optics," in *Thin-Film Coatings for Optical Applications IV*, edited by M. J. Ellison (SPIE, Bellingham, WA, 2007), Vol. 6674, p. 667407.

K. L. Marshall, J. Gan, G. Mitchell, S. Papernov, A. L. Rigatti, A. W. Schmid, and S. D. Jacobs, "Laser-Damage-Resistant Photoalignment Layers for High-Peak-Power Liquid Crystal Device Applications," in *Liquid Crystals XII*, edited by I. C. Khoo (SPIE, Bellingham, WA, 2008), Vol. 7050, Paper 70500L.

K. L. Marshall, K. Hasman, M. Leitch, G. Cox, T. Z. Kosc, A. Trajkovska-Petkoska, and S. D. Jacobs, "Doped Multilayer Polymer Cholesteric-Liquid-Crystal (PCLC) Flakes: A Novel Electro-Optical Medium for Highly Reflective Color Flexible Displays," in the *SID 07 Digest*, edited by J. Morreale (Society for Information Display, San Jose, CA, 2007), Vol. XXXVIII, Book II, pp. 1741–1744.

K. L. Marshall, A. Trajkovska-Petkoska, K. Hasman, M. Leitch, G. Cox, T. Z. Kosc, and S. D. Jacobs, "Polymer Cholesteric-Liquid-Crystal (PCLC) Flake/Fluid Host Electro-Optic Suspensions and Their Applications in Color Flexible Reflective Displays," in the *Proceedings of The International Display Manufacturing Conference 2007*, edited by C. H. Chen and Y.-S. Tsai (Society for Information Display, Hsinchu, Taiwan, 2007), pp. 70–73.

K. L. Marshall, R. Wang, M. Coan, A. G. Noto, K. Leskow, R. Pauszek, and A. Moore, "Using Time-Dependent Density Functional Theory (TDDFT) in the Design and Development of Near-IR Dopants for Liquid Crystal Device Applications," in *Liquid Crystals XI*, edited by I. C. Khoo (SPIE, Bellingham, WA, 2007), Vol. 6654, p. 66540F.

D. N. Maywar, J. H. Kelly, L. J. Waxer, S. F. B. Morse, I. A. Begishev, J. Bromage, C. Dorrer, J. L. Edwards, L. Folnsbee, M. J. Guardalben, S. D. Jacobs, R. Jungquist, T. J. Kessler, R. W. Kidder, B. E. Kruschwitz, S. J. Loucks, J. R. Marciante, R. L. McCrory, D. D. Meyerhofer, A. V. Okishev, J. B. Oliver, G. Pien, J. Qiao, J. Puth, A. L. Rigatti, A. W. Schmid, M. J. Shoup III, C. Stoeckl, K. A. Thorp, and J. D. Zuegel, "OMEGA EP High-Energy Petawatt Laser: Progress and Prospects," J. Phys., Conf. Ser. **112**, 032007 (2008).

D. N. Maywar, K. P. Solomon, and G. P. Agrawal, "Remote Optical Control of an Optical Flip-Flop," Opt. Lett. **32**, 3260 (2007).

R. L. McCrory, D. D. Meyerhofer, R. Betti, R. S. Craxton, J. A. Delettrez, D. H. Edgell, V. Yu. Glebov, V. N. Goncharov, D. R. Harding, D. W. Jacobs-Perkins, J. P. Knauer, F. J. Marshall, P. W. McKenty, P. B. Radha, S. P. Regan, T. C. Sangster, W. Seka, R. W. Short, S. Skupsky, V. A. Smalyuk, J. M. Soures, C. Stoeckl, B. Yaakobi, D. Shvarts, J. A. Frenje, C. K. Li, R. D. Petrasso, and F. H. Séguin, "Progress in Direct-Drive Inertial Confinement Fusion Research," Phys. Plasmas **15**, 055503 (2008) (invited).

R. L. McCrory, D. D. Meyerhofer, S. J. Loucks, S. Skupsky, R. Betti, T. R. Boehly, T. J. B. Collins, R. S. Craxton, J. A. Delettrez, D. H. Edgell, R. Epstein, K. A. Fletcher, C. Freeman, J. A. Frenje, V. Yu. Glebov, V. N. Goncharov, D. R. Harding, I. V. Igumenshchev, R. L. Keck, J. D. Kilkenny, J. P. Knauer, C. K. Li, J. Marciante, J. A. Marozas, F. J. Marshall, A. V. Maximov, P. W. McKenty, S. F. B. Morse, J. Myatt, S. Padalino, R. D. Petrasso, P. B. Radha, S. P. Regan, T. C. Sangster, F. H. Séguin, W. Seka, V. A. Smalyuk, J. M. Soures, C. Stoeckl, B. Yaakobi, and J. D. Zuegel, "Progress in Direct-Drive Inertial Confinement Fusion Research at the Laboratory for Laser Energetics," Eur. Phys. J. D **44**, 233 (2007).

C. Miao, K. M. Bristol, A. E. Marino, S. N. Shafrir, J. E. DeGroote, and S. D. Jacobs, "Magnetorheological Fluid Template for Basic Studies of Mechanical-Chemical Effects During Polishing," in *Optical Manufacturing and Testing VII*, edited by J. H. Burge, O. W. Faehnle, and R. Williamson (SPIE, Bellingham, WA, 2007), Vol. 6671, p. 667110.

M. Mikulics, M. Marso, S. Wu, A. Fox, M. Lepsa, D. Grützmacher, R. Sobolewski, and P. Kordoš, "Sensitivity Enhancement of Metal–Semiconductor–Metal Photodetectors on Low-Temperature-Grown GaAs Using Alloyed Contacts," IEEE Photon. Technol. Lett. **20**, 1054 (2008).

J. E. Miller, T. R. Boehly, D. D. Meyerhofer, and J. H. Eggert, "Equation-of-State Measurements in Ta_2O_5 Aerogel," in *Shock Compression of Condensed Matter–2007*, edited by M. Elert, M. D. Furnish, R. Chau, N. Holmes, and J. Nguyen (American Institute of Physics, Melville, NY, 2007), Vol. 955, pp. 71–74.

M. Nakatsutsumi, J. R. Davies, R. Kodama, J. S. Green, K. L. Lancaster, K. U. Akli, F. N. Beg, S. N. Chen, D. Clark, R. R. Freeman, C. D. Gregory, H. Habara, R. Heathcote, D. S. Hey, K. Highbarger, P. Jaanimagi, M. H. Key, K. Krushelnick, T. Ma, A. MacPhee, A. J. MacKinnon, H. Nakamura, R. B. Stephens, M. Storm, M. Tampo, W. Theobald, L. Van Woerkom, R. L. Weber, M. S. Wei, N. C. Woolsey, and P. A. Norreys, "Space

and Time Resolved Measurements of the Heating of Solids to Ten Million Kelvin by a Petawatt Laser," New J. Phys. **10**, 043046 (2008).

P. Nilson, W. Theobald, J. Myatt, C. Stoeckl, M. Storm, O. V. Gotchev, J. D. Zuegel, R. Betti, D. D. Meyerhofer, and T. C. Sangster, "High-Intensity Laser-Plasma Interactions in the Refluxing Limit," Phys. Plasmas **15**, 056308 (2008) (invited).

P. M. Nilson, L. Willingale, M. C. Kaluza, C. Kamperidis, S. Minardi, M. S. Wei, P. Fernandes, M. Notley, S. Bandyopadhyay, M. Sherlock, R. J. Kingham, M. Tatarakis, Z. Najmudin, W. Rozmus, R. G. Evans, M. G. Haines, A. E. Dangor, and K. Krushelnick, "Bidirectional Jet Formation During Driven Magnetic Reconnection in Two-Beam Laser–Plasma Interactions," Phys. Plasmas **15**, 092701 (2008).

A. V. Okishev, C. Dorrer, V. I. Smirnov, L. B. Glebov, and J. D. Zuegel, "ASE Suppression in a Diode-Pumped Nd:YLF Regenerative Amplifier Using a Volume Bragg Grating," in *Frontiers in Optics 2007/Laser Science XXIII/Organic Materials and Devices for Displays and Energy Conversion* (Optical Society of America, Washington, DC, 2007), Paper LTuB4.

A. V. Okishev, V. I. Smirnov, L. B. Glebov, and J. D. Zuegel, "An Optical Differentiator Based on a Regenerative Amplifier with an Intracavity Tunable Volume Bragg Grating Amplifier," in *Advanced Solid-State Photonics on CD-ROM* (Optical Society of America, Washington, DC, 2008), Paper WE32.

O. Okunev, G. Chulkova, I. Milostnaya, A. Antipov, K. Smirnov, D. Morozov, A. Korneev, B. Voronov, G. Gol'tsman, W. Slysz, M. Wegrzecki, J. Bar, P. Grabiec, M. Górska, A. Pearlman, A. Cross, J. Kitaygorsky, and R. Sobolewski, "Registration of Infrared Single Photons by a Two-Channel Receiver Based on Fiber-Coupled Superconducting Single-Photon Detectors," in the *Second International Conference on Advanced Optoelectronics and Lasers*, edited by I. A. Sukhoivanov, V. A. Svich, and Y. S. Shmaliy (SPIE, Bellingham, WA, 2008), Vol. 7009, p. 70090V.

S. Papernov and A. W. Schmid, "Testing Asymmetry in Plasma-Ball Growth Seeded by a Nanoscale Absorbing Defect Embedded in a SiO_2 Thin-Film Matrix Subjected to UV Pulsed-Laser Radiation," J. Appl. Phys. **104**, 063101 (2008).

S. Papernov, A. W. Schmid, J. B. Oliver, and A. L. Rigatti, "Damage Thresholds and Morphology of the Front- and Back-Irradiated SiO_2 Thin Films Containing Gold Nanoparticles

as Artificial Absorbing Defects," in *Laser-Induced Damage in Optical Materials: 2007*, edited by G. J. Exarhos, A. H. Guenther, K. L. Lewis, D. Ristau, M. J. Soileau, and C. J. Stolz (SPIE, Bellingham, WA, 2007), Vol. 6720, p. 67200G.

L. Parlato, G. P. Pepe, D. Pan, C. De Lisio, V. Pagliarulo, A. Cosentino, N. Marrocco, D. Dalena, G. Peluso, A. Barone, and R. Sobolewski, "Time-Resolved Optical Characterization of Proximized Nano-Bilayers for Ultrafast Photodetector Applications," J. Phys., Conf. Ser. **97**, 012317 (2008).

J. Qiao, A. Kalb, T. Nguyen, J. Bunkenburg, D. Canning, and J. H. Kelly, "Demonstration of Large-Aperture Tiled-Grating Compressors for High-Energy, Petawatt-Class, Chirped-Pulse Amplification Systems," Opt. Lett. **33**, 1684 (2008).

M. J. Quinlan, W. T. Shmayda, S. Lim, S. Salnikov, Z. Chambers, E. Pollock, and W. U. Schröder, "Effects of H_2O and H_2O_2 on Thermal Desorption of Tritium from Stainless Steel," Fusion Sci. Technol. **54**, 519 (2008).

S. P. Regan, T. C. Sangster, D. D. Meyerhofer, W. Seka, R. Epstein, S. J. Loucks, R. L. McCrory, C. Stoeckl, V. Yu. Glebov, O. S. Jones, D. Callahan, P. A. Amendt, N. B. Meezan, L. J. Suter, M. D. Rosen, O. L. Landen, E. L. DeWald, S. H. Glenzer, C. Sorce, S. Dixit, R. E. Turner, and B. MacGowan, "Hohlraum Energetics and Implosion Symmetry with Elliptical Phase Plates Using a Multi-Cone Beam Geometry on OMEGA," J. Phys., Conf. Ser. **112**, 022077 (2008).

T. C. Sangster, V. N. Goncharov, P. B. Radha, V. A. Smalyuk, R. Betti, R. S. Craxton, J. A. Delettrez, D. H. Edgell, V. Yu. Glebov, D. R. Harding, D. Jacobs-Perkins, J. P. Knauer, F. J. Marshall, R. L. McCrory, P. W. McKenty, D. D. Meyerhofer, S. P. Regan, W. Seka, R. W. Short, S. Skupsky, J. M. Soures, C. Stoeckl, B. Yaakobi, D. Shvarts, J. A. Frenje, C. K. Li, R. D. Petrasso, and F. H. Séguin, "High-Areal-Density Fuel Assembly in Direct-Drive Cryogenic Implosions," Phys. Rev. Lett. **100**, 185006 (2008).

T. C. Sangster, R. L. McCrory, V. N. Goncharov, D. R. Harding, S. J. Loucks, P. W. McKenty, D. D. Meyerhofer, S. Skupsky, B. Yaakobi, B. J. MacGowan, L. J. Atherton, B. A. Hammel, J. D. Lindl, E. I. Moses, J. L. Porter, M. E. Cuneo, M. K. Matzen, C. W. Barnes, J. C. Fernandez, D. C. Wilson, J. D. Kilkenny, T. P. Bernat, A. Nikroo, B. G. Logan, S. Yu, R. D. Petrasso, J. D. Sethian, and S. Obenschain, "Overview of Inertial Fusion Research in the United States," Nucl. Fusion **47**, S686 (2007).

H. Sawada, S. P. Regan, D. D. Meyerhofer, I. V. Igumenshchev, V. N. Goncharov, T. R. Boehly, R. Epstein, T. C. Sangster, V. A. Smalyuk, B. Yaakobi, G. Gregori, S. H. Glenzer, and O. L. Landen, "Diagnosing Direct-Drive, Shock-Heated, and Compressed Plastic Planar Foils with Noncollective Spectrally Resolved X-Ray Scattering," Phys. Plasmas **14**, 122703 (2007).

W. Seka, D. H. Edgell, J. P. Knauer, J. F. Myatt, A. V. Maximov, R. W. Short, T. C. Sangster, C. Stoeckl, R. E. Bahr, R. S. Craxton, J. A. Delettrez, V. N. Goncharov, I. V. Igumenshchev, and D. Shvarts, "Time-Resolved Absorption in Cryogenic and Room-Temperature Direct-Drive Implosions," Phys. Plasmas **15**, 056312 (2008) (invited).

S. N. Shafrir, J. C. Lambropoulos, and S. D. Jacobs, "MRF Spotting Technique for Studying Subsurface Damage in Deterministic Microground Polycrystalline Alumina," in *Optical Manufacturing and Testing VII*, edited by J. H. Burge, O. W. Faehnle, and R. Williamson (SPIE, Bellingham, WA, 2007), Vol. 6671, p. 66710J.

S. N. Shafrir, J. C. Lambropoulos, and S. D. Jacobs, "Toward Magnetorheological Finishing of Magnetic Materials," J. Manuf. Sci. Eng. **129**, 961 (2007).

D. Shvarts, V. A. Smalyuk, R. Betti, J. A. Delettrez, D. H. Edgell, V. Yu. Glebov, V. N. Goncharov, R. L. McCrory, P. W. McKenty, D. D. Meyerhofer, F. J. Marshall, P. B. Radha, S. P. Regan, T. C. Sangster, W. Seka, S. Skupsky, C. Stoeckl, B. Yaakobi, J. A. Frenje, C. K. Li, R. D. Petrasso, and F. H. Séguin, "The Role of Fast-Electron Preheating in Low-Adiabat Cryogenic Implosions on OMEGA," J. Phys., Conf. Ser. **112**, 022005 (2008).

A. Simon, "An Alternative Analysis of Some Recent Diffusion Experiments on the Large Plasma Device," Phys. Plasmas **15**, 022507 (2008).

A. Simon, "Comment on 'Two-Dimensional Equilibrium of a Low Temperature Magnetized Plasma,' " Plasma Sources Sci. Technol. **17**, 028001 (2008).

A. Simon, "Response to 'Comment on "An Alternative Analysis of Some Recent Diffusion Experiments on the Large Plasma Device" ' [Phys. Plasmas **15**, 074701 (2008)]," Phys. Plasmas **15**, 074702 (2008).

T. P. Simula, N. Nygaard, S. X. Hu, L. A. Collins, B. I. Schneider, and K. Mølmer, "Angular Momentum Exchange

Between Coherent Light and Matter Fields," Phys. Rev. A **77**, 015401 (2008).

V. A. Smalyuk, S. X. Hu, V. N. Goncharov, D. D. Meyerhofer, T. C. Sangster, D. Shvarts, C. Stoeckl, B. Yaakobi, J. A. Frenje, and R. D. Petrasso, "Rayleigh–Taylor Growth Stabilization in Direct-Drive Plastic Targets at Laser Intensities of ~1 × 10^{15} W/cm^2," Phys. Rev. Lett. **101**, 025002 (2008).

V. A. Smalyuk, S. X. Hu, V. N. Goncharov, D. D. Meyerhofer, T. C. Sangster, C. Stoeckl, and B. Yaakobi, "Systematic Study of Rayleigh–Taylor Growth in Directly Driven Plastic Targets in a Laser-Intensity Range of ~2 × 10^{14} to ~1.5 × 10^{15} W/cm^2," Phys. Plasmas **15**, 082703 (2008).

V. A. Smalyuk, D. Shvarts, R. Betti, J. A. Delettrez, D. H. Edgell, V. Yu. Glebov, V. N. Goncharov, R. L. McCrory, D. D. Meyerhofer, P. B. Radha, S. P. Regan, T. C. Sangster, W. Seka, S. Skupsky, C. Stoeckl, B. Yaakobi, J. A. Frenje, C. K. Li, R. D. Petrasso, and F. H. Séguin, "Role of Hot-Electron Preheating in the Compression of Direct-Drive Imploding Targets with Cryogenic D$_2$ Ablators," Phys. Rev. Lett. **100**, 185005 (2008).

A. A. Solodov and R. Betti, "Stopping Power and Range of Energetic Electrons in Dense Plasmas of Fast-Ignition Fusion Targets," Phys. Plasmas **15**, 042707 (2008).

C. Stoeckl, T. R. Boehly, J. A. Delettrez, S. P. Hatchett, J. A. Frenje, V. Yu. Glebov, C. K. Li, J. E. Miller, R. D. Petrasso, F. H. Séguin, V. A. Smalyuk, R. B. Stephens, W. Theobald, B. Yaakobi, and T. C. Sangster, "Hydrodynamics Studies of Direct-Drive Cone-in-Shell, Fast-Ignitor Targets on OMEGA," Phys. Plasmas **14**, 112702 (2007).

W. Theobald, R. Betti, C. Stoeckl, K. S. Anderson, J. A. Delettrez, V. Yu. Glebov, V. N. Goncharov, F. J. Marshall, D. N. Maywar, R. L. McCrory, D. D. Meyerhofer, P. B. Radha, T. C. Sangster, W. Seka, D. Shvarts, V. A. Smalyuk, A. A. Solodov, B. Yaakobi, C. D. Zhou, J. A. Frenje, C. K. Li, F. H. Séguin, R. D. Petrasso, and L. J. Perkins, "Initial Experiments on the Shock-Ignition Inertial Confinement Fusion Concept," Phys. Plasmas **15**, 056306 (2008).

A. Trajkovska, C. Kim, J. U. Wallace, and S. H. Chen, "Photo-alignment of Monodisperse Glassy-Nematic Oligofluorenes," in *Liquid Crystals XI*, edited by I. C. Khoo (SPIE, Bellingham, WA, 2007), Vol. 6654, p. 665409.

A. Trajkovska Petkoska, T. Z. Kosc, K. L. Marshall, K. Hasman, and S. D. Jacobs, "Motion of Doped-Polymer-Cholesteric Liquid Crystal Flakes in a Direct-Current Electric Field," J. Appl. Phys. **103**, 094907 (2008).

J. U. Wallace, R. H. Young, C. W. Tang, and S. H. Chen, "Charge-Retraction Time-of-Flight Measurement for Organic Charge Transport Materials," Appl. Phys. Lett. **91**, 152104 (2007).

M. S. Wei, A. A. Solodov, J. Pasley, R. B. Stephens, D. R. Welch, and F. N. Beg, "Study of Relativistic Electron Beam Production and Transport in High-Intensity Laser Interaction with a Wire Target by Integrated LSP Modeling," Phys. Plasmas **15**, 083101 (2008).

L. Welser-Sherrill, R. C. Mancini, J. A. Koch, N. Izumi, R. Tommasini, S. W. Haan, D. A. Haynes, I. E. Golovkin, J. J. MacFarlane, J. A. Delettrez, F. J. Marshall, S. P. Regan, V. A. Smalyuk, and G. Kyrala, "Spectroscopic Determination of Temperature and Density Spatial Profiles and Mix in Indirect-Drive Implosion Cores," Phys. Rev. E **76**, 056403 (2007).

S. Wu, J. Zhang, A. Belousov, J. Karpinski, and R. Sobolewski, "Dynamics of Intervalley Transitions and Propagation of Coherent Acoustic Phonons in GaN Single Crystals Studied by Femtosecond Pump-Probe Spectroscopy," in *Gallium Nitride Materials and Devices III*, edited by H. Morkoç, C. W. Litton, J.-I. Chyi, Y. Nanishi, and E. Yoon, (SPIE, Bellingham, WA, 2008), Vol. 6894, p. 68940K.

S. Wu, J. Zhang, A. Belousov, J. Karpinski, and R. Sobolewski, "Ultra-Long-Lived Coherent Acoustic Phonons in GaN Single Crystals," J. Phys., Conf. Ser. **92**, 012021 (2007).

B. Yaakobi, T. R. Boehly, T. C. Sangster, D. D. Meyerhofer, B. A. Remington, P. G. Allen, S. M. Pollaine, H. E. Lorenzana, K. T. Lorenz, and J. A. Hawreliak, "Extended X-Ray Absorption Fine Structure Measurements of Quasi-Isentropically Compressed Vanadium Targets on the OMEGA Laser," Phys. Plasmas **15**, 062703 (2008).

OMEGA External Users' Publications

P. Amendt, C. Cerjan, D. E. Hinkel, J. L. Milovich, H.-S. Park, and H. F. Robey, "Rugby-Like Hohlraum Experimental Designs for Demonstrating X-Ray Drive Enhancement," Phys. Plasmas **15**, 012702 (2008).

S. Atzeni, A. Schiavi, J. J. Honrubia, X. Ribeyre, G. Schurtz, Ph. Nicolaï, M. Olazabal-Loumé, C. Bellei, R. G. Evans, and J. R. Davies, "Fast Ignitor Target Studies for the HiPER Project," Phys. Plasmas **15**, 056311 (2008) (invited).

H. Azechi and FIREX Project, "The FIREX Program on the Way to Inertial Fusion Energy," J. Phys., Conf. Ser. **112**, 012002 (2008).

A. Benuzzi-Mounaix, B. Loupias, M. Koenig, A. Ravasio, N. Ozaki, M. Rabec le Gloahec, T. Vinci, Y. Aglitskiy, A. Faenov, T. Pikuz, and T. Boehly, "Density Measurement of Low-*Z* Shocked Material from Monochromatic X-Ray Two-Dimensional Images," Phys. Rev. E **77**, 045402(R) (2008).

D. Besnard, "Fusion with the Megajoule Laser," J. Phys., Conf. Ser. **112**, 012004 (2008).

B. Canaud, F. Garaude, P. Ballereau, J. L. Bourgade, C. Clique, D. Dureau, M. Houry, S. Jaouen, H. Jourdren, N. Lecler, L. Masse, A. Masson, R. Quach, R. Piron, D. Riz, J. Van der Vliet, M. Temporal, J. A. Delettrez, and P. W. McKenty, "High-Gain Direct-Drive Inertial Confinement Fusion for the Laser Mégajoule: Recent Progress," Plasma Phys. Control. Fusion **49**, B601 (2007).

C. Cherfils-Clérouin, M. Bonnefille, E. Dattolo, P. Fremerye, D. Galmiche, P. Gauthier, J. Giorla, S. Laffite, S. Liberatore, P. Loiseau, G. Malinie, L. Masse, F. Poggi, and P. Seytor, "New Designs of LMJ Targets for Early Ignition Experiments," J. Phys., Conf. Ser. **112**, 022023 (2008).

E. L. Dewald, M. Rosen, S. H. Glenzer, L. J. Suter, F. Girard, J. P. Jadaud, J. Schein, C. Constantin, F. Wagon, G. Huser, P. Neumayer, and O. L. Landen, "X-Ray Conversion Efficiency of High-Z Hohlraum Wall Materials for Indirect Drive Ignition," Phys. Plasmas **15**, 072706 (2008).

L. Divol, D. Froula, N. Meezan, R. Berger, R. London, P. Michel, and S. H. Glenzer, "Laser-Plasma Interaction in Ignition Relevant Plasmas: Benchmarking Our 3D Modelling Capabilities Versus Recent Experiments," J. Phys., Conf. Ser. **112**, 022032 (2008).

D. C. Eder, A. E. Koniges, O. L. Landen, N. D. Masters, A. C. Fisher, O. S. Jones, T. I. Suratwala, and L. J. Suter, "Debris and Shrapnel Mitigation Procedure for NIF Experiments," J. Phys., Conf. Ser. **112**, 032023 (2008).

J. Eggert, S. Brygoo, P. Loubeyre, R. S. McWilliams, P. M. Celliers, D. G. Hicks, T. R. Boehly, R. Jeanloz, and G. W. Collins, "Hugoniot Data for Helium in the Ionization Regime," Phys. Rev. Lett. **100**, 124503 (2008).

W. J. Garbett, S. James, G. A. Kyrala, D. C. Wilson, J. Benage, F. J. Wysocki, M. Gunderson, J. Frenje, R. Petrasso, V. Yu. Glebov, and B. Yaakobi, "Constraining Fundamental Plasma Physics Processes Using Doped Capsule Implosions," J. Phys., Conf. Ser. **112**, 022016 (2008).

S. H. Glenzer, P. Neumayer, T. Döppner, O. L. Landen, R. W. Lee, R. J. Wallace, S. Weber, H. J. Lee, A. L. Kritcher, R. Falcone, S. P. Regan, H. Sawada, D. D. Meyerhofer, G. Gregori, C. Fortmann, V. Schwarz, and R. Redmer, "Compton Scattering Measurements from Dense Plasmas," J. Phys., Conf. Ser. **112**, 032071 (2008).

G. P. Grim, P. A. Bradley, R. D. Day, D. D. Clark, V. E. Fatherly, J. P. Finch, F. P. Garcia, S. A. Jaramillo, A. J. Montoya, G. L. Morgan, J. A. Oertel, T. A. Ortiz, J. R. Payton, P. Pazuchanics, D. W. Schmidt, A. C. Valdez, C. H. Wilde, M. D. Wilke, and D. C. Wilson, "Neutron Imaging Development for MegaJoule Scale Inertial Confinement Fusion Experiments," J. Phys., Conf. Ser. **112**, 032078 (2008).

L. Guazzotto, J. P. Freidberg, and R. Betti, "A General Formulation of Magnetohydrodynamic Stability Including Flow and a Resistive Wall," Phys. Plasmas **15**, 072503 (2008).

J. F. Hansen, S. G. Glendinning, R. F. Heeter, and S. J. E. Brockington, "Dynamic *Hohlraums* as X-Ray Sources in High-Energy Density Science," Rev. Sci. Instrum. **79**, 013504 (2008).

H. W. Herrmann, S. E. Caldwell, D. Drew, S. C. Evans, V. Yu. Glebov, C. J. Horsfield, J. M. Mack, G. S. Macrum, E. K. Miller, P. Sanchez, T. Sedillo, C. Stoeckl, D. S. Wilson, and C. S. Young, "Improved Gamma Bang Time Measurements on OMEGA," J. Phys., Conf. Ser. **112**, 032084 (2008).

D. E. Hinkel, D. A. Callahan, A. B. Langdon, S. H. Langer, C. H. Still, and E. A. Williams, "Analyses of Laser-Plasma

Interactions in National Ignition Facility Ignition Targets," Phys. Plasmas **15**, 056314 (2008) (invited).

N. M. Hoffman, D. C. Wilson, M. J. Edwards, D. H. Kalantar, G. A. Kyrala, S. R. Goldman, S. V. Weber, N. Izumi, D. A. Callahan, N. Meezan, N. D. Delamater, I. L. Tregillis, M. J. Schmitt, P. A. Bradley, A. Seifter, O. S. Jones, J. L. Milovich, and C. A. Thomas, "Tuning NIF Drive Symmetry with Symmetry Capsules," J. Phys., Conf. Ser. **112**, 022075 (2008).

I. Kang, S. Chandrasekhar, L. Buhl, P. G. Bernasconi, X. Liu, C. R. Giles, C. Kazmierski, N. Dupuis, J. Decobert, F. Alexandre, C. Jany, A. Garreau, J. Landreau, M. Rasras, M. Cappuzzo, L. T. Gomez, Y. F. Chen, M. P. Earnshaw, J. Lee, A. Leven, and C. Dorrer, "A Hybrid Electroabsorption Modulator Device for Generation of High Spectral-Efficiency Optical Modulation Formats," Opt. Express **16**, 8480 (2008).

I. Kang, C. Dorrer, L. Zhang, M. Dinu, M. Rasras, L. L. Buhl, S. Cabot, A. Bhardwaj, X. Liu, M. A. Cappuzzo, L. Gomez, A. Wong-Foy, Y. F. Chen, N. K. Dutta, S. S. Patel, D. T. Neilson, C. R. Giles, A. Piccirilli, and J. Jaques, "Characterization of the Dynamical Processes in All-Optical Signal Processing Using Semiconductor Optical Amplifiers," IEEE J. Sel. Top. Quantum Electron. **14**, 758 (2008) (invited).

S. Kar, M. Borghesi, P. Audebert, A. Benuzzi-Mounaix, T. Boehly, D. Hicks, M. Koenig, K. Lancaster, S. Lepape, A. Mackinnon, P. Norreys, P. Patel, and L. Romagnani, "Modeling of Laser-Driven Proton Radiography of Dense Matter," High Energy Density Phys. **4**, 26 (2008).

M. H. Key, J. C. Adam, K. U. Akli, M. Borghesi, M. H. Chen, R. G. Evans, R. R. Freeman, H. Habara, S. P. Hatchett, J. M. Hill, A. Heron, J. A. King, R. Kodama, K. L. Lancaster, A. J. MacKinnon, P. Patel, T. Phillips, L. Romagnani, R. A. Snavely, R. Stephens, C. Stoeckl, R. Town, Y. Toyama, B. Zhang, M. Zepf, and P. A. Norreys, "Fast Ignition Relevant Study of the Flux of High Intensity Laser-Generated Electrons Via a Hollow Cone into a Laser-Imploded Plasma," Phys. Plasmas **15**, 022701 (2008).

M. H. Key, K. Akli, F. Beg, R. Betti, D. S. Clark, S. N. Chen, R. R. Freeman, S. Hansen, S. P. Hatchett, D. Hey, J. A. King, A. J. Kemp, B. F. Lasinski, B. Langdon, T. Ma, A. J. MacKinnon, D. Meyerhofer, P. K. Patel, J. Pasley, T. Phillips, R. B. Stephens, C. Stoeckl, M. Foord, M. Tabak, W. Theobald, M. Storm, R. P. J. Town, S. C. Wilks, L. VanWoerkom, M. S. Wei, R. Weber, and B. Zhang, "On Point Designs for High Gain Fast Ignition," J. Phys., Conf. Ser. **112**, 022056 (2008).

J. L. Kline, D. S. Montgomery, H. A. Rose, S. R. Goldman, D. H. Froula, J. S. Ross, R. M. Stevenson, and P. M. Lushnikov, "Mitigation of Stimulated Raman Scattering in Hohlraum Plasmas," J. Phys., Conf. Ser. **112**, 022030 (2008).

J. A. Koch, N. Izumi, L. A. Welser, R. C. Mancini, S. W. Haan, R. W. Lee, P. A. Amendt, T. W. Barbee, Jr., S. Dalhed, K. Fujita, I. E. Golovkin, L. Klein, O. L. Landen, F. J. Marshall, D. D. Meyerhofer, H. Nishimura, Y. Ochi, S. Regan, T. C. Sangster, V. Smalyuk, and R. Tommasini, "Core Temperature and Density Profile Measurements in Inertial Confinement Fusion Implosions," High Energy Density Phys. **4**, 1 (2008).

O. L. Landen, D. K. Bradley, D. G. Braun, V. A. Smalyuk, D. G. Hicks, P. M. Celliers, S. Prisbrey, R. Page, T. R. Boehly, S. W. Haan, D. H. Munro, R. G. Wallace, A. Nikroo, A. Hamza, J. Biener, C. Wild, E. Woerner, R. E. Olson, G. A. Rochau, M. Knudson, D. C. Wilson, H. F. Robey, G. W. Collins, D. Ho, J. Edwards, M. M. Marinak, B. A. Hammel, D. D. Meyerhofer, and B. J. MacGowan, "Experimental Studies of ICF Indirect-Drive Be and High Density C Candidate Ablators," J. Phys., Conf. Ser. **112**, 022004 (2008).

C. K. Li, F. H. Séguin, J. R. Rygg, J. A. Frenje, M. Manuel, R. D. Petrasso, R. Betti, J. Delettrez, J. P. Knauer, F. Marshall, D. D. Meyerhofer, D. Shvarts, V. A. Smalyuk, C. Stoeckl, O. L. Landen, R. P. J. Town, C. A. Back, and J. D. Kilkenny, "Monoenergetic-Proton-Radiography Measurements of Implosion Dynamics in Direct-Drive Inertial-Confinement Fusion," Phys. Rev. Lett. **100**, 225001 (2008).

M. K. Matzen, "Status and Plans of the United States ICF Program," J. Phys., Conf. Ser. **112**, 012001 (2008).

S. C. McDuffee, J. A. Frenje, F. H. Séguin, R. Leiter, M. J. Canavan, D. T. Casey, J. R. Rygg, C. K. Li, and R. D. Petrasso, "An Accelerator Based Fusion-Product Source for Development of Inertial Confinement Fusion Nuclear Diagnostics," Rev. Sci. Instrum. **79**, 043302 (2008).

K. Mima, "Impact of Fast Ignition on Laser Fusion Energy Development," J. Phys., Conf. Ser. **112**, 012005 (2008).

M. Modestov, V. Bychkov, R. Betti, and L.-E. Eriksson, "Bubble Velocity in the Nonlinear Rayleigh–Taylor Instability at a Deflagration Front," Phys. Plasmas **15**, 042703 (2008).

E. I. Moses, "Ignition on the National Ignition Facility," J. Phys., Conf. Ser. **112**, 012003 (2008).

A. N. Mostovych, D. G. Colombant, M. Karasik, J. P. Knauer, A. J. Schmitt, and J. L. Weaver, "Enhanced Direct-Drive Implosions with Thin High-Z Ablation Layers," Phys. Rev. Lett. **100**, 075002 (2008).

T. Nagayama, R. C. Mancini, L. A. Welser-Sherrill, S. Louis, I. E. Golovkin, R. Tommasini, J. A. Koch, N. Izumi, J. Delettrez, S. P. Regan, and V. Smalyuk, "Four-Objective Analysis Including an Optically Thick Line to Extract Electron Temperature and Density Profiles in ICF Implosion Cores," J. Phys., Conf. Ser. **112**, 022014 (2008).

M. Nakatsutsumi, R. Kodama, Y. Aglitskiy, K. U. Akli, D. Batani, S. D. Baton, F. N. Beg, A. Benuzzi-Mounaix, S. N. Chen, D. Clark, J. R. Davies, R. R. Freeman, J. Fuchs, J. S. Green, C. D. Gregory, P. Guillou, H. Habara, R. Heathcote, D. S. Hey, K. Highbarger, P. Jaanimagi, M. H. Key, M. Koenig, K. Krushelnick, K. L. Lancaster, B. Loupias, T. Ma, A. Macphee, A. J. Mackinnon, K. Mima, A. Morace, H. Nakamura, P. A. Norreys, D. Piazza, C. Rousseaux, R. B. Stephans, M. Storm, M. Tampo, W. Theobald, L. V. Woerkom, R. L. Weber, M. S. Wei, and N. C. Woolsey, "Heating of Solid Target in Electron Refluxing Dominated Regime with Ultra-Intense Laser," J. Phys., Conf. Ser. **112**, 022063 (2008).

P. Neumayer, R. L. Berger, D. Callahan, L. Divol, D. H. Froula, R. A. London, B. J. MacGowan, N. B. Meezan, P. A. Michel, J. S. Ross, C. Sorce, K. Widmann, L. J. Suter, and S. H. Glenzer, "Energetics of Multiple-Ion Species Hohlraum Plasmas," Phys. Plasmas **15**, 056307 (2008).

H. Park, B. A. Remington, D. Braun, P. Celliers, G. W. Collins, J. Eggert, E. Giraldez, S. Le Pape, T. Lorenz, B. Maddox, A. Hamza, D. Ho, D. Hicks, P. Patel, S. Pollaine, S. Prisbey, R. Smith, D. Swift, and R. Wallace, "Quasi-Isen-tropic Material Property Studies at Extreme Pressures: From OMEGA to NIF," J. Phys., Conf. Ser. **112**, 042024 (2008).

H.-S. Park, B. R. Maddox, E. Giraldez, S. P. Hatchett, L. T. Hudson, N. Izumi, M. H. Key, S. Le Pape, A. J. MacKinnon, A. G. MacPhee, P. K. Patel, T. W. Phillips, B. A. Remington, J. F. Seely, R. Tommasini, R. Town, J. Workman, and E. Brambrink, "High-Resolution 17–75 keV Backlighters for High Energy Density Experiments," Phys. Plasmas **15**, 072705 (2008).

H. Reimerdes, A. M. Garofalo, M. Okabayashi, E. J. Strait, R. Betti, M. S. Chu, B. Hu, Y. In, G. L. Jackson, R. J. La Haye, M. J. Lanctot, Y. Q. Liu, G. A. Navratil, W. M. Solomon,

H. Takahashi, R. J. Groebner, and the DIII-D team, "Resistive Wall Mode Stabilization in Slowly Rotating High Beta Plasmas," Plasma Phys. Control. Fusion **49**, B349 (2007).

H. F. Robey, D. H. Munro, B. K. Spears, M. M. Marinak, O. S. Jones, M. V. Patel, S. W. Haan, J. D. Salmonson, O. L. Landen, T. R. Boehly, and A. Nikroo, "An Assessment of the 3D Geometric Surrogacy of Shock Timing Diagnostic Techniques for Tuning Experiments on the NIF," J. Phys., Conf. Ser. **112**, 022078 (2008).

J. R. Rygg, J. A. Frenje, C. K. Li, F. H. Séguin, R. D. Petrasso, F. J. Marshall, J. A. Delettrez, J. P. Knauer, D. D. Meyerhofer, and C. Stoeckl, "Observations of the Collapse of Asymmetrically Driven Convergent Shocks," Phys. Plasmas **15**, 034505 (2008).

J. R. Rygg, F. H. Séguin, C. K. Li, J. A. Frenje, M. J.-E. Manuel, R. D. Petrasso, R. Betti, J. A. Delettrez, O. V. Gotchev, J. P. Knauer, D. D. Meyerhofer, F. J. Marshall, C. Stoeckl, and W. Theobald, "Proton Radiography of Inertial Fusion Implosions," Science **319**, 1223 (2008).

T. P. Simula, N. Nygaard, S. X. Hu, L. A. Collins, B. I. Schneider, and K. Mølmer, "Angular Momentum Exchange Between Coherent Light and Matter Fields," Phys. Rev. A **77**, 015401 (2008).

B. Spears, D. Hicks, C. Velsko, M. Stoyer, H. Robey, D. Munro, S. Haan, O. Landen, A. Nikroo, and H. Huang, "Influence and Measurement of Mass Ablation in ICF Implosions," J. Phys., Conf. Ser. **112**, 022003 (2008).

M. Temporal, J. J. Honrubia, and S. Atzeni, "Proton-Beam Driven Fast Ignition of Inertially Confined Fuels: Reduction of the Ignition Energy by the Use of Two Proton Beams with Radially Shaped Profiles," Phys. Plasmas **15**, 052702 (2008).

M. Vandenboomgaerde, S. Liberatore, D. Galmiche, A. Casner, G. Huser, J.-P. Jadaud, and B. Villette, "Planar Hydrodynamic Instability Computations and Experiments with Rugby-Shaped Hohlraums at the OMEGA Laser," J. Phys., Conf. Ser. **112**, 022019 (2008).

L. Welser-Sherrill, J. H. Cooley, D. A. Haynes, D. C. Wilson, M. E. Sherrill, R. C. Mancini, and R. Tommasini, "Application of Fall-Line Mix Models to Understand Degraded Yield," Phys. Plasmas **15**, 072702 (2008).

D. C. Wilson, G. A. Kyrala, J. F. Benage Jr., F. J. Wysocki, M. A. Gunderson, W. J. Garbett, V. Yu. Glebov, J. Frenje, B. Yaakobi, H. W. Herrman, J. H. Cooley, L. Welser-Sherrill, C. J. Horsfield, and S. A. Roberts, "The Effects of Pre-Mix on Burn in ICF Capsules," J. Phys., Conf. Ser. **112**, 022015 (2008).

Conference Presentations

T. C. Sangster, R. Betti, K. S. Anderson, J. A. Delettrez, V. Yu. Glebov, V. N. Goncharov, F. J. Marshall, D. N. Maywar, R. L. McCrory, D. D. Meyerhofer, P. B. Radha, D. Shvarts, V. A. Smalyuk, R. B. Stephens, C. Stoeckl, B. Yaakobi, C. D. Zhou, J. A. Frenje, C. K. Li, F. H. Séguin, and R. D. Petrasso, "Fast-Ignition Research at the Laboratory for Laser Energetics," 1st International Conference on Ultra-Intense Laser Interaction Sciences, Bordeaux, France, 1–5 October 2007.

The following presentations were made at the 6th International Laser Operations Workshop, Bordeaux, France, 9–11 October 2007:

J. L. Edwards, "Accessing Information and Maintaining Configuration Control of the OMEGA EP Laser System."

R. Janezic, L. M. Elasky, D. R. Harding, and S. J. Loucks, "Cryogenic DT Target Operations in the LLE OMEGA Facility."

B. E. Kruschwitz, L. J. Waxer, and J. H. Kelly, "OMEGA EP Activation Status."

S. J. Loucks, "LLE Overviews."

S. F. B. Morse, "Availability and Effectiveness Planning on OMEGA EP."

G. Pien, "Multi-Facility Diagnostic Development."

A. L. Rigatti, "Operational Issues Related to OMEGA and OMEGA EP Optics."

B. Ashe, K. L. Marshall, D. Mastrosimone, and C. McAtee, "Minimizing Contamination to Multilayer Dielectric Diffraction Gratings Within a Large Vacuum System," 54th AVS International Symposium, Seattle, WA, 14–19 October 2007.

J. R. Marciante, W. R. Donaldson, and R. G. Roides, "Enhanced-Dynamic-Range, Single-Shot Measurement of Nanosecond Pulses via Optical Replication," IEEE/LEOS, Lake Buena Vista, FL, 21–25 October 2007.

T. J. Kessler, "Laser Development at the Laboratory for Laser Energetics," 10th Annual Directed Energy Symposium, Huntsville, AL, 5–8 November 2007.

The following presentations were made at the 49th Annual Meeting of the APS Division of Plasma Physics, Orlando, FL, 12–16 November 2007:

K. S. Anderson, R. Betti, I. V. Igumenshchev, P. W. McKenty, P. B. Radha, W. Theobald, C. Stoeckl, and M. M. Marinak, "Direct-Drive Fuel-Assembly Simulations of Fast-Ignition Cone-in-Shell Implosions."

R. Betti and C. D. Zhou, "Measurable Lawson Criterium and Hydro-Equivalent Curves for Inertial Confinement Fusion."

T. R. Boehly, M. A. Barrios, D. E. Fratanduono, T. C. Sangster, D. D. Meyerhofer, P. M. Celliers, D. Munro, G. W. Collins, O. L. Landen, and R. E. Olson, "Development of Shock-Timing Techniques for the National Ignition Facility."

M. Braaten, C. Brown, S. Padalino, V. Glebov, T. C. Sangster, and T. Duffy, "Measuring Positron Annihilation in Na(Tl) Detectors as the Final Stage in a Carbon Diagnostic."

D. T. Casey, J. A. Frenje, S. C. McDuffee, C. K. Li, J. R. Rygg, F. H. Séguin, R. D. Petrasso, V. Yu. Glebov, D. D. Meyerhofer, S. Roberts, and T. C. Sangster, "The CR-39 Coincidence Counting Technique for Enhanced Signal-to-Background in a Large Range of Charged-Particle Measurements on OMEGA and the NIF."

T. J. B. Collins, J. A. Marozas, P. W. McKenty, P. B. Radha, S. Skupsky, and J. D. Zuegel, "Single-Beam Smoothing

Requirements for Wetted-Foam, Direct-Drive NIF Ignition Target Designs."

J. H. Cooley, L. Welser-Sherrill, D. C. Wilson, H. W. Herrmann, J. M. Mack, S. C. Evans, T. J. Sedillo, C. J. Horsfield, D. W. Drew, E. K. Miller, and V. Yu. Glebov, "Evaluation and Modeling of Neutron Reaction Histories Using a Directly Driven Capsule with Two Laser Pulses."

R. S. Craxton, A. M. Cok, and P. W. McKenty, "Initial Polar-Direct-Drive Designs to Optimize Neutron Yields on the NIF."

M. Cummings, K. Donovan, S. Padalino, V. Glebov, and T. C. Sangster, "Elemental Analysis of Carbon Disks Using Proton Induced X-Ray Emission."

J. A. Delettrez, D. Shvarts, P. B. Radha, C. Stoeckl, V. A. Smalyuk, A. V. Maximov, T. C. Sangster, R. D. Petrasso, and J. A. Frenje, "Transport of Energetic Electrons Produced from Two-Plasmon Decay in the 1-D Hydrodynamic Code *LILAC*."

D. H. Edgell, W. Seka, J. A. Delettrez, R. S. Craxton, V. N. Goncharov, I. V. Igumenshchev, J. Myatt, A. V. Maximov, R. W. Short, T. C. Sangster, and R. E. Bahr, "Scattered-Laser-Light Spectroscopy in Direct-Drive Implosion Experiments."

R. Epstein, J. A. Delettrez, V. N. Goncharov, J. P. Knauer, P. W. McKenty, F. J. Marshall, D. Li, P. B. Radha, S. P. Regan, H. Sawada, and B. Yaakobi, "Radiative Transport Modeling Relevant to Cryogenic Implosion Simulation and Diagnosis."

S. H. Fay, C. M. Kuhn, E. E. Smith, S. L. Stephenson, T. C. Sangster, V. Glebov, and S. J. Padalino, "Modeling a Carbon Diagnostic System Using MCNPX."

D. E. Fratanduono, M. A. Barrios, T. R. Boehly, D. D. Meyerhofer, D. G. Hicks, P. M. Celliers, S. Wilks, and J. E. Miller, "Nonequilibrium Conditions in a Shock Front."

J. A. Frenje, D. T. Casey, C. K. Li, J. R. Rygg, F. H. Séguin, R. D. Petrasso, V. Yu. Glebov, D. D. Meyerhofer, and T. C. Sangster, "First Measurements of the Neutron Spectrum Using the Magnetic Recoil Spectrometer (MRS) at OMEGA."

M. Ghilea, D. D. Meyerhofer, T. C. Sangster, D. J. Lonobile, A. Dillenbeck, R. A. Lerche, and L. Disdier, "First Tests on OMEGA of a Bubble Chamber for Neutron Detection."

V. Yu. Glebov, T. C. Sangster, C. Stoeckl, S. Roberts, W. Bittle, J. L. Bourgade, J. L. Leray, and R. A. Lerche, "Neutron-Induced Signal Measurements in Coaxial Cables on OMEGA."

V. N. Goncharov, T. C. Sangster, P. B. Radha, T. R. Boehly, T. J. B. Collins, R. S. Craxton, J. A. Delettrez, R. Epstein, V. Yu. Glebov, S. X. Hu, I. V. Igumenshchev, R. Janezic, S. J. Loucks, J. R. Marciante, J. A. Marozas, F. J. Marshall, D. N. Maywar, J. P. Knauer, P. W. McKenty, S. P. Regan, R. G. Roides, W. Seka, S. Skupsky, V. A. Smalyuk, J. M. Soures, C. Stoeckl, R. Betti, R. L. McCrory, D. D. Meyerhofer, D. Shvarts, J. A. Frenje, R. D. Petrasso, and C. K. Li, "Performance of Direct-Drive Cryogenic Targets on OMEGA" (invited).

O. V. Gotchev, P. Y. Chang, N. W. Jang, J. P. Knauer, D. D. Meyerhofer, R. Betti, C. K. Li, J. A. Frenje, F. H. Séguin, and R. D. Petrasso, "Laser-Driven Magnetic-Flux Compression Experiments on the OMEGA Laser."

D. R. Harding, D. H. Edgell, and L. M. Elasky, "Forming Cryogenic DT Targets for OMEGA."

S. X. Hu, V. A. Smalyuk, V. N. Goncharov, P. B. Radha, J. P. Knauer, T. C. Sangster, D. D. Meyerhofer, I. V. Igumenshchev, J. A. Marozas, and S. Skupsky, "Validation of Thermal Transport Modeling in Direct-Drive Targets Using Planar-Foil Experiments on OMEGA."

I. V. Igumenshchev, V. N. Goncharov, F. J. Marshall, M. J. Bonino, P. W. McKenty, D. D. Meyerhofer, and T. C. Sangster, "The Effect of Target Mounts in Direct-Drive Implosions on OMEGA."

J. P. Knauer, P. B. Radha, V. N. Goncharov, I. V. Igumenshchev, R. Betti, R. Epstein, F. J. Marshall, S. P. Regan, V. A. Smalyuk, D. D. Meyerhofer, and S. Skupsky, "Rayleigh–Taylor Growth and Spherical Compression Measurements of Silicon-Doped Ablators."

G. A. Kyrala, A. Seifter, N. M. Hoffman, D. C. Wilson, S. R. Goldman, N. D. Delamater, V. Glebov, C. Stoeckl, F. Marshall, C. K. Li, and J. Frenje, "Using Beam Pushing and Pointing to Control Indirect Drive Implosion Symmetry."

D. Li, V. N. Goncharov, I. V. Igumenshchev, and S. Skupsky, "Modeling Ion Heat Transport in ICF Targets."

G. Li, C. Ren, R. Yan, V. N. Goncharov, T. L. Wang, W. B. Mori, and J. Tonge, "Laser Channeling in Millimeter-Scale Underdense Plasmas of Fast Ignition."

J. Lundgren, B. Esham, S. J. Padalino, T. C. Sangster, and V. Glebov, "VELoCiRaPTORS."

J. Mack, C. Young, S. Evans, H. Herrmann, M. Moran, R. Malone, and V. Glebov, "NIF Conceptual Design Studies of Bang Time Diagnostics Using d-t Fusion Gamma Rays."

J. A. Marozas, T. J. B. Collins, C. Dorrer, and J. D. Zuegel, "Alternative Laser-Speckle-Smoothing Schemes for the NIF."

F. J. Marshall, J. P. Knauer, T. C. Sangster, J. A. Delettrez, P. W. McKenty, R. Epstein, V. N. Goncharov, and B. Yaakobi, "X-Ray Spectral Measurements of Cryogenic Capsules Imploded by OMEGA."

A. V. Maximov, J. Myatt, R. W. Short, W. Seka, and C. Stoeckl, "Two-Plasmon-Decay Instability Driven by Incoherent Laser Irradiation."

R. L. McCrory, D. D. Meyerhofer, R. Betti, R. S. Craxton, J. A. Delettrez, D. H. Edgell, V. Yu. Glebov, V. N. Goncharov, D. R. Harding, D. W. Jacobs-Perkins, J. P. Knauer, F. J. Marshall, P. W. McKenty, P. B. Radha, S. P. Regan, T. C. Sangster, W. Seka, R. W. Short, S. Skupsky, V. A. Smalyuk, J. M. Soures, C. Stoeckl, B. Yaakobi, D. Shvarts, J. A. Frenje, C. K. Li, R. D. Petrasso, and F. H. Séguin, "Progress in Direct-Drive Inertial Confinement Fusion Research" (review talk).

P. W. McKenty, A. Shvydky, T. J. B. Collins, J. A. Marozas, S. Skupsky, D. Keller, D. D. Meyerhofer, and R. L. McCrory, "Multidimensional Numerical Investigation of NIF Saturn PDD Designs with 3-D Laser Ray Tracing."

D. D. Meyerhofer, J. H. Kelly, S. J. Loucks, R. L. McCrory, S. F. B. Morse, and C. Stoeckl, "OMEGA EP: Status and Use Planning."

J. Myatt, A. V. Maximov, R. W. Short, and D. D. Meyerhofer, "Design of a Positron–Electron Pair-Plasma Production Experiment on OMEGA EP."

P. Nilson, W. Theobald, J. Myatt, C. Stoeckl, C. Mileham, M. Storm, O. V. Gotchev, I. A. Begishev, J. Brown, J. D. Zuegel, R. Betti, D. D. Meyerhofer, and T. C. Sangster, "High-Intensity Laser–Plasma Interactions in the Refluxing Limit" (invited).

S. Padalino, "Plasma Physics Research at an Undergraduate Institution."

E. Pogozelski, B. See, C. Kieffer, W. Becker, S. Padalino, and C. Sangster, "Impact of Cryogenic Temperatures on the Mechanical Properties of *Steatoda Triangulosa* Spider Silk."

P. B. Radha, J. P. Knauer, T. C. Sangster, V. N. Goncharov, I. V. Igumenshchev, R. Betti, R. Epstein, D. D. Meyerhofer, S. P. Regan, V. A. Smalyuk, S. Skupsky, J. A. Frenje, C. K. Li, and R. D. Petrasso, "Using Doped Ablators on OMEGA to Achieve a Low-Adiabat Cryogenic Implosion at High Intensities."

S. P. Regan, T. C. Sangster, D. D. Meyerhofer, W. Seka, B. Yaakobi, R. L. McCrory, C. Stoeckl, V. Yu. Glebov, N. B. Meezan, B. Kruer, L. J. Suter, E. A. Williams, O. S. Jones, D. A. Callahan, M. D. Rosen, O. L. Landen, S. H. Glenzer, C. Sorce, and B. J. MacGowan, "Hohlraum Hot-Electron Production."

T. C. Sangster, V. N. Goncharov, V. A. Smalyuk, R. Betti, D. Shvarts, P. B. Radha, J. A. Delettrez, D. H. Edgell, R. Epstein, V. Yu. Glebov, R. L. McCrory, P. W. McKenty, D. D. Meyerhofer, F. J. Marshall, W. Seka, S. Skupsky, C. Stoeckl, B. Yaakobi, J. A. Frenje, C. K. Li, R. D. Petrasso, and F. H. Séguin, "High-Areal-Density Cryogenic D_2 Implosions on OMEGA."

H. Sawada, S. P. Regan, P. B. Radha, R. Epstein, V. N. Goncharov, D. D. Meyerhofer, V. A. Smalyuk, T. C. Sangster, B. Yaakobi, and R. C. Mancini, "Investigation of Shock Heating and Heat-Front Penetration in Direct-Drive Targets Using Absorption Spectroscopy."

W. Seka, D. H. Edgell, J. P. Knauer, J. Myatt, A. V. Maximov, R. W. Short, T. C. Sangster, R. E. Bahr, R. S. Craxton, J. A. Delettrez, V. N. Goncharov, I. V. Igumenshchev, and D. Shvarts, "Time-Resolved Absorption in Cryogenic and Room-Temperature, Direct-Drive Implosions" (invited).

R. W. Short and J. Myatt, "Kinetic and Fluid Models of the Filamentation Instability of Relativistic Electron Beams for Fast-Ignition Conditions."

A. Shvydky, I. V. Igumenshchev, D. Keller, J. A. Marozas, P. W. McKenty, and S. Skupsky, "Irradiation Uniformity in Direct-Drive Simulations Using 3-D Ray Trace."

S. Skupsky, V. N. Goncharov, and D. Li, "Nonlocal Ion-Heat Transport and Viscosity in ICF Implosions Using a Quasi-Monte Carlo Approach."

V. A. Smalyuk, J. A. Delettrez, V. N. Goncharov, S. X. Hu, D. D. Meyerhofer, S. P. Regan, T. C. Sangster, D. Shvarts, C. Stoeckl,

B. Yaakobi, J. A. Frenje, and R. D. Petrasso, "Effects of Pre-heating on Compression and Rayleigh–Taylor Growth in Planar Plastic Targets on OMEGA."

A. A. Solodov, K. S. Anderson, R. Betti, V. Gotcheva, J. Myatt, J. A. Delettrez, and S. Skupsky, "Integrated Simulation of Fast-Ignition ICF."

C. Stoeckl, W. Theobald, P. A. Jaanimagi, P. Nilson, M. Storm, J. A. Delettrez, R. Epstein, T. C. Sangster, D. Hey, A. J. MacKinnon, H.-S. Park, P. K. Patel, R. Shepherd, J. Green, K. L. Lancaster, and P. A. Norreys, "High-Brightness ~keV Source Development."

M. Storm, D. D. Meyerhofer, C. Mileham, J. Myatt, P. Nilson, T. C. Sangster, C. Stoeckl, and W. Theobald, "High Spatially Resolved Measurements of MeV Electron Beam Transport Through Solids Using Coherent Transition Radiation."

J. Strain, G. Rawcliffe, J. Katz, K. Fletcher, J. Frenje, and S. MacMullin, "Preparation of Deuterated Polymer Targets for the OMEGA Magnetic Recoil Spectrometer."

S. Sublett, J. P. Knauer, D. D. Meyerhofer, and A. Frank, "OMEGA Laser-Driven Hydrodynamic Plasma Jet Experiments with Relevance to Astrophysics."

W. Theobald, R. Betti, C. Stoeckl, K. S. Anderson, J. A. Delettrez, V. Yu. Glebov, V. N. Goncharov, F. J. Marshall, D. N. Maywar, R. L. McCrory, D. D. Meyerhofer, P. B. Radha, T. C. Sangster, D. Shvarts, V. A. Smalyuk, A. A. Solodov, B. Yaakobi, C. D. Zhou, J. A. Frenje, C. K. Li, F. H. Séguin, R. D. Petrasso, and L. J. Perkins, "Initial Experiments of the Shock-Ignition ICF Concept" (invited).

G. T. Young, S. M. Hupcher, C. G. Freeman, M. A. Stoyer, and T. C. Sangster, "Noble Gas Analysis for the OMEGA Gas Sampling System."

C. D. Zhou and R. Betti, "Hydrodynamic Relations for Direct-Drive, Fast-Ignition Inertial Confinement Fusion Implosions."

———

V. Yu. Glebov, T. C. Sangster, C. Stoeckl, S. Roberts, C. Mileham, O. Landoas, L. Disdier, M. Houry, M. Briat, B. Brullot, Ph. Bergonzo, H. Hamrita, and D. Tromson, "Development of Fast CVD Diamond Detectors for Inertial Confinement Fusion Experiments," Materials Research

Society 2007 Fall Meeting, Boston, MA, 26–30 November 2007.

———

J. M. Soures, "Research Plans for OMEGA EP," FPA Annual Symposium, Oak Ridge, TN, 4–5 December 2007.

———

A. V. Okishev, V. I. Smirnov, L. B. Glebov, and J. D. Zuegel, "Optical Differentiator Based on a Regenerative Amplifier with an Intracavity Tunable Volume Bragg Grating Filter," Advanced Solid-State Photonics, Nara, Japan, 27–30 January 2008.

———

T. C. Sangster, "OMEGA EP High-Energy Petawatt Laser: Status and Progress," JOWOG '08, Los Alamos, NM, 4–8 February 2008.

———

W. T. Shmayda, "Fusion-Power and Hydrogen-Economy Community Material Issues," American Ceramic Society Conference, Cocoa Beach, FL, 24–27 February 2008.

———

J. M. Soures and D. D. Meyerhofer, "OMEGA and OMEGA EP Provide Unique Capabilities for NLUF Programs," NNSA–SSAA Symposium, Washington, DC, 26–28 February 2008.

———

A. V. Okishev, "The OMEGA/OMEGA EP Laser System: New Frontiers in ICF and HEDP Research," X Khariton's Topical Scientific Readings, Sarov, Russia, 11–14 March 2008.

———

The following presentations were made at the NIF Diagnostic Workshop, Los Alamos National Laboratory, Los Alamos, NM, 28 March 2008:

V. Yu. Glebov, T. C. Sangster, C. Stoeckl, M. Cruz, S. Roberts, M. Moran, and R. A. Lerche, "A Neutron Bang Time (NBT) Detector for the THD Campaign on the NIF."

V. Yu. Glebov, T. C. Sangster, C. Stoeckl, T. Duffy, M. Cruz, S. Roberts, M. Moran, and R. A. Lerche, L. Dauffy,

R. Tommasini, A. Throop, J. Celeste, Z. A. Ali, and C. J. Horsfield, "The NIF Neutron Time-of-Flight (nTOF) Diagnostic Status and Plans."

———————

The following presentations were made at HEDP/HEDLA–08, St. Louis, MO, 11–15 April 2008:

D. D. Meyerhofer, "HED Physics Opportunities on OMEGA/ OMEGA EP."

S. P. Regan, H. Sawada, D. D. Meyerhofer, P. B. Radha, J. A. Delettrez, R. Epstein, V. N. Goncharov, D. Li, V. A. Smalyuk, T. C. Sangster, B. Yaakobi, and R. C. Mancini, "Creating and Probing Matter Compressed and Heated by Shock Waves on OMEGA."

———————

J. P. Knauer, S. Sublett, R. S. Craxton, T. J. B. Collins, I. V. Igumenshchev, D. D. Meyerhofer, A. Frank, and R. P. Drake, "Hydrodynamic Jet Experiments at LLE," APS April Meeting 2008, St. Louis, MO, 12–15 April 2008.

———————

C. Miao, S. N. Shafrir, S. Adar, H. Romanofsky, and S. D. Jacobs, "*In-Situ* Drag Force and Normal Force Measurement for Magnetorheological Finishing (MRF) of Hard Ceramics," 16th Symposium on Materials Research, Rochester, NY, 22 April 2008.

———————

S. N. Shafrir, S. D. Jacobs, S. Adar, C. Miao, H. Romanofsky, and J. C. Lambropoulos, "Drag Force and Surface Texture in Material Removal with MRF on Optical Glass and Hard Ceramics," 12th Department of Defense Electromagnetic Windows Symposium, Redstone Arsenal, AL, 28 April–1 May 2008.

———————

The following presentations were made at CLEO 2008, San Jose, CA, 6–8 May 2008:

S.-W. Bahk, J. Bromage, J. D. Zuegel, and J. R. Fienup, "Application of Phase Retrieval for Predicting a High-Intensity-Focused Laser Field."

C. Dorrer, "Effect of Jitter on Linear Self-Referencing Pulse-Characterization Techniques."

C. Dorrer, I. A. Begishev, A. V. Okishev, and J. D. Zuegel, "Extreme-Contrast Front End for High-Power Laser Systems."

C. Dorrer, J. Bromage, and J. D. Zuegel, "High-Dynamic-Range, Single-Shot Cross-Correlator Using a Pulse Replicator."

C. Dorrer, A. V. Okishev, I. A. Begishev, J. D. Zuegel, V. I. Smirnov, and L. B. Glebov, "Optical Parametric Chirped-Pulse–Amplification Contrast Enhancement by Regenerative Pump Spectral Filtering."

W. Guan and J. R. Marciante, "Suppression of Self-Pulsations in Dual-Clad Ytterbium-Doped Fiber Lasers."

A. V. Okishev, "Multimillijoule Picosecond Regenerative Differentiator-Amplifier."

J. Qiao, A. Kalb, J. H. Kelly, D. Canning, T. Nguyen, and J. Bunkenburg, "Realization of Tiled-Grating Compressors for the OMEGA EP Petawatt Laser System."

L. J. Waxer, M. J. Guardalben, J. H. Kelly, B. E. Kruschwitz, J. Qiao, I. A. Begishev, J. Bromage, C. Dorrer, J. L. Edwards, L. Folnsbee, S. D. Jacobs, R. Jungquist, T. J. Kessler, R. W. Kidder, S. J. Loucks, J. R. Marciante, D. N. Maywar, R. L. McCrory, D. D. Meyerhofer, S. F. B. Morse, A. V. Okishev, J. B. Oliver, G. Pien, J. Puth, and A. L. Rigatti, "The OMEGA EP High-Energy, Short-Pulse Laser System" (invited).

———————

The following presentations were made at the 17th Topical Conference on High-Temperature Plasma Diagnostics, Albuquerque, NM, 11–15 May 2008:

Z. A. Ali, V. Yu. Glebov, M. Cruz, T. Duffy, C. Stoeckl, S. Roberts, T. C. Sangster, R. Tommasini, and S. Throop, "Tests and Calibration of the NIF Neutron Time-of-Flight Diagnostic."

C. G. Freeman, C. Stoeckl, T. C. Sangster, T. Duffy, and C. Mileham, "A Thomson Parabola for the Multiterawatt Laser Facility."

V. Yu. Glebov, M. Moran, C. Stoeckl, T. C. Sangster, and M. Cruz, "Neutron Bang Time Detector Based on a Light Pipe."

M. Storm, C. Guo, D. D. Meyerhofer, J. Myatt, T. C. Sangster, and C. Stoeckl, "Relativistic Electron-Beam Transport Measurements" (invited).

The following presentations were made at the 18th Target Fabrication Meeting, Lake Tahoe, CA, 11–15 May 2008:

M. J. Bonino, D. R. Harding, and L. M. Elasky, "Effects of Target Assembly on the Quality of Cryogenic Ice Layers."

D. H. Edgell, M. D. Wittman, R. S. Craxton, L. M. Elasky, D. R. Harding, and W. Seka, "Three-Dimensional Characterization of Cryogenic Targets Using X-Ray Phase-Contrast Imaging and Shadowgraphy."

L. M. Elasky, S. J. Verbridge, A. J. Weaver, and D. R. Harding, "Success of Layering with DT and Developments with D_2 in OMEGA Cryogenic Targets."

D. R. Harding, T. B. Jones, Z. Bei, D. H. Edgell, and S. H. Chen, "Cryogenic-DT-Foam Targets: The New Frontier."

T. B. Jones, Z. Bei, and D. R. Harding, "Electric-Field-Assisted Target Fabrication."

S. J. Verbridge, A. J. Weaver, D. R. Harding, and L. M. Elasky, "Effects of Process Limitations and Shell Composition on Cryogenic Target Layers."

G. P. Wainwright and W. T. Shmayda, "Tritium Management on OMEGA at the Laboratory for Laser Energetics."

M. D. Wittman and D. R. Harding, "Performance and Capabilities of the Cryogenic Fill-Tube Target Test Facility at LLE."

The following presentations were made at the 38th Annual Anomalous Absorption Conference, Williamsburg, VA, 1–6 June 2008:

R. S. Craxton, P. W. McKenty, J. A. Marozas, and A. M. Cok, "Optimization of Neutron Yields on the NIF from Room-Temperature DT Targets."

J. A. Delettrez, V. N. Goncharov, P. B. Radha, D. Shvarts, C. Stoeckl, B. Yaakobi, A. V. Maximov, W. Seka, J. A. Frenje, J. F. Myatt, T. C. Sangster, and V. A. Smalyuk, "Simulations of

the Effect of Energetic Electrons Produced from Two-Plasmon Decay in the 1-D Hydrodynamic Code *LILAC*."

D. H. Edgell, W. Seka, J. A. Delettrez, R. S. Craxton, V. N. Goncharov, I. V. Igumenshchev, J. F. Myatt, A. V. Maximov, R. W. Short, T. C. Sangster, and R. E. Bahr, "Time-Dependent Scattered-Laser-Light Spectroscopy in Direct-Drive Inertial Confinement Fusion Experiments."

R. Epstein, J. A. Delettrez, V. N. Goncharov, P. W. McKenty, F. J. Marshall, P. B. Radha, H. Sawada, and B. Yaakobi, "Radiative-Transport Modeling Relevant to Cryogenic Implosion Simulation and Diagnosis."

A. V. Maximov, J. F. Myatt, R. W. Short, W. Seka, C. Stoeckl, and J. A. Delettrez, "Modeling of Two-Plasmon-Decay Instability Driven by Crossing Laser Beams."

J. Myatt, D. H. Edgell, W. Seka, A. V. Maximov, and R. W. Short, "Two-Plasmon-Decay Hot-Electron Distribution from Anistropic Thick-Target Bremsstrahlung Measurements."

T. C. Sangster, J. H. Kelly, S. J. Loucks, D. D. Meyerhofer, S. F. B. Morse, R. L. McCrory, and C. Stoeckl, "Status of the OMEGA EP Laser System."

W. Seka, D. H. Edgell, J. F. Myatt, A. V. Maximov, R. W. Short, C. Stoeckl, R. E. Bahr, R. S. Craxton, J. A. Delettrez, and V. N. Goncharov, "Two-Plasmon-Decay Instability in Direct-Drive Implosion Experiments."

R. W. Short, "Two-Plasmon Decay of Multiple Obliquely Incident Laser Beams in Direct-Drive Geometry."

A. A. Solodov, K. S. Anderson, R. Betti, V. Gotcheva, J. F. Myatt, J. A. Delettrez, and S. Skupsky, "Integrated Simulations of Hot-Electron Transport and Ignition for Direct-Drive, Fast-Ignition Fusion Targets."

C. Stoeckl, K. S. Anderson, R. Betti, T. R. Boehly, J. A. Delettrez, J. A. Frenje, V. N. Goncharov, V. Yu. Glebov, J. H. Kelly, A. J. Mackinnon, R. L. McCrory, D. D. Meyerhofer, S. F. B. Morse, J. F. Myatt, P. A. Norreys, P. M. Nilson, R. D. Petrasso, T. C. Sangster, A. A. Solodov, R. B. Stephens, M. Storm, W. Theobald, L. J. Waxer, B. Yaakobi, and C. D. Zhou, "Fast-Ignition Target Design and Experimental-Concept Validation on OMEGA," 10th International Workshop on

Fast Ignition of Fusion Targets, Crete, Greece, 12–18 June 2008 (invited).

———————

O. V. Gotchev, P. Chang, J. P. Knauer, D. D. Meyerhofer, R. Betti, F. H. Séguin, C. K. Li, J. A. Frenje, and R. D. Petrasso, "Magnetized Hot-Spot Implosions on OMEGA," ICC 2008 Workshop, Reno, NV, 24–27 June 2008.

———————

T. Pfuntner and S. D. Jacobs, "The Optics Suitcase and Liquid Crystal Mood Patches," Boulder Workshop on Light-Controlled Liquid Crystalline Complex Adaptive Materials, Boulder, CO, 6 August 2008.

———————

The following presentations were made at SPIE Optics and Photonics, San Diego, CA, 10–14 August 2008:

B. Ashe, G. Myhre, D. Mastrosimone, and C. McAtee, "Minimizing Contamination to Multilayer Dielectric Diffraction Gratings Within a Large Vacuum System."

K. L. Marshall, J. Gan, G. Mitchell, S. Papernov, A. L. Rigatti, A. W. Schmid, and S. D. Jacobs, "Laser-Damage Resistant Photoalignment Layers for High-Peak-Power Liquid Crystal Device Applications."

———————

The following presentations were made at the HEDLP FESAC Workshop, Washington, DC, 25–27 August 2008:

W. Theobald, R. Betti, C. Stoeckl, K. S. Anderson, T. R. Boehly, J. A. Delettrez, J. A. Frenje, V. N. Goncharov, V. Yu. Glebov, C. K. Li, R. L. McCrory, D. D. Meyerhofer, L. J. Perkins, R. D. Petrasso, P. B. Radha, T. C. Sangster, W. Seka, A. A. Solodov, B. Yaakobi, and C. D. Zhou, "Driving Gigabar Shocks with High-Power Lasers and Their Applications to Shock Ignition."

W. Theobald, C. Stoeckl, R. Betti, K. S. Anderson, T. R. Boehly, J. A. Delettrez, R. R. Freeman, J. A. Frenje, V. N. Goncharov, V. Yu. Glebov, D. R. Harding, M. H. Key, A. J. MacKinnon, R. L. McCrory, D. D. Meyerhofer, J. F. Myatt, P. M. Nilson, A. V. Okishev, P. K. Patel, R. D. Petrasso, C. Ren, T. C. Sangster, W. Seka, R. B. Stephens, A. A. Solodov, L. Van Woerkom, B. Yaakobi, and C. D. Zhou, "Fast Ignition with OMEGA/OMEGA EP."

———————

The following presentations were made at the Boulder Damage Symposium, Boulder, CO, 22–24 September 2008:

J. B. Oliver, S. Papernov, A. W. Schmid, and J. C. Lambropoulos, "Optimization of Laser-Damage Resistance of Evaporated Hafnia at 351 nm."

S. Papernov and A. W. Schmid, "Laser-Induced Surface Damage of Optical Materials: Absorption Sources, Initiation, Growth, and Mitigation."

———————

The following presentations were made at the 18th Topical Meeting on the Technology of Fusion, San Francisco, CA, 28 September–2 October 2008:

R. Betti, P. W. McKenty, W. Theobald, C. D. Zhou, C. Stoeckl, K. S. Anderson, J. A. Delettrez, D. D. Meyerhofer, V. N. Goncharov, P. B. Radha, T. C. Sangster, A. A. Solodov, V. A. Smalyuk, S. Skupsky, C. K. Li, R. D. Petrasso, J. A. Frenje, L. J. Perkins, D. Shvarts, and A. Schmitt, "Shock Ignition of Thermonuclear Fuel with High Areal Density."

S. F. B. Morse, J. Bromage, C. Dorrer, M. J. Guardalben, J. H. Kelly, B. E. Kruschwitz, S. J. Loucks, R. L. McCrory, D. D. Meyerhofer, J. Qiao, and L. J. Waxer, "OMEGA Extended Performance Short-Pulse Laser: Technology and Operational Flexibility."

J. M. Soures, "The OMEGA Facility: Providing Unique Capabilities for Inertial Fusion and High-Energy-Density Physics Experiments."